NUMERICAL MODELLING OF STABLE MINIMAL SURFACES

Peter David Gosling, B.Eng., MSc.(Eng.), D.I.C..

A Thesis submitted for the Higher Degree of Doctor of Philosophy
in Engineering at the University of Warwick, September 1992.

In loving memory of my Father,
Edward William Gosling,
July 16th 1939 - 6th August 1973.

Contents

List of Tables

List of Figures

List of Plates

Acknowledgements

Firstly, I should like to express my gratitude to Dr. W.J. Lewis, for her assiduous supervision, and for our many lengthy and fruitful discussions. In recognition of his technical support, I should like to mention Mr. A.J. Hulme, whose efforts to maintain and improve the computing facilities have been invaluable.

The Science and Engineering Research Council and the Department of Engineering (SERC), University of Warwick, have both financed this research. For this support, I am also extremely grateful. In addition, I very much appreciate the funding by the SERC and the Fellowship of Engineering, of two research visits to the Institute of Lightweight Structures (IL), University of Stuttgart, Germany. Attendance at the NATO/DFG Advanced Study Institute, Berchtesgaden, Germany, was facilitated by the generous scholarship awarded by NATO.

I should like to thank Dr.-Ing. Siegfried Gass for his interest in my work, and for the many hours spent generating minimal surfaces at the Institute of Lightweight Structures (IL). At the same time, I acknowledge too my debt to Dr.-Ing. Maria Haase (Institute of Statics and Dynamics, University of Stuttgart, Germany), for her assistance in aspects of the mathematical treatise presented in this thesis. For his comradeship during my second visit to Stuttgart, I would like to express my thanks also to Dr. Sergei Federov.

Finally, on a more personal note, I express my heartfelt thanks to my future wife, Clare, for her uninterrupted support, friendship, and encouragement, without which this thesis would not have been written. I should also like to express my sincere gratitude to my family, for their support and tolerance during my years of study.

Synopsis

This thesis examines the numerical representation of stable minimal surfaces. In particular, the work presented concentrates on the formulation of a finite element, suitable for the analysis of systems subjected to large strains and large displacements.

In order to obtain an understanding of the physical properties of a minimal surface, and to verify the proposed numerical solution algorithms, the surfaces developed by several soap-film models are given. The mechanisms involved in the formation of a soap-film (minimal) surface is summarised. Several types of minimal surfaces are investigated, including general surfaces between rigid boundaries, single minimal surfaces between two frames, and those with internal and external flexible boundaries. In addition, the question of the stability of minimal surfaces is discussed, in terms of a finite and an infinitesimal perturbation.

The numerical modelling of minimal surfaces is presented, based initially on the discretisation of the form using plane linear (line) and triangular elements. The application of the matrix-based element formulations to the vector-based Dynamic Relaxation solution algorithm is described. The formulations of the elements are assessed in the context of large strains and large displacements. Subsequently, the effects of the violations of the assumptions inherent in the derivation of the element stiffness matrices on the accuracy of the numerical solution are demonstrated, and measures proposed to maintain the stability of the solution algorithm. The numerical solutions to several minimal surfaces are provided, based on the linear and triangular element discretisations respectively.

An intended improvement on the plane linear and triangular element formulations is proposed by the derivation of a higher order finite element. A 24 degrees-of-freedom finite element is formulated, representing a general curved elastic (or inelastic) geometrically non-linear continuum, and modelling the condition of plane stress. The element equations are derived with special consideration of the simulation of the effects of large strains and large displacements. An appraisal of the quality of the element formulation is made through the application of the Patch test and the Eigenvalue test. The solutions to several minimal surfaces are presented, from which the effects of the assumptions in the element formulation on the accuracy of the proposed numerical solution algorithm are demonstrated.

Chapter 1

Introduction

"I do not suppose that there is anyone in this room
who has not occasionally blown a common soap-bubble,
and while admiring the perfection of its form,
and the marvellous brilliancy of its colours, wondered
how it is that such a magnificent object can be so
easily produced." [1]

Aside from its aesthetic quality, the soap-bubble represents the primordial pneumatic structural membrane. Stable minimal surfaces are developed (where possible) by a soap-film when the pressure is equal on each side of the surface. A minimal surface is characterised by equal and opposite principal curvatures (at a point) and by minima in the potential energy and surface area for the given boundary conditions (Section 3.2, Chapter 3). The form of the surface complies with the principle of virtual work, and is generated by equal stresses (tensile) in all directions. Being created in nature, the minimal surface membrane represents an optimal structural system and can be used to simulate the forms of surface stressed structures such as tents, air-houses (pneumatics), thin shells, and mechanical devices such as sails and balloons. As Boys pointed out [1], and Otto and his co-workers demonstrated through the work of the Institute of Lightweight Structures (University of Stuttgart, Germany), several graceful minimal surfaces can be easily produced using soap-films.

The mathematical classification and definition of minimal surfaces was attempted in the late 18th and early 19th centuries, by the French geometer Meusnier, and by Young, amongst others (Section 3.2, Chapter 3). In the late 19th, Boys [1] presented a series of three lectures entitled "SOAP-BUBBLES and the forces which mould them". The lectures comprised the demonstration of several practical experiments to illustrate the phenomenon of surface tension, and the

---

1

Acknowledgement to the text, *SOAP-BUBBLES and the forces which mould them.*, by C.V. Boys, The Science Study Series, Heinemann, Number 3, page 19.

influences of electricity, wax, and other products on the formation of minimal surfaces.

The properties of surface tension were exploited by Otto in the 1950's - 1970's to generate optimised surface forms, the measurements of which were used to develop the shapes of the structural membranes forming, for example, the Munich Olympic Stadium. The generation of the surface geometry was termed "form-finding". More precisely, form-finding may be defined as that method by which the prestressed equilibrium form is developed. The objective of the form-finding procedure is to create a model of the intended surface, from which the geometric properties can be established (in the form of a cutting pattern) and the response of the structural system to externally applied forces and stresses can be assessed.

In parallel with the work of Otto, Trostel published the closed form solution to the catenoid, and addressed the question of stable and unstable minimal surfaces (Section 3.6.2.2, Chapter 3). In an attempt to add a firmer mathematical basis to the understanding of the formation of minimal surfaces in nature, investigations were carried out into the physical properties of the soap-film, and the generation of the elasticity of the fluid (Section 3.3, Chapter 3). However, the progress of such efforts was contained by the necessary simplifying assumptions made in these purely mathematical techniques.

Little previous work has been published on the numerical representation (or form-finding) of minimal surfaces. Papers by Ishii and Suzuki, and by Suzuki and Hangai, produced solutions based on the assumption of zero mean curvature, and on a finite element discretisation of the surface using plane triangular elements, respectively. These numerical solution algorithms produced both stable and unstable minimal surfaces (Section 2.1, Chapter 2). However, the unstable minimal surface cannot be reproduced by a soap-film model (or a structural membrane).

A membrane is a geometrically non-linear system. The term "geometrically non-linear" is used to denote that changes in the geometry of the surface (which occur during its deformation, due to both internal (form-finding) and external (static analysis) forces), must be taken into account when defining the equilibrium state. Consequently, an iterative type of solution procedure is required, which recognises changes in the directions and magnitudes (where appropriate) of the internal and external forces acting on the system, and the changes in the stiffnesses of the surface, arising from a change in shape. With the repeated application of the solution algorithm, the displacements are reduced and the system becomes geometrically linear as the true equilibrium configuration is approached.

Various algorithms have been proposed to represent numerically the response of geometrically non-linear systems (Section 2.2, Chapter 2). Attention was directed initially towards beams, frames, cable networks, and other skeletal type systems. The geometrically non-linear analysis of membranes and shells was complicated further by the need to represent a continuum. Green and Adkin presented a significant work on the theory of plane stress for finite deformations, and the

membrane theory for thin shells. However, the application of the theory was restricted to axi-symmetric problems. Further solutions were developed from the Karman equations for the large deflections of plates, and from the Foeppl equations for laterally loaded membranes. However, the generality of the solutions were restricted by the adoption of an assumed final configuration for the membrane, or flat regular geometries, for example (Section 2.3, Chapter 3).

From the restrictions of these essentially "closed-form" solution approaches, the need to discretise a complex system into a number of pre-defined components was realised. Such components were termed finite elements, and the method of solution (which was based on the discretisation of a system by finite elements) was termed the Finite Element method.

Unfortunately, subsequent to its inception, the terminology associated with the Finite Element method has become somewhat vague. Here, the Finite Element method is taken to be the solution algorithm which initially involves the discretisation of the system by a number of finite elements. A global stiffness matrix is then compiled, representing the total coupled response of the system. After applying the boundary conditions, the reduced stiffness matrix is inverted. The resulting flexibility matrix is then used to calculate the element nodal displacements. In the case of a geometrically non-linear system, this procedure is repeated until the condition of equilibrium is satisfied.

Oden and Sato presented in 1967 the first application of the Finite Element method to the analysis of membranes exhibiting finite strains (Section 2.3, Chapter 3). The success of the proposed approach was limited however, by the effects of ill-conditioning. Other finite element approaches were developed, including those by, for example, Haug and Powell, and by Argyris, which aimed to improve the performance of the overall algorithm, by the careful formulation of the finite element.

Emphasis was placed on the "strain free" rigid body rotation of the element. This term refers to the requirement that as the element moves in space without a change in shape (rigid body), the finite element formulation should indicate zero straining. However, the strains of an element are not obtained directly. The element flexibilities are combined with the out-of-balance forces at the element nodes, to evaluate the nodal displacements. These properties are then used, with the geometric properties of the element, to yield the element strains. The flexibility of the element is the inverse of its stiffness. Consequently, the adequate representation of the element rigid body rotations is a function of the element stiffness terms. The introduction of fictitious stiffnesses into the element formulation lead, indirectly, to erroneous (or imaginary) strains which are alleged to be induced in the element as it undergoes a rigid body rotation. Therefore, the term "strain free" is avoided (where possible) in this thesis, and replaced by "adequate representation".

The continued development of the Finite Element method led to formulations involving large strains and large displacements. However, with an increase in the complexity of the formulations,

the sensitivities of the numerical model to large displacements (associated with geometrically non-linear systems) rendered difficult the convergence of the system to the condition of equilibrium. The finite difference approach to the solution of the non-linear governing partial differential equations (describing the deflection response of a membrane) was investigated. The algorithm developed by Kao and Perrone (Section 2.3, Chapter 2) was shown to be both efficient and relatively insensitive to the assumed starting configuration in the case of the analysis of an axi-symmetric circular membrane. However, the need to express the form of the surface in terms of partial differential equations limited its application to simple regular membranes.

In 1965 Day presented the Dynamic Relaxation algorithm (Section 2.4, Chapter 2), and applied it to the analytical investigation of complex concrete pressure vessels. The method was founded on the D' Alembert principle of a body in motion, and rewritten using a finite difference scheme (Section 4.2, Chapter 4). As the analysis of the system was based on the imposition of a pseudo oscillation, the approximations of the finite difference formulation failed to compromise the accuracy of the solution. The representation of the discrete or continuous system could be provided either by using a further finite difference approximation to the characteristic partial differential equations, or by a discretisation of finite elements. The simplicity of the algorithm, its efficiency and flexibility, have been heralded as the main advantages of the approach. Though the system may be represented by a discretisation of finite elements, the solutions presented in this thesis are not obtained from the Finite Element Method.

This thesis presents work in the realm of the numerical modelling of stable minimal surfaces. The specific objective of the work is the adequate formulation of an element which is suited to the discretisation of a continuous system, whilst representing a state of plane stress, and being capable of modelling the effects of large displacements and large strains. Though having a direct application to structural membranes, the aspects of cutting patterns and static analysis are not discussed. The emphasis of the work is focused, instead, on the rigorous derivation of a doubly curved quadratic quadrilateral membrane finite element, for use in conjunction with the Dynamic Relaxation Algorithm.

A critical appraisal is made of the linear and triangular element formulations used most often in the analysis of structural membranes (Section 4.3 and Section 4.4, Chapter 4, respectively). The assumptions which are inherent in the derivation of the element matrices are highlighted, and the adaptation of these matrix-based formulations to the vector approach of the Dynamic Relaxation algorithm is described. Certain phenomena related to the inadequacy of the linear and triangular element formulations to model large strains and large displacements are demonstrated, and measures recommended to prevent their development (Section 4.3.2.2, Chapter 4). The effectiveness of the proposed techniques is illustrated by the numerical solutions to several minimal surfaces, culminating in the solution to a complex form denoted as "Siegfried's Tent"

(Section 4.5.4, Chapter 4).

The derivation of a higher order finite element is intended as an improvement on the linear and triangular element formulations. The general element equations, as they relate to the Finite Element method are presented, and the assumptions made, are assessed within the context of the analysis of inelastic continua (Section 5.2, Chapter 5). With reference to the outline formulation given by Irons and Ahmad, the proposed element is described (Section 5.3.1, Chapter 5), while two alternative formulations of the element shape functions are given, based on small and large displacement theory respectively (Section 5.3.2, Chapter 5).

A rigorous mathematical derivation of the expressions describing the strains within a general curved surface is offered, with a subsequent demonstration of the order of the strain-displacement terms necessary to represent adequately the deformation of the surface (Section 5.6, Chapter 5). From this mathematical treatise, expressions for the element matrices are established (Section 5.7, Chapter 5) with an assessment made of the order of quadrature required to evaluate the element integrands. The formulation is concluded by the presentation of the theory to model adequately the rigid body rotations in the element geometric stiffness matrix (Section 5.9, Chapter 5).

The quality of the proposed element formulation is assessed on a local level by the application of the Patch test and the Eigenvalue test. These single element tests verify the correctness of the elastic and geometric stiffness matrices of the element. In addition, the Patch test, when passed, indicates that the formulation will converge to the exact solution with mesh refinement. An "implicit" Patch test is proposed, and steps recommended to suppress the singular form of the element elastic stiffness matrix arising in the case of a flat element (Section 6.2 and Section 6.3, Chapter 6). The effects of the approach adopted for the representation of large strains is discussed with respect to the form-finding of minimal surfaces (Section 6.4.2.2), in conjunction with the combined consequences of geometric and topological distortion of the element. The accuracy of the proposed numerical solution method is demonstrated by comparisons with experimental models of several minimal surfaces (Section 6.5, Chapter 6). Finally, based on the work presented in this thesis, several conclusions are recommended, and possibilities for further investigations proposed (Chapter 7).

Chapter 2

Recent Developments in the Analysis of Surfaces and of Geometrically Non-linear Systems.

2.1. Introduction - the Mathematical Formulation and the Optimisation of Surfaces.

A mathematical treatise on the application of differential geometry to the form-finding and to the cutting-patterns of air-supported structures has been presented by Williams [2.1]. A method was given in which the equilibrium state of the surface and the cutting pattern of the membrane were defined simultaneously. A subsequent paper by the same author, presented the mathematical solutions to "equal mesh" and to principal curvature cable nets, in addition to that to constant tension coefficient surfaces [2.2].

Sobotka later published a catalogue of analytical solutions to surfaces generated by "perfectly flexible" membranes and cable nets, subjected to vertical loads and suspended in the horizontal plane [2.3]. The surface of the hanging form was related to the vertical load by a second order differential equation in the out-of-plane co-ordinate. Based on various plan geometries and assumed displacement fields, solutions were presented for the maximum sag of the surface, for the horizontal components of tension forces, and for the maximum surface tension.

Several publications have been presented on the optimisation of structural membranes. For example, Kostem used a penalty functional on the membrane stresses to determine the optimum geometry for single skinned pneumatic roofs, comprising spherical segments and subjected to an axi-symmetrical load [2.4]. It was shown that the shallow type of surface was less efficient at resisting normal external loads.

The dependencies of the static response and the eigenvalues of a membrane on its shape were subsequently investigated by Rousselet [2.5]. Differential operator properties and transformation techniques of integral calculus were employed to show that the static response and the eigenvalues of the membrane depended in a continuous and in a differentiable way on the shape of the membrane.

Surfaces optimised in terms of surface area and surface energy were modelled physically using soap-films, by Otto and his co-workers from the 1960's. Such surfaces were termed "minimal surfaces" [2.6],[2.7]. A considerable volume of papers has been published concerned with the mathematical description of minimal surfaces (see Bibliography of reference [2.8]). Subject areas such as the "Plateau problem", "minimal surfaces and homology", the "theory of currents and varifolds", have been addressed. The solutions obtained were, in the most part, esoteric and extremely specialised in application. The numerical investigation of minimal surfaces has received less attention, however.

In a paper presented by Ishii and Suzuki, a general minimal surface was expressed through a set of non-linear differential equations [2.9]. A finite difference approximation to the non-linear equations, in conjunction with the Gauss-Seidel iterative method, was used to obtain the solution to the form. The approach was based on the assumption of zero mean curvature at all points on the minimal surface. However, this is only a necessary and not a sufficient condition for the description of a stable minimal surface (Section 3.6.2.2, Chapter 3).

Suzuki and Hangai applied the finite element method to the analysis of minimal surfaces [2.10]. The first fundamental quantities of the surface were generated from a triangular finite element discretisation of the form. The variation of these quantities, combined with an assumed element stress field, were used to obtain an expression for the equilibrium of the surface. This expression was solved iteratively by a standard incremental procedure. As in the case of the preceding reference, both stable and unstable minimal surfaces were obtained via this approach.

Barnes treated the question of form-finding of minimal surface membranes briefly, using the Dynamic Relaxation algorithm and a constant strain triangular element discretisation as the bases of the analyses [2.11]. The paper was concerned primarily with the stability of the solution algorithm when used to analyse surfaces of neutral equilibrium or quasi-instability, as represented typically by minimal surfaces.

As stated in the Introduction (Chapter 1), this thesis aims to fill the lacunae which exist in the accurate representation of general, stable minimal surfaces. By way of a prologue to the subject matter, the following aspects related to the analysis of geometrically non-linear systems are reviewed in this chapter;

- numerical representation of geometrically non-linear systems,
- analysis of membranes,
- Dynamic Relaxation algorithm,
- aspects of the formulation of a finite element.

2.2. Numerical Representation of Geometrically Non-linear Systems.

Derivations for the elastic and geometric stiffness matrices of a bar, and for the overall global stiffness matrix of the complete discretised system, were presented by Turner *et al* in 1959 [2.12]. The theory was initially developed for aeronautical applications. Subsequently, Argyris and Scharpf adapted it to the non-linear analysis of prestressed networks [2.13]. Due to the geometric non-linearity of the system it was shown that an iterative type procedure was required in order to establish the condition of equilibrium. The solution to the surface at equilibrium was achieved using a Newton-Raphson method for the solution of a system of non-linear equations. The approach required the inversion of the total, global stiffness matrix of the discretisation.

Results of a similar analysis were presented simultaneously by Haug and Powell [2.14]. It was shown that the basic Newton-Raphson procedure may not converge, or may exhibit a slow rate of convergence when used as the solution algorithm in the analysis of three-dimensional cable nets. A procedure of limiting the maximum admissible nodal displacements, or of scaling the out-of-balance force vector at each nodal point, was suggested to improve the stability. However, it was found that these measures lead to the divergence of the solution in strongly geometrically non-linear cases.

An initial value algorithm for the analysis of cable nets was presented by West and Kar in 1973 [2.15]. A discrete mathematical model was used to represent the cable net. The non-linear response of the system was traced through a series of linear solutions, obtained from the Newton-Raphson iterative scheme. In the case of each linear solution the governing boundary-value problem was solved as a set of initial-value problems. This method therefore dispensed with the need to solve a large number of simultaneous equations. Due to the mathematical sensitivities of the initial-value algorithm, it was necessary however, to select the displacements of the surface judiciously, in order to control the distortion of the surface, as the solution algorithm proceeded.

Irvine presented analytical solutions to pretensioned cable nets based on a membrane analogy approach [2.16]. It was assumed that an orthogonal network of uniform flexible cables was replaced by an equivalent membrane, with zero shear resistance. The geometry of the network was taken as flat, initially, with the form of the surface dictated by the application of a uniform load vector, acting over the whole of the membrane. The differential and the integral equations of the equivalent membrane were rearranged and non-dimensionalised, so as to circumvent the use of a double Fourier series in the final solution. The resulting single series for the solution to the surface of a rectangular membrane was given, and shown to be more rapidly convergent than the double Fourier series. It was conceded in the paper however, that the analytical solutions were limited in their application, and that the solution accuracy was reduced by the assumption of small displacements.

A curvilinear finite difference energy formulation was applied by Kwok [2.17], to the geometrically non-linear analysis of general thin shells of arbitrary geometry. Based on the thin shell theory subjected to the Kirchoff's hypothesis, finite difference techniques were used to replace the partial derivatives which appeared in the energy functional, with algebraic expressions. The adoption of a curvilinear finite difference algorithm, relaxed the condition of regular mesh spacing. Consequently, the requirement that the grid lines were parallel to the co-ordinate axes, usually encountered in the finite difference algorithm, was dispensed with. The Newton-Raphson iterative method was used to solve for the non-linear displacements of the surface. Several solutions to the static response of thin elastic shells subjected to an external load vector were presented, showing good agreement with the available analytical solutions. The accuracy of the approach was limited directly, however, by the inability of the finite difference approximation to represent accurately the continuous response of the shell.

The application of the Finite Element method to the analysis of geometrically linear and geometrically non-linear systems has appeared extensively in the literature. For example, Brebbia and Connor presented a review of the works which investigated the (assumed) linear buckling response of beams, plates, and membranes, based on the Finite Element method [2.18]. Furthermore, a summary of the works concerned with the linearised incremental and with the mathematical iterative techniques for determining the geometrically non-linear behaviour of a system were also presented.

In 1975 Bathe, Ramm, and Wilson presented a paper which gave a consistent summary of, and an evaluation and a comparison of, the fully non-linear formulations which had been derived in order to represent the geometric non-linearity of a system [2.19]. These formulations also included the effects of large displacements and large strains. Two different approaches which had been pursued in the incremental non-linear Finite Element analyses were highlighted - the Eulerian (or Updated Lagrangian) and the Total Lagrangian approaches. In the Eulerian procedure, the static and the kinematic variables were referred to an updated configuration (or co-ordinate system) at each iteration. Adopting the Total Lagrangian approach, all static and kinematic variables were referred to an initial configuration. It was concluded by Bathe *et al* that the Total Lagrangian formulation was computationally more efficient when considering the geometrically non-linear system as a continuum.

A definitive paper by Wood and Zienkiewicz was published in 1977, presenting a combination of the Total Lagrangian formulation with a continuum approach, for the geometrically non-linear analysis of beams, frames, arches, and axi-symmetric shells [2.20]. In the derivation of the non-linear equations of equilibrium, it was shown that in the Total Lagrangian formulation, the internal work of the system was a function of the variation of the linear and the non-linear parts of Green's strain. The equilibrium equations of a single element were considered initially, with

the equations of equilibrium for the complete system established under the conditions of nodal equilibrium and nodal compatibility. Expressions were developed for the vectors of equivalent nodal loads due to body forces and surface tractions, and for a prescribed internal element stress. A "tangent" stiffness matrix was derived in which the large displacement and the geometrically non-linear stiffness terms were included.

The Newton-Raphson iterative scheme was adopted as the solution algorithm, and was applied to the non-linear equations of equilibrium to solve for the displacements of the system. A load increment procedure was proposed in order to define the complete equilibrium path. The overall solution procedure was demonstrated by the implementation of an in-plane "paralinear" isoparametric element, yielding accurate results when compared with the analytical solutions to an elastically loaded column, to hinged and clamped arches, and to a spherical cap. The approach of Wood and Zienkiewicz [2.20] was subsequently applied to several examples of the geometrically non-linear analyses of shells subjected to large strains and to large rotations [2.21],[2.22],[2.23].

2.3. Analysis of Membranes.

A significant work on the theory of elastic membranes was published by Green and Adkins [2.25]. The theory of plane stress for finite deformations, and the membrane theory for thin shells were developed. The application of the theory was confined to axi-symmetrical problems. In this case, the equations governing the deformation of the surface reduced to a system of ordinary differential equations. These equations were then integrated using numerical methods.

Boyer and Gutkowski adopted the theory of Green and Adkins to investigate the deformation of liquid filled membranes, in which the inflation pressure acting on the membrane was not constant [2.26]. The governing equations of the membrane were solved using a method of successive approximations - the Picard method. It was shown, by a comparison of the numerical solution with the experimental, that if the membrane deformations were small, the presented mathematical formulation was invalid. Furthermore, it was found that the method of successive approximations exhibited a slow rate of convergence when used to solve the governing large deformation equations of the membrane.

Several papers have been published on alternative analytical solutions to the deformation of membranes. For example, Kondo and Uemura investigated the mechanical behaviour of an orthotropic rectangular membrane subjected to uniform lateral pressure [2.27]. The Ritz and the Galerkin methods, based on the principle of stationary potential energy in the finite deformation theory, were used to obtain the geometrically non-linear relationships between the lateral pressure and the membrane deformations and stresses. It was assumed that the membrane possessed little bending stiffness and resistance to compressive stresses, and that no wrinkling occurred. The

effects on the membrane deformations and stresses of various parameters, including initial sag, aspect ratio of the membrane, orthotropic elastic constants and the principal directions of elasticity, were investigated. However, the proposed approach was limited by the necessary anticipation of the deformation modes of the membrane prior to the analysis. In this way the form of the membrane was dictated.

Nachman presented solutions to the geometrically exact equations of pressurised axi-symmetric membranes [2.28]. A derivation of the geometrically exact, axi-symmetric equations of equilibrium for an elastic membrane material, with completely general stress-strain laws, was given. The generality of the method was enhanced by the explicit choices of the axi-symmetric reference configuration, from which the analysis was commenced. An estimate of the deformation mode was also required, however. Results pertaining to a membrane in the form of a spherical cap were presented, and showed the effects of various stress-strain laws on the performance of the membrane.

Two papers have been published on the application of the geometrically non-linear zero moment theory of thin shells to the analysis of membranes undergoing large deformations. In the first paper by Sibgatullin, a circular membrane with a movable rigid centre, subjected to a pressure differential, was considered [2.29]. The Karman equations for the large deflections of circular plates were employed to define the equilibrium of the membrane. With the final membrane shape defined by truncated Chebyshev polynomials, it was shown that as the size of the rigid inclusion increased, the error in the membrane solution decreased.

In the second paper by Kabrits and Kolpak, a similar method was used to investigate a plane rectangular membrane [2.30]. Two approaches were described, with one based on a variational principle, and the other on a finite difference representation of a rudimentary membrane element. It was shown that the necessary modelling of the complicated stress field in the corners of the membrane, increased the complexity of the analytical solution considerably. As in the case of the preceding approach of Sibgatullin, an estimate of the final form of the surface was required.

Seide presented an alternative formulation for the large displacement analysis of rectangular membranes loaded by uniform pressure [2.31]. The approach was established on the large deflection equations for laterally loaded membrane plates (with little or zero bending stiffness) developed by Foeppl. The coupled non-linear membrane equations were expanded by means of the Fourier series in terms of the lateral deflection and the Airy stress function. An infinite number of coupled non-linear cubic equations in the deflection function coefficients were obtained. These were truncated and solved by means of an iterative procedure. In excess of one hundred equations were necessary in order to establish a solution of sufficient accuracy, leading to a computationally expensive solution algorithm.

The application of the "Framework" method to the geometrically non-linear analysis of transversely loaded membranes was presented by Allen and Al-Qarra [2.32]. In this method, the solid continuum of the elastic membrane was replaced by a pin-jointed truss. The elements of the truss were arranged in a definite pattern, and possessed appropriate values of elastic stiffness and natural force in order to represent accurately the substituted continuum. The solution to the displacements of the membrane were obtained through an iterative type procedure, relying on the inversion of the global stiffness matrix of the complete equivalent "framework". The approach was shown to work effectively for the calculation of deflections and stresses of transversely loaded membranes, but was limited to the case of flat, regular geometries and to small membrane strains.

Oden and Sato presented the first application of the Finite Element method to the analysis of membranes exhibiting finite strains in 1967 [2.33]. A triangular finite element was formulated for the analysis of large displacements and finite strains in elastic membranes of arbitrary shape. The element was taken to be plane, and to be defined with straight sides. It was assumed that the node points of the element were sufficiently close together to permit the displacement fields within each element to be approximately linear functions of the local nodal co-ordinates. The deformation of the continuous body was described by the Lagrangian strain tensor, while the geometrically non-linear stiffness relationship was derived from the principle of virtual work. The Newton-Raphson scheme was applied to the global stiffness matrix of the discretised surface to solve for the element nodal displacements. Solutions to several membranes, obtained using this approach, were presented. It was found, however, that an improper choice of starting values for the undetermined nodal displacements could lead to ill-conditioned stiffness matrices and to no solution.

A subsequent paper by Haug and Powell described a quadrilateral membrane element [2.34]. The element was warped in three-dimensional space, with straight sides, and was based on the isoparametric principle. An expression for the metric tensor describing the straining of the element in any deformed geometry, and applicable to the case of large deformations, was derived. A "prestress element" was defined, possessing zero elastic stiffness, and formulated so as to remain in a prescribed, isotropic state of stress, irrespective of the element deformations. The element was therefore presented as suitable for the analysis of constant stress inflated forms and minimal surfaces. The solutions to the geometrically non-linear surfaces presented in the paper were solved for by the Newton-Raphson iterative scheme. The proposed method was described by the authors as being theoretically consistent and computationally efficient. No measure of the accuracy of the approach was given, however.

An alternative finite element formulation was presented by Argyris *et al*, and was termed the "Natural Approach" [2.35],[2.36]. The method was based on the use of separate rigid body

displacements and natural (or strain inducing) deformations for the description of the current state of the finite element. The "natural approach" was devised in order to derive, in an exact and in a simple manner, the geometrical stiffness matrix of an element, which was suitable for application to the analysis of systems undergoing large displacements, but small strains. Subsequently, the effects of large strains were introduced into the formulation through the Green's measure of strain [2.36].

Using the proposed "natural approach", it was necessary, however, to separate the components of the rigid body and the natural displacements from the general displacement vector, prior to the calculation of the element matrices. It was suggested by Argyris *et al* that for general curved elements, the rigid body modes may prove difficult to define accurately. In order to overcome this difficulty, it was shown that an arbitrarily shaped element could be represented by a set of regularly shaped sub-elements. The elastic and the geometric stiffness matrices of the finite element were then obtained by the integration, over the strain energy, of the local sub-elements. As a consequence, an extra approximation (and therefore, error) was introduced into the formulation, the effects of which increased with an increase in the distortion of the element.

In addition to that work presented by Kabrits and Kolpak [2.30], various alternative procedures have been proposed for the geometrically non-linear analysis of membranes, in which the finite difference method was adopted as the basis of the solution algorithm. For example, several papers have been published on the analytical solutions to the deformations of membranes, where the finite difference method was used to solve the governing differential equations of the response of the system [2.37],[2.38],[2.39],[2.40].

Kao and Perrone presented a non-linear relaxation method to solve the governing partial differential equations which described the deflection response of an axi-symmetric circular membrane [2.41]. The governing equations of the membrane were rewritten in a finite difference format. The equilibrium of the surface was obtained using the derivative of the finite difference equations as "relaxation operators", in order to reduce systematically the out-of-balance force vector at each grid point to a value close to zero. It was shown that the algorithm was efficient and relatively insensitive to the assumed starting configuration of the membrane. The approach was only applicable, however, to surfaces for which the differential equations could be defined explicitly.

The generalised finite difference method was used by Tworzydlo to analyse membrane shells undergoing large deformations [2.42]. A "star" type pattern was adopted for the finite difference grid in order to permit the analysis of arbitrary geometries. The differential equations of the membrane shell were obtained from an equation of motion involving the first Piola-Kirchoff stress resultant tensor and a viscous damping tensor. These non-linear equations, rewritten in the proposed finite difference format, were solved initially by the Newton-Rapshon scheme, and

separately by the viscous relaxation method of Webster [2.42]. The overall algorithm, based on both the Newton Raphson scheme and the viscous relaxation method, was shown to produce good results, but to be computationally inefficient.

An application of the finite difference method to the analysis of membranes, in the form of the Dynamic Relaxation algorithm, was presented by Barnes and Wakefield, and Barnes [2.43],[2.11]. A summary of the work presented in these papers is given in Chapter 4.

2.4. Dynamic Relaxation Algorithm.

Several alternative numerical solution algorithms have been proposed for the analyses of discrete and continuous surfaces, and geometrically non-linear systems [2.44],[2.45],[2.46],[2.47]. However, efficiency studies conducted by Barnes [2.44] and by Lewis [2.48] concluded that the Dynamic Relaxation algorithm was the more expedient method in the cases of the form-finding and static analysis of lightweight tension structures.

The Dynamic Relaxation algorithm was first presented in a paper published in 1965 in "The Engineer" [2.49]. The algorithm was devised by the author of the paper, A.S. Day, as a solution method for the analytical investigation of complex prestressed concrete pressure vessels comprising nuclear reactors. Used mainly at the time for structural problems, which depended essentially on the solution of governing differential equations, the author concluded that the Dynamic Relaxation algorithm could be applied to solutions based on both finite elements and finite differences. The main disadvantages of the method were given as the derivation of the time interval for the integration of the fundamental finite difference equations, and the need to establish the damping factor necessary to attenuate the pseudo oscillations of the system. Conversely, the simplicity of the algorithm, and the ease with which the method could be implemented with existing analytical software to solve complex problems, were heralded as the main advantages [2.49].

Methods for determining the critical damping factor and the optimum time increment were presented by Rushton in 1968 [2.50]. It was found that, when analysing a flat plate subjected to tensile stress, the stress function followed the vibration of the fundamental mode of the plate closely, from which the critical damping factor could be calculated. In addition, the critical time interval, below which the algorithm remained stable, was related to the square of the smallest finite difference mesh interval by a factor of $\frac{1}{4}$. A method for optimising the algorithm when adopting an irregular mesh interval was also presented [2.50]. Using this approach, artificial (unequal) masses were introduced at the nodal points, such that the time increment throughout the mesh adopted the minimum value possible for the current mesh intervals. In this way, the rate of convergence of the solution algorithm was enhanced.

In 1970, Day and Bunce applied the Dynamic Relaxation scheme to the analysis of cable networks, and presented a comparison of the algorithm with the matrix method approach [2.51]. It was found that for the case of the "skeletal" type of structures with several degrees of freedom, the matrix method approach was uneconomical due to the large bandwidth of the global stiffness matrix of the system. Day and Bunce also highlighted the fact that if the element prestresses were assumed to be zero, such that the geometric stiffness matrix was a null matrix, and the stiffness of the system was derived from elasticity only, then the global stiffness matrix of the cable network was singular. In the case of the Dynamic Relaxation Algorithm with Viscous Damping, it was shown that a singularity in the stiffness of the surface, failed to affect the solution, as only the elastic stiffness terms were used in a remote or in a tertiary sense to calculate the current element forces. An approximate upper-bound on the time increment was also given by the least value of the quantity $\sqrt{\frac{M.L}{A.E}}$, where M was the nodal mass, L the current length, A the cross-sectional area, and E the elastic modulus of the element used in the analysis.

An alternative Dynamic Relaxation procedure was suggested by Cundall and applied to rock mechanics problems [2.52]. Using the revised procedure, the pseudo oscillations of the system were attenuated by Kinetic Damping (Section 4.2, Chapter 4). It was found that in arresting the system using technique, a generally more stable and a more rapidly convergent solution algorithm was obtained. Furthermore, the revised procedure was shown to be particularly appropriate to the analysis of systems exhibiting large "local disturbances", such as geometrically non-linear surfaces undergoing large displacements and large strains. The application of both the Viscous Damping and the Kinetic Damping procedures to the investigation of cable networks, can be found in references [2.53], [2.54], and [2.55].

More recently, Zhang and Yu have presented a modified adaptive Dynamic Relaxation ("maDR") algorithm, based on the viscous damping approach [2.56]. In this case, the damping coefficient was based on a function of the current system configuration, the internal element force, and the mass matrix. The numerical stability of the "maDR" algorithm was assured through the mass matrix, the terms of which were given by the Gerschgorin theorem. When applied to the analyses of elastic-plastic plate bending, and to the wrinkling of circular plates, it was shown that the "maDR" algorithm was stable and displayed a small increase in computational efficiency, when compared with the standard viscously damped Dynamic Relaxation algorithm.

A mathematical treatise on the convergence of the Dynamic Relaxation algorithm to the solution of a set of simultaneous linear equations was presented by Wood in 1971 [2.57]. A comparison was made between the Dynamic Relaxation algorithm and the degenerated Chebyshev method, which it closely resembles. It was shown, through the calculation of the spectral radius of the iteration matrix of each approach, that the convergence of the Dynamic Relaxation algorithm was assured in this case, and that it gave a faster rate of asymptotic convergence by a factor of $\sqrt{2}$ when

compared with the Chebyshev method.

In 1984 a similar paper was published in which the convergence of the Dynamic Relaxation algorithm for problems of axi-symmetric loading of elastic shells of revolution was investigated [2.58]. The convergence of the solution algorithm was proved by showing that as the time, t, tended to infinity, the kinetic energy and the potential energy of the shell tended to zero.

2.5. Aspects of the Formulation of a Finite Element.

2.5.1. The "Isoparametric" Approach.

Ergatoudis, Irons, and Zienkiewicz introduced a new "family" of "Isoparametric" elements in 1968 [2.59]. From the developments of the Finite Element method and from the establishment of the principles of the technique, it was found that the derivation of the matrices of an element followed a prescribed path, once the shape functions had been selected. It was suggested, therefore, that the possibilities of improving the finite element approximation were confined to the development of new shape functions. The impetus behind the "Isoparametric" approach, was the formulation of elements which may, if desired, have curved sides.

A derivation of the isoparametric shape functions was provided by Ergatoudis *et al.* It was shown that the convergence criteria of an element were satisfied by the new approach - that a state of constant strain could be satisfied by the element formulation, and that the displacements were continuous between adjacent elements. The elastic stiffness matrix of a general plane element, based on the isoparametric shape functions, was given. Quadrilateral elements with eight and twelve nodes were used to represent a cantilever beam which was subjected to a vertical load at the free end, and a moment at the encastre´ end. It was shown that significant improvements in the accuracies of both the stress and the displacement solutions were obtained with the curved isoparametric elements, when compared with the standard triangle and quadrilateral.

A subsequent paper by Irons and Zienkiewicz gave some of the basic definitions used in the isoparametric formulation, and indicated the progress and the range of applications of the approach [2.60]. In particular, the fundamental relationship between the "parent" and "curvilinear" elements was described. Furthermore, the basic isoparametric definition was presented - "the same shape functions are used to define the element co-ordinates, as were used to define the variation of the unknown" (displacements). The extension of the isoparametric approach to the analysis of general curved non-linear systems has been illustrated in several publications.

For example, Ahmad, Irons, and Zienkiewicz presented a comprehensive paper on the application of curved isoparametric finite elements to the analysis of thick and thin shells [2.61]. The limitations of the current alternative techniques applicable to the analysis of shells, such as shallow curvatures, and the omission of shear deformation effects, were shown to be overcome

through the adoption of the curved isoparametric formulation. However, the application of the isoparametric approach to curved, three dimensional elements, was found to lead to ill-conditioning of the global stiffness matrix of the discretised system, as the thickness of the shell was reduced.

Webster presented a curved two-dimensional finite element with nodal derivatives, based on the isoparametric approach [2.62]. A four node quadrilateral element was developed in which the displacement components at each node, and the first derivative of the displacements with respect to the local co-ordinates, were taken as the element degrees-of-freedom. When compared with the theoretical solutions to a straight and to a curved cantilever beam, the proposed finite element model showed good agreement. It was commented by the author however, that elements in which nodal derivatives comprise some of the element degrees-of-freedom, suffered the disadvantage of not being suitable for those cases where strain discontinuities existed at the element interfaces, such as the cases of material or thickness changes.

Papers by Parisch [2.63] and by Skvortsov and Khazanov [2.64] presented works on the use of the isoparametric formulation to investigate shells undergoing large displacements and exhibiting elasto-plastic material behaviour (large strains). These papers, in conjunction with that of Wood and Zienkiewicz [2.20], illustrated the suitability of the isoparametric approach to the analysis of curved systems subjected to large displacements and large strains.

2.5.2. Patch Test.

Irons formally presented the "Patch Test" in a paper in 1965 [2.65]. The test was devised in order to verify that an arbitrary "patch" of assembled elements reproduced exactly the behaviour of an elastic solid material, when it was subjected to boundary displacements, or to boundary equivalent nodal forces, which were consistent with a state of constant straining. Several papers have been published on the Patch Test, dealing with both the theory and with the implementation of the test.

For example, Irons and Razzaque presented work which showed that the Patch Test provided a necessary condition for the convergence of a discretised system to the exact solution with mesh refinement [2.66]. A comprehensive list of the applications of the Patch Test to various element formulations was also presented in the same paper.

At the same time, Strang presented a mathematical treatise on the Patch Test [2.67]. In reference [2.67] it was suggested that the Finite Element method amounted to a special case of the Rayleigh-Ritz technique. The modifications of the Ritz procedure which had been made in order to achieve an efficient Finite Element system were examined. In doing so, the effects of irregular meshes, non-conforming elements, and numerical integration, on the accuracy of the finite element solution were considered. Ultimately, Strang gave mathematical support to the Patch

Test by showing that the convergence of a numerically integrated finite element was conditional on the element passing the test.

A further mathematical treatise by Fraeijs de Veubeke showed that the Patch Test was contained in the variational formulations of the Finite Element method, and illustrated the validity of the Patch Test for conforming elements (or elements possessing a full complement of the displacement terms in the derivation of the shape functions) [2.68]. However, it was also shown that non-conforming elements only passed the Patch Test when they became exactly conforming under a common state of uniform stress.

The question of non-conforming elements and the Patch Test was investigated further by Stummel [2.69]. Stummel showed that an approximation of the solutions to a simple one-dimensional boundary value problem by a mesh of non-conforming finite elements, passed the Patch Test, but did not converge to the exact solution of the problem with mesh refinement. Subsequent to the papers by Fraeijs de Veubeke [2.68] and Stummel [2.69], a wealth of literature was published in the defence of the Patch Test [2.70],[2.71],[2.72].

Of particular note was a paper by Taylor *et al*, in which it was shown that the work of Stummel [2.69] was in error, and that the Patch Test was applicable to both conforming and non-conforming finite elements [2.73]. It was also shown that the Patch Test was a necessary and a sufficient condition for finite element convergence with mesh refinement.

2.5.3. Technique of Reduced Integration.

The technique of reduced, or selective, integration was first proposed by Doherty, Wilson, and Taylor in 1969 [2.74]. The procedure was devised in order to alleviate the effects of "parasitic shear" in the pure bending mode of the four node plane quadrilateral element. It was found that by reducing the order of the numerical integration algorithm for the shear strain component, the accuracy of the finite element in bending was enhanced significantly.

Zienkiewicz, Taylor, and Too, applied the technique to the analysis of plates and shells using an isoparametric degenerated shell element [2.75]. The degenerated shell element had been shown to work well in the case of thick shells, but became ill-conditioned as the thickness was reduced. Zienkiewicz *et al* showed that very accurate solutions to thin laterally loaded plates and shells could be obtained by calculating the direct and shearing strains using the technique of reduced integration. It was shown further that the stiffness of the displacement based elements was reduced as the order of the numerical integration was reduced. In addition, the convergence of the numerically integrated elements was shown to be guaranteed in all cases, provided that the order of the integration technique allowed sufficient accuracy in the calculation of the integrand, such that the volume of the element was evaluated exactly.

A paper similar to that of Zienkiewicz *et al* [2.75] was presented subsequently by Pawsey and Clough [2.76]. Whereas Zienkiewicz *et al* [2.75] recommended a uniform reduced integration technique, Pawsey and Clough proposed a selective integration scheme for calculating the stiffness matrix of the finite element. Using the proposed selective integration approach, each component of the strain energy was evaluated separately, with a different Gaussian integration rule for each contributing term, so as to optimise the performance of the element. It was commented further, that when using the techniques of selective or reduced integration, the integration procedure must evaluate exactly the energy associated with the element constant strain states, in order to assure convergence of the solution with mesh refinement. In addition, a warning was given, regarding the implementation of the approaches, in that deformation modes could exist, for which zero strain energy was given when adopting a low order of numerical integration. Such a phenomenon was realised in the form of a singular element stiffness matrix.

Zienkiewicz and Hinton addressed the reasons why the reduced integration technique yielded an improvement in the accuracy of the finite element formulation [2.77]. It was shown that an optimum number of sampling or "Gauss" points existed, for which the strains of the element were calculated with increased accuracy. The optimal Gauss points were found to coincide with an order of numerical integration which was one order below that necessary to calculate the integrand "exactly". The improvement in the accuracy of the strain calculations was shown to be achieved through an optimisation of the error in the numerical integration algorithm.

The techniques of reduced and selective integration have been used to improve the accuracy and the performance of mixed formulation finite element models, where a combination of displacement and stress degrees-of-freedom were invoked as the total element degrees-of-freedom [2.78],[2.79]. Furthermore, the problem of shear or membrane "locking" in curved elements arising from the adoption of low order shape functions in the element formulation, was shown to be overcome by the under-integration of the shear terms comprising the overall element strains [2.80]. Publications have also been presented on the efforts to optimise the reduced integration algorithm, and to eliminate or evade the undersirable effects of the technique.

For example, Stander and Wilson presented an eight point, modified reduced integration scheme, which was applied to a four node, plane quadrilateral element [2.81]. It was found, however, that the weights associated with the eight point integration rule took optimal values which made the modified rule resemble very closely the standard 2×2 Gauss. The eight point rule therefore required twice the computational effort of the four point rule to produce similar results.

A paper by Sandhu and Singh [2.82] proposed a method to circumvent the limitation of the reduced integration technique highlighted by Pawsey and Clough [2.76] (who revealed that it could be used only on a selective basis, in order to avoid a singular form of the stiffness matrix comprising zero energy modes). The approach was based on the inclusion of additional terms in the element shape

functions, such that the singularity of the element stiffness matrix was eliminated. A technique was suggested for the derivation of the additional terms which were just sufficient to achieve the desired effect, without generating an over-stiff element formulation.

2.5.4. Requirement of Strain Free Rigid Body Motion.

In the derivation of the displacement functions used to construct the stiffness matrix of a finite element, the satisfaction of several conditions were shown generally to be required. Firstly, the displacement functions should contain all the lower terms of a complete polynomial, in order to ensure monotonic convergence of the finite element solution with mesh refinement. Secondly, a minimum degree of element compatibility should be maintained between adjacent elements - in-plane and out-of-plane displacement components. Finally, rigid body motions of the element should be represented accurately, and therefore should be strain free. The final requirement was included to ensure the internal equilibrium of the element.

A great number of papers have been published on the aspect of strain free rigid body motions of a finite element. For example, Haisler and Stricklin considered the rigid body displacements of curved elements in the analysis of shells [2.83]. It was shown that the explicit inclusion of strain free rigid body motions in the displacement function of a curved finite element, where the displacement function was defined as a truncated power series, was not necessary for "practical problems". This was done by demonstrating that the internal energy associated with a vertical rigid body displacement of an element, approached zero as the change in slope between the element nodes became sufficiently small. This work was rather limited in its rigour however, as only a single type of rigid body motion was considered.

Mebane and Stricklin presented an implicit representation of strain free rigid body modes for the case of axi-symmetric shells of revolution [2.84]. The suggested method was based on the careful selection of the terms of the polynomials used to relate the element nodal displacements to the displacements at any arbitrary point within the element. The implicit strain free rigid body modes were shown to be much better represented when adopting a quadratic displacement function as opposed to a linear one. Furthermore, the same rigid body modes were shown to be revived with mesh refinement, when the displacement functions were not adequate to model them. It was stated that a relatively fine discretisation of elements was required, in order to include implicitly the strain free rigid body deformation modes of the element with sufficient accuracy. Such a condition, rendered the proposed approach computationally inefficient, particularly in the analyses of geometrically non-linear systems.

Papers published by Cantin and Clough [2.85], and by Cantin [2.86], illustrated the explicit "inclusion" of the strain free rigid body deformation modes in the element displacement vector of a curved element, used to represent a cylindrical shell. In this case, expressions for the actual

rigid body deformations were established, and were subtracted from the combined displacements of the element, to leave only the true, strain inducing components. It was shown that curved elements corrected by the proposed method, showed a significant improvement in the accuracy of the solution to problems in which some rigid body displacements of the elements were required. The approach was, however, only applicable to axi-symmetric systems, discretised by regularly shaped elements.

In addition to the papers of Cantin and Clough [2.85] and Cantin [2.86], several additional papers have been published on the explicit inclusion of strain free rigid body motions in curved shell elements [2.87],[2.88],[2.89],[2.90]. The techniques proposed were all subjected to the constraints of regular surface, or axi-symmetric geometries, however.

A paper by Jagannathan, Epstein and Christiano presented work in which it was shown that the exclusion of the higher order terms in the strain-displacement relationships of the element formulation (based on the Total Lagrangian approach), gave rise to the induction of fictitious strains when the element was subjected to a rigid body rotation [2.91]. It was conceded, that though the Total Lagrangian formulation was computationally more efficient than the Eulerian, especially when analysing systems subjected to large strains and large displacements, the inclusion of the higher order strain-displacement terms lead to stiffness matrices that contained displacement gradients which were to the third or fourth powers. It was suggested further that these elements were difficult to formulate. An example of a simple beam element was presented in the paper to illustrate the effects of including or omitting the higher order strain-displacement terms in the element stiffness matrix. In conclusion, it was shown that, in general, all of the second order terms of the strain-displacement relationship of the element formulation, needed to be retained in order to model accurately the response of a system subjected to large strains and large displacements, and to negate the strains induced by rigid body motions.

A test which checked for strain free rigid body motions of a finite element, and for the legitimacy of it for use in a geometrically non-linear analysis, was proposed by Yang and Chiou [2.92]. The test was based on the observations of common physical phenomena, and stated that when a finite element with initial (natural) forces was subjected to a rigid body motion, the initial forces of that element had to rotate or translate with the rigid body motion, while their magnitudes remained unchanged.

A complementary paper was subsequently published by Lui and Yang giving an eigenvalue procedure to establish the correctness of a geometrically non-linear finite element [2.93]. In addition, a method was proposed to include explicitly the strain free rigid body rotations of a geometrically non-linear finite element, subjected to initial stress. It was necessarily assumed that, in the incremental equation of equilibrium of the finite element, the stiffness terms of the element and the element equivalent nodal loads remain unchanged in direction, during the

iterative step. As a consequence of this assumption, pseudo strains were induced into the element when it was subjected to a rigid body rotation. For the case of a simple plane linear beam element, it was demonstrated that the disparity in the element nodal forces prior and subsequent to the application of the rigid body rotation, could be written as a fictitious (or a strain inducing) stiffness matrix. A subtraction of this stiffness matrix from the total stiffness matrix of the element was undertaken in order to suppress the strains induced by the rigid body rotation of the element.

2.5.5. Remedies to Other Element Deficiencies, and Additional Measures of Element Accuracy.

MacNeal presented a "catalogue" of element deficiencies or failure modes which were shown to exist in the various derivations of the four node membrane element, and which could be found equally in a general finite element formulation [2.94]. The primary element failure modes included "spurious mechanisms" arising from the under integration of the element stiffness integrand, "shear locking" caused by the presence of a dominating in-plane shear strain during an in-plane bending deformation, "Poisson's ratio locking", and "trapezoidal locking" occurring in slender beams. In addition, a failure of the Patch Test was cited as a collective failure mechanism, implying that the rigid body modes and the constant strain states of the element formulation were improperly represented.

The failure modes of shear and membrane locking were addressed by Braissoulis [2.95]. In a paper concerned with the displacement continuous, or C^0, type plate, shell, and beam elements, it was shown that the stiffness terms which induced the locking phenomenon, could be extracted from the general element stiffness matrix. The proposed approach was similar to that of Liu and Yang [2.93] which was concerned with the explicit inclusion of strain free rigid body rotations (Section 2.5.4). Though effective in a linear element formulation, the work presented by Braissoulis [2.95], was not applicable to the geometrically non-linear case.

In the papers by Zienkiewicz, Taylor, and Too [2.75], and by Pawsey and Clough [2.76], the techniques of reduced or selective integration were also shown to be effective in alleviating the shear locking and the membrane locking phenomena. However, spurious modes were found to degrade the performance of the element as a result of this approach.

Cook and Zhao-Hua presented a paper which showed that "static condensation" could be used to suppress the spurious modes arising from the use of reduced or selective integration [2.96]. The procedure consisted of detecting the erroneous stiffness terms which cancelled with the legitimate ones, and which thus permitted the formation of the zero strain deformation modes. The offending terms were then removed by condensing of the appropriate degrees-of-freedom, giving rise to a reduced order for the element stiffness matrix. It was also shown that similar results were

obtained by applying a factor, with a magnitude of greater than unity, to the stiffness terms of the spurious modes.

A comprehensive mathematical treatise on the derivation of a curved degenerated shell element was presented by Vu-Quoc and Mora [2.97]. In this work it was shown that the filtering of spurious zero energy modes, arising from the technique of reduced integration, could be achieved through the introduction of a small perturbation to the under integrated element stiffness matrix. The perturbation was taken as a fraction of the maximum absolute value of the diagonal coefficients of the element stiffness matrix. In the case of systems which exhibited a high level of geometric non-linearity, it was found, however, that the filtered element was slower to converge than the same element with unfiltered spurious modes. Furthermore, the accuracy of the filtered element was shown to be compromised when the numerical solution was compared with the analytical.

The effects of initial element stress on the development of spurious zero energy modes, was not considered in either the paper by Cook and Zhao-Hua [2.96] or in that by Vu-Quoc and Mora [2.97].

In a letter to the Editor of the *Journal of Sound and Vibration*, Fried highlighted the possible loss of accuracy in curved isoparametric finite elements [2.98]. It was shown that as the element distortion increased, the order of the error in the strain energy of the element was reduced. Furthermore, the same error was shown to increase as the element side nodes moved away from the mid-point of the element sides. In a study by Henshell, Walters and Warburton, it was shown that the error in the strain energy was attributed to the existence of a pole in the expression for the element strains [2.99]. The presence of the pole (just outside the physical element) caused the strain energy of the element to take unrealistic values at certain locations within the element. Consequently, the accuracies of the solutions obtained using distorted isoparametric elements was poor.

In a subsequent paper by Celia and Gray, it was shown that the pole mentioned by Henshell, Walters and Warburton, was generated by the assumption that the element side nodes remained at, or very near to, the centre of the interval (defined by the element side) in the derivation of the element shape functions [2.100]. An improved isoparametric transformation was proposed in which, the element side nodes in the global and natural spaces were at the same relative location. The true relative position of the side nodes were then used in the derivation of the element shape functions to provide a compatible mapping between the global and the natural spaces. Applied to a plane two-dimensional quadratic element, it was shown that the proposed transformation yielded a consistently low error in the strain energy of the element as the position of the element side node was varied.

Several additional papers have been published related to the effects of distortion on the accuracy of finite elements. For example, Robinson presented work on distortion measures for the plane four node quadrilateral element [2.101]. It was shown that the element shape parameters defined in

the paper could be related directly to the Jacobian matrix of the element. Tests were also given which could be implemented to illustrate the amount of warping of the element, and to detect re-entrant angles in the element geometry.

The results of a series of tests on the accuracy and on the robustness of certain shell finite elements for the linear elastic and for the geometrically non-linear problems were published in a paper by White and Abel [2.102]. Based on the results of the tests, it was concluded that an element derived using the Total Lagrangian formulation, and with characteristic matrices evaluated by the technique of reduced integration, was the least sensitive to geometric distortion. In addition it was found to exhibit the highest level of accuracy, when used to analyse several geometrically non-linear systems.

2.6. Summary.

As presented in Chapter 4, the element formulation proposed by Turner [2.12] and adapted by Argyris and Scharpf [2.13] to the geometrically non-linear analysis of prestressed networks, has been used, in conjunction with the Dynamic Relaxation algorithm, to provide a low-order approximation to the solution of stable minimal energy forms. In addition, the non-linear equilibrium equations, and the Total Lagrangian formulation presented by Wood and Zienkiewicz [2.20], in association with the outline element formulation given by Irons and Ahmad [2.24], have been employed to represent numerically the geometrically non-linear and the continuous response of arbitrarily shaped elastic membranes (Chapter 6).

The work done by Day and Bunce [2.51] on the analysis of cable networks, with modifications to the Dynamic Relaxation algorithm to include Kinetic Damping proposed by Cundall [2.52], have been drawn upon. Contributions from Barnes related to the re-initialisation of the algorithm subsequent to an energy peak when using the Kinetic Damping scheme [2.55], and to the maximum time interval which could be employed to ensure the numerical stability of the solution algorithm [2.53], have also been adopted. The suggestion made by Day [2.49] that the Dynamic Relaxation algorithm could be applied to solutions based on finite elements (in addition to those established on finite differences), has provided the impetus to combine finite elements with a (predominantly) non-matrix approach solution algorithm.

The Patch Test has been used extensively to assess the validity and the accuracy of the existing and proposed element formulations. The technique of reduced integration, recommended in place of selective integration by Zienkiewicz *et al* [2.75], has been adopted in order to reduce the sensitivity of the high-order membrane finite element (formulated in Chapter 5) to large displacements and rapid changes in the element geometry.

Furthermore, the principles presented in references [2.91], [2.92], and [2.93], have been implemented to include explicitly the strain free rigid body motion of the proposed element, while the techniques presented in the papers by Celia and Gray [2.100], and by White and Abel [2.102], have been used to assess and to improve the quality of the finite element formulation.

2.7. References.

[2.1] Williams, C.J.K.

"Form-finding and Cutting Patterns for Air-supported Structures."

Symposium on Air-supported Structures: the State of the Art., I.Struct.E, London, June 1980, pages 99-120.

[2.2] Williams, C.J.K.

"Defining and Designing Curved Flexible Tensile Surface Structures."

The Mathematics of Surfaces., Conference Proceedings, Institute of Mathematics and its Applications, University of Manchester, 17-19 September 1984, pages 143-177.

[2.3] Sobotka, Z.

"Shapes, Sags and Tensions of the Hanging Roofs with Horizontal Boundaries."

Acta Technica Csav, Volume 33, Part 2, 1988, pages 233-268.

[2.4] Kostem, C.N.

"Optimum Shaped Pneumatic Roofs."

Symposium on Ind. Spat. and Shell Struct., Int. Assoc. for Shell and Spatial Structures, Celt, Kielce, Poland, 18-23 June 1973, pages 77-87.

[2.5] Rousselet, B.

"Shape Design Sensitivity of a Membrane."

Journal of Optimisation Theory and Applications. Volume 40, Number 4, August 1983, pages 595-623.

[2.6] Bach, K., Burkhardt, B., Otto, F.

Forming Bubbles.

IL. (Institute of Lightweight Structures, Stuttgart University, Germany.) Publication Number 18, 1987.

[2.7] Gass, S.

Experiments.

IL. (Institute of Lightweight Structures, Stuttgart University, Germany.) Publication Number 25, 1990.

[2.8] Dao Trong Thi, Fomenko, A.T.

Minimal Surfaces, Stratified Multi-varifolds and the Plateau Problem.

American Mathematical Society, 1991, pages 381-399.

[2.9] Ishii, K., Suzuki, T.

"Shape of Membrane Structures."

Proceedings of IASS Symposium Part II on Tension Structures and Space Frames. Tokyo and Kyoto, 1972, pages 127-136.

[2.10] Suzuki, T., Hangai, Y.

"Shape Analysis of Minimal Surface by the Finite Element Method."

Proceedings of IASS Symposium. Copenhagen, September 1991, pages 103-110.

[2.11] Barnes, M.R.

"Form-finding of Minimum Surface Membranes."

Proceedings of IASS World Congress on Space Enclosures. Building Research Centre, Concordia University, Montreal, July 1976, pages 115-124.

[2.12] Turner, M.J., Dill, E.H., Martin, H.C., Melosh, R.J.

"Large Deflections of Structures Subjected to Heating and External Loads."

Journal of Aero-space Sciences. Volume 27, February 1960, pages 97-106.

[2.13] Argyris, J.H., Scharpf, D.W.

"Large Deflection Analysis of Prestressed Networks."

Journal of the Structural Division, ASCE. Volume 98, Number ST3, March 1972, pages 633-654.

[2.14] Haug, E., Powell, G.H.

"Analytical Shape Finding for Cable Nets."

Proceedings of IASS Symposium Part II on Tension Structures and Space Frames. Tokyo and Kyoto, 1972, pages 83-92.

[2.15] West, H.H., Kar, A.K.

"Discretised Initial-value Analysis of Cable Nets."

Int. Journal Solids and Structures. Volume 9, 1973, pages 1403-1420.

[2.16] Irvine, H.M.

"Analytical Solutions for Pretensioned Cable Nets."

Journal of the Engineering Mechanics Division, ASCE. Volume 102, Number EM1, February 1976, pages 43-57.

[2.17] Kwok, S.K.

"Geometrically Non-linear Analysis of General Thin Shells Using a Curvilinear Finite Difference (CFD) Energy Approach."

Computers and Structures. Volume 20, Number 4, 1985, pages 683-697.

[2.18] Brebbia, C., Connor, J.

"Geometrically Non-linear Finite Element Analysis."

Journal of the Engineering Mechanics Division ASCE. Volume 95, Number EM2, April 1969, pages 463-483.

[2.19] Bathe, K.-J., Ramm, E., Wilson, E.L.

"Finite Element Formulations for Large Deformation Dynamic Analysis."

Int. Journal for Num. Methods Eng.. Volume 9, 1975, pages 353-386.

[2.20] Wood, R.D., Zienkiewicz, O.C.

"Geometrically Non-linear Finite Element Analysis of Beams, Frames, Arches, and Axi-symmetric Shells."

Computers and Structures. Volume 7, 1977, pages 725-735.

[2.21] Misley, M.

"Finite Element Analysis of Anisotropic Shells Including Large Displacements and Large Rotations."

Periodica Polytechnia Mechanical Engineering. Volume 33, Part 1-2, 1989, pages 85-94.

[2.22] Hughes, T.J.R., Carnoy, E.

"Non-linear Finite Element Shell Formulation Accounting for Large Membrane Strains."

Computer Methods in Applied Mechanics and Engineering. Volume 39, 1983, pages 69-82.

[2.23] Surana, K.S.

"Geometrically Non-linear Formulation for the Curved Shell Elements."

Int. Journal for Num. Methods Eng.. Volume 19, 1983, pages 581-615.

[2.24] Irons, B., Ahmad, S.

Techniques of Finite Elements.

Ellis Horwood Series in Engineering Science, 1980, pages 77-79, 443-445.

[2.25] Green, A.E., Adkins, J.E.

Large Elastic Deformations.

Clarendon Press, Oxford, 1970, pages 133-173.

[2.26] Boyer, D.L., Gutkowski, W.

"Liquid Filled Membranes."

Int. Journal of Non-linear Mechanics. Volume 5, 1970, pages 299-310.

[2.27] Kondo, K., Uemura, M.

"Deformations and Stresses of Orthotropic Rectangular Membrane Under Uniform Lateral Pressure."

Proceedings of IASS Symposium Part II on Tension Structures and Space Frames. Tokyo and Kyoto, 1972, pages 211-222.

[2.28] Nachman, A.

"Some Results on the Geometrically Exact Equations of Pressurised, Axis-symmetric Membranes."

Acta Mechanica. Volume 57, Part 3-4, December 1985, pages 233-239.

[2.29] Sibgatullin, N.R.

"Calculating Large Deflections of Rigid-centre Elastic Membranes Under a Pressure Differential."

Moscow Univ. Mechanics Bulletin. Volume 32, Part 1-2, 1977, pages 29-35.

[2.30] Kabrits, S.A., Kolpak, E.P.

"Square Membrane Under Large Deformations."

Mechanics of Solids. Volume 21, 1986, pages 182-186.

[2.31] Seide, P.

"Large Deflections of Rectangular Membranes Under Uniform Pressure."

Int. Journal Non-linear Mechanics. Volume 12, 1977, pages 397-406.

[2.32] Allen, H.G., Al-Qarra, H.H.

"The Geometrically Non-linear Analysis of Transversely Loaded Membranes."

Int. Journal of Mech. Sci.. Volume 28, Number 7, 1986, pages 455-461.

[2.33] Oden, J.T., Sato, T.

"Finite Strains and Finite Displacements of Elastic Membranes by the Finite Element Method."

Int. Journal Solids and Structures. Volume 3, 1967, pages 471-488.

[2.34] Haug, E., Powell, G.H.

"Finite Element Analysis of Non-linear Membrane Structures."

Proceedings of IASS Symposium Part II on Tension Structures and Space Frames. Tokyo and Kyoto, 1972, pages 165-175.

[2.35] Argyris, J.H., Dunne, P.C., Haase, M., Orkisz, J.

"Higher-order Simplex Elements for Large Strain Analysis - Natural Approach."

Computer Methods in Applied Mechanics and Engineering. Volume 16, 1978, pages 369-403.

[2.36] Argyris, J.H., Balmer, H., Doltsinis, J.St., Dunne, P.C., Haase, M., *et al*

"Finite Element Method - the Natural Approach."

Computer Methods in Applied Mechanics and Engineering. Volume 17/18, 1979, pages 1-106.

[2.37] Smith, D.G., Peddieson, J., Chung, C.-J.

"Finite Deflection of a Shallow Spherical Membrane."

AIAA Journal. Volume 11, Number 5, May 1973, pages 736-738.

[2.38] Vishwanath, T., Glockner, P.G.

"Effects of Axi-symmetric Loads on Inflated Non-linear Membranes."

Int. Journal of Non-linear Mechanics. Volume 8, 1973, pages 345-369.

[2.39] Ueng, C.E.S., Sun, Y.S.

"Large Elastic Deformation of an Inflatable Membrane of Revolution."

AIAA Journal. Volume 12, Number 6, June 1974, pages 761-766

[2.40] Tseng, C.-G., Peddieson, J.

"Arbitrarily Large Deflections of Circular Membranes Due to Transverse Loading."

Journal of the Industrial Mathematics Society. Volume 34, Part 2, 1984, pages 181-191.

[2.41] Kao, R., Perrone, N.

"Large Deflections of Axi-symmetric Circular Membranes."

Int. Journal Solids and Structures. Volume 7, 1971, pages 1601-1612.

[2.42] Tworzydlo, W.W.

"Analysis of Large Deformations of Membrane Shells by the Generalised Finite Difference Method."

Computers and Structures. Volume 27, Number 1, 1987, pages 39-59.

[2.43] Barnes, M.R., Wakefield, D.

"Dynamic Relaxation Applied to Interactive Form-finding and Analysis of Air-supported Structures."

Proceedings of Conference on the Design of Air-supported Structures. I.Struct.E., Bristol, 1984, pages 147-161.

[2.44] Barnes, M.R.

"Non-linear Numerical Solution Methods for Static and Dynamic Analysis."

IL. (Institute of Lightweight Structures, Stuttgart University, Germany.) Publication Number 15, 1982, pages 150-166.

[2.45] Lewis, W.J., *et al*

"Dynamic Relaxation Analysis of the Non-linear Static Response of Pretensioned Cable Roofs."

Computers and Structures. Volume 18, Number 6, 1984, pages 989-997.

[2.46] Grindig, L.

"The Force-density Approach and Numerical Methods for the Calculation of Network s."

Proceedings 3rd Int. Symposium Weiggespannte Flachentragwerke, University of Stuttgart, 1985, pages 99-105.

[2.47] Bucholdt, H.A.

An Introduction to Cable Roof Structures.

Cambridge University Press, 1985.

[2.48] Lewis, W.J.

"The Efficiency of Numerical Methods for the Analysis of Prestressed and Pin-jointed Frame Structures."

Computers and Structures. Volume 33, Number 3, 1989, pages 791-800.

[2.49] Day, A.S.

"An Introduction to Dynamic Relaxation."

The Engineer. January 29th 1965, pages 218-221.

[2.50] Rushton, K.R.

"The Dynamic Relaxation Method Used for Stress Analysis."

Proceedings of Conference on Recent Advances in Stress Analysis. Royal Aeronautical Society, 26-29 March 1968, London, pages 3.41-3.46.

[2.51] Day, A.S., and Bunce, J.W.

"Analysis of Cable Networks by Dynamic Relaxation."

Civil Engineering Public Works Review. Number 4, 1970, pages 383-386.

[2.52] Cundall, P.A.

"Explicit Finite Difference Methods in Geomechanics."

Proceedings of E.F. Conference on the Numerical Methods in Geomechanics., Blacksburg, V.A., 1976.

[2.53] Barnes, M.R.

"Dynamic Relaxation Analysis of Tension Networks."

Proceedings of the Int. Conference on Tension Roof Structures. London, 1974, pages 1-11.

[2.54] Lewis, W.J., Jones, M.S., Rushton, K.R.

"Dynamic Relaxation Analysis of the Non-linear Static Response of Pretensioned Cable Roofs."

Computers and Structures. Volume 18, Number 6, 1984, pages 989-997.

[2.55] Barnes, M.R.

"Form-finding and Analysis of Prestressed Nets and Membranes."

Proceedings of the Int. Conference on Non-conventional Structures. Volume 1, 1987, pages 327-338.

[2.56] Zhang, L.G., Yu, T.X.

"Modified Adaptive Dynamic Relaxation Method and its Application to Elastic-plastic Bending and Wrinkling of Circular Plates."

Computers and Structures. Volume 33, Number 2, 1989, pages 609-614.

[2.57] Wood, W.L.

"Note on Dynamic Relaxation."

Int. Journal for Numerical Methods in Engineering. Volume 3, 1971, pages 145-147.

[2.58] Tarakanov, S.I.

"Convergence of the "Dynamic Relaxation" Method in Problems of Loading of Elastic Shells of Revolution."

Moscow University Mechanics Bulletin. Volume 39, Part 5, 1984, pages 53-56.

[2.59] Ergatoudis, I., Irons, B.M., Zienkiewicz, O.C.

"Curved, Isoparametric, "Quadrilateral" Elements for Finite Element Analysis."

Int. Journal of Solids and Structures. Volume 4, 1968, pages 31-42.

[2.60] Irons, B.M., Zienkiewicz, O.C.

"The Isoparametric Finite Element System - a New Concept in Finite Element Analysis."

Proceedings of Conference on Recent Advances in Stress Analysis. Royal Aeronautical Society, 26-29 March 1968, London, pages 3.35-3.40.

[2.61] Ahmad, S., Irons, B.M., Zienkiewicz, O.C.

"Analysis of Thick and Thin Shell Structures by Curved Finite Elements."

Int. Journal for Numerical Methods in Engineering. Volume 2, 1970, pages 419-451.

[2.62] Webster, W.D.

"An Isoparametric Finite Element with Nodal Derivatives."

Journal of Applied Mechanics, Transactions of the ASME. volume 48, March 1981, pages 64-68.

[2.63] Parisch, H.

"Non-linear Analysis of Shells Using Isoparametric Elements."

AMD Symp. Ser. ASME Applied Mechanics Division, Non-linear Finite Element Analysis of Plates and Shells. Presented at the Winter Annual Meeting of ASME, Washington, November 15-20, Volume 48, 1981, pages 47-63.

[2.64] Skvortsov, Yu.V., Khazanov, Kh.S.

"Non-linear Analysis of Arbitrary Shell Structures with Use of a Curvilinear Isoparametric Element."

Soviet Aeronautics. Volume 32, Part 2, 1989, pages 15-19.

[2.65] Bezeley, G.P., Cheung, Y.K., Irons, B.M., Zienkiewicz, O.C.

"Triangular Elements in Plate Bending, Conforming and Non-conforming Solutions."

Proceedings of the First Conference on Matrix Methods in Structural Mechanics. AFFDL-TR-CC-80, Wright-Patterson Air-Force Base, Ohio, 1965, pages 547-576.

[2.66] Irons, B.M., Razzaque, A.

"Experience with the Patch Test for Convergence of the Finite Element Method."

The Mathematical Foundations of the Finite Element Method with Applications to Partial Differential Equations. Ed. A.K. Aziz, Academic Press, 1972, pages 557-587.

[2.67] Strang, G.

"Variational Crimes and the Finite Element Method."

The Mathematical Foundations of the Finite Element Method with Applications to Partial Differential Equations. Ed. A.K. Aziz, Academic Press, 1972, pages 689-710.

[2.68] Fraeijs de Veubeke, B.

"Variational Principles and the Patch Test."

Int. Journal Numerical Methods in Engineering. Volume 8, 1974, pages 783-801.

[2.69] Stummel, F.

"The Limitations of the Patch Test."

Int. Journal Numerical Methods in Engineering. Volume 15, 1980, pages 177-188.

[2.70] de Arantes e Oliveira, E.R.

"The Patch Test and the General Convergence Criteria of the Finite Element Method."

Int. Journal Solids and Structures. Volume 13, 1977, pages 159-178.

[2.71] Robinson, J.

"The Patch Test - is it or isn't it ?" A Collection of Letters to the Editor by B.M. Irons, G. Strang, and F. Stummel.

Finite Element News. Issue 1, February 1982, pages 30-34.

[2.72] Razzaque, A.

"The Patch Test for Elements."

Int. Journal Numerical Methods in Engineering. Volume 22, 1986, pages 63-71.

[2.73] Taylor, R.L., Simo, J.C.

"The Patch Test - a Condition for Assessing FEM Convergence."

Int. Journal Numerical Methods in Engineering. Volume 22, 1986, pages 39-62

[2.74] Doherty, W.P., Wilson, E.L., Taylor, R.L.

"Stress Analysis of Axis-symmetric Solids Utilising High Order Quadrilateral Finite Elements."

Structural Engineering Laboratory. University of California, Berkeley, California, 1969.

[2.75] Zienkiewicz, O.C., Taylor, R.L., Too, J.M.

"Reduced Integration Technique in General Analysis of Plates and Shells."

Int. Journal Numerical Methods in Engineering. Volume 3, 1971, pages 275-290.

[2.76] Pawsey, S.F., Clough, R.W.

"Improved Numerical Integration of Thick Shell Finite Elements."

Int. Journal Numerical Methods in Engineering. Volume 3, 1971, pages 575-586.

[2.77] Zienkiewicz, O.C., Hinton, E.

"Reduced Integration, Function Smoothing and Non-conformity in Finite Element Analysis (with Special Reference to Thick Plates)."

Journal of the Franklin Institute. Volume 302, Numbers 5 & 6, November/December 1976, pages 443-461.

[2.78] Noor, A.K., Andersen, C.M.

"Mixed Models and Reduced/Selective Integration Displacement Models for Non-linear Shell Analysis."

AMD Symp. Ser. ASME Applied Mechanics Division, Non-linear Finite Element Analysis of Plates and Shells. Presented at the Winter Annual Meeting of ASME, Washington, November 15-20, Volume 48, 1981, pages 119-146.

[2.79] Malkus, D.S., Hughes, T.J.R.

"Mixed Finite Element Methods - Reduced and Selective Integration Techniques: a Unification of Concepts."

Computer Methods in Applied Mechanics and Engineering. Volume 15, 1978, pages 63-81.

[2.80] Stolarski, H., Belytschko, T.

"Shear/Membrane Locking in Curved Finite Elements."

Proceedings of Conference on the Recent Advances in Engineering Mechanics. Fourth Speciality Conference, Volume 2, 1983, pages 830-833.

[2.81] Stander, N., Wilson, E.L.

"A 4-Node Quadrilateral Membrane Element with In-plane Vertex Rotations and Modified Reduced Quadrature."

Eng. Comput. Volume 6, December 1989, pages 266-271.

[2.82] Sandhu, R.S., Singh, K.J.

"Reduced Integration for Improved Accuracy of Finite Element Approximations."

Computer Methods in Applied Mechanics and Engineering. Volume 14, 1978, pages 23-37.

[2.83] Haisler, W.E., Stricklin, J.A.,

"Rigid Body Displacements of Curved Elements in the Analysis of Shells by the Matrix-displacement Method."

AIAA Journal. Volume 5, Number 8, August 1967, pages 1525-1527.

[2.84] Mebane, P.M., Stricklin, J.A.

"Implicit Rigid Body Motion in Curved Finite Elements."

AIAA Journal. Volume 9, Number 2, February 1971, pages 344-345.

[2.85] Cantin, G., Clough, R.W.

"A Curved, Cylindrical Shell, Finite Element."

AIAA Journal. Volume 6, Number 6, pages 1057-1062.

[2.86] Cantin, G.

"Rigid Body Motions in Curved Finite Elements."

AIAA Journal. Volume 8, Number 7, pages 1252-1255.

[2.87] Dawe, D.J.

"Rigid Body Motions and Strain Displacement Equations of Curved Shell Finite Elements."

Int. Journal Mech. Sci.. Volume 14, 1972, pages 569-578.

[2.88] Fonder, G.A., Clough, R.W.

"Explicit Addition of Rigid Body Motions in Curved Finite Elements."

AIAA Journal. Volume 11, Number 3, March 1973, pages 305-312.

[2.89] Hansen, J.S., Heppler, G.R.

"A Mindlin Shell Element that Satisfies Rigid Body Requirements."

AIAA Journal. Volume 23, Number 2, February 1985, pages 288-295.

[2.90] Yang, T.Y., Kapania, R.K., Saigal, S.

"Accurate Rigid Body Modes Representation for a Non-linear Curved Thin Shell Element."

AIAA Journal. Volume 27, Number 2, February 1989, pages 211-218.

[2.91] Jagannathan, D.S., Epstein, H.I., Christiano, M.

"Fictitious Strains Due to Rigid Body Rotation."

Journal of the Structural Division, ASCE. Volume 101, Number ST11, November 1975, pages 2472-2476.

[2.92] Yang Y.-B., Chiou, H.-T.

"Rigid Body Motion Test for Non-linear Analysis with Beam Elements."

Journal of Engineering Mechanics. Volume 113, Number 9, September, 1987, pages 1404-1419.

[2.93] Lui, W., Yang Y.-B.

"General Eigenvalue Test for Non-linear Finite Elements."

Proceedings of the Fourth Int. Conference Civil Structural Eng. Comp., Civil Comp. 89. London, September 19-21, 1989, pages 345-350.

[2.94] MacNeal, R.H.

"Toward a Defect-Free Four-Noded Membrane Element."

Finite Elements in Analysis and Design. Volume 5, 1989, pages 31-37.

[2.95] Brailloulis, D.

"The C^0 Shell Plate and Beam Elements Freed from their Deficiencies."

Computer Methods in Applied Mechanics and Engineering. Volume 72, 1989, pages 243-266.

[2.96] Cook, R.D., Zhao-Hua, F.

"Control of Spurious Modes in the Nine Node Quadrilateral Element."

Int. Journal Numerical Methods in Engineering. Volume 18, Number 10, October 1982, pages 1576-1580.

[2.97] Vu-Quoc, L., Mora, J.A.

"A Class of Simple and Efficient Degenerated Shell Elements - Analysis of Global Spurious Mode Filtering."

Computer Methods in Applied Mechanics and Engineering. Volume 74, 1989, pages 117-175.

[2.98] Fried, I.

"Possible Loss of Accuracy in Curved (Isoparametric) Finite Elements - Comment on a Paper by Henshell, Walters and Warburton."

Journal of Sound and Vibration. Volume 23, pages 507-510.

[2.99] Henshell, D., Walters, D., Warburton, G.B.,

"Possible Loss of Accuracy in Curved (Isoparametric) Finite Elements."

Journal of Sound and Vibration. Volume 23, pages 510-513.

[2.100] Celia, M.A., Gray, W.G.

"An Improved Isoparametric Transformation for Finite Element Analysis."

Int. Journal Numerical Methods in Engineering. Volume 20, 1984, pages 1443-1459.

[2.101] Robinson, J.

"Some New Distortion Measures for Quadrilaterals."

Finite Elements in Analysis and Design. Volume 3, 1987, pages 183-197.

[2.102] White, D.W., Abel, J.F.

"Testing of Shell Finite Element Accuracy and Robustness."

Finite Elements in Analysis and Design. Volume 6, 1989, pages 129-151.

Chapter 3

Experimental Solutions to Stable Minimal Surfaces.

3.1. Introduction.

This chapter presents the following aspects related to the modelling of stable minimal surfaces:

- a historical summary of "minimal surfaces",
- the mechanisms involved in the formation of a soap-film,
- descriptions of the apparatus for the experimental measurements of surfaces and of the modelling technique,
- the experimental solutions, and the question of the stability of minimal surfaces.

3.2. Historical Summary of "Minimal Surfaces" [3.1].

Minimal surfaces are described as three-dimensional surfaces whose mean curvature, H, is zero at all points on the surface. Minimal surfaces can therefore be characterised mathematically as,

$$H = \frac{k_1 + k_2}{2} = 0 . \qquad \text{eqn(3.2.1)}$$

where k_1 and k_2 are the principal curvatures of the surface at the point of interest.

From eqn(3.2.1), for a surface to be a minimal surface, the two principal curvatures, k_1 and k_2, can be seen to be of equal magnitude and of opposite sign. Consequently, all non-flat minimal surfaces are locally anti-clastic, or have the shape of a saddle surface.

The relationship between the geometrical classification of "minimal surface" and eqn(3.2.1) is based on the requirement that the surface with a minimum area (within a given boundary) must necessarily comply with eqn(3.2.1) for all points on the surface. This finding is attributed to the French geometer Meusnier and was published in a paper in 1785. Furthermore, surfaces possessing a minimum area are minimal surfaces, but minimal surfaces are not necessarily surfaces of minimum area - in general for the minimal surface, ms_1, there exists another surface, ms_2, which is local to ms_1, but possesses a smaller surface area when bounded by the same

boundary contour. This is often the case when one of the lamellae comprising the surface ms_1 is removed, for example.

The connection between the minimal surface and a surface of minimum area, can be realised through the physical theory of soap-films. This constitutes part of the phenomenological theory of capillary action, published in 1805 by Young, and derived later from the principle of virtual work by Gauss [3.1].

The principle of virtual work can be stated as [3.1];

(i) "the stable states of equilibrium (or states of rest) of a physical system are characterised in that, in such a state, the potential energy of the system is smaller than in any other possible (or "virtual") local state",

(ii) "the equilibrium states of a physical system are the stationary states of its potential energy".

According to the work by Gauss (1880) a soap-film can be analysed as a physical system, where the potential energy of the surface is proportional to its area, given that the factor of proportionality is a material constant. The surfaces of minimum area can therefore be described as the mathematical models of a soap-film in a state of stable equilibrium. It is thus appropriate to use soap-film models as analogues to stable minimal surfaces.

3.3. Mechanisms Involved in the Formation of a Soap-film [3.2].

The formation of the soap-film and the regulation of its behaviour are controlled by the principle of virtual work given above. In the case of a soap-film, the energy of the surface is described in terms of the surface tension of the constituent liquid. Considering the case of water initially, the surface tension of the liquid is generated by the forces of attraction between the separate molecules and the imbalance of these forces on the boundary of the surface. The effect of the forces of attraction is to transform the liquid film, located at the interface between the liquid (water) and the external medium (air), into an elastic film which tends to minimise its own area, and consequently to minimise the energy of the surface tension taken over a unit area. It is assumed in this case that the existence of gravity and of a pressure differential across the surface, are ignored and so do not contribute to the energy of the surface. The effects of adding a soap or a detergent material to water are summarised below [3.3].

In contrast to the polar molecules of water, the molecules of a soap or of a detergent consist typically of long, slender, non-polar hydrocarbon chain with a highly polar oxygen-rich group attached at one end. When such molecules are added to water, they tend to migrate to the surface of the liquid, and orientate themselves so that their non-polar ends are protruding through the liquid film. This has the effect of reducing the surface tension of the liquid and increasing the general elasticity of the surface.

When the layer of soap molecules is stretched however, by a moving wire for example, the surface tension is increased, due to a temporary decrease in the number of soap molecules per unit area. This has the effect of giving the surface additional stabilising elastic properties, very much like a prestress in a structural membrane. Furthermore, the addition of a soap material or a detergent to water limits the thinness of the film made from a soap-water solution to the length of two soap molecules stacked end to end. By combining the above effects, it is therefore possible to establish a thin elastic membrane, spanning a given contour, when a thin wire contour is dipped into a soap solution.

3.4. Soap-film Formulation [3.1].

In the case of all of the experimental solutions presented subsequently, the fundamental constituent of the soap-film solution is a commercially available detergent, "Pustefix", produced by Messrs. Dr. Rolf Hein KG, Tuebingen, Stuttgart, Germany. The "Pustefix" solution consists mainly of a negatively charged detergent, in conjunction with chemical products, wetting agents and a thickening substance. In addition, the mixture also contains a dissolving agent and a bacteriacide. It is highlighted in reference [3.1] that the substances listed above are not chemically pure. A solution which is chemically very pure has been found, in the past, to produce very much more stable surfaces. However, such solutions are not available commercially.

To increase the workability of the "Pustefix" solution, a solvent in the form of distilled water is added, along with glycerine to improve the durability of the film. In the case of the surfaces presented in Plates 3.1 - 3.13, the "Pustefix" solution is diluted in the ratio of one part "Pustefix" to two parts of distilled water, with 10% of glycerine (by volume). Conversely, for the two dimensional surfaces (Plates 3.14 - 3.19) a total of approximately 30% of glycerine was added in order to enhance the stability of the soap-film further.

3.5. Minimal Surface Apparatus [3.1].

In order to make a permanent record of the minimal surface forms described by the soap-film models, the soap film must be sufficiently durable. The durability of the surface film can be enhanced by altering the chemical composition of the solution as described in the preceding section. In addition, the durability of the surface can be augmented by protecting the model from air turbulence, and by placing it in a dust free environment, possessing a high degree of humidity and a low temperature.

The purpose-built apparatus, illustrated by the schematic diagram presented in Figure 3.1, has been designed according to the above criteria at the Institute of Lightweight Structures (IL), University of Stuttgart, Germany. This apparatus has been used to make the permanent records of the soap-film models, Plates 3.1 - 3.19, presented in this chapter. A brief description of the main details of the apparatus is given below.

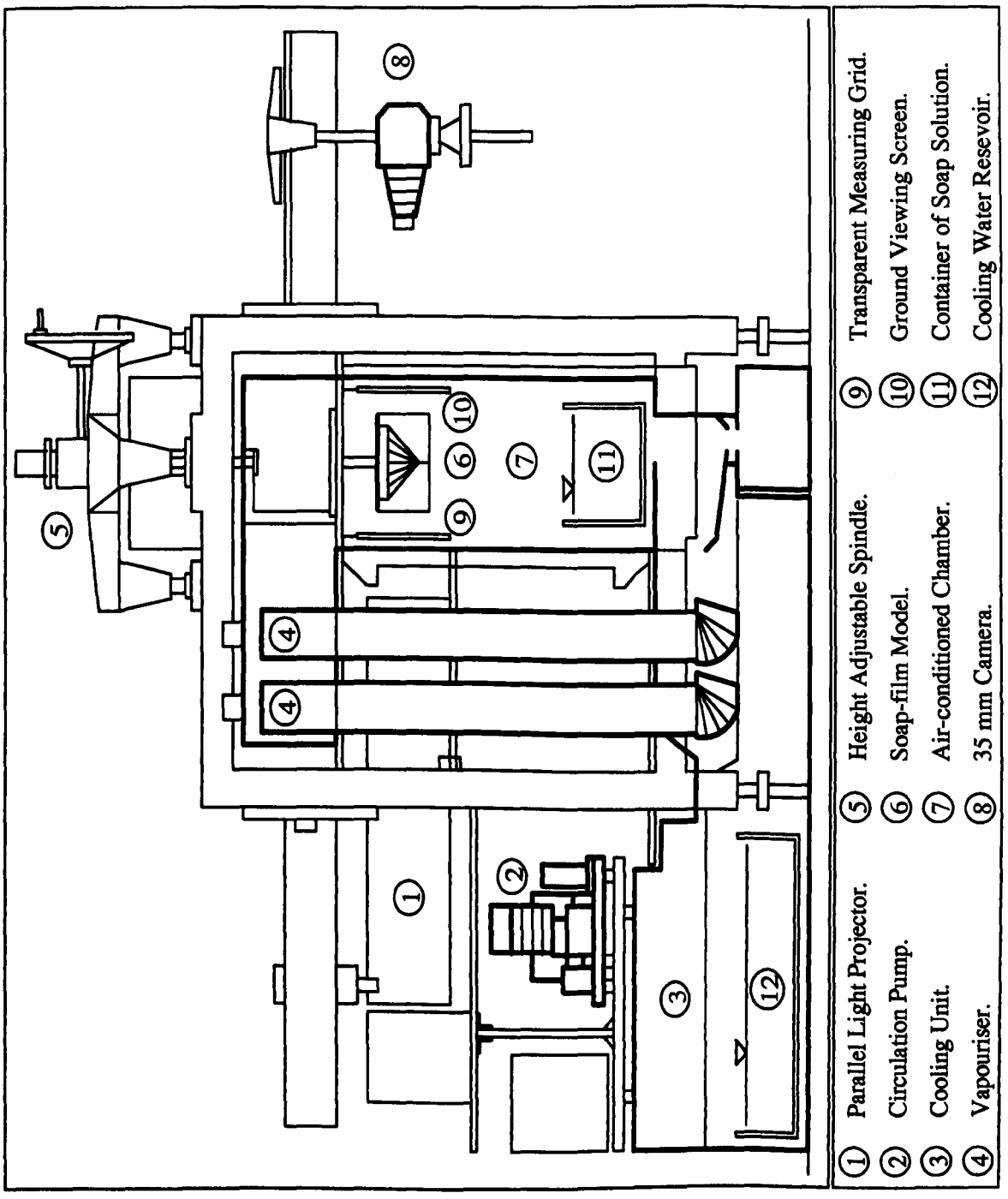

Figure 3.1 - Minimal Surface Apparatus.[3.1]

The air-conditioned chamber (3), into which the soap-film model (6) is placed, comprises four vertical glass walls and two acrylic sheets, located at the base and at the top, connected and sealed with rubber gaskets. A steel frame is used to support the chamber, on top of which a height-adjustable spindle (5) is located. The latter projects into the chamber and supports the "model ring". The "model ring" comprises a thin aluminium frame and a Perspex ring through which screw tappings can be made, and is used to support the model under investigation. It is capable of rotating through 360° in the horizontal plane, and through 180° in the vertical plane, to permit viewing of the model from all angles.

A container holding the soap solution (11) is located beneath the model and can be lifted in the air-conditioned chamber for immersion of the model. External to the rear side of the chamber, a parallel light projector is located (1), with a 35 mm camera (8) placed external to the opposite side. To aid the measurement of the geometry of the soap-film surfaces from the photographs, a transparent measuring grid (9), with centimetre divisions, and a ground screen (10), are suspended inside the air-conditioned chamber, in front of the parallel light projector and the camera respectively. The shadow of the model is therefore projected on the ground screen, from which the permanent record is made. The light source is provided by a high pressure mercury vapour lamp.

A reservoir of cooling water (12) is located behind the main body of the apparatus, from above which cool air is extracted. The cooling water is continuously circulated by a diaphragm pump (2), and vapourised by two multi-nozzle tubes (4) positioned in the side of the air-conditioned chamber. The descending water vapour ensures a good circulation of cooling air in the chamber without disturbing the model. The vibrations of the water pump and of the cooling unit are isolated from the chamber by rubber bearings, to prevent blurring of the photographs and the possible destruction of the soap-film.

3.6. Soap-films.

3.6.1. Model Construction.

Minimal surfaces which are formed from a soap solution are termed "self-generating" [3.1] surfaces - no external loading is used to dictate the geometry of the form. The shape of the model (and therefore the geometry of the surface) is a function of the boundary. The boundary in the physical model (comprising rigid wires, deformable threads, or intersecting lamellae) may deviate from the ideal (assumed) form adopted for the numerical representation of the surface, due to the practical tolerances of forming the physical boundary. Consequently, disparities between the experimental and numerical solutions are introduced. A further error can an also be incurred by the effects of the self-weight of the soap-film. For this reason, and for the practical

consideration of the immersion of the model, suitable overall dimensions of the model have been recommended as 150 mm - 200 mm [3.1].

In the case of the models illustrated in Plates 3.1 - 3.9, a thin copper wire, with a diameter of 1.25 mm, is used to form the "rigid" boundary of the surface. The wire is bent into shape and soldered at the two free ends to form a "closed" boundary. The influences of the boundary on the geometry of the soap-film surface can be minimised by the use of a thin wire for this purpose [3.1]. However, the adoption of a wire which is too thin can lead to errors in the physical model, arising from deformations of the boundary due to the effects of the surface tension of the soap-film.

The models illustrated in Plate 3.10 and Plate 3.11 represent an elliptical form of the catenoid shown in Plates 3.7 - 3.9. The use of thin wire to form the boundaries of the elliptical models leads to difficulties in the theoretical definition of the boundary of the physical model which deviate from the assumed elliptical shape. The initially straight wire tends to form a circle when the two ends are joined, an effect arising from the natural stiffness of the wire. Therefore the wire needs to be deformed plastically in order to achieve the desired shape. This procedure is found to be impractical.

The design of the more complicated model illustrated in Plate 3.10 and Plate 3.11, is based on the requirements that the boundaries are geometrically accurate, that they are concentric, and that they are made from a thin material, so as to keep the distortion of the soap-film surface to a minimum. In addition it is also required that the separation of the boundaries can be measured accurately.

The model comprises two Perspex discs with the profile of the ellipse engraved by a computer controlled lathe, to a depth of 3.0 mm, and to a width of 1.0 mm. Into each groove a vertical copper strip is inserted and soldered together at the two free ends. The copper strip projects approximately 2.0 mm above the surface of the Perspex disc, and provides the fixed boundary for the soap-film. The Perspex discs are connected by two threaded bars, along which the lower disc can be moved in order to increase or to decrease the separation of the discs.

A thin acrylic thread is used to form the boundaries of the of the models illustrated in Plates 3.16 - 3.19. The boundary threads are supported by four Perspex stanchions, which are, in turn, located on a circular base plate of the same material. The stanchions are positioned in the form of a square. The boundary thread, which is used to generate the hole in the soap-film (Plates 3.17 - 3.19), is formed as a loop at the end of a long thread, and suspended above the centre of the surface from an additional stanchion.

The boundaries of the surfaces illustrated in Plates 3.20 - 3.22 are established in a similar manner to that described in the preceding paragraph. The physical modelling of the surface illustrated in Plates 3.20 - 3.22 is acknowledged to the Institute of Lightweight Structures (IL), University of Stuttgart, Germany (Section 3.6.4.2).

3.6.2. Experimental Solutions.

3.6.2.1. General Surfaces with Rigid Boundaries.

The soap-film surface illustrated in Plate 3.1 and Plate 3.2 has overall dimensions on plan of 152.5 mm × 232.0 mm. The longer side of the model possesses a discontinuity of slope at approximately the mid-point, giving rise to an overall depth of the model of 31.8 mm.

The wire frame is not precisely rectangular (Plate 3.1 and Plate 3.2). In particular, it is shown that at the extreme right of the model (as viewed in Plate 3.1) the boundary wire appears much thicker than in other regions, indicating a distortion of the frame out of the plane of the photograph. Similar features can be seen in Plate 3.2, and lead to errors in the measurement of the soap-film surface profile. The low value for the ratio of the length of the longer side of the model to the depth out-of-plane, gives rise to a surface of slowly changing curvatures.

Plate 3.3 and Plate 3.4 illustrate a similar surface to the preceding example. In this case however, the discontinuity of slope is located at approximately the mid-point of the shorter side. The model overall dimensions are 126.0 mm × 188.7 mm on plan, with an overall depth of 63.5 mm.

In order to satisfy eqn(3.2.1), the soap-film surface can be seen to exhibit rapidly changing principal curvatures. This leads to an almost vertical surface at the discontinuities of slope in the boundary of the model, as illustrated in Plate 3.3. Consequently, the soap-film surface is obscured by the boundary wire in this region. A measurement of the surface profile of the model is also not possible at the left side of the model (as viewed in Plate 3.3), due to the positioning of the supporting wire to the "model ring".

Plate 3.5 and Plate 3.6 present the experimental solution to a curved, sinusoidal type of boundary. The overall dimensions of the model are 124.0 mm × 146.0 mm on plan, with an overall depth of 106.0 mm.

It was intended that the model should be symmetrical about each principal plane. However, the obvious disparity in the geometry of the boundary in the foreground and in the background when viewing the model along the principal axes, Plate 3.5 and Plate 3.6, illustrates, again, the

difficulties in producing an accurate, curved (non-circular) boundary, when formed from a thin wire. The resulting soap-film surface is, nevertheless, characterised by curvatures of similar magnitude in the principal directions.

An error has been introduced when photographing the soap-film surface (Plate 3.5, Plate 3.6), by not ensuring that the wire model was positioned vertically in the air-conditioned chamber of the apparatus. The error is realised by a difference between the position of the central point of the soap-film surface in the global z direction, when viewing the model along the two principal axes. The profiles of the soap-film surface as given by Plate 3.5 and by Plate 3.6, possessing this error, have been used in Chapter 4 (Figure 4.12 (a)&(b), Figure 4.22 (a)&(b))and in Chapter 6 (Figure 6.21, Figure 6.22), for comparison of the experimental and numerical solutions.

In the case of the three examples presented above, the soap-film surfaces have been obtained by the total immersion of the wire models in the soap solution, and by their subsequent withdrawal. No further manipulations of the models, including the breaking of superfluous lamellae, are required in these cases.

3.6.2.2. Single Minimal Surfaces Between Two Frames and the Question of the Stability of Minimal Surfaces.

Two unconnected frames can be joined by a soap lamella exhibiting a single minimal surface. Such a minimal surface, when generated between two concentric rings, is an axi-symmetric surface, or a surface of revolution (Plate 3.7). The shape of the surface is termed a catenoid and can be generated geometrically by rotating a catenary line around a vertical axis. The surface was described by Euler in 1744 and is the only minimal surface which is, at the same time, a surface of revolution.

The height of the catenoid has a maximum attainable value, as given by the separation of the rings. For the case of the catenoid formed between two circular rings of the same diameter, the maximum separation is directly proportional to the radius of the rings. A classical solution to the surface description of the catenoid, for the axi-symmetric case of two circular rings of differing diameters connected by a soap-film (with equal pressures on each side), has been presented by Trostel [3.4]. This solution is summarised below.

Considering the case of a ring of radius $r = r_a$, and a concentric ring of radius $r = r_i$, with the separation of the rings denoted as h, the surface of the soap-film can be described by the expression,

$$z = C_1 \int_r^{r_a} \left[\sqrt{r^2 - C_1^2} \right]^{-1} dr$$

$$= C_1 \left[\cosh^{-1}\left[\frac{r_a}{C_1} \right] - \cosh^{-1}\left[\frac{r}{C_1} \right] \right], \qquad \text{eqn(3.6.2.2.1)}$$

where z is the position of a circle of radius r, which describes part of the surface of the catenoid, above the ring of radius $r = r_a$, and where C_1 is a constant of integration.

Writing $\frac{z}{r_a} = \xi$, $\frac{C_1}{r_a} = \overline{C_1}$, and, $\frac{r_i}{r_a} = \zeta$, eqn((3.6.2.2.1) can be rewritten as,

$$\zeta = \overline{C_1} \cosh \left[\frac{\xi - \overline{C_1} \cosh^{-1}\left[\frac{1}{\overline{C_1}} \right]}{\overline{C_1}} \right] \qquad \text{eqn(3.6.2.2.2)}$$

Several values of $\overline{C_1}$ can be selected to generate a family of curves, relating the separation of the rings, h, to the ratio $\frac{r_i}{r_a}$ [3.4]. However, due to the characteristics of the hyperbolic cosine curve expressed in eqn(3.6.2.2.2), if $r = r_i$ is given, h cannot be selected arbitrarily. For example, in the case of two circular rings of equal diameter such that $\zeta = \frac{r_i}{r_a} = \frac{r}{r_a} = 1.0$, eqn(3.6.2.2.2) is written as,

$$\xi = 2\ \overline{C_1}\ \cosh^{-1}\left[\frac{1}{\overline{C_1}} \right] \qquad \text{eqn(3.6.2.2.3)}$$

To find the maximum attainable separation of the rings, it is necessary to maximise the preceding equation with respect to $\overline{C_1}$. With a trial method of solution, ξ is maximised at the value of 1.3255, with $\overline{C_1} = 0.552$. Therefore, for the case of a single surface, generated between two circular rings of equal diameter, the maximum attainable separation is 1.3255 times the radius of the rings.

Physical model experiments conducted at the Institute of Lightweight Structures (IL), University of Stuttgart, Germany, have also shown that the maximum attainable separation of the equal diameter rings, is approximately 1.3 times the ring radius [3.1]. An example of these experiments is presented in Plate 3.7. In this case two 80.0 mm diameter concentric rings were used to generate the form.

The rings are initially placed at a separation of 1 - 2 mm, and the complete model immersed in the soap solution. Upon removal of the model from the soap solution, the lower ring was displaced in a vertical direction by approximately 25 mm, so that it remained concentric with the upper one, yielding a minimal surface. The minimal surface which is obtained from this procedure is shown in Plate 3.8.

This minimal surface comprises four lamellae - a vertical lamella filling the right region of the model, and generating a surface between the wires used to support the rings, and two symmetrical lamellae, one commencing from the upper and from the lower ring respectively, and connected by a fourth horizontal lamella, located at the mid-point between the rings.

Breaking the vertical lamella yields the minimal surface illustrated in Plate 3.9. This surface clearly possesses a lower surface area than the minimal surface illustrated in Plate 3.8. The catenoid is obtained by removing the horizontal lamella shown in Plate 3.9, and can be described as a minimal surface with a minimum surface area for the wire boundary configuration (Plate 3.7). A comparison of 3.9 with Plate 3.7 clearly illustrates the statement presented in Section 3.2 - "minimal surfaces are not necessarily surfaces of minimum area".

It is suggested in reference 3.2 that an infinite-dimensional space can be established, in which the set of all two dimensional surfaces that span wire contours, exists. An area functional can then be defined which associates an area with each point on the surface, such that a change in the geometry of the surface, changes the value of the area functional. At equilibrium, the two dimensional surface describes a critical state for the area functional, which may be classified as a local maximum, local minimum, or as a point of inflection (saddle point) [3.2].

If the area functional is at a local minimum the condition of the state of equilibrium of the surface is described as "stable". Conversely, a point of inflection reflects an unstable equilibrium state - the application of a small perturbation (displacement) to the surface gives rise to a change in the geometry of the surface, such that it does not return to its original form. In this case the surface adopts a configuration with a lower energy, and which can be considerably different to the original one. The subsequent paragraphs describe the manifestation of stable and unstable surfaces.

It is suggested here that the classification of the stability of the equilibrium state of the surface can be assessed by two criteria - the geometry of the surface subsequent to the application of a finite perturbation, and the geometry of the surface after the application of an infinitesimal perturbation.

For example, in the case of the catenoid minimal surface, the boundary rings may be placed at the maximum separation. A finite perturbation in the form of a displacement causing a small increase in the separation of the rings, can lead to the catenoid soap-film surface breaking, and forming two independent minimal surface discs in the upper and lower rings. The original minimal surface is clearly not recovered after the removal of the perturbation, indicating the instability of the original catenoid surface in this case. It is further suggested here that a surface which is classified as "unstable" when it is subjected to a finite perturbation can be formed by using a soap-film model. The "unstable" equilibrium state which is defined by an infinitesimal perturbation is described below.

In the case of the catenoid, the geometric requirement given by eqn(3.2.1) can be expressed diagrammatically, as illustrated by Figure 3.2 [3.2].

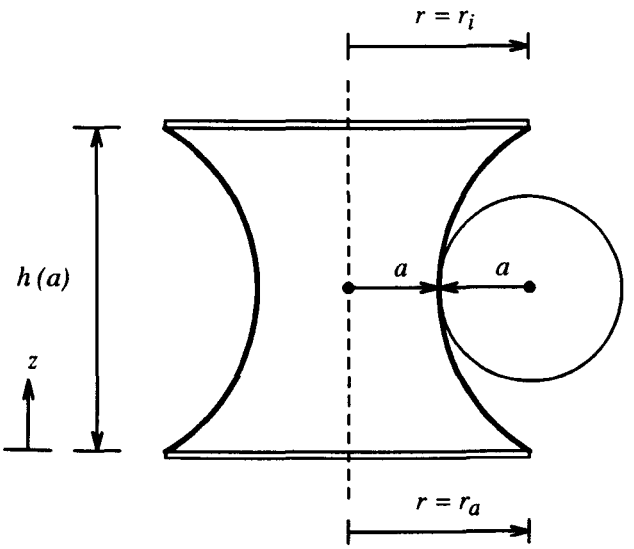

Figure 3.2 - Diagrammatic Representation of Eqn(3.2.1).

At $z = \frac{h(a)}{2}$, the curvature of the surface in the horizontal plane can be seen to be measured by the radius of the catenoid $r = a$, describing the surface at that point. It follows that, in order to satisfy eqn(3.2.1), the curvature of the surface in the vertical plane is similarly described by a circle of radius a. It is suggested in reference [3.2] that the parameter a (taken as the radius of the circle in this case) varies from zero to infinity. However, if $a > r$, where r is the radius of the rings used to form the catenoid, then a minimal surface cannot be formed if eqn(3.2.1) is to be satisfied. In the case that $a = r$, the sides of the catenoid are vertical, indicating that $h(a) = 0$ and that the rings are in contact (Figure 3.2).

Due to the nature of the hyperbolic cosine curve describing the surface geometry of the catenoid, it is found that as a is decreased from $a = r$ the separation of the rings, $h(a)$, increases until a maximum value of separation is attained. As a tends to zero, $h(a)$ also tends to zero. The relationship between a and $h(a)$ is presented in Figure 3.3 [3.2].

It is shown that for a single value of ring separation, $h(a)$, two values of a are obtained, indicating the possible existence of two minimal surfaces (Figure 3.4). It was conjectured by Plateau, and subsequently proven, that the minimal surface with the smaller value of a is an "unstable" minimal surface, and cannot be modelled using a soap-film [3.2]. It is suggested here that such minimal surfaces are unstable when subjected to an infinitesimal perturbation - as the soap-film surface is developed both the surface geometry and the soap-film itself are in a state of flux, which is sufficient to make the surface pass through the configuration given by the lower value of a, and to continue to the stable state at $a = a_1$ (Figure 3.3).

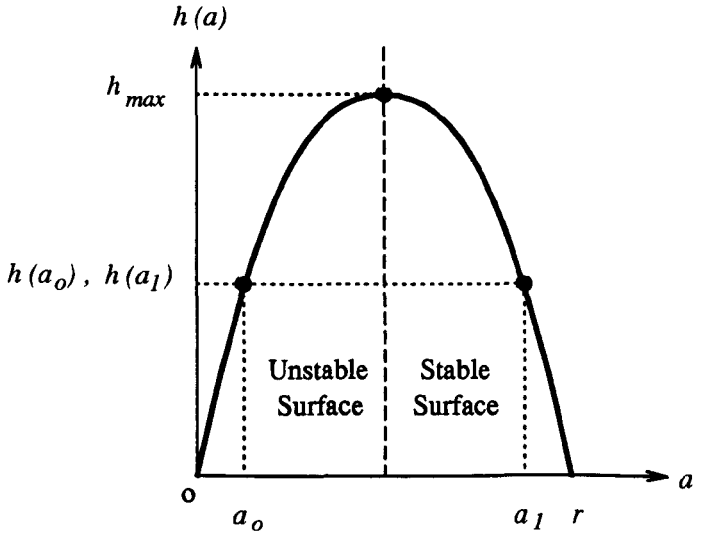

Figure 3.3 - Variation of the Ring Separation, h, with the Parameter a.

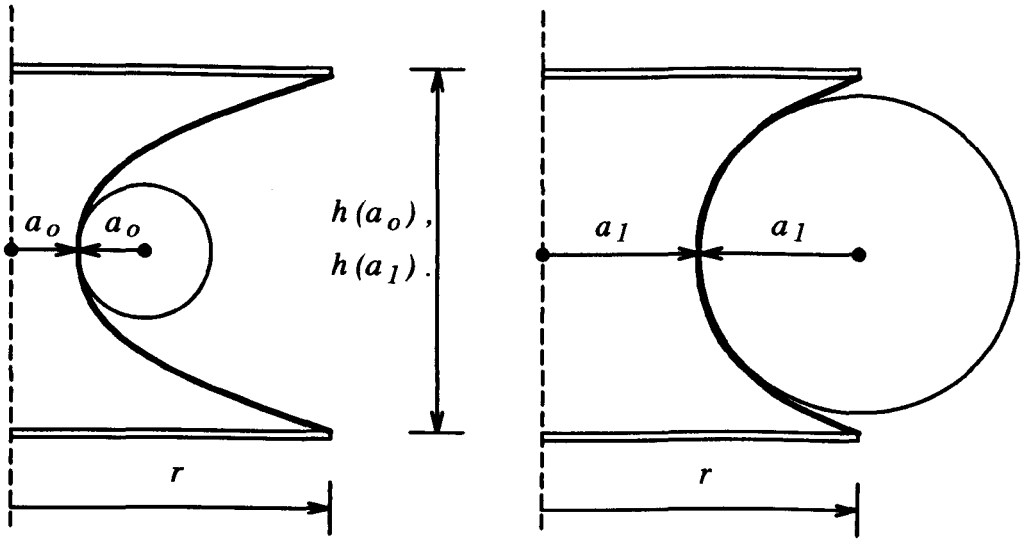

Figure 3.4 - Example of Two Minimal Surfaces with the Same Ring Separation, and Satisfying Eqn(3.2.1).

Therefore, the condition of equilibrium classified as "unstable" when the surface is subjected to an infinitesimal perturbation, cannot be illustrated by a soap-film model. In addition, the preceding example clearly shows that eqn(3.2.1) is a necessary, and not a sufficient, condition for a surface to be a stable minimal surface. Instead, the condition of minimum surface energy (or minimum surface area) must be satisfied.

The minimal surface illustrated in Plate 3.12 and Plate 3.13, is obtained from the model shown in Plate 3.10 and Plate 3.11. The boundaries of the model are given by ellipses, and the resulting minimal surface constitutes a more general form of the catenoid. Three models of this type have

been investigated. Two of the models are described by a minor axis diameter of 80.0 mm, and by major axis diameters of 120.0 mm and 160.0 mm, respectively. These dimensions give the values for the ratio of the major axis diameter to the minor axis diameters, of 1.5 and 2.0 respectively. In the case of the third model, the minor axis diameter is 66.5 mm, with the corresponding major axis diameter equal to 200.0 mm. The soap-film surface illustrated in Plate 3.12 and Plate 3.13 is generated in the manner described below.

The Perspex blocks which are visible on the underside of the lower sheet of Perspex in Plate 3.11, are unscrewed down the threaded rods to a pre-determined level below the top sheet of Perspex - 65.0 mm, 78.0 mm, and 70.0 mm for the three models described above, respectively. The lower sheet of Perspex is next raised to meet the top sheet, and wedged into position so that a gap of not greater than 10 mm existed between the two sheets. The complete model is then immersed in the soap-solution.

After removing the superfluous lamellae, which typically forms between the threaded bars and the copper ellipses, the lower Perspex sheet is carefully lowered onto the pre-positioned Perspex blocks. With equal rotations of these blocks, the lower Perspex sheet is lowered in order to increase the separation of the ellipses. At this intermediate stage, photographs are taken (Plates 3.10 - 3.13). Subsequently the separation of the ellipses is increased, until the soap-film surface collapses, and fills the upper and lower ellipses, respectively. At the point of collapse the separation of the ellipses is measured. An average value for the measurements of the separation, made using this technique, are presented in Table 4.8 (Section 4.5.3), Chapter 4.

3.6.2.3. Minimal Surfaces with Internal and External Flexible Boundary Elements.

A comparison of Plate 3.14 with Plate 3.15 shows the effect of increasing the length of the boundary threads on the form of a plane minimal surface. Prior to the immersion of the model in the soap solution, the threads are adjusted to the required lengths, and are unstressed (ignoring self-weight). Withdrawing the model from the solution reveals a soap-film surface spanning between the boundary threads. The boundary threads are uniformly stressed, and their geometries define an arc, which is also given by the equation of a circle [3.1].

From Plate 3.14 and Plate 3.15 the adoption of boundary threads which are significantly longer than the distance between the fixed boundary points at the corners of the model, can be seen to lead to the merging of the boundary threads in the vicinity of these points. This feature arises as the soap-film attempts to minimise its surface area, and therefore to minimise its surface energy, in order to satisfy the condition of equilibrium.

To obtain the minimal surfaces illustrated in Plates 3.16 - 3.19, a similar procedure to that described above is adopted. In this case however, the external boundary threads (spanning between the fixed boundary points), are chosen to have unequal lengths, in order to show the

more general form of the plane minimal surface (Plates 3.16 - 3.19). The hole in the soap-film is introduced by placing the loop on the surface, and by ensuring that the thread is completely wetted initially (Plate 3.16). Subsequently, the soap-film inside the loop is broken by a blunt, dry object (a sharp object simply punctures the film, which then immediately self-repairs).

In order to equilibriate the form, the loop is immediately stressed by the surface tension of the soap-film, and adopts the form of a circle (Plate 3.17). Due to the nature of the soap-film solution, the stressed loop moves freely about the surface, without affecting either the form of the loop, or the form of the boundary threads. This phenomenon is illustrated in Plate 3.18, and reflects, in addition to the circular form of the boundary threads, the uniform and the constant surface tension exhibited by the soap-film. This feature is also shown by Plate 3.19, where effectively two minimal surfaces are generated by the introduction of a loop in the corner region of the original soap-film.

Plates 3.20 - 3.22 illustrate the general three-dimensional minimal surface, "Siegfried's Tent". The model comprises nine fixed boundary points, and the same number of boundary threads. The surface is characterised by rapidly changing curvatures, generated primarily through the adoption of a high central mast head. The co-ordinates of the fixed boundary points, and the lengths of the boundary threads, are presented in Table 4.9 (Section 4.6, Chapter 4). Further details related to the conception of the model can be found in reference [3.5].

Plate 3.20 and Plate 3.21 illustrate the minimal surface spanning the given boundary contour, represented by a soap-film surface. Plate 3.22 show the same surface, described using a hexagonal tulle. In this case, the shape of the hexagonal patterns of the fabric are kept constant during the stretching of the tulle between the boundary contours. This condition is required in order to model the condition of uniform surface stress [3.5].

3.6.2.4. Acknowledgement.

The copies of the Plates 3.20 - 3.22, supplied by the Institute of Lightweight Structures (IL), University Stuttgart, Germany, are gratefully acknowledged. These Plates may be identified under the following IL references: Plate 3.20 → 5.20.132, Plate 3.21 → 5.20.122, Plate 3.22 → 5.20.110.

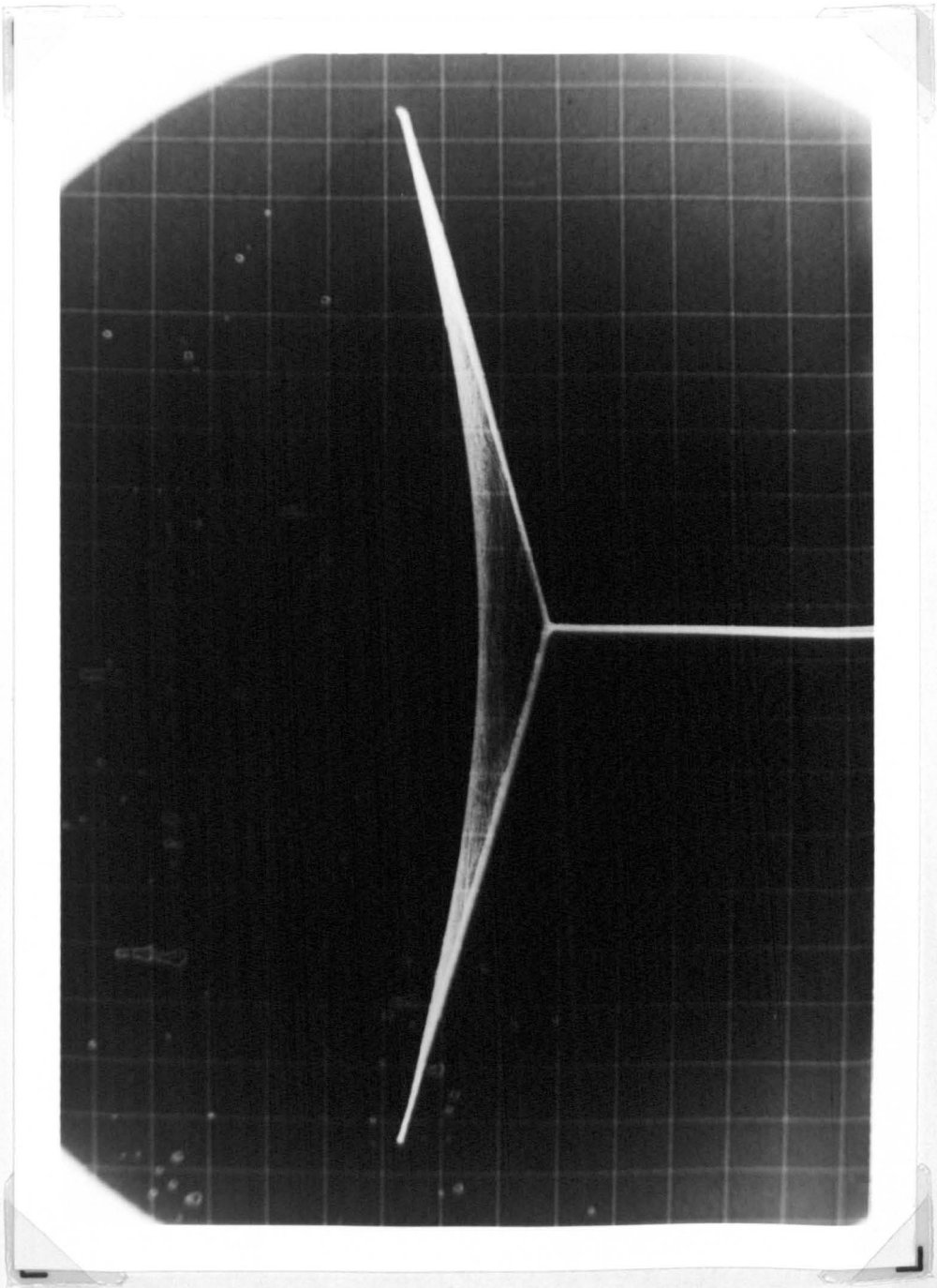

Plate 3.1 - General Surface with Rigid Boundaries - z –x Central Plane.

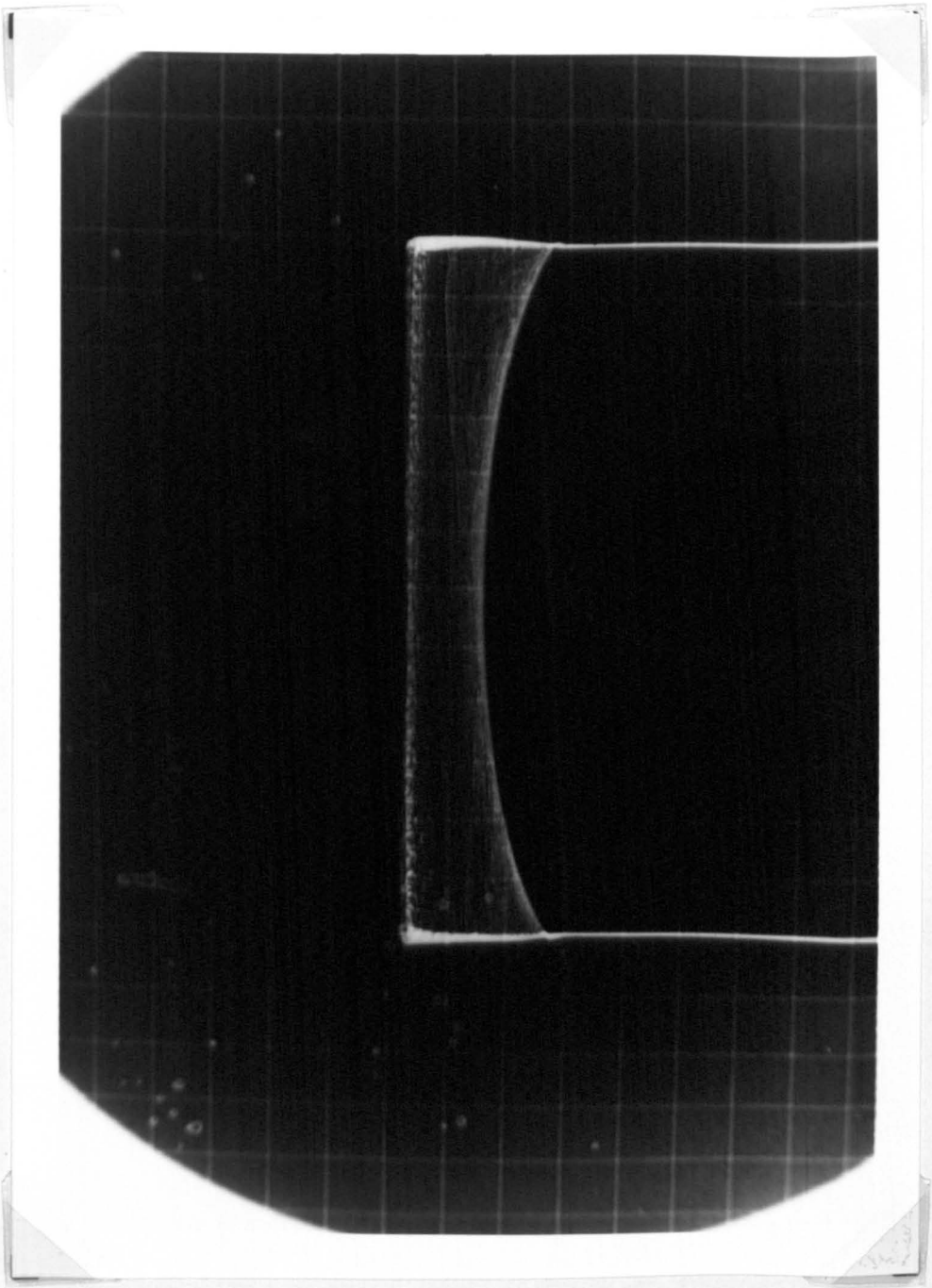

Plate 3.2 - General Surface with Rigid Boundaries - $z-y$ Central Plane.

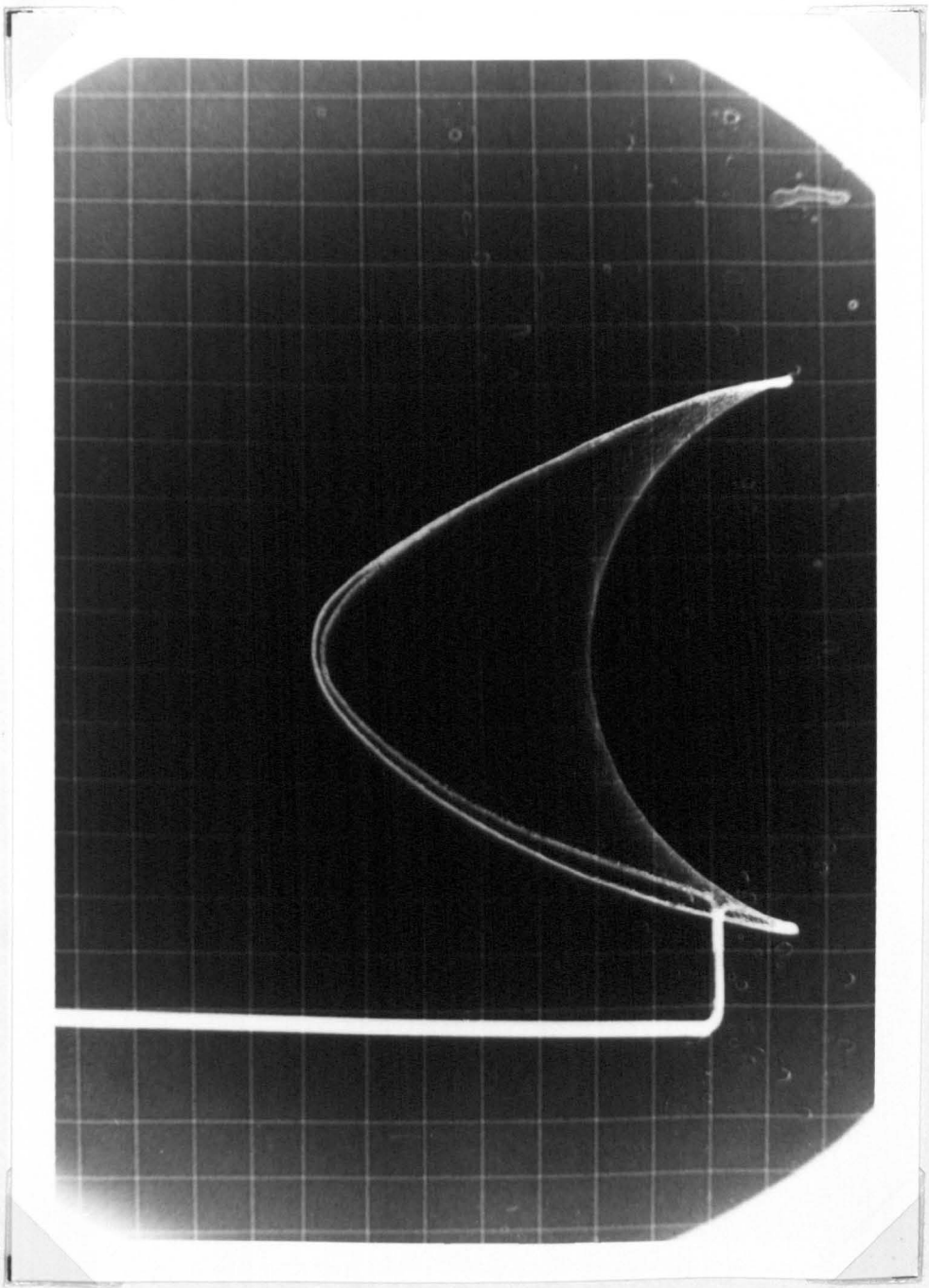

Plate 3.3 - General Surface with Rigid Boundaries - $z-x$ Central Plane.

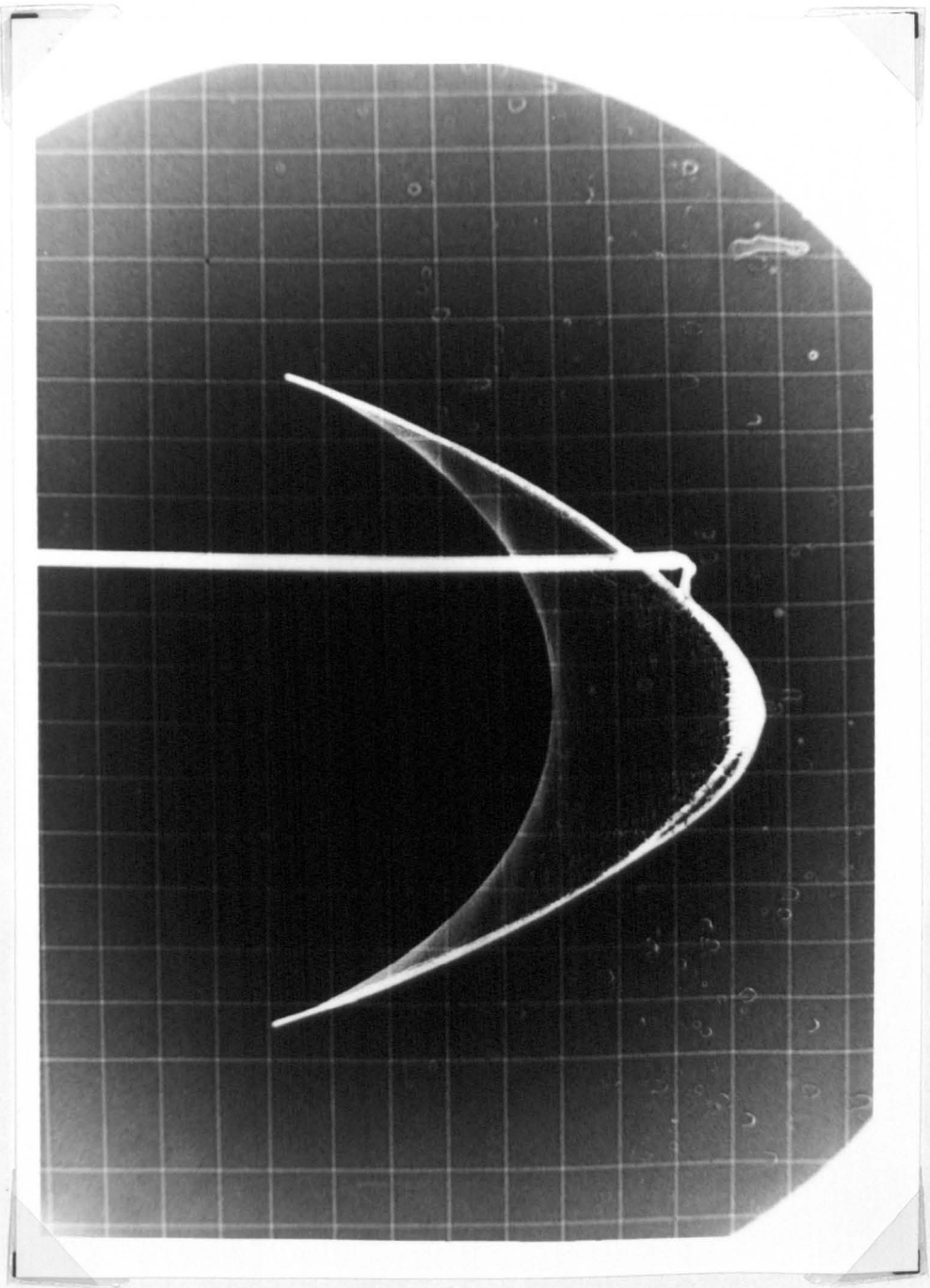

Plate 3.4 - General Surface with Rigid Boundaries - $z-y$ Central Plane.

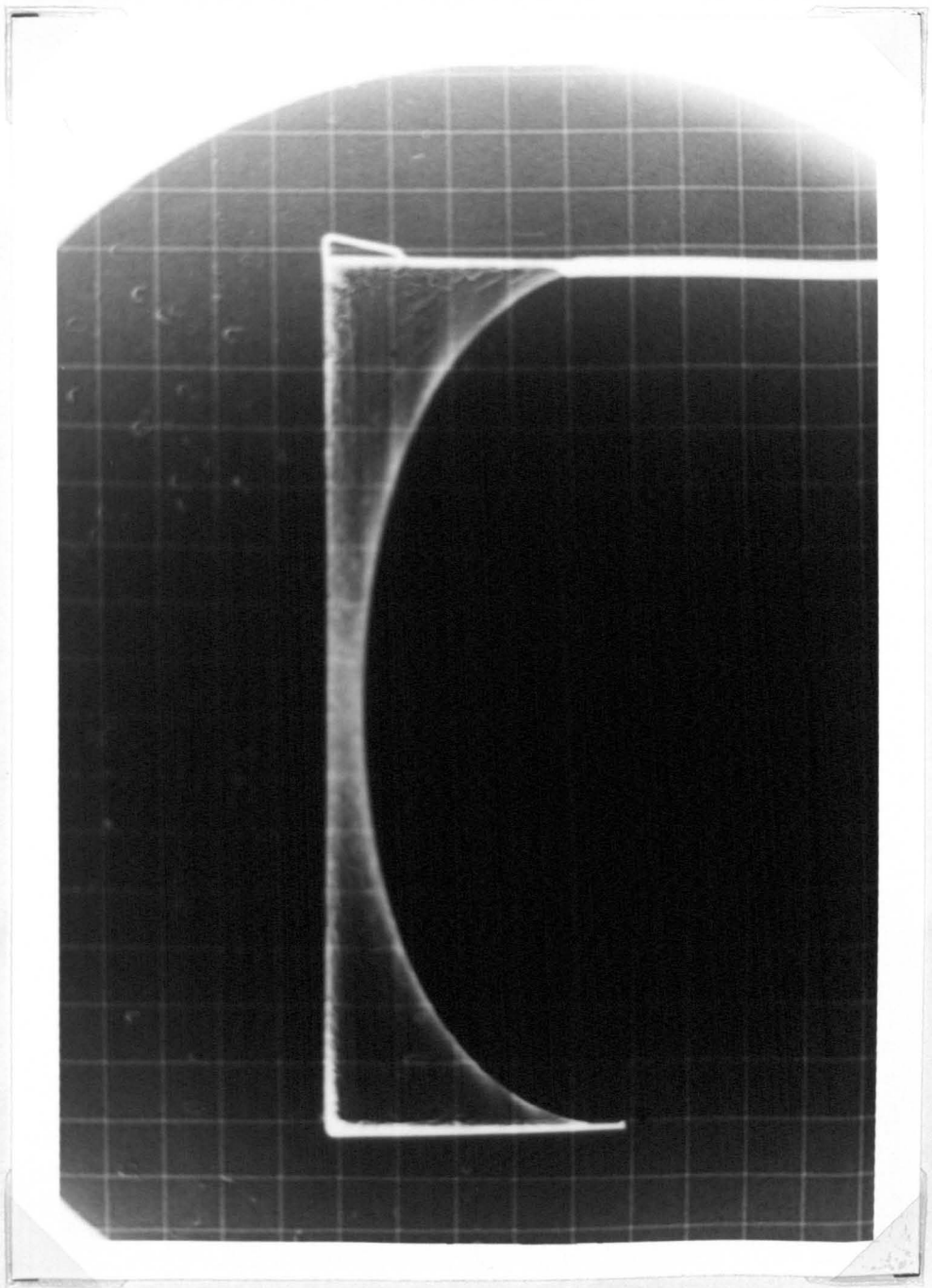

Plate 3.5 - General Surface with Rigid Boundaries - $z-x$ Central Plane.

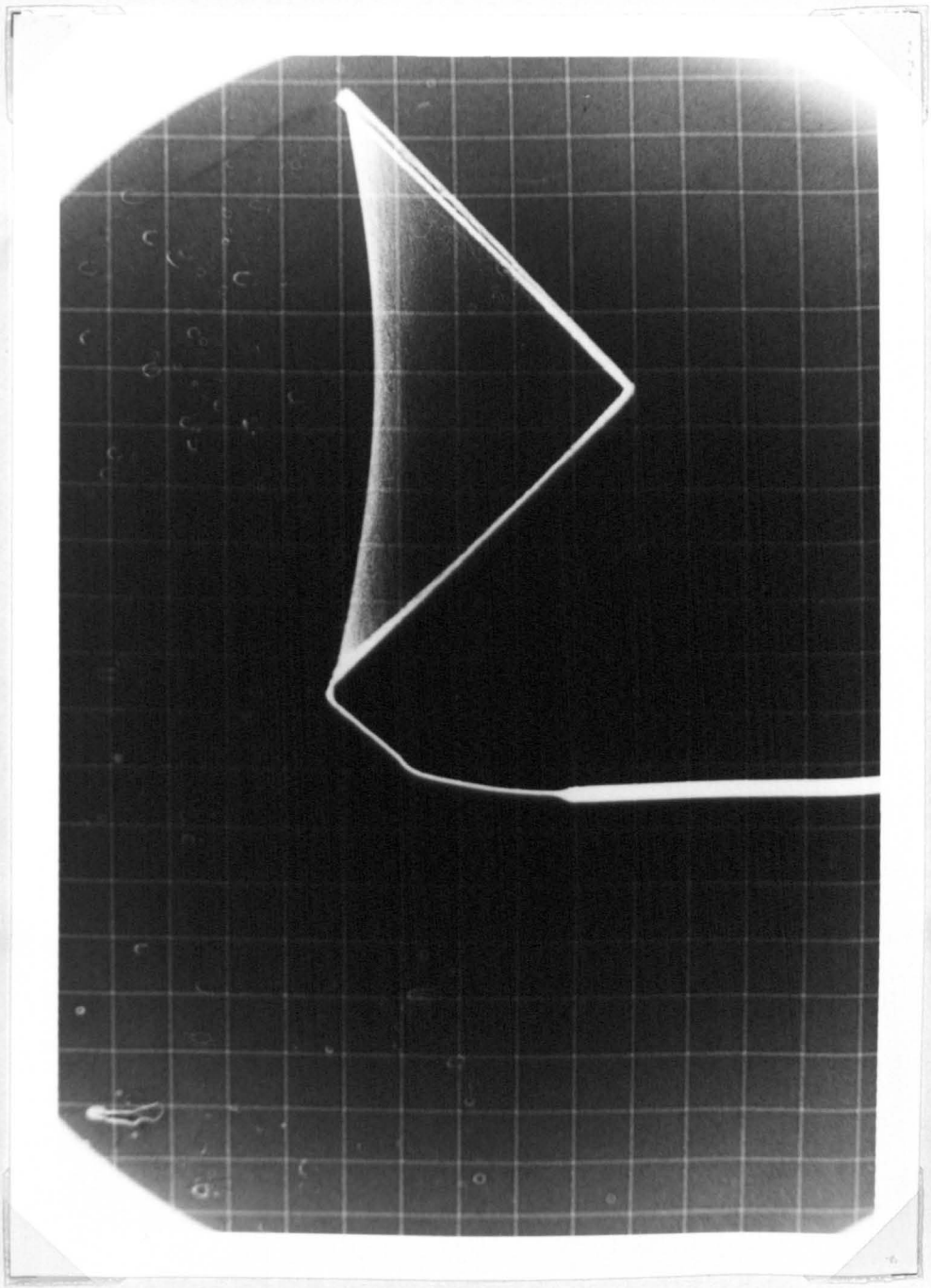

Plate 3.6 - General Surface with Rigid Boundaries - $z-y$ Central Plane.

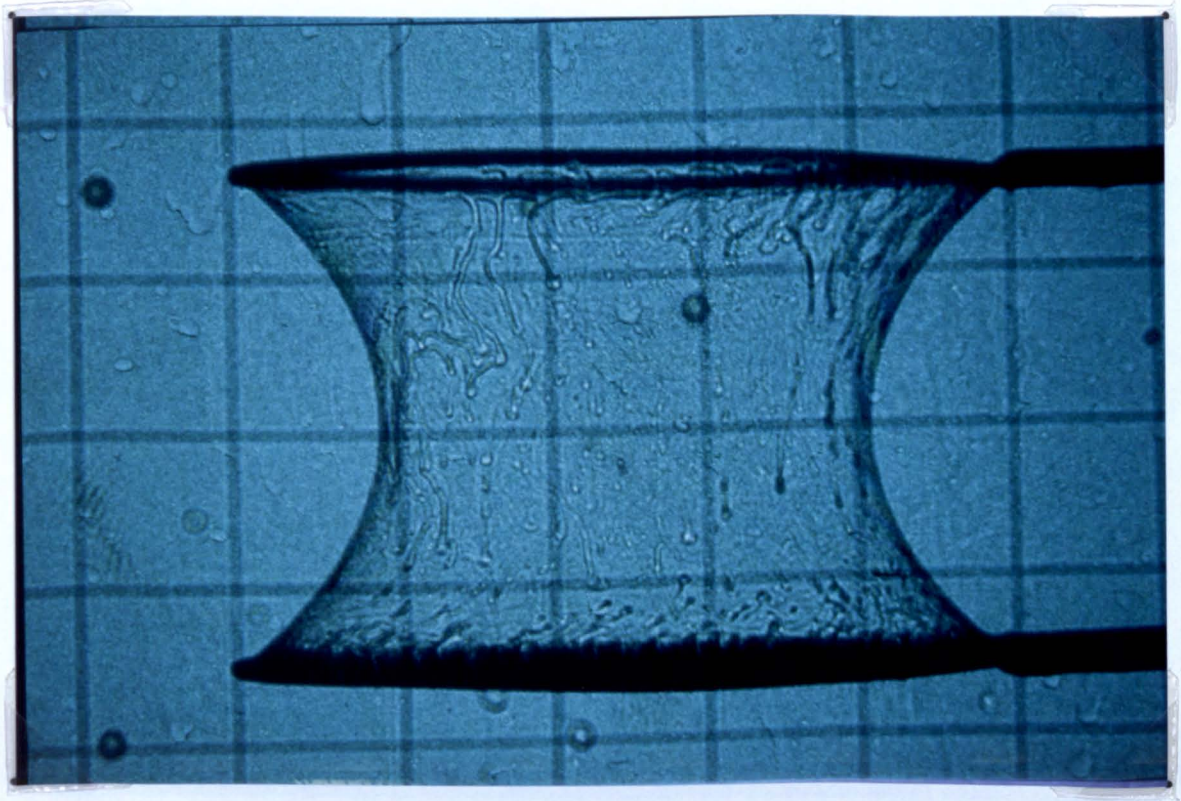

Plate 3.7 - Catenoid Surface (80. mm Diameter Rings, h = 53.0 mm).

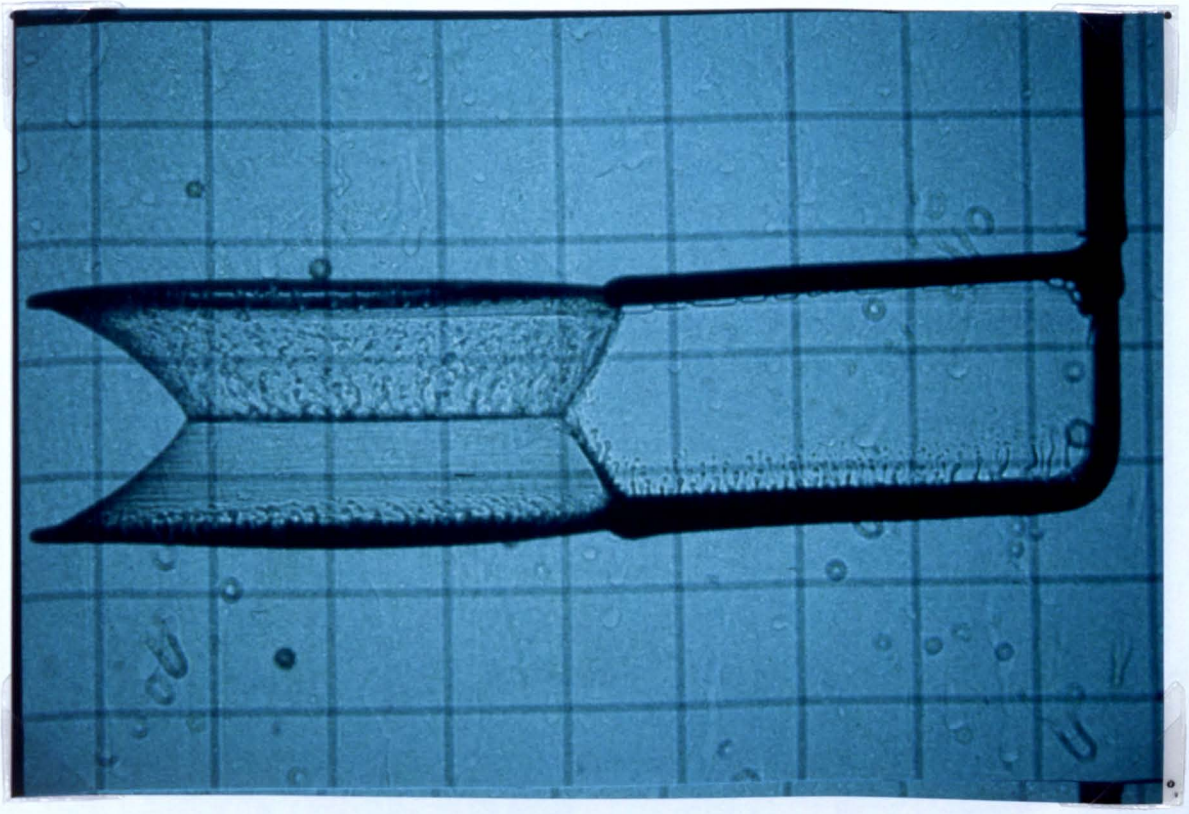

Plate 3.8 - Multiple Lamellae Minimal Surface - Four Lamellae.

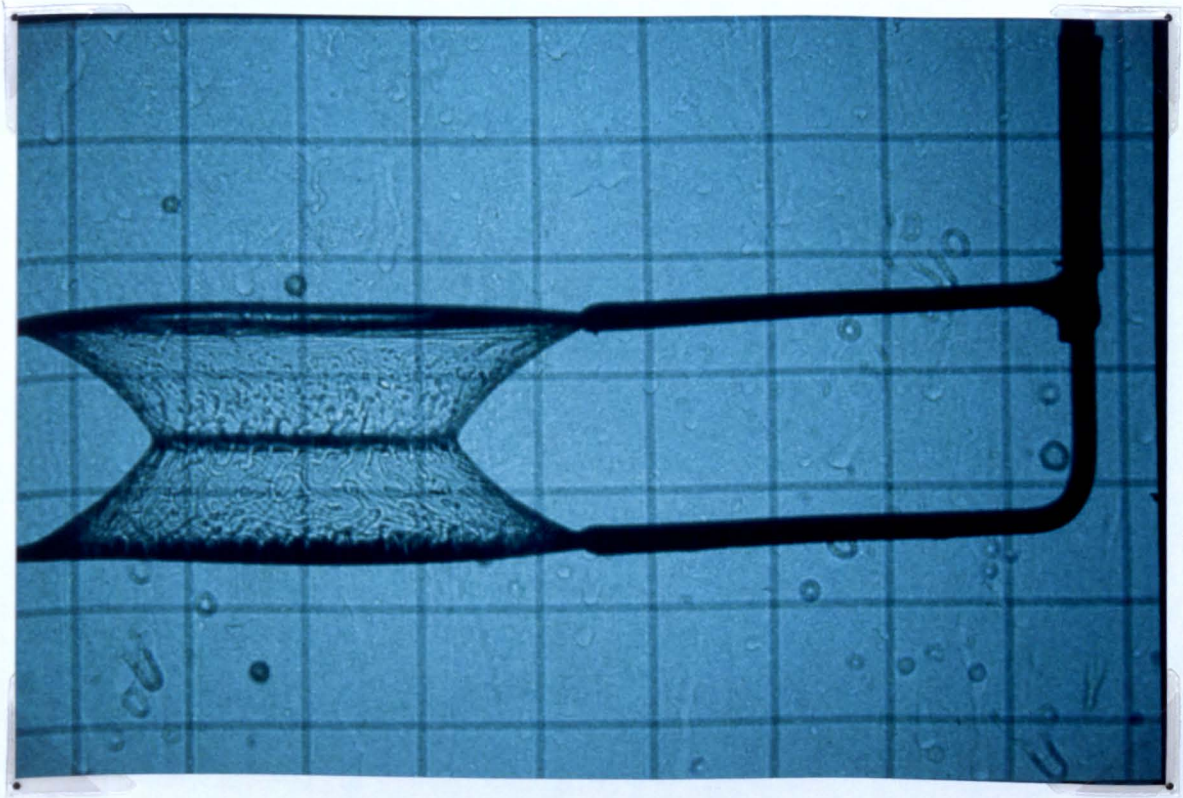

Plate 3.9 - Multiple Lamellae Minimal Surface - Three Lamellae.

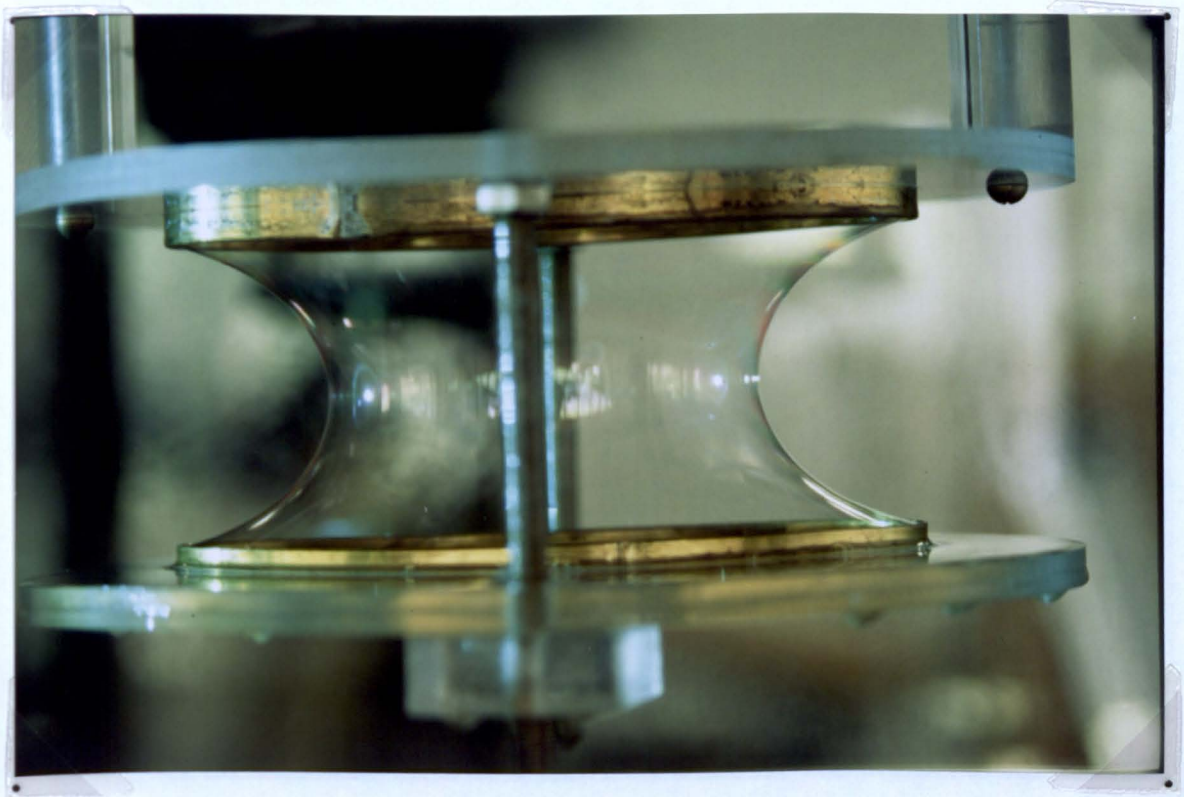

Plate 3.10 - Physical Model to Generate a Single Minimal Surface Between two Elliptical Rings.

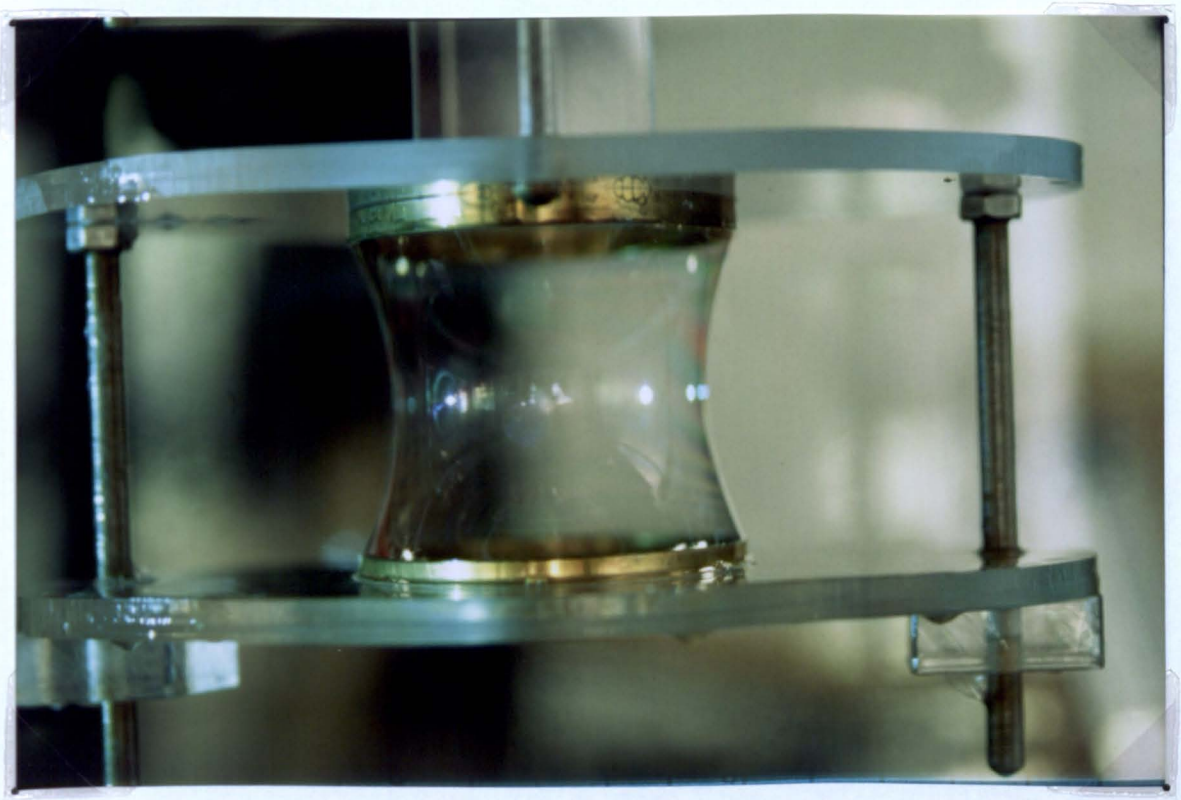

Plate 3.11 - Physical Model to Generate a Single Minimal Surface Between two Elliptical Rings.

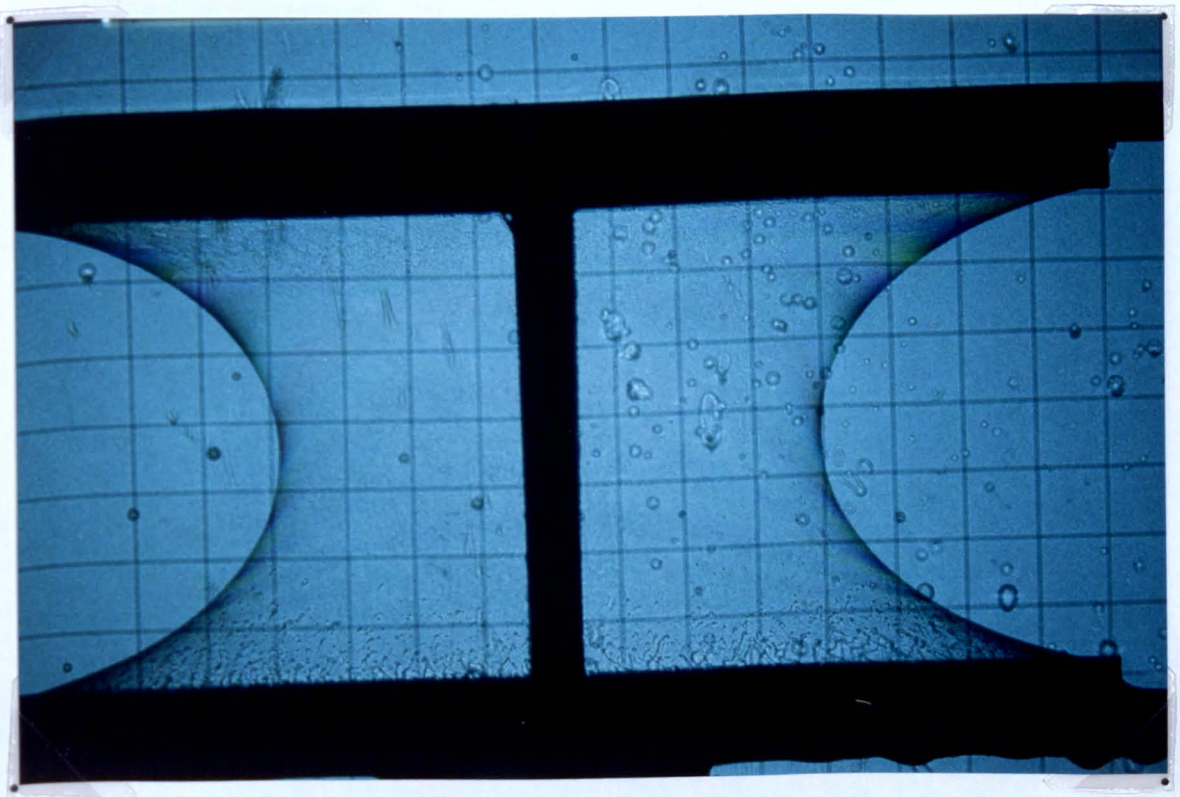

Plate 3.12 - Single Minimal Surface Between two Elliptical Rings.

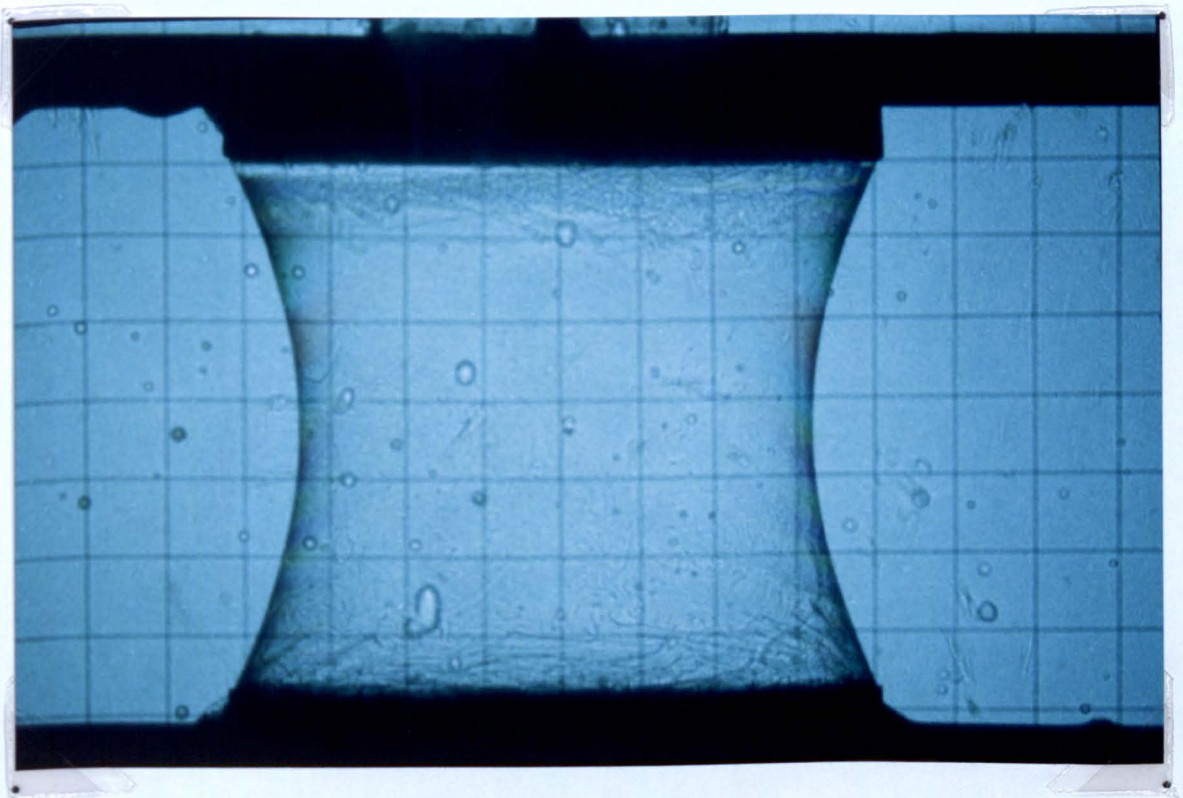

Plate 3.13 - Single Minimal Surface Between two Elliptical Rings.

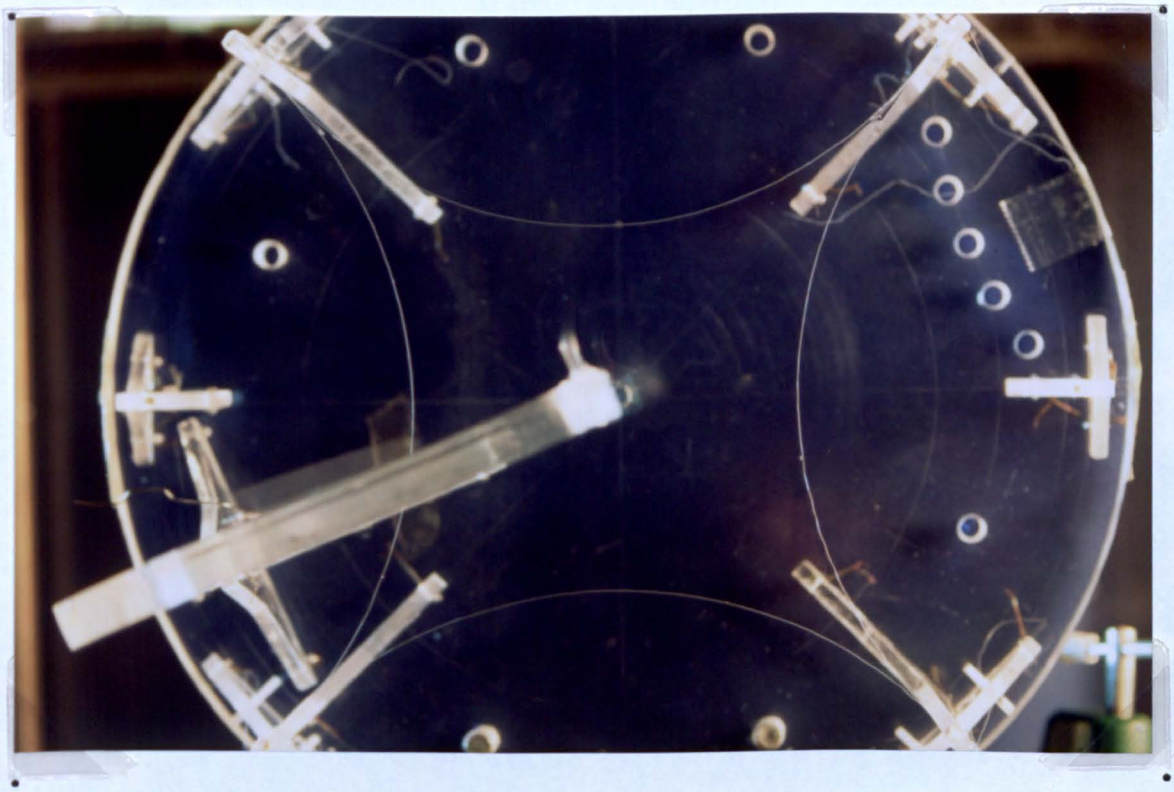

Plate 3.14 - 2-dimensional Minimal Surface Bounded by External Flexible Boundary Elements.

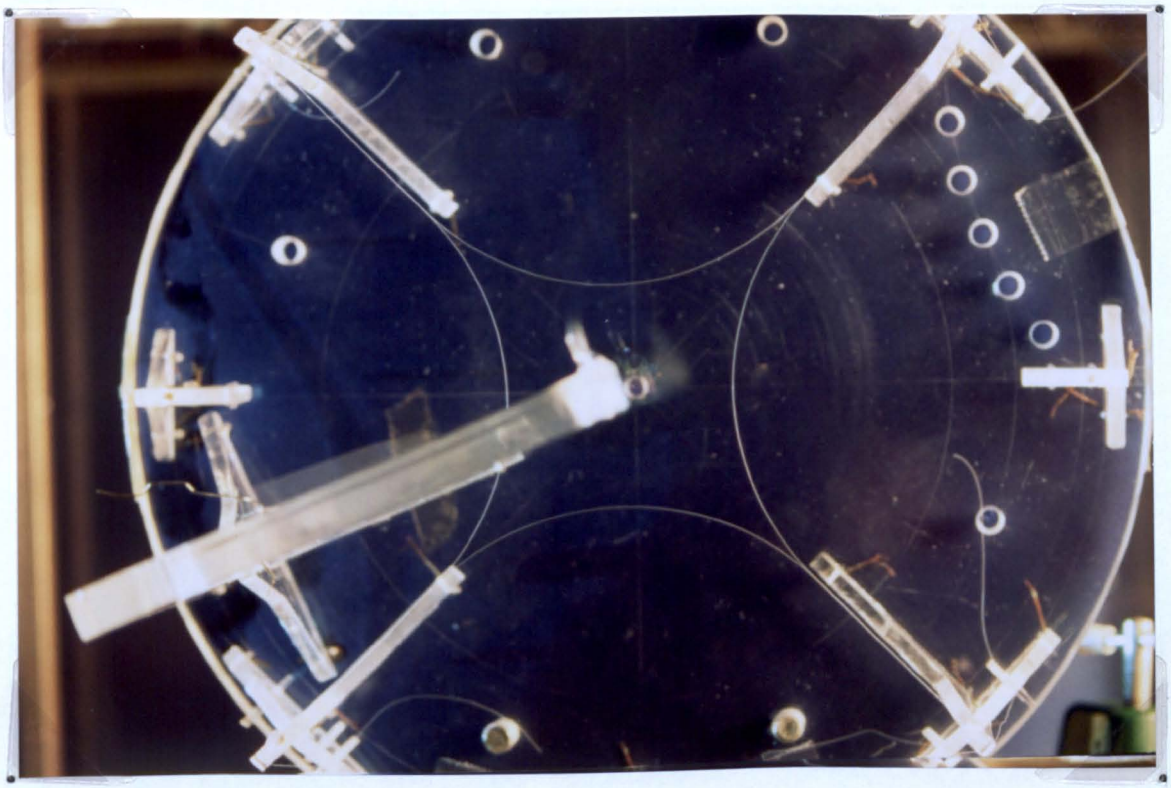

Plate 3.15 - 2-dimensional Minimal Surface Bounded by External Flexible Boundary Elements.

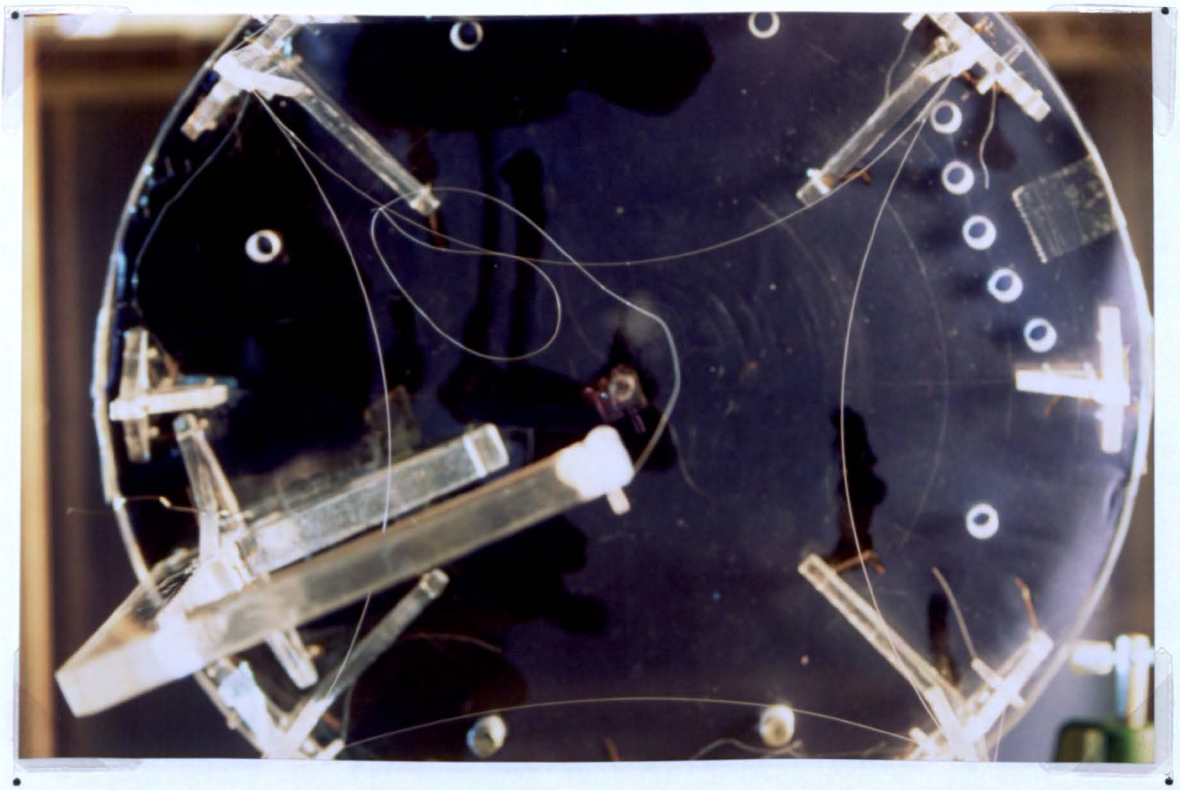

Plate 3.16 - 2-dimensional Minimal Surface Bounded by Internal and External Flexible Boundary Elements. (Internal Boundary Elements Unstressed.)

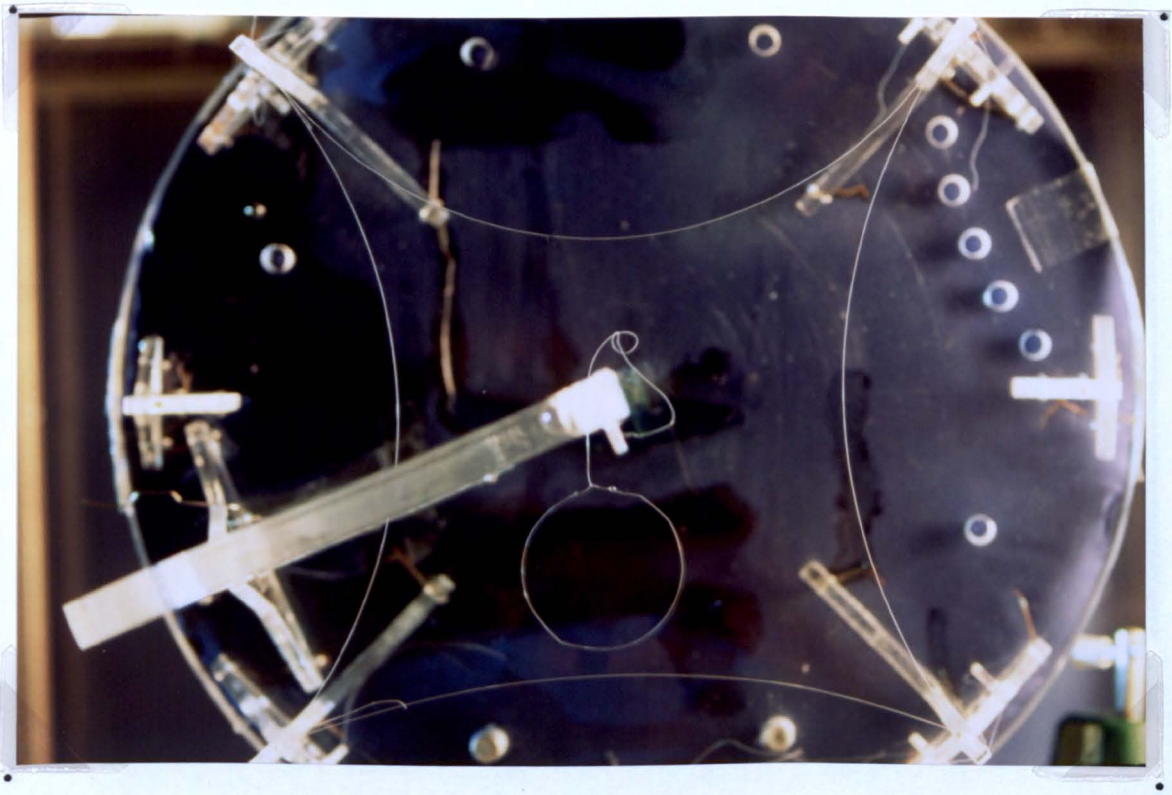

Plate 3.17 - 2-dimensional Minimal Surface Bounded by Internal and External Flexible Boundary Elements.

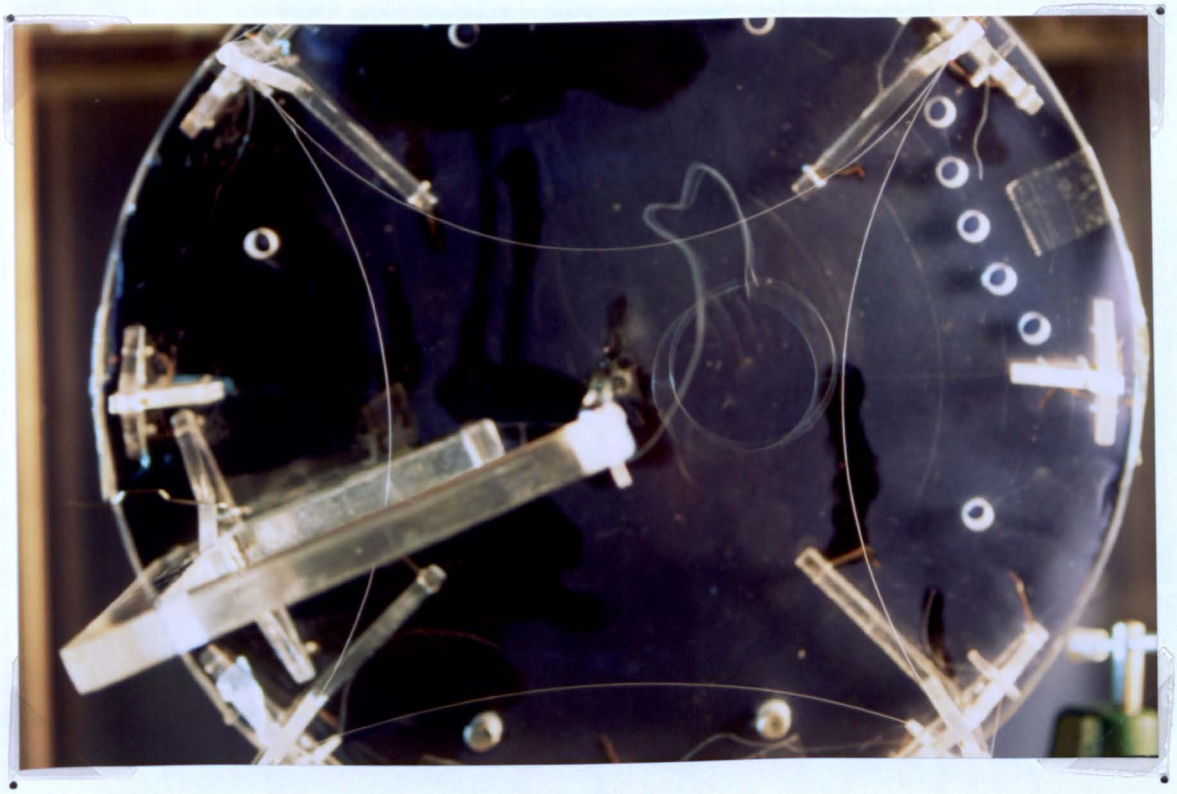

Plate 3.18 - Feature of Constant and Uniform Surface Stress.

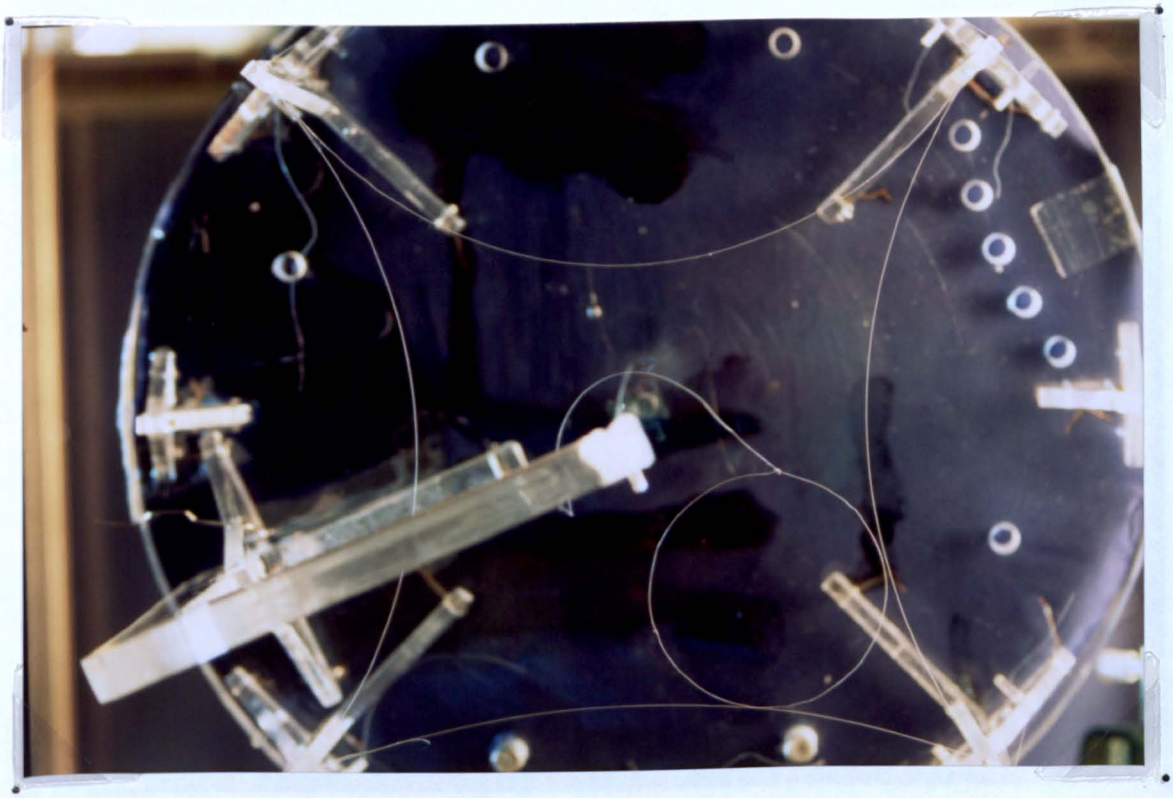

Plate 3.19 - 2-dimensional Minimal Surface Bounded by Internal and External Flexible Boundary Elements. (Formation of Two Minimal Surfaces.)

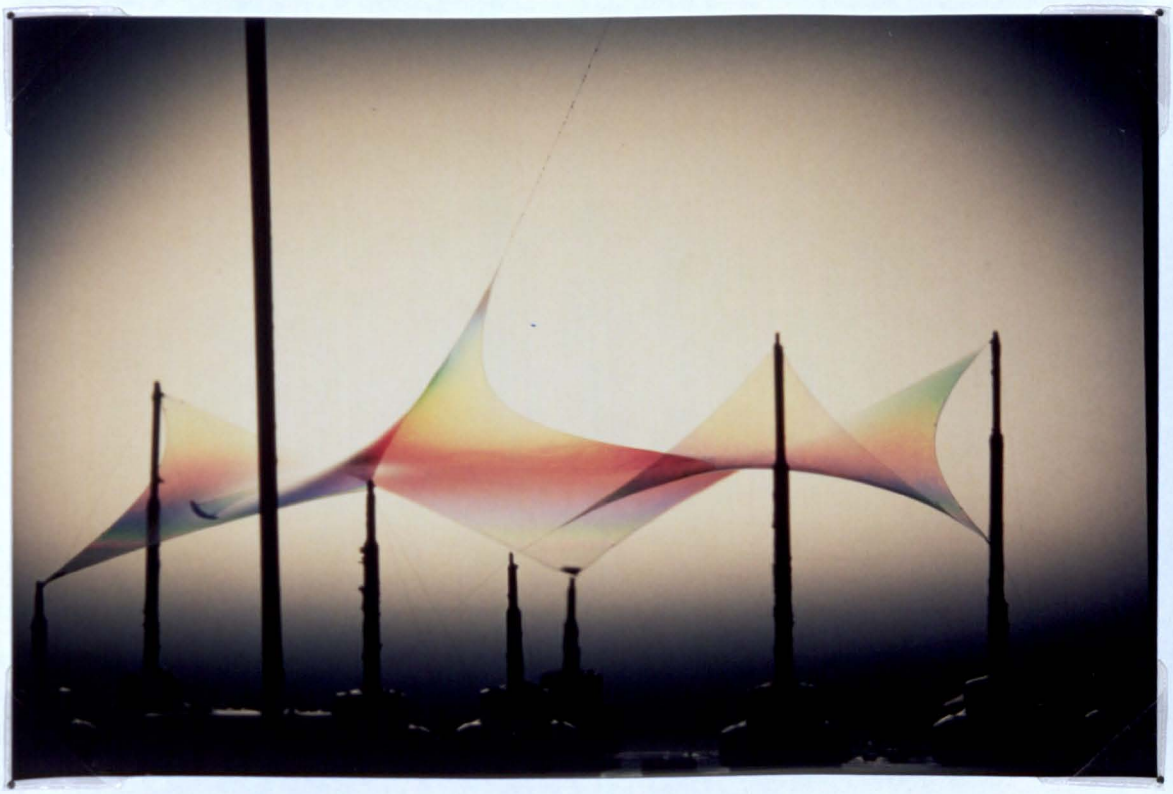

Plate 3.20 - "Siegfried's" Tent (Soap-film Model).

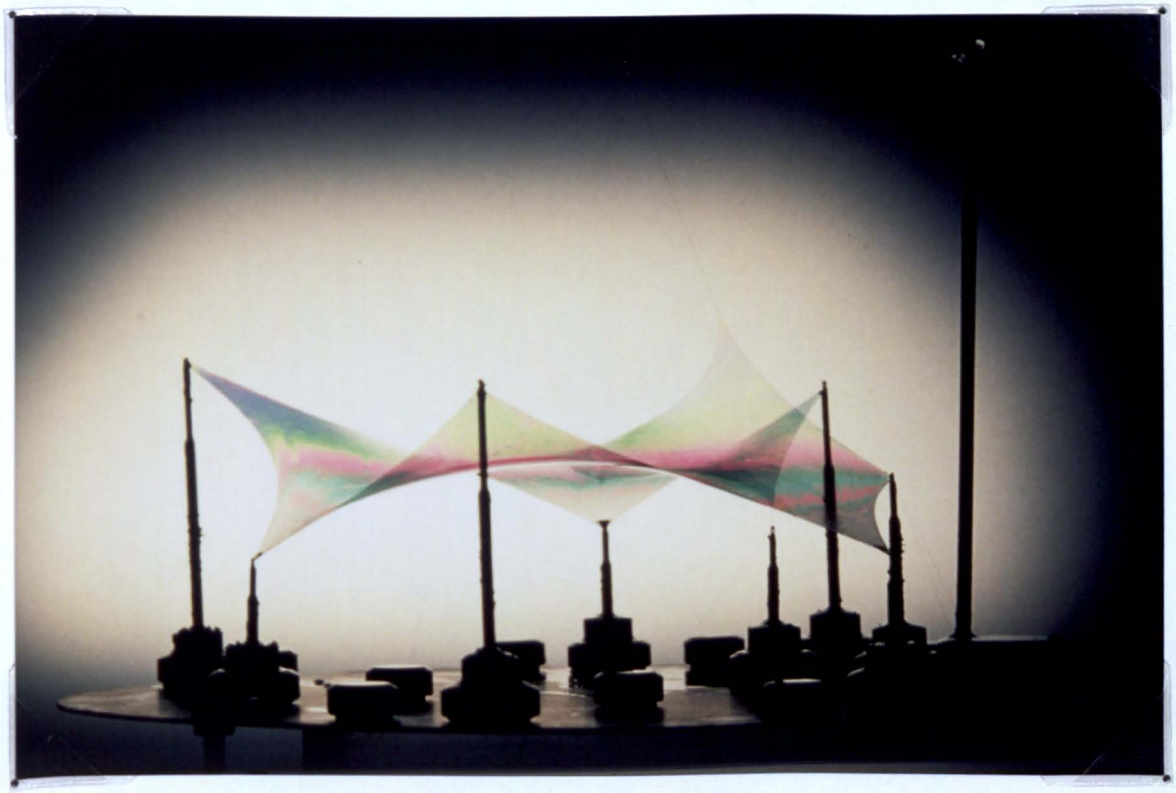

Plate 3.21 - "Siegfried's" Tent (Soap-film Model).

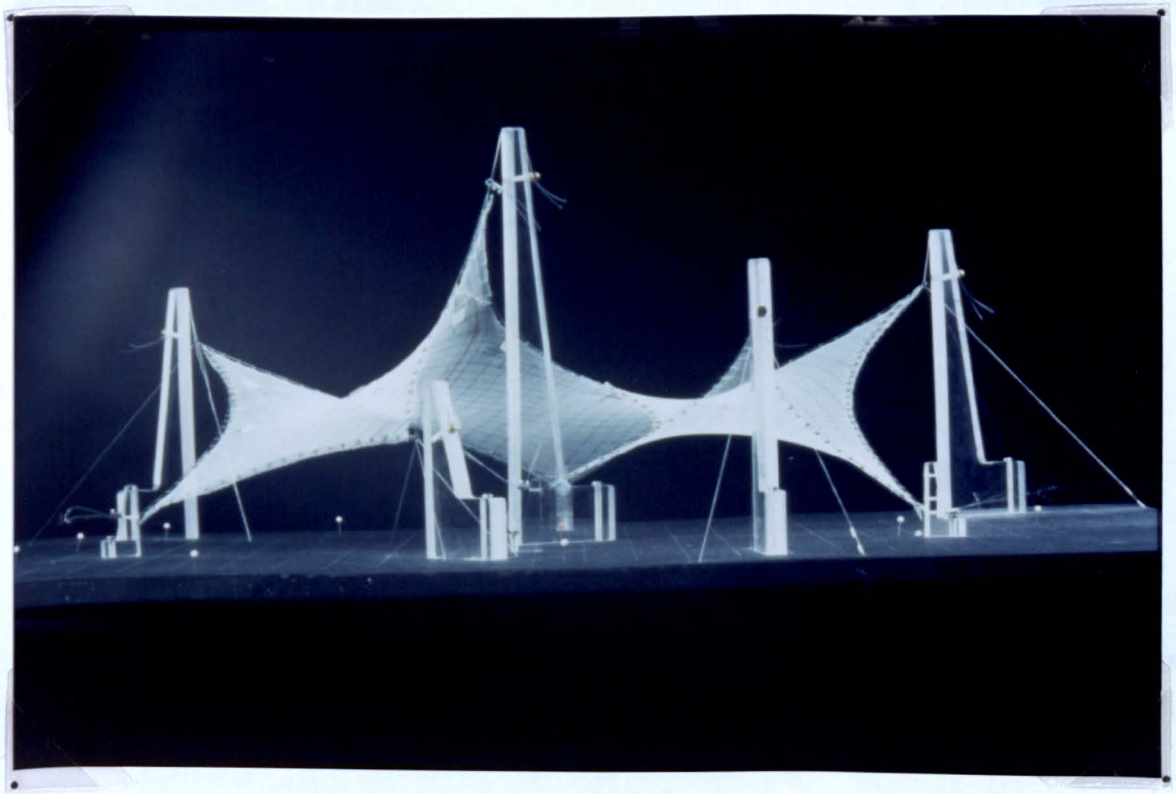

Plate 3.22 - "Siegfried's" Tent (Hexagonal Tulle Model).

3.7. References.

[3.1] Bach, K., Burkhardt, B., Otto, F.

Forming Bubbles.

IL. (Institute of Lightweight Structures, Stuttgart University, Germany.) Publication Number 18, 1987, pages 310-312, pages 332-334.

[3.2] Dao Trong Thi, Fomenko, A.T.

Minimal Surfaces, Stratified Multi-varifolds and the Plateau Problem.

American Mathematical Society, 1991, pages 32-34.

[3.3] Almgren, F.J., Taylor, J.E.

"The Geometry of Soap-films and Soap Bubbles."

Scientific American, July 1976, pages 82-93.

[3.4] Otto, F., Trostel, R.

Tensile Structures.

The MIT Press, Cambridge, Volume 1, 1967, pages 290-296.

[3.5] Gass, S.

Experiments.

IL. (Institute of Lightweight Structures, Stuttgart University, Germany.) Publication Number 25, 1990, pages 7.4-7.13.

Chapter 4

Numerical Modelling of Minimal Surface Membranes Using Linear and Triangular Elements.

4.1. Introduction.

It is suggested that the sub-division of a continuous system is often necessary so as to obtain an understanding of the behaviour of the complete continuum, when it is subjected to a series of boundary conditions [4.1]. An adequate model may be obtained by using a limited number of well defined components. Alternatively, the sub-division may be continued indefinitely such that the mathematical phenomenon of an infinitesimal may be used. This usually results in the manipulation of a set of differential equations, which may be solved to obtain a "continuous" solution to the problem.

Success has been achieved in the case of vaults and sails, where it has been shown that the Biot-Savart law (used in electro-magnetic theory) may be applied to calculate the state of stress in the vault or sail, when it is subjected to a dominant load case [4.2]. However, in general, difficulty is encountered when generating the necessary differential equations. This is particularly pertinent in the case of stable minimal surfaces used to model structural membranes, where extremely complex forms may render the generation of the governing equations of the surface impractical. For example, the accurate mathematical description of the surface represented by a soap-film model, is only possible for a few special cases [4.3],[4.4].

Therefore, discretisation of the surface into a finite number of components with known properties is desirable. In doing so an approximation is made. The aim of the discretisation must be such as to minimise the error of the approximation, as the number of components or variables is increased. Ultimately, therefore, in the limit, the true continuous solution is reached. Furthermore, the behaviour of the finite components (elements) is controlled by a finite number of parameters and degrees of freedom. Thus, as the element size tends to zero, in the limit, the error in the individual element must also tend to zero, if an accurate solution is to ensue.

In this chapter the discretisation of the stable minimal energy surface is undertaken using linear and triangular elements respectively. The condition of equilibrium is solved for by the Dynamic Relaxation algorithm with Kinetic Damping. The derivation of the characteristic matrices of both the linear and triangular elements are summarised. The assumptions which are inherent in these formulations have been highlighted, along with the effects these can have on the performance of the elements when used to analyse systems exhibiting large strains and large displacements. Measures to improve the stability and the performance of the triangular element formulation are proposed.

Several parametric studies are also presented, related to the accuracy and to the stability of the solution method. Finally, a comparison is made between the numerical solution to (obtained using both linear and triangular element discretisations), and the experimental measurements of, three soap-film models, representing stable minimal surfaces. The numerical solutions to minimal surfaces of revolution and to a more general surface are also presented.

4.2. Dynamic Relaxation Algorithm.

The Dynamic Relaxation algorithm is based on the principle that any body which is in motion will come to rest only when it is at a state of equilibrium. The system is forced into a pseudo oscillation, with equal amplitude about the equilibrium position. Both the frequency and the amplitude of the fictitious dynamic motion are controlled artificially. As illustrated subsequently, this is achieved through the components of stiffness and of out-of-balance force at each node of the discretisation, and by the associated nodal mass.

The motion of the system is described by the D' Alembert principle, written as,

$$\underline{P_{pq}} = M_{pq}\,\ddot{\delta}_{pq} + C\,\dot{\delta}_{pq} + \underline{K_{pq}}\,\delta_{pq}\,, \qquad \text{eqn(4.2.1)}$$

or,

$$\underline{P_{pq}} - \underline{K_{pq}}\,\delta_{pq} = M_{pq}\,\ddot{\delta}_{pq} + C\,\dot{\delta}_{pq}\,, \qquad \text{eqn(4.2.2)}$$

and,

$$\underline{R_{pq}} = M_{pq}\,\ddot{\delta}_{pq} + C\,\dot{\delta}_{pq} \qquad \text{eqn(4.2.3)}$$

where the subscripts pq refer to the p^{th} node in the q^{th} direction. q can take the values $1 \rightarrow 3$, corresponding to the global axis directions $\{x, y, z\}$, respectively. The remaining coefficients are defined below.

$\underline{P_{pq}}$ is the external load vector, including terms representing the effects of surface prestress or initial strains,

$\underline{K_{pq}}$ is the nodal stiffness selected from the terms of the element stiffness matrix,

$\underline{R_{pq}}$ is the out-of-balance nodal force (or residual),

M_{pq} is the fictitious nodal mass,

$\ddot{\delta}_{pq}$ is the nodal acceleration,

$\dot{\delta}_{pq}$ is the nodal velocity,

δ_{pq} is the nodal displacement.

Kinetic Damping has been shown to be a more stable and a more rapidly convergent technique of damping the pseudo dynamic oscillations of the discretised system, when compared with the Viscous Damping approach (eqn(4.2.1)) [4.10]. Using this technique the system is allowed to vibrate freely without attenuation of displacement or frequency. During this motion the kinetic energy of the entire system is monitored. As the system passes the equilibrium configuration the kinetic energy of the system is maximised.

When a maximum value is observed the current oscillation is halted. The pseudo motion is then restarted from this new configuration. As more peaks in the kinetic energy of the system are detected, the proximity of the system to the true equilibrium configuration is increased. The procedure culminates in the minimisation of the sum of the kinetic and potential energies of the system at equilibrium. Using this approach, eqn(4.2.2) may be written more simply as,

$$\underline{P_{pq}} - \underline{K_{pq}}\,\delta_{pq} = \underline{R_{pq}} = M_{pq}\,\ddot{\delta}_{pq} \qquad \text{eqn(4.2.4)}$$

The acceleration term given in the right side of eqn(4.2.4) is written as the variation of the velocity over the time increment δt using a central difference approximation, such that,

$$\ddot{\delta}_{pq} = \frac{\dot{\delta}_{pq}^{\,t+\frac{\delta t}{2}} - \dot{\delta}_{pq}^{\,t-\frac{\delta t}{2}}}{\delta t}. \qquad \text{eqn(4.2.5)}$$

Substitution of eqn(4.2.5) into eqn(4.2.4) leads to the following recurrent equation for the nodal velocity, $\dot{\delta}_{pq}^{\,t+\frac{\delta t}{2}}$, as,

$$\dot{\delta}_{pq}^{\,t+\frac{\delta t}{2}} = \dot{\delta}_{pq}^{\,t-\frac{\delta t}{2}} + \underline{R_{pq}}^{t}\,\frac{\delta t}{M_{pq}} \qquad \text{eqn(4.2.6)}$$

In order to ensure numerical stability of the solution algorithm, the following expression has been suggested [4.11],

$$\delta t \le \sqrt{2\,\frac{M_{pq}}{\underline{K_{pq}}}} \qquad \text{eqn(4.2.7)}$$

or,

$$M_{pq} \ge \frac{\underline{K_{pq}}}{2}\cdot \delta t^2 \qquad \text{eqn(4.2.8)}$$

Substitution of eqn(4.2.8) into eqn(4.2.6) gives,

$$\dot{\delta}_{pq}^{\,t+\frac{\delta t}{2}} = \dot{\delta}_{pq}^{\,t-\frac{\delta t}{2}} + \underline{R_{pq}}^{t} \left[\frac{2}{\delta t \cdot \underline{K_{pq}}} \right] \qquad \text{eqn(4.2.9)}$$

The velocities at time $t+\frac{\delta t}{2}$ can be used to calculate the current nodal displacements as in,

$$\delta_{pq}^{\,t+\frac{\delta t}{2}} = \dot{\delta}_{pq}^{\,t+\frac{\delta t}{2}} . \delta t \; . \qquad \text{eqn(4.2.10)}$$

Therefore, through the recurrent use of eqn(4.2.4), eqn(4.2.9) with eqn(4.2.10), the pseudo dynamic behaviour of the structure is defined. During each iterative cycle, the current kinetic energy of the system, $U_k^{\,t+\frac{\delta t}{2}}$ is monitored and compared with the preceding value, denoted respectively as,

$$U_k^{\,t+\frac{\delta t}{2}} = \frac{1}{2} \sum_{p=1}^{p=N} \sum_{q=1}^{q=3} M_{pq} \left(\dot{\delta}_{pq}^{\,t+\frac{\delta t}{2}} \right)^2 , \qquad \text{eqn(4.2.11)}$$

and,

$$U_k^{\,t-\frac{\delta t}{2}} = \frac{1}{2} \sum_{p=1}^{p=N} \sum_{q=1}^{q=3} M_{pq} \left(\dot{\delta}_{pq}^{\,t-\frac{\delta t}{2}} \right)^2 , \qquad \text{eqn(4.2.12)}$$

where N is the total number of nodes of the discretised system.

An energy peak is deemed to have occurred during the time interval $t-\frac{\delta t}{2} \le t \le t+\frac{\delta t}{2}$ when the magnitude of $U_k^{\,t+\frac{\delta t}{2}}$ is less than that of $U_k^{\,t-\frac{\delta t}{2}}$. If it is assumed that the kinetic energy peak occurs at the time t^*, where $t-\frac{\delta t}{2} \le t^* \le t+\frac{\delta t}{2}$, it may be estimated that t^* is at the mid point of the interval, $t-\frac{\delta t}{2} \le t \le t+\frac{\delta t}{2}$, such that $t^* = t$.

Alternatively, a parabola may be fitted through the current and the two previous values of the kinetic energy ($U_k^{\,t-\frac{\delta t}{2}}, U_k^{\,t-\frac{3\delta t}{2}}$), yielding an improved estimate of the true position of the kinetic energy peak, written as [4.12],

$$t^* = t - \alpha . \delta t = t - \delta t^* \qquad \text{eqn(4.2.13(a))}$$

where,

$$\alpha = \frac{U_k^{\,t+\frac{\delta t}{2}} - U_k^{\,t-\frac{\delta t}{2}}}{U_k^{\,t-\frac{3\delta t}{2}} - 2\,U_k^{\,t-\frac{\delta t}{2}} + U_k^{\,t+\frac{\delta t}{2}}} \qquad \text{eqn(4.2.13(b))}$$

The pseudo dynamic motion may be restarted therefore, from the configuration described by the following expression [4.12];

$$\delta^{t^*} = \delta^{t+\frac{\delta t}{2}} - \dot{\delta}^{t+\frac{\delta t}{2}} \cdot \delta t - \dot{\delta}^{t-\frac{\delta t}{2}} \cdot \delta t^* \qquad \text{eqn(4.2.14)}$$

Using eqn(4.2.9) and eqn(4.2.13), eqn(4.2.14) may be rewritten as,

$$\delta^{t^*} = \delta^{t+\frac{\delta t}{2}} - (1+\alpha)\,\dot{\delta}^{t+\frac{\delta t}{2}} \cdot \delta t + \delta t \cdot \alpha \cdot \underline{R_{pq}}^t \left[\frac{2}{\delta t \cdot \underline{K_{pq}}} \right] \qquad \text{eqn(4.2.15)}$$

Through the recurrent use of eqn(4.2.4), eqn(4.2.9) and eqn(4.2.10), the condition of static equilibrium of a system can be satisfied by damping its pseudo dynamic behaviour. The pseudo dynamic behaviour of the system has been shown to be controlled by the components of both stiffness and of out-of-balance force at each node of the discretisation.

4.3. Linear Element Discretisation.

4.3.1. Introduction.

The linear or line element represents the most basic of the element formulations. As described in the subsequent paragraphs, it is defined with translational degrees of freedom only, and with a constant cross-section. A minimal surface may be discretised using a mesh of intersecting linear elements which are approximately orthogonal. In this case the uniform stress characterising a minimal surface is modelled by the imposition of a constant and equal tension in all internal elements of the discretisation.

The stiffness of the surface is obtained from the summation of both the elastic and geometric stiffness matrices of the individual elements. The element elastic stiffness matrix, $[\,K_E{}^c\,]$, is given as the rate of change of the axial force of the element with the axial displacement. The geometric stiffness matrix, $[\,K_\sigma{}^c\,]$, represents the non-linearity of the system. This additional stiffness is activated by the combination of axial tension in the element with displacements normal to its longitudinal direction. A linear (line) element, suitable for the analysis of minimal energy forms, is illustrated in Figure 4.1 [4.13],

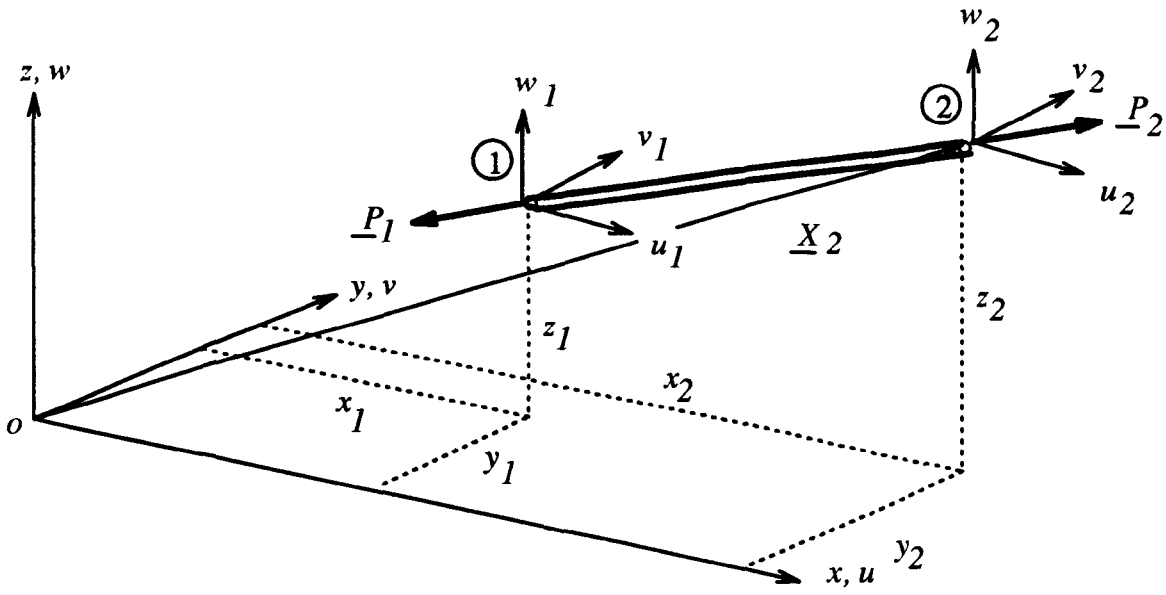

Figure 4.1 - Geometry, Degrees-of-Freedom, and Forces of the Linear Element.

where, u_1, v_1, w_1, are the displacements of node 1 in the global directions x, y, z, and are denoted by the vector, $\underline{\delta}_1$,

x_1, y_1, z_1 are the co-ordinates of node 1 in the global directions x, y, z, and are denoted by the vector, $\underline{X}_1$, and,

$\underline{P}_1$ is the vector of nodal loads written in the global directions x, y, z as, $\underline{P}_1 = \{P_{1x}, P_{1y}, P_{1z}\}$.

The element is assumed to remain straight during all modes of deformation, and to model a state of constant strain. The derivations of the element matrices may be found in reference [4.13]. They are summarised in the subsequent section for reasons of completeness, and to highlight certain aspects which are significant.

4.3.2. Geometrical, Displacement and Loading Matrices.

The position of an element in the global $\{x, y, z\}$ space is given by the vector,

$$\underline{X} = \{\{x_1 \underline{i} + y_1 \underline{j} + z_1 \underline{k}\}, \{x_2 \underline{i} + y_2 \underline{j} + z_2 \underline{k}\}\} \qquad \text{eqn(4.3.2.1)}$$

where, $\underline{i}, \underline{j}, \underline{k}$, are unit vectors aligned with the global co-ordinate directions $\{x, y, z\}$.

The length of the element, l, may be written simply as,

$$l = \sqrt{(x_1 - x_2)^2 + (y_1 - y_2)^2 + (z_1 - z_2)^2}\,. \qquad \text{eqn(4.3.2.2)}$$

The direction of the element, assumed to be in the longitudinal sense, may be specified by the unit vector $[\acute{c}]$, where $[\acute{c}]$ is expressed as,

$$[\acute{c}] = \begin{bmatrix} c_x \\ c_y \\ c_z \end{bmatrix} = \frac{1}{l} \begin{bmatrix} x_2 - x_1 \\ y_2 - y_1 \\ z_2 - z_1 \end{bmatrix} \qquad \text{eqn(4.3.2.3)}$$

and, c_x, c_y, and c_z are the direction cosines of the element corresponding to the global x, y, z directions.

By defining the elongation of the element as the natural deformation, δ_N, and the axial force in the element as the natural force, P_N, the following relationships may be written in matrix form;

$$\delta_N = [\acute{c}]^t \cdot \underline{\delta}_2 - [\acute{c}]^t \cdot \underline{\delta}_1 , \qquad \text{eqn(4.3.2.4(a))}$$

and,

$$[\underline{P}_1] = -[\acute{c}] \cdot P_N ; \quad [\underline{P}_2] = +[\acute{c}] \cdot P_N , \qquad \text{eqn(4.3.2.4(b))}$$

or,

$$\delta_N = [T_N] \cdot \begin{Bmatrix} \delta_1 \\ \delta_2 \end{Bmatrix} = [T_N] \cdot \{\delta_G\} , \qquad \text{eqn(4.3.2.5(a))}$$

where, $\{\delta_1\}^T = \{u_1, v_1, w_1\}$, and $\{\delta_2\}^T = \{u_2, v_2, w_2\}$,

and,

$$\begin{bmatrix} \underline{P}_1 \\ \underline{P}_2 \end{bmatrix} = [T_N]^t \cdot P_N , \qquad \text{eqn(4.3.2.5(b))}$$

where,

$$[T_N] = [-[\acute{c}]^t \; [\acute{c}]^t] , \qquad \text{eqn(4.3.2.6)}$$

and is a transformation matrix between the natural and global co-ordinate systems.

4.3.3. Elastic Stiffness Matrix, $[K_E{}^c]$

Given that the natural co-ordinate system of a one-dimensional element lies in the direction of the element, the natural elastic stiffness, K_N, is obtained from the expression,

$$P_N = \frac{EA}{l} \cdot \delta_N = K_N \cdot \delta_N \qquad \text{eqn(4.3.3.1)}$$

where, E, is the elastic modulus, and, A, the cross-sectional area, of the element.

Eqn(4.3.3.1) may be transformed to the global co-ordinate directions using eqn(4.3.2.6), as [4.14],

$$P_g = [T_N]^t \; [K_N] \; [T_N] \; \{\delta_G\} , \qquad \text{eqn(4.3.3.2)}$$

yielding the elastic element stiffness matrix [$K_E{}^c$] as,

$$[K_E{}^c] = [T_N]^t [K_N] [T_N] = \frac{EA}{l} \begin{bmatrix} [\acute{c}][\acute{c}]^t & -[\acute{c}][\acute{c}]^t \\ -[\acute{c}][\acute{c}]^t & [\acute{c}][\acute{c}]^t \end{bmatrix} \qquad \text{eqn(4.3.3.3)}$$

4.3.4. Geometric Stiffness Matrix, [$K_\sigma{}^c$]

The geometric stiffness matrix, [$K_\sigma{}^c$], recognises the contribution of the natural element force to the total stiffness of the element. Unlike the elastic stiffness matrix which relies on a change in the length of the element, the matrix [$K_\sigma{}^c$] responds to a change in the orientation of the element in the global $\{x, y, z\}$ space. A summary of the derivation of the geometric stiffness matrix, [$K_\sigma{}^c$] [4.13], is presented below.

Figure 4.2 illustrates a linear element possessing a natural force, P_N, prior and subsequent to the application of the global displacements vectors $\underline{\delta}_1$ and $\underline{\delta}_2$.

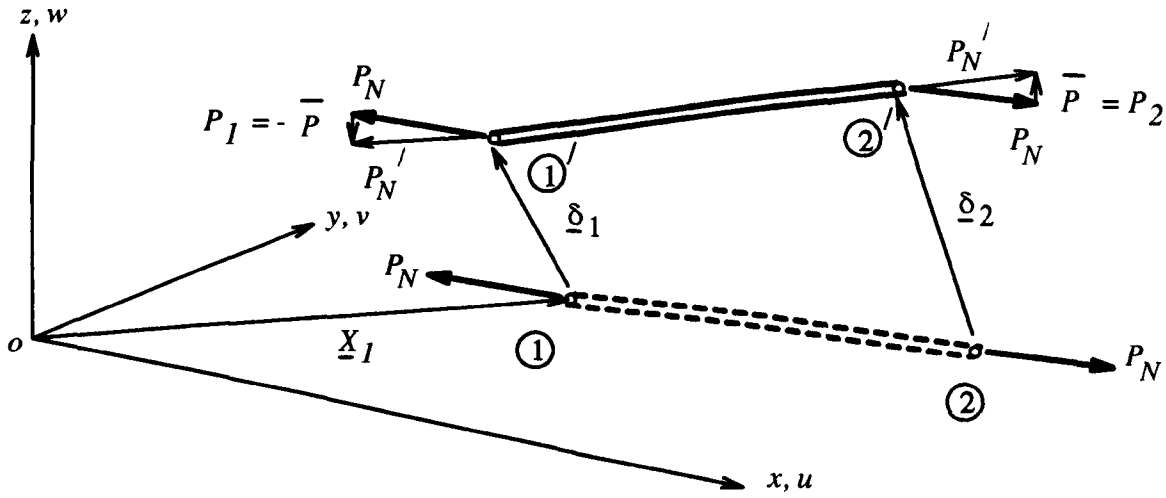

Figure 4.2 - Derivation of the Geometric Stiffness of the Linear Element.

The displacement vectors $\underline{\delta}_1$ and $\underline{\delta}_2$ can be resolved into components which are parallel and orthogonal to the natural co-ordinate of the element, as,

$$\{\delta_i\} = \{\delta_i\}_{par} + \{\delta_i\}_{orth} \qquad \text{eqn(4.3.4.1)}$$

where $i = 1, 2$, corresponding to the element nodes, and

$$\{\delta_i\}_{par} = [\acute{c}][\acute{c}]^t \cdot \{\delta_i\}, \qquad \text{eqn(4.3.4.2)}$$

with,

$$\{\delta_i\}_{orth} = \{\delta_i\} - \{\delta_i\}_{par} = \left[[I_3] - [\acute{c}][\acute{c}]^t \right] \cdot \{\delta_i\}. \qquad \text{eqn(4.3.4.3)}$$

$[I_3]$ is a 3×3 identity matrix.

The rotation of the element is measured by the expression,

$$\{\delta^r\} = \underline{\delta}_{2orth} - \underline{\delta}_{1orth} = \left[[I_3] - [\acute{c}][\acute{c}]^t \right] . \{ \underline{\delta}_2 - \underline{\delta}_1 \}. \qquad \text{eqn(4.3.4.4)}$$

The natural force P_N acting with the displacement vector $\{\delta^r\}$, generates a moment M^r, as $M^r = P_N . \left| \{\delta^r\} \right|$ (Figure 4.2). This moment is equilibriated by the nodal loads P_1 and P_2, where,

$$P_1 = -\bar{P} ; \quad P_2 = +\bar{P} , \qquad \text{eqn(4.3.4.5)}$$

with,

$$\bar{P} = \frac{P_N}{l} . \{\delta^r\}. = P_N . \theta^c{}_r , \qquad \text{eqn(4.3.4.6)}$$

where $\theta^c{}_r$ is the angle of rigid body rotation.

Writing eqn(4.3.4.5) and eqn(4.3.4.6) in matrix form yields the matrix $[P_G]$, as in,

$$[P_G] = \frac{P_N}{l} \begin{bmatrix} -\{\delta^r\} \\ \{\delta^r\} \end{bmatrix} = \frac{P_N}{l} \begin{bmatrix} ([I_3] - [\acute{c}][\acute{c}]^t) & -([I_3] - [\acute{c}][\acute{c}]^t) \\ -([I_3] - [\acute{c}][\acute{c}]^t) & ([I_3] - [\acute{c}][\acute{c}]^t) \end{bmatrix} . \{\delta_i\}$$

eqn(4.3.4.7)

From eqn(4.3.4.7) the geometric stiffness matrix is written as,

$$[K_\sigma{}^c] = \frac{P_N}{l} \begin{bmatrix} ([I_3] - [\acute{c}][\acute{c}]^t) & -([I_3] - [\acute{c}][\acute{c}]^t) \\ -([I_3] - [\acute{c}][\acute{c}]^t) & ([I_3] - [\acute{c}][\acute{c}]^t) \end{bmatrix} \qquad \text{eqn(4.3.4.8)}$$

The total element stiffness matrix, $[K_t{}^c]$, is obtained by the summation of eqn(4.3.3.3) with eqn(4.3.4.8), yielding,

$$[K_t{}^c] = [K_E{}^c] + [K_\sigma{}^c] = \begin{bmatrix} [K_{t\,sub}{}^c] & -[K_{t\,sub}{}^c] \\ -[K_{t\,sub}{}^c] & [K_{t\,sub}{}^c] \end{bmatrix} \qquad \text{eqn(4.3.4.9)}$$

where the sub-matrix $[K_{t\,sub}{}^c]$ is given by,

$$[K_{t\,sub}{}^c] = \frac{EA - P_N}{l} . [\acute{c}][\acute{c}]^t + \frac{P_N}{l} [I_3] . \qquad \text{eqn(4.3.4.10)}$$

Assuming symmetry, the terms of the stiffness sub-matrix, $[K_{t\,sub}{}^c]$, may be written as,

$$K_{11} = \frac{EA - P_N}{l} . c_x{}^2 + \frac{P_N}{l} ; \quad K_{22} = \frac{EA - P_N}{l} . c_y{}^2 + \frac{P_N}{l} ;$$

$$K_{33} = \frac{EA - P_N}{l} . c_z{}^2 + \frac{P_N}{l} ; \quad K_{12} = \frac{EA - P_N}{l} . c_x c_y = K_{21}$$

$$K_{13} = \frac{EA - P_N}{l} . c_x c_z = K_{31} ; \quad K_{23} = \frac{EA - P_N}{l} . c_y c_z = K_{32}$$

eqn(4.3.4.11)

The inclusion of the geometric stiffness matrix, $[K_\sigma{}^c]$, is vital to the analysis of a system undergoing large displacements and large strains for two reasons. Firstly, it represents an additional element stiffness generated by a combination of the out-of-plane displacements of the element with the element natural force. Secondly, it takes into account a change in the stiffness of the element arising from elastic straining.

4.3.5. Adoption of the Linear Element Formulation with the Dynamic Relaxation Algorithm.

4.3.5.1. Solution Procedure.

In the Dynamic Relaxation algorithm the component of out-of-balance force at each element node is divided by the direct component of the element stiffness ($\underline{K_{pq}}$), in order to calculate the nodal velocity $\dot{\delta}_{pq}{}^{t+\frac{\delta t}{2}}$ (eqn(4.2.9)). The stiffness term which appears in the denominator of eqn(4.2.9) represents the direct stiffness components of all the elements meeting at the node p. Eqn(4.3.3.3) and eqn(4.3.4.9) show that the elastic and the geometric stiffnesses of a linear element are given by two 6×6 matrices. The required stiffness term, $\underline{K_{pq}}$ (eqn(4.2.9)), should be obtained initially therefore, by the summation of the element stiffness matrices corresponding to the node p to form the matrix $[K_p{}^c]$. This matrix should then be inverted to yield the direct flexibility terms, taking into account the coupling effects of all the element degrees-of-freedom.

Since the determinant of the stiffness matrix of an unconstrained element is zero, it follows that the inversion of the matrix $[K_p{}^c]$ cannot be calculated. It is proposed therefore that only the corresponding diagonal terms of the element stiffness matrices are summed at the node p. The reciprocal of each of these figures (representing the direct stiffnesses in the directions, x, y, and z), are then used in eqn(4.2.9) to obtain the velocities of the nodes at each end of the element in the corresponding global directions. The resulting flexibility term is uncoupled therefore.

The selection of only the diagonal terms of the element stiffness matrices, can be shown to be an efficacious and a legitimate means of controlling the pseudo dynamic motion of the discretised system (Section 4.5). Only the first three terms of eqn(4.3.4.11) need to be calculated for

substitution into the Dynamic Relaxation algorithm therefore. Furthermore, this procedure dispenses with the need to invert an element stiffness matrix (or a global stiffness matrix representing the complete discretisation) [1].

The effects of using the decoupled diagonal element stiffness terms only, are two fold. Firstly, the sensitivity of the element formulation to large displacements is reduced. Secondly, the minimum time increment necessary to maintain the numerical stability of the algorithm is increased as the nodal stiffness $\underline{K_{pq}}$ is reduced (eqn(4.2.7)). The rate of convergence of the solution algorithm to the condition of equilibrium is enhanced therefore.

The solution procedure for the Dynamic Relaxation Algorithm with the linear element formulation is summarised below.

The surface is discretised into an adequate number of elements initially. They are arranged in the form of an orthogonal mesh, in which the element natural co-ordinate direction is aligned with either of the principal stress directions. The initial lengths of the elements are calculated according to eqn(4.3.2.2), and maintained as the current length.

Within each iterative cycle, the global stiffnesses of the elements are established and assigned to the element nodes, using the first three terms of eqn(4.3.4.11). Dynamic Relaxation uses the technique of the relaxation of residuals at each node in turn. Consequently, the current nodal velocities and nodal displacements, given by eqn(4.2.9) and by eqn(4.2.10), respectively, are calculated as a function of the nodal out-of-balance force vector (eqn(4.2.2) and eqn(4.2.3)). Consistent with the current vector of nodal displacements, the geometry of the surface is updated, and an evaluation of the total kinetic energy of the system is made (eqn(4.2.11)). This iterative cycle is repeated until a peak in the total kinetic energy of the system is identified.

The nodal velocities are then reset to zero, and the lengths of the elements updated in accordance with the current surface geometry. The analysis is re-commenced from the new element configurations. This procedure is reiterated until the out-of-balance force vectors, corresponding to all the internal degrees-of-freedom of the discretisation, are less than, or equal to, the error residual, Er.

1

Conversely, all of the elastic stiffness terms presented in eqn(4.3.3.3) must be included when calculating the change in the element natural force, P_N, arising from the elastic straining of the element. If eqn(4.3.3.3) is used, the natural force P_N is transformed into the global $\{x, y, z\}$ directions directly. Alternatively, the elongation of the element may be calculated from the nodal displacements. Using Hook's Law, the natural force P_N can then be calculated and resolved subsequently into the global $\{x, y, z\}$ directions.

4.3.5.2. Aspects of the Linear Element Formulation.

In the derivation of the geometric stiffness matrix, $[K_\sigma{}^c]$ (Section 4.3.4) it is assumed that the direction and the magnitude of the element nodal load, P_N, remain unchanged after the element has undergone a rigid body rotation (Figure 4.2). It is shown that as a consequence of this assumption a pair of fictitious loads, $\{P_1, P_2\}$, are required in order to maintain the equilibrium of the element. The vector addition of P_N and P_2 at the element node $2'$, gives the magnitude of the updated nodal force $P_N{}'$ as $\sqrt{P_N{}^2 + \bar{P}^2}$ (eqn(4.3.4.5)).

The magnitudes of the forces P_N and $P_N{}'$ are clearly different. Subsequent to a rigid body rotation the nodal forces P_N and $P_N{}'$ should be identical however. The fact that there is a difference between the magnitudes of the forces indicates that an error is present in the formulation of the geometric stiffness matrix, $[K_\sigma{}^c]$. The error arises through the necessary assumption that the direction and magnitude of the element nodal forces remain unchanged during the incremental step of the solution algorithm. Theoretically, the direction of the nodal forces varies with the element direction as a continuous function of time. The disparity between the forces P_N and $P_N{}'$ can be used as one measure of the ability of the incremental solution procedure to model the continuous response of a system discretised by the current linear element.

The error introduced into the geometric stiffness matrix, $[K_\sigma{}^c]$, is manifested in the form of fictitious stiffness terms. These terms, in conjunction with the displacement vector $\{\delta^r\}$ (eqn(4.3.4.4)) (describing the rigid body rotation of the element) account directly for the disparity between the nodal forces P_N and $P_N{}'$. The error is shown to reduce with a decrease in the equilibriating force $\bar{P}$ and thus with a decrease in the angle of the rigid body rotation, $\theta^c{}_r$ (eqn(4.3.4.6)). The linear element formulation can therefore be described as accurate for small angles of rigid body rotation only.

However, it is shown subsequently, that in the case of the proposed higher order finite element formulation, the fictitious terms in the element geometric stiffness matrix (arising from a violation of the assumption of small rigid body rotations) fail to affect significantly the correctness of the numerical solution obtained using Dynamic Relaxation (Section 6.4.3.3 of Chapter 6). Using the same arguements and, given that the error in the formulation of the geometric stiffness matrix does not induce numerical instability therefore, an accurate numerical solution to the system can be obtained when using a geometric stiffness matrix of the type derived in Section 4.3 with the Dynamic Relaxation algorithm.

4.3.6. Summary - Linear Element Formulation.

The following points are summarised regarding the adoption of the linear element formulation (Section 4.3.4) with the Dynamic Relaxation Algorithm (Section 4.2):

i) The linear element is adapted to the Dynamic Relaxation algorithm by using only the diagonal terms of the element stiffness matrix, $[K_t^c]$, in order to control the time increment of the iterative step and the magnitude of the nodal displacements.

ii) The geometric stiffness matrix, $[K_\sigma^c]$, is accurate for small angles of rigid body rotation only.

The numerical solutions to stable minimal energy forms obtained from the linear element formulation with the Dynamic Relaxation algorithm are presented in Section 4.5 of this chapter.

4.4. Triangular Element Discretisation.

4.4.1. Introduction.

In order to model a state of uniform surface stress, the linear element formulation presented in the preceding section assumes that the elements remain orthogonal and that they are aligned in either directions of the principal stresses, σ_x and σ_y. If the elements deviate from the condition of orthogonality during the application of the solution algorithm, the uniform pretension within the elements no longer models a state of constant surface stress, but an approximation to it. An increase in the violation of the condition of orthogonality causes the numerical solution to drift from the truly minimal form.

In the case of surfaces whose boundaries are not rectangular on plan or whose boundaries exhibit rapidly changing curvatures, it may not be possible to define initially or to maintain an orthogonal discretisation of linear elements prior to, or during, the form-finding procedure. It is required therefore, to find the level of element (linear) pretension which models a state of uniform stress within the surface, when the elements are orientated arbitrarily in space.

4.4.2. Element Formulation.

4.4.2.1. Introduction.

The plane constant strain triangular element in its original form has six degrees-of-freedom [4.14]. These comprise two (U, V) translations at each node, within a local two-dimensional co-ordinate system (Figure 4.3(a)). The element stiffness matrices (elastic and geometric) and the vector of equivalent nodal loads may be obtained through the adoption of an assumed displacement field and the minimisation of the total potential energy of the discretised system [4.14]. This may be described as a standard Finite Element method approach to the generation of the characteristic matrices of the element. However, with two degrees of freedom at each node, the element is only applicable to two-dimensional problems. Provision of the third translational degree-of-freedom at each node increases significantly the complexity of the element formulation.

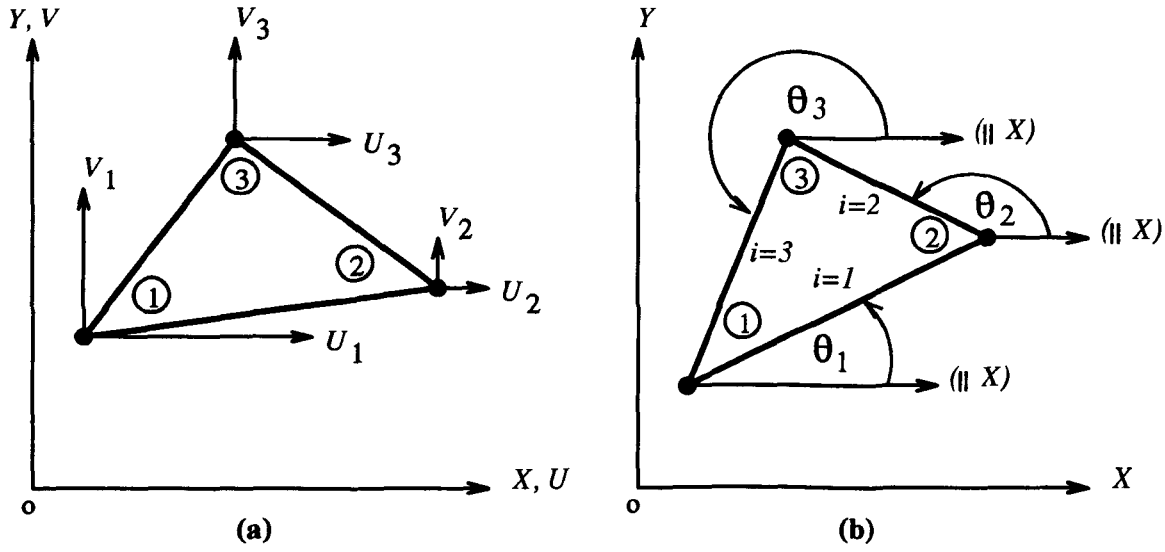

Figure 4.3 - Constant Strain Triangular Element.
(a) Original Form - 6 Degrees-of-Freedom Formulation.
(b) Alternative Form - 3 Degrees-of-Freedom Formulation.

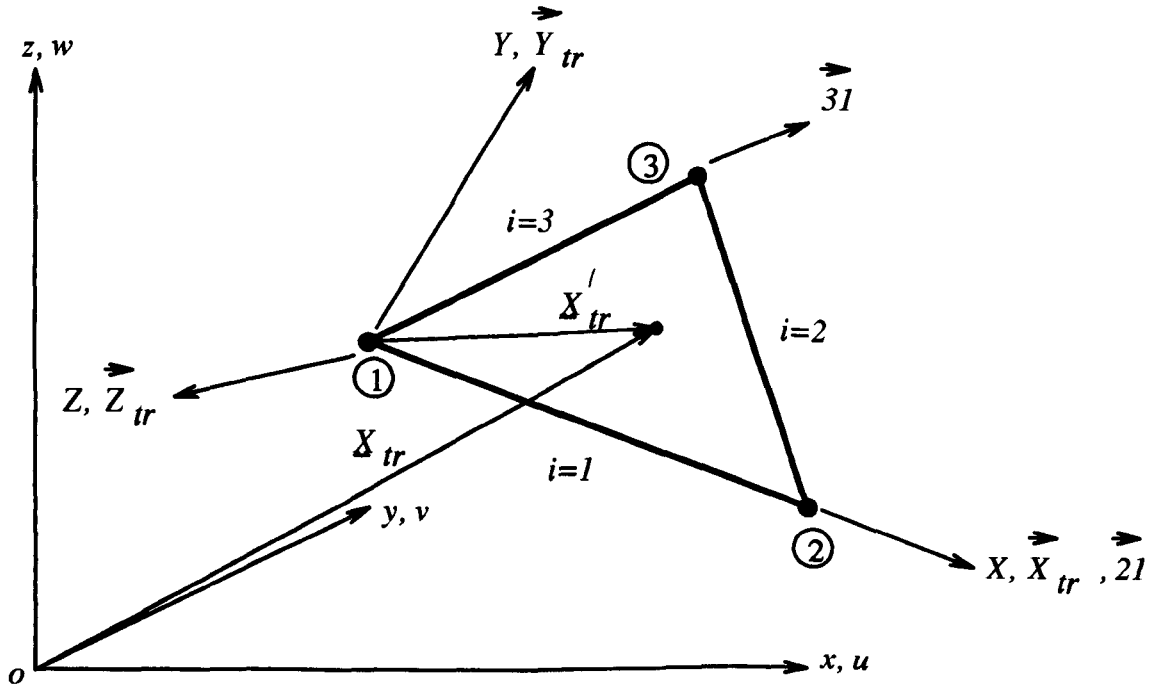

Figure 4.4 - Local Co-ordinate System of the Plane Triangular Element.

Alternatively, the degrees-of-freedom of the triangular element can be reselected as the change in lengths of the element sides [4.16]. Such an approach is valid in this case since the triangular element exhibits a state of constant strain. The strains defined at all points within the element, and those on the boundary of the element, are identical therefore. The continuum based triangular element can be represented by a triplet of discrete pseudo cables simulating the geometry and the

mechanical properties of the original continuous element [4.16]. The formulation of the element using this approach is summarised below.

The typical element illustrated in Figure 4.3(b) is shown in the local X, Y co-ordinate system. The elastic properties and stress state of the element are defined within the local co-ordinate system, and thus move with the surface as it is displaced. So that the elastic stiffness terms and the vector of equivalent nodal loads (defining the element stress field) are represented correctly, it is necessary that the element sides ($i = 1, i = 2, i = 3$) are numbered anti-clockwise as shown (Figure 4.3(b)). In addition, it is required that the angles ($\theta_1, \theta_2, \theta_3$) are measured in a similar manner. The formulation and the evaluation of the characteristic matrices of the element are carried out in a local planar system of co-ordinates. This is established in the manner described below.

4.4.2.2. Element Local Co-ordinate System.

It is assumed that the local X co-ordinate direction is aligned with the element side $i = 1$ ($\theta_1 = 0$, Figure 4.3). The angles θ_2 and θ_3 are measured relative to the local X co-ordinate. The rigid body rotation of the element is modelled correctly therefore, as the local element strains move with the element under this type of motion, and are a function of the angles θ_1, θ_2, and θ_3.

The local Z co-ordinate direction is defined normal to the surface of the element and calculated as,

$$\vec{Z_{tr}} = \vec{21} \times \vec{31} = \begin{vmatrix} \underline{i} & \underline{j} & \underline{k} \\ (x_2 - x_1) & (y_2 - y_1) & (z_2 - z_1) \\ (x_3 - x_1) & (y_3 - y_1) & (z_3 - z_1) \end{vmatrix} . \qquad \text{eqn(4.4.2.1)}$$

where $\{\{x_1, y_1, z_1\}, \{x_2, y_2, z_2\}, \{x_3, y_3, z_3\}\}$ are the global co-ordinates of the element side intercepts $\{i_3, i_1\}, \{i_1, i_2\}, \{i_2, i_3\}$ respectively.

The vector $\vec{Y_{tr}}$ defining the direction of the local Y co-ordinate, is given by the cross product of the vectors $\vec{Z_{tr}}$ with $\vec{X_{tr}}$. $\vec{X_{tr}}$ is a vector in the local X direction. The transformation matrix, $[\Lambda]$, relating the local co-ordinate system to the global co-ordinate system, is obtained from the components of the unit vectors in the local X, Y, and Z directions, $\hat{X}_{tr}, \hat{Y}_{tr}, \hat{Z}_{tr}$, and is written as,

$$\left.\begin{aligned} \hat{X}_{tr} &= \frac{\vec{X}_{tr}}{|\vec{X}_{tr}|} = \{ l_1, m_1, n_1 \} \\ \hat{Y}_{tr} &= \frac{\vec{Y}_{tr}}{|\vec{Y}_{tr}|} = \{ l_2, m_2, n_2 \} \\ \hat{Z}_{tr} &= \frac{\vec{Z}_{tr}}{|\vec{Z}_{tr}|} = \{ l_3, m_3, n_3 \} \end{aligned}\right\} \longrightarrow [\Lambda] = \begin{bmatrix} l_1 & m_1 & n_1 \\ l_2 & m_2 & n_2 \\ l_3 & m_3 & n_3 \end{bmatrix}$$

eqn(4.4.2.2)

As the triangular element is flat, only transformation into the local X, Y plane is necessary. The direction cosines describing the vector $\hat{Z}_{tr}$ are not required therefore. A reduced transformation matrix, $[\Lambda_r]$, may thus be written in the form,

$$[\Lambda_r] = \begin{bmatrix} l_1 & m_1 & n_1 \\ l_2 & m_2 & n_2 \end{bmatrix} \qquad \text{eqn(4.4.2.3)}$$

If the position of a point P on the element is denoted by the vector $\underline{X}_{tr}$ in the global co-ordinate system (Figure 4.4), such that,

$$\underline{X}_{tr} = \{ x^P \underline{i} + y^P \underline{j} + z^P \underline{k} \}, \qquad \text{eqn(4.4.2.4)}$$

where $\underline{i}$, $\underline{j}$, and $\underline{k}$, are unit vectors in the global x, y, and z, co-ordinate directions respectively,

then the position vector of the same point P in the local system of co-ordinates, $\underline{X}_{tr}'$, is written as,

$$\begin{aligned} \underline{X}_{tr}' &= [\Lambda_r] \underline{X}_{tr}^T \\ &= \{ (l_1 x^P + m_1 y^P + n_1 z^P) \} \underline{i} + \{ (l_2 x^P + m_2 y^P + n_2 z^P) \} \underline{j} \end{aligned}$$

eqn(4.4.2.5)

Using an equation of the form of eqn(4.4.2.5) therefore, an element described in the global system of co-ordinates may be transformed into the local X, Y plane.

4.4.2.3. Generation of Element Matrices.

Appendix 4-A presents a formulation to relate the surface strains in an inclined direction to the vector of local principal strains $\{\varepsilon\}^T = \{ \varepsilon_X, \varepsilon_Y, \gamma_{XY} \}$. If the direct strain in the element side i is denoted as ε_i, then from Appendix 4-A,

$$\varepsilon_i = \varepsilon_X \cos^2 \theta_i + \varepsilon_Y \sin^2 \theta_i + \gamma_{XY} \sin \theta_i \cos \theta_i , \qquad \text{eqn(4.4.2.6)}$$

where, θ_i is the anti-clockwise angle between the element side i and the local X axis, and $i = 1 \rightarrow 3$. ε_X and ε_Y are the direct strains in the local X and Y directions respectively, with γ_{XY} the local shear stress.

Application of eqn(4.4.2.6) to each side of the element leads to three equations of the form,

$$a_1 \varepsilon_X + b_1 \varepsilon_Y + c_1 \gamma_{XY} = \varepsilon_1 \qquad \text{eqn(4.4.2.7(a))}$$

$$a_2 \varepsilon_X + b_2 \varepsilon_Y + c_2 \gamma_{XY} = \varepsilon_2 \qquad \text{eqn(4.4.2.7(b))}$$

$$a_3 \varepsilon_X + b_3 \varepsilon_Y + c_3 \gamma_{XY} = \varepsilon_3 \qquad \text{eqn(4.4.2.7(c))}$$

where $a_i = \cos^2 \theta_i$, $b_i = \sin^2 \theta_i$, and $c_i = \sin \theta_i \cos \theta_i$. $\varepsilon_i = \dfrac{\delta_i}{l_i}$, in which δ_i is the extension of the element side i, and l_i is the unstrained length of the element side i, respectively.

By writing the expressions given in eqn(4.4.2.7(a)-(c)) in a determinant form,

$$\frac{\varepsilon_X}{\begin{vmatrix} b_1 & c_1 & \varepsilon_1 \\ b_2 & c_2 & \varepsilon_2 \\ b_3 & c_3 & \varepsilon_3 \end{vmatrix}} = \frac{-\varepsilon_Y}{\begin{vmatrix} a_1 & c_1 & \varepsilon_1 \\ a_2 & c_2 & \varepsilon_2 \\ a_3 & c_3 & \varepsilon_3 \end{vmatrix}} = \frac{\gamma_{XY}}{\begin{vmatrix} a_1 & b_1 & \varepsilon_1 \\ a_2 & b_2 & \varepsilon_2 \\ a_3 & b_3 & \varepsilon_3 \end{vmatrix}} = \frac{1}{\begin{vmatrix} a_1 & b_1 & c_1 \\ a_2 & b_2 & c_2 \\ a_3 & b_3 & c_3 \end{vmatrix}},$$

eqn(4.4.2.8)

the solution to the local principal strains $\{\varepsilon_X, \varepsilon_Y, \gamma_{XY}\}$ may be obtained in the manner outlined below.

Defining $\det [A] = \begin{vmatrix} a_1 & b_1 & c_1 \\ a_2 & b_2 & c_2 \\ a_3 & b_3 & c_3 \end{vmatrix}$ then, from eqn(4.4.2.8),

$$\varepsilon_X = \frac{1}{\det [A]} \begin{vmatrix} b_1 & c_1 & \varepsilon_1 \\ b_2 & c_2 & \varepsilon_2 \\ b_3 & c_3 & \varepsilon_3 \end{vmatrix}$$

$$= \frac{1}{\det [A]} \left(b_1 (c_2\varepsilon_3 - c_3\varepsilon_2) - c_1 (b_2\varepsilon_3 - b_3\varepsilon_2) + \varepsilon_1 (b_2c_3 - b_3c_2) \right)$$

eqn(4.4.2.9)

or,

$$\varepsilon_X = \frac{1}{\det [A]} \left(\varepsilon_1 (b_2c_3 - b_3c_2) - \varepsilon_2 (c_1b_3 - b_1c_3) - \varepsilon_3 (b_1c_2 - c_1b_2) \right)$$

eqn(4.4.2.10)

Similar expressions can be established for the strains ε_Y and γ_{XY}.

The vector of principal strains $\{\varepsilon\}$, can be written therefore in matrix form as,

$$\{\varepsilon\} = \begin{Bmatrix} \varepsilon_X \\ \varepsilon_Y \\ \gamma_{XY} \end{Bmatrix} = \frac{1}{\det[A]} \begin{bmatrix} (b_2c_3 - b_3c_2)(b_3c_1 - b_1c_3)(b_1c_2 - b_2c_1) \\ (a_3c_2 - a_2c_3)(a_1c_3 - a_3c_1)(a_2c_1 - a_1c_2) \\ (a_2b_3 - a_3b_2)(a_3b_1 - a_1b_3)(a_1b_2 - a_2b_1) \end{bmatrix} \begin{Bmatrix} \frac{\delta_1}{l_1} \\ \frac{\delta_2}{l_2} \\ \frac{\delta_3}{l_3} \end{Bmatrix}$$

$$= \frac{1}{\det[A]} \begin{bmatrix} (b_2c_3 - b_3c_2)(b_3c_1 - b_1c_3)(b_1c_2 - b_2c_1) \\ (a_3c_2 - a_2c_3)(a_1c_3 - a_3c_1)(a_2c_1 - a_1c_2) \\ (a_2b_3 - a_3b_2)(a_3b_1 - a_1b_3)(a_1b_2 - a_2b_1) \end{bmatrix} \begin{bmatrix} l_1^{-1} & 0 & 0 \\ 0 & l_2^{-1} & 0 \\ 0 & 0 & l_3^{-1} \end{bmatrix} \begin{Bmatrix} \delta_1 \\ \delta_2 \\ \delta_3 \end{Bmatrix}$$

$$= \frac{1}{\det[A]} \begin{bmatrix} (b_2c_3 - b_3c_2)l_1^{-1} & (b_3c_1 - b_1c_3)l_2^{-1} & (b_1c_2 - b_2c_1)l_3^{-1} \\ (a_3c_2 - a_2c_3)l_1^{-1} & (a_1c_3 - a_3c_1)l_2^{-1} & (a_2c_1 - a_1c_2)l_3^{-1} \\ (a_2b_3 - a_3b_2)l_1^{-1} & (a_3b_1 - a_1b_3)l_2^{-1} & (a_1b_2 - a_2b_1)l_3^{-1} \end{bmatrix} \begin{Bmatrix} \delta_1 \\ \delta_2 \\ \delta_3 \end{Bmatrix}$$

or

$$\{\varepsilon\} = [B^{tr}]\{\delta^{tr}\} \qquad \text{eqn(4.4.2.11)}$$

where $[B^{tr}]$ is a transformation matrix between the element side extensions $\{\delta_1, \delta_2, \delta_3\}$ and the vector of local element strains $\{\varepsilon\}$, and $\{\delta^{tr}\}$ is the vector of side extensions $\{\delta_1, \delta_2, \delta_3\}$.

The element stresses can be calculated as,

$$\{\sigma\} = \begin{Bmatrix} \sigma_X \\ \sigma_Y \\ \tau_{XY} \end{Bmatrix} = \begin{bmatrix} d_{11} & d_{12} & 0 \\ d_{21} & d_{22} & 0 \\ 0 & 0 & d_{33} \end{bmatrix} \begin{Bmatrix} \varepsilon_X \\ \varepsilon_Y \\ \gamma_{XY} \end{Bmatrix} = [E][B^t]\{\delta^{tr}\}, \qquad \text{eqn(4.4.2.12)}$$

where the matrix $[E]$ is the elasticity matrix relating the element strains to the element stresses.

Assuming isotropic plane stress and that the element remains in tension, the coefficients of $[E]$ may be written as,

$$d_{11} = d_{22} = \frac{E}{(1-\upsilon^2)}; \quad d_{12} = d_{21} = \upsilon d_{11}; \quad d_{33} = \frac{E}{(2(1+\upsilon))}.$$

eqn(4.4.2.13)

The contribution of elastic straining to the vector of side forces of the element, $\{T\}$, (or the forces in the pseudo cables) can therefore be obtained from,

$$\{T\} = \begin{Bmatrix} T_1 \\ T_2 \\ T_3 \end{Bmatrix} = \left[[B^{tr}]^T [E] [B^{tr}] V \right] \{\delta^{tr}\} \qquad \text{eqn(4.4.2.14)}$$

where V is the volume of the element under consideration.

The element elastic stiffness matrix $[K_E{}^{tr}]$ can be obtained directly from the definition that $\{T\} = [K_E{}^{tr}] \{\delta^{tr}\}$. Thus, with reference to eqn(4.4.2.14), $[K_E{}^{tr}]$ may be written as,

$$[K_E{}^{tr}] = \left[[B^{tr}]^T [E] [B^{tr}] \right] V , \qquad \text{eqn(4.4.2.15)}$$

During the form-finding procedure it is often desirable to maintain the stresses within the element at prescribed values, whilst taking into account changes in the element geometry. Denoting the constant stress state as $\{\sigma_c\}$ and pre-multiplying both sides of eqn(4.4.2.12) by $[B^{tr}]^T$ and V, leads to the expression,

$$V [B^{tr}]^T \{\sigma_c\} = \left[[B^{tr}]^T [E] [B^{tr}] V \right] \{\delta^{tr}\} . \qquad \text{eqn(4.4.2.16)}$$

Comparing eqn(4.4.2.16) with eqn(4.4.2.14) yields,

$$\{T_c\} = \begin{Bmatrix} T_{c1} \\ T_{c2} \\ T_{c3} \end{Bmatrix} = V [B^{tr}]^T \{\sigma_c\} , \qquad \text{eqn(4.4.2.17)}$$

where $\{T_c\}$ is the vector of element side forces representing an invariant state of element stress, $\{\sigma_c\}$, as the element deforms. The geometry of the element is described by the matrix $[B^{tr}]$.

The geometric stiffness matrix $[K_\sigma{}^{pc}]$ is obtained from the pseudo cable analogy . The terms of $[K_\sigma{}^{pc}]$ are written as a function of the element side forces $\{T_c\}$ (assuming an invariant stress field), the length of the pseudo cables, and the element orientation in the global $\{x, y, z\}$ space for each pseudo cable i (eqn(4.3.4.9)). The diagonal terms are therefore given as,

$$[K_{\sigma 11}{}^{pc}]_i = \frac{T_{ci}}{l_i} - \frac{T_{ci}}{l_i} c_{xi}{}^2 ;$$

$$[K_{\sigma 22}{}^{pc}]_i = \frac{T_{ci}}{l_i} - \frac{T_{ci}}{l_i} c_{yi}{}^2 ;$$

$$[K_{\sigma 33}{}^{pc}]_i = \frac{T_{ci}}{l_i} - \frac{T_{ci}}{l_i} c_{zi}{}^2 ; \qquad \text{eqn(4.4.2.18)}$$

where c_{xi}, c_{yi}, and c_{zi} are the direction cosines of the of the pseudo cable i in the global x, y, z co-ordinate directions, and $i = 1 \rightarrow 3$.

The total stiffness matrix of the triangular element $[K_t^{tr}]$ is therefore written as,

$$[K_t^{tr}] = [K_E^{tr}] + [K_\sigma^{pc}], \qquad \text{eqn(4.4.2.19)}$$

4.4.2.4. Summary.

The continuum based triangular element may be represented therefore by a triplet of pseudo cables possessing the elastic and geometric properties described by eqn(4.4.2.18) and by eqn(4.4.2.19). The invariant stress field of the element is represented by natural forces in the pseudo cables (eqn(4.4.2.17)). These forces can be tensile or compressive, dependent on the geometry and the orientation of the triangular element.

4.4.3. Adoption of the Triangular Element Formulation with the Dynamic Relaxation Algorithm.

4.4.3.1. Solution Procedure.

The solution procedure for the Dynamic Relaxation Algorithm with the triangular element formulation is summarised below.

i) Discretise the surface into an adequate number and into a suitable arrangement of elements,

For each element it is required further to:

ii) Calculate the normal vectors and establish the local system of co-ordinates (eqn(4.4.2.1) and eqn(4.4.2.2)),

iii) Transform the element from the global to the local co-ordinate systems (eqn(4.4.2.5)),

iv) Calculate the element side lengths. If the analysis is at the first loop after a kinetic energy peak has been detected, then the these calculated lengths are set as the initial current side lengths, and the nodal displacements set at zero,

v) Calculate the element elastic stiffness matrix $[K_E^{tr}]$ (eqn(4.4.2.15)) and extract the diagonal terms $K_E{}^{tr}{}_{11}$, $K_E{}^{tr}{}_{22}$, and,$K_E{}^{tr}{}_{33}$,

vi) Calculate the element side tensions (eqn(4.4.2.17)), assuming an invariant stress field.

Within the Dynamic Relaxation algorithm, for each node, it is required to:

vii) Treat the element side as pseudo cables, calculate the diagonal geometric stiffness terms (eqn(4.4.2.18)),

viii) Calculate the nodal out-of-balance force vector,

ix) Calculate the nodal velocities and the nodal displacements, in the global $\{x, y, z\}$ co-ordinate directions,

x) Calculate the total kinetic energy of the system, and update the surface geometry according to ix),

xi) If a kinetic energy peak is detected, return to ii), else viii),

xii) Continue the process until the out-of-balance force vector, at every node, is less than or equal to the error residual Er.

4.4.3.2. Aspects of the Triangular Element Formulation and the Stability and Convergence of the Solution Algorithm.

4.4.3.2.1. Introduction.

The iterative time step and the element formulation are recognised as factors which affect directly the numerical stability of the Dynamic Relaxation algorithm. An adequate value of the time step δt must be used to ensure that sufficient samples of the algorithm are made during a complete cycle of the pseudo oscillation of the surface, in order to negate instability. This condition is satisfied when the discrete sampling of the algorithm represents adequately the continuous response of the discretisation. Such a condition is represented mathematically by eqn(4.2.7).

The effect of the element formulation on the numerical stability and on the rate of convergence of the numerical algorithm, is described below. The assumptions which are inherent in the derivation of the equations of the characteristic matrices (Section 4.4.2), are shown to have significant effects on the performance of the element formulation. These effects are demonstrated by the solutions to systems undergoing large strains and large displacements.

4.4.3.2.2. Constant Element Strains.

The triangular element models a state of constant strain such that changes in the rate of straining of the surface may occur across element boundaries only. The characteristic of constant element strains can cause a buckling type of instability. This feature is most pronounced in the numerical algorithm as the value of the error residual Er (at which the condition of equilibrium is assumed to be satisfied) is reduced. It can be demonstrated by the analysis of the simple example surface illustrated in Figure 4.5.

The surface has overall plan dimensions of 24.m and 16.m in the global x and y directions respectively. It is discretised by 48 triangular elements. The geometrical boundary conditions are given in Table 4.1. A uniform surface stress vector, $\{\sigma_c\}$, has been assumed, corresponding to

$\sigma_x = \sigma_y = 5.\times10^{+6}$ kN.m^{-2} and $\tau_{xy} = 0.$ kN.m^{-2}. The stiffness of the surface is derived from prestress only, while a uniform thickness of the membrane of $1.\times10^{-3}$m is adopted.

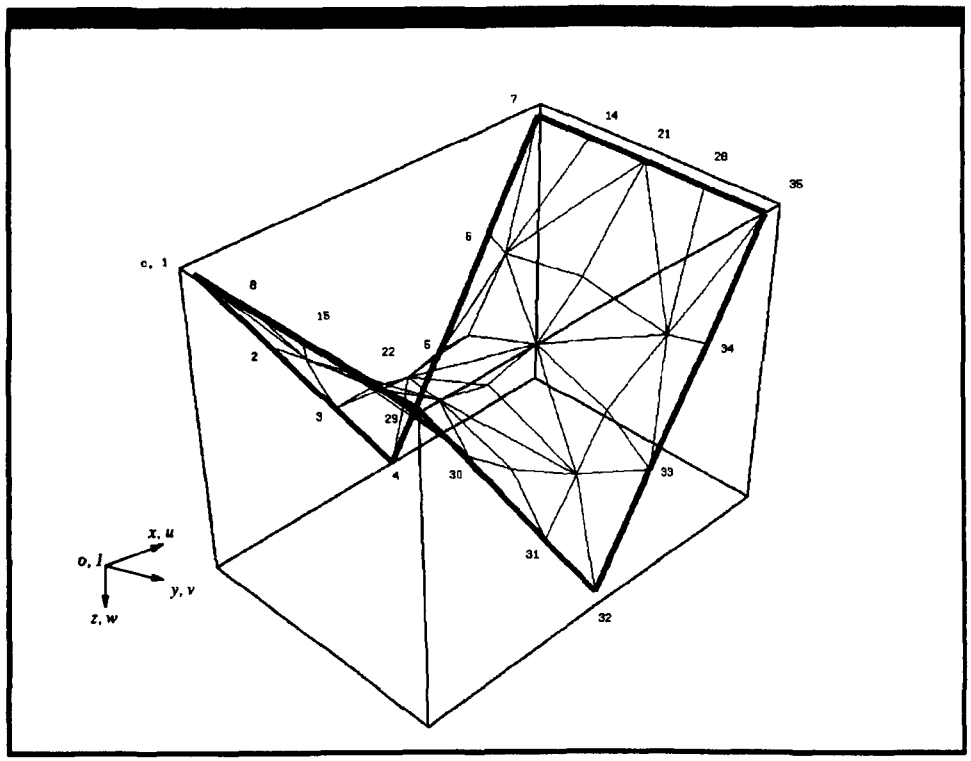

Table 4.1 - Boundary Conditions.					
Nodes	2, 30	3, 31	4, 32	5, 33	6, 34
z co-ord. (m)	6.000	12.000	18.000	12.000	6.000

Figure 4.5 - Simple 3-Dimensional Surface - Example 4.1.

Using the solution procedure described in Section 4.3.5.1, and assuming that Er = 0.1% of the maximum pseudo cable force, the condition of equilibrium is satisfied after 423 iterations. If, however, the value of Er is reduced to 0.025% of the maximum pseudo cable force, for example, the condition of equilibrium cannot be satisfied when using the same procedure (Section 4.3.5.1).

Instead it is found that in attempting to reduce the magnitude of the error residual throughout the surface, the elements buckle about the equilibrium position. Subsequent to the onset of this phenomenon, after each deformation cycle, the elements can be shown to maintain an approximately constant surface area and a constant out-of-balance force vector. Increasing the number of admissible iterations of the Dynamic Relaxation algorithm fails to improve the accuracy of the solution significantly, and may lead to numerical instability. In order to satisfy

the condition of equilibrium to the required accuracy (0.025% of the maximum pseudo cable force) the procedure described below has been devised.

Following the approach outlined in Section 4.3.5.1 initially, the membrane is permitted to vibrate about the equilibrium position with reducing amplitude and out-of-balance force vector. The element side forces are updated as the geometries of the elements change according to eqn(4.4.2.17). After a specified number of kinetic energy peaks, a revised routine is adopted. As described subsequently, in this procedure, the element side forces are held constant, while changes in the geometry of the element are permitted.

As the elastic modulus of the membrane, E, is assumed to be zero the element side forces remain unaffected by elastic straining of the surface (eqn(4.4.2.14)). Similarly, if the matrix $[B^{tr}]$ is held constant, no changes in the element side forces will occur due to changes in the geometry of the element (eqn(4.4.2.17)).

The element matrices $[B^{tr}]$, calculated at the end of the initial routine are adopted for the remainder of the analysis therefore. The terms in these matrices are held constant (in the revised procedure) irrespective of any further changes in the geometries of the elements. Subsequent to the adoption of the revised procedure, the surface is equilibriated using the direction cosines and the natural forces of the pseudo cables as before. The magnitudes of the element natural forces are a function of the matrix, $[B^{tr}]$, and are fixed, therefore. They are consistent with the stress field and with the element geometries at the end of the initial routine.

By keeping the element side forces constant during the revised routine, the condition of uniform stress is relaxed temporarily. The surface is less constrained therefore. Consequently, the revised procedure can be shown to permit the satisfaction of the condition of equilibrium to a greater accuracy. In the case of the Example 4.1 (Figure 4.5), a reduction in the error residual, Er, to a value of $1.\times10^{-10}$ % of the maximum pseudo cable force has been achieved.

At equilibrium, the natural forces in the pseudo cables combined with the final geometry of the triangular element, may no longer satisfy the required condition of uniform surface stress, however. A measure of the deviation of the surface stress from the constant stress state at equilibrium can be obtained as outlined below.

For each element i, the vector $\{T_{eq}\}_i$ and the matrix $[B_{eq}{}^{tr}]^T{}_i$ are related, at equilibrium, by the expression (eqn(4.4.2.17)),

$$\{T_{eq}\}_i = \begin{Bmatrix} T_{c1} \\ T_{c2} \\ T_{c3} \end{Bmatrix}_i = V\,[B_{eq}{}^{tr}]^T{}_i\,\{\sigma_{eq}\}_i\,, \qquad \text{eqn(4.4.3.1)}$$

where the subscript eq refers to the equilibrium state, and the natural forces T_{c1}, T_{c2}, and T_{c3} are those at the end of the initial solution procedure.

The vector of element stresses, at equilibrium, can thus be obtained through the equation,

$$\{\sigma_{eq}\}_i = \frac{1}{V}\left[[B_{eq}{}^{tr}]^T{}_i\right]^{-1}\{T_{eq}\}_i \ . \qquad \text{eqn(4.4.3.2)}$$

The vector of stress deviations for the element i are therefore given as,

$$\{\Delta\sigma\}_i = \{\sigma_c\}_i - \{\sigma_{eq}\}_i \qquad \text{eqn(4.4.3.3)}$$

NRPF	$\Delta\sigma_X{}^{max}$	$\Delta\sigma_Y{}^{max}$	$\Delta\tau_{XY}{}^{max}$	$\overline{\Delta\sigma_X}$	$\overline{\Delta\sigma_Y}$	$\overline{\Delta\tau_{XY}}$	δ_z (NRPF) ^{centre}
1	40.40 %	45.04 %	-29.11 %	21.61 %	13.22 %	9.80 %	11.20498 m (32.4 %)
2	4.43 %	36.65 %	-11.65 %	5.23 %	7.07 %	4.96 %	9.92173 m (17.3 %)
3	4.92 %	11.69 %	-8.31 %	3.68 %	2.53 %	2.76 %	9.04275 m (6.7 %)
4	2.49 %	9.22 %	-7.46 %	2.31 %	2.70 %	2.32 %	8.87468 m (4.9 %)
5	1.89 %	6.47 %	-4.89 %	1.52 %	2.09 %	1.48 %	8.67688 m (2.6 %)
10	1.60 %	2.75 %	1.84 %	0.82 %	0.86 %	0.70 %	8.51619 m (0.3 %)
20	1.13 %	1.41 %	0.79 %	0.43 %	0.46 %	0.37 %	8.48213 m (0.1 %)
50	0.51 %	0.25 %	0.55 %	0.09 %	0.12 %	0.12 %	8.46113 m (0.1 %)
60	**0.28 %**	**0.23 %**	**0.50 %**	**0.04 %**	**0.10 %**	**0.10 %**	**8.46079 m -**
70	0.07 %	0.23 %	0.44 %	0.03 %	0.11 %	0.10 %	8.46125 m (0.1 %)
90	0.12 %	0.27 %	-0.34 %	0.08 %	0.13 %	0.09 %	8.46347 m (0.1 %)
100	0.13 %	0.29 %	-0.32 %	0.10 %	0.13 %	0.09 %	8.46493 m (0.1 %)

Table 4.2 - Variation of Surface Accuracy with NRPF - Example 4.1.

Table 4.2 presents the deviations of the local principal stresses from the condition of uniform surface stress for the Example 4.1 (Figure 4.5). The results are quoted as a function of the number of kinetic energy peaks, NRPF, detected during the implementation of the initial solution procedure. The range $1 \leq \text{NRPF} \leq 100$ has been assumed. The maximum element stress deviations are given ($\Delta\sigma_X{}^{max}$, $\Delta\sigma_Y{}^{max}$, and $\Delta\tau_{XY}{}^{max}$), with the absolute averages ($\overline{\Delta\sigma_X}$, $\overline{\Delta\sigma_Y}$, and $\overline{\Delta\tau_{XY}}$), taken over all the elements.

The numerical estimate of the central node z co-ordinate, δ_z (NRPF) ^{centre}, obtained as a function of the repeat factor, NRPF, is also given. The disparity between the magnitude of δ_z (NRPF) ^{centre} and the accurate solution (assumed) is presented in parentheses in the final column of Table 4.2.[2]

The deviations in the principal stresses are presented as maximum percentage values, and as absolute averages of the percentage deviations over all elements of the discretisation. Since the prescribed shear stress τ_{XY} is zero (in order to model the condition of uniform surface stress) the percentage deviation, $\Delta\tau_{XY}$, is based on the average of the two direct principal stresses σ_X and σ_Y. The initial surface of the numerical model is assumed to be in the plane of the boundary.

As more kinetic energy peaks are permitted within the initial procedure (Section 4.3.5.1) (in which both the element side forces and the nodal displacements are updated) the magnitudes of the terms in the vector $\{\Delta\sigma\}_i$ are shown to reduce significantly (Table 4.2). As demonstrated below, the proximity of the numerical solution to the truly minimal surface is increased consequently.

By assuming a single kinetic energy peak (NRPF = 1) prior to the adoption of the revised routine, the condition of uniform stress is satisfied to within 45. % (approximately) (Table 4.2). The maximum of the average stress deviations is 21.6 %. In addition the central node z co-ordinate of the surface is accurate to within 68. % (approximately).

Assuming NRPF = 10, the accuracy of the surface geometry is increased to 99.3 % at the centre (for the discretisation presented in Figure 4.5). The maximum element stress deviation is reduced to 2.75 %, with the maximum of the average stress deviations given as <1. %. Increasing the number of admissible kinetic energy peaks to 50 realises a further, though a less marked, enhancement in the accuracy of the surface (Table 4.2).

At NRPF = 60 the central node z co-ordinate attains a minimum value (taken as the true value for the Example 4.1). The corresponding deviations in the element stresses are also shown to be at a minimum (in general). As the number of admissible kinetic peaks is augmented from 60 to 100 (and therefore the number of applications of the initial procedure is augmented) the deviations in the element stresses increase. Furthermore, the surface is shown to drift from the true solution (assumed). An explanation of this loss of accuracy from the numerical solution is proposed below.

2

The triangular element formulation (Section 4.4.2) can be shown to give an over estimate of the z co-ordinates of the minimal surface when compared with the experimental solution. The accurate estimate of the central node z co-ordinate is assumed to be the minimum value of those solutions obtained for the range $1 \leq \text{NRPF} \leq 100$ therefore. Consequently, in the case of the discretisation illustrated in Figure 4.5, the accurate numerical solution to the central node z co-ordinate is assumed to be 8.46079 m.

As the number of admissible kinetic energy peaks is increased beyond 60, the assumption of constant strains (in the triangular element formulation) forces the elements of the discretisation to buckle about the equilibrium position (Section 4.4.3.2.2). After further iterations of the initial solution procedure the buckling modes of the discretised surface begin to interfere with the pseudo oscillations of the numerical model (described by the Dynamic Relaxation algorithm). This phenomenon induces erroneous peaks in the kinetic energy of the system. Numerical inaccuracies and instabilities are therefore introduced into the numerical solution (Table 4.2).

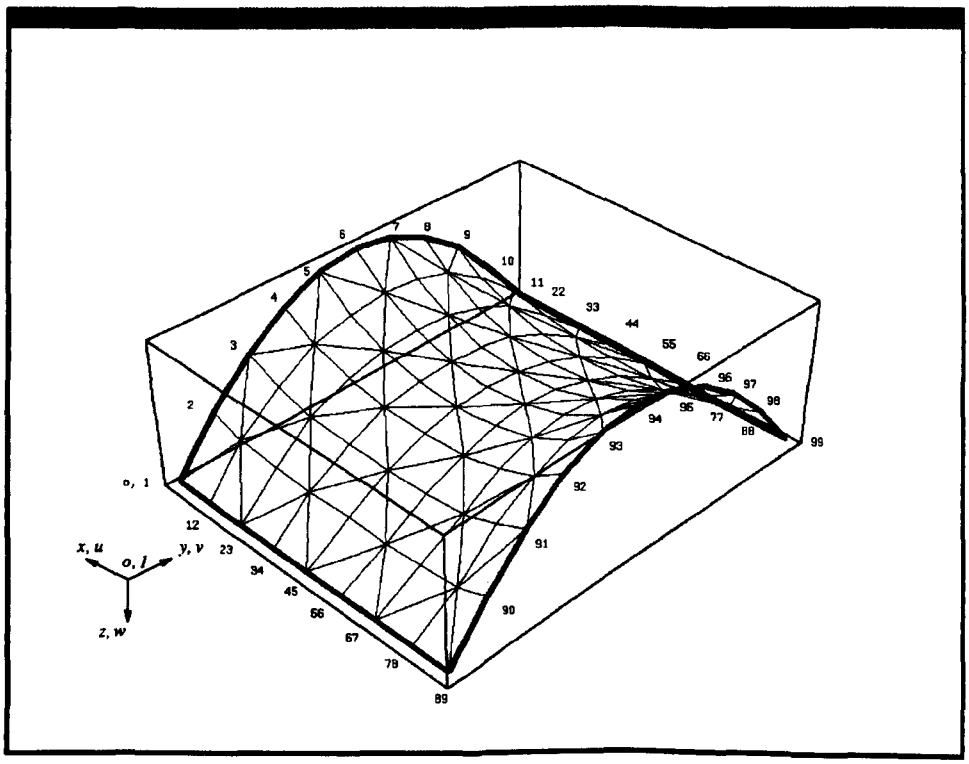

Table 4.3 - Boundary Conditions (Symmetrical).					
Nodes	2, 90	3, 91	4, 92	5, 93	6, 94
z co-ord. (m)	-6.156	-10.944	-14.364	-16.416	-17.100

Figure 4.6 - Simple 3-Dimensional Surface - Example 4.2.

The results of a similar analysis conducted on the surface illustrated in Figure 4.6 (Example 4.2) are presented in Table 4.4.

The surface has overall plan dimensions of 40.m and 50.m in the global x and y directions respectively. It is discretised by 160 triangular elements. Table 4.2 presents the geometrical boundary conditions of the surface. The remaining elastic and surface constants are assumed to be the same as those given in the case of Example 4.1. The initial surface of the numerical model is assumed to be in the plane of the boundary. (The accurate numerical solution to the central node z co-ordinate of the surface is taken as -9.14950 m.)

NRPF	$\Delta\sigma_X{}^{max}$	$\Delta\sigma_Y{}^{max}$	$\Delta\tau_{XY}{}^{max}$	$\overline{\Delta\sigma_X}$	$\overline{\Delta\sigma_Y}$	$\overline{\Delta\tau_{XY}}$	δ_z (NRPF) *centre*
1	3.47 %	5.59 %	-3.95 %	2.38 %	1.91 %	1.01 %	-9.27298 m (1.3 %)
2	26.94 %	22.10 %	-7.36 %	9.10 %	6.66 %	2.12 %	-9.24207 m (0.9 %)
3	7.16 %	7.11 %	-2.99 %	3.62 %	2.56 %	0.90 %	-9.22861 m (0.8 %)
4	4.07 %	4.97 %	2.72 %	2.84 %	2.03 %	0.74 %	-9.22762 m (0.8 %)
5	3.70 %	2.16 %	-2.11 %	1.91 %	1.18 %	0.52 %	-9.21387 m (0.6 %)
10	1.85 %	0.58 %	-1.06 %	0.67 %	0.49 %	0.34 %	-9.19938 m (0.5 %)
20	0.76 %	0.48 %	0.68 %	0.32 %	0.32 %	0.25 %	-9.18458 m (0.3 %)
50	0.35 %	0.33 %	0.56 %	0.10 %	0.17 %	0.12 %	-9.16496 m (0.2 %)
100	0.19 %	0.28 %	0.34 %	0.06 %	0.12 %	0.06 %	-9.15548 m (0.1 %)
180	**0.17 %**	**0.37 %**	**0.20 %**	**0.08 %**	**0.08 %**	**0.04 %**	**-9.14950 m -**

Table 4.4 - Variation of Surface Accuracy with NRPF - Example 4.2.

Though a direct comparison between Table 4.2 and Table 4.4 cannot be made (due to the dissimilarities of the surfaces and of the boundary conditions of Example 4.1 and Example 4.2) the following additional observations can be made, common to both sets of results;

i) Using NRPF = 10 the central node z co-ordinate of both example surfaces are accurate to within 1. % when compared with the same surface described using NRPF = 100.

ii) A maximum stress deviation of 1. % generates less than a 0.5 % error in the central node z co-ordinate when the corresponding figure is compared with the accurate numerical solution.

iii) A critical value of NRPF exists, beyond which, numerical inaccuracy and instability may corrupt the solution. In the case of Example 4.1 the critical value of NRPF is 60, and for Example 4.2 is 180.

iv) For the examples investigated, the accuracy of the surface may be related to the condition of uniform stress and the element discretisation. This is done by expressing the element size as a percentage of the overall dimensions of the surface. This figure is then related to the maximum of the average element stress deviations. The procedure is described more fully below with reference to a specific example.

The discretisation illustrated in Figure 4.5 is characterised by an initial element size corresponding to 16.67 % and 25.0 % of the surface dimensions in the global x direction and y direction respectively. Similarly, the element size in Example 4.2 is 10.0 % and 12.5 % of the corresponding surface dimensions, respectively.

The maximum of the average element stress deviations, 0.26 %, corresponds to an error in the central node z co-ordinate of 0.1 % (Table 4.2, Example 4.1). In the case of the Example 4.2 the same surface accuracy can be achieved with a maximum of the average element stress deviations of 0.13 % (Table 4.4).

The maximum of the average stress deviations in the surface of Example 4.1 and of Example 4.2 (0.26 % and 0.13 % respectively), may be related to the maximum element size $\Delta_G{}^{max}$ (25.0 % and 12.5 % respectively), by a factor of approximately 100 (96.2 in both cases) therefore. Consequently, the maximum of the average element stress deviations (expressed as a percentage) must not exceed $\frac{\Delta_G{}^{max}(\%)}{100.}$ if the resulting numerical model is to be accurate to within 0.1 % of the same surface discretisation, but equilibriated with "uniform stress".[3]

Through this approach, a measure of the accuracy of the discretisation may be made via the magnitude of the maximum of the average principal stresses and the relative size of the elements of the discretisation.

4.4.3.2.3. Assumption of Small Strains.

In the preceding section it is has been shown that the constant strain characteristics of the element can result in a locking type of phenomenon. A "softening" of the element formulation, by releasing the constraint of constant surface stress during the latter part of the analysis, permits the full equilibrium of the surface to a high level of accuracy. However, violation of the assumptions inherent in the element formulation can also be shown to lead to numerical instability and to a loss of convergence.

3

In Example 4.1 the state of "uniform stress" is assumed to exist when $-0.10\ \% \leq \overline{\Delta\sigma^{max}} \leq +0.10\ \%$, and for Example 4.2 when $-0.08\ \% \leq \Delta\sigma^{max} \leq +0.08\ \%$. The ranges of $\Delta\sigma^{max}$ presented here have been found to be the minimum attainable values for Example 4.1 and Example 4.2 respectively.

Appendix 4-A summarises the derivation of the relationship between the principal strains and the strains in an inclined direction (used to generate the element strain-displacement expressions (eqn(4.4.2.11))). In the derivation of this relationship it is assumed that the strains $\{\varepsilon_x, \varepsilon_y, \gamma_{xy}\}$ are small, such that the angles θ and θ' (Figure 4-A.1) are approximately equal (Appendix 4-A). A measure of the effect of this assumption can be made by comparing the numerical solution with the exact solution to a particular problem. This procedure is known as the "Patch Test". (The basis of the test is described more fully in Chapter 6.)

A suitable "patch" of elements is illustrated in Figure 4.7. The numerical model (Figure 4.7) is intended to represent a thin plate or membrane subjected to axial tension in the global x direction. The axial tension is applied through an external stress, σ_x. The nodes 1 and 5 are free to displace in the global y direction so as to permit the accurate modelling of the Poisson's ratio effect (Figure 4.7).

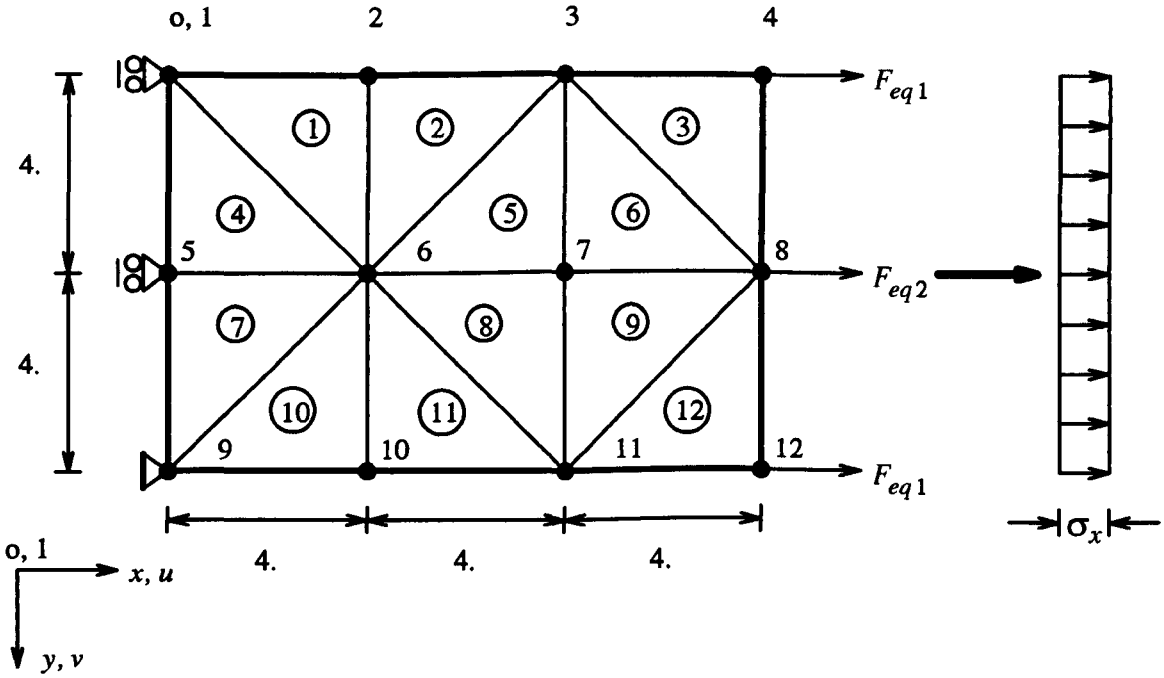

Figure 4.7 - "Patch" of Triangular Elements with Boundary Conditions.

The magnitude of the external stress, σ_x, is assumed to be $3.\times10^{+5}$ kN.m^{-2} It is represented by the equivalent nodal loads F_{eq1} and F_{eq2} (600 kN and 1200 kN respectively, Figure 4.7), derived using the shape functions of the six degree-of-freedom triangular finite element [4.18]. A value of $1.\times10^{-3}$ m is adopted for the thickness of the plate. The elastic modulus, E, is assumed to be a variable (but constant for all elements). Poisson's ratio, υ, is taken as 0.1

Through the selection of different values of the elastic modulus, E, the amount of straining in the plate can be varied. A comparison may thus be made between the exact and the numerical solutions to the element stresses and the displacements of the nodal degrees-of-freedom, as the

strains of the model are increased. The disparity between the numerical and exact solutions can be used as a measure of the ability of the triangular element formulation (Section 4.4.2) to model large strains. The results of this study are presented in Table 4.5.

Elastic Modulus E	Maximum Stress Error	Maximum Displacement Error	Exact Strain ε_x
$1.\times10^{+8}$ kN.m^{-2}	0.013 %	0.20 %	0.3 %
$1.\times10^{+7}$ kN.m^{-2}	0.14 %	1.91 %	3.0 %
$1.\times10^{+6}$ kN.m^{-2}	1.80 %	7.67 %	30.0 %
$3.\times10^{+5}$ kN.m^{-2}	3.37 %	34.1 %	100.0 %
$1.\times10^{+5}$ kN.m^{-2}	8.91 %	84.0 %	300.0 %

Table 4.5 - Patch Test Results for the Discretisation Illustrated in Figure 4.7.

As the strains in the model increase, the errors in the numerical solutions to the element stresses and to the nodal displacements, are shown to increase also (Table 4.5). The accumulation of error in the numerical solution can be attributed to the violation of the assumption of small strains in the element formulation, directly. The violation of this assumption is shown to induce much larger errors in the numerical solution to the nodal displacements, than to the element stresses. For example, in the case of a strain of 300.0 % the maximum error in the nodal displacements is 84.0 %. Conversely, the error in the element stresses is only 8.91 % (Table 4.5).

A significant error in the nodal displacements of an individual element can cause the element to collapse, or to invert, as the apex node passes through the side opposite to it. As demonstrated below, this phenomenon can be induced through large membrane strains occurring during the form-finding procedure (where element strains may readily exceed 100. %).

The surface illustrated in Figure 4.8(a) has overall dimensions of 24.m and 16.m in the global x and y directions respectively, and is discretised by 768 triangular elements. The element width and height are approximately equal to unity (initially) for all elements. The boundary conditions of the numerical model are similar to those described in the case of Example 4.1, but with the exception that the maximum z co-ordinate is 3.0 m. The initial surface of the form is described using Hermitian polynomials [4.21] with the factor $\lambda_s = 0.5$ [4].

[4] Those curves defined by the Hermitian polynomial are controlled by the z co-ordinate and by the slope of the curve at the end points. The latter has been taken as the z co-ordinate divided by the dimension of the elements in the direction of the curve. In order to influence the shape further, the factor λ_s has been applied to the slopes at each end.

The condition of uniform stress is given as $\sigma_x = \sigma_y = 5.e^{+6}$ kN.m^{-2} and $\tau_{xy} = 0.$ kN.m^{-2}. A thickness of the $1.\times10^{-3}$ m has been assumed for the membrane. The stiffness of the membrane is derived from prestress only.

Using the solution procedure proposed in Section 4.4.3.2.2 the surface is equilibriated after 399 iterations (Figure 4.8(a)). The maximum error residual, Er, is 0.025 % of the maximum pseudo cable force, and the surface stress is uniform to within 2.12 %.

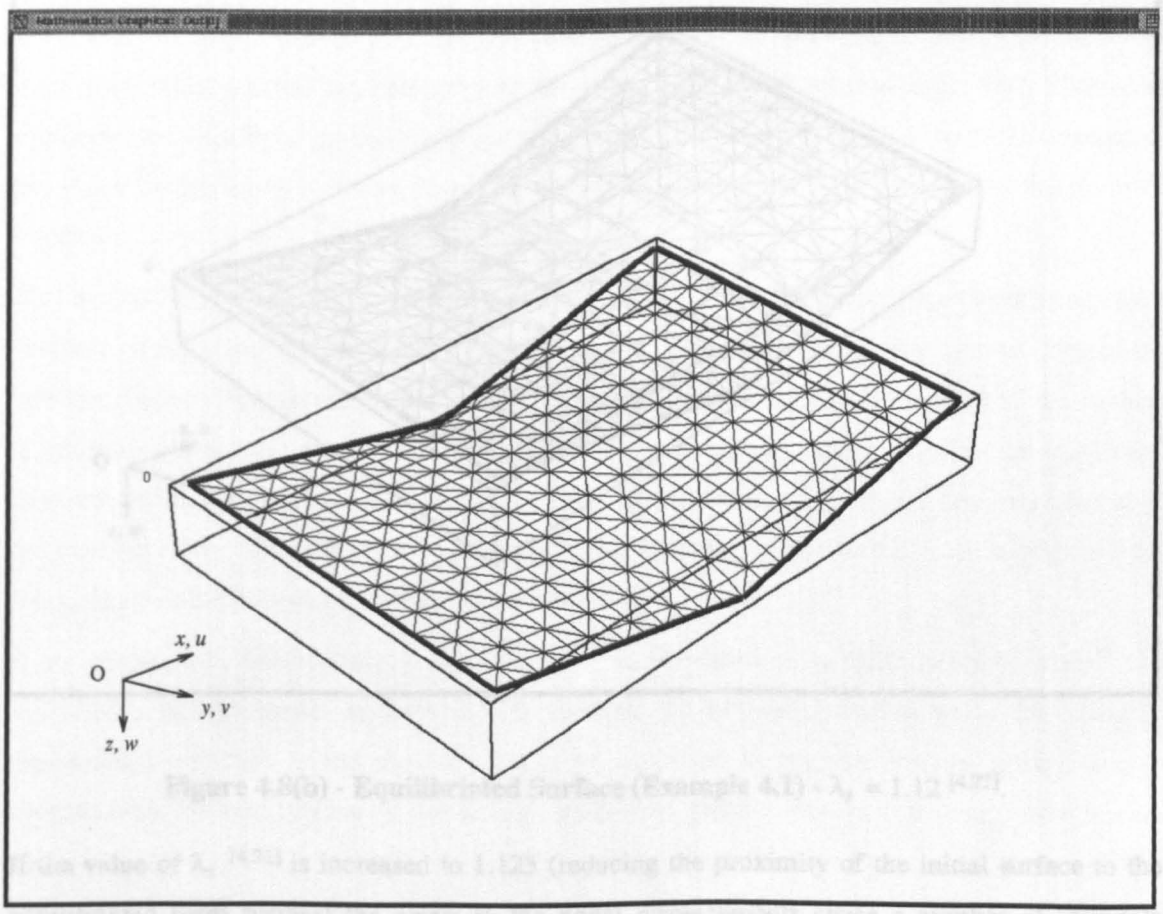

Figure 4.8(a) - Equilibriated Surface (Example 4.1) - $\lambda_s = 0.5$ [4.21].

If the initial surface is defined with $\lambda_s = 1.12$ [4.21] (such that it is more remote from the final form than when $\lambda_s = 0.5$ [4.21]) the equilibriated surface shown in Figure 4.8(b) is obtained. In this case 783 iterations are required to equilibriate the surface to the same error residual (0.025 % of the maximum pseudo cable force). The condition of uniform stress is not satisfied however. This is demonstrated by a value for the maximum element stress deviation of 420.48 %.

Significant distortions of the elements of the discretisation are shown to occur during the form-finding procedure (Figure 4.8(b)). The poor representation of the condition of uniform stress in the case of the surface illustrated in Figure 4.8(b), and the geometrical disparity between the solutions (Figure 4.8(a) and Figure 4.8(b)) can be attributed to errors in the element nodal

displacements (predominantly). These errors are induced by a violation of the assumption of small strains in the element formulation [5].

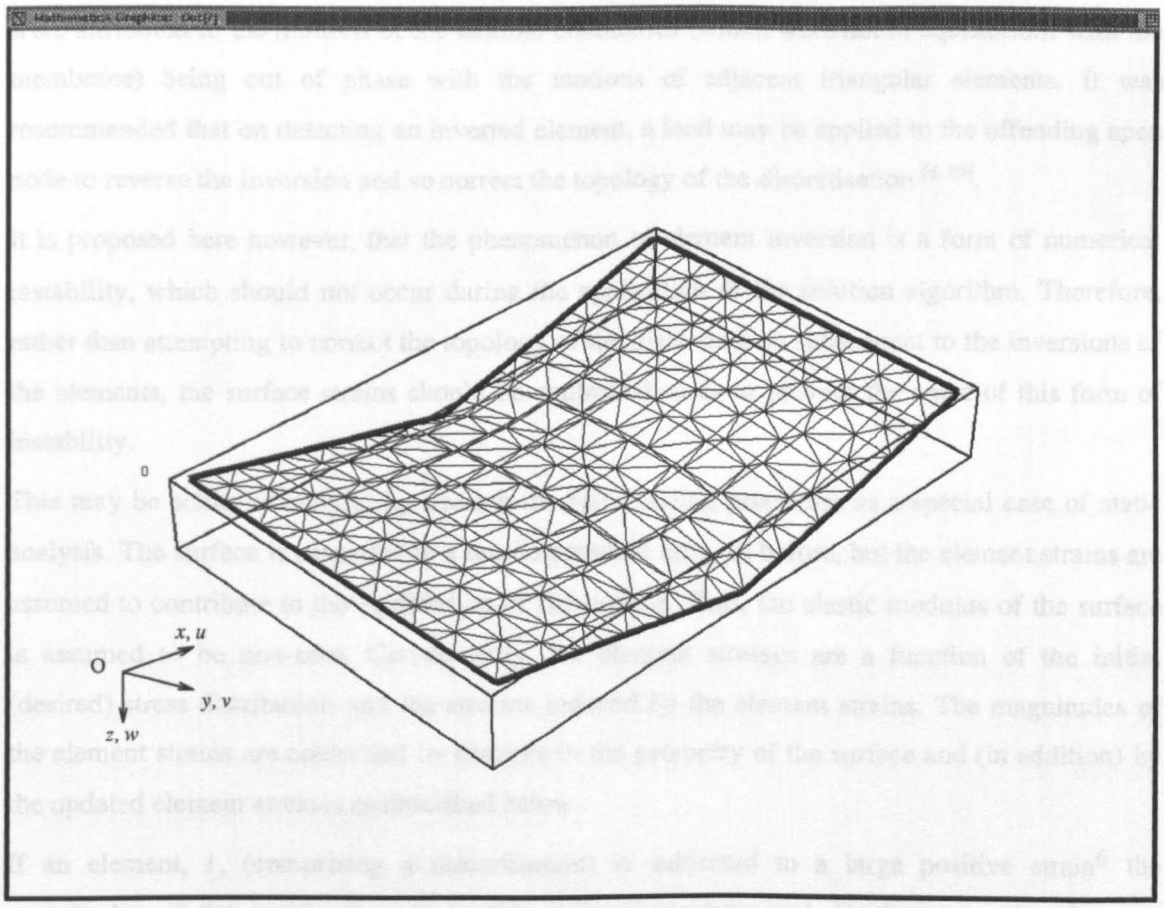

Figure 4.8(b) - Equilibriated Surface (Example 4.1) - $\lambda_s = 1.12$ [4.21].

If the value of λ_s [4.21] is increased to 1.125 (reducing the proximity of the initial surface to the equilibriated form further) the errors in the nodal displacements cause a number of elements comprising the discretisation to invert. The inversion of any element immediately yields an erroneous topology for the discretisation. This introduces additional errors into the numerical model and causes the solution algorithm to diverge.

The inversion of an element may be visualised as a fold in the material of the surface. In the case of a soap-film surface, folds of this type are not generated. The numerical representation of a minimal (soap-film) surface is in error therefore, when the phenomenon of element inversion occurs.

---

5 In the solution represented by Figure 4.8(b), the magnitudes of the element strains have been increased (when compared with the strains in the preceding solution (Figure 4.8(a))) by reducing the proximity of the initial surface to the equilibriated form.

Minimal surfaces have been investigated with the triangular element formulation (Section 4.4.2) previously [4.19]. The surfaces investigated in reference [4.19] were bounded by flexible elastic cable elements. In this case, the inversions of certain triangular elements of the discretisation were attributed to the motions of the flexible boundaries (which were not in equilibrium with the membrane) being out of phase with the motions of adjacent triangular elements. It was recommended that on detecting an inverted element, a load may be applied to the offending apex node to reverse the inversion and so correct the topology of the discretisation [4.19].

It is proposed here however, that the phenomenon of element inversion is a form of numerical instability, which should not occur during the application of the solution algorithm. Therefore, rather than attempting to correct the topology of the discretisation subsequent to the inversions of the elements, the surface strains should be controlled so as to prevent the onset of this form of instability.

This may be achieved simply, by treating the form-finding procedure as a special case of static analysis. The surface is subjected to a tensile prestress only, as before, but the element strains are assumed to contribute to the equilibrium of the surface. Thus, the elastic modulus of the surface is assumed to be non-zero. Consequently, the element stresses are a function of the initial (desired) stress distribution and the stresses induced by the element strains. The magnitudes of the element strains are controlled by changes in the geometry of the surface and (in addition) by the updated element stresses as described below.

If an element, i, (comprising a discretisation) is subjected to a large positive strain[6] the magnitudes of the tensile stresses in this element are increased. Furthermore, the elements immediately adjacent to the element i will be subjected to negative strains, giving rise to decreases in the magnitudes of the tensile stresses in these elements (assuming they remain stable).

In order to establish equilibrium, the geometry of the surface (and therefore of the elements) must change. The large imbalance of stresses in the plane of the surface cause the stretched element to contract and the compressed elements to expand. Subsequent to this cycle of expansion and contraction, the sizes of the elements are unchanged (approximately). The sustained collapse and enlargement of adjacent elements (central region of Figure 4.8(b)) is negated therefore, and the stability of the solution algorithm is maintained. The stability of the solution algorithm is enhanced further by the contribution of the elastic stiffness terms to the overall stiffness of the

6

In the form-finding of stable minimal energy forms, adjacent elements are usually subjected to similar strains. An individual element may be subjected to a large positive (or negative) strain as a result of the effects of the solution algorithm becoming unstable. Errors introduced into the numerical solution, by a violation of an inherent assumption in the element formulation for example, can have a similar consequence.

surface.

The mathematical application of this approach is outlined below.

At the time $t = i\ \delta t$, the vector of element side forces $\{T_E\}^t$, may be given by the expression, (eqn(4.4.2.9) & eqn(4.4.2.12)),

$$\{T_E\}^t = \left\{ \begin{matrix} T_{E1} \\ T_{E2} \\ T_{E3} \end{matrix} \right\}^t = V\,[B^{tr}]^T\,\{\sigma_c\}\Big|^{t=0}$$

$$+ \sum_{i=1}^{i=n} \left[\ [B^{tr}]^T\,[D]\,[B^{tr}]\,V\ \right]\Big|^{t=i\,\delta t} \left[\ \{\delta^{tr}\}\Big|^{t=i\,\delta t} - \{\delta^{tr}\}\Big|^{t=(i-1)\,\delta t}\ \right]$$

eqn(4.4.3.4)

where i is the current iterative loop, and n is the maximum number of admissible loops. The vector of element side forces, $\{T_E\}^t$, is a function of the elasticity of the surface, denoted by the subscript E.

The first term on the far right side of eqn(4.4.3.4) constitutes the element side forces describing the initial (desired) element stresses. The term in the summation sign gives the contribution of the elastic straining of the element to the element side forces at each iterative step. The element stresses are given by the vector $\{\sigma_E\}^t$, written as,

$$\{\sigma_E\}^t = \{\sigma_c\}\Big|^{t=0} + \sum_{i=1}^{i=n} \left[\ [D]\,[B^{tr}]\ \right]\Big|^{t=i\,\delta t} \left[\ \{\delta^{tr}\}\Big|^{t=i\,\delta t} - \{\delta^{tr}\}\Big|^{t=(i-1)\,\delta t}\ \right]$$

eqn(4.4.3.5)

If it is found at the time interval $t = i\ \delta t$ that the element stresses are negative, it is assumed that the element has wrinkled. In this case the offending principal direct stress(es) is set to zero and the shear stress prescribed according to the Mohr's circle of stress. The revised vector of element stresses, $\{\sigma_W\}$, are then used to recalculate the vector of element side forces $\{T_W\}$, as,

$$\{T_W\}^t = V\,[B^{tr}]^T\Big|^{t=i\,\delta t}\,\{\sigma_W\}^t\ . \qquad \text{eqn(4.4.3.6)}$$

The remainder of the analysis follows a similar procedure to that outlined in Section 4.4.3.1.

Due to the contribution of the element strains to the element stress vector, $\{\sigma_E\}^t$, the condition of uniform stress is violated at equilibrium (generally). As demonstrated below, by re-imposing the constant stress vector, $\{\sigma_c\}$, and re-equilibriating the surface, the condition of uniform stress can be represented more closely.

Table 4.6 presents the maximum and the average element stress deviations for the surface illustrated in Figure 4.8(a). The results are presented for the first five re-impositions ($N_{GI} = 1 \rightarrow 5$) of the constant stress vector, $\{\sigma_c\}$. The numbers of iterations of the solution algorithm to achieve equilibrium (N_{IT}) for each re-imposition of the vector $\{\sigma_c\}$ are presented in the second column (Table 4.6).

The initial surface of the form is defined with $\lambda_s = 1.12$ [4.21]. A value of $5.\times10^{+6}$ kN.m^{-2} has been assumed for the elastic modulus of the membrane, with Poisson's ratio $\upsilon = 0.1$. The error residual, Er, is taken as 0.025 % of the maximum pseudo cable force.

N_{GI}	N_{IT}	$\Delta\sigma_X{}^{max}$	$\Delta\sigma_Y{}^{max}$	$\Delta\tau_{XY}{}^{max}$	$\overline{\Delta\sigma_X}$	$\overline{\Delta\sigma_Y}$	$\overline{\Delta\tau_{XY}}$
1	1392	18.35 %	17.76 %	12.99 %	1.85 %	1.51 %	1.06 %
2	1208	2.31 %	2.23 %	1.65 %	0.20 %	0.19 %	0.14 %
3	899	-0.31 %	-0.31 %	0.23 %	0.03 %	0.03 %	0.02 %
4	627	-0.38 %	-0.37 %	-0.17 %	0.02 %	0.02 %	0.01 %
5	505	-0.39 %	-0.38 %	-0.18 %	0.01 %	0.02 %	0.01 %

Table 4.6 - Variation of Element Stress Deviation with N_{GI} ($E = 5.\times10^{+6}$ kN.m^{-2}).

The maximum element stress deviation is shown to converge to 0.4 % (approximately). Figure 4.8(b) illustrates the solution to the same surface in which the elastic modulus, E, was assumed to be zero. In this case the maximum element stress deviation was 420.48 % at equilibrium. [7] The disparity between the maximum element stress deviations of the solutions can be attributed to the effects of the violation of the assumption of small strains in the element formulation. By including elasticity in the solution algorithm it is shown that the effects of a violation of this assumption are negated.

As demonstrated below a minimum value of elastic modulus, E, should be adopted which will maintain the numerical stability of the solution algorithm and maximise its rate of convergence to the conditions of equilibrium and uniform surface stress.

The results presented in Table 4.6 are based on a conservative value of E so as to illustrate the application of the revised procedure. If the elastic modulus of the surface is reduced to $5.\times10^{+5}$ kN.m^{-2}, the results given in Table 4.7. are obtained. The solutions presented in Table 4.6 and in

7

The initial surface of the numerical model was described with $\lambda_s = 1.12$ [4.21] in both cases.

Table 4.7 converge to the same final definition of the surface. The latter solution (Table 4.7) demonstrates a saving of 48 % in computational effort over the former (Table 4.6) however.

The minimum value of E which will ensure numerical stability of the solution algorithm can be used as a measure of the complexity of the form. Thus, as the intricacy of the geometry of a surface is increased (by the application of additional boundary conditions) the minimum value of E necessary to ensure the numerical stability of the solution algorithm is similarly augmented, and vice versa.

N_{GI}	N_{IT}	$\Delta\sigma_X{}^{max}$	$\Delta\sigma_Y{}^{max}$	$\Delta\tau_{XY}{}^{max}$	$\overline{\Delta\sigma_X}$	$\overline{\Delta\sigma_Y}$	$\overline{\Delta\tau_{XY}}$
1	1566	1.93 %	1.87 %	1.48 %	0.20 %	0.17 %	0.12 %
2	823	-0.38 %	-0.37 %	-0.17 %	0.01 %	0.02 %	0.01 %

Table 4.7 - Variation of Element Stress Deviation with N_{GI} ($E = 5.\times10^{+5}$ kN.m^{-2}).

4.4.4. Summary - Triangular Element Formulation.

The following points are summarised from the studies presented in the preceding sections, regarding the triangular element formulation.

i) The characteristic of constant element strain can lead to a buckling type of phenomenon. This may result in the divergence of the numerical algorithm.

ii) By releasing the constraint of uniform surface stress in the numerical model after a specified number of kinetic energy peaks (NRPF), the buckling type of phenomenon associated with the constant strain element can be prevented. A critical value of NRPF exists beyond which the accuracy of the solution is reduced.

iii) The accuracy of the equilibriated surface can be related to the condition of uniform stress and the element discretisation in the following way - the maximum of the average stress deviations in the surface (expressed as a percentage) must not exceed $\frac{\Delta_G{}^{max}(\%)}{100}$ if the resulting surface is to be accurate to within 0.1 % of the same surface discretisation, but equilibriated with uniform stress. ($\Delta_G{}^{max}$ is the maximum element size (maximum overall dimension)).

iv) By violating the assumption of small element strains errors in the numerical solution can be induced, which may lead to the divergence of the solution algorithm. The effects of a violation of this assumption can be negated by introducing elasticity into the numerical model.

4.5. Verification of the Numerical Solution Methods.

4.5.1. Introduction.

Soap-film models may be adopted as useful physical analogues to stable minimal energy forms. In this section the results of investigations into the accuracy of the numerical representation of various soap-film models is presented.

4.5.2. Single Minimal Surfaces with Fixed Boundaries.

4.5.2.1. Linear Elements.

Figure 4.9 shows the equilibriated surface of the soap-film model illustrated in Plates 3.1 & 3.2 (Example 4.3). The surface of the model is sub-divided into an orthogonal mesh with element lengths corresponding to 1.25 % of the overall x dimension of the model in the global x direction, and 2.00 % of the of the overall y dimension in the global y direction. A mathematically defined initial surface has been assumed, based on the Hermitian polynomial with the factor $\lambda_s = 7.0$ [4.21]. The stabilising factor $\lambda_A = 2.0$ [8] [4.21] has been adopted with the error residual Er equal to 0.025 % of the element pretensions [9]. The element pretensions are taken as 50. kN in all elements. The elasticity of the surface is assumed to be zero.

The condition of equilibrium is satisfied after 467 iterations, with a corresponding Cpu time of 871.3u [10] . The main curvatures of the surface along the two central planes $z-x$ and $z-y$ are shown in Figure 4.10(a) and Figure 4.10(b). Excellent agreement is demonstrated between the numerical and the experimental solutions. The deviation of the solutions (experimental and numerical) in certain regions of Figure 4.10(a) may be attributed to differences in the assumed and in the actual boundary conditions, arising from a distortion of the wire model.

8

The factor λ_A [4.21] is applied to all the stiffness terms of the discretisation. An increase in the geometric stiffness of the surface is obtained therefore. This is achieved without increasing the pretensions in the elements and thus increasing the out-of-balance forces at the element nodes. The numerical stability of the solution algorithm is enhanced in this way, therefore.

9

The error residual Er equal to 0.025 % of the element pretensions has been assumed for all subsequent examples unless otherwise stated. This also applies in the case of the triangular element discretisation, where the natural forces in the pseudo cables are used as the basis for the error residual.

10

All Cpu times are quoted for a "Sparc-1" Sun Workstation.

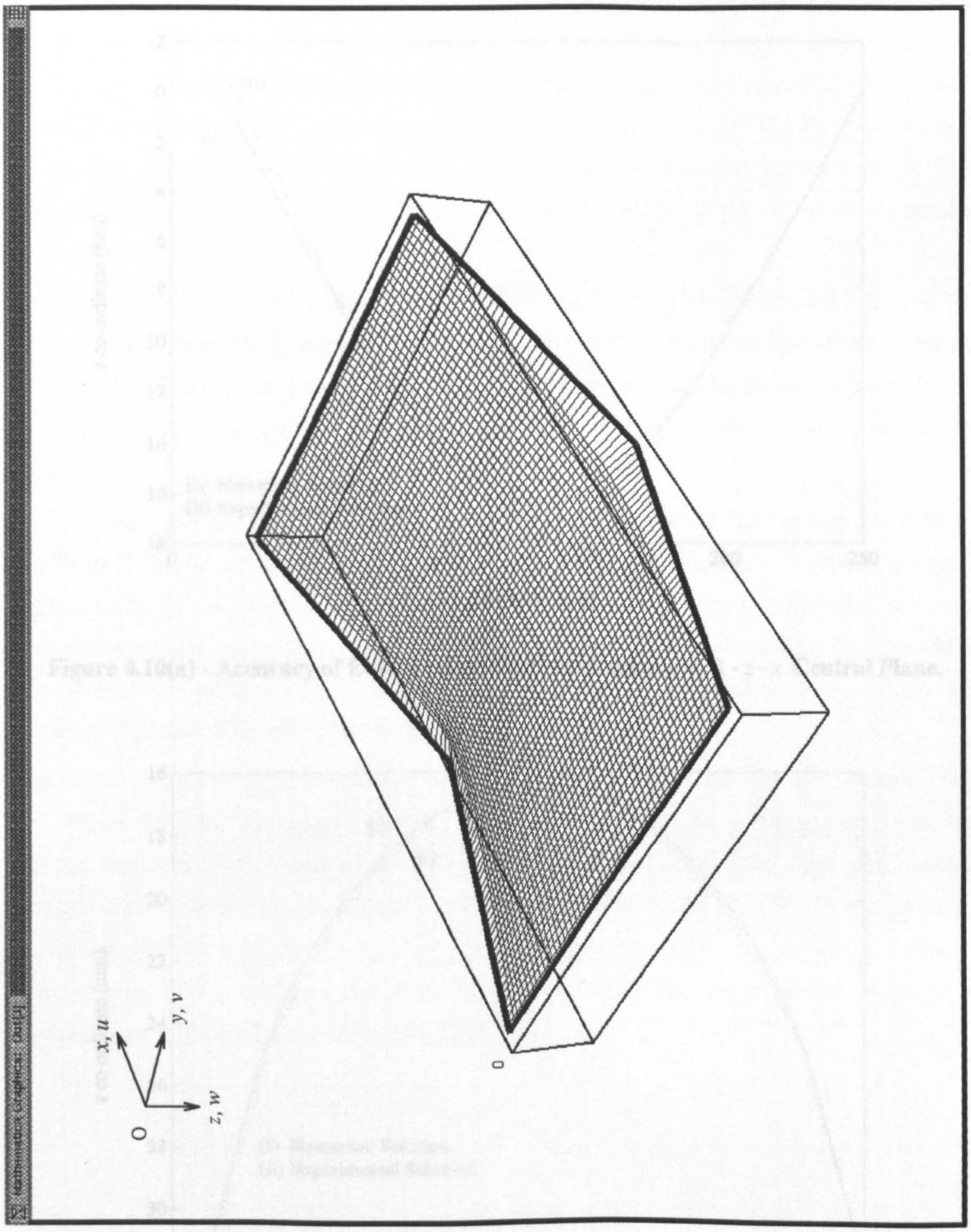

Figure 4.9 - Equilibriated Surface (Example 4.3).

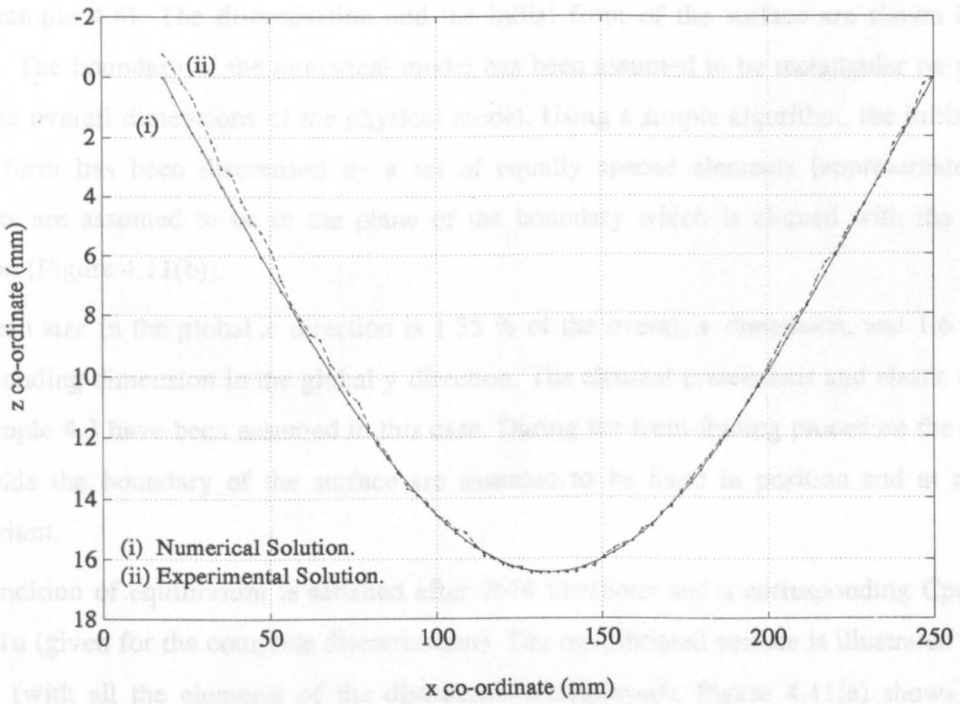

Figure 4.10(a) - Accuracy of Equilibriated Surface (Example 4.3) - z–x Central Plane.

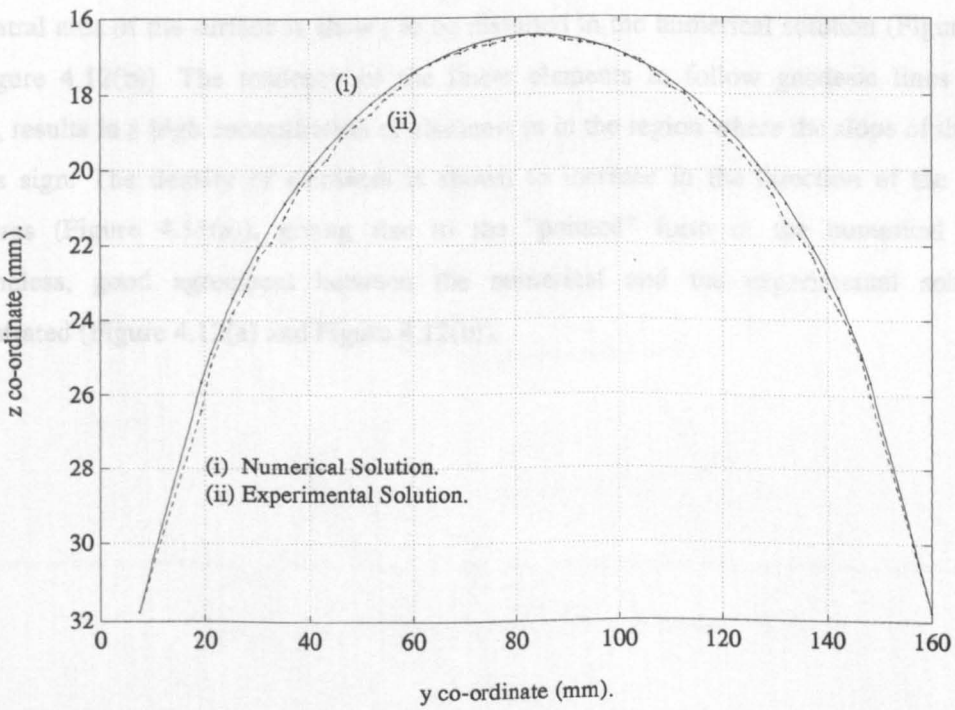

Figure 4.10(b) - Accuracy of Equilibriated Surface (Example 4.3) - z–y Central Plane.

Figure 4.11(a) shows the equilibriated surface of the soap-film model illustrated in Plates 3.3 & 3.4 (Example 4.4). The discretisation and the initial form of the surface are shown in Figure 4.11(b). The boundary of the numerical model has been assumed to be rectangular on plan with the same overall dimensions of the physical model. Using a simple algorithm, the initial surface of the form has been discretised by a set of equally spaced elements (approximately). The elements are assumed to be in the plane of the boundary which is aligned with the global x direction (Figure 4.11(b)).

The mesh size in the global x direction is 1.35 % of the overall x dimension, and 1.6 % of the corresponding dimension in the global y direction. The element pretensions and elastic constants of Example 4.3 have been assumed in this case. During the form-finding procedure the nodes on or outside the boundary of the surface are assumed to be fixed in position and at a state of equilibrium.

The condition of equilibrium is satisfied after 2674 iterations and a corresponding Cpu time of 12988.1u (given for the complete discretisation). The equilibriated surface is illustrated in Figure 4.11(c) (with all the elements of the discretisation displayed). Figure 4.11(a) shows only the elements which are assumed to contribute to the formation of the numerical solution to the soap-film surface. The main curvatures of the surface along the two central planes $z-x$ and $z-y$ are shown in Figure 4.12(a) and Figure 4.12(b) respectively [11].

The central area of the surface is shown to be distorted in the numerical solution (Figure 4.12(a) and Figure 4.12(b)). The tendency of the linear elements to follow geodesic lines over the surface, results in a high concentration of elements in in the region where the slope of the surface changes sign. The density of elements is shown to increase in the direction of the principal curvatures (Figure 4.11(a)), giving rise to the "pointed" form of the numerical solution. Nevertheless, good agreement between the numerical and the experimental solutions is demonstrated (Figure 4.12(a) and Figure 4.12(b)).

11

The discrepancy between the numerical and the experimental boundaries may be attributed to the modelling technique, as outlined in Section 3.6.2.1, Chapter 3. An additional approximation is present in the numerical solution therefore.

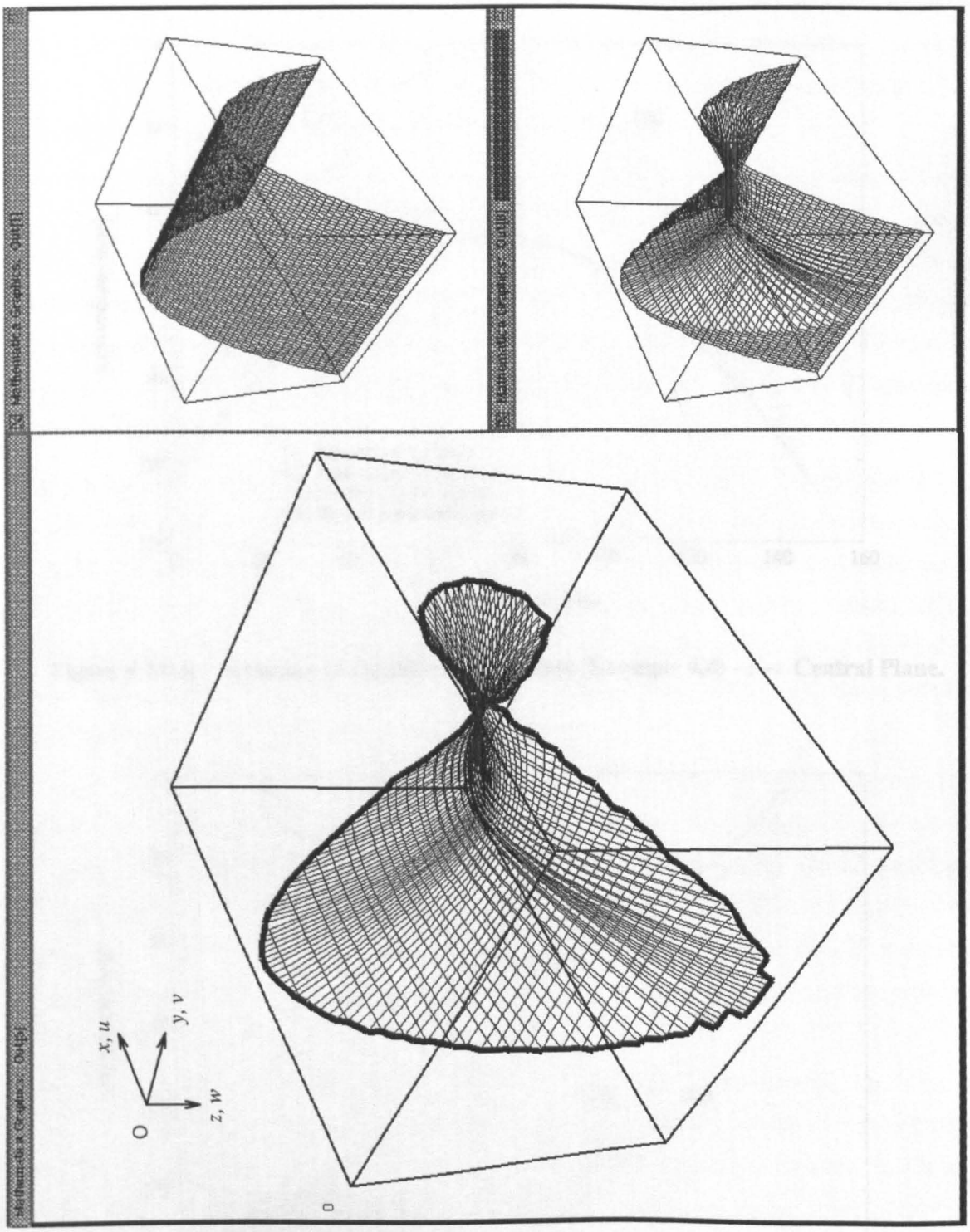

Figure 4.11 - Equilibriated Surface (Example 4.4).

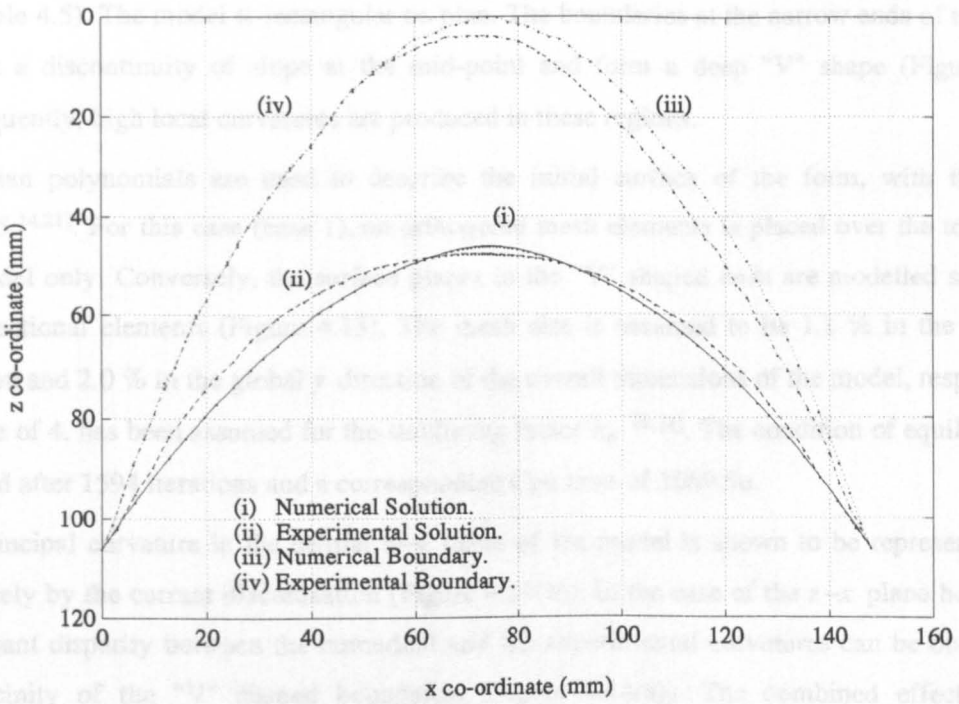

Figure 4.12(a) - Accuracy of Equilibriated Surface (Example 4.4) - z–x Central Plane.

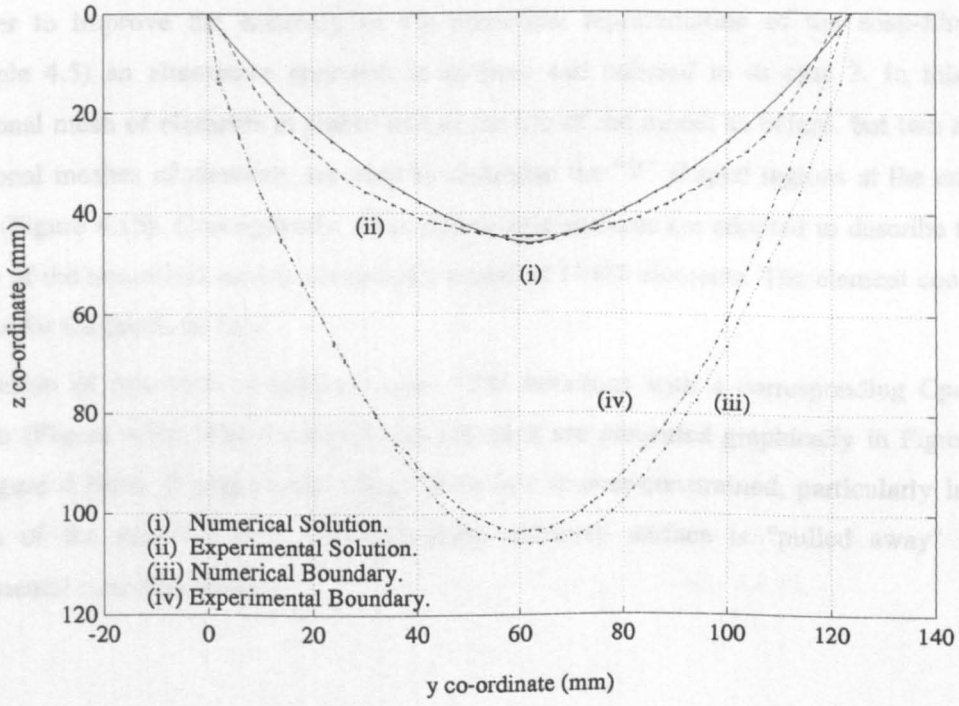

Figure 4.12(b) - Accuracy of Equilibriated Surface (Example 4.4) - z–y Central Plane.

Figure 4.13 shows the equilibriated surface of the soap-film model illustrated in Plates 3.5 & 3.6 (Example 4.5). The model is rectangular on plan. The boundaries at the narrow ends of the model possess a discontinuity of slope at the mid-point and form a deep "V" shape (Figure 4.13). Consequently, high local curvatures are produced in these regions.

Hermitian polynomials are used to describe the initial surface of the form, with the factor $\lambda_s = 0.5$ [4.21]. For this case (case 1), an orthogonal mesh elements is placed over the top part of the model only. Conversely, the surface planes in the "V" shaped ends are modelled simply by uni-directional elements (Figure 4.13). The mesh size is assumed to be 1.1 % in the global x direction and 2.0 % in the global y direction of the overall dimensions of the model, respectively. A value of 4. has been assumed for the stabilising factor λ_A [4.21]. The condition of equilibrium is satisfied after 1594 iterations and a corresponding Cpu time of 3069.5u.

The principal curvature in the central $z-y$ plane of the model is shown to be represented very accurately by the current discretisation (Figure 4.14(b)). In the case of the $z-x$ plane however, a significant disparity between the numerical and the experimental curvatures can be observed in the vicinity of the "V" shaped boundaries (Figure 4.14(a)). The combined effects of the propensity of the linear elements to follow geodesic lines over the surface and an inadequate representation of the "V" shaped regions of the surface, can be attributed to the disparity referred to previously and illustrated in Figure 4.14(a).

In order to improve the accuracy of the numerical representation of the soap-film surface (Example 4.5) an alternative approach is adopted and referred to as case 2. In this case an orthogonal mesh of elements is placed across the top of the model as before, but two additional orthogonal meshes of elements are used to discretise the "V" shaped regions at the ends of the model (Figure 4.15). Consequently, three planar type surfaces are adopted to describe the initial surface of the numerical model, comprising a total of 11488 elements. The element constants are taken as for the previous case.

Equilibrium of this form is achieved after 1267 iterations with a corresponding Cpu time of 3116.7u (Figure 4.15). The results of this approach are presented graphically in Figure 4.16(a) and Figure 4.16(b). It can be seen that the surface is over-constrained, particularly in the end regions of the model where the numerically achieved surface is "pulled away" from the experimental soap-film surface.

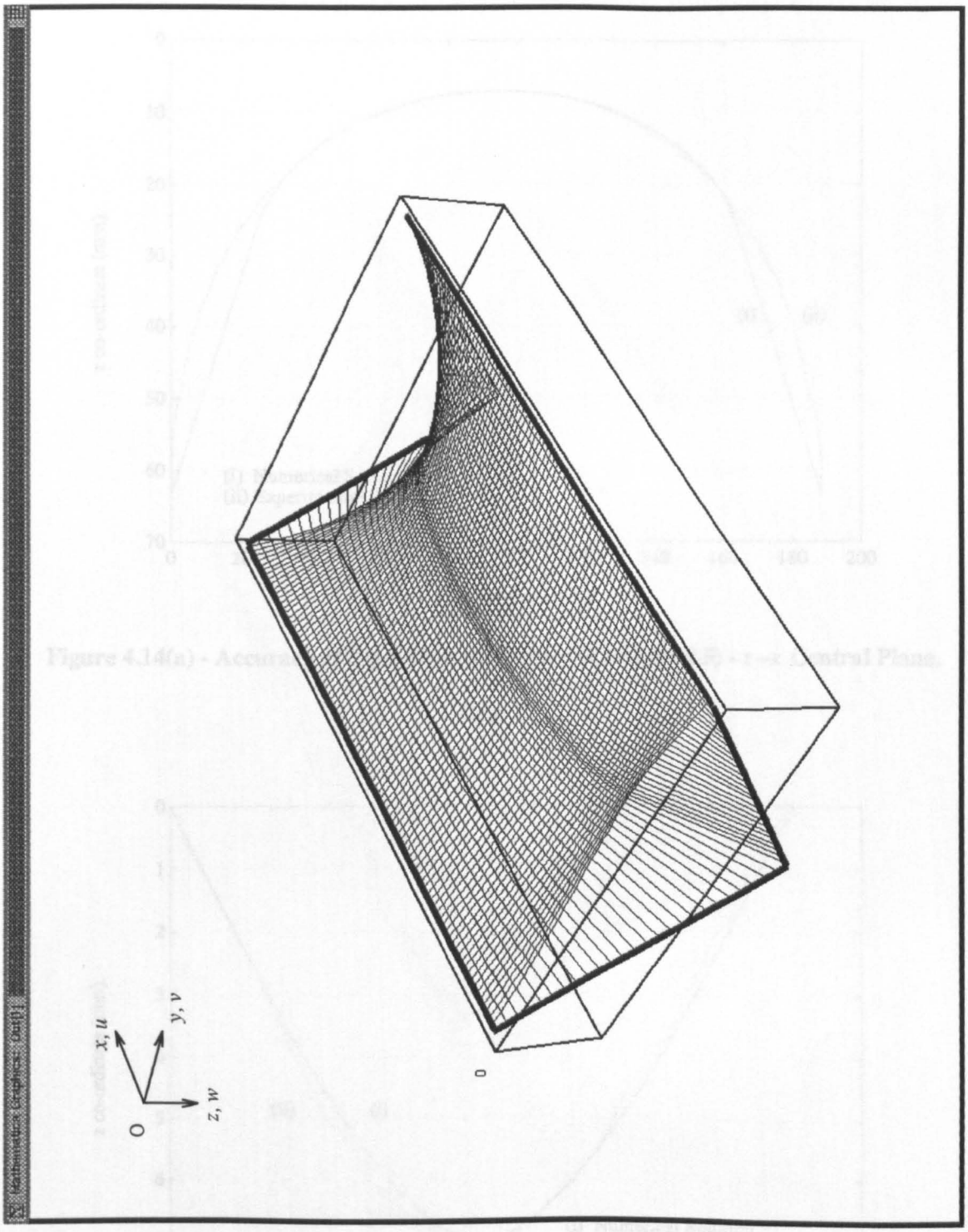

Figure 4.13 - Equilibriated Surface (Example 4.5).

Case 1.

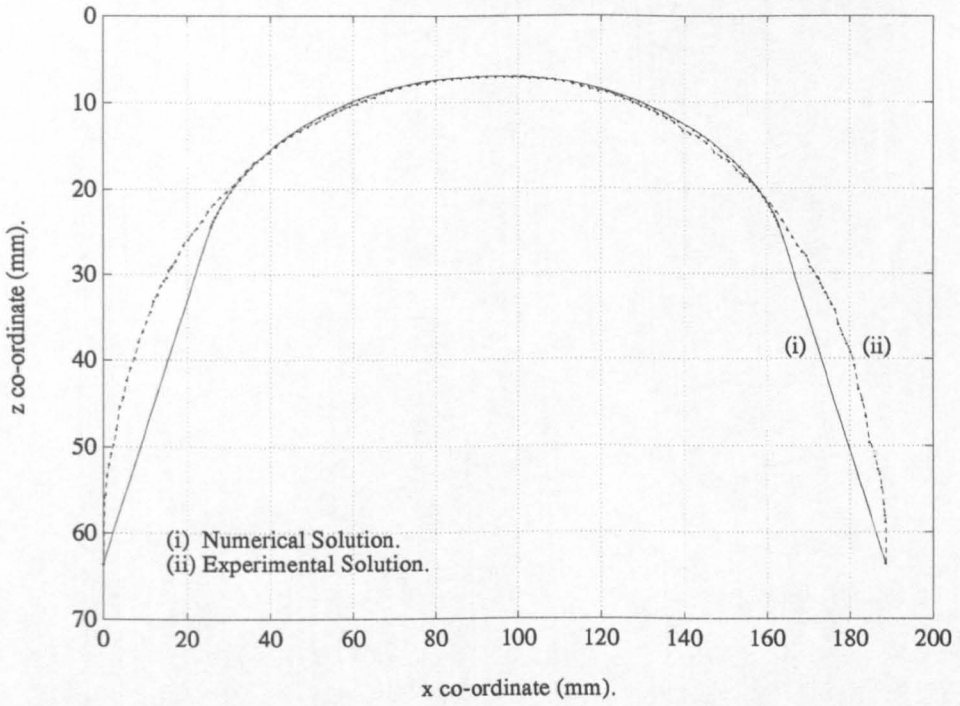

Figure 4.14(a) - Accuracy of Equilibriated Surface (Example 4.5) - $z-x$ Central Plane.

Case 1.

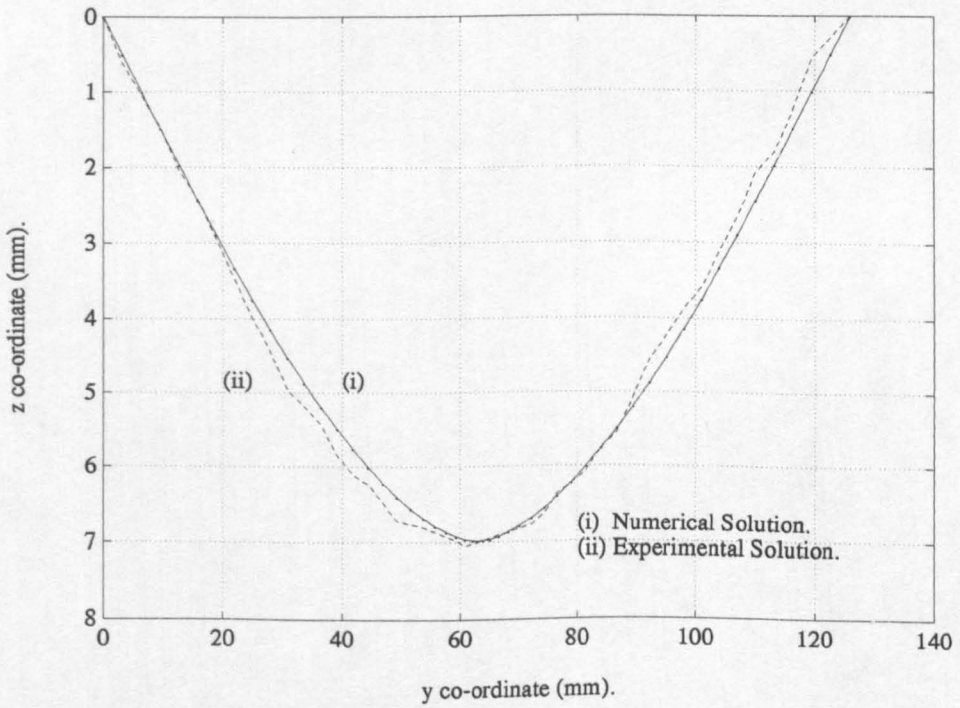

Figure 4.14(b) - Accuracy of Equilibriated Surface (Example 4.5) - $z-y$ Central Plane.

Case 1.

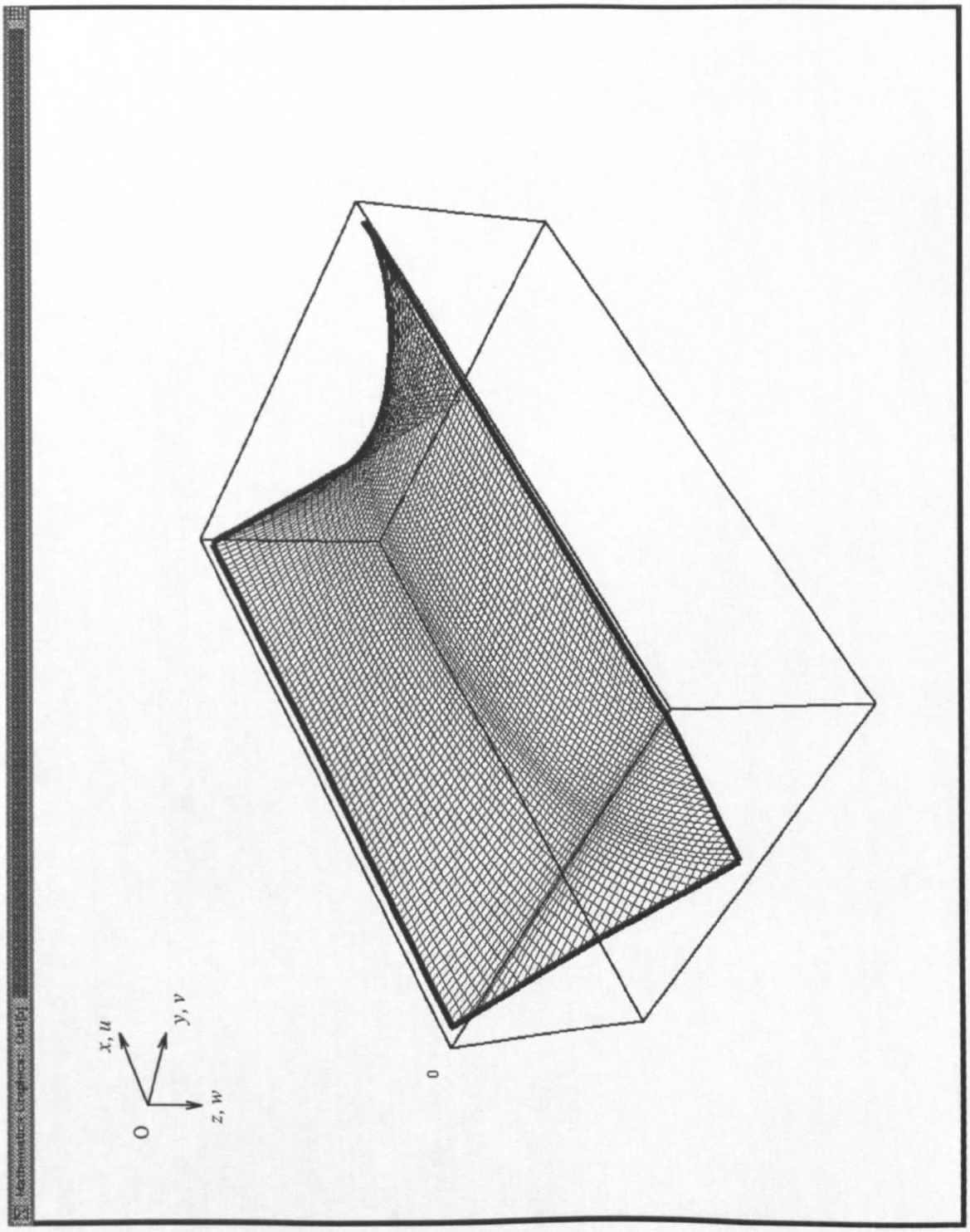

Figure 4.15 - Equilibriated Surface (Example 4.5).

Case 2.

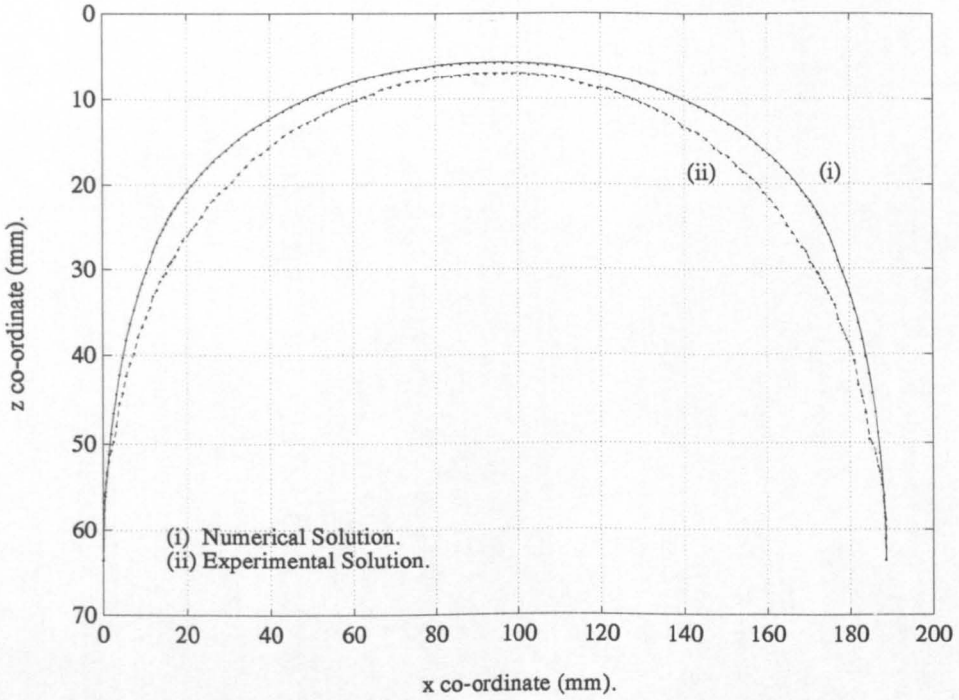

Figure 4.16(a) - Accuracy of Equilibriated Surface (Example 4.5) - $z-x$ Central Plane.

Case 2.

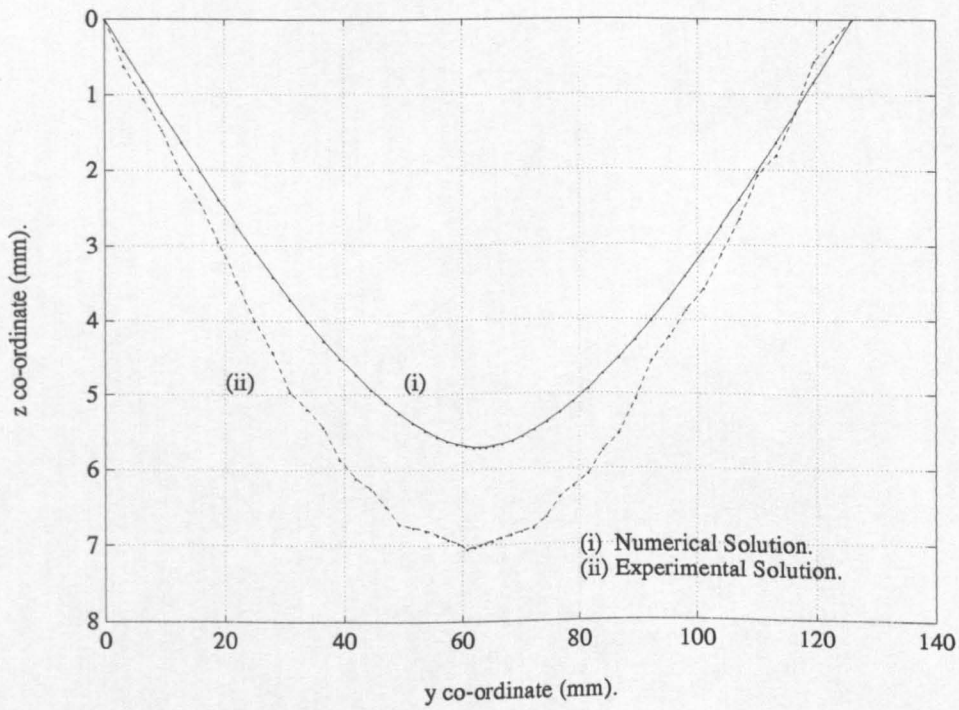

Figure 4.16(b) - Accuracy of Equilibriated Surface (Example 4.5) - $z-y$ Central Plane.

Case 2.

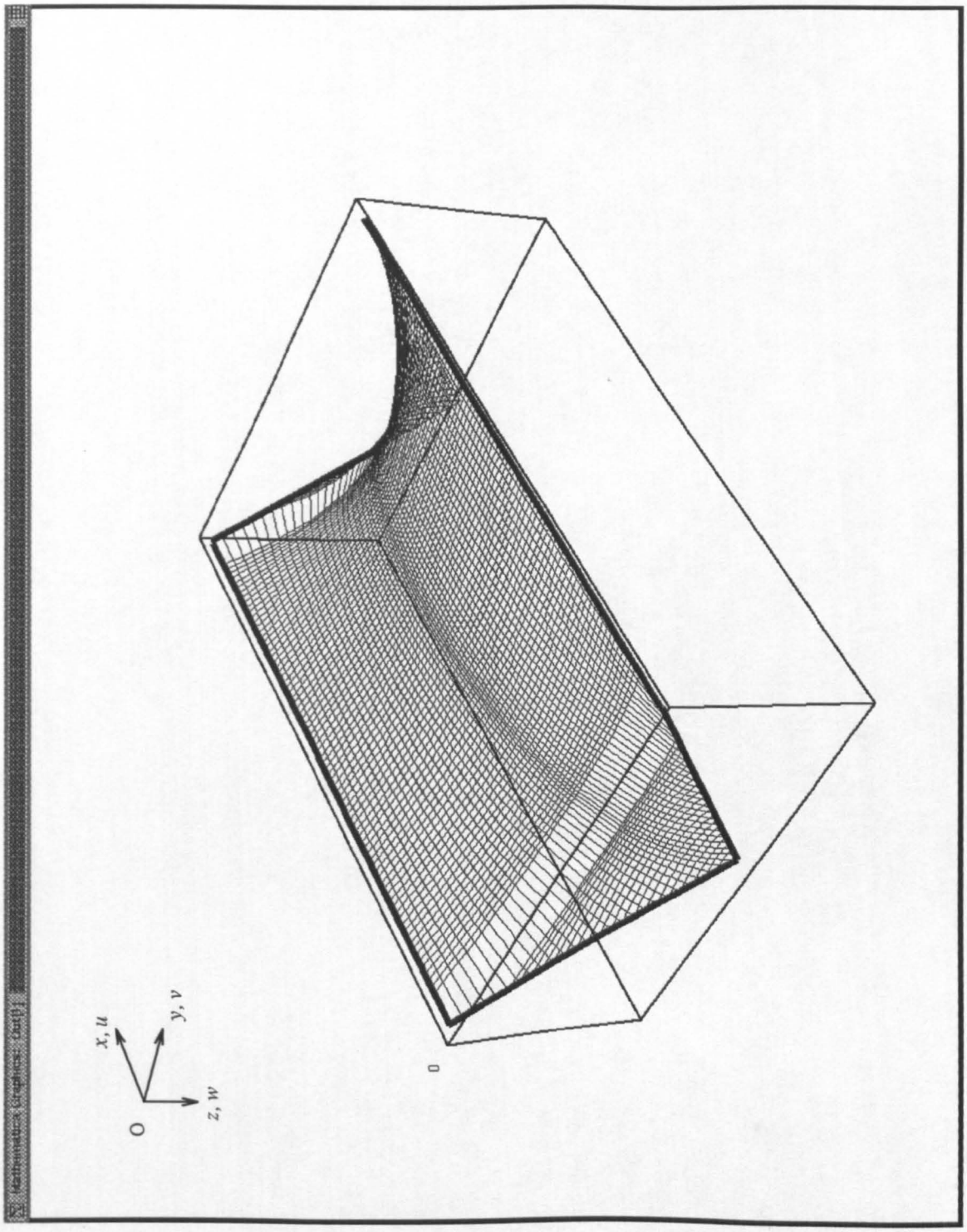

Figure 4.17 - Equilibriated Surface (Example 4.5).

Case 3.

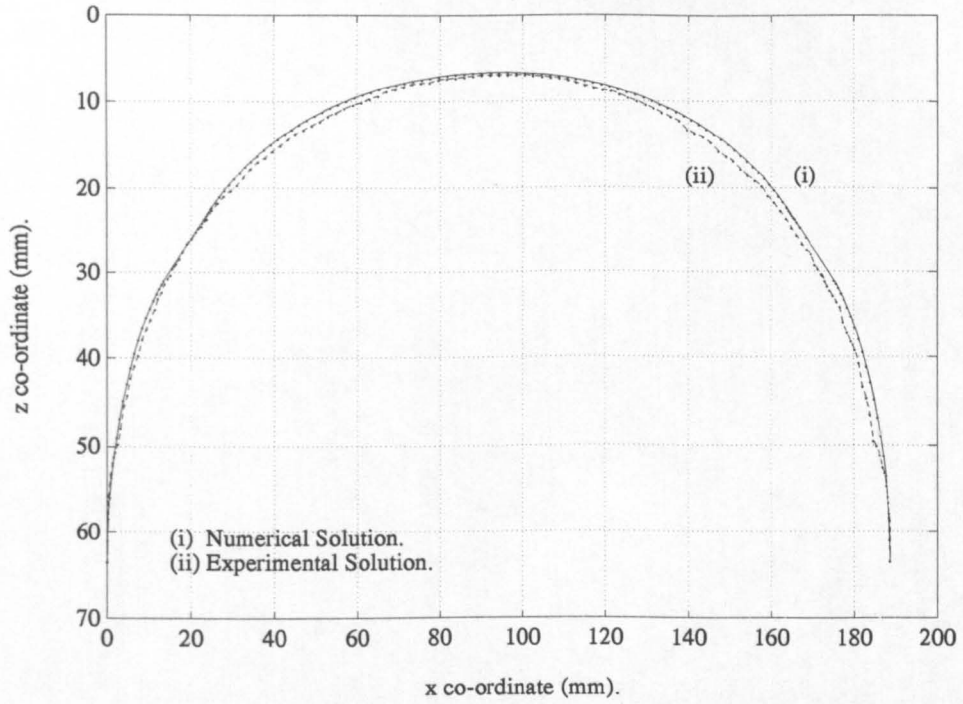

Figure 4.18(a) - Accuracy of Equilibriated Surface (Example 4.5) - $z-x$ Central Plane.

Case 3.

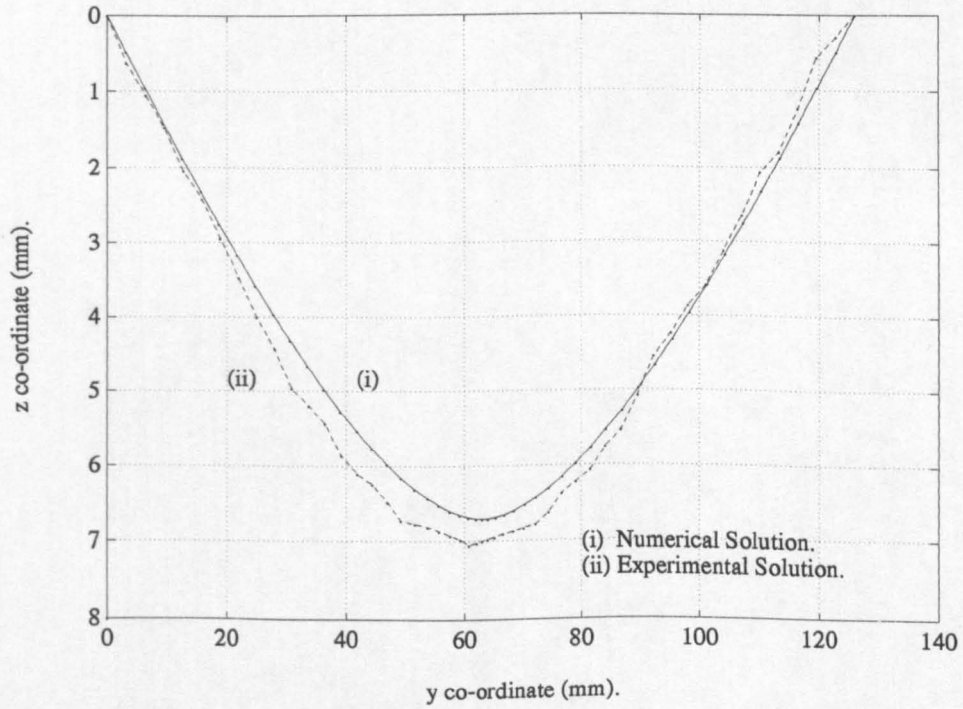

Figure 4.18(b) - Accuracy of Equilibriated Surface (Example 4.5) - $z-y$ Central Plane.

Case 3.

The solutions from the studies "case 1" and "case 2" suggest that more careful modelling (with elements placed partly over the top and partly over the end planes) is required in order to enhance the accuracy of the numerical model (case 3, Figure 4.17). The condition of equilibrium for this case is satisfied after 2213 iterations and a corresponding Cpu time of 5483.7u. The equilibriated surface is illustrated in Figure 4.17, with the main curvatures in the $z-x$ and $z-y$ planes shown in Figure 4.18(a) and Figure 4.18(b) respectively.

An improvement in the accuracy of the numerical solution is achieved through the adoption of the discretisation illustrated in Figure 4.17. This solution (Figure 4.18(a) and Figure 4.18(b)) is not unique however. As demonstrated by a comparison of the solutions obtained from case 1, case 2 and case 3, it is sensitive to both the number and the position of the linear elements.

The number and the position of the linear elements may be varied in order to achieve an accurate solution to a known form (Figure 4.17). By simply increasing the number of linear elements in the discretisation however, an accurate solution to the minimal surface may not be obtained necessarily.

4.5.2.2. Triangular Elements.

The equilibriated surface of the soap-film model illustrated in Plates 3.1 & 3.2 (Example 4.3) is shown in Figure 4.19. A discretisation of triangular elements with dimensions equal to 10 % (approximately) of the overall dimensions of the physical model in the global x and y direction respectively, has been adopted (Figure 4.19). The surface is therefore sub-divided with 24 elements along the greater length and 16 elements in the orthogonal direction [12] . The initial surface of the numerical model has been generated mathematically using Hermitian polynomials ($\lambda_A = 2.0$ [4.21]).

It is assumed that 75 kinetic energy peaks (NRPF = 75) are permitted prior to the commencement of the revised routine (Section 4.4.3.1). The condition of uniform stress is modelled as $\sigma_x = \sigma_y = 1.\times10^{+6}$ kN.m^{-2} and $\tau_{xy} = 0.$ kN.m^{-2}. The thickness of the membrane is taken as $1.\times10^{-3}$m.

The condition of equilibrium is satisfied after a total of 589 iterations and a corresponding Cpu time of 111.4u. At equilibrium the condition of uniform stress is represented within a maximum surface stress deviation of 0.38 %, and a maximum of the average element stress deviations of 0.04 %. The numerical solution to the surface is presented graphically in Figure 4.20(a) and

12

By increasing the number of elements comprising the discretisation, the description of the surface is not altered significantly. The term "significantly" is taken to mean a change of greater than 0.02 % in the z co-ordinate of any node arising from an increase in the number of elements of the discretisation.

Figure 4.20(b) as profiles of the central planes of the membrane, $z-x$ and $z-y$ respectively.

Small deviations of the numerical solution from the experimental solution can be observed (Figure 4.20(b)). The disparities between the numerical and the experimental solutions arise (predominantly) from the effects of the characteristics of the discretisation (Figure 4.19) given below.

The triangular elements are plane and therefore provide a linear piecewise approximation to the curved profile of the surface. Furthermore, in the $z-x$ central plane the surface is described at the apex nodes only. This is not the case in the orthogonal direction where information is provided at two nodes of each element (Figure 4.19). Consequently, the numerical solution exhibits the marked discontinuities of slope in the $z-y$ central plane (Figure 4.20(a)) which are not identified in the $z-x$ central plane (Figure 4.20(b)).

Nevertheless, a coarse discretisation of plane triangular elements (Figure 4.19) can provide an improved numerical solution to a curved minimal surface (when compared with the linear (line) element discretisation (Figure 4.9)) for the following reasons:

(i) the condition of uniform surface stress can be represented adequately by the continuum based triangular element formulation (Section 4.4.2). Consequently, arbitrarily shaped elements may be used to discretise the surface as opposed to an orthogonal mesh of linear elements. Large changes of the internal geometry of the discretisation can tolerated therefore, while maintaining the condition of uniform surface stress [13],

(ii) the magnitudes of the natural forces in the pseudo cables (representing the sides of the triangular element) are not constant (necessarily). Instead they relate the geometries of the triangular elements to the vector of surface stresses, $\{\sigma_c\}$, (eqn(4.4.2.17)). Therefore, geodesic lines (which can cause a distortion of the numerical solution) are not necessarily simulated by the pseudo cable elements comprising the triangular element formulation.

Example 4.4 and Example 4.5 demonstrate the implementation of the triangular element formulation with the Dynamic Relaxation algorithm further.

13

If the elasticity of the surface is assumed to be non-zero (in order to maintain the numerical stability of the solution algorithm for example) then changes in the geometry of the element will affect the condition of uniform surface stress (represented by the vector $\{\sigma_c\}$) (eqn(4.4.3.5)). The condition of uniform stress can be recovered in this case by re-applying the vector $\{\sigma_c\}$ and re-equilibriating the surface repeatedly (Section 4.4.3.2.3).

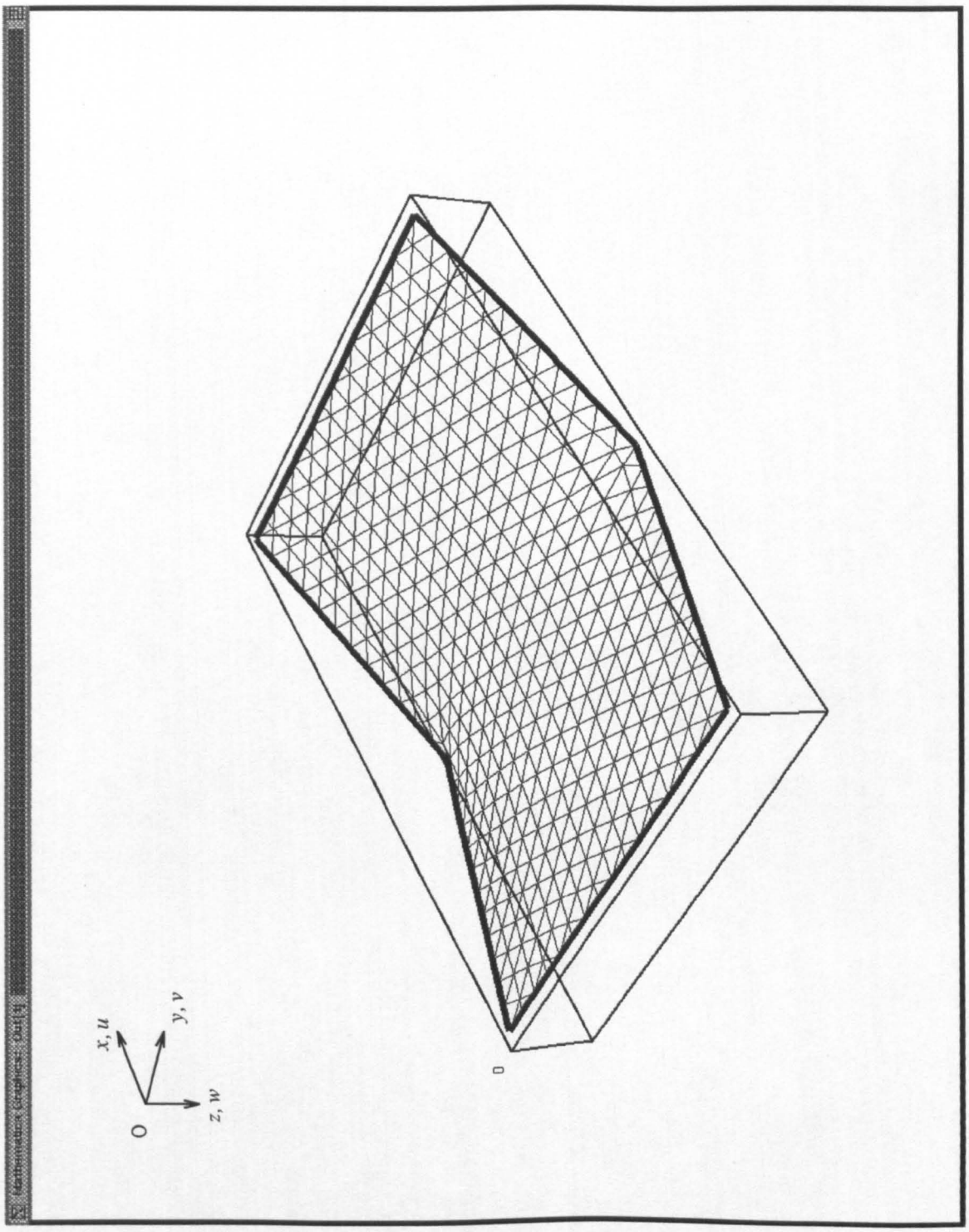

Figure 4.19 - Equilibriated Surface (Example 4.3).

(Triangular Elements.)

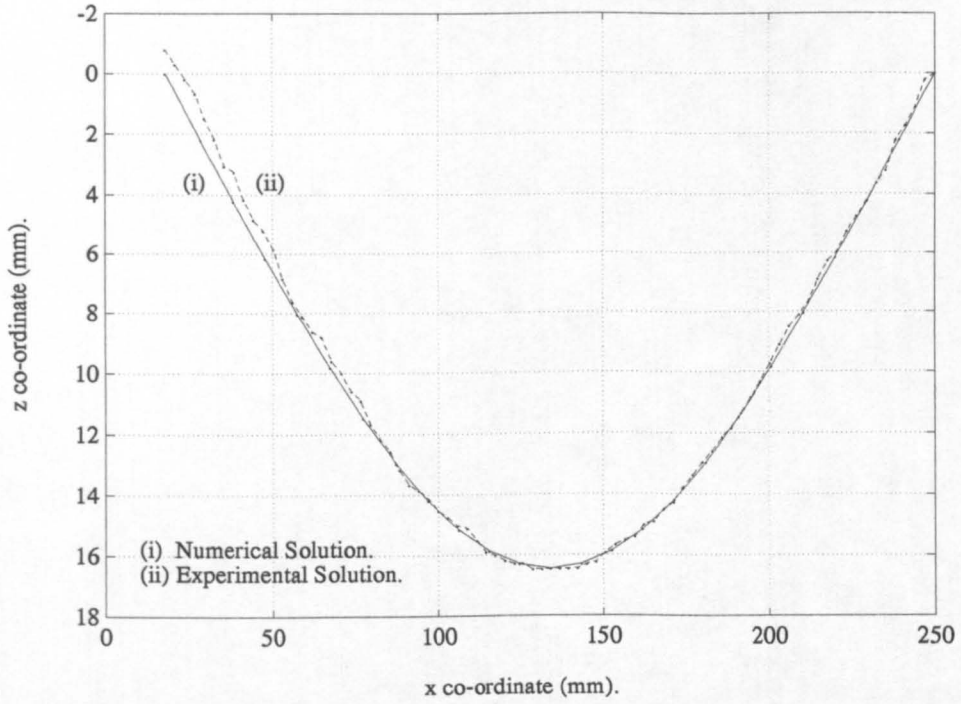

Figure 4.20(a) - Accuracy of Equilibriated Surface (Example 4.3) - z–x Central Plane.

(Triangular Elements.)

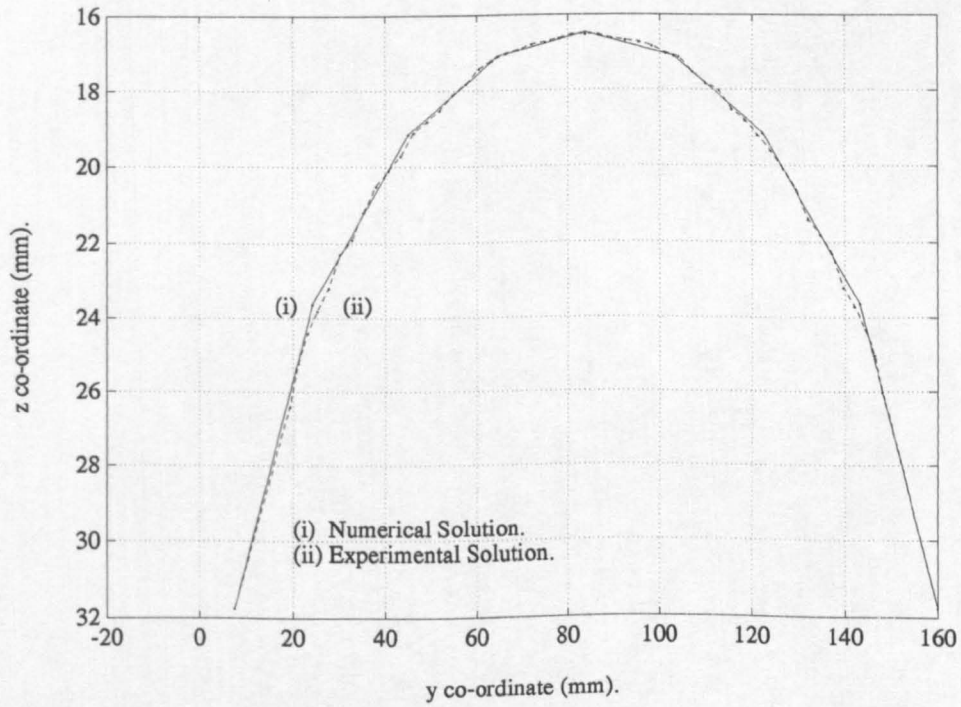

Figure 4.20(b) - Accuracy of Equilibriated Surface (Example 4.3) - z–y Central Plane.

(Triangular Elements.)

The equilibriated surface of the soap-film model illustrated in Plates 3.3 & 3.4 (Example 4.4) is shown in Figure 4.21. Due to the complexity of the form a relatively fine discretisation of the surface has been adopted. Thus, the triangular elements possess dimensions of up to 3.5 % of the associated overall dimension of the physical model. The non-symmetrical form of the boundary is modelled by a layer of irregularly shaped elements, permitting a regular mesh of elements within the main body of the surface (Figure 4.21). The total number of elements is 1124.

The initial surface of the numerical model has been defined using Hermitian polynomials with $\lambda_s = 2$. [4.21]. It is assumed that 100 kinetic energy peaks (NRPF = 100) are permitted prior to the commencement of the revised routine (Section 4.4.3.1). This relatively high value is adopted in order to reduce the magnitude of element stress deviations arising from the poor aspect ratios of some elements [14] . The remaining surface constants are taken as for Example 4.3.

The condition of equilibrium is satisfied after a total of 840 iterations and a corresponding Cpu time of 300.0u. The condition of uniform surface stress is represented adequately (at equilibrium) with the maximum element stress deviation equal to 1.09 %, and the maximum of the average element stress deviations equal to 0.09 %.

Figure 4.22(a) and Figure 4.22(b) show the profiles of the central $z-x$ and $z-y$ planes of the membrane respectively. Good agreement is demonstrated between the numerical and the experimental solutions. (As before, the discrepancy between the two solutions in certain regions of Figure 4.22(a) and Figure 4.22(b) may be attributed to errors in the physical model.) The triangular element discretisation is shown to provide an improvement in the accuracy of the numerical solution to the soap-film surface when compared with the linear element discretisation (Figures 4.36 (a) & (b) with Figures 4.26 (a) & (b)).

14

Due to the trigonometric terms which comprise some of the characteristic matrices of the triangular element formulation (eqn(4.4.2.11) and eqn(4.4.2.17)), errors are introduced into the numerical solution when the angles θ_2 and θ_3 (Figure 4.3), approach 0 or 2 π.

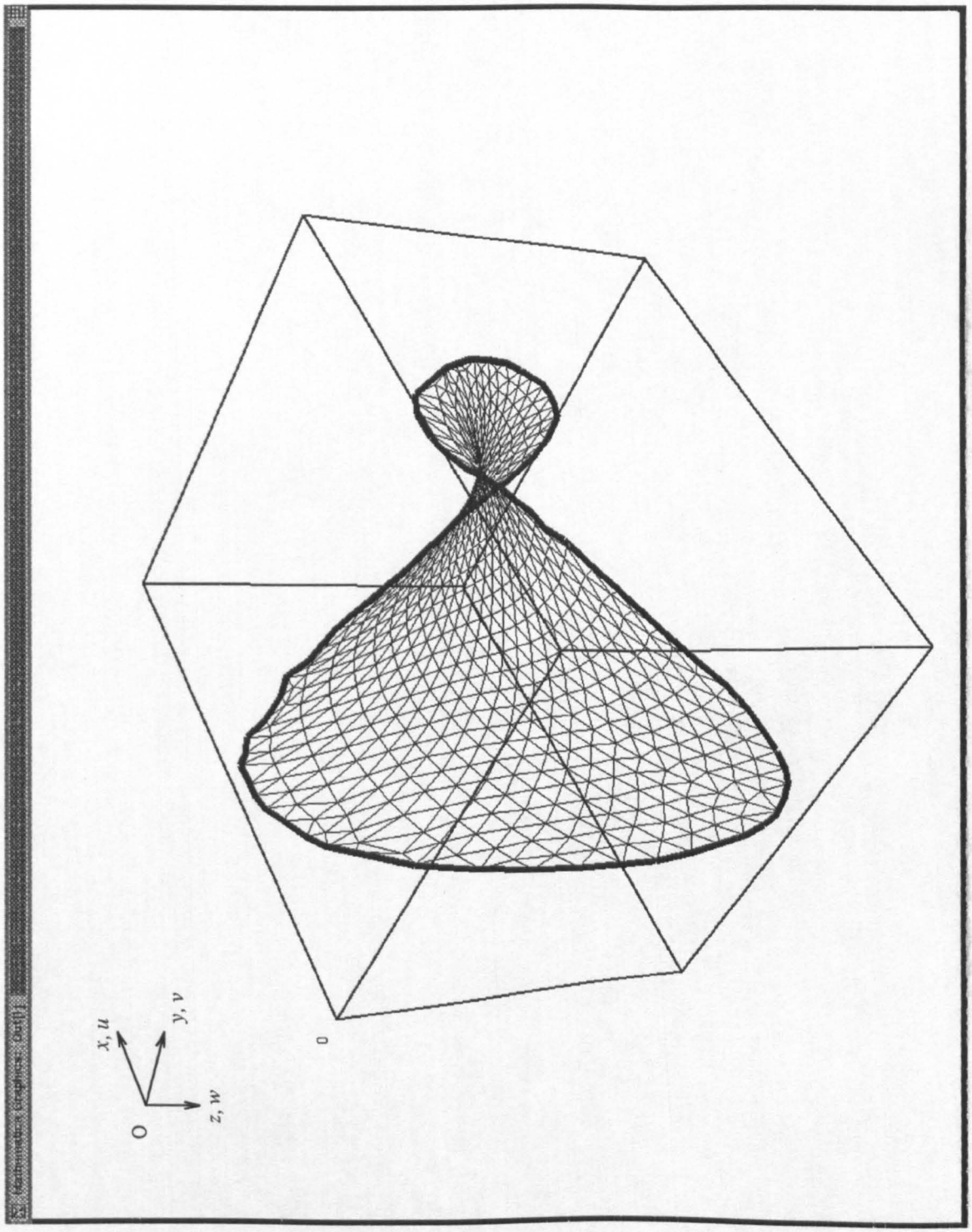

Figure 4.21 - Equilibriated Surface (Example 4.4).

(Triangular Elements.)

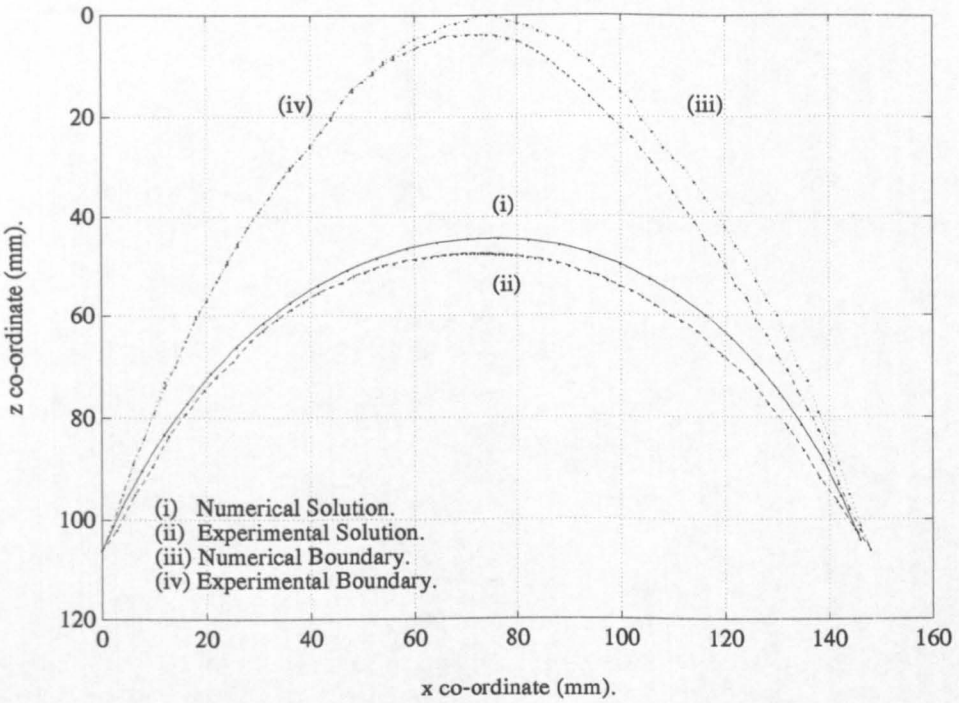

Figure 4.22(a) - Accuracy of Equilibriated Surface (Example 4.4) - $z-x$ Central Plane.

(Triangular Elements.)

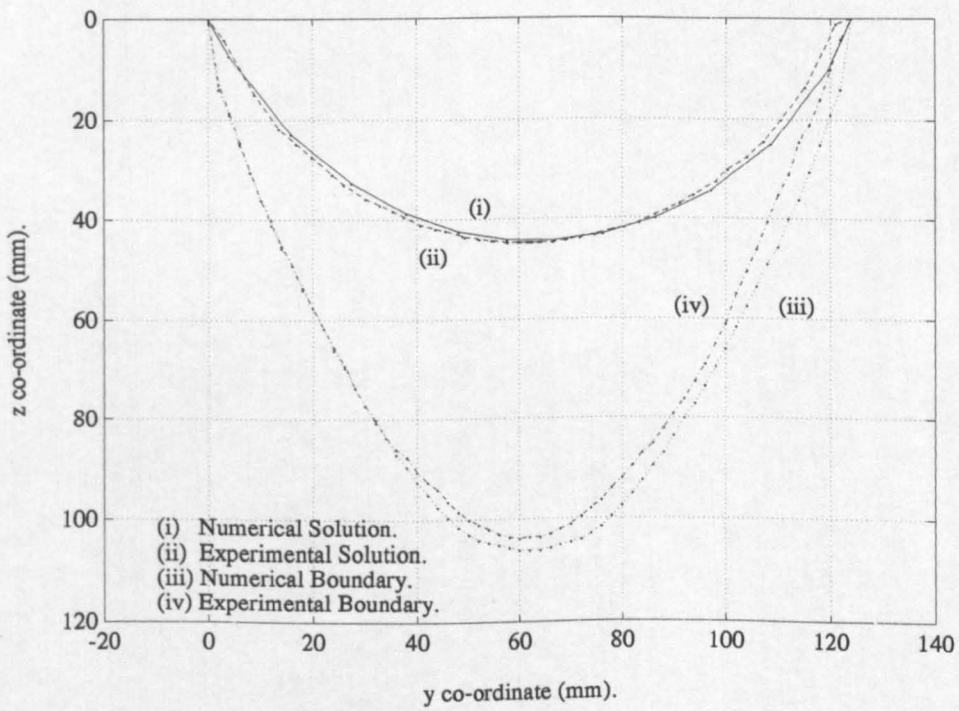

Figure 4.22(b) - Accuracy of Equilibriated Surface (Example 4.4) - $z-y$ Central Plane.

(Triangular Elements.)

Figure 4.23 shows the equilibriated surface of the soap-film model illustrated in Plates 3.5 & 3.6. A fine discretisation of elements has been assumed in order to model accurately the high curvatures of the surface. Consequently, the numerical model comprises 20 elements in the global y direction (5. % of the overall y dimension) and 34 elements in the global x direction (2.9 % of the overall x dimension). The initial surface is generated using Hermitian polynomials with factor $\lambda_s = 3$. [4.21]. It is assumed that 75 kinetic energy peaks (NRPF = 75) are permitted prior to the adoption of the revised procedure (Section 4.3.3.1).

A total of 1028 iterations are required to equilibriate the form with a corresponding Cpu time of 296.6u. The central $z-x$ and $z-y$ planes are plotted in Figure 4.24(a) and Figure 4.24(b) respectively.

A disparity of approximately 0.8 mm (constituting an error of around 11 %.) is shown to exist between the numerical and the experimental solutions at the centre of the model (Figure 4.24(b)). As presented below, an explanation related to the measurement of the physical soap-film surface rather than to the numerical modelling technique is proposed for the disparity between the two solutions.

The numerical model assumes that the soap-film surface commences at the centre-line of the wire frame of the physical model. Conversely, measurements of the physical soap-film surface have been taken using the inside of the wire frame as the datum.

The actual location of the soap-film on the wire frame is defined such that a vector in the plane of the membrane is normal to the surface of the boundary. In the case of a boundary comprising a tube (circular wire) the soap film moves around the wire until this vector passes through the centre of radius of the tube. Therefore, as the curvatures of the membrane change (normal to the boundary), the location of the soap-film on the wire frame changes also.

In the case of the surface illustrated in Plates 3.5 & 3.6, the soap-film is approximately vertical at the boundary with the discontinuity of slope (Plate 3.5). Therefore, the soap-film is attached to the top surface of the wire frame at this point. An over-estimate of the z co-ordinate of the surface is thus made, equivalent to the radius of the tubular frame (0.625 mm). Consequently, the central node z co-ordinate of the numerical model may be amended to (7.820 mm - 0.625 mm) $\approx$ 7.2 mm. The error between the numerical solution and the experimental solution is reduced to 3 % (approximately) subsequently. The remaining co-ordinates of the numerical solution may be amended pro rata.

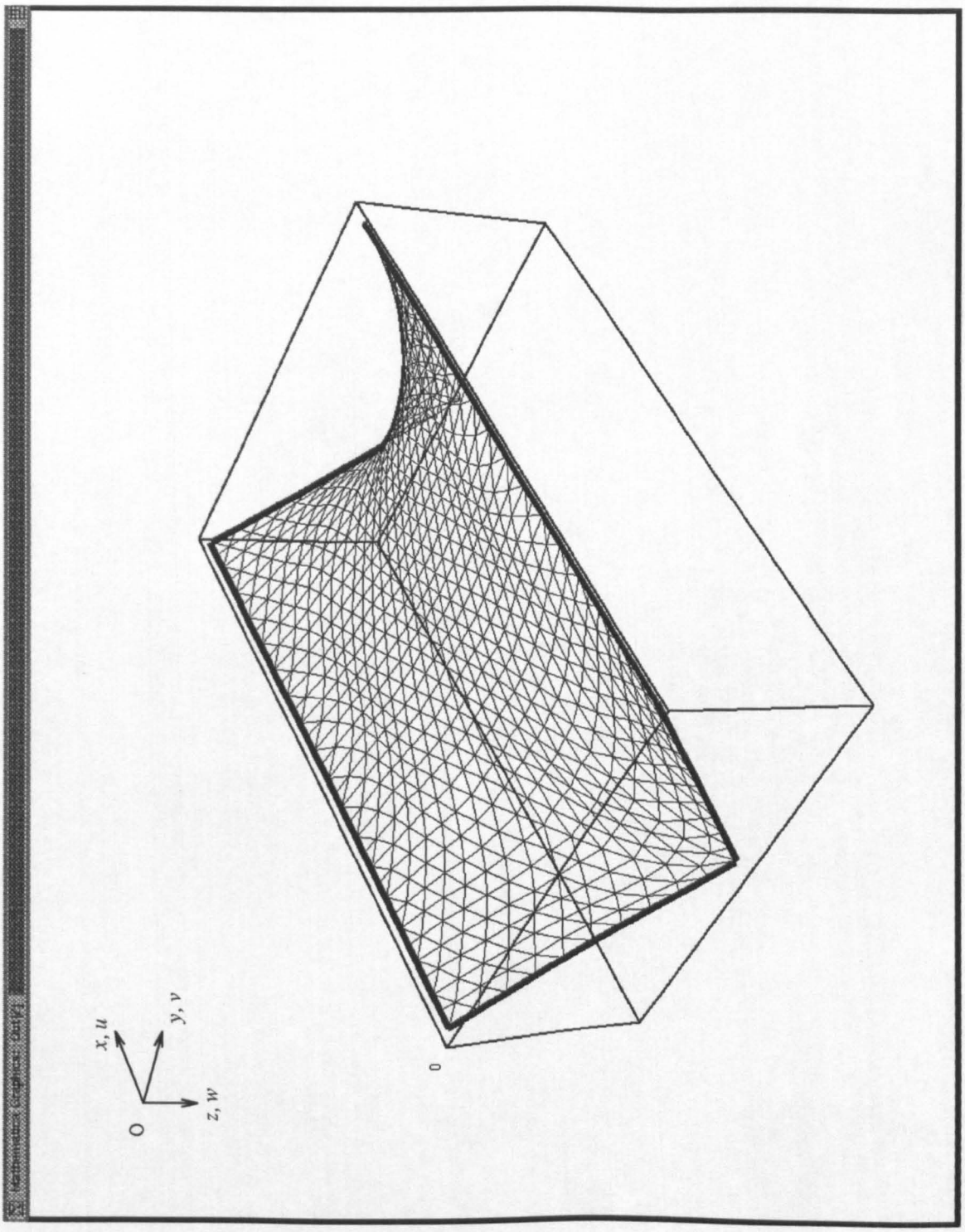

Figure 4.23 - Equilibriated Surface (Example 4.5).

(Triangular Elements.)

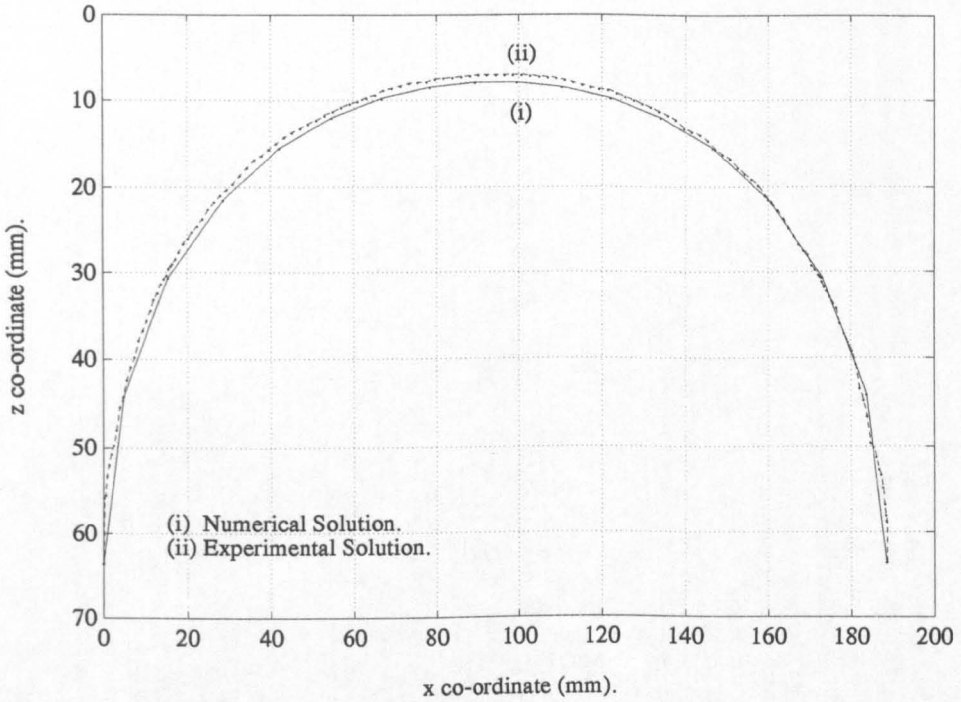

Figure 4.24(a) - Accuracy of Equilibriated Surface (Example 4.5) - $z-x$ Central Plane.

(Triangular Elements.)

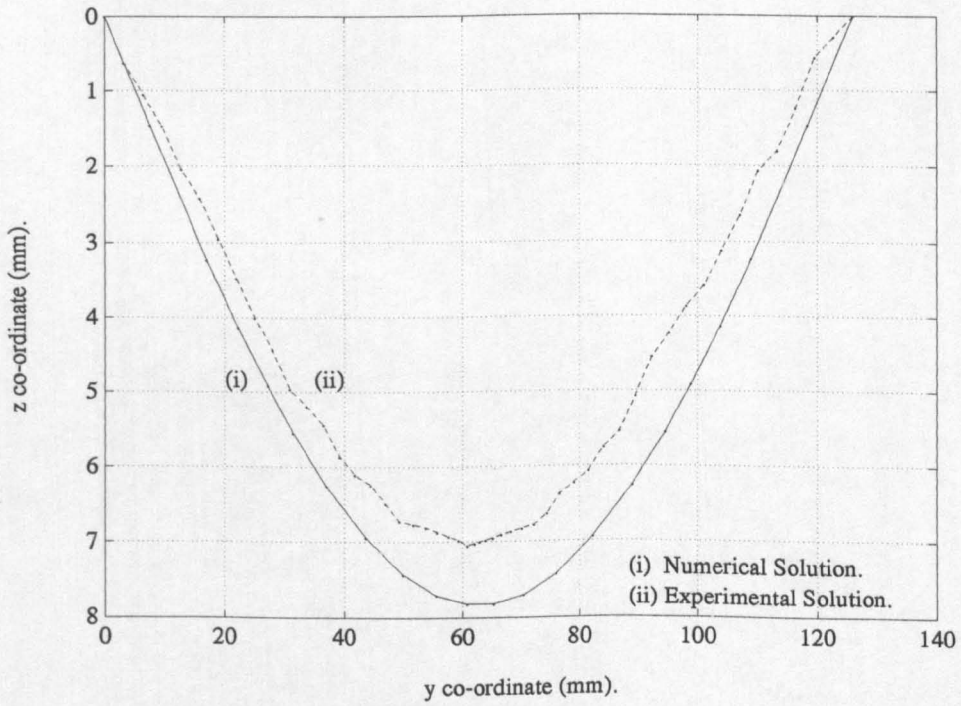

Figure 4.24(b) - Accuracy of Equilibriated Surface (Example 4.5) - $z-y$ Central Plane.

(Triangular Elements.)

4.5.3. Single Minimal Surfaces Between Two Independent Frames.

Two independent frames may be connected by a single soap lamella to form a minimal surface (Plate 3.7). The classical solution to a single surface formed between two circular rings of equal diameter is summarised in Section 3.6.2.2, Chapter 3 [4.20].

In order to assess the accuracy of the numerical solution method further, three surfaces of the type illustrated in Plate 3.7 are analysed. The ring diameters are assumed to be 40 mm, 80 mm, and 150 mm. The same surface discretisation is used in each case, with 24 elements around the circumference of the surface and with eight rows of elements in the vertical direction (Figure 4.25(a)). The initial surface of the form is taken to be cylindrical for each example (unless otherwise stated). The constant stress vector $\{\sigma_c\}$, is defined as, $\sigma_x = \sigma_y = 1.\times10^{+6}$ kN.m^{-2} and $\tau_{xy} = 0.$ kN.m^{-2}. At equilibrium the condition of uniform stress is satisfied to within 1. % in all cases.

During the experimental modelling of the catenoid surface, if the maximum attainable separation of the rings is exceeded, the soap-film collapses inwards and breaks. The membrane then fills the upper and lower rings, causing them to become disconnected (Section 3.6.2.2, Chapter 3). As demonstrated below, in the case of the numerical model, the criterion to establish the maximum attainable separation of the rings is based on this phenomenon.

Figure 4.25(a) shows the equilibriated surface between two 80 mm diameter rings at the maximum attainable separation of 53.0 mm. Using this equilibriated form as the initial surface but extended to 53.1 mm, an attempt is made to equilibriate the updated model. Figures 4.39 (b) - (d) show the progressive collapse of the surface. The collapse of the surface is caused by the rings exceeding the maximum value of separation. In the case of the 80 mm diameter rings, the maximum attainable separation of 53.0 mm corresponds to a value of the factor $\xi_{max} = \frac{z_{max}}{r_a}$ (Section 3.6.2.2, Chapter 3) of 1.325.

Using this approach the remaining two examples, (40 mm and with the 150 mm diameter rings) both yield $\xi_{max} = 1.315$. These results correspond to less than a 1. % deviation from the classical solution (Section 3.6.2.2, Chapter 3).

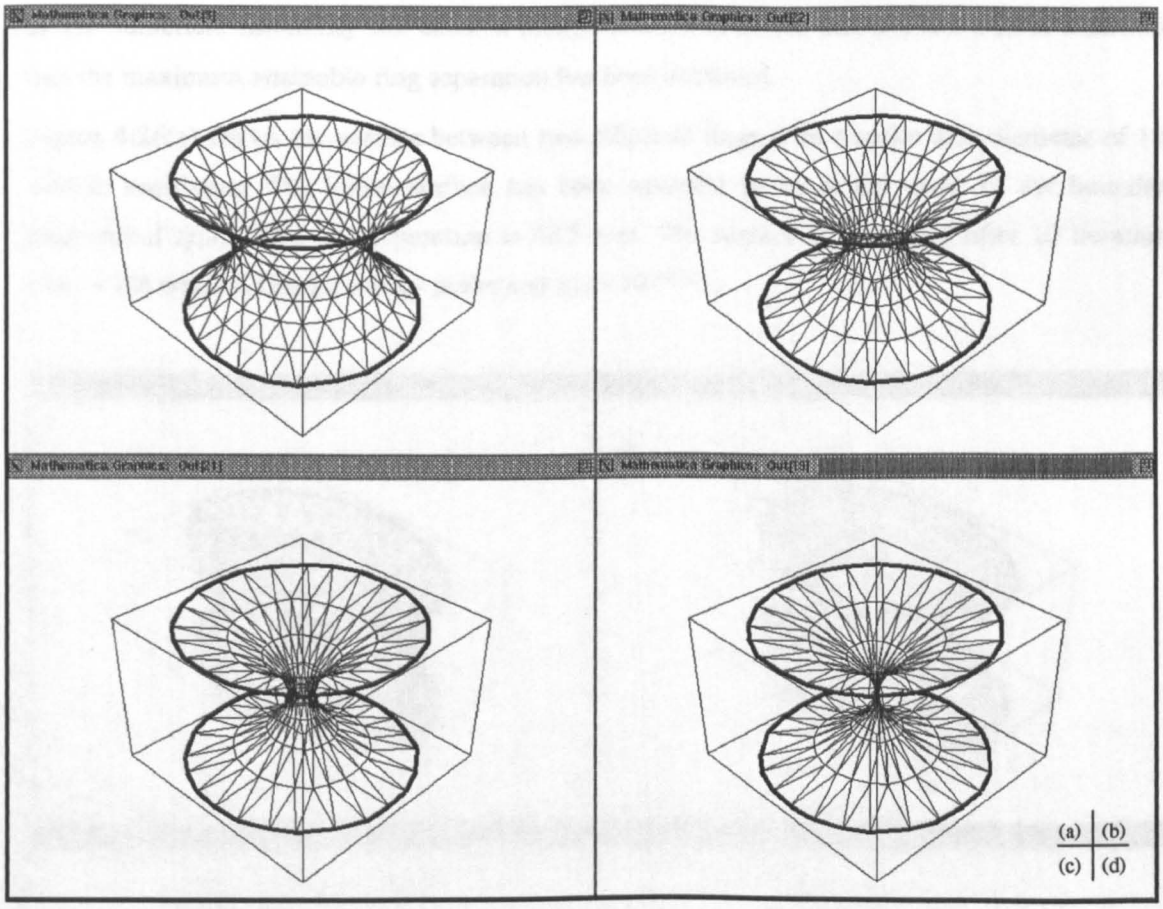

Figure 4.25 - (a) Catenoid - 80 mm Rings at Maximum Separation (53.0 mm). (b) - (d) Progressive Collapse of Catenoid Surface (Separation = 53.1 mm).

Three examples using concentric elliptical rings, for which the closed form solution does not exist, have also been investigated. The minor axis of the ellipse is maintained at 80 mm while the major axis diameter has assumed values of 120 mm, 160 mm, and 240 mm respectively. The surface discretisation is taken as for the circular ring examples, except that 36 elements are used around the circumference of the surface. For the example where the major axis diameter is 120 mm the initial surface is assumed to be in the plane of the boundary (forming a cylindrical type surface between the two rings). In the case of the remaining examples, the initial surfaces are obtained as scaled versions of the equilibriated surface, established between the 120 mm major axis ellipses.

If the initial surface of the numerical model is assumed to be in the plane of the boundary (for the examples where the major axis diameter exceeds 120. mm) the solution algorithm becomes unstable [15] . Similarly, in the case of the smallest ellipse, if the assumed ring separation is too

15

great (but less than the maximum) numerical instability can result. As described below, the form of the numerical instability can cause a misrepresentation of the surface, and a false indication that the maximum attainable ring separation has been achieved.

Figure 4.26(a) shows the surface between two elliptical rings with a major axis diameter of 120 mm in each case. The initial surface has been assumed to be in the plane of the boundary (cylindrical type). The ring separation is 58.5 mm. The surface is illustrated after 10 iterations ($N_{IT} = 10$) with no kinetic energy peaks and $\lambda_A = 10$ [4.21].

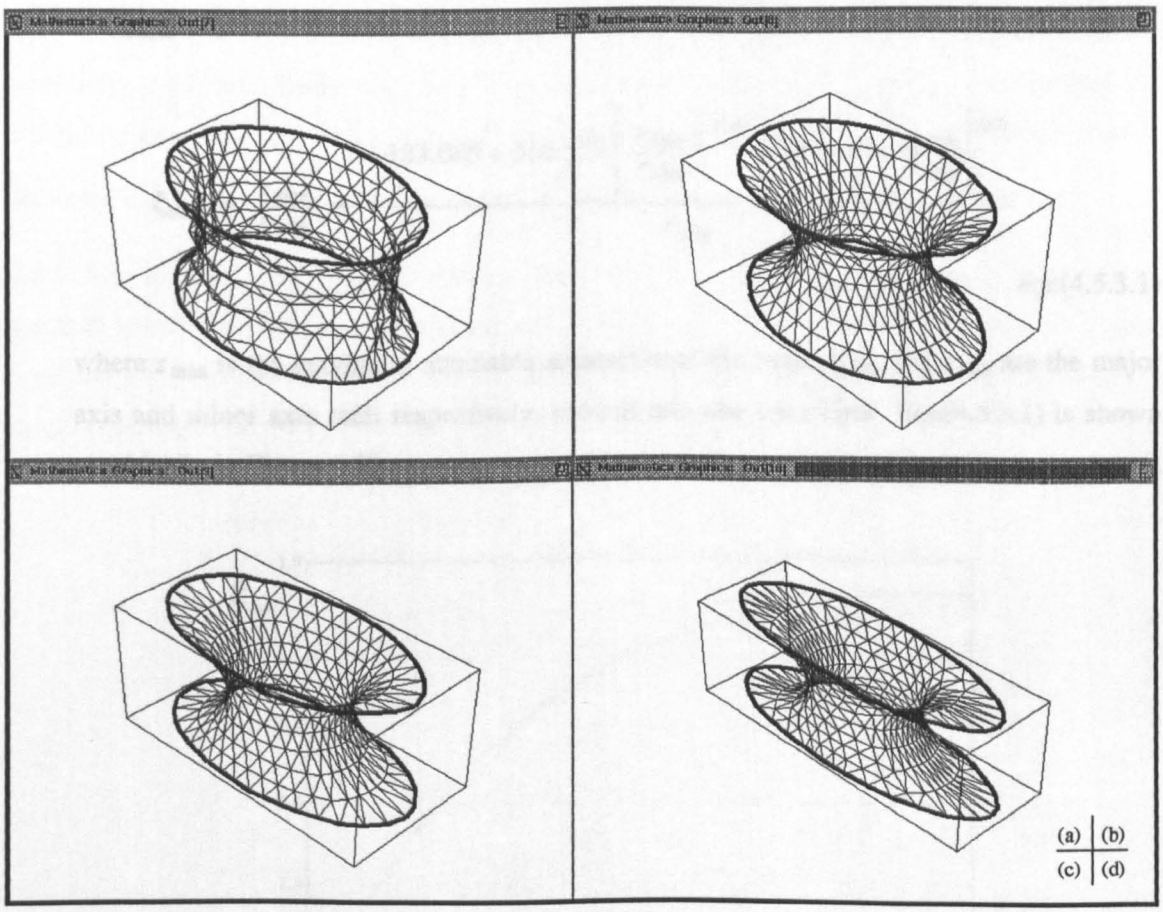

Figure 4.26 - (a) Surface Exhibiting Numerical Instability.
(b) - (d) Equilibriated Surfaces at Maximum Attainable Ring Separation
Major Axis Diameters of 120 mm, 160 mm, and 240 mm, Respectively.

A comparison of Figure 4.26(a) with Figure 4.25(d) suggests that the modes of surface collapse are dissimilar. Particular attention is drawn to the central region of the surface shown in Figure 4.26(a) where it can be seen that the surface has tended to buckle and wrinkle.

By using a smaller ring separation, an equilibriated surface with uniform element stress can be established. This surface is then extended to give a new initial surface for the subsequent increase in ring separation. The surface resulting from this approach is shown in Figure 4.26(b). The

maximum ring separation is 62.8 mm. This value of separation can be compared with the misrepresented maximum separation of 58.5 mm, and constitutes an increase of around 7 %.

Therefore, in the case of the ellipses in which major axis diameter is 120 mm, $\xi_{max} = \frac{68.3}{40.} = 1.57$. In the examples where the major axis diameters are 160 mm and 240 mm, it is found that $\xi_{max} = \frac{68.3}{40.} = 1.71$ and $\xi_{max} = \frac{73.3}{40.} = 1.83$, respectively. The corresponding surfaces are illustrated in Figure 4.26(c) and Figure 4.26(d) respectively.

Given the solutions to the examples presented above, an expression for obtaining intermediate values of ξ_{max} may be written as,

$$\xi_{max} = \frac{z_{max}}{r_{min}} = \frac{-183.085 + 366.575\left[\frac{r_{max}}{r_{min}}\right]^{0.25} - 130.486\left[\frac{r_{max}}{r_{min}}\right]^{0.5}}{r_{min}}$$

eqn(4.5.3.1)

where z_{max} is the maximum attainable separation of the rings. r_{max} and r_{min} are the major axis and minor axis radii respectively, used to describe the ellipse. Eqn(4.5.3.1) is shown graphically in Figure 4.27.

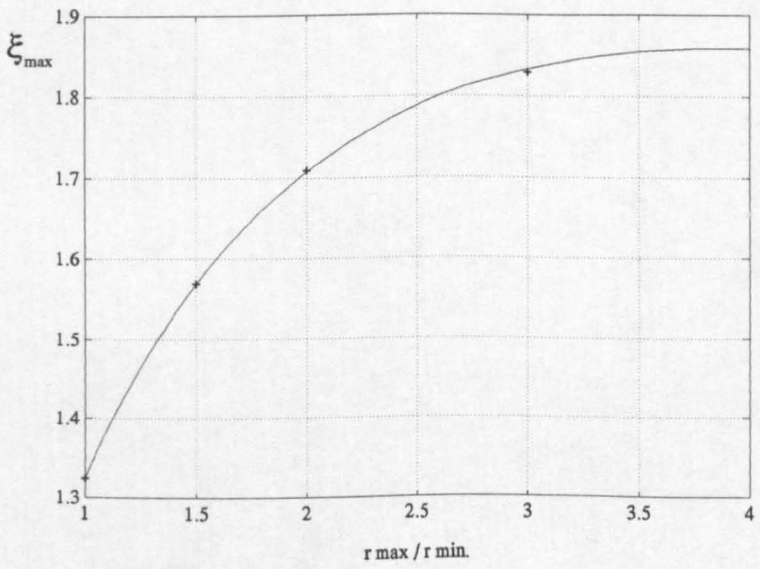

Figure 4.27 Variation of ξ_{max} with $\frac{r_{max}}{r_{min}}$ (eqn(4.5.3.1)).

Differentiation of eqn(4.5.3.1) leads to,

$$\frac{dz_{max}}{da} = \frac{91.644}{a^{0.75}} - \frac{65.243}{a^{0.5}}$$

eqn(4.5.3.2)

where a is the ratio $\frac{r_{max}}{r_{min}}$.

Equating the right hand side of eqn(4.5.3.2) to zero leads to $\xi_{max}{}^{max} = 1.859$ at $\frac{r_{max}}{r_{min}} \geq 3.893$. This compares with the value of $\xi_{max} = 1.325$ for the case of the circular concentric rings ($\frac{r_{max}}{r_{min}} = 1.$).

The maximum attainable separation may be increased when the rings are of an elliptical shape instead of circular (for the same minor axis diameter). As the major axis diameter of the elliptical rings is increased the extremes of the surface (in the direction of the major axis diameter) assume horizontal positions. Therefore, these areas are almost redundant in terms of enhancing the maximum attainable separation of the rings for a constant value of minor axis diameter. This is demonstrated by the levelling of the plot of $\frac{r_{max}}{r_{min}}$ against ξ_{max} (Figure 4.27).

Table 4.8 presents a comparison of the numerical with the experimental solutions to the minimal surfaces generated between two circular and between two elliptical rings, illustrated in Figure 4.25 and Figure 4.26. An adequate representation of the maximum attainable separation of the rings is demonstrated by the proposed numerical model.

Solution	Numerical		Experimental		
$\frac{r_{max}}{r_{min}}$	z_{max} (mm)	ξ_{max}	z_{max} (mm)	ξ_{max}	Error
1.5	62.8	1.57	61.7	1.54	1.8 %
2.0	68.3	1.71	66.9	1.67	2.4 %
3.0	73.3	1.83	60.9	1.82	0.5 %

Table 4.8 - Comparison of Numerical Solution with Experimental (Elliptical Rings) [16].

4.5.4. Minimal Surfaces with Internal and External Flexible Boundary Elements.

Those surfaces whose boundaries are flexible and fixed at a minimum number of points to maintain equilibrium, comprise an additional group of minimal energy forms. The numerical solutions to the surfaces shown in Plates 3.14 - 3.19 are presented in this section. The membrane

16

Due to the constraints of the modelling apparatus, the minor axis diameter, r_{min}, of the physical model in which $\frac{r_{max}}{r_{min}}$ = 3.0 is 33.325 mm. Consequently, the maximum attainable separation is 60.9 mm.

is discretised by triangular elements, representing a state of constant surface stress. The boundary elements (linear (line) in this case) are assumed to act in an elastic manner such the strains in these elements induce natural forces.

Consequently, the shape of the surface is controlled by both the position of the fixed boundary points (as before), and the length of the boundary elements. Figure 4.28 shows the effect of increasing the lengths of the boundary elements on the final form. The lengths of the elements are increased by reducing the elastic modulus of the boundary elements progressively.

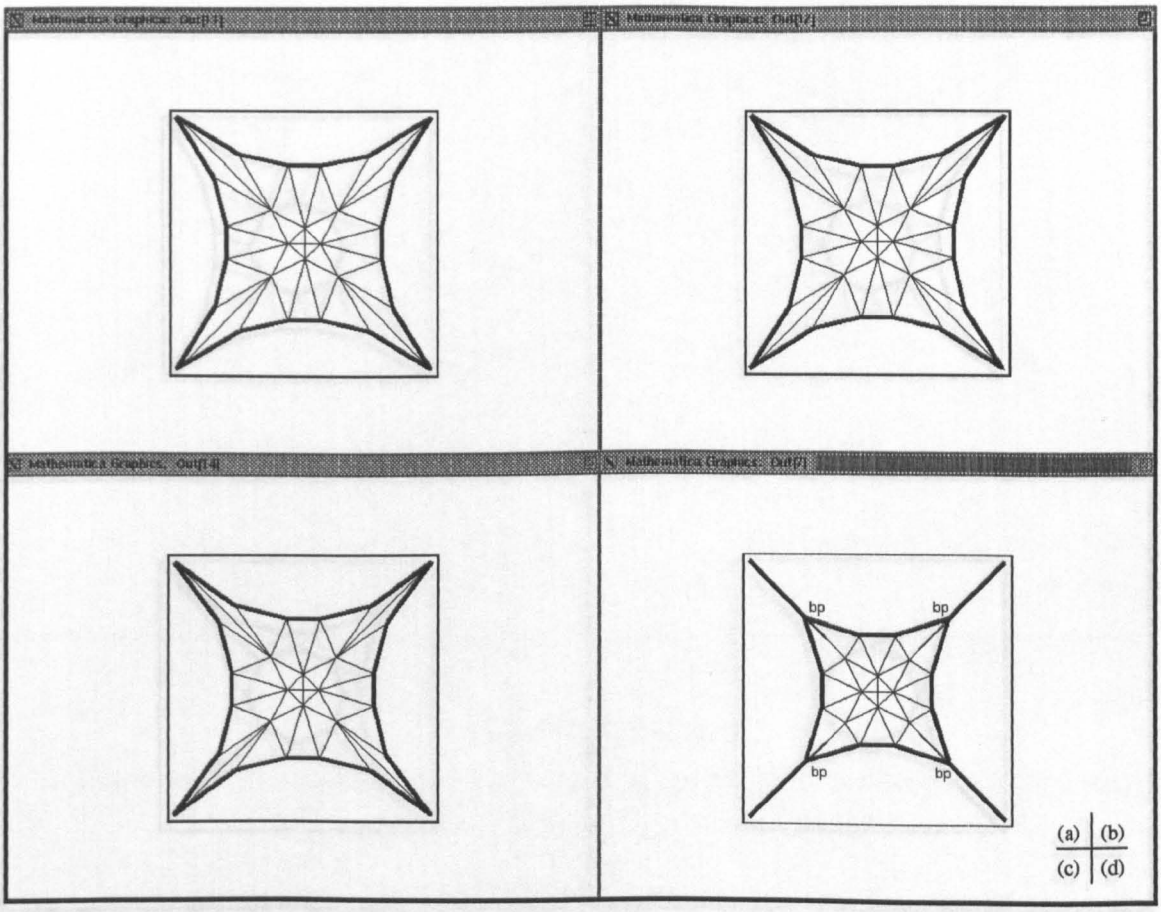

Figure 4.28 (a) - (d)
Surface Forms Generated by Increasing the Length of the Boundary Elements.
(External Boundary Elements Only).

The numerical solutions presented in Figure 4.28 (a) - (d) can be compared with the experimental solutions illustrated in Plates 3.14 & 3.15. The element stresses in all of the examples illustrated in Figure 4.28 are uniform to within 0.01 %. In the case of the experimental solution the individual boundary cables exhibit a constant natural force. The natural forces in the boundary elements of the numerical model vary by up to 3 % (approximately). This figure can be reduced if a finer discretisation of elements is adopted. (The initial prestress of the boundary elements has

been assumed to be zero).

If the boundary elements become too long then a minimal surface cannot be formed between the actual fixed boundary points (Figure 4.28(d)). Instead the boundary cable elements merge and new "fixed" boundary points are generated by the minimal surface. These are marked as "bp" in Figure 4.28(d). This phenomenon can also be recognised in the physical models (Plate 3.15).

The numerical solutions to plane membranes with internal and external boundary elements of varying length are presented in Figure 4.29.

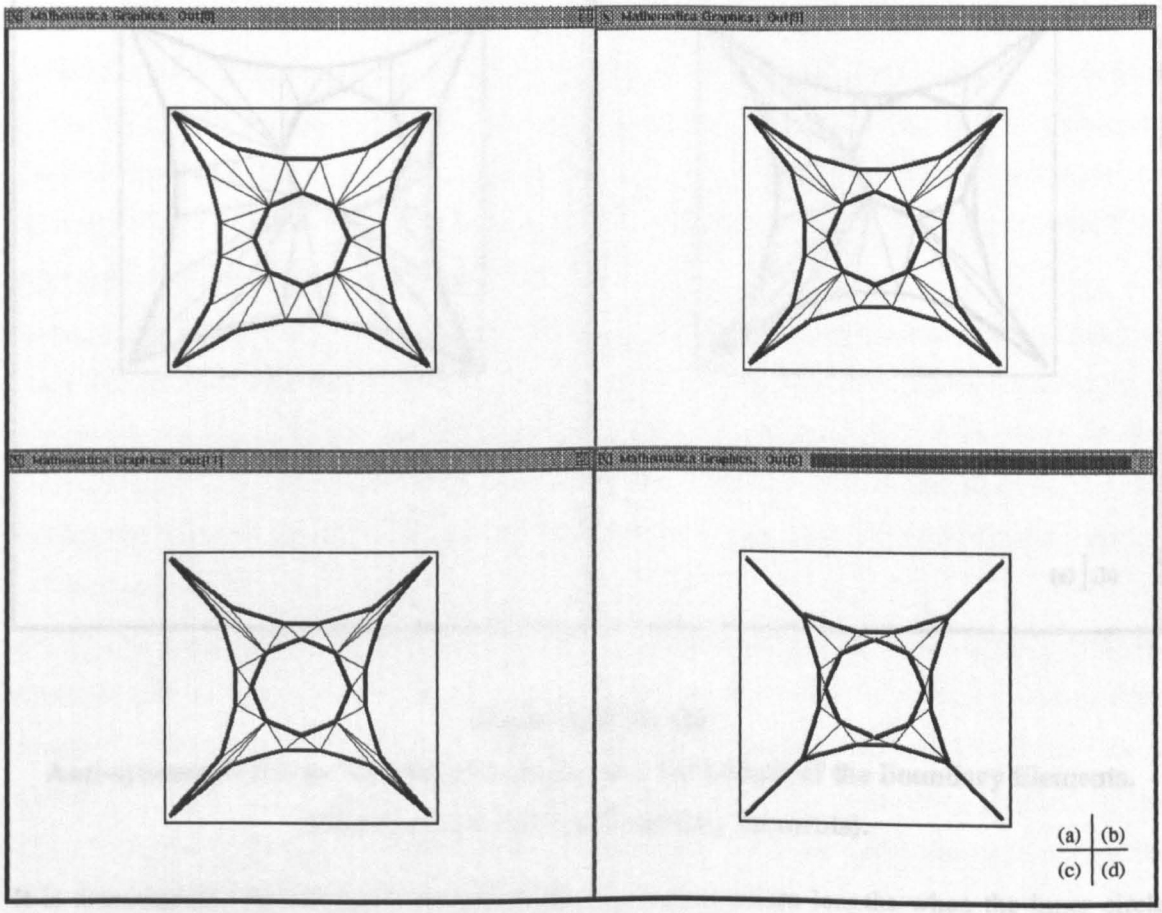

Figure 4.29 (a) - (d)
Surface Forms Generated by Increasing the Length of the Boundary Elements.
(External and Internal Boundary Elements).

The internal boundary elements are shown to form a linear piecewise approximation to a circle (Figure 4.29). In the numerical model the natural forces of the internal boundary elements vary by less than 0.03 %. In the case of a pure circle (Plate 3.17) the natural forces are constant. Consequently, the numerical model may be seen to provide an excellent approximation to the physical model.

Figure 4.30 shows the effect of assuming that the internal boundary cables are remote from the centre of the membrane as the length of the boundary elements are increased.

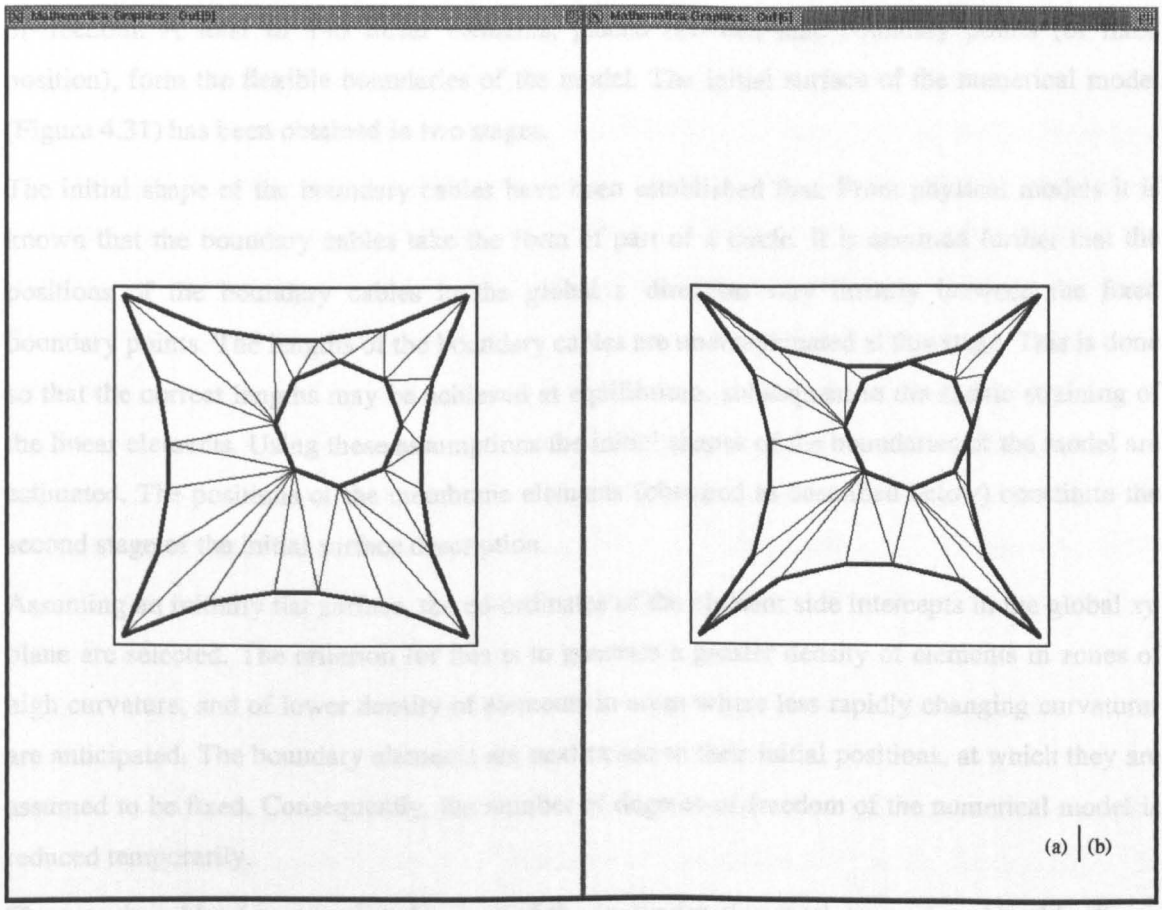

Figure 4.30 (a), (b)
Anti-symmetric Forms Generated by Increasing the Length of the Boundary Elements. (External and Internal Boundary Elements).

It is demonstrated that the boundary elements achieve maximum lengths when the inner circle comes into contact with the external boundaries. In this case the shape of the external boundaries remain unchanged. They continue to describe an arc whose form is given by the equation of a circle. This feature is also shown experimentally in Plate 3.19.

4.5.5. A General 3-dimensional Minimal Surface with Flexible Boundary Elements - "Siegfried's Tent".

The experimental solution to the surface illustrated in Plates 3.20 - 3.22 is presented in this section. The form is characterised by a surface of rapidly changing curvatures and by flexible boundary cables of specified unequal lengths and determinable positions in space. The surface is established through the imposition of the condition of a constant surface stress (approximately)

and the equilibrium state of the boundary and internal elements. The numerical representation of the form is described below.

The surface is discretised by 1240 constant strain triangular elements constituting 2046 degrees-of-freedom. A total of 140 linear elements, placed between nine boundary points (of fixed position), form the flexible boundaries of the model. The initial surface of the numerical model (Figure 4.31) has been obtained in two stages.

The initial shape of the boundary cables have been established first. From physical models it is known that the boundary cables take the form of part of a circle. It is assumed further that the positions of the boundary cables in the global z direction vary linearly between the fixed boundary points. The lengths of the boundary cables are underestimated at this stage. This is done so that the correct lengths may be achieved at equilibrium, subsequent to the elastic straining of the linear elements. Using these assumptions the initial shapes of the boundaries of the model are estimated. The positions of the membrane elements (obtained as described below) constitute the second stage of the initial surface description.

Assuming an initially flat surface, the co-ordinates of the element side intercepts in the global xy plane are selected. The criterion for this is to generate a greater density of elements in zones of high curvature, and of lower density of elements in areas where less rapidly changing curvatures are anticipated. The boundary elements are next raised to their initial positions, at which they are assumed to be fixed. Consequently, the number of degrees-of-freedom of the numerical model is reduced temporarily.

The pseudo cables (representing the sides of the triangular elements) are next replaced by linear elements (for the purposes of establishing the initial surface only). The linear elements are assumed to possess a constant and uniform pretension throughout. Consequently, the surface is analysed as a linear element model initially. To prevent the surface from being distorted by the linear elements following geodesic lines, movements of the surface nodes are permitted in the global z direction only. The surface is therefore equilibriated in a partial sense, with the condition of equilibrium in the global xy plane ignored temporarily. The resulting initial surface is illustrated in Figure 4.31. The triangular elements are reinstated subsequently.

Due to the complexity of the form the revised procedure (Section 4.4.3.2.3) is adopted in order to maintain the stability of the solution algorithm. The elastic modulus of the surface is thus assumed to be $3.\times10^{+6}$ kN.m^{-2}, and Poisson's ratio υ to be 0.1. A thickness of $1.\times10^{-3}$ m is assumed for the membrane. The uniform stress vector $\{\sigma_c\}$ is given as $\sigma_x = \sigma_y = 5.\times10^{+6}$ kN.m^{-2} and $\tau_{xy} = 0.$ kN.m^{-2}.

The geometric and elastic properties of the boundary cables are assumed to be constant between the fixed boundary points. The areas of the boundary cables are taken as unity throughout, except in the case of the cable f-g (Figure 4.32) where it is assumed to be $2.2\times10^{+3}$ m^2. The elastic

modulus of all boundary cables is 1.0 kN.m^{-2}. A list of the assumed element prestresses is given in Table 4.9. [17]

After a total of 20,000 iterations (N_{GI} = 40), corresponding to a Cpu time of 20707.3u, the surface illustrated in Figure 4.32 is obtained. The condition of equilibrium is satisfied globally to within an error residual, Er, equal to 0.25% of the maximum pseudo cable force. Due to the merging of the boundary cables g-h and f-g in the vicinity of the mast head (g), some elements of the discretisation collapse (while remaining stable). The effects of the poor aspect ratio of these elements introduce errors into the numerical solution. Consequently, local equilibrium of the surface is not achieved at some nodes of the discretisation. A global satisfaction of the condition of equilibrium can be assumed however.

Table 4.9 presents a summary of the boundary cable forces at equilibrium (N_{GI} = 40). The natural forces in the linear elements comprising each boundary cable are constant at equilibrium (N_{GI} = 40). This is with the exception of the cable f-g. A 4 % (approximately) deviation in natural force from the mean value (given in Table 4.9) exists in this boundary cable at equilibrium (N_{GI} = 40) [18] . Also given in Table 4.9 is a comparison between the numerical and the experimental values of the lengths of the boundary cable (b.c.l.).

Table 4.10 gives the values of the maximum and the average element stress deviations for the first four and for the last two re-impositions of the uniform stress vector, $\{\sigma_c\}$ (N_{GI} = 1→4, 39, and 40). The low magnitudes of the average element stress deviations indicate that the condition of uniform surface stress is represented adequately at equilibrium (N_{GI} = 40, Table 4.10). [19] In addition, the lengths of the boundary cable f-g are given as a function of the number of re-impositions of the uniform stress vector $\{\sigma_c\}$ (N_{GI}). The magnitudes of the maximum element stress deviations and the increases in the length of the boundary cable element f-g indicate the substantial straining of the surface during the initial stages of the form-finding procedure (N_{GI} = 1→5). The numerical solution given in Figure 4.32 may be compared with the experimental solution shown in Plates 3.20 & 3.21.

17

The boundary cable data has been selected so as to provide good agreement between the required (experimental) and the numerical boundary cable lengths. This has been achieved through an iterative procedure, using both the area and the prestress of the boundary elements as variables to control the lengths.

18

The variation of the natural forces along the boundary cable f-g may be attributed to the adoption of an insufficient number of elements to represent the curvatures of the cable adequately.

19

It is inferred through the magnitudes of the maximum element stress deviations, that the condition of uniform surface stress is not represented adequately at equilibrium (N_{GI} = 40). However, the highest element stress deviations appear in the collapsed elements in the vicinity of the mast head (g) and therefore do not contribute significantly to the complete numerical solution (Figure 4.32).

Boundary Cable	Prestress (kN)	Force at Equilibrium (kN) ($N_{GI} = 40$)	b.c.l. (m) (Numerical)	b.c.l. (m) (Experimental)	Error
a-b	$0.1900 \times 10^{+5}$	$0.1900 \times 10^{+5}$	9.438	9.437	0.01 %
b-c	$0.1900 \times 10^{+5}$	$0.1900 \times 10^{+5}$	10.178	10.178	0. %
c-d	$0.1889 \times 10^{+5}$	$0.1889 \times 10^{+5}$	12.254	12.254	0. %
d-e	$0.1307 \times 10^{+5}$	$0.1307 \times 10^{+5}$	7.322	7.322	0. %
e-f	$0.1319 \times 10^{+5}$	$0.1319 \times 10^{+5}$	7.043	7.043	0. %
f-g	$0.2270 \times 10^{+5}$	$0.3386 \times 10^{+5}$	12.491	12.500	0.07 %
g-h	$0.1240 \times 10^{+5}$	$0.1240 \times 10^{+5}$	7.769	7.769	0. %
h-i	$0.1341 \times 10^{+5}$	$0.1341 \times 10^{+5}$	7.162	7.162	0. %
i-a	$0.1912 \times 10^{+5}$	$0.1912 \times 10^{+5}$	10.184	10.184	0. %

Table 4.9 - Boundary Cable Data. [20]

N_{GI}	$\Delta\sigma_X{}^{max}$	$\Delta\sigma_Y{}^{max}$	$\Delta\tau_{XY}{}^{max}$	$\overline{\Delta\sigma_X}$	$\overline{\Delta\sigma_Y}$	$\overline{\Delta\tau_{XY}}$	b.c.l. f-g (m)
1	79.63 %	-99.74 %	74.18 %	4.95 %	9.24 %	4.78 %	9.019
2	-49.55 %	-95.31 %	-37.97 %	2.58 %	5.68 %	2.89 %	9.758
3	-37.51 %	-69.06 %	21.85 %	1.69 %	3.97 %	1.87 %	10.342
4	-27.57 %	-57.89 %	19.52 %	1.17 %	2.93 %	1.30 %	10.787
39	-0.98 %	-7.54 %	2.55 %	0.07 %	0.15 %	0.08 %	12.489
40	-0.95 %	-7.45 %	2.51 %	0.07 %	0.14 %	0.08 %	12.491

Table 4.10 - Variation of Element Stress Deviation with N_{GI}.

20

The boundary cable references given in Table 4.9 refer to Figure 4.32.

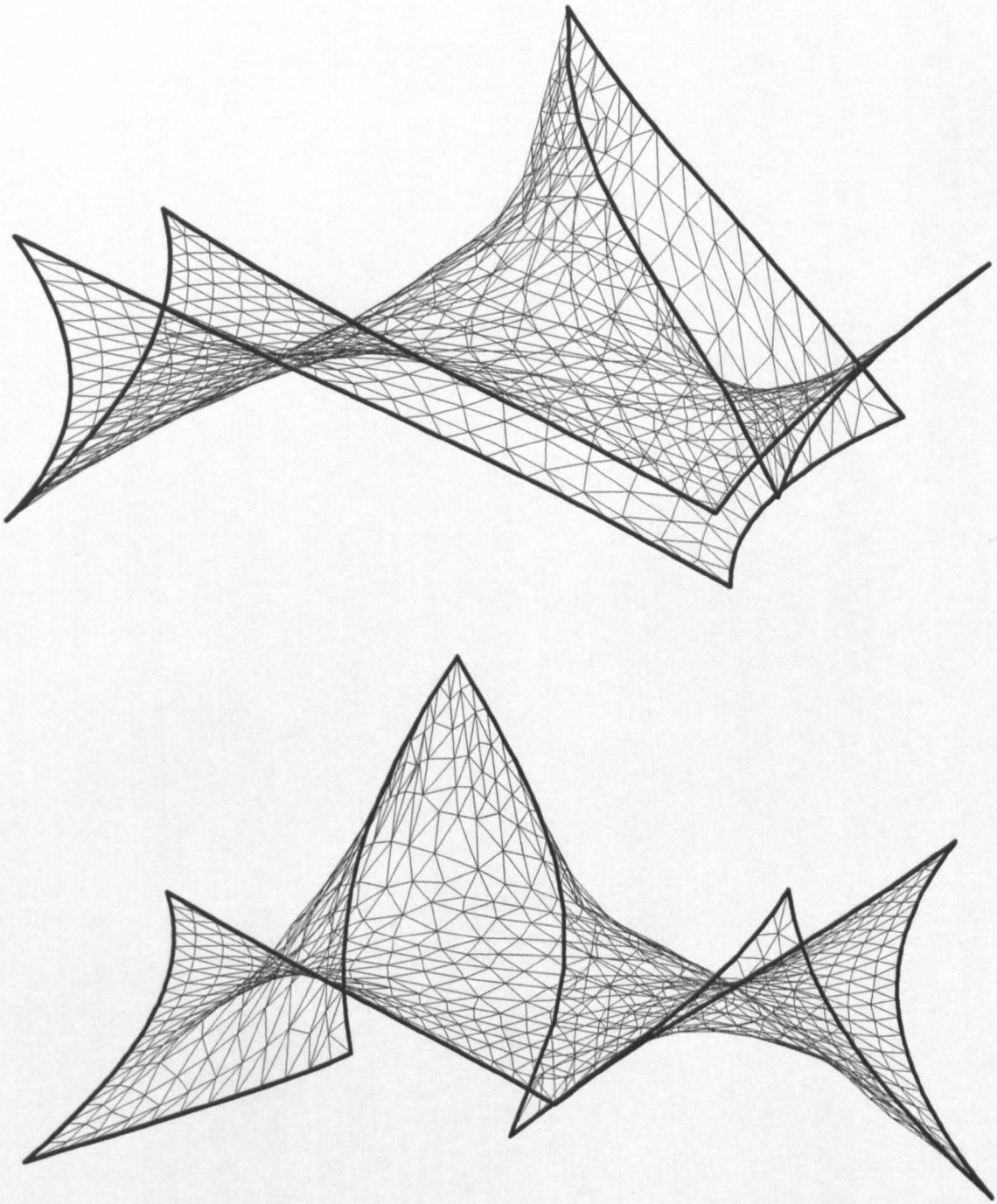

Figure 4.31 - "Siegfried's" Tent.
Initial Surface.

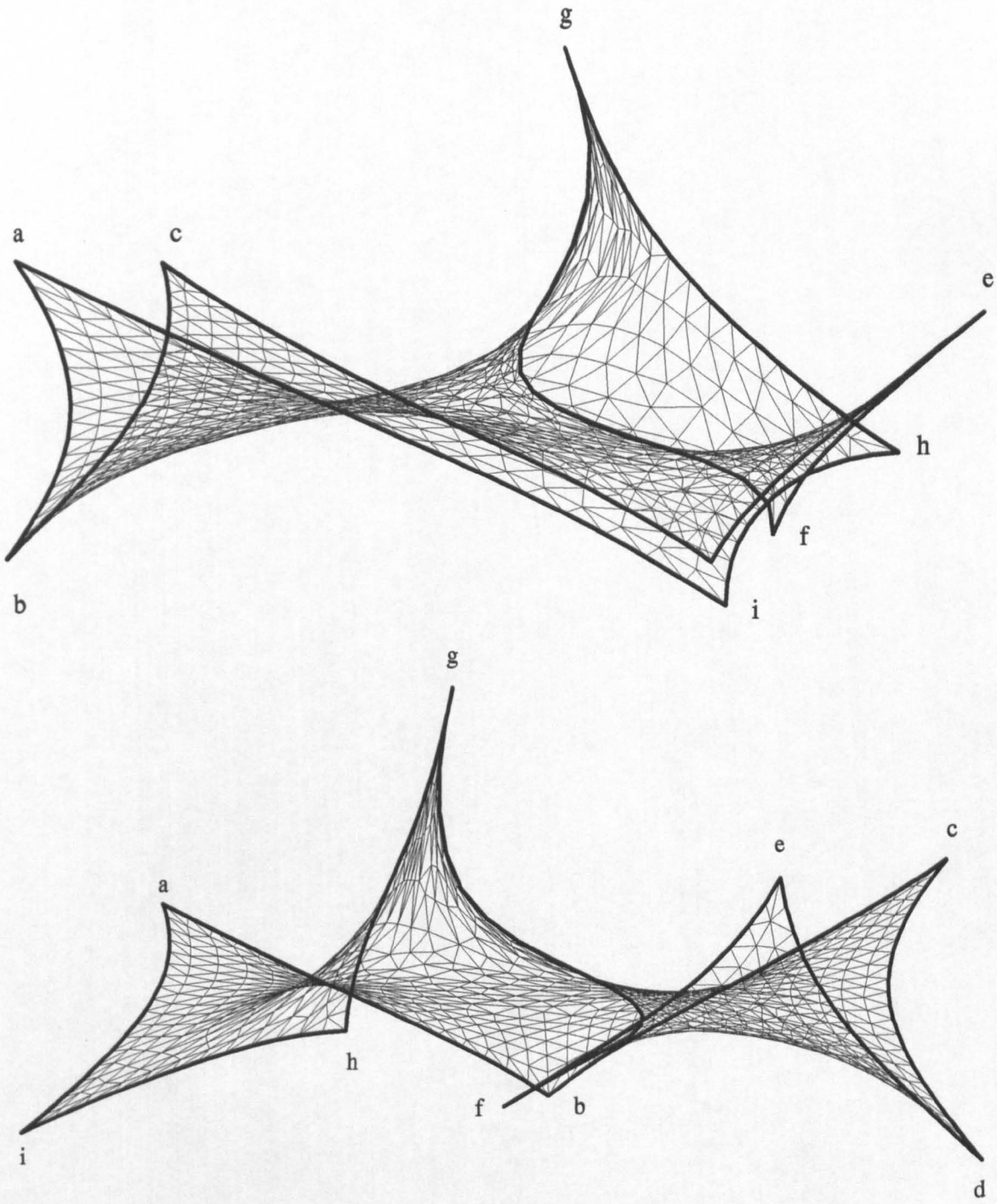

Figure 4.32 - "Siegfried's" Tent.
Equilibriated Surface.

If the elasticity of the surface is assumed to be non-zero (during the form-finding procedure), the magnitudes of the maximum element stress deviations can be used to assess the proximity of the equilibriated surface to the local minimal surface. The elements in which the highest element stress deviations occur identify the areas of the discretisation in which need to be revised. The basis of the approach is described below.

A measure of the straining of the surface can be made by observing the changes in the element stresses during the form-finding procedure. As the surface approaches the condition of uniform stress, the magnitude of the surface strains (and therefore of the element stress deviations) reduce. However, if the form cannot represent a minimal surface (due to the choice of the boundary conditions for example) then a straining the surface occurs after each re-imposition of the constant stress vector $\{\sigma_c\}$. As illustrated below, if the surface is over-constrained the magnitude of the strains are equal (approximately) after each re-imposition, and represent the collapsing and breaking of the surface.

The flexible boundary cables of the surface illustrated in Figure 4.31 are replaced by straight lines of fixed boundary points between the points a $\rightarrow$ i. The surface is subjected to a uniform surface stress, given by the vector $\{\sigma_c\}$. At equilibrium, the element stress deviations presented in Table 4.11 are obtained. The results are given for the first five re-impositions of the constant stress vector $\{\sigma_c\}$ (N_{GI} = 1$\rightarrow$5).

N_{GI}	$\Delta\sigma_X{}^{max}$	$\Delta\sigma_Y{}^{max}$	$\Delta\tau_{XY}{}^{max}$	$\overline{\Delta\sigma_X}$	$\overline{\Delta\sigma_Y}$	$\overline{\Delta\tau_{XY}}$
1	-60.09 %	-76.61 %	38.67 %	3.17 %	3.95 %	2.76 %
2	-46.16 %	-46.09 %	-25.55 %	2.45 %	2.86 %	2.01 %
3	-39.54 %	-41.47 %	-19.82 %	2.33 %	2.70 %	1.86 %
4	-36.11 %	-39.70 %	18.15 %	2.21 %	2.59 %	1.73 %
5	-34.25 %	-39.16 %	16.40 %	2.12 %	2.50 %	1.64 %

Table 4.11 - Variation of Element Stress Deviation with N_{GI}.

The convergence of the maximum element stress deviation to 39 % (approximately) indicates that a minimal surface is not developable with the assumed boundary conditions. The relatively low average direct stress deviation of 2.5 % (relative to the maximum of 39 % (approximately)) suggests that areas of the form represent local minimal surfaces however. The maximum element stress deviations may be reduced by partially relaxing the over-constraining boundary conditions.

In the case of the surface illustrated in Figure 4.32, a minimal surface cannot be established with the boundary conditions given in Table 4.9. This is demonstrated by the merging of the boundary cables g-h and f-g in the vicinity of the mast head (g) (Figure 4.32). Through a sufficient revision of the current topology, the separation of the boundary cables g-h and f-g may be detected and the local minimal surface obtained [21] . The separation of the boundary cables is indicated by the convergence of the maximum element stress deviations (corresponding to the elements around the mast head (g) (Figure 4.32)) to minimum values. In this way the geometry of a general surface with flexible boundaries (which are initially too long) can be amended to obtain the minimal surface which is local to the original topology.

4.5.6. Summary - Verification of Soap-film Models.

The following points are summarised regarding the verification of the soap-film models presented in the preceding section.

i) A linear element discretisation of the form can provide an accurate solution to the surface when the principal curvatures are low. A large number of linear elements is required to model the surface accurately.

ii) Linear elements with uniform and constant pretensions tend to follow geodesic lines over the surface. This can give rise to distortion of the final form. With careful modelling an accurate solution can be achieved to a known surface.

iii) A numerical model using triangular elements can produce an accurate solution to a minimal surface when compared with the experimental solution. A relatively coarse discretisation of arbitrarily shaped elements can be used.

v) The introduction of elasticity into the form-finding procedure has been shown to be successful in maintaining the stability of the numerical solution algorithm when the surface is subjected to large strains and to large displacements.

iv) A method has been proposed, based on the maximum and average element stress deviations, for assessing the proximity of the current form to the local minimal surface. The same approach can be used modifying the existing boundaries of the current form in order to obtain the minimal surface which is local to the original topology.

21

A minimal surface can be obtained by either lowering the mast head (g) or decreasing the length of the boundary cable f-g.

4.6. Appendix 4-A - Strains in an Inclined Direction.

In a system of 2-dimensional strains, the direct and shearing strains can be calculated in any in-plane direction provided that the direct and shearing strains in two mutually perpendicular directions are known [4.17]. A summary of the proof of this statement is presented below.

The flat rectangular element of elastic material, illustrated in Figure 4-A.1., has side intercepts OABC and is located in the local XY plane. The position of a point on the boundary of the element is defined as $\underline{X}^l$. It is assumed that the element is subjected to a general displacement vector $\underline{\delta}^l$ [22].

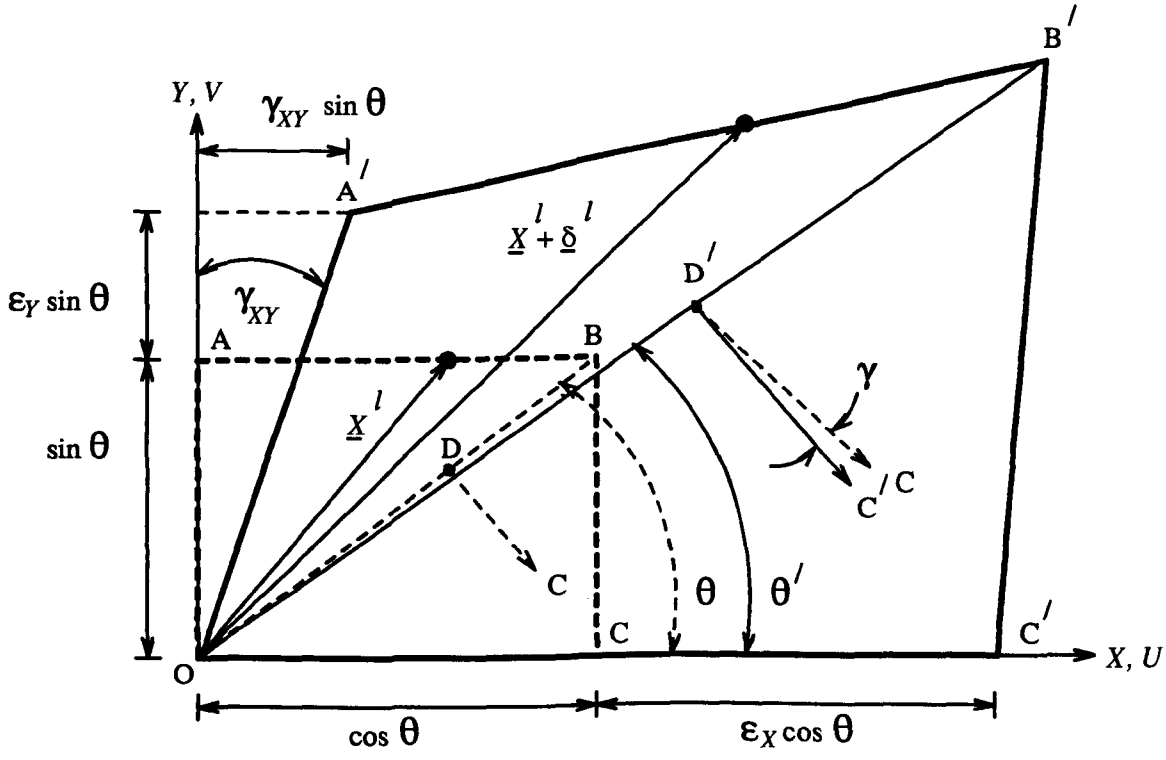

Figure 4-A.1 - Plane Element Subjected to a Displacement Vector $\underline{\delta}^l$.

The length of the diagonal OB is assumed to be unity, while the angle subtended by OB to the X axis is denoted by θ. The undeformed lengths OC and OA may thus be written as cos θ and sin θ respectively.

Subsequent to the application of the displacement vector $\underline{\delta}^l$ the element strains to the deformed shape OA'B'C' (Figure 4-A.1). In the strained condition, the side OA extends by a small amount ε_Y sin θ and OC by a small amount ε_X cos θ. Due to the shearing strain, the side OA rotates through a small angle γ_{XY}, to OA' (Figure 4-A.1).

22

Both $\underline{X}^l$ and $\underline{\delta}^l$ are given in the local co-ordinate system as indicated by the superscript l.

In the strained condition, the point B moves to B′ by an amount $\varepsilon_X \cos\theta + \gamma_{XY} \sin\theta$ in the direction OC, and by an amount $\varepsilon_Y \sin\theta$ in the direction OA (Figure 4-A.1). These two components may be transformed to give the movement of the point B in the direction OB, $\vec{B}^{OB}$, as,

$$\vec{B}^{OB} = (\varepsilon_X \cos\theta + \gamma_{XY} \sin\theta)\cos\theta + \varepsilon_Y \sin^2\theta$$

eqn(4-A.1)

By assuming that the strains $\{\varepsilon_X, \varepsilon_Y, \gamma_{XY}\}$ are small, and that the angles θ and θ' (Figure 4-A.1) are approximately equal, it follows that the movement, $\vec{B}^{OB}$, is the direct strain ε^{OB} in the direction OB, arising from the vector of strains $\{\varepsilon\}$. Therefore, from eqn(4-A.1),

$$\varepsilon^{OB} = \varepsilon_X \cos^2\theta + \varepsilon_Y \sin^2\theta + \gamma_{XY} \cos\theta \sin\theta .$$

eqn(4-A.2)

4.7. References.

[4.1] Zienkiewicz, O.C.

The Finite Element Method in Engineering Science.

McGraw-Hill, London, 1971

[4.2] Williams, C.J.K.

"The Generation of a Class of Structural Forms for Vaults and Sails."

The Structural Engineer, Volume 68, Number 12, June 1990.

[4.3] Bach, K., Burkhardt, B., Otto, F.

Forming Bubbles.

IL. (Institute of Lightweight Structures, Stuttgart University, Germany.) Publication Number 18, 1987.

[4.4] Otto, F., Trostel, R.

Tensile Structures.

The MIT Press, Cambridge, Volume 1, 1967.

[4.10] Cundall, P.A.

"Explicit Finite Difference Methods in Geometrics."

Proceedings E.F. Conference, Numerical Methods in Geomechanics, Blacksburg, VA., 1976.

[4.11] Barnes, M.R.

"Non-linear Numerical Solution Methods for Static and Dynamic Analysis of Tension Structures."

Symposium on Air Supported Structures, IStructE, London, 1980.

[4.12] Barnes, M.R.

"Form-finding and Analysis of Prestressed Nets and Membranes."

Int. Conf. Non-conventional Structures, Volume 1, 1987, pages 327-338.

[4.13] Argyris, J.H., Scharpf, D.W.

"Large Deflection Analysis of Prestress Networks."

Journal of the Structural Division, ASCE, volume 98, ST3, March 1972.

[4.14] Cook, R.D., Malkus, D.S., Plesha, M.E.

Concepts and Applications of Finite Element Analysis.

John Wiley and Sons, 1989.

[4.15] Faux, I.D., Pratt M.J.

Computational Geometry for Design and Manufacture.

Mathematics and its Applications Series, Ellis Horwood, 1979

[4.16] Oden, J.T.

Finite Elements of Non-linear Continua.

McGraw-Hill Advanced Engineering Series, 1972.

[4.17] Case and Chilver

Strength of Materials of Structures, an Introduction to the Mechanics of Solids and Structures.

2nd Edition, Edward Arnold, London, 1971.

[4.18] Cook, R.D.

Concepts and Applications of Finite Element Analysis, a Treatment of the Finite Element Method as Used for the Analysis of Displacement, Strain and Stress.

Willey, London, 1974.

[4.19] Barnes, M.R.

"Form-finding of Minimum Surface Membranes."

IASS World Congress on Space Structures, Building Research Centre, Concordia University, Montreal, July 1976.

[4.20] Otto, F., Trostel R.

Zugbeanspruchte Konstruktionen, Bd. 1, (ZK 1), 1962.

[4.21] Lewis, W.J., Gosling, P.D.

"Computer Modelling of Stable Minimal Surfaces."

Research Report CE32, University of Warwick, November 1990.

Chapter 5

24 Degrees-of-Freedom Quadratic Quadrilateral Finite Element for the Investigation of Stable Minimal Energy Forms - Element Formulation.

5.1. Introduction.

In order to move away from the restrictions and the assumptions of the plane type of elements summarised in Section 4.3 and Section 4.4 of Chapter 4, the element formulation presented in this chapter is proposed for the analysis of stable minimal energy forms. The element is doubly curved and suited to the analysis of systems subjected to both large displacements and large strains, and which are characterised by surfaces of rapidly changing curvatures.

In this chapter the following aspects of the element formulation are presented:

- the derivation of the general element equations as they relate to the Finite Element method (Section 5.2),
- a description of the proposed element (Section 5.3.1),
- the derivation of the element shape functions assuming both small and large nodal displacements respectively (Section 5.3.2 and Section 5.3.3)
- the derivation of the relationship between the natural, local, and global co-ordinate systems, and of the expressions for the element local strains (Section 5.4 and Section 5.5 respectively),
- the generation of the element elastic and initial stress stiffness matrices, and of the element equivalent nodal force vector (Section 5.7),
- the techniques of numerical (Gauss Quadrature) and of reduced integration (Section 5.8),
- the adequate representation of rigid body rotations of the element in the geometric stiffness matrix, $[K_{\sigma}^{e}]$ (Section 5.9).

5.2. Derivation of the General Element Equations.

5.2.1. General Expression for the Potential Energy of an Elastic Continuum.

The derivation of the general element equations is presented in this section. As demonstrated below, the derivation is based on the minimisation of the total potential energy of the discretised system [5.1].

In the case of a general three-dimensional body in which it is assumed that all six components of stress act in a linear elastic manner, the vector of body stresses $\{\sigma\}$, may be written as,

$$\{\sigma\} = \{\sigma_x, \sigma_y, \sigma_z, \tau_{xy}, \tau_{yz}, \tau_{zx}\}, \qquad \text{eqn(5.2.1.1)}$$

where $\sigma_x, \sigma_y, \sigma_z$ are the principal direct stresses, and $\tau_{xy}, \tau_{yz}, \tau_{zy}$ are the principal shear stresses.

The vector of corresponding strains, $\{\varepsilon\}$, is,

$$\{\varepsilon\} = \{\varepsilon_x, \varepsilon_y, \varepsilon_z, \gamma_{xy}, \gamma_{yz}, \gamma_{zx}\}. \qquad \text{eqn(5.2.1.2)}$$

If it is assumed initially, that a first order approximation to the strains may be made, then, $\varepsilon_x = \frac{\partial u}{\partial x}$, $\varepsilon_y = \frac{\partial v}{\partial y}$, and $\gamma_{xy} = \frac{\partial u}{\partial y} + \frac{\partial v}{\partial x}$ etc., where u, v, w are the global displacements at a point in the body, corresponding to the global x, y, z directions.

The vectors of stresses, $\{\sigma\}$, and of strains, $\{\varepsilon\}$, are related by the expression,

$$\{\sigma\} = [E]\left\{\{\varepsilon\} - \{\varepsilon_o\}\right\} + \{\sigma_o\}$$

$$= [E]\{\varepsilon\} - [E]\{\varepsilon_o\} + \{\sigma_o\}$$

$$\text{or} \quad = [E]\{\delta\varepsilon\} + \{\sigma_o\}, \qquad \text{eqn(5.2.1.3)}$$

where, $\{\sigma_o\}$, is the vector of initial stress, and, $[E]$, is the matrix of isotropic or anisotropic elastic constants [1].

1

The vector of initial stress, $\{\sigma_o\}$, can be used to represent the prestress applied to a fabric membrane in order to establish the surface of the form, and, at the same time, to invoke sufficient out-of-plane stiffness to prevent the onset of aero-elastic flutter.

The increment of strain energy generated when a unit volume of material is subjected to an infinitesimal distortion, may be written as [2],

$$\begin{aligned} \delta U_o &= \{ \sigma + \delta\sigma \}\{ \delta\varepsilon \}^T \\ &\approx \{ \sigma \}\{ \delta\varepsilon \}^T \end{aligned} \qquad \text{eqn(5.2.1.4)}$$

Taking the variation of the strain energy with respect to each of the strains, eqn(5.2.1.5) may be written in the form,

$$\frac{\partial U_o}{\partial \varepsilon_x} = \sigma_x, \quad \frac{\partial U_o}{\partial \varepsilon_y} = \sigma_y \quad \ldots\ldots \quad \frac{\partial U_o}{\partial \gamma_{xy}} = \tau_{xy}. \qquad \text{eqn(5.2.1.6)}$$

Collecting the terms of eqn(5.2.1.6) into matrix form and substituting eqn(5.2.1.3), yields,

$$\left\{ \frac{\partial U_o}{\partial \varepsilon_x} \right\} = \{ \sigma \} = [E]\{ \varepsilon \} - [E]\{ \varepsilon_o \} + \{ \sigma_o \}. \qquad \text{eqn(5.2.1.7)}$$

Integrating eqn(5.2.1.7) and discarding the superfluous constant of integration, leads to an expression for the strain energy per unit volume as,

$$U_o = \frac{1}{2} \{\varepsilon\}^T [E]\{ \varepsilon \} - \{\varepsilon\}^T [E]\{ \varepsilon_o \} + \{ \varepsilon \}^T \{ \sigma_o \} \qquad \text{eqn(5.2.1.8)}$$

Denoting $\{ F \}$ as the vector of body forces per unit volume, and $\{ \Phi \}$ as the vector of surface traction per unit area acting on the boundaries of the volume gives,

$$\{ F \} = \{ F_x, F_y, F_z, \}, \text{ and } \{ \Phi \} = \{ \Phi_x, \Phi_y, \Phi_z \}, \qquad \text{eqn(5.2.1.9)}$$

2

Changes in the vector, $\{ \sigma \}$, arising from an infinitesimal strain increment $\{ \delta\varepsilon \}$ are discarded as a necessary approximation in order to simplify the remaining formulation (eqn(5.2.1.4)). Consequently, when the strain energy of the distorted volume is calculated, the additional strain energy due to the strains, $\{ \delta\varepsilon \}$, acting on the stresses generated by those strains, $\{ \delta\sigma \}$, are ignored. For example, if the strain increment $\{ \delta\varepsilon \}$ is subdivided into s sub-increments and applied to a unit volume of material, it is assumed that after the application of each sub-increment, the material stress is held constant at the initial value until the last sub-increment has been applied.

During the form-finding of a minimal surface membrane, it is effective to assume that the elastic modulus of the surface is zero, and hence $[E] = 0$. From eqn(5.2.1.3) a variation in strain can be seen not to produce a variation in stress when the elastic modulus is zero. Therefore, eqn(5.2.1.4) may be rewritten as,

$$\begin{aligned} \delta U_o &= \{ \sigma + \delta\sigma \}\{ \delta\varepsilon \}^T \\ &= \{ \sigma \}\{ \delta\varepsilon \}^T + \{ \delta\sigma \}\{ \delta\varepsilon \}^T \\ &= \{ \sigma \}\{ \delta\varepsilon \}^T \\ &= \{ \sigma_x \delta\varepsilon_x + \sigma_y \delta\varepsilon_y \quad \ldots\ldots \quad \tau_{zx} \delta\gamma_{zx} \} \end{aligned} \qquad \text{eqn(5.2.1.5)}$$

when $[E] = 0$.

Hence, with the assumption that the elastic modulus of the surface is zero, no approximation is made when calculating the strain energy of a distorted element in the case of the form-finding of continua.

assumed positive when acting in the positive co-ordinate directions. The generalised functional of the total potential energy of the volume can be written as [5.8],

$$\Pi_p = \int_{vol} \left[\frac{1}{2} \{\varepsilon\}^T [E] \{\varepsilon\} - \{\varepsilon\}^T [E] \{\varepsilon_o\} + \{\varepsilon\}^T \{\sigma_o\} \right] dV$$

$$- \int_{vol} \{\delta\}^T \{F\} dV - \int_{surface} \{\delta\}^T \{\Phi\} dS, \qquad \text{eqn(5.2.1.10)}$$

where $\{\delta\}$ is the vector of volume displacements.

The vector of displacements, $\{\delta\}$, in the surface integral is calculated at the position that the surface traction is applied. The first integral represents the strain energy and hence energy stored, while those remaining represent lost potential energy when the body and surface forces are displaced in the direction in which they act.

5.2.2. Application of the Assumed Displacement Field.

The adoption of the principle of minimum potential energy automatically invokes the displacements of the system as the primary unknowns. This is particularly suited to a mechanics type problem where the initial boundary conditions may be prescribed and where the system is statically indeterminate. The application of an external load vector causes displacement of the system, which in turn generates strains and ultimately a change in stress. For systems undergoing small displacements, the governing equations of equilibrium need to be solved once only, as the magnitudes of the displacements are deemed not to cause significant changes to the geometry and stiffness of the system. Conversely, for systems exhibiting large displacements, a non-linear analysis procedure is necessary, where the governing equations of equilibrium are applied repeatedly.

According to the principle of stationary potential energy, it is required that Π_p, eqn(5.2.1.10), assumes a stationary value. This is achieved when the displacements of the system (described by the nodal degrees of freedom comprising the discretisation), take the appropriate values. Therefore, it is required that eqn(5.2.1.10) is rewritten with the nodal degrees of freedom as the unknown variable. This may be achieved as explained below.

In the case of a general body, the displacement of an arbitrary point within the body may be defined as,

$$\{\delta\} = \{u, v, w\} \approx [N] \{\delta\}_i, \qquad \text{eqn(5.2.2.1)}$$

where $\{\delta\}_i$ is a vector of nodal generalised displacements, and the right hand side of eqn(5.2.2.1) represents the assumed displacement field within the body. The matrix, $[N]$,

describes a normalised interpolation scheme, valid for any of the generalised nodal displacements [5.14]. The vector $\{\delta\}_i$ may possess both translational and rotational displacements according to the description used for the nodal degrees of freedom.

The terms of eqn(5.2.1.2) describing the element strains, may be collected into a matrix form (after substitution of eqn(5.2.2.1)) and written as,

$$\{\varepsilon\} = [B]\{\delta\}_i, \qquad \text{eqn(5.2.2.2)}$$

where $[B]$ contains differentials of the assumed displacement field $[N]\{\delta\}_i$.

Eqn(5.2.2.2) may describe all six components of strain. In the case of the analysis of thin elastic continua, the three components of strain describing plane stress are sufficient [3].

Substitution of eqn(5.2.2.1) and eqn(5.2.2.2) into eqn(5.2.1.10) (and assuming that the vectors, $\{F\}$ and $\{\Phi\}$, are zero (eqn(5.2.1.9)), with an assumed displacement field $\{\delta\} = [N]\{\delta\}_i$), leads to an expression for the total potential energy of one element, Π_{pe}, of the form,

$$\Pi_{pe} = \frac{1}{2}\{\delta\}_i^T \left[\int_{vol} [B]^T [E][B]\, dV \right] \{\delta\}_i$$

$$- \{\delta\}_i^T \int_{vol} [B]^T [E]\{\varepsilon_o\}\, dV + \{\delta\}_i^T \int_{vol} [B]^T \{\sigma_o\}\, dV$$

eqn(5.2.2.3)

The total potential energy of the system is calculated as the sum of the total potential energies of the individual elements comprising the discretisation. Therefore, if a system is discretised into m elements, the total potential energy of the system, Π_{ps}, may be written as,

$$\Pi_{ps} = \left[\sum_{i=1}^{i=m} \Pi_{pe}i \right] - \{D\}^T \{P\} \qquad \text{eqn(5.2.2.4)}$$

The vector $\{D\}$ is the "system vector" of nodal displacements, and is obtained as the vector summation of the corresponding terms of the element displacement vectors $\{\delta\}_i$ to generate a "system array". Similarly, the element matrices held in the square parentheses of eqn(5.2.2.4) may be rearranged and summed to give an expression for the total internal potential energy of the system. Therefore, eqn(5.2.2.3) may be rewritten in the form of eqn(5.2.2.4) for the complete system, discretised by m elements as,

---

3

The assumption of plane stress is valid for the category of problem being investigated, and simplifies the element formulation from three dimensions to two. The magnitude and direction of the principal strain components are thus taken to be invariant with the thickness of the surface.

$$\Pi_{ps} = \frac{1}{2}\{D\}^T \left[\sum_{i=1}^{i=m} \left[\int_{vol} [B]^T [E][B] \, dV \right]_i \right] \{D\}$$
$$- \{D\}^T \sum_{i=1}^{i=m} \left[\int_{vol} [B]^T [E]\{\varepsilon_o\} \, dV \right]_i$$
$$+ \{D\}^T \sum_{i=1}^{i=m} \left[\int_{vol} [B]^T \{\sigma_o\} \, dV \right]_i - \{D\}\{P\}.$$

eqn(5.2.2.5)

Hence, the system may be replaced by a discretisation of elements whose potential energy is a function of the overall vector of nodal degrees of freedom, $\{D\}$. In order to obtain a stationary value of Π_{ps}, and therefore to establish an expression for the equilibrium of the system, it is necessary to differentiate eqn(5.2.2.5) with respect to all the nodal degrees of freedom, and set the resulting expressions to zero. This may be written as,

$$\frac{\partial \Pi_{ps}}{\partial D_1} = 0., \quad \frac{\partial \Pi_{ps}}{\partial D_2} = 0., \quad ....., \quad \frac{\partial \Pi_{ps}}{\partial D_n} = 0., \qquad \text{eqn(5.2.2.6)}$$

where n is the number of degrees of freedom of the discretisation.

By applying eqn(5.2.2.6) to eqn(5.2.2.5) and rearranging the result, the equation of equilibrium for the complete system is,

$$\sum_{i=1}^{i=m} \left[\int_{vol} [B]^T [E][B] \, dV \right]_i \{D\} = \sum_{i=1}^{i=m} \left[\int_{vol} [B]^T [E]\{\varepsilon_o\} \, dV \right]_i$$
$$+ \sum_{i=1}^{i=m} \left[- \int_{vol} [B]^T \{\sigma_o\} \, dV \right]_i + \{P\}$$

eqn(5.2.2.7)

The expression within the summation sign on the left side of eqn(5.2.2.7) represents the element elastic stiffness matrix, $[K_E{}^e]$. The integrals on the right side denote the components of the vector of element nodal forces, $\{f_e\}$. They simulate initial surface strains and stresses, respectively, such that,

$$\{ f_e \} = \sum_{i=1}^{i=m} \left[\int_{vol} [B]^T [E] \{ \varepsilon_o \} \, dV \right]_i - \sum_{i=1}^{i=m} \left[\int_{vol} [B]^T \{ \sigma_o \} \, dV \right]_i$$

eqn(5.2.2.8)

The difference between the left side and the right side of eqn(5.2.2.7) constitutes an unbalanced or residual force vector, $\{ R \}$.

5.3. 24 Degrees-of-Freedom "Isoparametric" Quadrilateral Element.

5.3.1. Introduction to the "Isoparametric Formulation".

The co-ordinate system used within the isoparametric formulation may be described as *intrinsic* or *natural*. To illustrate the principle of a natural co-ordinate system, it is convenient to consider a straight bar with length L, whose longitudinal axis is assumed to be aligned with the global x co-ordinate direction. The centre of the bar is at the origin and the ends at $\pm\frac{L}{2}$. Another co-ordinate system is established along the centre-line of the bar, denoted as ξ, where ξ is defined as $\xi = \frac{2x}{L}$, such that ξ has the limits +1 and −1. If the co-ordinate system ξ remains attached to the centre-line of the bar, and describes the position of a point along that axis only (regardless of the orientation of the bar in the global co-ordinate system), then ξ is termed a "natural co-ordinate".

In isoparametric formulation, the same interpolation functions are used to describe both the element geometry and displacements within the element. Two-dimensional "Isoparametric elements" are formulated using a conventional natural co-ordinate system ξ, η. As described below, the application of a natural co-ordinate system makes it possible to generate elements which are non-rectangular and which may have curved sides [4].

Figure 5.1(a) shows a plane four noded isoparametric quadrilateral element in global $\{x, y\}$ space. Figure 5.1(b) illustrates the same element but in the natural $\{\xi, \eta\}$ space. The mapping procedure relates, in this case, an arbitrarily shaped quadrilateral element to a square element with side lengths of 2 units. For a four noded element, the axes ξ and η pass through the mid-points of opposite sides as shown. In general ξ and η will not be orthogonal and are not required to be parallel to the global $\{x, y\}$ axis system.

The mapped element (Figure 5.1(b)) is of a regular shape and therefore standard mathematical procedures such as differentiation and integration can be applied. The distorted element shown in Figure 5.1(a) is mapped to the square element (Figure 5.1(b)) by a set of interpolation (or shape)

[4] A discussion of the advantages of the "Isoparametric" approach is presented in Section 2.5.1, Chapter 2.

functions. The shape functions (in the case being considered) relate the global $\{x, y\}$ space to the isoparametric $\{\xi, \eta\}$ space. In conjunction with other standard techniques (such as the chain rule for differentiation), they provide a change of variable.

An element formulation termed the "Natural Approach", which is based primarily on the use of vector algebra to relate the global and natural co-ordinate systems directly, can be found in reference [5.3] [5] . In the case of the formulation presented subsequently, expressions are derived which relate the natural, the local and the global co-ordinate systems. These relationships are then used to establish the local element strains (Sections 5.5 & 5.6).

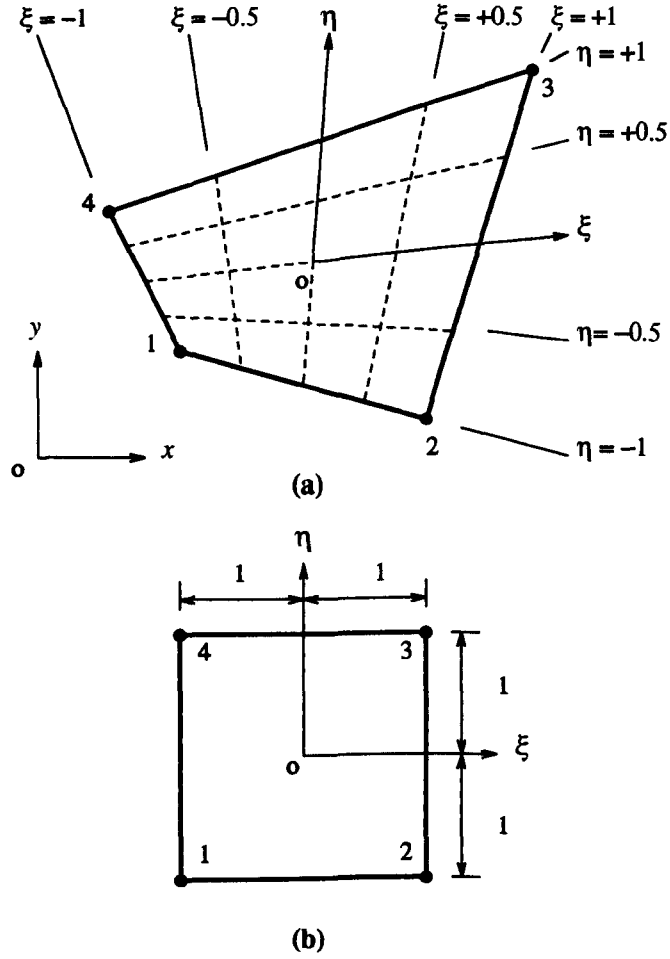

Figure 5.1 - (a) Four-Node Isoparametric Quadratic Quadrilateral Element in Global { x , y } Space.
(b) Plane Isoparametric Element in { ξ, η } Space.

5

A resume of the "Natural Approach" is provided in Section 2.3, Chapter 2.

5.3.2. Element Description.

The 24 degrees-of-freedom isoparametric quadratic quadrilateral element has eight nodes, each with three translational displacements, $\{u, v, w\}$, Figure 5.2(a). The element is chosen to be two dimensional (constant thickness) so as to model plane stress, but in general, it may be curved in three dimensional space. The element shape is described according to the position of the nodes in the global x, y, z space, which are located at the four corners and at arbitrary positions along each of the element sides. The element illustrated in Figure 5.2(a) is a distorted form of the quadrilateral "parent" element shown in Figure 5.2(b).

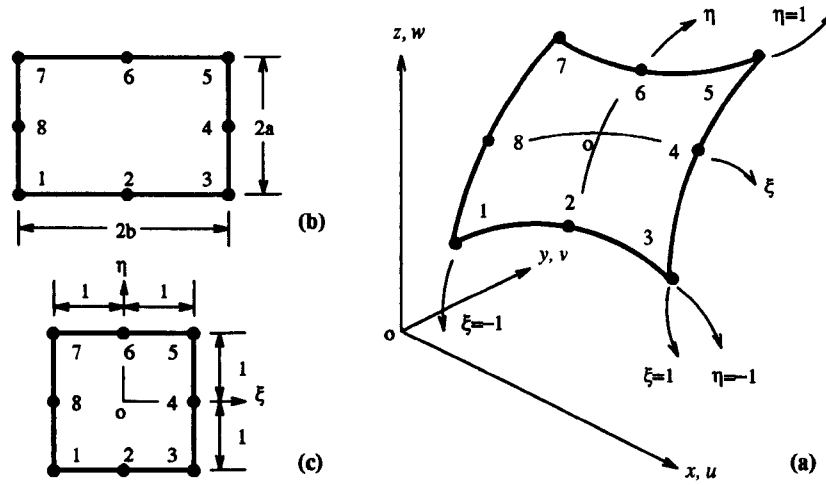

Figure 5.2 - (a) 24 DOF Isoparametric Quadratic Quadrilateral Element. (b) Parent Element. (c) Mapping into a Square.

By adopting a general mapping function,[5.4] the global co-ordinates of a point within the element, may be written as,

$$\begin{Bmatrix} x \\ y \\ z \end{Bmatrix} = \begin{bmatrix} N_1 & 0 & 0 & N_2 & 0 & 0 & \cdots & N_8 & 0 & 0 \\ 0 & N_1 & 0 & 0 & N_2 & 0 & \cdots & 0 & N_8 & 0 \\ 0 & 0 & N_1 & 0 & 0 & N_2 & \cdots & 0 & 0 & N_8 \end{bmatrix} \begin{Bmatrix} x_1 \\ y_1 \\ z_1 \\ \cdot \\ \cdot \\ x_8 \\ y_8 \\ z_8 \end{Bmatrix}, \qquad \text{eqn(5.3.2.1)}$$

such that, $N_1, N_2, \ldots\ldots N_8$ are the element shape functions corresponding to node 1, node 2 ....., node 8 respectively, and similarly $\{x_1, y_1, z_1\}, \ldots\ldots, \{x_8, y_8, z_8\}$ are the global nodal co-ordinates.

The mapping described in eqn(5.3.2.1) relates a unit square in isoparametric co-ordinates (ξ, η), Figure 5.1(c), to the quadratic quadrilateral element in (x, y, z) co-ordinates defined by the eight sets of nodal co-ordinates $\{x_1, y_1, z_1\}, \ldots\ldots, \{x_8, y_8, z_8\}$. The mapping is an interpolation scheme which describes any point (x, y, z) within the distorted element (Figure 5.2(a)) when

the corresponding (ξ, η) co-ordinates are given from the mapped element (Figure 5.2(c)).

According to the definition of the isoparametric formulation, the global displacements within the element are described by the same interpolation algorithm. Therefore, eqn(5.3.2.1) may be rewritten in terms of the nodal displacements as,

$$\begin{aligned} \{\delta\}^T &= \{u, v, w\} \\ &\approx [N]\{u_1, v_1, w_1, \ldots\ldots, u_8, v_8, w_8\} \\ &= [N]\{\delta\}^T_i , \end{aligned} \qquad \text{eqn(5.3.2.2)}$$

where $\{u, v, w\}$ are global displacements within the element in the x, y, and z directions respectively.

5.3.3. Element Shape Functions.

5.3.3.1. Introduction - Small Displacement Theory.

The derivation of the element shape functions denoted in eqn(5.3.2.1) as $N_1, N_2, \ldots\ldots, N_8$ (or as $N^s{}_1, N^s{}_2, \ldots\ldots, N^s{}_8$ in the case of the small displacement theory) is summarised in this section. The order of the element under consideration is quadratic, where the element geometry and element displacements vary with up to the second power the natural co-ordinates, (ξ, η). As demonstrated subsequently, this allows for a pseudo linear variation in the element strains (Section 5.6). Consequently, changes in the surface strains may occur within each element and across element boundaries. As demonstrated below, the element shape functions are based on a characteristic interpolation polynomial.

In the case of a quadratic element (Figure 5.2(a)), an interpolation polynomial, applicable to both the element shape and displacements, may be written as,[5.4]

$$\phi_i = a_1 + a_2\xi + a_3\eta + a_4\xi^2 + a_5\xi\eta + a_6\eta^2 + a_7\xi^2\eta + a_8\xi\eta^2 \qquad \text{eqn(5.3.3.1)}$$

The nodal co-ordinates of the distorted element can be expressed in terms of the natural co-ordinates of the mapped element (ξ, η) with the limits ($\pm 1, \pm 1$) (Figure 5.2(a), Figure 5.2(c)). It is shown in the subsequent paragraphs, that the successive substitution of the natural co-ordinates of the element nodes into eqn(5.3.3.1) leads to eight simultaneous equations, with the coefficients ($a_1, a_2, \ldots\ldots, a_8$) as the unknowns.

Assuming that the displacement δ is interpolated according to eqn(5.3.3.1), with the vector of nodal displacements $\{\delta\}_i$ as the basis for the scheme, then, from eqn(5.3.3.1),

$$\delta = \{a\}^T\{i\} = \{i\}^T\{a\} \qquad \text{eqn(5.3.3.2)}$$

where,

$$\{ a \}^T = \{ a_1, a_2, \ldots\ldots\ldots, a_8 \} ,$$

and,

$$\{ i \}^T = \{ 1, \xi, \eta, \xi^2, \xi\eta, \eta^2, \xi^2\eta, \xi\eta^2 \}.$$

By substituting the natural co-ordinates of each of the element nodes into eqn(5.3.3.2) the vector of known nodal displacements, $\{ \delta \}_i$, is related to the assumed interpolation polynomial, ϕ_i, by the expression,

$$\{ \delta \}_i = [C^s] \{ a \}, \qquad \text{eqn(5.3.3.3)}$$

where $[C^s]$ is a square matrix containing coefficients with values of either $\{ 0, \pm 1 \}$, and written as,

$$[C^s] = \begin{bmatrix} 1 & -1 & -1 & 1 & 1 & 1 & -1 & -1 \\ 1 & 0 & -1 & 0 & 0 & 1 & 0 & 0 \\ 1 & 1 & -1 & 1 & -1 & 1 & -1 & 1 \\ 1 & 1 & 0 & 1 & 0 & 0 & 0 & 0 \\ 1 & 1 & 1 & 1 & 1 & 1 & 1 & 1 \\ 1 & 0 & 1 & 0 & 0 & 1 & 0 & 0 \\ 1 & -1 & 1 & 1 & -1 & 1 & 1 & -1 \\ 1 & -1 & 0 & 1 & 0 & 0 & 0 & 0 \end{bmatrix} \qquad \text{eqn(5.3.3.4)}$$

From eqn(5.3.3.3),

$$\{ a \} = [C^s]^{-1} \{ \delta \}_i \qquad \text{eqn(5.3.3.5)}$$

Back substitution of eqn(5.3.3.5) into eqn(5.3.3.2) yields,

$$\{ \delta \} = \{ i \}^T [C^s]^{-1} \{ \delta \}_i = \{ n \} \{ \delta \}_i \qquad \text{eqn(5.3.3.6)}$$

where $\{ n \}$ is a row vector of the form $\{ N^s{}_1, N^s{}_2, \ldots\ldots, N^s{}_8 \}$, with $N^s{}_i$ the shape function for element node i ($i = 1 \rightarrow 8$). Expressions for all the element shape functions $\{ n \}$ are given in Table 5.1 [5.15].

Therefore, the co-ordinate or displacement of any point within the element may be calculated as,

$$x = \sum_{i=1}^{i=8} N_i (\xi, \eta) x_i , \qquad \delta = \sum_{i=1}^{i=8} N_i (\xi, \eta) \delta_i , \qquad \text{eqn(5.3.3.7)}$$

where δ_i represents the displacement components u, v and w, and $N_i (\xi, \eta)$ is calculated at the point of interest, as defined by the mapped element. Similar expressions can be obtained for the global co-ordinates, y and z.

Element Node	Shape Function
$N^s{}_1$	$\frac{1}{4}(1-\xi)(1-\eta)(-\xi-\eta-1)$
$N^s{}_2$	$\frac{1}{2}(1-\xi^2)(1-\eta)$
$N^s{}_3$	$\frac{1}{4}(1+\xi)(1-\eta)(\xi-\eta-1)$
$N^s{}_4$	$\frac{1}{2}(1+\xi)(1-\eta^2)$
$N^s{}_5$	$\frac{1}{4}(1+\xi)(1+\eta)(\xi+\eta-1)$
$N^s{}_6$	$\frac{1}{2}(1-\xi^2)(1+\eta)$
$N^s{}_7$	$\frac{1}{4}(1-\xi)(1+\eta)(-\xi+\eta-1)$
$N^s{}_8$	$\frac{1}{2}(1-\xi)(1-\eta^2)$

Table 5.1 - Shape Functions for 24 DOF Quadratic Quadrilateral Element. (Small Displacement Theory.)

5.3.3.2. Large Displacement Theory.

The derivation of the shape functions given in Table 5.1 is based on small displacement theory, as denoted by the superscript s. In this case the position of the side nodes are assumed to remain at, or very close to, the centre of the element side. However, in the analysis of highly flexible systems, large displacements may occur, which can cause the side nodes to move significantly from the central position. The resulting violation of this assumption can lead to a loss of accuracy, and in some cases, no solution, due to the induced numerical instability and arithmetic errors (Section 6.2.3, Chapter 6).

It has been shown [5.17], that as the side nodes of the element move away from the centre of the interval, the mapping defined by the element shape functions becomes distorted. Thus, the quadratic shape functions, which are usually parabolic when represented graphically, tend to a skew form, and the isoparametric co-ordinate transformation is no longer valid. This distortion generates errors in the co-ordinate transformation, between the natural (ξ, η) and the local (X, Y) co-ordinate systems given by the Jacobian matrix $[J]$ (eqn(5.5.7.6)). Significant deviations of the side nodes from the centre of the element side can result in the derivative of the shape functions becoming zero and in a singular form of the Jacobian matrix $[J]$.

Celia and Gray [5.17] have proposed an improved isoparametric transformation to overcome the difficulties outlined above. The approach, as applied to two dimensional elements, is described in

full in reference [5.17]. For completeness however, a summary of the principles behind the theory is presented in the subsequent paragraphs. This is followed by the extension of the approach to the three dimensional case, as presented below.

The positions of the side nodes in the natural (ξ , η) space, are determined using the criterion that they minimise magnitudes of the derivatives of the Jacobian matrix, $[J]$. It is shown [5.17] that this may be achieved by locating the side nodes, such that the relative position of the side node along the edge of the element on which it occurs, is the same in the global (x , y , z), and the natural (ξ , η), spaces. The procedure is demonstrated for a typical edge of the plane two-dimensional element in Figure 5.3, in which $\underline{X}_i$ represents the position vector of the element node i.

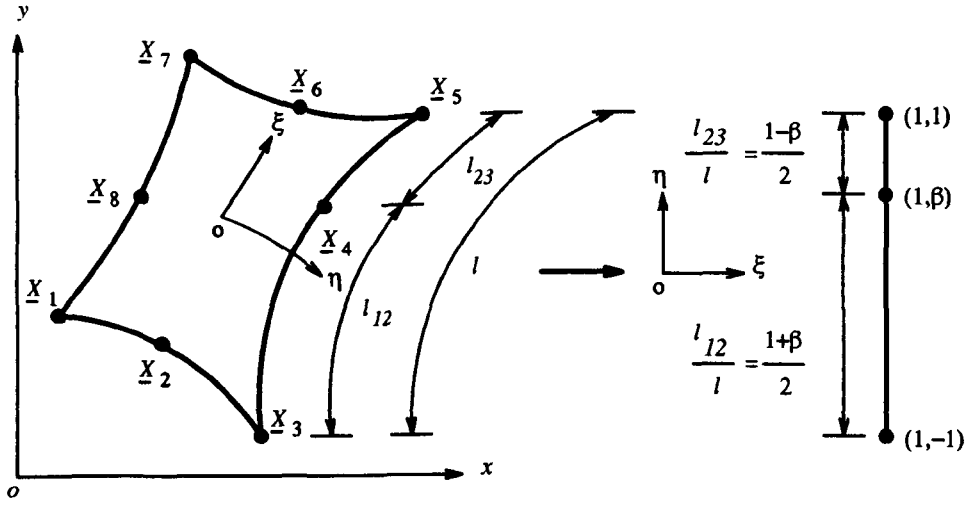

Figure 5.3 - (a) 2-Dimensional Quadratic Quadrilateral Element. (b) Mapping into { ξ, η } Space.

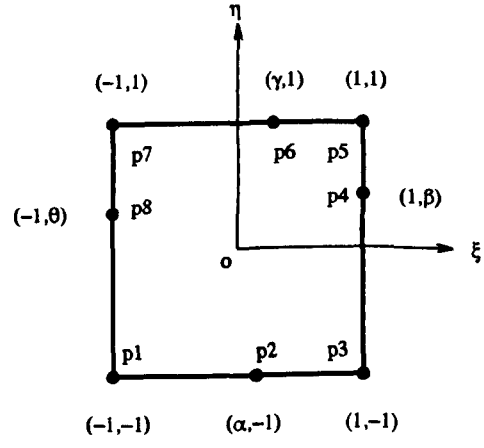

Figure 5.4 - 3-Dimensional Quadratic Quadrilateral Element Mapped into a Square in the { ξ, η } Space.

By repeating the same procedure for the remaining three sides of the quadrilateral element, the nodal locations in the natural (ξ , η) space, and illustrated in Figure 5.4, are obtained. Therefore, assuming the interpolation polynomial given in eqn(5.3.3.1), and with reference to eqn(5.3.3.3), the matrix [C] may be written as,

$$[C] = \begin{bmatrix} 1 & -1 & -1 & 1 & 1 & 1 & -1 & -1 \\ 1 & \alpha & -1 & \alpha^2 & -\alpha & 1 & -\alpha^2 & \alpha \\ 1 & 1 & -1 & 1 & -1 & 1 & -1 & 1 \\ 1 & 1 & \beta & 1 & \beta & \beta^2 & \beta & \beta^2 \\ 1 & 1 & 1 & 1 & 1 & 1 & 1 & 1 \\ 1 & \gamma & 1 & \gamma^2 & \gamma & 1 & \gamma^2 & \gamma \\ 1 & -1 & 1 & 1 & -1 & 1 & 1 & -1 \\ 1 & -1 & \theta & 1 & -\theta & \theta^2 & \theta & -\theta^2 \end{bmatrix} \qquad \text{eqn(5.3.3.8)}$$

where [C] is a general matrix, relating the element nodal co-ordinates in the natural (ξ , η) space, Figure 5.4, to the coefficients $\{ a_1, a_2, \ldots, a_8 \}$ of eqn(5.3.3.1).

Substituting the matrix [C] for [C^s] in eqn(5.3.3.6), yields the set of large displacement element nodal shape functions as given in Table 5.2.

Element Node	Shape Function
N_1	$\frac{-((-1+\xi)(-1+\eta)(1+\xi+\eta+\alpha\eta-\alpha\theta+\xi\theta))}{4(1+\alpha)(1+\theta)}$
N_2	$\frac{-((-1+\xi)(1+\xi)(-1+\eta))}{2(-1+\alpha)(1+\alpha)}$
N_3	$\frac{(1+\xi)(-1+\eta)(-1-\alpha\beta+\xi+\beta\xi-\eta+\alpha\eta)}{4(-1+\alpha)(1+\beta)}$
N_4	$\frac{(1+\xi)(-1+\eta)(1+\eta)}{2(-1+\beta)(1+\beta)}$
N_5	$\frac{-((1+\xi)(1+\eta)(1-\xi+\beta\xi-\beta\gamma-\eta+\gamma\eta))}{4(-1+\beta)(-1+\gamma)}$
N_6	$\frac{(-1+\xi)(1+\xi)(1+\eta)}{2(-1+\gamma)(1+\gamma)}$
N_7	$\frac{(-1+\xi)(1+\eta)(-1-\xi+\eta+\gamma\eta+\xi\theta-\gamma\theta)}{4(1+\gamma)(-1+\theta)}$
N_8	$\frac{-((-1+\xi)(-1+\eta)(1+\eta))}{2(-1+\theta)(1+\theta)}$

Table 5.2 - Shape Functions for 24 DOF Quadratic Quadrilateral Element. (Large Displacement Theory.)

It remains to find the location of the side nodes in the natural co-ordinate system (ξ , η), as defined by the values { α, β, γ, θ }, (Figure 5.4). Adopting a similar procedure to Celia and Gray,[5.17] but extending the approach to three-dimensional space, the side nodes of the element can be located as explained below.

Considering first the location of the element node p_2 and the corresponding value of α (Figure 5.4), the position vector of the nodes p_1, p_2, p_3, may be written in terms of the natural co-ordinates, with $\eta = -1$, as,

$$\underline{X} = \bar{x}\,\underline{i} + \bar{y}\,\underline{j} + \bar{z}\,\underline{k} \qquad \text{eqn(5.3.3.9(a))}$$

where,

$$\bar{x} = \sum_{i=1}^{i=3} N_i^*(\xi)\, x_i \;,\; \bar{y} = \sum_{i=1}^{i=3} N_i^*(\xi)\, y_i \;,\; \text{and,} \quad \bar{z} = \sum_{i=1}^{i=3} N_i^*(\xi)\, z_i \;. \qquad \text{eqn(5.3.3.9(b))}$$

and the shape functions $N_i^*(\xi)$, with $i = 1, 2, 3$, are taken from a one dimensional quadratic element presented below.

Figure 5.5 represents the side of the element p_1, p_2, p_3 in both the global and natural co-ordinate systems.

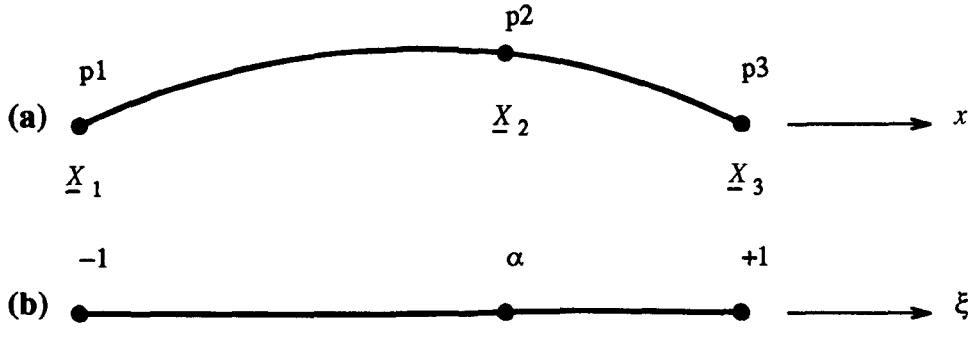

Figure 5.5 - (a) 2-Dimensional Quadratic Line Element.
(b) Mapping into { ξ } Space.

The shape functions $N_i^*(\xi)$ may be drawn from the polynomial,

$$\phi_i^* = a_1 + \xi_i\, a_2 + \xi_i^2\, a_3, \qquad \text{eqn(5.3.3.10)}$$

where $i = 1, 2, 3$, and $\xi_1 = -1$, $\xi_2 = \alpha$, $\xi_3 = +1$, and are written as,

$$N_1^*(\xi) = \frac{(-1+\xi)(-\alpha+\xi)}{2(1+\alpha)} \qquad \text{eqn(5.3.3.11(a))}$$

$$N_2^*(\xi) = \frac{(-1+\xi^2)}{((-1+\alpha)(1+\alpha)} \qquad \text{eqn(5.3.3.11(b))}$$

$$N_3^*(\xi) = \frac{-((1+\xi)(-\alpha+\xi))}{2(-1+\alpha)} \qquad \text{eqn(5.3.3.11(c))}$$

The location of any point along the element side p_1, p_2, p_3 can be seen to depend only on the position of the three nodes p_1, p_2, and p_3, and the natural co-ordinate ξ. This ensures that the adjacent elements are compatible, and that the shape functions are continuous in the displacement terms (or are C^o continuous).

The requirement of equal relative positions of the side node in the global and natural co-ordinate systems, may be written mathematically as,[5.17]

$$\frac{\int_{p_1}^{p_2} \sqrt{(d\underline{X} \cdot d\underline{X})}}{\int_{p_1}^{p_3} \sqrt{(d\underline{X} \cdot d\underline{X})}} = \frac{\int_{-1}^{\alpha} d\xi}{\int_{-1}^{+1} d\xi} \qquad \text{eqn(5.3.3.12)}$$

The integrals on the right side of eqn(5.3.3.12) may be calculated explicitly. Those on the left side may be rewritten in terms of the natural co-ordinate ξ, so that,

$$f(\alpha) = \frac{\int_{-1}^{\alpha} \sqrt{\left(\frac{\partial \bar{x}}{\partial \xi}\right)^2 + \left(\frac{\partial \bar{y}}{\partial \xi}\right)^2 + \left(\frac{\partial \bar{z}}{\partial \xi}\right)^2}\, d\xi}{\int_{-1}^{+1} \sqrt{\left(\frac{\partial \bar{x}}{\partial \xi}\right)^2 + \left(\frac{\partial \bar{y}}{\partial \xi}\right)^2 + \left(\frac{\partial \bar{z}}{\partial \xi}\right)^2}\, d\xi} - \frac{\alpha+1}{2} = 0\,,$$

eqn(5.3.3.13)

Writing,

$$\Delta_x = x_3 - x_1 \ , \ \delta_x = x_2 - x_1 \ ,$$

$$\Delta_y = y_3 - y_1 \ , \ \delta_y = y_2 - y_1 \ ,$$

$$\Delta_z = z_3 - z_1 \ , \ \delta_z = z_2 - z_1 \ , \qquad \text{eqn(5.3.3.14)}$$

and substituting eqn(5.3.3.9(b)) into eqn(5.3.3.13) together with eqns(5.3.3.11 (a)-(c)) and eqn(5.3.3.14), yields,

$$f(\alpha) = \frac{\int_{-1}^{\alpha} \sqrt{(f_a \xi^2 + f_b \xi + f_c)}\, d\xi}{\int_{-1}^{+1} \sqrt{(f_a \xi^2 + f_b \xi + f_c)}\, d\xi} - \frac{\alpha+1}{2} = 0 \ , \qquad \text{eqn(5.3.3.15(a))}$$

where,

$$f_a = \frac{1}{(1-\alpha^2)^2} \left\{ [(1+\alpha)\Delta_x - 2\delta_x]^2 + [(1+\alpha)\Delta_y - 2\delta_y]^2 + [(1+\alpha)\Delta_z - 2\delta_z]^2 \right\}, \qquad \text{eqn(5.3.3.15(b))}$$

$$f_b = \frac{1}{(1-\alpha^2)} \left\{ [(1+\alpha)\Delta_x - 2\delta_x] + [(1+\alpha)\Delta_y - 2\delta_y] + [(1+\alpha)\Delta_z - 2\delta_z] \right\} . \qquad \text{eqn(5.3.3.15(c))}$$

and,

$$f_c = \frac{1}{4} [\Delta_x^2 + \Delta_y^2 + \Delta_z^2] \qquad \text{eqn(5.3.3.15(d))}$$

As demonstrated below, the integrals given in equations eqn(5.3.3.15(b)-(d)) may be computed by completing the square of the integrand.[5.18]

$$\sqrt{(f_a \xi^2 + f_b \xi + f_c)} = \sqrt{(\xi + \frac{f_b}{2f_a})^2 f_a + (\frac{f_c}{f_a} - \frac{f_b^2}{4f_a^2}) f_a}$$

$$= \sqrt{f_a}\ \sqrt{f^2(\xi) + A^2} \qquad \text{eqn(5.3.3.16)}$$

given that, $f(\xi) = \xi + \frac{f_b}{2f_a}$, and, $A^2 = (\frac{f_c}{f_a} - \frac{f_b^2}{4f_a^2})$.

Using a standard mathematical result,[5.19]

$$\int_{-1}^{\alpha} \sqrt{(f_a \xi^2 + f_b \xi + f_c)}\, d\xi =$$

$$\frac{f(\xi)}{2}\sqrt{A^2 f_a + f^2(\xi) f_a} + \frac{A^2}{2}\sqrt{f_a}\log_e\left[f(\xi) + \sqrt{A^2 + f^2(\xi)} \right] \Bigg|_{-1}^{\alpha}$$

eqn(5.3.3.17)[6]

Substitution of the definitions for $f(\xi)$ and A^2 into eqn(5.3.3.17) leads to,

$$\int_{-1}^{\alpha} \sqrt{(f_a \xi^2 + f_b \xi + f_c)}\, d\xi = \frac{2f_a\xi + f_b}{4f_a}\sqrt{(f_a \xi^2 + f_b \xi + f_c)} \Bigg|_{-1}^{\alpha} +$$

$$\frac{4f_a f_c - f_b^2}{8f_a}\,\frac{1}{\sqrt{f_a}}\log_e\left[\frac{2f_a\xi + f_b + 2\sqrt{f_a^2\xi^2 + f_a f_b \xi + f_a f_c}}{2f_a} \right] \Bigg|_{-1}^{\alpha}$$

eqn(5.3.3.18)

Therefore, eqn(5.3.3.15(a)) may be simply written as,[5.17]

$$f(\alpha) = \frac{g(\alpha) - g(-1)}{g(1) - g(-1)} - \frac{\alpha + 1}{2} = 0. \qquad \text{eqn(5.3.3.19)}$$

where $g(\alpha)$ is the value of the integral of the numerator of eqn(5.3.3.15(a)) with the value of α substituted for ξ, and similarly for the remaining terms.

The Secant Method [5.20] may be used to solve eqn(5.3.3.19) iteratively, such that,

$$\alpha^{(n+1)} = \alpha^{(n)} - f(\alpha^{(n)}) \left[\frac{\alpha^{(n)} - \alpha^{(n-1)}}{f(\alpha^{(n)}) - f(\alpha^{(n-1)})} \right] \qquad \text{eqn(5.3.3.20)}$$

For the continuous real function $f(\alpha)$, the solution procedure is commenced by bracketing the real root between approximations $\alpha^{(n)}$ and $\alpha^{(n-1)}$, in order that $f(\alpha^{(n)})$ and $f(\alpha^{(n-1)})$ have opposite signs.[5.20]

Through the adaptation of eqn(5.3.3.15(a)) to the remaining three sides of the quadrilateral element, the preceding formulation, as summarised in eqn(5.3.3.20), can be used to obtain the remaining values of β, γ, and θ. These values may then be substituted into the shape functions given in Table 5.2. When the values of $\{\alpha, \beta, \gamma, \theta\}$ are equal to zero, the shape functions presented in Table 5.2 revert to those in Table 5.1. Results related to the application of the modified shape-functions (Table 5.2) to the form-finding of an elastic continua, are presented in Section 6.2.3, Chapter 6.

6

In order to avoid a negative or zero log, $\sqrt{A^2 + f^2(\xi)} > f(\xi)$. This implies that A^2 must be positive, or that $\frac{f_c}{f_a} - \frac{f_b^2}{4f_a^2} > 0$.. In the case that $f_a < 1.$, A^2 may be negative. This phenomenon can be avoided by scaling the global co-ordinates of the discretised system, such that when squared the magnitudes of Δ_x and δ_x are greater than unity.

5.4. Element Local Co-ordinate System.

The contributions to the vectors describing force, $\{f_e\}$, stiffness, $[K_t^e]$, and initial stress, $\{\sigma_o\}$, from each element comprising the discretisation are required (eqn(5.2.2.7) and eqn(5.2.2.8)). Consequently, expressions relating the global (in which the overall system is defined) and the local (in which the vector quantities of each element are calculated) co-ordinate systems, are required.

In general the proposed element is curved. Therefore, the local co-ordinate systems vary continuously across the surface of the element. (This feature is not present in the case of a plane element, where only a single local co-ordinate system is defined.) For the purposes of calculating the characteristic matrices of the 24 degrees-of-freedom quadrilateral element, local co-ordinate systems are constructed at the element nodes, and also at the element Gauss Points (Section 5.8). The development of the element local co-ordinate systems is presented in the subsequent paragraphs.

Two base vectors are established at each point of interest initially. As described below, they are derived such that they are tangential to the middle surface of the element.

The base vector $\vec{\xi}$, aligned with the natural co-ordinate direction ξ, (Figure 5.2(a)) may be given as [5.5],[5.6],

$$\vec{\xi} = \left[\frac{\partial x}{\partial \xi} \underline{i} + \frac{\partial y}{\partial \xi} \underline{j} + \frac{\partial z}{\partial \xi} \underline{k} \right] \qquad \text{eqn(5.4.1)}$$

where, $\{\underline{i}, \underline{j}, \underline{k}\}$, are coincident with the direction of the global co-ordinate system $\{x, y, z\}$ respectively.

Substitution of equations of the form given in eqn(5.3.3.7) into eqn(5.4.1) gives,

$$\vec{\xi} = \left[\sum_{i=1}^{i=8} \frac{\partial N_i}{\partial \xi} x_i \underline{i} + \sum_{i=1}^{i=8} \frac{\partial N_i}{\partial \xi} y_i \underline{j} + \sum_{i=1}^{i=8} \frac{\partial N_i}{\partial \xi} z_i \underline{k} \right]. \qquad \text{eqn(5.4.2)}$$

Similarly, a base vector in the natural co-ordinate direction η may be established and written as,

$$\vec{\eta} = \left[\sum_{i=1}^{i=8} \frac{\partial N_i}{\partial \eta} x_i \underline{i} + \sum_{i=1}^{i=8} \frac{\partial N_i}{\partial \eta} y_i \underline{j} + \sum_{i=1}^{i=8} \frac{\partial N_i}{\partial \eta} z_i \underline{k} \right]. \qquad \text{eqn(5.4.3)}$$

As the element may be curved in three dimensions, it is not necessarily true that $\vec{\xi}$ and $\vec{\eta}$ are orthogonal vectors [7] . It is necessary, therefore, to use these base vectors to generate an orthogonal system of local co-ordinates.

7

A special case arises when the element is rectangular with straight sides, in which case the vectors $\vec{\xi}$ and $\vec{\eta}$ are orthogonal.

Following the approach suggested by Irons,[5.7] a unit vector can be defined in the local X direction as $\hat{X}$,

$$\hat{X} = \frac{\vec{\xi}}{\left|\vec{\xi}\right|}. \qquad \text{eqn(5.4.4)}$$

The vectors $\hat{Y}$ and $\hat{Z}$ are next established, such that $\hat{X}$, $\hat{Y}$, and $\hat{Z}$ are orthogonal unit vectors.

The base vectors $\vec{\xi}$ and $\vec{\eta}$ lie in a plane at the local point of interest. Since by eqn(5.4.4), $\hat{X}$ is parallel to this plane, the cross product of $\vec{\xi}$ and $\vec{\eta}$ generates a vector $\vec{Z}$ orthogonal to $\hat{X}$, and written as,

$$\vec{Z} = \vec{\xi} \times \vec{\eta} \;\rightarrow\; \hat{Z} = \frac{\vec{\xi} \times \vec{\eta}}{\left|\vec{\xi} \times \vec{\eta}\right|}, \qquad \text{eqn(5.4.5)}$$

where,

$$\vec{\xi} \times \vec{\eta} = \begin{vmatrix} \underline{i} & \underline{j} & \underline{k} \\ \sum_{i=1}^{i=8} \frac{\partial N_i}{\partial \xi} x_i & \sum_{i=1}^{i=8} \frac{\partial N_i}{\partial \xi} y_i & \sum_{i=1}^{i=8} \frac{\partial N_i}{\partial \xi} z_i \\ \sum_{i=1}^{i=8} \frac{\partial N_i}{\partial \eta} x_i & \sum_{i=1}^{i=8} \frac{\partial N_i}{\partial \eta} y_i & \sum_{i=1}^{i=8} \frac{\partial N_i}{\partial \eta} z_i \end{vmatrix} \qquad \text{eqn(5.4.6)}$$

The local co-ordinate system is completed by generating the vector $\hat{Y}$, normal to the vectors $\hat{X}$ and $\hat{Z}$. This may be written as,

$$\vec{Y} = \hat{Z} \times \hat{X} \;\rightarrow\; \hat{Y} = \frac{\hat{Z} \times \hat{X}}{\left|\hat{Z} \times \hat{X}\right|}, \qquad \text{eqn(5.4.7)}$$

where, $\hat{Z} \times \hat{X}$ may be calculated in a similar manner to eqn(5.4.6).

This procedure is repeated at each node and at the element Gauss Points.

However, the approach described above, based on eqn(5.4.4), can be shown to produce an erroneous element formulation. The errors in the terms of the element characteristic matrices arise as the requirement that the directions of the element local co-ordinates are a function of the orientation of the element in the global space only (and not of the geometry of the element in addition), is not upheld [8]. The dependence of the preceding approach on both the orientation and the shape of the element is demonstrated by the element illustrated in Figure 5.6. The local co-ordinate systems at each of the element nodes, for a flat element in the global x, y plane, (a) prior, and (b) subsequent, to a clockwise rotation through an angle of $\frac{\pi}{2}$, are displayed.

8

The effects of the element geometry are related to the element characteristic matrices, through the Jacobian of the transformation (Section 5.5).

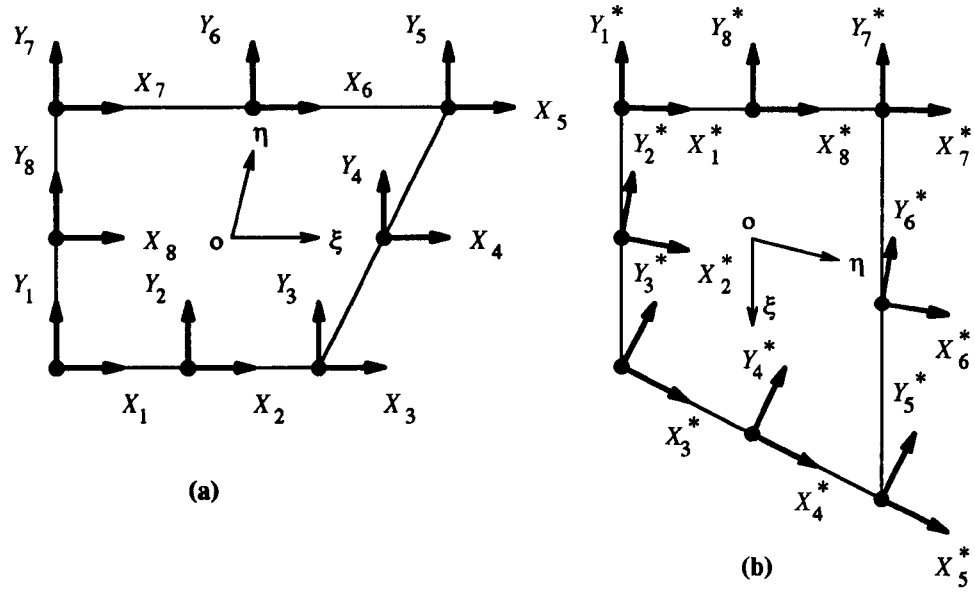

Figure 5.6 - Local Co-ordinate Systems - (a) prior, and (b) subsequent, to the Application of a Clockwise Rigid Body Rotation.

The local co-ordinate systems in Figure 5.6(a) and (b) are clearly dissimilar, and are influenced by both the orientation and shape of the element, rather than by its orientation alone. The orientation of the (rotated) element in the global x, y plane can be seen to be indeterminate, and to vary across its surface (Figure 5.6(b)).

In the approach suggested by Irons,[5.7] the vector $\vec{\xi}$ is normalised to yield the local co-ordinate direction X (eqn(5.4.4)). However, the vector $\vec{\xi}$ (eqn(5.4.2)) is dependent on the geometry of the element. Consequently, the local co-ordinate system demonstrates a similar dependence (Figure 5.6 (a) & (b)). As described below, an alternative method of establishing the element local co-ordinate system, is to select an additional base vector of unit length, in a direction which is independent of the element geometry [5.21].

A unit vector in the global y direction may be selected as the additional independent base vector. Thus, as before, the vector $\hat{Z}$ in the local Z direction can be constructed using the cross product of the two base vectors $\vec{\xi}$ and $\vec{\eta}$. Defining the additional independent base vector as,

$$\hat{j} = \{ 0\underline{i} + 1\underline{j} + 0\underline{k} \}, \qquad \text{eqn(5.4.8)}$$

the vector in the local X direction, $\vec{X}$, may be calculated as,

$$\vec{X} = \hat{j} \times \vec{Z}. \qquad \text{eqn(5.4.9)}$$

Thus, the unit vector in the local Y direction, $\hat{Y}$, may be calculated as before,

$$\hat{Y} = \hat{Z} \times \hat{X}. \qquad \text{eqn(5.4.10)}$$

Considering the element described in Figure 5.6, the local vector normal to the element surface, $\vec{Z}$, may be written as,

$$\vec{Z} = \{\, 0\,\underline{i} + 0\,\underline{j} + Z_{\vec{k}}\,\underline{k} \,\} \qquad \text{eqn(5.4.11)}$$

where, $Z_{\vec{k}}$ is a positive real number.

Consequently, the vector $\vec{X}$ is given as (eqn(5.4.9)),

$$\vec{X} = \begin{vmatrix} \underline{i} & \underline{j} & \underline{k} \\ 0 & 1 & 0 \\ 0 & 0 & Z_{\vec{k}} \end{vmatrix} = Z_{\vec{k}}\,\underline{i} + 0\,\underline{j} + 0\,\underline{k} \qquad \text{eqn(5.4.12)}$$

where, $\{\, \underline{i}, \underline{j}, \underline{k} \,\}$, are aligned with the global co-ordinate directions, $\{\, x, y, z \,\}$.

From eqn(5.4.12), the vector $\vec{X}$ can be seen to coincide with the global x direction, at any point on the surface of the element. Similarly, computing $\vec{Y} = \vec{Z} \times \vec{X}$, yields the local vector $\vec{Y}$, acting in the same direction as the global y direction, at any point on the surface of the element. Therefore, since the geometry of the element is not constant, the fact that the vectors $\vec{X}$ and $\vec{Y}$ are invariant across the surface of the element, infers that they are independent of the element geometry. Conversely, dependence exists on the vector normal to the surface of the element, $\vec{Z}$, and the chosen additional vector, $\hat{\underline{i}}$.

By adopting this approach, Figure 5.6 may be redrawn, giving the revised sets of local co-ordinate systems at the element nodes as shown in Figure 5.7,

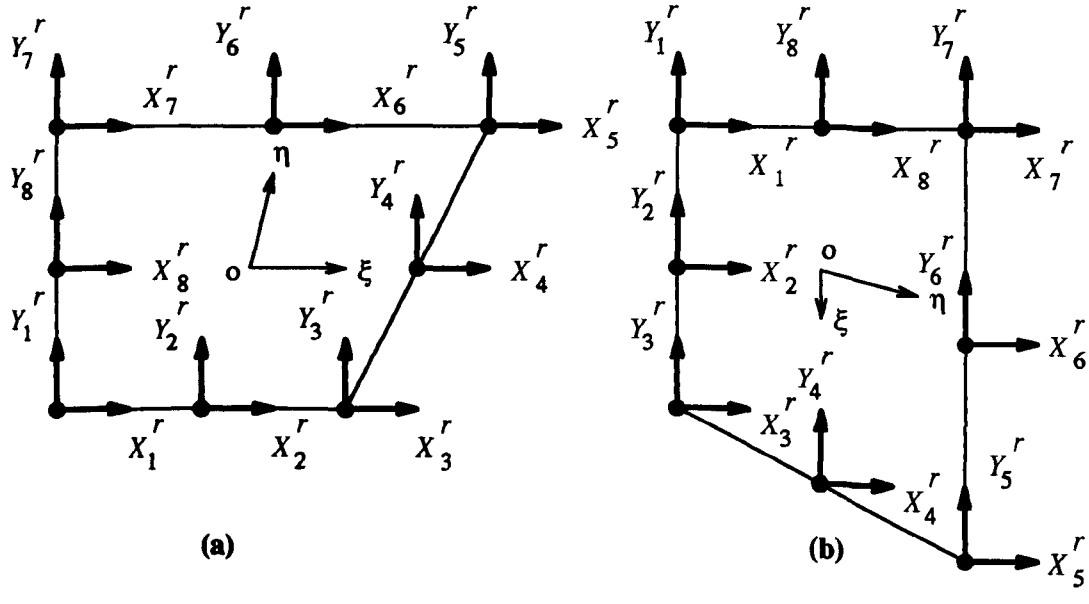

Figure 5.7.

Revised Local Co-ordinate Systems - (a) prior, and (b) subsequent, to the Application of a Clockwise Rigid Body Rotation.

Thus, regardless of the orientation of the element in the global x, y plane, a unique set of local co-ordinate axes is defined at the element nodes (Figure 5.7).

In general, as the element rotates in the global $\{ x, y, z \}$ space, the vector $\vec{Z}$ becomes,

$$\vec{Z} = \{ Z_{\vec{i}} \underline{i} + Z_{\vec{j}} \underline{j} + Z_{\vec{k}} \underline{k} \} \qquad \text{eqn(5.4.13)}$$

where $Z_{\vec{i}}, Z_{\vec{j}}$, and $Z_{\vec{k}}$ are the components of the vector $\vec{Z}$ in the global $\{ x, y, z \}$ space, and may take the value of a real number including zero.

Consequently, in general, $\vec{X} \neq \vec{x}$ and $\vec{Y} \neq \vec{y}$. Instead, they are defined by the successive application of eqn(5.4.13), eqn(5.4.9) and eqn(5.4.10), at each point of interest [9].

The vector $\hat{j}$ (eqn(5.4.8)), aligns the element variables with the global x direction (when the element is flat and orientated in the global xy plane). However, the components of the vector $\hat{j}$ may be chosen arbitrarily (but with constant magnitudes within each element), so as to permit the modelling of direction dependent characteristics [10].

The adoption of the general approach described by eqn(5.4.13), eqn(5.4.9) and eqn(5.4.10), produces an improved element formulation. This is demonstrated by the solutions to the Patch Test (Section 6.2, Chapter 6).

5.5. Change of Variable for Differentiation.

The displacements within the element are written as functions of the natural co-ordinates (ξ, η) (eqn(5.3.3.7)). However, it is required to calculate the strains based on the general local co-ordinate system and not the normalised natural co-ordinates. Therefore, a change of variable is necessary, relating the differentiation with respect to the local co-ordinate, X and Y, to the differentiation with respect to the natural co-ordinate, (ξ, η). Though strain is a vector quantity, equations of the form of eqn(5.3.3.7) are differentiable scalar functions of position (ξ, η) ($N_i = f(\xi, \eta)$ and (ξ, η) are scalar quantities in the range $-1 \leq (\xi, \eta) \leq +1$). In the subsequent paragraphs, the derivation of the change of variable for differentiation is summarised [5.7].

The scalar quantity, Ω, is established at the position (ξ, η), (where Ω may be a component of displacement in the global x direction, for example). If the position of Ω is moved from (ξ, η) to $(\xi + d\xi, \eta + d\eta)$ the change in Ω, $d\Omega$, is given as,

---

9

When the base vector $\vec{\xi}$ coincides with the local X direction and the element is rectangular, the preceding approach, and the approach by Irons,[5.7] produce the same definition for the local co-ordinate systems across the surface of the element. Therefore, the method proposed by Irons may be seen as a special case of the general solution.

10

The ability to pre-select the direction of the vector $\hat{j}$ is significant to the analysis of structural membranes, where the membrane material may possess orthotropic properties.

$$d\Omega = \frac{\partial \Omega}{\partial \xi} . d\xi + \frac{\partial \Omega}{\partial \eta} . d\eta \qquad \text{eqn(5.5.1)}$$

A change in position of $d\xi$ implies a shift in position given as $\vec{\xi} . d\xi$. Resolving this shift into the local X and Y directions yields,

$$dX_\xi = \vec{\xi} . \hat{X}\, d\xi \quad \text{and} \quad dY_\xi = \vec{\xi} . \hat{Y}\, d\xi . \qquad \text{eqn(5.5.2)}$$

Similarly, in the natural co-ordinate direction η, a change in position by $d\eta$ gives,

$$dX_\eta = \vec{\eta} . \hat{X}\, d\eta \quad \text{and} \quad dY_\eta = \vec{\eta} . \hat{Y}\, d\eta . \qquad \text{eqn(5.5.3)}$$

Rewriting eqn(5.5.1) in terms of the local element co-ordinate system yields,

$$d\Omega = \frac{\partial \Omega}{\partial X} . dX + \frac{\partial \Omega}{\partial Y} . dY , \qquad \text{eqn(5.5.4)}$$

where, $dX = dX_\xi + dX_\eta$ and, $dY = dY_\xi + dY_\eta$

Substitution of eqn(5.5.3) and eqn(5.5.2) into eqn(5.5.4), and rearranging the resulting expression gives,

$$d\Omega = \left[\vec{\xi} . \hat{X} \frac{\partial \Omega}{\partial X} + \vec{\xi} . \hat{Y} \frac{\partial \Omega}{\partial Y} \right] d\xi + \left[\vec{\eta} . \hat{X} \frac{\partial \Omega}{\partial X} + \vec{\eta} . \hat{Y} \frac{\partial \Omega}{\partial Y} \right] d\eta$$

$$= \frac{\partial \Omega}{\partial \xi} . d\xi + \frac{\partial \Omega}{\partial \eta} . d\eta \qquad \text{eqn(5.5.5)}$$

Collection of common terms in eqn(5.5.5) leads to the matrix formulation,[5.7]

$$\begin{bmatrix} \frac{\partial \Omega}{\partial \xi} \\ \frac{\partial \Omega}{\partial \eta} \end{bmatrix} = \begin{bmatrix} \vec{\xi} . \hat{X} & \vec{\xi} . \hat{Y} \\ \vec{\eta} . \hat{X} & \vec{\eta} . \hat{Y} \end{bmatrix} \begin{bmatrix} \frac{\partial \Omega}{\partial X} \\ \frac{\partial \Omega}{\partial Y} \end{bmatrix} , \qquad \text{eqn(5.5.6)}$$

or more usefully,

$$\begin{bmatrix} \frac{\partial \Omega}{\partial X} \\ \frac{\partial \Omega}{\partial Y} \end{bmatrix} = \frac{1}{\det[J]} \begin{bmatrix} \vec{\eta} . \hat{Y} & -\vec{\xi} . \hat{Y} \\ -\vec{\eta} . \hat{X} & \vec{\xi} . \hat{X} \end{bmatrix} \begin{bmatrix} \frac{\partial \Omega}{\partial \xi} \\ \frac{\partial \Omega}{\partial \eta} \end{bmatrix} , \qquad \text{eqn(5.5.7(a))}$$

where,

$$[J] = \begin{bmatrix} \vec{\xi} . \hat{X} & \vec{\xi} . \hat{Y} \\ \vec{\eta} . \hat{X} & \vec{\eta} . \hat{Y} \end{bmatrix} \qquad \text{eqn(5.5.7(b))}$$

The square matrix in eqn(5.5.7(b)) is termed the Jacobian, and has the effect of a scaling factor, relating the mapped element of Figure 5.2(c) to the distorted parent element illustrated in Figure 5.2(b). Calculation of the determinant of the Jacobian matrix yields the area of the element.

5.6. Using the Jacobian to Compute Local Strains.

In the present formulation the primary unknowns are the nodal displacements. Compilation of an overall system array generates displacements in the fixed global co-ordinate system, permitting the description of the element, and hence system, rigid body motions. It has been suggested that, when computing local strains at discrete points within the element, based on global displacements, variation in the local X and Y co-ordinate directions may be ignored.[5.7] This results in the global displacements being interpreted onto the local axes, which are assumed fixed in direction, at the point of interest. A summary of this approach is presented below.

By transforming the components of the global displacements at the element nodes into the local $\vec{X}$ direction, the local deflection U is given as,

$$U = \hat{X} \cdot \left\{ \sum_{i=1}^{i=8} N_i \, u_i \, \underline{i} + \sum_{i=1}^{i=8} N_i \, v_i \, \underline{j} + \sum_{i=1}^{i=8} N_i \, w_i \, \underline{k} \right\}$$

$$= \hat{X} \cdot [N] \{\delta\}_i \, . \qquad \text{eqn(5.6.1)}$$

Assuming small displacements, the local direct strain in the local X direction,, $\varepsilon_X = \frac{\partial U}{\partial X}$, may be written as [5.7],

$$\frac{\partial U}{\partial X} = \frac{\partial [\hat{X} \cdot [N] \{\delta\}_i]}{\partial X} \, . \qquad \text{eqn(5.6.2)}$$

Since $\hat{X}$ is a unit vector, it is simple to show that eqn(5.6.1) may be rewritten as,

$$U = \hat{X}^T [N] \{\delta\}_i \, . \qquad \text{eqn(5.6.3)}$$

Differentiating eqn(5.6.3) yields,

$$\frac{\partial U}{\partial X} = \hat{X}^T \frac{\partial [N(\xi, \eta)]}{\partial X} \{\delta\}_i + \hat{X}^T [N] \frac{\partial \{\delta\}_i}{\partial X}$$

$$+ \frac{\partial \hat{X}^T}{\partial X} [N] \{\delta\}_i \, . \qquad \text{eqn(5.6.4)}$$

The first term on the right side of eqn(5.6.4) indicates zero strain under rigid body motion (necessary in order to satisfy the conditional requirement of a valid element [5.8]). In reference [5.7] it is suggested that the second term of the expression is zero for all cases of displacement, since the displacement vector $\{\delta\}_i$ is given at discrete points. Consequently, the variation of $\{\delta\}_i$ is zero. However, as described below, the magnitude of the third term on the right side of eqn(5.6.4) is primarily dependent on the curvature of the element, irrespective of whether the global displacement vector $\{\delta\}_i$ describes rigid body motion or not.

The differential $\frac{\partial \hat{X}^T}{\partial X}$ is a measure of the curvature of the element. Therefore, if the element has straight sides, the magnitude of the final term of eqn(5.6.4) will be zero, and is independent of the displacement field, $\{ \delta \}_i$. Conversely, if the element exhibits curved sides, the final term will yield a non-zero value even though the displacement vector $\{ \delta \}_i$ describes rigid body motion. Therefore, it is suggested that this term of the expression must be neglected, as a necessary assumption [5.7].

A more rigorous investigation is presented below, in which it is shown that this assumption is not intrinsic. It is shown explicitly that the computation of local strains does not depend on variation in the orientation of the local X, Y axes, to the end of providing a true description of the state of strain within an elastic continuum [11].

Examination of eqn(5.6.1) indicates that the dot product transforms the global displacements δ_i into displacements in the local co-ordinate system. Subsequently these are differentiated to give the local strains. An alternative formulation it is proposed in which the local element strains are calculated by the differentiation of the global displacements with respect to the local co-ordinates prior to transformation into the local co-ordinate system.

In order to show the validity of the approach presented in reference [5.7] and that proposed above, a general elastic continuum is examined with respect to the global co-ordinate system.

Figure 5.8 shows a general elastic continuum, where, $\underline{X}$ is the position vector of the point P_o, and $\underline{\delta}$ is an assumed general displacement vector, given in global co-ordinates as,

$$\underline{X} = \{ x\,\underline{i} + y\,\underline{j} + z\,\underline{k} \} \qquad \text{eqn(5.6.5(a))}$$

$$\underline{\delta} = \{ u\,\underline{i} + v\,\underline{j} + w\,\underline{k} \}. \qquad \text{eqn(5.6.5(b))}$$

Using the definition for strain given by Green,[5.9] ε_G, the strain induced in the continuum at the point $P_o(\xi, \eta)$, due to a displacement vector $\underline{\delta}$, may be given in terms of the distance squared as,

$$\varepsilon_G = \frac{ds^2 - ds_o^2}{2\,ds_o^2}, \qquad \text{eqn(5.6.6)}$$

where ds_o is a given initial infinitesimal arc length on the surface at the point P_o in the direction of the natural co-ordinate ξ, and ds is the arc length after application of the assumed displacement field $\underline{\delta}$. (When calculating the straining of the arc ds_o due to a global

11

When calculating element properties such as stiffness and equivalent nodal forces which rely on the integration of a continuous functional, the effects of the variation in the orientation of the local X, Y co-ordinate directions cannot be ignored. They may be included by the adoption of discrete sampling, however. For example, Gauss Quadrature is used to compute the integrals given in eqn(5.2.2.7). In this method the functional is evaluated at discrete locations within the element, to give the exact (continuous) solution when sufficient Gauss Points are used (Section 5.8).

displacement vector $\{\ \underline{\delta}\ \}$, it is assumed that the rate of straining along the arc is constant.)

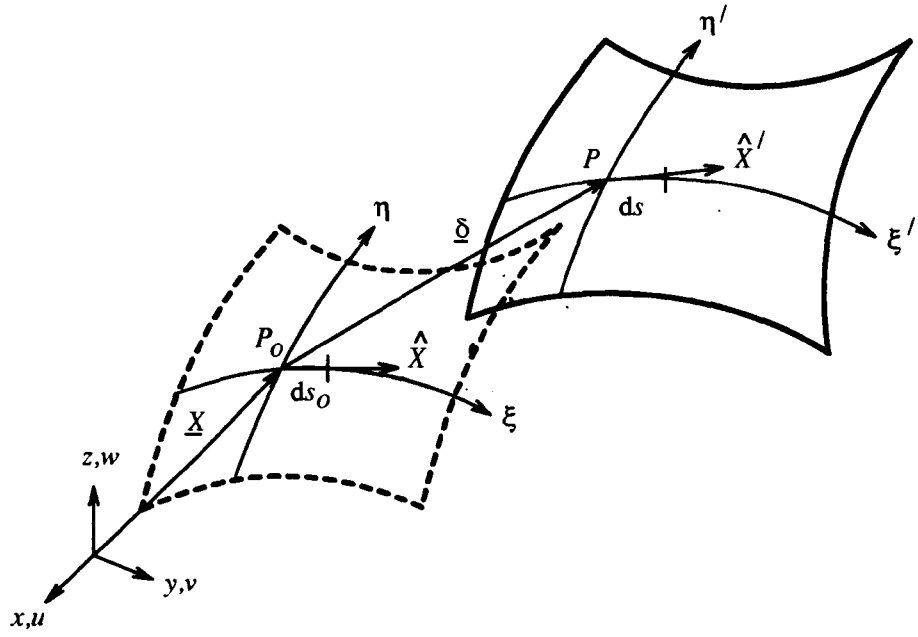

Figure 5.8 - General 3-Dimensional Elastic Continuum Subjected to a Displacement Vector $\underline{\delta}$

The position vector $\underline{X}$ may be written as a function of the curvilinear co-ordinates (ξ, η). For a constant value of η, and assuming that the expression for $\underline{X}$ is differentiable, then,

$$d\underline{X} = \frac{\partial \underline{X}}{\partial \xi}\, d\xi\,. \qquad \text{eqn(5.6.7(a))}$$

Taking $d\xi$ as unity, the square of the original arc length, ds_o may be calculated as,[5.9]

$$ds_o^{\,2} = d\underline{X} \cdot d\underline{X} = \frac{\partial \underline{X}}{\partial \xi} \cdot \frac{\partial \underline{X}}{\partial \xi}\,, \qquad \text{eqn(5.6.7(b))}$$

and of ds as,

$$\begin{aligned} ds^2 &= \frac{\partial(\underline{X}+\underline{\delta})}{\partial \xi} \cdot \frac{\partial(\underline{X}+\underline{\delta})}{\partial \xi} \\ &= \left[\frac{\partial \underline{X}}{\partial \xi} + \frac{\partial \underline{\delta}}{\partial \xi}\right] \cdot \left[\frac{\partial \underline{X}}{\partial \xi} + \frac{\partial \underline{\delta}}{\partial \xi}\right] \\ &= \frac{\partial \underline{X}}{\partial \xi} \cdot \frac{\partial \underline{X}}{\partial \xi} + 2\,\frac{\partial \underline{\delta}}{\partial \xi} \cdot \frac{\partial \underline{X}}{\partial \xi} + \frac{\partial \underline{\delta}}{\partial \xi} \cdot \frac{\partial \underline{\delta}}{\partial \xi}\,. \end{aligned} \qquad \text{eqn(5.6.7(c))}$$

Substitution of eqn(5.6.7(b)) into eqn(5.6.7(c)) yields,

$$ds^2 = ds_o^{\,2} + 2\,\frac{\partial \underline{\delta}}{\partial \xi} \cdot \frac{\partial \underline{X}}{\partial \xi} + \frac{\partial \underline{\delta}}{\partial \xi} \cdot \frac{\partial \underline{\delta}}{\partial \xi}\,. \qquad \text{eqn(5.6.8)}$$

Substitution of eqn(5.6.8) into eqn(5.6.6) and making use of eqn(5.6.7(b)), leads to the expression for the strain in the continuum at the point P, $\varepsilon_G{}^P$, as,

$$\varepsilon_G{}^P = \frac{2\,\frac{\partial \delta}{\partial \xi} \cdot \frac{\partial X}{\partial \xi} + \frac{\partial \delta}{\partial \xi} \cdot \frac{\partial \delta}{\partial \xi}}{2\left|\frac{\partial X}{\partial \xi}\right|^2} \qquad \text{eqn(5.6.9)}$$

in which the dot product in eqn(5.6.7(b)) is given in terms of scalar quantities, *i.e.*, as the square of the modulus of $\frac{\partial X}{\partial \xi}$.

The second term in the numerator of eqn(5.6.9) is a higher order term and may be neglected initially, leading to the expression for the first order approximation to Green's strain, ε_G, as in,

$$\varepsilon_G{}^P \approx \frac{\frac{\partial \delta}{\partial \xi} \cdot \frac{\partial X}{\partial \xi}}{\left|\frac{\partial X}{\partial \xi}\right|^2}. \qquad \text{eqn(5.6.10)}$$

Differentiating $\underline{X}$ (eqn(5.6.5(a)) and $\underline{\delta}$ (eqn(5.6.5(b)) with respect to the natural co-ordinate ξ, gives,

$$\frac{\partial \delta}{\partial \xi} = \left\{ \frac{\partial u}{\partial \xi}\underline{i} + \frac{\partial v}{\partial \xi}\underline{j} + \frac{\partial w}{\partial \xi}\underline{k} \right\}, \qquad \text{eqn(5.6.11)}$$

and,

$$\frac{\partial X}{\partial \xi} = \left\{ \frac{\partial x}{\partial \xi}\underline{i} + \frac{\partial y}{\partial \xi}\underline{j} + \frac{\partial z}{\partial \xi}\underline{k} \right\}. \qquad \text{eqn(5.6.12)}$$

Therefore, from eqn(5.6.11) and eqn(5.6.12),

$$\frac{\partial \delta}{\partial \xi} \cdot \frac{\partial X}{\partial \xi} = \left\{ \frac{\partial u}{\partial \xi}\frac{\partial x}{\partial \xi} + \frac{\partial v}{\partial \xi}\frac{\partial y}{\partial \xi} + \frac{\partial w}{\partial \xi}\frac{\partial z}{\partial \xi} \right\}, \qquad \text{eqn(5.6.13)}$$

Substituting eqn(5.6.13) into eqn(5.6.10) gives,

$$\varepsilon_G{}^P \approx \frac{\left\{ \frac{\partial u}{\partial \xi}\frac{\partial x}{\partial \xi} + \frac{\partial v}{\partial \xi}\frac{\partial y}{\partial \xi} + \frac{\partial w}{\partial \xi}\frac{\partial z}{\partial \xi} \right\}}{\left|\frac{\partial X}{\partial \xi}\right|^2}. \qquad \text{eqn(5.6.14(a))}$$

where eqn(5.6.14(a)) describes the strain in the ξ direction.

As described below, in order to simplify the following mathematical analysis, a special case of the general solution (eqn(5.6.14(a))) is considered.

If it is assumed that the local X co-ordinate direction is aligned with the natural co-ordinate, ξ, then the vectors $\vec{\xi}$ and $\hat{Y}$ are orthogonal (Figure 5.8). Consequently, the vector product $\vec{\xi} \cdot \hat{Y} = 0$. By substituting this result into eqn(5.5.7(a)), the strain in the ξ direction, $\varepsilon_G{}^P$ (eqn(5.6.14(a))),

can be shown to correspond to the local direct strain in the X co-ordinate direction. Therefore, denoting the local direct strain in the X co-ordinate direction as, $\frac{\partial U}{\partial X}$, this can be written as,

$$\varepsilon_G{}^P \approx \frac{\partial U}{\partial X} . \qquad \text{eqn(5.6.14(b))}$$

Given that $\frac{\partial X}{\partial \vec{\xi}} = \vec{\xi}$ (eqn(5.4.1)), and using the simplifying assumption that $\hat{X} = \frac{\vec{\xi}}{|\vec{\xi}|}$, (eqn(5.4.4)), then from eqn(5.6.10(a)),

$$\varepsilon_G{}^P \approx \frac{\partial U}{\partial X} = \frac{\frac{\partial \delta}{\partial \vec{\xi}}}{\left|\frac{\partial X}{\partial \vec{\xi}}\right|} \cdot \frac{\frac{\partial X}{\partial \vec{\xi}}}{\left|\frac{\partial X}{\partial \vec{\xi}}\right|} = \frac{\frac{\partial \delta}{\partial \vec{\xi}}}{\left|\frac{\partial X}{\partial \vec{\xi}}\right|} \cdot \hat{X} \qquad \text{eqn(5.6.14(c))}$$

In order to calculate the local strain, $\varepsilon_G{}^P$, of an elastic continuum, subjected to an assumed global displacement field $\{ \underline{\delta} \}$, it can be seen from eqn(5.6.14(c)) that the global displacements must be first differentiated with respect to the natural variable. Subsequently, this result is transformed to the local axes. This is done by computing the dot product $\frac{\partial \delta}{\partial \vec{\xi}} \cdot \hat{X}$. The calculation is completed by the application of a further transformation, as given by eqn(5.5.7(a)). This transformation arises from the change of variable for differentiation, which is required when calculating the strains from partial derivatives, $\varepsilon_x \approx \frac{\partial u}{\partial x}$, for example. By adopting this approach, an expression for the local strain, $\frac{\partial U}{\partial X}$, is derived below.

Using the notation of Figure 5.8, eqn(5.6.1) may be rewritten as,

$$U = \hat{X} \cdot \underline{\delta} , \qquad \text{eqn(5.6.15(a))}$$

which, upon differentiation of the displacement term with respect to the local variable X gives,

$$\frac{\partial U}{\partial X} = \hat{X} \cdot \frac{\partial \delta}{\partial X} , \qquad \text{eqn(5.6.15(b))}$$

or, using the result from eqn(5.6.3), yields,

$$\frac{\partial U}{\partial X} = \hat{X}^T \frac{\partial [N(\xi, \eta)]}{\partial X} \{ \delta_i \} . \qquad \text{eqn(5.6.15(c))}$$

Considering the first term on the right side of eqn(5.6.15(b)) initially, and rewriting eqn(5.5.7(a)) in terms of the global displacement vector $\underline{\delta}$, yields,

$$\begin{bmatrix} \frac{\partial \delta}{\partial X} \\ \frac{\partial \delta}{\partial Y} \end{bmatrix} = \frac{1}{\det[J]} \begin{bmatrix} \vec{\eta} \cdot \hat{Y} & -\vec{\xi} \cdot \hat{Y} \\ -\vec{\eta} \cdot \hat{X} & \vec{\xi} \cdot \hat{X} \end{bmatrix} \begin{bmatrix} \frac{\partial \delta}{\partial \vec{\xi}} \\ \frac{\partial \delta}{\partial \vec{\eta}} \end{bmatrix} . \qquad \text{eqn(5.6.16)}$$

Assuming, as before, that $\hat{X}$ and $\hat{Y}$ are orthogonal vectors such that $\hat{X} = \frac{\vec{\xi}}{|\vec{\xi}|}$, and $\hat{Y} \approx \frac{\vec{\eta}}{|\vec{\eta}|}$, it follows that,

$$(\vec{\xi} \cdot \hat{Y}) = 0, \quad \text{and} \quad (\vec{\eta} \cdot \hat{X}) \approx 0. \qquad \text{eqn(5.6.17)}$$

Therefore, substituting eqn(5.6.17) into eqn(5.6.16) gives an expression for the pseudo local strain, $\frac{\partial \delta}{\partial \hat{X}}$, as [12],

$$\frac{\partial \delta}{\partial \hat{X}} = \frac{1}{(\vec{\eta} \cdot \hat{Y})(\vec{\xi} \cdot \hat{X})} \left[\vec{\eta} \cdot \hat{Y} \right] \frac{\partial \delta}{\partial \vec{\xi}}$$

$$= \frac{1}{(\vec{\xi} \cdot \hat{X})} \frac{\partial \delta}{\partial \vec{\xi}}. \qquad \text{eqn(5.6.18)}$$

By substituting eqn(5.6.11) into eqn(5.6.18) and the resulting expression into eqn(5.6.15(b)), the local strain $\frac{\partial U}{\partial \hat{X}}$ is written as,

$$\frac{\partial U}{\partial \hat{X}} = \left[\frac{1}{(\vec{\xi} \cdot \hat{X})} \left\{ \frac{\partial u}{\partial \vec{\xi}} \underline{i} + \frac{\partial v}{\partial \vec{\xi}} \underline{j} + \frac{\partial w}{\partial \vec{\xi}} \underline{k} \right\} \right] \cdot \hat{X}. \qquad \text{eqn(5.6.19)}$$

Rewriting the dot product in the denominator of eqn(5.6.19), $(\vec{\xi} \cdot \hat{X})$, with eqn(5.4.1) and eqn(5.4.4) gives,

$$(\vec{\xi} \cdot \hat{X}) = \frac{\vec{\xi} \cdot \vec{\xi}}{|\vec{\xi}|}$$

$$= \frac{\left[\frac{\partial x}{\partial \vec{\xi}}\right]^2 + \left[\frac{\partial y}{\partial \vec{\xi}}\right]^2 + \left[\frac{\partial z}{\partial \vec{\xi}}\right]^2}{\sqrt{\left[\frac{\partial x}{\partial \vec{\xi}}\right]^2 + \left[\frac{\partial y}{\partial \vec{\xi}}\right]^2 + \left[\frac{\partial z}{\partial \vec{\xi}}\right]^2}}$$

$$= \sqrt{\left[\frac{\partial x}{\partial \vec{\xi}}\right]^2 + \left[\frac{\partial y}{\partial \vec{\xi}}\right]^2 + \left[\frac{\partial z}{\partial \vec{\xi}}\right]^2} \qquad \text{eqn(5.6.20)}$$

12

The term "pseudo" is used here, since eqn(5.6.18) expresses variation of global displacements with respect to the local co-ordinate system, prior to transformation to the local system of co-ordinates yielding the true local strain.

Given that, in the current notation, $\vec{\xi} = \frac{\partial X}{\partial \xi}$, the final term in eqn(5.6.20) can be seen to represent the magnitude of the base vector $\vec{\xi}$. Substituting this result into eqn(5.6.19) gives,

$$\frac{\partial U}{\partial X} = \left[\frac{1}{\left| \frac{\partial X}{\partial \xi} \right|} \left\{ \frac{\partial u}{\partial \xi} \underline{i} + \frac{\partial v}{\partial \xi} \underline{j} + \frac{\partial w}{\partial \xi} \underline{k} \right\} \right] \cdot \hat{X}$$

$$= \underline{d} \cdot \hat{X} = \left| \underline{d} \right| \left| \hat{X} \right| \cos \alpha . \qquad \text{eqn(5.6.21)}$$

in which the magnitude of $\underline{d}$ may be written as,

$$\left| \underline{d} \right| = \frac{1}{\left| \frac{\partial X}{\partial \xi} \right|} \left| \frac{\partial \delta}{\partial \xi} \right| , \qquad \text{eqn(5.6.22)}$$

and the angle, α, between vectors $\underline{d}$ and $\hat{X}$ given as,

$$\cos\alpha = \frac{\underline{d} \cdot \hat{X}}{\left| \underline{d} \right| \left| \hat{X} \right|} . \qquad \text{eqn(5.6.23)}$$

From the definition $| \hat{X} | = 1$, and substituting for $\underline{d}$ (eqn(5.6.21(b))), and for $\hat{X}$ (eqn(5.6.20(b)) and eqn(5.4.4)), into eqn(5.6.23), leads to,

$$\cos\alpha = \frac{\frac{1}{\left| \frac{\partial X}{\partial \xi} \right|} \left\{ \frac{\partial u}{\partial \xi} \underline{i} + \frac{\partial v}{\partial \xi} \underline{j} + \frac{\partial w}{\partial \xi} \underline{k} \right\} \cdot \frac{1}{\left| \vec{\xi} \right|} \left\{ \frac{\partial x}{\partial \xi} \underline{i} + \frac{\partial y}{\partial \xi} \underline{j} + \frac{\partial z}{\partial \xi} \underline{k} \right\}}{\left| \underline{d} \right|}$$

$$= \frac{\frac{1}{\left| \frac{\partial X}{\partial \xi} \right|} \left\{ \frac{\partial u}{\partial \xi} \underline{i} + \frac{\partial v}{\partial \xi} \underline{j} + \frac{\partial w}{\partial \xi} \underline{k} \right\} \cdot \frac{1}{\left| \vec{\xi} \right|} \left\{ \frac{\partial x}{\partial \xi} \underline{i} + \frac{\partial y}{\partial \xi} \underline{j} + \frac{\partial z}{\partial \xi} \underline{k} \right\}}{\frac{1}{\left| \frac{\partial X}{\partial \xi} \right|} \left| \frac{\partial \delta}{\partial \xi} \right|}$$

$$= \frac{1}{\left| \vec{\xi} \right|} \frac{1}{\left| \frac{\partial \delta}{\partial \xi} \right|} \left[\frac{\partial u}{\partial \xi} \frac{\partial x}{\partial \xi} + \frac{\partial v}{\partial \xi} \frac{\partial y}{\partial \xi} + \frac{\partial w}{\partial \xi} \frac{\partial z}{\partial \xi} \right] . \qquad \text{eqn(5.6.24)}$$

Therefore, noting that $\left| \vec{\xi} \right| = \left| \frac{\partial X}{\partial \xi} \right|$, the cosine of the angle between the two vectors $\underline{d}$ and $\hat{X}$, α, may be written as,

$$\cos\alpha = \frac{1}{\left| \frac{\partial X}{\partial \xi} \right|} \frac{1}{\left| \frac{\partial \delta}{\partial \xi} \right|} \left[\frac{\partial u}{\partial \xi}\frac{\partial x}{\partial \xi} + \frac{\partial v}{\partial \xi}\frac{\partial y}{\partial \xi} + \frac{\partial w}{\partial \xi}\frac{\partial z}{\partial \xi} \right] . \qquad \text{eqn(5.6.25)}$$

Substitution of eqn(5.6.22) and eqn(5.6.25) into eqn(5.6.21) yields,

$$\frac{\partial U}{\partial X} = \frac{\left[\frac{\partial u}{\partial \xi}\frac{\partial x}{\partial \xi} + \frac{\partial v}{\partial \xi}\frac{\partial y}{\partial \xi} + \frac{\partial w}{\partial \xi}\frac{\partial z}{\partial \xi} \right]}{\left| \frac{\partial X}{\partial \xi} \right|^2} . \qquad \text{eqn(5.6.26)}$$

Eqn(5.6.26) can be seen to be identical to eqn(5.6.14(a)), and therefore to validate eqn(5.6.14(c)).

Consequently, by comparing eqn(5.6.14(c)) with eqn(5.6.26), it has been shown that in order to calculate the local strain of an elastic continuum, $\varepsilon_G{}^P$, subjected to an assumed global displacement field, $\underline{\delta}$, the global displacements must first be differentiated with respect to the local variable, prior to transformation to the local co-ordinate system.

Returning to the formulation presented in reference [5.7] in which eqn(5.6.15(a)) has been presented as,

$$U = \hat{X} \cdot \underline{\delta} = \underline{\delta} \cdot \hat{X} . \qquad \text{eqn(5.6.15(a))}$$

Differentiation of eqn(5.6.15(a)) with respect to the local co-ordinate direction X, leads to the expression for the local strain in the local X direction as [5.7],

$$\frac{\partial U}{\partial X} = \frac{\partial \delta}{\partial X} \cdot \hat{X} + \underline{\delta} \cdot \frac{\partial \hat{X}}{\partial X} . \qquad \text{eqn(5.6.27)}$$

Comparisons of eqn(5.6.27) with eqn(5.6.15(b)) and eqn (5.6.26) with eqn(5.6.14(c)) demonstrate that the additional term on the right side of eqn(5.6.27), which has been suggested in reference [5.7], is superfluous and should not be included in the formulation for the expression of the local strain due to an imposed global displacement vector.

In the preceding derivation, it has been assumed that the base vector $\vec{\varepsilon}$ is aligned with the local X co-ordinate direction. The relaxation of this simplifying assumption to obtain a general form of the solution, leads to the formulation presented in Appendix 5-A. It is shown in Table 5-A.2 (Appendix 5-A) that eqn(5.6.15(b)) is valid in the general case.

Furthermore, in the formulation presented thus far in this section, it has been convenient to disregard the second term of the numerator of eqn(5.6.9). In Appendix 5-B it is shown that,

regardless of the magnitude of the assumed displacement vector $\{ \underline{\delta} \}$, the higher order terms of the expression for strain must be included when calculating the total strain of an elastic continuum.

However, the expressions for strain in the form of eqn(5.6.26), eqn(5-B.7) and eqn(5-B.8), are only applicable to "homogeneous strains", where "homogeneous" means that, within the element considered, the state of strain is constant throughout that element, though the strains may be finite rather than infinitesimal.

Ford [5.10], presented a derivation for the case of "Finite Homogeneous Strains" in a solid body, and remarked that the case of non-homogeneous strains is mathematically impractical. Consequently, though the element formulation may describe up to a linear variation in strain, the expression relating the global displacements to the local strains assumes that those strains are constant across the element. Therefore, it is proposed here, that up to a pseudo linear variation of strain may be described by the present formulation.

5.7. Derivation of Element Matrices.

5.7.1. Element Local Elastic Stiffness Matrix.

The generation of the terms of the local element elastic stiffness matrix $[K_E{}^e]$ is presented in this section.

From the term on the left side of eqn(5.2.2.7), $[K_E{}^e]$ may be written as,

$$\left[K_E{}^e \right] = \int_{vol} [B]^T [E] [B] \, dV . \qquad \text{eqn(5.7.1.1)}$$

Matrix $[B]$ eqn(5.2.2.2), relates the element global displacements to the element local strains. From eqn(5-B.8), and eqn(5-B.7), the local strain in the local X direction, $\frac{\partial U'}{\partial X}$, is given as,

$$\frac{\partial U'}{\partial X} = \frac{\partial U}{\partial X} + \frac{1}{2} \left[\left[\frac{\partial U}{\partial X} \right]^2 + \left[\frac{\partial V}{\partial X} \right]^2 + \left[\frac{\partial W}{\partial X} \right]^2 \right] . \qquad \text{eqn(5.7.1.2)}$$

The first term of eqn(5.7.1.2) represents the linear contribution to the total strain of the continuum, and may be written as,

$$\frac{\partial U}{\partial X} = [b_o] \left\{ \underline{\delta} \right\} , \qquad \text{eqn(5.7.1.3)}$$

where, $[b_o]$ is an element matrix relating the global displacement vector $\{ \underline{\delta} \}$ to the first order contribution of strain to $\frac{\partial U'}{\partial X}$.

The term in parentheses on the right side of eqn(5.7.1.2), representing the non-linear (second order) contribution of strain, $\frac{\partial U^{ho}}{\partial X}$, to $\frac{\partial U^{t}}{\partial X}$, is written as,

$$\frac{\partial U^{ho}}{\partial X} = [\, b_L \,] \left\{ \underline{\delta} \right\}, \qquad \text{eqn(5.7.1.4)}$$

where, $[\, b_L \,]$ is an element matrix of similar form to $[\, b_o \,]$.

Substituting eqn(5.7.1.3) and eqn(5.7.1.4) into eqn(5.7.1.2) gives,

$$\frac{\partial U^{t}}{\partial X} = \left[\, [\, b_o \,] + [\, b_L \,] \, \right] \left\{ \underline{\delta} \right\} = [\, \bar{b} \,] \left\{ \underline{\delta} \right\}. \qquad \text{eqn(5.7.1.5)}$$

For the situation of plane stress, eqn(5.7.1.5) may be written as,

$$\{ \varepsilon \} = \begin{Bmatrix} \varepsilon_X \\ \varepsilon_Y \\ \gamma_{XY} \end{Bmatrix} = \left[\, [B_o \,] + [B_L \,] \, \right] \left\{ \delta \right\}_i$$

$$= [\, \bar{B} \,] \left\{ \delta \right\}_i, \qquad \text{eqn(5.7.1.6)}$$

where,

$$\varepsilon_X = \frac{\partial U}{\partial X} + \frac{1}{2} \left[\left(\frac{\partial U}{\partial X} \right)^2 + \left(\frac{\partial V}{\partial X} \right)^2 + \left(\frac{\partial W}{\partial X} \right)^2 \right],$$

$$\varepsilon_Y = \frac{\partial V}{\partial Y} + \frac{1}{2} \left[\left(\frac{\partial U}{\partial Y} \right)^2 + \left(\frac{\partial V}{\partial Y} \right)^2 + \left(\frac{\partial W}{\partial Y} \right)^2 \right],$$

and,

$$\gamma_{XY} = \frac{\partial U}{\partial Y} + \frac{\partial V}{\partial X} + \left[\left(\frac{\partial U}{\partial X} \right)\left(\frac{\partial U}{\partial Y} \right) + \left(\frac{\partial V}{\partial X} \right)\left(\frac{\partial V}{\partial Y} \right) + \left(\frac{\partial W}{\partial X} \right)\left(\frac{\partial W}{\partial Y} \right) \right],$$

with, $\{ \delta \}_i$, the global displacement vector of the element i.

Therefore, for a thin elastic continuum subjected to large strains and large displacements, the local element elastic stiffness matrix, $\left[\overline{K_E{}^e} \right]$, is given by the expression, (eqn(5.7.1.1)),

$$\left[\overline{K_E{}^e} \right] = \int_{vol} [\, \bar{B} \,]^T [\, E \,] [\, \bar{B} \,] \, dV = [\, K_o \,] + [\, K_L \,]. \qquad \text{eqn(5.7.1.7)}$$

5.7.2. Derivation of the Strain - Displacement Matrix [B_o].

The first order contribution to the total strain given by eqn(5.7.1.3), may be rewritten in the form,

$$\frac{\partial U}{\partial X} = \frac{\partial \delta}{\partial X} \cdot \{ \hat{X}^T \} . \qquad \text{eqn(5.7.2.1)}$$

By rewriting the displacement vector, $\{ \underline{\delta} \}$, in terms of the element shape functions and the natural co-ordinate system (eqn(5.6.1)), eqn(5.7.2.1) may be expressed in the form,

$$\frac{\partial U}{\partial X} = \left[\sum_{i=1}^{i=8} \frac{\partial N_i(\xi,\eta)}{\partial X} u_i \underline{i} + \sum_{i=1}^{i=8} \frac{\partial N_i(\xi,\eta)}{\partial X} v_i \underline{j} + \sum_{i=1}^{i=8} \frac{\partial N_i(\xi,\eta)}{\partial X} w_i \underline{k} \right] \cdot \{ \hat{X}^T \} . \qquad \text{eqn(5.7.2.2)}$$

The local co-ordinate unit vector at element node i, $\{ \hat{X} \}_i$ may be given as,

$$\{ \hat{X} \}_i = \left\{ \hat{X}^i{}_i \underline{i} + \hat{X}^j{}_i \underline{j} + \hat{X}^k{}_i \underline{k} \right\} \qquad \text{eqn(5.7.2.3)}$$

Substituting eqn(5.7.2.3) into eqn(5.7.2.2) yields,

$$\frac{\partial U}{\partial X} = \sum_{i=1}^{i=8} \hat{X}^i{}_i \frac{\partial N_i(\xi,\eta)}{\partial X} u_i + \sum_{i=1}^{i=8} \hat{X}^j{}_i \frac{\partial N_i(\xi,\eta)}{\partial X} v_i + \sum_{i=1}^{i=8} \hat{X}^k{}_i \frac{\partial N_i(\xi,\eta)}{\partial X} w_i . \qquad \text{eqn(5.7.2.4)}$$

Similarly,

$$\frac{\partial V}{\partial Y} = \sum_{i=1}^{i=8} \hat{Y}^i{}_i \frac{\partial N_i(\xi,\eta)}{\partial Y} u_i + \sum_{i=1}^{i=8} \hat{Y}^j{}_i \frac{\partial N_i(\xi,\eta)}{\partial Y} v_i + \sum_{i=1}^{i=8} \hat{Y}^k{}_i \frac{\partial N_i(\xi,\eta)}{\partial Y} w_i , \qquad \text{eqn(5.7.2.5)}$$

$$\frac{\partial U}{\partial Y} = \sum_{i=1}^{i=8} \hat{X}^i{}_i \frac{\partial N_i(\xi,\eta)}{\partial Y} u_i + \sum_{i=1}^{i=8} \hat{X}^j{}_i \frac{\partial N_i(\xi,\eta)}{\partial Y} v_i + \sum_{i=1}^{i=8} \hat{X}^k{}_i \frac{\partial N_i(\xi,\eta)}{\partial Y} w_i , \qquad \text{eqn(5.7.2.6)}$$

and,

$$\frac{\partial V}{\partial X} = \sum_{i=1}^{i=8} \hat{Y}^i{}_i \frac{\partial N_i(\xi,\eta)}{\partial X} u_i + \sum_{i=1}^{i=8} \hat{Y}^j{}_i \frac{\partial N_i(\xi,\eta)}{\partial X} v_i + \sum_{i=1}^{i=8} \hat{Y}^k{}_i \frac{\partial N_i(\xi,\eta)}{\partial X} w_i . \qquad \text{eqn(5.7.2.7)}$$

Therefore, the matrix, $[B_o]$, representing the small strain-displacement theory (eqn(5.7.1.6)), may be written as,

$$[B_o] =$$

$$\begin{bmatrix} \hat{X^i}_1 \frac{\partial N_1}{\partial X} & \hat{X^j}_1 \frac{\partial N_1}{\partial X} & \hat{X^k}_1 \frac{\partial N_1}{\partial X} & \rightarrow & \hat{X^k}_8 \frac{\partial N_8}{\partial X} \\ \hat{Y^i}_1 \frac{\partial N_1}{\partial Y} & \hat{Y^j}_1 \frac{\partial N_1}{\partial Y} & \hat{Y^k}_1 \frac{\partial N_1}{\partial Y} & \rightarrow & \hat{Y^k}_8 \frac{\partial N_8}{\partial Y} \\ \hat{X^i}_1 \frac{\partial N_1}{\partial Y} + \hat{Y^i}_1 \frac{\partial N_1}{\partial X} & \hat{X^j}_1 \frac{\partial N_1}{\partial Y} + \hat{Y^j}_1 \frac{\partial N_1}{\partial X} & \hat{X^k}_1 \frac{\partial N_1}{\partial Y} + \hat{Y^k}_1 \frac{\partial N_1}{\partial X} & \rightarrow & \hat{X^k}_8 \frac{\partial N_8}{\partial Y} + \hat{Y^k}_8 \frac{\partial N_8}{\partial X} \end{bmatrix},$$

eqn(5.7.2.8)

which, multiplied by the displacement vector $\{ u_1, v_1, w_1, \ldots\ldots u_8, v_8, w_8 \}$, gives the first order contribution to the local strains, ε_X, ε_Y, and γ_{XY}.

Equations of the form given by eqn(5.5.7(a)), may be substituted into eqn(5.7.2.8) to give $[B_o] = [B_o(\xi, \eta)]$ only.

5.7.3. Non-linear Strain Displacement Matrix $[B_L]$

The second order (non-linear) contributions ($\{\varepsilon^{o\,2}\}$) to the local strains, $\{\varepsilon\}$ (eqn(5.7.1.6)), are given by,

$$\left\{ \varepsilon^{o\,2} \right\} = \begin{Bmatrix} \frac{1}{2} \left[\left(\frac{\partial U}{\partial X} \right)^2 + \left(\frac{\partial V}{\partial X} \right)^2 + \left(\frac{\partial W}{\partial X} \right)^2 \right] \\ \frac{1}{2} \left[\left(\frac{\partial U}{\partial Y} \right)^2 + \left(\frac{\partial V}{\partial Y} \right)^2 + \left(\frac{\partial W}{\partial Y} \right)^2 \right] \\ \left(\frac{\partial U}{\partial X} \right)\left(\frac{\partial U}{\partial Y} \right) + \left(\frac{\partial V}{\partial X} \right)\left(\frac{\partial V}{\partial Y} \right) + \left(\frac{\partial W}{\partial X} \right)\left(\frac{\partial W}{\partial Y} \right) \end{Bmatrix}.$$

eqn(5.7.3.1)

Following a similar procedure to Zienkiewicz,[5.11] the higher order strains, $\{\varepsilon^{o\,2}\}$ (eqn(5.7.3.1)), may be expressed in the form,

$$\left\{ \varepsilon^{o\,2} \right\} = \frac{1}{2} \begin{bmatrix} \{\Delta_X\}^T & \{0\} \\ \{0\} & \{\Delta_Y\}^T \\ \{\Delta_Y\}^T & \{\Delta_X\}^T \end{bmatrix} \begin{bmatrix} \{\Delta_X\} \\ \{\Delta_Y\} \end{bmatrix}$$

$$= \frac{1}{2} [A][\Delta], \qquad \text{eqn(5.7.3.2)}$$

where $\{ \Delta_X \}^T = \left[\frac{\partial U}{\partial X}, \frac{\partial V}{\partial X}, \frac{\partial W}{\partial X} \right]$, and, $\{ \Delta_Y \}^T = \left[\frac{\partial U}{\partial Y}, \frac{\partial V}{\partial Y}, \frac{\partial W}{\partial Y} \right]$.

Taking the variation of eqn(5.7.3.2) gives,

$$d\{ \varepsilon^{o2} \} = \frac{1}{2} d[A][\Delta] + \frac{1}{2} [A] d[\Delta] . \qquad \text{eqn(5.7.3.3)}$$

Examination of the matrices $[A]$ and $[\Delta]$, reveals the following properties,

$$d[A][\Delta] = \begin{bmatrix} d\{\Delta_X\}^T & \{0\} \\ \{0\} & d\{\Delta_Y\}^T \\ d\{\Delta_Y\}^T & d\{\Delta_X\}^T \end{bmatrix} \begin{bmatrix} \{\Delta_X\} \\ \{\Delta_Y\} \end{bmatrix}$$

$$= \begin{bmatrix} \{\Delta_X\}^T & \{0\} \\ \{0\} & \{\Delta_Y\}^T \\ \{\Delta_Y\}^T & \{\Delta_X\}^T \end{bmatrix} \begin{bmatrix} d\{\Delta_X\} \\ d\{\Delta_Y\} \end{bmatrix} = [A] d[\Delta] . \qquad \text{eqn(5.7.3.4)}$$

Substitution of eqn(5.7.3.4) into eqn(5.7.3.3) yields,

$$d\{ \varepsilon^{o2} \} = [A] d\{\Delta\} = [A] \left[[G] d\{\delta\}_i \right] , \qquad \text{eqn(5.7.3.5)}$$

where, as described below, $[G]$ is a matrix relating the local displacement derivatives, $\{ \frac{\partial U}{\partial X}, \frac{\partial V}{\partial X}, \ldots, \frac{\partial W}{\partial Y} \}$ to the global nodal displacements $\{\delta\}_i$.

The matrix $[\Delta]$ (eqn(5.7.3.2)), may be written as,

$$\{\Delta\}^T = \left[\frac{\partial U}{\partial X}, \frac{\partial V}{\partial X}, \frac{\partial W}{\partial X}, \frac{\partial U}{\partial Y}, \frac{\partial V}{\partial Y}, \frac{\partial W}{\partial Y} \right] , \qquad \text{eqn(5.7.3.6(a))}$$

Substitution of equations of the form of eqn(5.7.2.4), yields,

$$[\Delta] = \begin{bmatrix} \sum_{i=1}^{i=8} \hat{X}^i{}_i \frac{\partial N_i}{\partial X}(\xi,\eta) u_i + \sum_{i=1}^{i=8} \hat{X}^j{}_i \frac{\partial N_i}{\partial X}(\xi,\eta) v_i + \sum_{i=1}^{i=8} \hat{X}^k{}_i \frac{\partial N_i}{\partial X}(\xi,\eta) w_i \\ \sum_{i=1}^{i=8} \hat{Y}^i{}_i \frac{\partial N_i}{\partial X}(\xi,\eta) u_i + \sum_{i=1}^{i=8} \hat{Y}^j{}_i \frac{\partial N_i}{\partial X}(\xi,\eta) v_i + \sum_{i=1}^{i=8} \hat{Y}^k{}_i \frac{\partial N_i}{\partial X}(\xi,\eta) w_i \\ \sum_{i=1}^{i=8} \hat{Z}^i{}_i \frac{\partial N_i}{\partial X}(\xi,\eta) u_i + \sum_{i=1}^{i=8} \hat{Z}^j{}_i \frac{\partial N_i}{\partial X}(\xi,\eta) v_i + \sum_{i=1}^{i=8} \hat{Z}^k{}_i \frac{\partial N_i}{\partial X}(\xi,\eta) w_i \\ \sum_{i=1}^{i=8} \hat{X}^i{}_i \frac{\partial N_i}{\partial Y}(\xi,\eta) u_i + \sum_{i=1}^{i=8} \hat{X}^j{}_i \frac{\partial N_i}{\partial Y}(\xi,\eta) v_i + \sum_{i=1}^{i=8} \hat{X}^k{}_i \frac{\partial N_i}{\partial Y}(\xi,\eta) w_i \\ \sum_{i=1}^{i=8} \hat{Y}^i{}_i \frac{\partial N_i}{\partial Y}(\xi,\eta) u_i + \sum_{i=1}^{i=8} \hat{Y}^j{}_i \frac{\partial N_i}{\partial Y}(\xi,\eta) v_i + \sum_{i=1}^{i=8} \hat{Y}^k{}_i \frac{\partial N_i}{\partial Y}(\xi,\eta) w_i \\ \sum_{i=1}^{i=8} \hat{Z}^i{}_i \frac{\partial N_i}{\partial Y}(\xi,\eta) u_i + \sum_{i=1}^{i=8} \hat{Z}^j{}_i \frac{\partial N_i}{\partial Y}(\xi,\eta) v_i + \sum_{i=1}^{i=8} \hat{Z}^k{}_i \frac{\partial N_i}{\partial Y}(\xi,\eta) w_i \end{bmatrix} .$$

eqn(5.7.3.6(b))

From the expression in parentheses on the right side of eqn(5.7.3.5) the matrix [G] is obtained therefore as,

$$[G] = \begin{bmatrix} \hat{X}^i{}_1 \frac{\partial N_1}{\partial X}(\xi,\eta) & \hat{X}^j{}_1 \frac{\partial N_1}{\partial X}(\xi,\eta) & \hat{X}^k{}_1 \frac{\partial N_1}{\partial X}(\xi,\eta) & \rightarrow \hat{X}^k{}_8 \frac{\partial N_8}{\partial X}(\xi,\eta) \\ \hat{Y}^i{}_1 \frac{\partial N_1}{\partial X}(\xi,\eta) & \hat{Y}^j{}_1 \frac{\partial N_1}{\partial X}(\xi,\eta) & \hat{Y}^k{}_1 \frac{\partial N_1}{\partial X}(\xi,\eta) & \rightarrow \hat{Y}^k{}_8 \frac{\partial N_8}{\partial X}(\xi,\eta) \\ \hat{Z}^i{}_1 \frac{\partial N_1}{\partial X}(\xi,\eta) & \hat{Z}^j{}_1 \frac{\partial N_1}{\partial X}(\xi,\eta) & \hat{Z}^k{}_1 \frac{\partial N_1}{\partial X}(\xi,\eta) & \rightarrow \hat{Z}^k{}_8 \frac{\partial N_8}{\partial X}(\xi,\eta) \\ \hat{X}^i{}_1 \frac{\partial N_1}{\partial Y}(\xi,\eta) & \hat{X}^j{}_1 \frac{\partial N_1}{\partial Y}(\xi,\eta) & \hat{X}^k{}_1 \frac{\partial N_1}{\partial Y}(\xi,\eta) & \rightarrow \hat{X}^k{}_8 \frac{\partial N_8}{\partial Y}(\xi,\eta) \\ \hat{Y}^i{}_1 \frac{\partial N_1}{\partial Y}(\xi,\eta) & \hat{Y}^j{}_1 \frac{\partial N_1}{\partial Y}(\xi,\eta) & \hat{Y}^k{}_1 \frac{\partial N_1}{\partial Y}(\xi,\eta) & \rightarrow \hat{Y}^k{}_8 \frac{\partial N_8}{\partial Y}(\xi,\eta) \\ \hat{Z}^i{}_1 \frac{\partial N_1}{\partial Y}(\xi,\eta) & \hat{Z}^j{}_1 \frac{\partial N_1}{\partial Y}(\xi,\eta) & \hat{Z}^k{}_1 \frac{\partial N_1}{\partial Y}(\xi,\eta) & \rightarrow \hat{Z}^k{}_8 \frac{\partial N_8}{\partial Y}(\xi,\eta) \end{bmatrix}, \qquad \text{eqn(5.7.3.7)}$$

with the corresponding global displacement vector,$\{ \delta \}$, as given by eqn(5.3.2.2)

The relationship between the non-linear local element strains and the element global displacement vector, $\{ \delta \}$, may be written as,

$$d\{ \varepsilon^{o\,2} \} = [B_L]\ d\{ \delta_i \} . \qquad \text{eqn(5.7.3.8)}$$

Therefore, by comparing eqn(5.7.3.8) with eqn(5.7.3.5) the expression for the second order strain displacement matrix, [B_L], is obtained as,

$$[B_L] = [A]\ [G] , \qquad \text{eqn(5.7.3.9)}$$

with the matrix [G] as defined by eqn(5.7.3.7) and the matrix [A] by eqn(5.7.3.2)

The matrix [A] (eqn(5.7.3.4)) may be written as a function of the element global displacements as given by the definitions of $\{ \frac{\partial U}{\partial X}, \frac{\partial V}{\partial X}, \ldots\ldots, \frac{\partial W}{\partial Y} \}$ in eqn(5.7.3.6(b)). Consequently, the non-linear terms of the element stiffness matrix, $\left[\overline{K_E{}^e} \right]$, can be seen to be linearly dependent on the nodal displacements, described by the vector $\{ \delta \}_i$ [5.11].

5.7.4. Element Initial Stress Stiffness Matrix.

Based on the principle of virtual work, Zienkiewicz [5.11] has suggested the following relationship for the element initial stress stiffness matrix, or geometric matrix, [$K_\sigma{}^e$],

$$[K_\sigma{}^e]\, d\{ \delta \}_i = \int_{vol} d[B_L]^T \{ \sigma_o \}\ dV , \qquad \text{eqn(5.7.4.1)}$$

where,

Taking the variation of the matrix $[B_L]^T$ (eqn(5.7.3.9)) with respect to the displacement vector $\{\delta\}_i$, yields,

$$d[B_L]^T = \left\{ d[A][G] + [A]\,d[G] \right\}^T \qquad \text{eqn(5.7.4.2)}$$

By substituting eqn(5.7.4.2) into eqn(5.7.4.1), and noting that $d[G] = 0$ and that $\{ d[A][G] \}^T = [G]^T d[A]^T$, gives,

$$[K_\sigma^e]\, d\{\delta_i\} = \int_{vol} [G]^T\, d[A]^T\, \{\sigma_o\}\, dV. \qquad \text{eqn(5.7.4.3)}$$

Substitution of the definition for the matrix $[A]$ (eqn(5.7.3.2)) into the part of eqn(5.7.4.3) written as $d[A]^T \{\sigma_o\}$, gives,

$$d[A]^T \{\sigma_o\} = \begin{bmatrix} d\{\Delta_X\} & \{0\} & d\{\Delta_Y\} \\ \{0\} & d\{\Delta_Y\} & d\{\Delta_X\} \end{bmatrix} \begin{Bmatrix} \sigma_x \\ \sigma_y \\ \tau_{xy} \end{Bmatrix}$$

$$= \begin{bmatrix} d\{\Delta_X\}\sigma_x + d\{\Delta_Y\}\tau_{xy} \\ d\{\Delta_Y\}\sigma_y + d\{\Delta_X\}\tau_{xy} \end{bmatrix}$$

$$= \begin{bmatrix} \sigma_x [I_3]\, d\{\Delta_X\} + \tau_{xy} [I_3]\, d\{\Delta_Y\} \\ \tau_{xy} [I_3]\, d\{\Delta_X\} + \sigma_y [I_3]\, d\{\Delta_Y\} \end{bmatrix}$$

$$= \begin{bmatrix} \sigma_x [I_3] & \tau_{xy} [I_3] \\ \tau_{xy} [I_3] & \sigma_y [I_3] \end{bmatrix} \begin{bmatrix} d\{\Delta_X\} \\ d\{\Delta_Y\} \end{bmatrix}$$

$$= \begin{bmatrix} \sigma_x [I_3] & \tau_{xy} [I_3] \\ \tau_{xy} [I_3] & \sigma_y [I_3] \end{bmatrix} d\{\Delta\} \qquad \text{eqn(5.7.4.4)}$$

where $[I_3]$ is a 3x3 identity matrix.

Substituting for $d\{\Delta\}$ (eqn(5.7.3.5)), into eqn(5.7.4.4), yields,

$$d[A]^T \{\sigma_o\} = [M][G]\, d\{\delta_i\}, \qquad \text{eqn(5.7.4.5)}$$

where the matrix $[M]$ is given as,

$$[M] = \begin{bmatrix} \sigma_x [I_3] & \tau_{xy} [I_3] \\ \tau_{xy} [I_3] & \sigma_y [I_3] \end{bmatrix} . \qquad \text{eqn(5.7.4.6)}^{13}$$

Substitution of eqn(5.7.4.5) into eqn(5.7.4.3) leads to the expression for the element initial stress (or geometric) stiffness matrix, $[K_\sigma{}^e]$, as,

$$[K_\sigma{}^e] = \int_{vol} [G]^T [M] [G] \, dV \qquad \text{eqn(5.7.4.7)}$$

where the matrix $[G]$ is a function of the natural co-ordinates ξ, η (eqn(5.7.3.7)) [14].

The total element stiffness matrix, $[K_t{}^e]$, is obtained as the sum of the large displacement elastic stiffness matrix, $[\overline{K_E{}^e}]$ (eqn(5.7.1.7)), and the initial stress stiffness matrix, $[K_\sigma{}^e]$ eqn(5.7.4.7), as in,

$$[K_t{}^e] = [\overline{K_E{}^e}] + [K_\sigma{}^e] . \qquad \text{eqn(5.7.4.8)}$$

5.7.5. Element Equivalent Nodal Forces.

The general formulation for the vector $\{fe\}$ has been presented in eqn(5.2.2.8). More specifically, in the case of a continuum undergoing large displacements and large strains, the surface stress vector, $\{\sigma_o\}$, is represented (for each element) by the vector, $\{fe\}$, written as,

$$\{fe\} = - \int_{vol} [\bar{B}]^T \{\sigma_o\} \, dV , \qquad \text{eqn(5.7.5.1)}$$

where, the expression for the matrix $[\bar{B}]$ is given in eqn(5.7.1.6) and $\{\sigma_o\}^T = \{\sigma_{xo}, \sigma_{yo}, \tau_{xyo}\} = \{\sigma_{Xo}, \sigma_{Yo}, \tau_{XYo}\}$.

13

In the case of an elastic continuum, the matrix $[M]$ is identical for both the local and global systems of co-ordinates, since the stress vector $\{\sigma_o\}$ is fixed to the membrane and moves with it. Therefore, in this case, eqn(5.7.4.6) may be rewritten as,

$$[M] = \begin{bmatrix} \sigma_x [I_3] & \tau_{xy} [I_3] \\ \tau_{xy} [I_3] & \sigma_y [I_3] \end{bmatrix} = \begin{bmatrix} \sigma_X [I_3] & \tau_{XY} [I_3] \\ \tau_{XY} [I_3] & \sigma_Y [I_3] \end{bmatrix} . \qquad \text{eqn(5.7.4.9)}$$

Consequently, eqn(5.7.4.6) does not need transformation to the local co-ordinate system in order to give the local element initial stress stiffness matrix $[K_\sigma{}^e]$.

14

In the derivation of the initial stress stiffness matrix,$[K_\sigma{}^e]$ (eqn(5.7.4.7)), it has been assumed that the stresses within the element remain constant during elastic straining (eqn(5.7.4.1)). Consequently, the formulation of the matrix, $[K_\sigma{}^e]$, is (in general) applicable to systems subjected to small strains and to small rotations. However, if the elastic modulus of the membrane is set to zero (which is usual in the case of form-finding) no approximation to the stress stiffness matrix is made arising from the violation of the assumption of small strains. The effects of the assumption of small rotations are negated by the removal of the erroneous terms from the stiffness matrix, $[K_\sigma{}^e]$ (Section 5.9).

5.8. Numerical Integration - Gauss Quadrature.

5.8.1. Introduction.

Due to the complexity of the element matrices, $[\bar{B}]$ (eqn(5.7.1.6)), $[A]$ (eqn(5.7.3.4)), and $[G]$ (eqn(5.7.3.7)), the integrals representing the elastic and geometric element stiffness matrices, $[\overline{K_E{}^e}]$ (eqn(5.7.1.7)) and $[K_\sigma{}^e]$ (eqn(5.7.4.3)) cannot be evaluated, in practice, using explicit mathematical techniques. Therefore, a numerical integration algorithm is adopted.

The most widely used form of numerical integration in the field of the finite element analyses, is Gauss Quadrature. Its popularity is based on the fact that it is the most accurate of the quadrature formulae in "ordinary use" [5.12].

The accuracy of the method is obtained by selecting the ordinates, for substitution into the algorithm, at the optimum position for accuracy of the approximation. Therefore, if it is required to calculate the definite integral, $\int_a^b f(x)\,dx$, the method by Gauss provides the locations of the ordinates, such that the interval (a, b) is sub-divided to give the greatest possible accuracy.

The derivation of Gauss Quadrature, for the interval $-1 \leq x \leq 1$, may be found in reference [5.13]. It is shown that, to minimise the error of the algorithm, the points of sub-division of the interval (a, b), should not be equidistant, but symmetrically placed with respect to the mid-point of the interval of integration. Also, it may be shown that Gauss Quadrature gives an exact solution to the definite integral $\int_a^b f(x)\,dx$, when the function $f(x)$, is a polynomial of order $(2n-1)$ or lower, where n is the order of quadrature used.[5.12] For example, if 2×2 quadrature is adopted, then a polynomial of O^3 or less will be integrated exactly by Gauss Quadrature.

5.8.2. Order of Quadrature Required.

The terms comprising the vector of element shape functions $\{N\}$ have been derived according to the interpolation polynomial (Section 5.3),

$$\phi_i = a_1 + a_2\xi + a_3\eta + a_4\xi^2 + a_5\xi\eta + a_6\eta^2 + a_7\xi^2\eta + a_8\xi\eta^2 . \qquad \text{eqn(5.3.3.1)}$$

Clearly, eqn(5.3.3.1) is an expression in two variables (ξ, η), both of O^2, resulting in quadratic element shape functions (Table 5.1). Substitution of the shape functions into the equation for $[K_e{}']$ for example, leads to an integrand with maximum O^3, obtained by expressions of the form $\frac{\partial N(\xi,\eta)}{\partial\xi} \cdot \frac{\partial N(\xi,\eta)}{\partial\eta}$.

Therefore, exact integration of the integrand may be achieved through the use of 2×2 Gauss Quadrature. However, the criterion that the rank of the stiffness matrix, in general, must not be greater than the number of sampled strains in the element must be satisfied also. If the rank of the

stiffness matrix is greater than the number of sampled strains, then the element stiffness matrices, $[\overline{K_E{}^e}]$, and $[K_\sigma{}^e]$, may exhibit spurious mechanisms (or zero energy modes) [5.14]. The phenomenon of a zero energy mode is explained below.

The element global nodal displacements may be related to the element local strains, through the expression (Section 5.7),

$$\{\varepsilon\} = [\bar{B}]\{\delta\}_i \,. \qquad \text{eqn(5.7.1.6)}$$

If the magnitudes of the stresses in the vector of initial stress, $\{\sigma_o\}$, are zero, then the strain energy U_o (eqn(5.2.1.8)), may be rewritten as,

$$U_o = \frac{1}{2}\{\varepsilon\}^T[E]\{\varepsilon\} = \frac{1}{2}\{\delta\}_i{}^T[\overline{K_E{}^e}]\{\delta\}_i$$

$$= \frac{1}{2}\{\delta_i\}^T \int_{vol} [\bar{B}]^T[E][\bar{B}]\, dV\{\delta\}_i \,. \qquad \text{eqn(5.8.2.1)}$$

The general element elastic stiffness matrix, $[\overline{K_E{}^e}]$, is calculated using Gauss Quadrature, in which the interval of integration is sampled at locations which minimise the error of the numerical solution, known as Gauss Points. If the location of the Gauss Points and the mode of element distortion given by the displacement vector, $\{\delta\}_i$, are such that the strains $\{\varepsilon\} = [\bar{B}]\{\delta\}_i$, are zero at all the sampling points, then the strain energy of the element will be zero also. Since the strain energy U_o, is zero for the particular displacement vector $\{\delta\}_i$, it follows that the determinant of the matrix $[\bar{B}]$ is zero also (eqn(5.7.1.6)). Consequently, from eqn(5.8.2.1), the determinant of the element elastic stiffness matrix, $[\overline{K_E{}^e}]$ is similarly zero.

It is expected that an element will exhibit zero strain energy when the displacement vector $\{\delta\}_i$, describes rigid body motion. However, if the strain energy is zero for a displacement vector which does not describe rigid body motion, then the existence of a spurious mode or zero energy mechanism, has been detected. This is typically the result of the application of a Gauss rule of insufficient order. An element which displays zero energy mechanisms is said to be rank deficient [5.14] [15]. The rank of a stiffness matrix is determined as described below.

In the case of an eight noded quadrilateral element, with only two translational degrees of freedom at each node, $\{u, v\}$, three rigid body modes are modelled. These comprise two translational and one in-plane rotation. Therefore, with 16 degrees of freedom, the rank of the element stiffness matrix is 13. If 2x2 Gauss Quadrature is used, then sampling the strains

15

The rank deficiency of a matrix can be demonstrated by factorisation. The resulting upper-triangular element displays zeros below the leading diagonal. The number of rows possessing all zero coefficients is a direct measure of the rank deficiency of the element.

$\{ \varepsilon_X, \varepsilon_Y, \gamma_{XY} \}$ (plane stress), at each Gauss Point, leads to a maximum admissible rank of 2×2×3 = 12 for the element stiffness matrix. Thus, with the 2×2 Gauss rule, the eight noded, 16 degree of freedom element, exhibits one zero energy mechanism, which is shown in Figure 5.9.

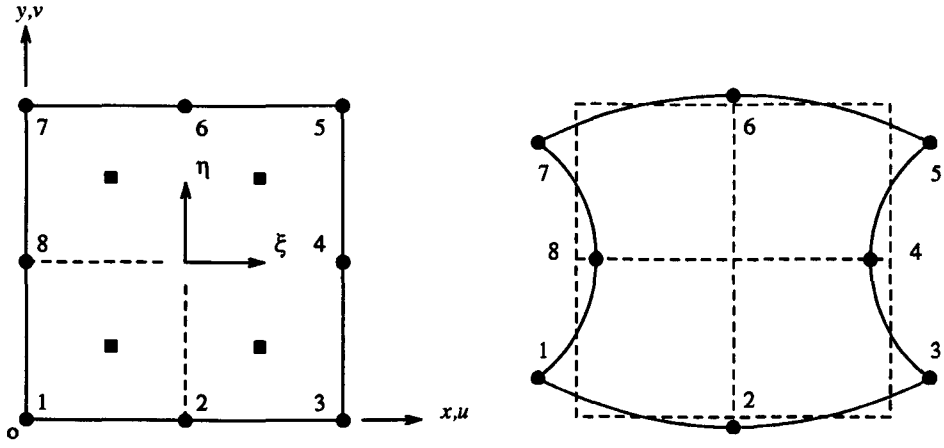

(a) Location of Gauss Points. ■
$(\xi, \eta) = (+-0.57735, +-0.57735)$

(b) Possible "Hour-glass" Mechanism.

Figure 5.9 - Possible Zero Energy Mechanism for 16 DOF Quadrilateral Element.[5.14]

This particular mechanism is suppressed by adjacent elements, through the requirements of displacement (or C^0) compatibility.

The stiffness matrix representing the eight noded quadrilateral element with three translational degrees of freedom at each node, $\{u, v, w\}$, possesses a maximum admissible rank of 12 when evaluated using 2×2 Gauss Quadrature [16]. With 24 degrees of freedom, the eight noded element may display up to six rigid body modes, incorporating three translations and three rotations. Therefore, the element stiffness matrix possesses a rank of 18. By comparing the admissible and the actual ranks of the element stiffness matrix, it can be seen that the use of 2×2 Gauss Quadrature leads to a rank deficiency of six. This implies the existence of six zero energy mechanisms.

Conversely, by adopting 3×3 Gauss Quadrature, then with nine sampling points and three strains at each point, a maximum admissible rank of 27 is obtained for the element stiffness matrix. This is significantly greater than the required value of 18. Selection of the 3×3 Gauss rule removes the possibility of zero energy mechanisms, as required. However, the computational effort is clearly increased when compared with the 2×2 quadrature. Furthermore, during the form-finding of an

16

The admissible rank of the element stiffness matrices of the four and eight noded elements are the same since, in both cases, the condition of plane stress is represented and 2×2 Gauss Quadrature is employed. Consequently, only three strains are sampled at four Gauss points in each element.

5.9. Adequate Representation of Rigid Body Rotations in the Element Stiffness Matrix, $[K_\sigma^e]$.

5.9.1. Introduction.

It is the requirement of any finite element formulation that, if a displacement vector which describes rigid body motion is applied to the element, the resulting motion does not induce strains (or forces at the element nodes). Satisfaction of this requirement not only illustrates that the element is able to model fundamental phenomena which may exist in the analysis of a system, but also, that as the finite element mesh is refined, convergence to the exact solution is assured. As demonstrated in Section 6.4.3.3, Chapter 6, these considerations are significant in the case of a linear element formulation and small displacement theory.

It is generally recognised that both the elastic stiffness matrix, $[\overline{K_E^e}]$, and the stress stiffness matrix, $[K_\sigma^e]$ of general non-linear finite elements, generate zero nodal forces under the application of a displacement vector describing rigid body translation only. Furthermore, the same results are true when an element, which possess elastic stiffness only, is subjected to a displacement vector representing small rigid body rotations. Large rigid body rotation, in general, are not represented as strain free for an element with elastic stiffness only. This is since the usual expressions describing the strain of an elastic continuum are approximate, and only include up to the quadratic displacement terms. Retention of all higher order terms in the expression for the direct and shear strains would result in the general strain free rigid body translation and rotation of an element with elastic stiffness only.[5.14] In such a case, it would be possible to translate, rotate and strain an element with finite displacements, from any location in the global space and, provided the straining component of the displacement vector remained constant, the strain energy would similarly remain constant, and at a minimum.

Conversely, in the case of an element possessing initial stress (or geometric) stiffness alone, only translational rigid body modes yield zero strain energy. This is demonstrated by conducting an eigenvalue analysis (Section 6.3, Chapter 6) on an element stress stiffness matrix, $[K_\sigma^e]$, from which three zero eigenvalues are obtained, as opposed to the required six which are displayed by the elastic stiffness matrix, $[\overline{K_E^e}]$. By displaying the corresponding eigenvectors, it is shown that the three zero eigenvalues correspond to two in-plane and one out-of-plane rigid body translations. As described below, the loss of the three zero eigenvalues, whose eigenvectors describe rigid body rotation, can be attributed to the modelling of the internal stress of the element.

Any stress state, described typically at the Gauss points, may be represented by a set of equivalent forces, acting at each of the element nodes. During the application of the rigid body rotation vector $\{\underline{\delta}\}_{Rr}$ it is required that the magnitude of the element nodal forces remain

unchanged, in order to describe the internal stress of the element consistently, and to maintain the internal equilibrium of the element. In addition, a change in direction of the forces, equal to that defined by the rigid body motion of the element, is required.

During both the eigenvalue analysis, and the incremental step of the analysis of a geometrically non-linear system, the magnitudes and directions of the nodal forces at the end of the iterative step are assumed to be the same as at the start of it. Consequently, as the element undergoes a rigid body rotation, additional fictitious nodal forces are generated by the change in direction of the element (given by the orientation of the element prior and subsequent to the application of the rigid body rotation vector, $\{\underline{\delta}\}_{Rr}$), while the directions of the element nodal forces remain unchanged. Thus, after the application of the vector $\{\underline{\delta}\}_{Rr}$, the nodal forces become inconsistent with the stress state within the element. The difference between the assumed values of the nodal forces before, and after, rigid body rotation, is treated as an external load vector. The external load vector can be assumed to induce strains into the element. These strains then give rise to non-zero eigenvalues which are associated with the rigid body rotations of the element. Conversely, when the displacement vector $\{\underline{\delta}\}_R$ describes rigid body translation alone, the direction and orientation of the element remains unchanged. Therefore, the assumption that the magnitudes and directions of the element equivalent nodal forces are constant, is valid. Thus, rigid body translation is strain free, as illustrated by the three zero eigenvalues mentioned previously.

Lui and Yang [5.22] have proposed a "General Eigenvalue Test for Non-linear Finite Elements". The theory presented in reference [5.22] may be used to include strain free rigid body rotation explicitly for non-linear finite elements with prestress. The relevant sections of the paper by Lui and Yang[5.22] are summarised below.

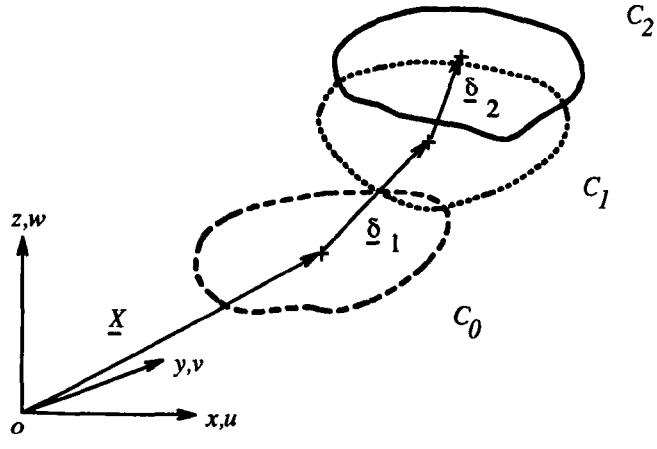

Figure 5.11 [5.22] - Path of a General Finite Element During an Incremental Solution.

Figure 5.11 shows a general finite element as it passes from an initial configuration C_0, through a known equilibrium configuration, C_1, and finally to a neighbouring desired equilibrium configuration C_2. It is assumed that C_2 is incrementally close to C_1.

For each finite element, an incremental equation of equilibrium may be written as the element moves from configuration C_1 to C_2, and is given as,

$$[\overline{K_E{}^e}]\Big|^1 \{\underline{\delta}\}\Big|_1^2 + [K_\sigma{}^e]\Big|^1 \{\underline{\delta}\}\Big|_1^2 = \{fe\}\Big|^2 - \{fe\}\Big|^1 \qquad \text{eqn(5.9.1.1)}$$

where;

$\{\underline{\delta}\}\Big|_1^2$ is the displacement vector as the finite element moves from C_1 to C_2,

$[\overline{K_E{}^e}]\Big|^1$ and $[K_\sigma{}^e]\Big|^1$ are the elastic and stress (geometric) stiffness matrices respectively, as evaluated at the configuration C_1, and,

$\{fe\}\Big|^2$ and $\{fe\}\Big|^1$ are the nodal force vectors as given at configuration C_1 and C_2.

The requirement that the equivalent nodal forces remain consistent with the internal equilibrium of the element during rigid body rotation, may be written as,

$$\{fe\}\Big|^2 = [R]_r \{fe\}\Big|^1 \qquad \text{eqn(5.9.1.2)}$$

where $[R]_r$ is a rotation matrix describing the rigid motion of the element.

For purely translational rigid body motion, the matrix $[R]_r$ becomes the identity matrix. For rigid body rotation angles which are small, the diagonal terms of eqn(5.9.1.2) remain as unity, with the other terms either zero or a function of the angle of rigid body rotation. Therefore, the right side of eqn(5.9.1.1) describes the vector of additional fictitious nodal forces, generated by the rigid body rotation of the element. A relationship between these additional nodal forces and the displacement vector describing rigid body rotation, $\{\underline{\delta}\}_{Rr}$, may be written as,

$$\{fe\}\Big|^2 - [R]_r \{fe\}\Big|^1 = [K_\sigma{}^e]_{ex} \{\underline{\delta}\}_{Rr} \qquad \text{eqn(5.9.1.3)}$$

where the matrix $[K_\sigma{}^e]_{ex}$ is termed the external stiffness matrix [5.22].

The terms of this matrix may be obtained by extracting the nodal displacement variables from the expressions for the additional fictitious nodal forces given by the left side of eqn(5.9.1.3).

By subtracting the external stiffness matrix $[K_\sigma{}^e]_{ex}$ from the stress stiffness matrix, $[K_\sigma{}^e]\Big|^1$, the internal [5.22] stiffness matrix, $[K_\sigma{}^e]_{in}$ may be obtained as,

$$[K_\sigma{}^e]_{in} = [K_\sigma{}^e]\Big|^1 - [K_\sigma{}^e]_{ex} \qquad \text{eqn(5.9.1.4)}$$

When performing an eigenvalue analysis on the internal stress matrix, $[K_\sigma{}^e]_{in}$, a full complement of six zero eigenvalues is obtained, with the associated eigenvectors displaying three

rigid body translations, plus three rigid body rotations (Section 6.3, Chapter 6). Therefore, through the use of eqn(5.9.1.2) to eqn(5.9.1.4), the fictitious stiffness terms generated when the element undergoes a rigid body rotation, can be suppressed explicitly in the formulation of a non-linear finite element, subjected to prestress.

Reference [5.22] presents an application of this approach to a simple in-plane, two dimensional beam element. However, it is possible to extend the same theory to the curved quadrilateral element, formulated in the preceding sections of this chapter. The main differences in the extended application of this theory to that given in reference [5.22], are as follows:

- the definition of the rigid body rotation angle, θ_r, necessary to generate the matrix, $[\,R\,]_r$, and,
- the terms of the external stiffness matrix, $[\,K_\sigma{}^e\,]_{ex}$.

5.9.2. Definition of the Rigid Body Rotation Angle, θ_r

In the case of a plane two dimensional element (Figure 5.12), the rotation matrix, $[\,R\,]_{rB}$, may be written as,

$$[\,R\,]_{rB} = \begin{bmatrix} 1 & -\theta_r & 0 & 0 \\ \theta_r & 1 & 0 & 0 \\ 0 & 0 & 1 & -\theta_r \\ 0 & 0 & \theta_r & 1 \end{bmatrix} \qquad \text{eqn(5.9.2.1)}$$

where $\theta_R = \dfrac{v^A - v^B}{L}$, with v^A the displacement in the direction y^1 at node A, and v^B similarly at node B. L is defined as the length of the bar at configuration C_1. (Angles of small rotation are assumed in the above.)

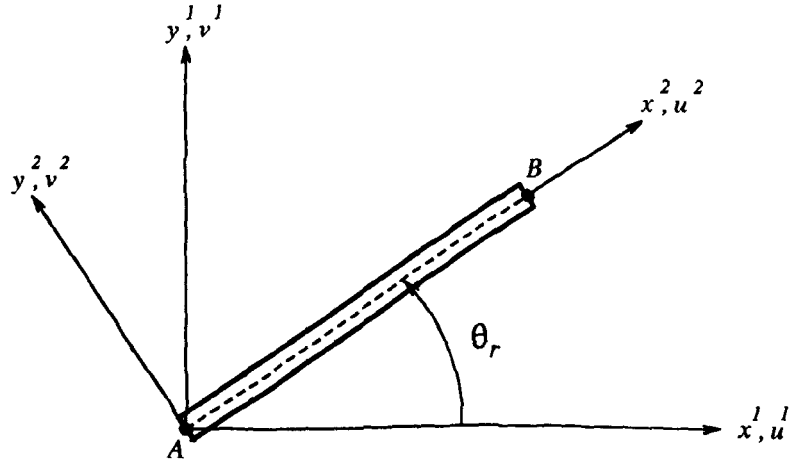

Figure 5.12 [5.22] - Beam Finite Element Subjected to a Rigid Body Rotation, θ_r.

However, for a general curved finite element, rigid body rotation may occur about three local axes - about a vector normal to the middle surface of the element, and about two orthogonal vectors tangential to the middle surface. Calculation of the rigid body rotation angle, θ_r, is clearly dependent on all of the element nodal degrees of freedom. Thus the initial problem is to assess the contribution of the individual nodal displacements to the overall element rigid body rotation angle, θ_r. Considering rotation about a vector normal to the middle surface of the element initially, an assessment of the magnitude of the angle, $\theta_r{}^{ip}$, is made in the subsequent paragraphs.

A plane quadratic element is shown in Figure 5.13, prior and subsequent to the application of a general displacement vector $\{\underline{\delta}\}$.

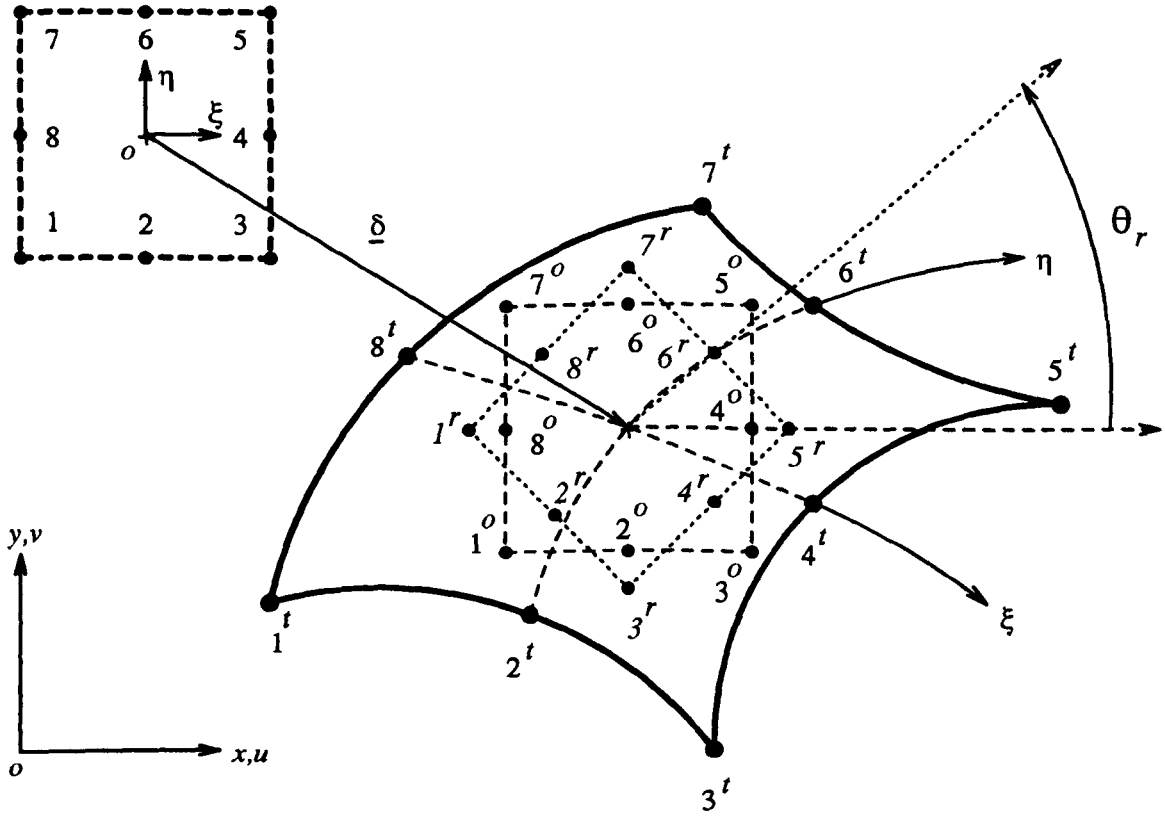

Figure 5.13 - Plane Quadrilateral Finite Element Subjected to a General Displacement Vector, $\underline{\delta}$.

where the element numbered with the superscript "*o*" is the original undeformed element subjected to the rigid body translation components of $\{\underline{\delta}\}$ only. The superscript "*r*" indicates the original element with both the rigid body translation and suggested rigid body rotation components of $\{\underline{\delta}\}$ applied, while the element with the superscript "*t*" denotes the original element subjected to all the terms of the displacement vector $\{\underline{\delta}\}$, i.e. rigid body translation, rigid body rotation, and the strain inducing terms.

It is postulated that during the deformation of the original element, both rigid body translation and rigid body rotation occur (Figure 5.13). Both types of rigid body displacements may be subtracted from the overall displacement vector to find the straining components of the vector $\{\underline{\delta}\}$.

When considering rigid body rotation in the finite element formulation, a fictitious increase in strain energy may be observed, with an increase in the angle of rigid body rotation. This is illustrated in Figure 5.14 which shows the strain energy associated with the variation of rigid body rotation angle θ_r for a plane quadratic element. The ordinate has been expressed as a percentage of the strain energy generated by a unit strain in both the global x and y directions.

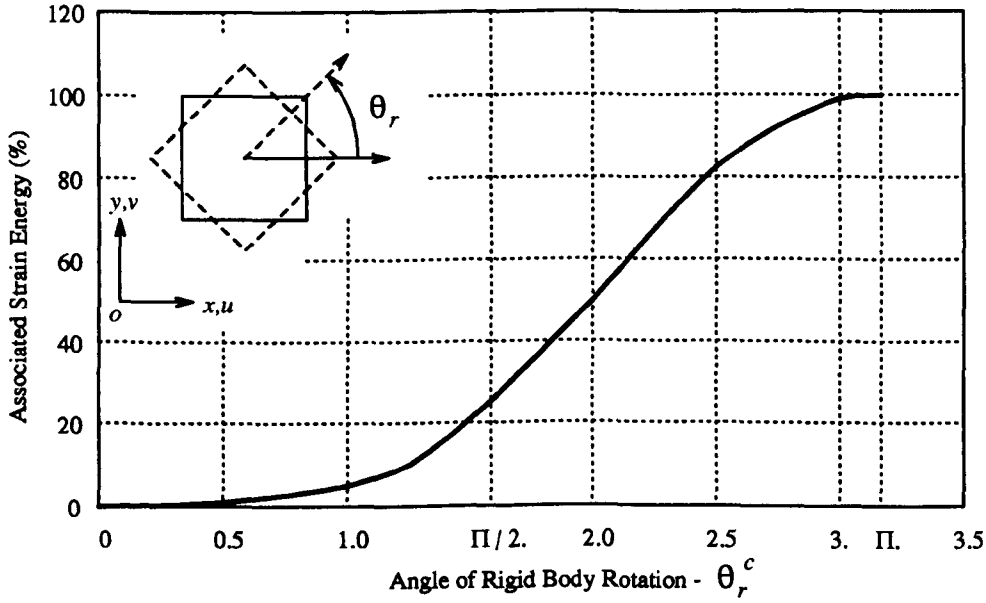

Figure 5.14 - Associated Strain Energy with Variation in Rigid Body Rotation, θ_r.

When the general displacement vector, $\{\underline{\delta}\}$, exhibits zero rigid body rotation, it can be seen that the strain energy of the deformed element is a minimum (Figure 5.14). Consequently, as described below, by monitoring the strain energy of an initially undeformed element subjected to a variable angle of rigid body rotation, an assessment of the amount of rigid body rotation contained within the displacement vector, $\{\underline{\delta}\}$, may be made.

As a first estimate, the evaluation of the characteristic matrices of the undeformed element is performed using the original orientation of the element. Thus it is only the nodal displacements which are amended with the varied angle of rigid body rotation. For example, with reference to eqn(5.8.2.1), the strain energy, U_o, generated within a finite element when subjected to a general displacement vector, $\{\underline{\delta}\}$, may be written as,

$$U_o = \frac{1}{2}\left[[\bar{B}]\{\underline{\delta}\}\right]^T [E][\bar{B}]\{\underline{\delta}\} \qquad \text{eqn(5.9.2.2)}$$

In order to assess the contribution of the rigid body rotation to the displacement vector $\{\underline{\delta}\}$, eqn(5.9.2.2) may be rewritten here as,

$$U_o = \frac{1}{2}\left[[B_s]\left(\{\underline{\delta}\} - \{\underline{\delta}_r(\theta_r)\}\right)\right]^T [E][B_s]\left(\{\underline{\delta}\} - \{\underline{\delta}_r(\theta_r)\}\right)$$

eqn(5.9.2.3)

where $\{\underline{\delta}_r(\theta_r)\}$ is a displacement vector describing the rigid body rotation of the element, as a function of the rotation angle θ_r. The matrix $[B_s]$ has been substituted for $[\bar{B}]$ in eqn(5.9.2.2), as it is assumed that no initial nodal displacements occur prior to the application of the displacement vector $\{\underline{\delta}\}$.

The value of the matrix $[B_s]$ is held constant and is based on the original undeformed element. As the vector $\{\underline{\delta}_r(\theta_r)\}$ is varied, the strain energy of the deformed element is monitored, until a minimum value is reached, with a corresponding value of θ_r.

When comparing the results for θ_r using this approach, with the known imposed rigid body rotation angle, good agreement is obtained provided the displacement vector $\{\underline{\delta}\}$ describes small strains and small rotations. Since the matrix $[B_s]$ is linear and only dependent on the first order terms of the strain-displacement relation, the higher order components of strain are not represented. This may result in an under-estimate of the strain energy of deformation. Thus, a false strain energy minimum can be encountered, giving an erroneous measure of the rigid body rotation angle, θ_r.

An alternative formulation is suggested below therefore, which seeks to minimise the error induced by the violation of the assumptions inherent in the derivation of the matrix $[B_s]$, whilst maximising the strain energy within the element.

Instead of establishing the matrix $[B_s]$ (eqn(5.9.2.3)) on the undeformed element in its original orientation, the terms of the matrix, $[B_s]$, may be written as a function of the rigid body rotation angle, θ_r. In this case, the undeformed element is rotated through an angle θ_r, and the matrix $[B_s(\theta_r)]$ is calculated, based on the updated element configuration. Consequently, eqn(5.9.2.3) may be rewritten as,

$$U_o = \frac{1}{2}\left[[B_s(\theta_r)]\left(\{\underline{\delta}\} - \{\underline{\delta}_r(\theta_r)\}\right)\right]^T [E][B_s(\theta_r)]\left(\{\underline{\delta}\} - \{\underline{\delta}_r(\theta_r)\}\right)$$

eqn(5.9.2.4)

By writing the matrix $[B_s]$ as a function of the rigid body rotation angle, θ_r, it is possible to maximise the components of local strain in the deformed element, with respect to the displacement vector, $\{\underline{\delta}\}$, and the rigid body rotation angle, θ_r. This, in turn, yields a maximum value of the strain energy of deformation. As demonstrated by the subsequent examples, the strain energy induced through any displacement terms in the vector $\{\underline{\delta}\}$ corresponding to those of

the rigid body rotation type, is not sufficient to give a false strain energy maximum.

Figure 5.15 presents the strain energy for a plane square element, subjected to a unit strain in both the global x and y directions. The strain energy, U_o, is quoted as the sum of the strain energies at the four element Gauss points, based on the elastic constants as presented in Figure 5.15.

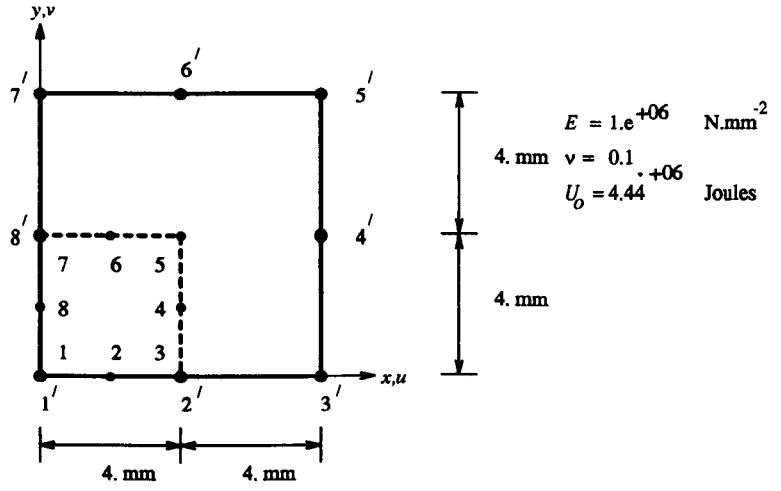

Figure 5.15 - Strain Energy of Plane Element Under Uniform Unit Strain.

The element is now subjected to an additional, arbitrary, rigid body translation, and a rigid body rotation of 0.75^c ($= \theta_r{}^{true}$). The relationship between the rigid body rotation angle, θ_r, as applied to the undeformed element (in the global xy plane), and the strain energy (eqn(5.9.2.4)) of the deformed element, is presented in Figure 5.16.

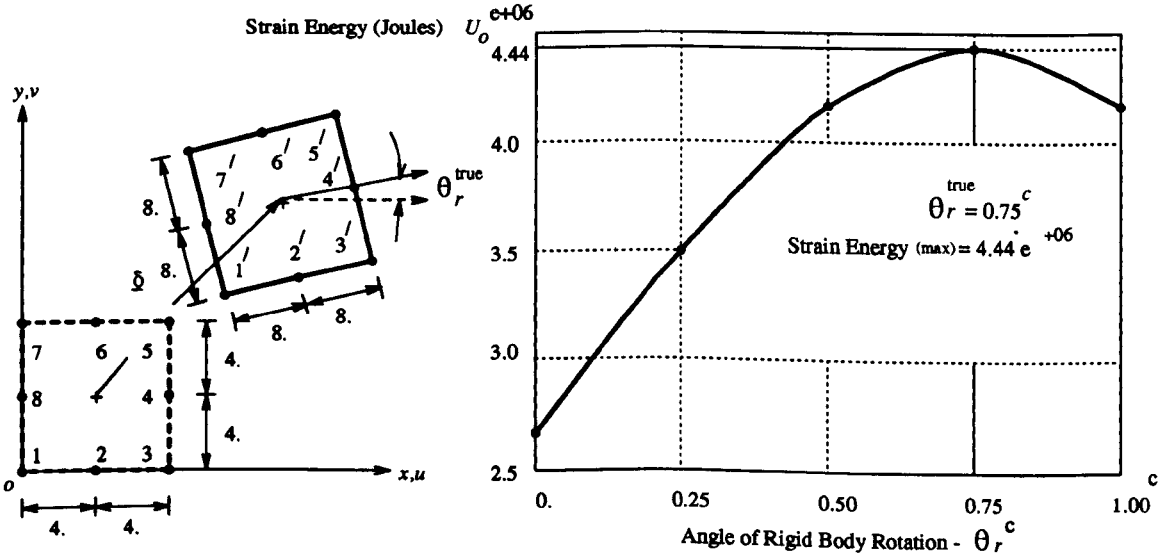

Figure 5.16 - Example 5.1

Associated Strain Energy with Variation in Rigid Body Rotation, θ_r.

As the rigid body rotation angle is increased from 0^c to 0.75^c, the strain energy can be seen to tend to the known exact value (Figure 5.16). The true (maximum) value is observed when θ_r

corresponds to the accurate value of the rigid body rotation.

The following examples are included to show the application of this procedure to elements of a similar undeformed shape to that shown in Figure 5.15, but under the application of various displacement vectors $\{\underline{\delta}\}$. The elements are considered to remain in the global x, y plane. The cases illustrated in Figure 5.17 (a)-(c) are assumed to have the same constants of elasticity as given in Figure 5.15, and the same notation as in Figure 5.13. The displacement vectors of each example (Figure 5.17 (a)-(c)) are presented in Appendix 5-C.

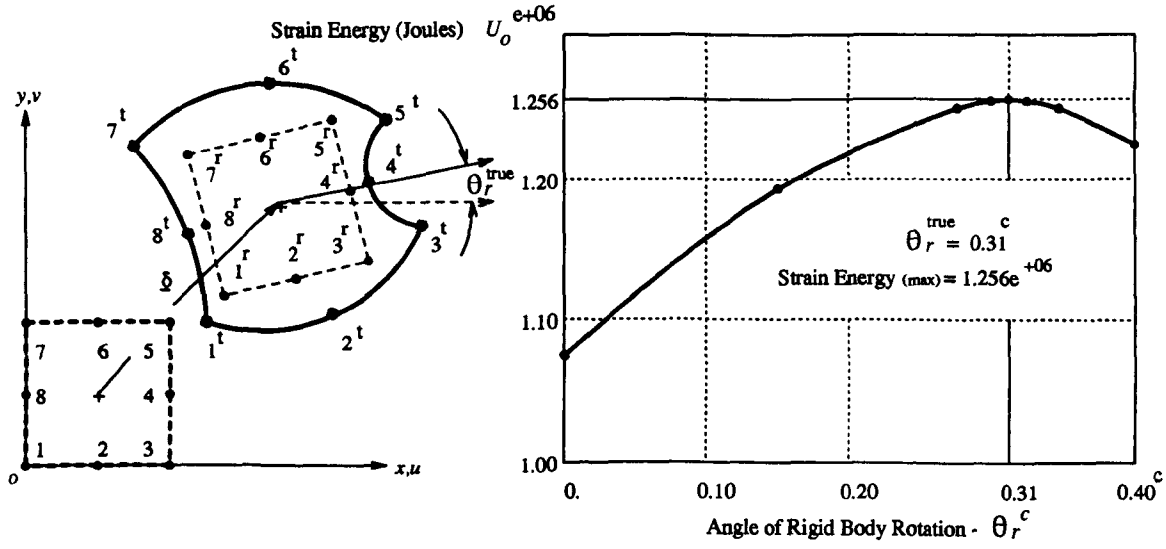

Figure 5.17(a) - Example 5.2

Associated Strain Energy with Variation in Rigid Body Rotation, θ_r.

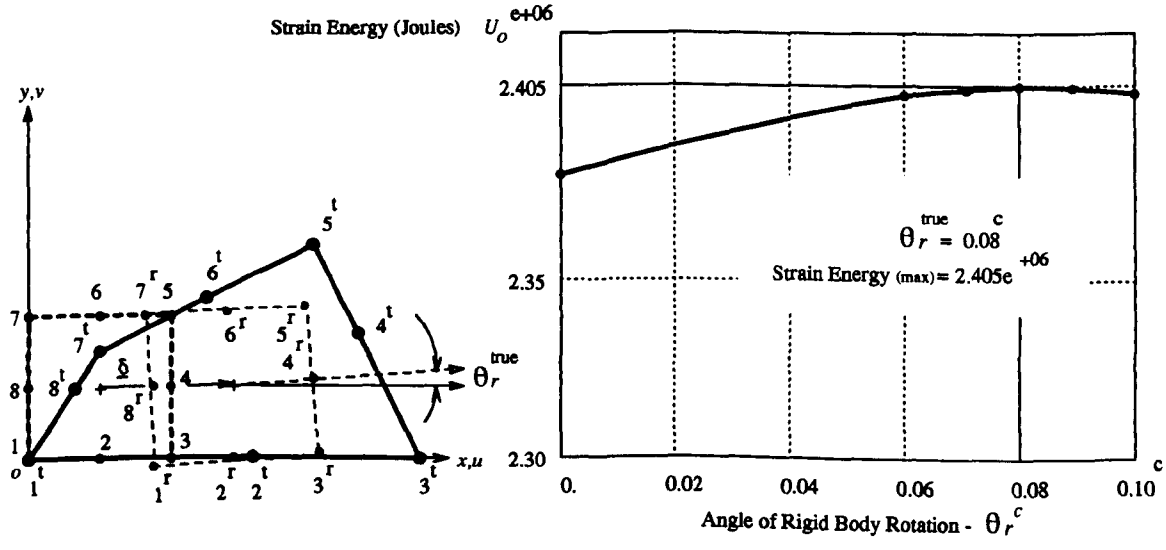

Figure 5.17(b) - Example 5.3

Associated Strain Energy with Variation in Rigid Body Rotation, θ_r.

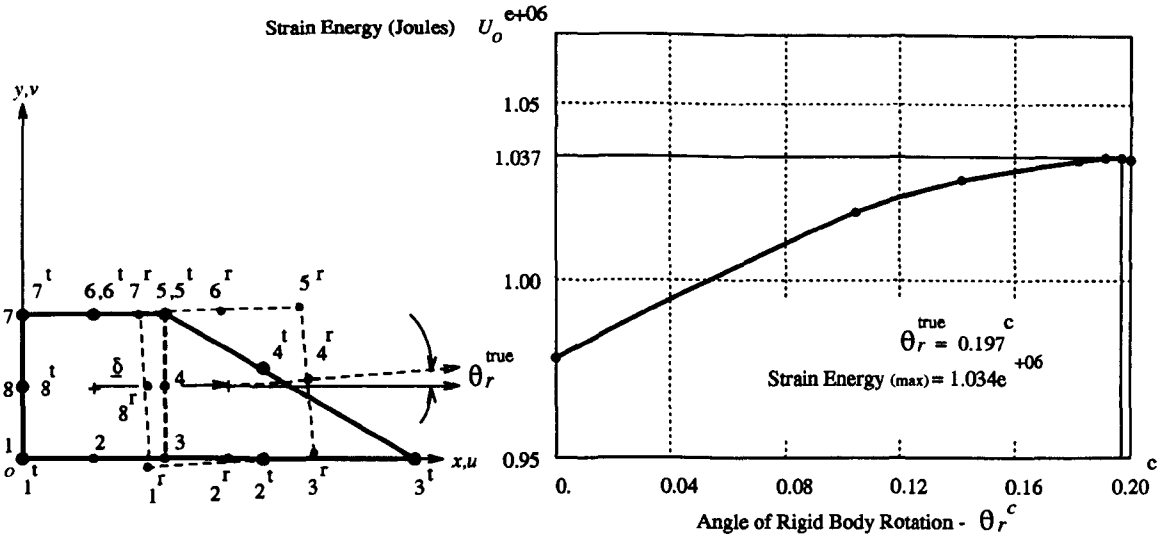

Figure 5.17(c) - Example 5.4

Associated Strain Energy with Variation in Rigid Body Rotation, θ_r.

The product of the element matrix $[B_s]$, calculated subsequent to the application of the rigid body rotation terms given in the displacement vector $\{\underline{\delta}\}$ to the undeformed element, with the net displacement $\{\underline{\delta}\} - \{\underline{\delta}_r(\theta_r)\}$ has been shown (Examples 5.2 - 5.4) to lead to a maximisation of the strain energy of the deformation, when the rigid body rotation angle θ_r is represented accurately. An adequate estimate of the rigid body rotation angle θ_r can therefore be made through this iterative type of approach. From these results, an algebraic expression is proposed below which relates explicitly the element nodal displacements, $\{\underline{\delta}\}$, to the angle of rigid body rotation, θ_r, through the element natural base vectors, $\vec{\xi}$ and $\vec{\eta}$.

Considering the angle of rigid body rotation, θ_r^{ip}, about a vector normal to the middle surface of the element, constructed at the origin of the natural co-ordinate system, (ξ, η), it is postulated that the magnitude of the angle θ_r^{ip} may be related to the change in the direction of the base vectors $\vec{\xi}$ and $\vec{\eta}$ as,

$$\theta_r^{ip} \approx \frac{(\Delta\vec{\xi} + \Delta\vec{\eta})}{2}, \qquad \text{eqn(5.9.2.5)}$$

where $\Delta\vec{\xi}$ is the angle through which the base vector $\vec{\xi}$ is moved, subsequent to the application of the displacement vector $\{\underline{\delta}\}$ (Figure 5.18). Similarly, $\Delta\vec{\eta}$ is the angle through which the base vector $\vec{\eta}$ is moved, due to the vector $\{\underline{\delta}\}$, as shown in Figure 5.19.

A comparison of eqn(5.9.2.5) with the results obtained through the maximisation of eqn(5.9.2.4), for the examples shown in Figure 5.16 and Figure 5.17(a)-(c) are presented in Table 5.4.

Example.	θ_r^{ip} (eqn(5.9.2.4)^{max})	θ_r^{ip} (eqn(5.9.2.5))	Error in eqn(5.9.2.5).
5.1	0.75^c	0.75^c	0.%
5.2	0.31^c	0.32^c	0.8%
5.3	0.080^c	0.062^c	22.5%
5.4	0.20^c	0.23^c	15.0%

Table 5.4 - Accuracy of eqn(5.9.2.5) in Estimating θ_r^{ip}.

A wide range of error values can be seen to exist for the examples tested (Table 5.4). This feature may be attributed to the violation of the assumption of uniform strain. For example, in writing eqn(5.9.2.5), it has been assumed that the strains in the local element directions X, Y, are equal or of similar magnitude. The elements in Example 5.3 and Example 5.4 (Figure 5.17(b) and Figure 5.17(c), respectively) are not characterised by deformation modes which generate a state of uniform strain. Thus, as illustrated by the error measures presented in Table 5.4, it can be seen that violation of the implicit assumption in eqn(5.9.2.5), leads to the generation of relatively large errors in the estimate for θ_r^{ip}.

However, in case of the form-finding of an elastic membrane subjected to a constant stress field, uniform straining within individual elements may be closely approximated with mesh refinement. Thus, eqn(5.9.2.5) may closely estimate the angle of rigid body rotation, θ_r^{ip}, when a global state of constant strain exists, or when the element size tends to zero.

The derivations of the expressions for $\Delta\vec{\xi}$ and $\Delta\vec{\eta}$ involving the nodal displacements of the element, are given below. The expression for $\Delta\vec{\xi}$ is presented initially. It is convenient to calculate the angle change $\Delta\vec{\xi}$ in an additional local co-ordinate system, tangential to the middle surface of the element, at the natural co-ordinate location $(\xi, \eta) = (0, 0)$ (Figure 5.18).

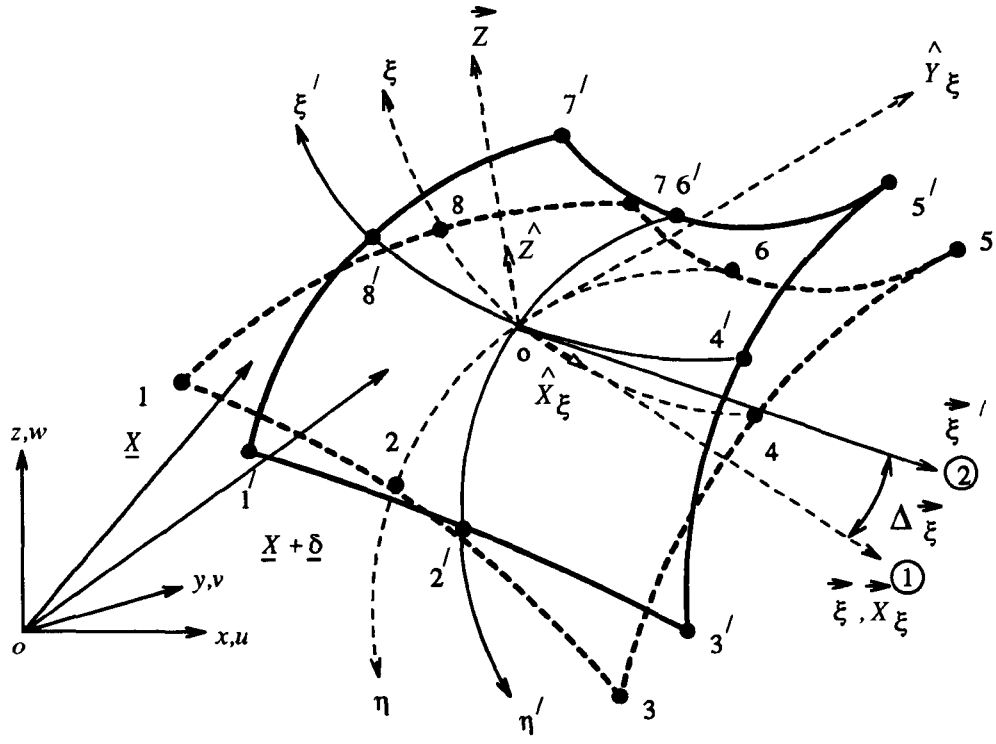

Figure 5.18 - An Element Subjected to a Rigid Body Rotation, θ_r^{ip}. The Component $\Delta\vec{\xi}$.

where $\vec{\xi}$ and $\vec{\xi}'$ are base vectors prior and subsequent to the application of the global displacement vector $\{\underline{\delta}\}$ respectively.

The vector $\vec{Z}$, normal to the middle surface of the element is defined by eqn(5.4.5). Using eqn(5.4.4) and eqn(5.4.7), the local co-ordinate directions $\vec{X}_\xi$ and $\vec{Y}_\xi$, may be described similarly. Taking the axis of the vector $\vec{Z}$ as the origin of the local co-ordinate system $(\vec{X}_\xi, \vec{Y}_\xi)$, the base vector $\vec{\xi}$ may be transformed into the $\vec{X}_\xi, \vec{Y}_\xi$ plane, as (eqn(5.4.4)),

$$\begin{Bmatrix} X_{\xi 1} \\ Y_{\xi 1} \end{Bmatrix} = \begin{Bmatrix} \hat{X}_\xi{}^i \frac{\partial x}{\partial \xi} + \hat{X}_\xi{}^j \frac{\partial y}{\partial \xi} + \hat{X}_\xi{}^k \frac{\partial z}{\partial \xi} \\ \hat{Y}_\xi{}^i \frac{\partial x}{\partial \xi} + \hat{Y}_\xi{}^j \frac{\partial y}{\partial \xi} + \hat{Y}_\xi{}^k \frac{\partial z}{\partial \xi} \end{Bmatrix} \qquad \text{eqn(5.9.2.6)}$$

where the superscripts, i, j and k, correspond to the global directions x, y and z, and $X_{\xi 1}, Y_{\xi 1}$ are the local co-ordinates of the base vector $\vec{\xi}$.

After application of the general displacement vector, $\{\underline{\delta}\}$, it is assumed that the vector $\vec{\xi}$ moves into a new direction $\vec{\xi}'$, as shown in Figure 5.18. The base vector $\vec{\xi}'$, may be similarly transformed into the local co-ordinate directions, $\vec{X}_\xi, \vec{Y}_\xi$, and written as,

$$\begin{Bmatrix} X_{\xi 2} \\ Y_{\xi 2} \end{Bmatrix} = \begin{Bmatrix} \hat{X}_\xi{}^i \frac{\partial x}{\partial \xi} + \hat{X}_\xi{}^i \frac{\partial u}{\partial \xi} + \hat{X}_\xi{}^j \frac{\partial y}{\partial \xi} + \hat{X}_\xi{}^j \frac{\partial v}{\partial \xi} + \hat{X}_\xi{}^k \frac{\partial z}{\partial \xi} + \hat{X}_\xi{}^k \frac{\partial w}{\partial \xi} \\ \hat{Y}_\xi{}^i \frac{\partial x}{\partial \xi} + \hat{Y}_\xi{}^i \frac{\partial u}{\partial \xi} + \hat{Y}_\xi{}^j \frac{\partial y}{\partial \xi} + \hat{Y}_\xi{}^j \frac{\partial v}{\partial \xi} + \hat{Y}_\xi{}^k \frac{\partial z}{\partial \xi} + \hat{Y}_\xi{}^k \frac{\partial w}{\partial \xi} \end{Bmatrix}$$

eqn(5.9.2.7)

where u, v and w are the components of the global displacement vector, $\{\underline{\delta}\}$, in the directions x, y and z, respectively. Assuming that the angle of the rigid body rotation is small, $\Delta\vec{\xi}$, may be given as,

$$\Delta\vec{\xi} \approx \frac{Y_{\xi 2} - Y_{\xi 1}}{\left|\vec{\xi}\right|} \qquad \text{eqn(5.9.2.8)}$$

A similar procedure may be adopted for calculating the term $\Delta\vec{\eta}$ (eqn(5.9.2.5)). In this case, however, the local co-ordinate direction, $\hat{X}_\eta$, is aligned with the base vector $\vec{\eta}$ (Figure 5.19), such that,

$$\hat{X}_\eta = \frac{\frac{\partial \underline{X}}{\partial \eta}}{\left|\frac{\partial \underline{X}}{\partial \eta}\right|} = \frac{\vec{\eta}}{\left|\vec{\eta}\right|} \qquad \text{eqn(5.9.2.9)}$$

where $\underline{X}$ is the position vector of the centre of the element in global co-ordinates.

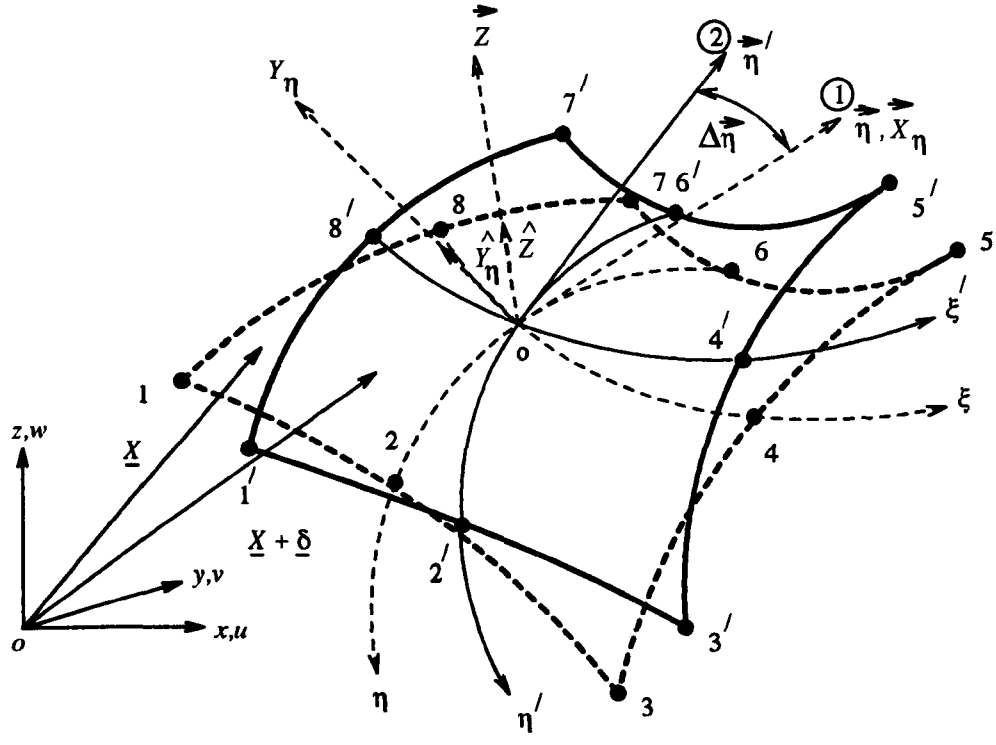

Figure 5.19 - An Element Subjected to a Rigid Body Rotation, $\theta_r{}^{ip}$. The Component $\Delta\vec{\eta}$.

Thus, the unit vector, $\hat{Y}_\eta$, in the local co-ordinate direction, $\vec{Y}_\eta$, may be written as,

$$\hat{Y}_\eta = \frac{\vec{Y}_\eta}{\left|\vec{Y}_\eta\right|} = \frac{\vec{Z} \times \hat{X}_\eta}{\left|\vec{Y}_\eta\right|} \qquad \text{eqn(5.9.2.10)}$$

where $\vec{Z}$ is as given in eqn(5.4.5)

The base vectors, $\vec{\eta}$ and $\vec{\eta}'$, may be transformed into the local co-ordinate system with eqn(5.9.2.9) and eqn(5.9.2.10). Assuming small angles, $\Delta\vec{\eta}$ may be written in a similar manner to eqn(5.9.2.8), as,

$$\Delta\vec{\eta} \approx \frac{Y_{\eta 2} - Y_{\eta 1}}{\left|\vec{\eta}\right|} \qquad \text{eqn(5.9.2.11)}$$

where,

$$Y_{\eta 1} = \hat{Y}_\eta{}^i \frac{\partial x}{\partial \eta} + \hat{Y}_\eta{}^j \frac{\partial y}{\partial \eta} + \hat{Y}_\eta{}^k \frac{\partial z}{\partial \eta}$$

and,

$$Y_{\eta 2} = \hat{Y}_\eta{}^i \frac{\partial x}{\partial \eta} + \hat{Y}_\eta{}^i \frac{\partial u}{\partial \eta} + \hat{Y}_\eta{}^j \frac{\partial y}{\partial \eta} + \hat{Y}_\eta{}^j \frac{\partial v}{\partial \eta} + \hat{Y}_\eta{}^k \frac{\partial z}{\partial \eta} + \hat{Y}_\eta{}^k \frac{\partial w}{\partial \eta}$$

Therefore, substitution of eqn(5.9.2.8) and eqn(5.9.2.11) into eqn(5.9.2.5) yields an expression for the angle of in-plane rigid body rotation, $\theta_r{}^{ip}$, in terms of the nodal displacements, as

$$\theta_r{}^{ip} \approx \frac{1}{2}\left[\frac{Y_{\xi 2} - Y_{\xi 1}}{\left|\vec{\xi}\right|} + \frac{Y_{\eta 2} - Y_{\eta 1}}{\left|\vec{\eta}\right|}\right] \qquad \text{eqn(5.9.2.12(a))}$$

or, more usefully,

$$\theta_r{}^{ip} \approx \frac{1}{2}\left[\frac{\hat{Y}_\xi{}^i}{\left|\vec{\xi}\right|}\frac{\partial u}{\partial \xi} + \frac{\hat{Y}_\eta{}^i}{\left|\vec{\eta}\right|}\frac{\partial u}{\partial \eta} + \frac{\hat{Y}_\xi{}^j}{\left|\vec{\xi}\right|}\frac{\partial v}{\partial \xi} + \frac{\hat{Y}_\eta{}^j}{\left|\vec{\eta}\right|}\frac{\partial v}{\partial \eta} + \frac{\hat{Y}_\xi{}^k}{\left|\vec{\xi}\right|}\frac{\partial w}{\partial \xi} + \frac{\hat{Y}_\eta{}^k}{\left|\vec{\eta}\right|}\frac{\partial w}{\partial \eta}\right]$$

eqn(5.9.2.12(b))

The angles of rigid body rotation about a pair of orthogonal vectors tangential to the middle surface of the element, $\theta_r{}^X$ and $\theta_r{}^Y$, may be obtained in a similar manner. An accurate estimate of this type of rigid body rotation may be obtained by calculating the change in direction of the vector $\hat{Z}$, normal to the surface of the element. The rigid body rotation, $\theta_r{}^X$, about the local co-ordinate direction $\hat{X}_X$ (Figure 5.20), is derived below.

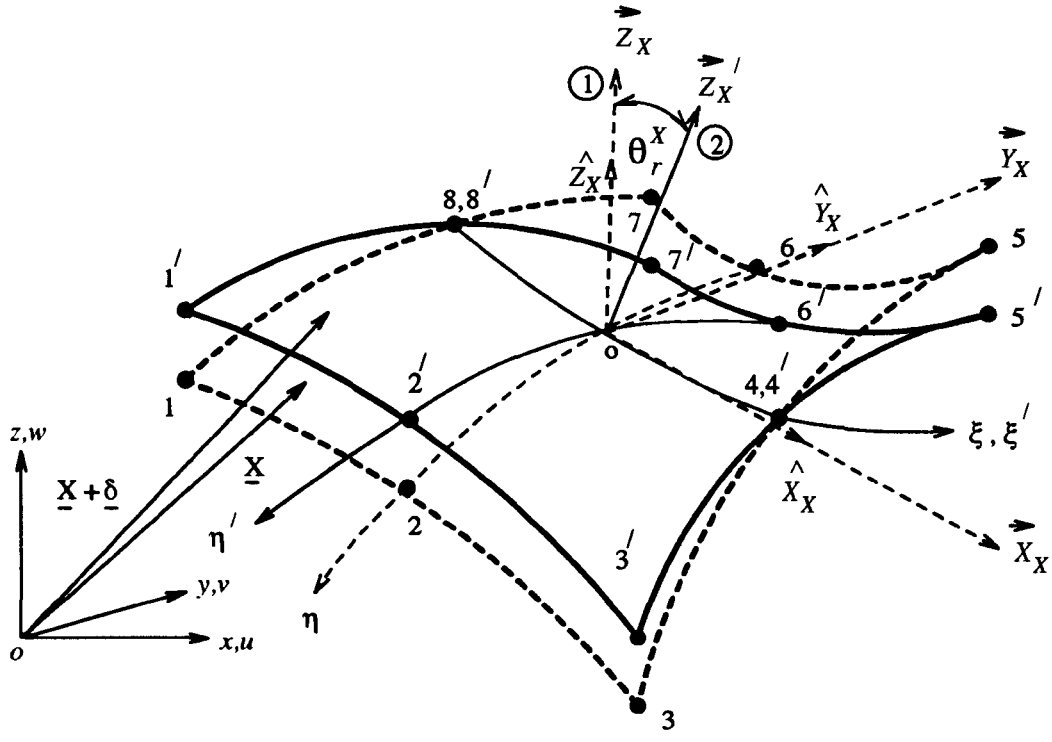

Figure 5.20 - An Element Subjected to a Rigid Body Rotation, θ_r^X.

The proposed axis of rigid body rotation, $\vec{X}_X$, may be established using an equation of the type given in eqn(5.4.4). Prior to the application of the rigid body rotation θ_r^X, a vector normal to the middle surface of the element, $\vec{Z}_X$, may be obtained as a vector product of $\vec{\xi}$ and $\vec{\eta}$ (eqn(5.4.5)). The updated normal vector, $\vec{Z}_X'$, may be calculated as,

$$\vec{Z}_X' = \begin{vmatrix} \underline{i} & \underline{j} & \underline{k} \\ \left(\frac{\partial x}{\partial \xi}+\frac{\partial u}{\partial \xi}\right) & \left(\frac{\partial y}{\partial \xi}+\frac{\partial v}{\partial \xi}\right) & \left(\frac{\partial z}{\partial \xi}+\frac{\partial w}{\partial \xi}\right) \\ \left(\frac{\partial x}{\partial \eta}+\frac{\partial u}{\partial \eta}\right) & \left(\frac{\partial y}{\partial \eta}+\frac{\partial v}{\partial \eta}\right) & \left(\frac{\partial z}{\partial \eta}+\frac{\partial w}{\partial \eta}\right) \end{vmatrix} \qquad \text{eqn(5.9.2.13)}$$

which, by evaluating the determinant, gives,

$$\begin{aligned} \vec{Z}_X' = & \left(\frac{\partial y}{\partial \xi}\frac{\partial z}{\partial \eta}+\frac{\partial y}{\partial \xi}\frac{\partial w}{\partial \eta}+\frac{\partial v}{\partial \xi}\frac{\partial z}{\partial \eta}+\frac{\partial v}{\partial \xi}\frac{\partial w}{\partial \eta}-\frac{\partial y}{\partial \eta}\frac{\partial z}{\partial \xi}-\frac{\partial y}{\partial \eta}\frac{\partial w}{\partial \xi}-\frac{\partial v}{\partial \eta}\frac{\partial z}{\partial \xi}-\frac{\partial v}{\partial \eta}\frac{\partial w}{\partial \xi} \right) \underline{i} \\ & - \left(\frac{\partial x}{\partial \xi}\frac{\partial z}{\partial \eta}+\frac{\partial x}{\partial \xi}\frac{\partial w}{\partial \eta}+\frac{\partial u}{\partial \xi}\frac{\partial z}{\partial \eta}+\frac{\partial u}{\partial \xi}\frac{\partial w}{\partial \eta}-\frac{\partial x}{\partial \eta}\frac{\partial z}{\partial \xi}-\frac{\partial x}{\partial \eta}\frac{\partial w}{\partial \xi}-\frac{\partial u}{\partial \eta}\frac{\partial z}{\partial \xi}-\frac{\partial u}{\partial \eta}\frac{\partial w}{\partial \xi} \right) \underline{j} \\ & + \left(\frac{\partial x}{\partial \xi}\frac{\partial y}{\partial \eta}+\frac{\partial x}{\partial \xi}\frac{\partial v}{\partial \eta}+\frac{\partial u}{\partial \xi}\frac{\partial y}{\partial \eta}+\frac{\partial u}{\partial \xi}\frac{\partial v}{\partial \eta}-\frac{\partial x}{\partial \eta}\frac{\partial y}{\partial \xi}-\frac{\partial x}{\partial \eta}\frac{\partial v}{\partial \xi}-\frac{\partial u}{\partial \eta}\frac{\partial y}{\partial \xi}-\frac{\partial u}{\partial \eta}\frac{\partial v}{\partial \xi} \right) \underline{k} \end{aligned}$$

eqn(5.9.2.14)

or,

$$\vec{Z}_X' = Z_X'^i \, \underline{i} - Z_X'^j \, \underline{j} + Z_X'^k \, \underline{k} \qquad \text{eqn(5.9.2.15)}$$

The expression for $\vec{Z}_X'$ given in eqn(5.9.2.15), contains terms such as $\frac{\partial v}{\partial \xi}\frac{\partial w}{\partial \eta}$, $\frac{\partial u}{\partial \xi}\frac{\partial w}{\partial \eta}$, etc., which are clearly products of the differentials of the element nodal displacements. Assuming that the rate of change of the interpolated displacements across the element are small, the second order terms of this type may be neglected as a necessary simplification.

With reference to Figure 5.20, and using an equation of the form given in eqn(5.4.7), the vector $\hat{Y}_X$, may be expressed as,

$$\hat{Y}_X = \hat{Z}_X \times \hat{X}_X = \{ Y_X{}^i \underline{i} - Y_X{}^j \underline{j} + Y_X{}^k \underline{k} \}. \qquad \text{eqn(5.9.2.16)}$$

The vector $\vec{Z}_X$ may be expanded to give (eqn(5-A.7)),

$$\vec{Z}_X = \left\{ \left(\frac{\partial y}{\partial \xi}\frac{\partial z}{\partial \eta} - \frac{\partial y}{\partial \eta}\frac{\partial z}{\partial \xi}\right)\underline{i} - \left(\frac{\partial x}{\partial \xi}\frac{\partial z}{\partial \eta} - \frac{\partial x}{\partial \eta}\frac{\partial z}{\partial \xi}\right)\underline{j} + \left(\frac{\partial x}{\partial \xi}\frac{\partial y}{\partial \eta} - \frac{\partial x}{\partial \eta}\frac{\partial y}{\partial \xi}\right)\underline{k} \right\}$$

$$= \left\{ Z_X{}^i \underline{i} - Z_X{}^j \underline{j} + Z_X{}^k \underline{k} \right\} \qquad \text{eqn(5.9.2.17)}$$

Eqn(5.9.2.16) and eqn(5.9.2.17) may be used to transform the vector $\vec{Z}_X$ into the local $\vec{Z}_X, \vec{Y}_X$ plane. For example, given that the co-ordinates Z_{X1}, Y_{X1} describe the end of the vector $\vec{Z}_X$ (point 1 (Figure 5.20)) in the local $\hat{Z}_X, \hat{Y}_X$ plane, the transformation may be written as,

$$\begin{Bmatrix} Z_{X1} \\ Y_{X1} \end{Bmatrix} = \begin{Bmatrix} \left| \vec{Z}_X \right| \\ \hat{Y}_X{}^i Z_X{}^i - \hat{Y}_X{}^j Z_X{}^j + \hat{Y}_X{}^k Z_X{}^k \end{Bmatrix} \qquad \text{eqn(5.9.2.18)}$$

Similarly, the vector $\vec{Z}_X'$ may be transformed into the same plane, $\hat{Z}_X, \hat{Y}_X$, to give the local co-ordinates of the point 2 (Figure 5.20), as,

$$\begin{Bmatrix} Z_{X2} \\ Y_{X2} \end{Bmatrix} = \begin{Bmatrix} \hat{Z}_X{}^i Z_X{}'^i - \hat{Z}_X{}^j Z_X{}'^j + \hat{Z}_X{}^k Z_X{}'^k \\ \hat{Y}_X{}^i Z_X{}'^i - \hat{Y}_X{}^j Z_X{}'^j + \hat{Y}_X{}^k Z_X{}'^k \end{Bmatrix} \qquad \text{eqn(5.9.2.19)}$$

where $\hat{Z}_X{}^i$, $\hat{Z}_X{}^j$, and $\hat{Z}_X{}^k$ are the respective direction cosines of the vector $\vec{Z}_X$, and the terms $Z_X{}'^i$, $Z_X{}'^j$, and $Z_X{}'^k$ are as presented in eqn(5.9.2.14).

Assuming small rotations, eqn(5.9.2.18) and eqn(5.9.2.19) may be used to obtain an expression for the rigid body rotation angle $\theta_r{}^X$, in terms of the element nodal displacements, as,

$$\theta_r{}^X \approx \frac{Y_{X2} - Y_{X1}}{Z_{X1}}, \qquad \text{eqn(5.9.2.20)}$$

or,

$$\theta_r{}^X \approx \frac{1}{\left| \vec{Z}_X \right|} \left[\hat{Y_X}{}^i \left(\frac{\partial y}{\partial \xi}\frac{\partial w}{\partial \eta} + \frac{\partial z}{\partial \eta}\frac{\partial v}{\partial \xi} - \frac{\partial y}{\partial \eta}\frac{\partial w}{\partial \xi} - \frac{\partial z}{\partial \xi}\frac{\partial v}{\partial \eta} \right) - \hat{Y_X}{}^j \left(\frac{\partial x}{\partial \xi}\frac{\partial w}{\partial \eta} + \frac{\partial z}{\partial \eta}\frac{\partial u}{\partial \xi} - \frac{\partial x}{\partial \eta}\frac{\partial w}{\partial \xi} - \frac{\partial z}{\partial \xi}\frac{\partial u}{\partial \eta} \right) + \hat{Y_X}{}^k \left(\frac{\partial x}{\partial \xi}\frac{\partial v}{\partial \eta} + \frac{\partial y}{\partial \eta}\frac{\partial u}{\partial \xi} - \frac{\partial x}{\partial \eta}\frac{\partial v}{\partial \xi} - \frac{\partial y}{\partial \xi}\frac{\partial u}{\partial \eta} \right) \right] \qquad \text{eqn(5.9.2.21)}$$

Adopting a similar procedure, the rigid body rotation angle about the local $\vec{Y}_X$ axis, $\theta_r{}^Y$, may be written as,

$$\theta_r{}^Y \approx \frac{1}{\left| \vec{Z}_X \right|} \left[\hat{X_X}{}^i \left(\frac{\partial y}{\partial \xi}\frac{\partial w}{\partial \eta} + \frac{\partial z}{\partial \eta}\frac{\partial v}{\partial \xi} - \frac{\partial y}{\partial \eta}\frac{\partial w}{\partial \xi} - \frac{\partial z}{\partial \xi}\frac{\partial v}{\partial \eta} \right) - \hat{X_X}{}^j \left(\frac{\partial x}{\partial \xi}\frac{\partial w}{\partial \eta} + \frac{\partial z}{\partial \eta}\frac{\partial u}{\partial \xi} - \frac{\partial x}{\partial \eta}\frac{\partial w}{\partial \xi} - \frac{\partial z}{\partial \xi}\frac{\partial u}{\partial \eta} \right) + \hat{X_X}{}^k \left(\frac{\partial x}{\partial \xi}\frac{\partial v}{\partial \eta} + \frac{\partial y}{\partial \eta}\frac{\partial u}{\partial \xi} - \frac{\partial x}{\partial \eta}\frac{\partial v}{\partial \xi} - \frac{\partial y}{\partial \xi}\frac{\partial u}{\partial \eta} \right) \right] \qquad \text{eqn(5.9.2.22)}$$

where $\hat{X_X}{}^i$, $\hat{X_X}{}^j$, and $\hat{X_X}{}^k$, are the direction cosines of the local co-ordinate direction $\vec{X}_X$.

Therefore, the total angle of rigid body rotation, $\theta_r{}^T$ may be estimated by eqn(5.9.2.12(b)), eqn(5.9.2.21) and eqn(5.9.2.22), as,

$$\theta_r{}^T \approx \theta_r{}^{ip} + \theta_r{}^X + \theta_r{}^Y \qquad \text{eqn(5.9.2.23)}$$

Thus, with reference to eqn(5.9.1.3), the expressions given for $\theta_r{}^{ip}$, $\theta_r{}^X$, and $\theta_r{}^Y$ in terms of the element nodal displacements (eqn(5.9.2.12(b)), eqn(5.9.2.21), eqn(5.9.2.22)), may be used to calculate the terms of the matrix $[\, K_\sigma{}^e \,]_{ex}$ as outlined below.

5.9.3. Generation of the Terms of the External Stiffness Matrix $[\, K_\sigma{}^e \,]_{ex}$.

Considering initially a rigid body rotation through a small angle $\theta_r{}^{ip}$, the corresponding rotation matrix, $[\, R \,]_r{}^{ip}$ (eqn(5.9.1.2)), may be written as,

$$[\, R \,]_r{}^{ip} = \begin{bmatrix} 1 & -\hat{Z}^k\,\theta_r{}^{ip} & \hat{Z}^j\,\theta_r{}^{ip} \\ \hat{Z}^k\,\theta_r{}^{ip} & 1 & -\hat{Z}^i\,\theta_r{}^{ip} \\ -\hat{Z}^j\,\theta_r{}^{ip} & \hat{Z}^i\,\theta_r{}^{ip} & 1 \end{bmatrix} \qquad \text{eqn(5.9.3.1)}$$

where $\hat{Z}^i$, $\hat{Z}^j$, and $\hat{Z}^k$ are the respective direction cosines of the vector $\hat{Z}$ (Figure 5.19), in the global x, y and z directions.

Substituting eqn(5.9.3.1) into the general equation, eqn(5.9.1.2), yields the vector of nodal forces, $\{fe\}_{ip}\Big|^{2}$, written as,

$$\{fe\}_{ip}\Big|^{2} \approx \left\{ \begin{array}{l} F_{1X^1} - \hat{Z}^k\,\theta_r{}^{ip}\,F_{1Y^1} + \hat{Z}^j\,\theta_r{}^{ip}\,F_{1Z^1} \\ \hat{Z}^k\,\theta_r{}^{ip}\,F_{1X^1} + F_{1Y^1} - \hat{Z}^i\,\theta_r{}^{ip}\,F_{1Z^1} \\ -\hat{Z}^j\,\theta_r{}^{ip}\,F_{1X^1} + \hat{Z}^i\,\theta_r{}^{ip}\,F_{1Y^1} + F_{1Z^1} \\ \vdots \\ F_{8X^8} - \hat{Z}^k\,\theta_r{}^{ip}\,F_{8Y^8} + \hat{Z}^j\,\theta_r{}^{ip}\,F_{8Z^8} \\ \hat{Z}^k\,\theta_r{}^{ip}\,F_{8X^8} + F_{8Y^8} - \hat{Z}^i\,\theta_r{}^{ip}\,F_{8Z^8} \\ -\hat{Z}^j\,\theta_r{}^{ip}\,F_{8X^8} + \hat{Z}^i\,\theta_r{}^{ip}\,F_{8Y^8} + F_{8Z^8} \end{array} \right\} \qquad \text{eqn(5.9.3.2)}$$

where F_{1X^1}, F_{1Y^1}, and F_{1Z^1}, are the equivalent nodal forces for the element node 1 in the local directions X^1, Y^1, and Z^1, respectively.

The additional fictitious nodal forces generated through the application of the rigid body rotation described by $\theta_r{}^{ip}$, is given by a similar form to that of the left side of eqn(5.9.1.3). Thus,

$$\{fe\}_{ip}\Big|^{2} - [R]_r{}^{ip}\,\{fe\}\Big|^{1} \approx \left\{ \begin{array}{l} (-\hat{Z}^k F_{1Y^1} + \hat{Z}^j F_{1Z^1}) \\ (\hat{Z}^k F_{1X^1} - \hat{Z}^i F_{1Z^1}) \\ (-\hat{Z}^j F_{1X^1} + \hat{Z}^i F_{1Y^1}) \\ \vdots \\ (-\hat{Z}^k F_{8Y^8} + \hat{Z}^j F_{8Z^8}) \\ (\hat{Z}^k F_{8X^8} - \hat{Z}^i F_{8Z^8}) \\ (-\hat{Z}^j F_{8X^8} + \hat{Z}^i F_{8Y^8}) \end{array} \right\} \theta_r{}^{ip}$$

eqn(5.9.3.3)

The rigid body rotation angle $\theta_r{}^{ip}$ (eqn(5.9.2.12(b)), may be expressed explicitly in terms of the element nodal degrees of freedom, through equations of the type given in eqn(5.3.3.7), such that,

$$\theta_r{}^{ip} \approx \frac{1}{2}\left[\sum_{n=1}^{n=8}\frac{\frac{\partial N_n}{\partial \xi}}{\left|\vec{\xi}\right|} u_n \hat{Y}_\xi{}^i + \sum_{n=1}^{n=8}\frac{\frac{\partial N_n}{\partial \eta}}{\left|\vec{\eta}\right|} u_n \hat{Y}_\eta{}^i\right]$$
$$+ \frac{1}{2}\left[\sum_{n=1}^{n=8}\frac{\frac{\partial N_n}{\partial \xi}}{\left|\vec{\xi}\right|} v_n \hat{Y}_\xi{}^j + \sum_{n=1}^{n=8}\frac{\frac{\partial N_n}{\partial \eta}}{\left|\vec{\eta}\right|} v_n \hat{Y}_\eta{}^j\right]$$
$$+ \frac{1}{2}\left[\sum_{n=1}^{n=8}\frac{\frac{\partial N_n}{\partial \xi}}{\left|\vec{\xi}\right|} w_n \hat{Y}_\xi{}^k + \sum_{n=1}^{n=8}\frac{\frac{\partial N_n}{\partial \eta}}{\left|\vec{\eta}\right|} w_n \hat{Y}_\eta{}^k\right] \qquad \text{eqn(5.9.3.4)}$$

Writing eqn(5.9.1.3) with eqn(5.9.3.3) and eqn(5.9.3.4), yields the coefficients of the external stiffness matrix, $[\,K_\sigma{}^e\,]_{ex}{}^{ip}$, due to the rigid body rotation angle $\theta_r{}^{ip}$. This is done by extracting the coefficients corresponding to the element nodal displacements and recompiling them to generate a 24 × 24 stiffness matrix.

For example, the first three terms of the first row of the matrix $[\,K_\sigma{}^e\,]_{ex}{}^{ip}$, may be written as,

$$[\,K_\sigma{}^e(1,1)\,]_{ex}{}^{ip} = \frac{1}{2}\left(-\hat{Z}^k F_{1Y^1} + \hat{Z}^j F_{1Z^1}\right)\left[\hat{Y}_\xi{}^i \frac{\frac{\partial N_1}{\partial \xi}}{\left|\vec{\xi}\right|} + \hat{Y}_\eta{}^i \frac{\frac{\partial N_1}{\partial \eta}}{\left|\vec{\eta}\right|}\right],$$

$$[\,K_\sigma{}^e(1,2)\,]_{ex}{}^{ip} = \frac{1}{2}\left(-\hat{Z}^k F_{1Y^1} + \hat{Z}^j F_{1Z^1}\right)\left[\hat{Y}_\xi{}^j \frac{\frac{\partial N_1}{\partial \xi}}{\left|\vec{\xi}\right|} + \hat{Y}_\eta{}^j \frac{\frac{\partial N_1}{\partial \eta}}{\left|\vec{\eta}\right|}\right],$$

$$[\,K_\sigma{}^e(1,3)\,]_{ex}{}^{ip} = \frac{1}{2}\left(-\hat{Z}^k F_{1Y^1} + \hat{Z}^j F_{1Z^1}\right)\left[\hat{Y}_\xi{}^k \frac{\frac{\partial N_1}{\partial \xi}}{\left|\vec{\xi}\right|} + \hat{Y}_\eta{}^k \frac{\frac{\partial N_1}{\partial \eta}}{\left|\vec{\eta}\right|}\right],$$

eqn(5.9.3.5(a))

while the final term of the matrix $[\,K_\sigma{}^e\,]_{ex}{}^{ip}$, is given by,

$$[\,K_\sigma{}^e(24,24)\,]_{ex}{}^{ip} = \frac{1}{2}\left(-\hat{Z}^j F_{8X^8} + \hat{Z}^i F_{8Y^8}\right)\left[\hat{Y}_\xi{}^k \frac{\frac{\partial N_8}{\partial \xi}}{\left|\vec{\xi}\right|} + \hat{Y}_\eta{}^k \frac{\frac{\partial N_8}{\partial \eta}}{\left|\vec{\eta}\right|}\right].$$

eqn(5.9.3.5(b))

A similar procedure may be adopted to obtain the contribution of a small rigid body rotation, $\theta_r{}^X$, about the local X_X axis to the total external stiffness matrix, $[\,K_\sigma{}^e\,]_{ex}$. In this case the

rotation matrix, matrix, $[\,R\,]_r{}^X$, is given as,

$$[\,R\,]_r{}^X = \begin{bmatrix} 1 & -\hat{X}_X{}^k\,\theta_r{}^X & \hat{X}_X{}^j\,\theta_r{}^X \\ \hat{X}_X{}^k\,\theta_r{}^X & 1 & -\hat{X}_X{}^i\,\theta_r{}^X \\ -\hat{X}_X{}^j\,\theta_r{}^X & \hat{X}_X{}^i\,\theta_r{}^X & 1 \end{bmatrix} \qquad \text{eqn(5.9.3.6)}$$

The additional fictitious nodal forces resulting from a rigid body rotation of magnitude $\theta_r{}^X$, may be written as,

$$\{\,fe\,\}_X\Big|^2 - [\,R\,]_r{}^X\,\{\,fe\,\}\Big|^1 \approx \begin{Bmatrix} \\ (-\hat{X}_X{}^k\,F_{1Y^1} + \hat{X}_X{}^j\,F_{1Z^1}) \\ (\hat{X}_X{}^k\,F_{1X^1} - \hat{X}_X{}^i\,F_{1Z^1}) \\ (-\hat{X}_X{}^j\,F_{1X^1} + \hat{X}_X{}^i\,F_{1Y^1}) \\ \cdot \\ \cdot \\ \cdot \\ (-\hat{X}_X{}^k\,F_{8Y^8} + \hat{X}_X{}^j\,F_{8Z^8}) \\ (\hat{X}_X{}^k\,F_{8X^8} - \hat{X}_X{}^i\,F_{8Z^8}) \\ (-\hat{X}_X{}^j\,F_{8X^8} + \hat{X}_X{}^i\,F_{8Y^8}) \\ \\ \end{Bmatrix} \theta_r{}^X \qquad \text{eqn(5.9.3.7)}$$

where $\{\,fe\,\}_X\Big|^2$ is the vector of equivalent nodal forces subsequent to the application of $\theta_r{}^X$.

Rewriting the rigid body rotation angle $\theta_r{}^X$ (eqn(5.9.2.21) in terms of the element nodal displacements (eqn(5.3.3.7)), leads to the following expression for $\theta_r{}^X$;

$$\begin{aligned}
\theta_r{}^X \approx\ & \sum_{n=1}^{n=8} \frac{\partial N_n}{\partial \xi}\frac{u_n}{|\,\vec{Z}_X\,|}\left[\,-\hat{Y}_X{}^j \sum_{m=1}^{m=8}\frac{\partial N_m}{\partial \eta} z_m + \hat{Y}_X{}^k \sum_{m=1}^{m=8}\frac{\partial N_m}{\partial \eta} y_m\,\right] \\
& + \sum_{n=1}^{n=8} \frac{\partial N_n}{\partial \eta}\frac{u_n}{|\,\vec{Z}_X\,|}\left[\,\hat{Y}_X{}^j \sum_{m=1}^{m=8}\frac{\partial N_m}{\partial \xi} z_m - \hat{Y}_X{}^k \sum_{m=1}^{m=8}\frac{\partial N_m}{\partial \xi} y_m\,\right] \\
& + \sum_{n=1}^{n=8} \frac{\partial N_n}{\partial \xi}\frac{v_n}{|\,\vec{Z}_X\,|}\left[\,\hat{Y}_X{}^i \sum_{m=1}^{m=8}\frac{\partial N_m}{\partial \eta} z_m - \hat{Y}_X{}^k \sum_{m=1}^{m=8}\frac{\partial N_m}{\partial \eta} x_m\,\right] \\
& + \sum_{n=1}^{n=8} \frac{\partial N_n}{\partial \eta}\frac{v_n}{|\,\vec{Z}_X\,|}\left[\,-\hat{Y}_X{}^i \sum_{m=1}^{m=8}\frac{\partial N_m}{\partial \xi} z_m + \hat{Y}_X{}^k \sum_{m=1}^{m=8}\frac{\partial N_m}{\partial \xi} x_m\,\right] \\
& + \sum_{n=1}^{n=8} \frac{\partial N_n}{\partial \xi}\frac{w_n}{|\,\vec{Z}_X\,|}\left[\,-\hat{Y}_X{}^i \sum_{m=1}^{m=8}\frac{\partial N_m}{\partial \eta} y_m + \hat{Y}_X{}^j \sum_{m=1}^{m=8}\frac{\partial N_m}{\partial \eta} x_m\,\right] \\
& + \sum_{n=1}^{n=8} \frac{\partial N_n}{\partial \eta}\frac{w_n}{|\,\vec{Z}_X\,|}\left[\,\hat{Y}_X{}^i \sum_{m=1}^{m=8}\frac{\partial N_m}{\partial \xi} y_m - \hat{Y}_X{}^j \sum_{m=1}^{m=8}\frac{\partial N_m}{\partial \xi} x_m\,\right]
\end{aligned} \qquad \text{eqn(5.9.3.8)}$$

Writing eqn(5.9.3.7) and eqn(5.9.3.8) in the form of the general equation, eqn(5.9.1.3), yields the coefficients of the external stiffness matrix, $[K_\sigma{}^e]_{ex}{}^X$, generated by a rigid body rotation of magnitude $\theta_r{}^X$.

For example, the first term of the first row of the matrix $[K_\sigma{}^e]_{ex}{}^X$, is given as,

$$[K_\sigma{}^e(1,1)]_{ex}{}^X = \frac{\left(-\hat{X}_X{}^k F_{1Y^1} + \hat{X}_X{}^j F_{1Z^1}\right)}{\left|\vec{Z}_X\right|}\left[[K_\sigma{}^e]_{ex}{}^X(A) + [K_\sigma{}^e]_{ex}{}^X(B)\right]$$

eqn(5.9.3.9)

where,

$$[K_\sigma{}^e]_{ex}{}^X(A) = \frac{\partial N_1}{\partial \xi}\left[-\hat{Y}_X{}^j \sum_{m=1}^{m=8}\frac{\partial N_m}{\partial \eta} z_m + \hat{Y}_X{}^k \sum_{m=1}^{m=8}\frac{\partial N_m}{\partial \eta} y_m\right]$$

and,

$$[K_\sigma{}^e]_{ex}{}^X(B) = \frac{\partial N_1}{\partial \eta}\left[\hat{Y}_X{}^j \sum_{m=1}^{m=8}\frac{\partial N_m}{\partial \xi} z_m - \hat{Y}_X{}^k \sum_{m=1}^{m=8}\frac{\partial N_m}{\partial \xi} y_m\right]$$

In the case of rigid body rotation about the local Y_X axis (Figure 5.20),the rotation matrix, $[R]_r{}^Y$, may be written as,

$$[R]_r{}^Y = \begin{bmatrix} 1 & -\hat{Y}_X{}^k \theta_r{}^Y & \hat{Y}_X{}^j \theta_r{}^Y \\ \hat{Y}_X{}^k \theta_r{}^Y & 1 & -\hat{Y}_X{}^i \theta_r{}^Y \\ -\hat{Y}_X{}^j \theta_r{}^Y & \hat{Y}_X{}^i \theta_r{}^Y & 1 \end{bmatrix}$$

eqn(5.9.3.10)

With reference to eqn(5.9.1.3), the additional fictitious nodal forces resulting from the application of a rigid body rotation of magnitude $\theta_r{}^Y$, may be written as follows;

$$\{fe\}_Y \Big|^2 - [R]_r{}^Y \{fe\} \Big|^1 \approx \left\{\begin{array}{c} \\ (-\hat{Y}_X{}^k F_{1Y^1} + \hat{Y}_X{}^j F_{1Z^1}) \\ (\hat{Y}_X{}^k F_{1X^1} - \hat{Y}_X{}^i F_{1Z^1}) \\ (-\hat{Y}_X{}^j F_{1X^1} + \hat{Y}_X{}^i F_{1Y^1}) \\ \cdot \\ \cdot \\ \cdot \\ (-\hat{Y}_X{}^k F_{8Y^8} + \hat{Y}_X{}^j F_{8Z^8}) \\ (\hat{Y}_X{}^k F_{8X^8} - \hat{Y}_X{}^i F_{8Z^8}) \\ (-\hat{Y}_X{}^j F_{8X^8} + \hat{Y}_X{}^i F_{8Y^8}) \\ \end{array}\right\} \theta_r{}^Y$$

eqn(5.9.3.11)

Writing eqn(5.9.2.22) in terms of the element nodal displacements, and substituting the resulting expression, with eqn(5.9.3.11), into the general equation, eqn(5.9.1.3), yields the coefficients of the external stiffness matrix, $[\,K_\sigma{}^e\,]_{ex}{}^Y$, due to an angle of rigid body rotation, $\theta_r{}^Y$. Thus, the first term of the first row of the matrix $[\,K_\sigma{}^e\,]_{ex}{}^X$, may be written as,

$$[\,K_\sigma{}^e(1,1)\,]_{ex}{}^Y = \frac{\left(-\hat{Y}_X{}^k\,F_{1Y^1} + \hat{Y}_X{}^j\,F_{1Z^1}\right)}{\left|\,\vec{Z}_X\,\right|}\left[\,[\,K_\sigma{}^e\,]_{ex}{}^Y(A) + [\,K_\sigma{}^e\,]_{ex}{}^Y(B)\right]$$

eqn(5.9.3.12)

where,

$$[\,K_\sigma{}^e\,]_{ex}{}^Y(A) = \frac{\partial N_1}{\partial\xi}\left[-\hat{X}_X{}^j\sum_{m=1}^{m=8}\frac{\partial N_m}{\partial\eta}z_m + \hat{X}_X{}^k\sum_{m=1}^{m=8}\frac{\partial N_m}{\partial\eta}y_m\right]$$

and,

$$[\,K_\sigma{}^e\,]_{ex}{}^Y(B) = \frac{\partial N_1}{\partial\eta}\left[\hat{X}_X{}^j\sum_{m=1}^{m=8}\frac{\partial N_m}{\partial\xi}z_m - \hat{X}_X{}^k\sum_{m=1}^{m=8}\frac{\partial N_m}{\partial\xi}y_m\right]$$

Finally, by combining the coefficients of the type described in eqn(5.9.3.5(a)&(b)), eqn(5.9.3.9), and eqn(5.9.3.12), the total external stiffness matrix, $[\,K_\sigma{}^e\,]_{ex}$ is obtained as,

$$[\,K_\sigma{}^e\,]_{ex} = [\,K_\sigma{}^e\,]_{ex}{}^{ip} + [\,K_\sigma{}^e\,]_{ex}{}^X + [\,K_\sigma{}^e\,]_{ex}{}^Y \qquad \text{eqn(5.9.3.13)}$$

where the matrices $[\,K_\sigma{}^e\,]_{ex}{}^{ip}$, $[\,K_\sigma{}^e\,]_{ex}{}^X$. and $[\,K_\sigma{}^e\,]_{ex}{}^Y$, correspond to the components of the matrix $[\,K_\sigma{}^e\,]_{ex}$, arising from rigid body rotation in a plane normal to the middle surface of the element (at $(\xi, \eta) = (0, 0)$), and about the local axes $\hat{X}_X$ and $\hat{Y}_X$, respectively.

Substituting eqn(5.9.3.13) into eqn(5.9.1.4) gives an expression for the element internal stiffness matrix, $[\,K_\sigma{}^e\,]_{in}$, as,

$$[\,K_\sigma{}^e\,]_{in} = [\,K_\sigma{}^e\,]_{ex} - [\,K_\sigma{}^e\,]_{ex}{}^{ip} - [\,K_\sigma{}^e\,]_{ex}{}^X - [\,K_\sigma{}^e\,]_{ex}{}^Y$$

eqn(5.9.3.14)

The results relating to the theoretical approach presented in this section are given in Section 6.3, Chapter 6.

5.10. Appendix 5-A - General Form of the Solution to the Direct Element Strain $\frac{\partial U}{\partial X}$.

The elastic continuum illustrated in Figure 5-A.1, is subjected to a general displacement vector $\underline{\delta}^*$. The strain at the point $P_o{}^*$, $\varepsilon_G{}^{P_o{}^*}$, is given in the general form, as in eqn(5.6.6), with the current notation (Figure 5-A.1) as,

$$\varepsilon_G{}^{P_o{}^*} = \frac{ds^{*2} - ds_o{}^{*2}}{2\, ds_o{}^{*2}} \qquad \text{eqn(5.6.6)}$$

where ds^* and $ds_o{}^{*2}$, are the infinitesimal arc lengths at the point of interest, prior and subsequent to the application of the displacement vector $\underline{\delta}^*$, respectively.

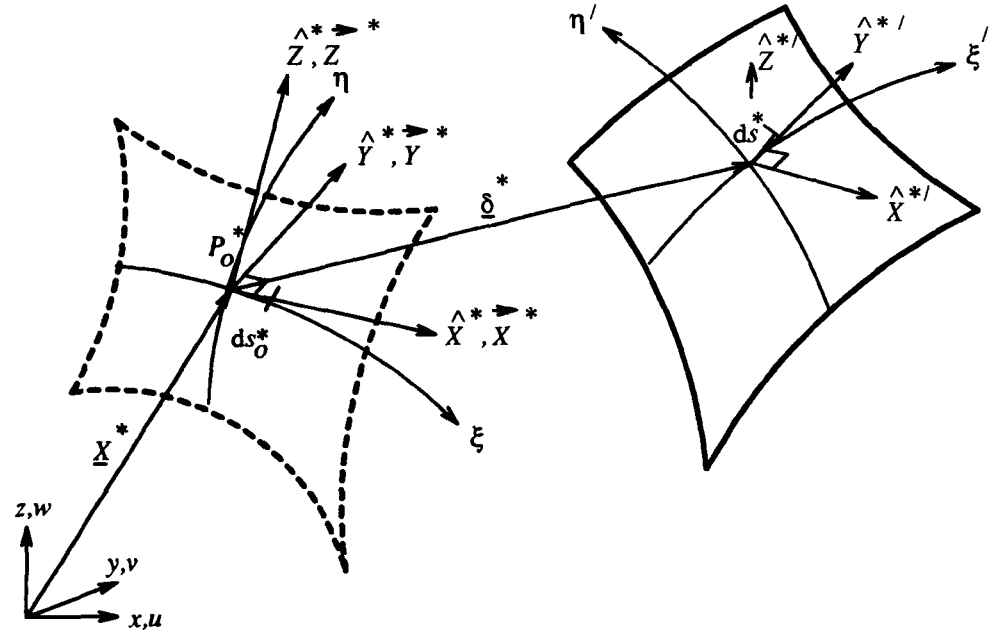

Figure 5-A.1 - General 3-Dimensional Elastic Continuum Subjected to a Displacement Vector $\underline{\delta}$

It is required to calculate the local strain, $\frac{\partial U^*}{\partial \hat{X}}$, in the direction of the vector $\hat{X}^*$, at the location $P_o{}^*$. Given that $ds_o{}^*$ is an initial infinitesimal arc length, on the surface at the point $P_o{}^*$ in the local direction $\hat{X}^*$, then,

$$ds_o{}^{*2} = \frac{\partial \underline{X}^*}{\partial X} \cdot \frac{\partial \underline{X}^*}{\partial X} \qquad \text{eqn(5-A.1)}$$

Similarly, if the point $P_o{}^*$ moves to a new location, P^* after application of the displacement vector $\underline{\delta}^*$, then the square of the strained infinitesimal arc length, ds^*, may be written as,

$$ds^{*2} = \frac{\partial(\underline{X}^* + \underline{\delta}^*)}{\partial X} \cdot \frac{\partial(\underline{X}^* + \underline{\delta}^*)}{\partial X} \qquad \text{eqn(5-A.2)}$$

Substitution of eqn(5-A.1) and eqn(5-A.2) into eqn(5.6.29) gives,

$$\varepsilon_G{}^{P_o^*} = \frac{2\,\frac{\partial \underline{\delta}^*}{\partial X}\cdot\frac{\partial \underline{X}^*}{\partial X} + \frac{\partial \underline{\delta}^*}{\partial X}\cdot\frac{\partial \underline{\delta}^*}{\partial X}}{2\left|\frac{\partial \underline{X}^*}{\partial X}\right|^2} \qquad \text{eqn(5-A.3(a))}$$

or, to the first order,

$$\varepsilon_G{}^{P_o^*} \approx \frac{\partial \underline{\delta}^*}{\partial X}\cdot\frac{\frac{\partial \underline{X}^*}{\partial X}}{\left|\frac{\partial \underline{X}^*}{\partial X}\right|^2} = \frac{\partial U^*}{\partial X} \qquad \text{eqn(5-A.3(b))}$$

From the form of eqn(5.6.15(a)) it may be written that,

$$U^* = \underline{\delta}^* \cdot \hat{X}^* , \qquad \text{eqn(5-A.4)}$$

and the direct strain in the local X direction from the form of eqn(5.6.15(b)) as,

$$\frac{\partial U^*}{\partial X} = \frac{\partial \underline{\delta}^*}{\partial X} \cdot \hat{X}^* , \qquad \text{eqn(5-A.5)}$$

By a comparison of eqn(5-A.3(b)) with eqn(5-A.5) it is shown that if eqn(5.6.15(b)) is to be valid for calculating the direct local strain, $\frac{\partial U}{\partial X}$ (or in the current notation $\frac{\partial U^*}{\partial X}$) in the general case, then the following equality

$$\hat{X}^* = \frac{\frac{\partial \underline{X}^*}{\partial X}}{\left|\frac{\partial \underline{X}^*}{\partial X}\right|^2} \qquad \text{eqn(5-A.6)}$$

must hold true.

Considering initially the left side of eqn(5-A.6), in the case of a general curved quadrilateral element in the global $\{x, y, z\}$ space (Figure 5-A.1), the local co-ordinate base vectors may be calculated from eqn(5.4.1), eqn(5.4.9), eqn(5.4.10), with eqn(5.4.13). For example, the co-ordinate direction $\vec{Z}^*$ may be written as,

$$\vec{Z}^* = \vec{\xi} \times \vec{\eta} = \left[\frac{\partial y}{\partial \xi}\frac{\partial z}{\partial \eta} - \frac{\partial y}{\partial \eta}\frac{\partial z}{\partial \xi}\right]\underline{i} - \left[\frac{\partial x}{\partial \xi}\frac{\partial z}{\partial \eta} - \frac{\partial x}{\partial \eta}\frac{\partial z}{\partial \xi}\right]\underline{j} + \left[\frac{\partial x}{\partial \xi}\frac{\partial y}{\partial \eta} - \frac{\partial x}{\partial \eta}\frac{\partial y}{\partial \xi}\right]\underline{k} \qquad \text{eqn(5-A.7)}$$

Assuming that $\hat{j} = \{0\,\underline{i} + 1\,\underline{j} + 0\,\underline{k}\}$, the base vector $\vec{X}^*$ may be given by,

$$\vec{X}^* = \hat{i} \times \vec{Z}^* = \left[\frac{\partial x}{\partial \xi} \frac{\partial y}{\partial \eta} - \frac{\partial x}{\partial \eta} \frac{\partial y}{\partial \xi} \right] \underline{i} + 0\,\underline{j} - \left[\frac{\partial y}{\partial \xi} \frac{\partial z}{\partial \eta} - \frac{\partial y}{\partial \eta} \frac{\partial z}{\partial \xi} \right] \underline{k}$$

eqn(5-A.8)

The left side of eqn(5-A.6) is therefore written as $\hat{X}^* = \dfrac{\vec{X}^*}{\left| \vec{X}^* \right|}$, with $\vec{X}^*$ given by eqn(5-A.8). In addition, the local base vector $\vec{Y}^*$ may be expressed as,

$$\begin{aligned} \vec{Y}^* = \vec{Z}^* \times \vec{X}^* = & \left[\left[\frac{\partial x}{\partial \xi} \frac{\partial z}{\partial \eta} - \frac{\partial x}{\partial \eta} \frac{\partial z}{\partial \xi} \right] \left[\frac{\partial y}{\partial \xi} \frac{\partial z}{\partial \eta} - \frac{\partial y}{\partial \eta} \frac{\partial z}{\partial \xi} \right] \right] \underline{i} \\ & + \left[\left[\frac{\partial y}{\partial \xi} \frac{\partial z}{\partial \eta} - \frac{\partial y}{\partial \eta} \frac{\partial z}{\partial \xi} \right]^2 + \left[\frac{\partial x}{\partial \xi} \frac{\partial y}{\partial \eta} - \frac{\partial x}{\partial \eta} \frac{\partial y}{\partial \xi} \right]^2 \right] \underline{j} \\ & + \left[\left[\frac{\partial x}{\partial \xi} \frac{\partial y}{\partial \eta} - \frac{\partial x}{\partial \eta} \frac{\partial y}{\partial \xi} \right] \left[\frac{\partial x}{\partial \xi} \frac{\partial z}{\partial \eta} - \frac{\partial x}{\partial \eta} \frac{\partial z}{\partial \xi} \right] \right] \underline{k} \end{aligned}$$

eqn(5-A.9)

Calculation of the right side of eqn(5-A.6) requires the Jacobian matrix describing the transformation between the local and natural co-ordinate systems, eqn(5.5.7(a)). The vector $\underline{X}^*$ may be rewritten as,

$$\underline{X}^* = x^* \underline{i} + y^* \underline{j} + z^* \underline{k} \qquad \text{eqn(5-A.10)}$$

where x^*, y^* and z^* are scalar quantities and the components of the vector $\underline{X}^*$ in the global $\{ x, y, z \}$ space.

As demonstrated below, the terms x^*, y^* and z^* may be substituted successively into eqn(5.5.7(a)) to obtain the components of the vector $\dfrac{\partial \underline{X}^*}{\partial \underline{X}}$, in terms of the natural co-ordinates ξ and η.

Substituting x^* into eqn(5.5.7(a)) leads to,

$$\frac{\partial x^*}{\partial X} = \frac{1}{(\vec{\xi} \cdot \hat{X}^*)(\vec{\eta} \cdot \hat{Y}^*) - (\vec{\eta} \cdot \hat{X}^*)(\vec{\xi} \cdot \hat{Y}^*)} \left[\vec{\eta} \cdot \hat{Y}^* \frac{\partial x^*}{\partial \xi} - \vec{\xi} \cdot \hat{Y}^* \frac{\partial x^*}{\partial \eta} \right]$$

eqn(5-A.11)

Similar expressions may be obtained for $\dfrac{\partial y^*}{\partial X}$ and $\dfrac{\partial z^*}{\partial X}$.

In the general case, since the unit vector, $\hat{X}$, is not aligned with the base vector $\vec{\xi}$, then the vector $\hat{Y}$ is not orthogonal to the vector $\vec{\xi}$ (Figure 5-A.1). Thus it no longer follows that $\vec{\xi} \cdot \vec{Y} \approx 0$. Therefore, all the terms in eqn(5-A.11) must be included in the expression for the differential component $\dfrac{\partial x^*}{\partial X}$, and similarly for $\dfrac{\partial y^*}{\partial X}$ and $\dfrac{\partial z^*}{\partial X}$.

Using the following notation,

$$\vec{\xi} = \xi^i \underline{i} + \xi^j \underline{j} + \xi^k \underline{k}\,, \quad \vec{\eta} = \eta^i \underline{i} + \eta^j \underline{j} + \eta^k \underline{k}\,,$$

$$\hat{X^*} = X^{i*} \underline{i} + X^{j*} \underline{j} + X^{k*} \underline{k}\,, \; \hat{Z^*} = Z^{i*} \underline{i} + Z^{j*} \underline{j} + Z^{k*} \underline{k}\,,$$

eqn(5-A.12)

the dot products in eqn(5-A.11) may be written as,

$$\vec{\xi} \cdot \hat{X^*} = \frac{1}{\left|\vec{\xi}\right|}\Big[(\xi^i)(X^{i*}) + (\xi^j)(X^{j*}) + (\xi^k)(X^{k*}) \Big]$$

eqn(5-A.13(a))

$$\vec{\eta} \cdot \hat{Y^*} = \frac{1}{\left|\vec{\eta}\right|}\Big[(\eta^i)((Z^{j*})(X^{k*}) - (X^{j*})(Z^{k*})) -$$

$$(\eta^j)((Z^{i*})(X^{k*}) - (X^{i*})(Z^{k*})) + (\eta^k)((Z^{i*})(X^{j*}) - (X^{i*})(Z^{j*}))\Big]$$

eqn(5-A.13(b))

$$\vec{\eta} \cdot \hat{X^*} = \frac{1}{\left|\vec{\eta}\right|}\Big[(\eta^i)(X^{i*}) + (\eta^j)(X^{j*}) + (\eta^k)(X^{k*}) \Big]$$

eqn(5-A.13(c))

$$\vec{\xi} \cdot \hat{Y^*} = \frac{1}{\left|\vec{\xi}\right|}\Big[(\xi^i)((Z^{j*})(X^{k*}) - (X^{j*})(Z^{k*})) -$$

$$(\xi^j)((Z^{i*})(X^{k*}) - (X^{i*})(Z^{k*})) + (\xi^k)((Z^{i*})(X^{j*}) - (X^{i*})(Z^{j*}))\Big]$$

eqn(5-A.13(d))

By writing eqns(5-A.13(a-d)) with eqn(5-A.7), with eqn(5-A.8) and with eqn(5-A.9), and substituting the resulting expression into eqn(5-A.11), a general equation is obtained for the differential component $\frac{\partial x^*}{\partial X}$. (This expression is not included here for reasons of brevity). The components $\frac{\partial y^*}{\partial X}$ and $\frac{\partial z^*}{\partial X}$ may be obtained in a similar manner.

The complexity of the general algebraic form of the right side of eqn(5-A.6) renders the explicit mathematical proof of the equality suggested in this equation, impractical. However, a numerical example may be used to illustrate the validity of eqn(5-A.6).

Thus, considering the general curved quadrilateral element described in Figure 5-A.2, the co-ordinates of the eight nodes are given in parentheses in the global co-ordinate system as shown. In addition the co-ordinates of the Gauss Points (Section 10.2 of the current chapter) are given in

the natural $\{\xi, \eta\}$ space. The base vectors $\vec{\xi}$ and $\vec{\eta}$ are also shown with the local X co-ordinate directions at each of the Gauss Points.

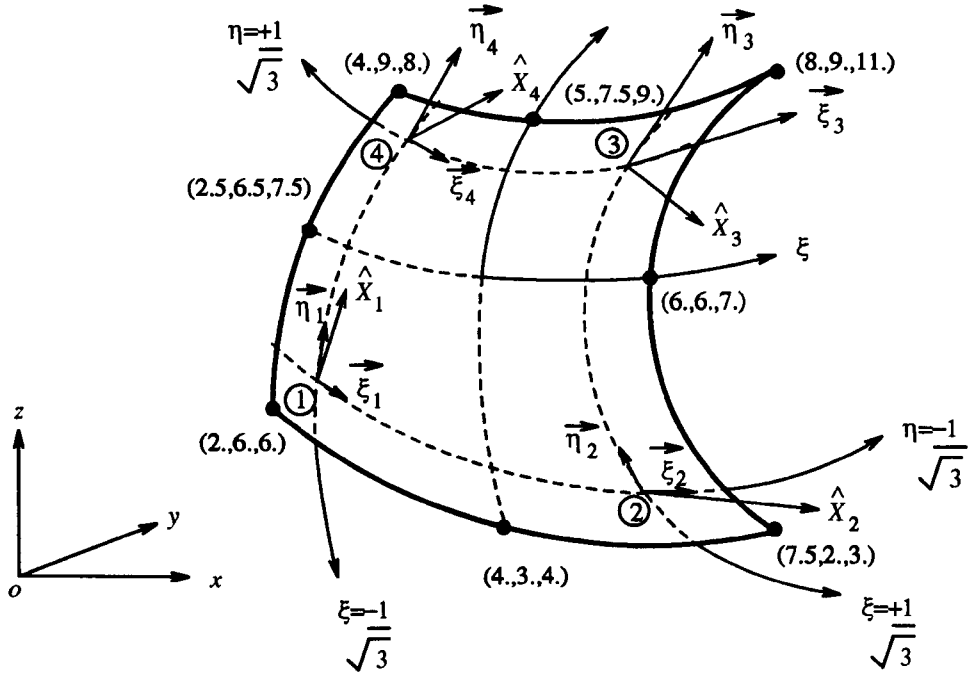

Figure 5-A.2 - General 3-Dimensional Curved Quadrilateral Element.

The coefficients comprising the vectors $\hat{X}^*$ and $\dfrac{\dfrac{\partial X^*}{\partial X}}{\left|\dfrac{\partial X^*}{\partial X}\right|^2}$,

(eqn(5-A.8), given that $\hat{X}^* = \dfrac{\vec{X}^*}{|\vec{X}^*|}$, and eqn(5-A.11)),

at the four element Gauss points (Section 5.8, Figure 5-A.2), are presented in Table 5-A.1. A comparison of the left side and the right side of eqn(5-A.6) is made in Table 5-A.2.

Component Terms	Gauss Point 1	Gauss Point 2	Gauss Point 3	Gauss Point 4
$\frac{\partial x}{\partial \xi}\frac{\partial y}{\partial \eta} - \frac{\partial x}{\partial \eta}\frac{\partial y}{\partial \xi}$	0.7001583	9.4645193	2.9520329	4.7985421
$\frac{\partial y}{\partial \xi}\frac{\partial z}{\partial \eta} - \frac{\partial y}{\partial \eta}\frac{\partial z}{\partial \xi}$	-3.8780513	2.4076056	3.7450884	-2.6072570
$\vec{\xi} \cdot \hat{X}^*$	-1.3798822	3.1357372	0.7708134	0.6086970
$\vec{\eta} \cdot \hat{Y}^*$	0.9310003	4.1723607	4.4576337	2.3872591
$\vec{\eta} \cdot \hat{X}^*$	2.0276869	-2.1918383	-1.3155410	2.0024447
$\vec{\xi} \cdot \hat{Y}^*$	-2.9024215	0.4164495	3.6774681	-2.0172717
$\frac{\partial x^*}{\partial \xi} = \sum_{i=1}^{i=8} \frac{\partial N_i}{\partial \xi} x_i$	1.2286701	3.1124970	2.8373375	0.6378043
$\frac{\partial y^*}{\partial \xi} = \sum_{i=1}^{i=8} \frac{\partial N_i}{\partial \xi} y_i$	-2.4861726	0.2905818	2.1195201	-2.0057115
$\frac{\partial z^*}{\partial \xi} = \sum_{i=1}^{i=8} \frac{\partial N_i}{\partial \xi} z_i$	-1.6240201	-0.4839456	1.2550200	0.1011159
$\frac{\partial x^*}{\partial \eta} = \sum_{i=1}^{i=8} \frac{\partial N_i}{\partial \eta} x_i$	-0.1124956	-1.3873537	2.0464879	1.6376550
$\frac{\partial y^*}{\partial \eta} = \sum_{i=1}^{i=8} \frac{\partial N_i}{\partial \eta} y_i$	0.7974814	2.9112901	2.5691710	2.3755785
$\frac{\partial z^*}{\partial \eta} = \sum_{i=1}^{i=8} \frac{\partial N_i}{\partial \eta} z_i$	2.0807796	3.4369155	3.2882204	1.1802548

Table 5-A.1 - Coefficients of the vectors $\hat{X}^*$ and $\frac{\frac{\partial \underline{X}^*}{\partial X}}{\left|\frac{\partial \underline{X}^*}{\partial X}\right|^2}$.

Gauss Point	$\hat{X}^*$	$\frac{\frac{\partial \underline{X}^*}{\partial X}}{\left\|\frac{\partial \underline{X}^*}{\partial X}\right\|^2}$
1	$0.1776714\,\underline{i} + 0\,\underline{j} + 0.9840899\,\underline{k}$	$0.1776714\,\underline{i} + 0\,\underline{j} + 0.9840899\,\underline{k}$
2	$0.9691350\,\underline{i} + 0\,\underline{j} - 0.2465307\,\underline{k}$	$0.9691350\,\underline{i} + 0\,\underline{j} - 0.2465307\,\underline{k}$
3	$0.6190478\,\underline{i} + 0\,\underline{j} - 0.7853533\,\underline{k}$	$0.6190478\,\underline{i} + 0\,\underline{j} - 0.7853533\,\underline{k}$
4	$0.8786742\,\underline{i} + 0\,\underline{j} + 0.4774220\,\underline{k}$	$0.8786742\,\underline{i} + 0\,\underline{j} + 0.4774220\,\underline{k}$

Table 5-A.2 - A Comparison of the Left Side and the Right Side of eqn(5-A.6).

By comparing the solutions given in Table 5-A.2, the equality presented in eqn(5-A.6) is shown to be true. Consequently, it is proposed that the validity of eqn(5.6.15(b)) is demonstrated implicitly for the general case.

5.11. Appendix 5-B - Necessary Inclusion of the Higher Order Terms of the Expression for Strain when Calculating the Total Strain of an Elastic Continuum.

The higher order term, $\frac{\partial U}{\partial X}^{ho}$, is written as (eqn(5.6.9)),

$$\frac{\partial U}{\partial X}^{ho} = \frac{\frac{\partial \delta}{\partial \vec{\xi}} \cdot \frac{\partial \delta}{\partial \vec{\xi}}}{2 \left| \frac{\partial X}{\partial \vec{\xi}} \right|^2} . \qquad \text{eqn(5-B.1)}$$

Expansion of the dot product in the numerator of eqn(5-B.1) leads to,

$$\frac{\partial U}{\partial X}^{ho} = \frac{1}{2} \frac{\left\{ \frac{\partial u}{\partial \xi}\frac{\partial u}{\partial \xi} + \frac{\partial v}{\partial \xi}\frac{\partial v}{\partial \xi} + \frac{\partial w}{\partial \xi}\frac{\partial w}{\partial \xi} \right\}}{\left| \frac{\partial X}{\partial \vec{\xi}} \right|^2} \qquad \text{eqn(5-B.2)}$$

Considering the first product in the parentheses of eqn(5-B.2), and substituting the scalar displacement u into eqn(5.5.6) yields,

$$\begin{bmatrix} \frac{\partial u}{\partial \xi} \\ \frac{\partial u}{\partial \eta} \end{bmatrix} = \begin{bmatrix} \vec{\xi} \cdot \hat{X} & \vec{\xi} \cdot \hat{Y} \\ \vec{\eta} \cdot \hat{X} & \vec{\eta} \cdot \hat{Y} \end{bmatrix} \begin{bmatrix} \frac{\partial u}{\partial X} \\ \frac{\partial u}{\partial Y} \end{bmatrix} . \qquad \text{eqn(5-B.3)}$$

By adopting the assumptions that $\hat{X} = \frac{\vec{\xi}}{|\vec{\xi}|}$ with $\hat{Y} \approx \frac{\vec{\eta}}{|\vec{\eta}|}$, then global displacement u is equivalent to the local displacement U. Therefore, the first term on the left side of eqn(5-B.3) (with eqn(5.5.7(a)) may be written as,

$$\frac{\partial u}{\partial \xi} = \frac{\partial U}{\partial \xi} = (\vec{\xi} \cdot \hat{X}) \frac{\partial U}{\partial X} . \qquad \text{eqn(5-B.4)}$$

Substitution of eqn(5.6.20) into eqn(5-B.4) leads to,

$$\frac{\partial u}{\partial \xi} = \left| \frac{\partial X}{\partial \vec{\xi}} \right| \frac{\partial U}{\partial X} . \qquad \text{eqn(5-B.5)}$$

Similarly, expressions may be derived for $\frac{\partial v}{\partial \xi}$ and $\frac{\partial w}{\partial \xi}$, where,

$$\frac{\partial v}{\partial \xi} = \left| \frac{\partial X}{\partial \vec{\xi}} \right| \frac{\partial V}{\partial X}, \text{ and, } \frac{\partial w}{\partial \xi} = \left| \frac{\partial X}{\partial \vec{\xi}} \right| \frac{\partial W}{\partial X} . \qquad \text{eqn(5-B.6)}$$

Rewriting eqn(5-B.2) with eqn(5-B.5) and eqn(5-B.6) yields the familiar expression,

$$\frac{\partial U}{\partial X}^{ho} = \frac{1}{2} \left[\left[\frac{\partial U}{\partial X} \right]^2 + \left[\frac{\partial V}{\partial X} \right]^2 + \left[\frac{\partial W}{\partial X} \right]^2 \right] . \qquad \text{eqn(5-B.7)}$$

The total direct strain in the local X direction, $\frac{\partial U^t}{\partial X}$, may therefore be given as,

$$\frac{\partial U^t}{\partial X} = \frac{\partial U}{\partial X} + \frac{\partial U^{ho}}{\partial X}, \qquad \text{eqn(5-B.8)}$$

and similarly for strains in the other local directions, Y and Z.

The contribution of the terms given by eqn(5-B.7) to the total strain of an elastic continuum subjected to a global displacement vector $\{ \underline{\delta} \}$, is demonstrated by the membrane illustrated in Figure 5-B.1.

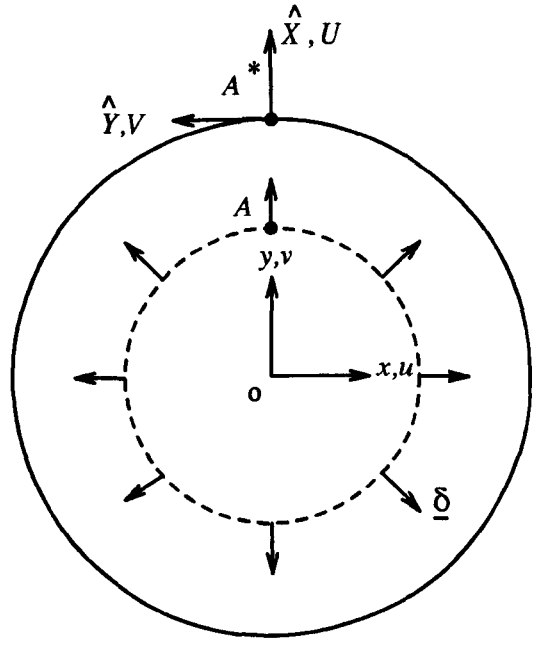

Figure 5-B.1 - General 2-Dimensional Elastic Continuum Subjected to a Displacement Vector $\underline{\delta}$

For simplicity, the membrane is assumed to be two dimensional with the global and local axes as indicated in Figure 5-B.1. It is assumed also that the global displacement vector, $\{ \underline{\delta} \}$, describes a radial stretching of the membrane.

To reduce the complexity of the calculations further, the point A is assumed to move to the new location A^*, after application of $\{ \underline{\delta} \}$, such that the local axes, rotated through ninety degrees, are parallel with the global co-ordinate system (Figure 5-B.1). Given that the membrane is discretised by a set of infinitesimally small quadratic quadrilateral elements, so that, at the point A, the global displacement vector describes displacements in the y direction as non-zero, and those in the x direction as zero, then the analysis continues as described below.

Rewriting eqn(5-B.8) for the two-dimensional problem given in Figure 5-B.1, the element strain in the local X direction may be given as,

$$\frac{\partial U'}{\partial X} = \frac{\partial U}{\partial X} + \frac{1}{2}\left[\left(\frac{\partial U}{\partial X}\right)^2 + \left(\frac{\partial V}{\partial X}\right)^2\right]. \qquad \text{eqn(5-B.9)}$$

Writing $\{\,\underline{\delta}\,\}$ as,

$$\{\,\underline{\delta}\,\} = \{\,u\,\underline{i} + v\,\underline{j}\,\}, \qquad \text{eqn(5-B.10)}$$

then,

$$\frac{\partial \delta}{\partial X} = \left\{\frac{\partial u}{\partial X}\,\underline{i} + \frac{\partial v}{\partial X}\,\underline{j}\right\}. \qquad \text{eqn(5-B.11)}$$

where, $\underline{i}$, $\underline{j}$ are unit vectors aligned with the global axes x, y.

Given that, $\vec{\xi} \cdot \hat{Y} = 0.$, and invoking the Jacobian Matrix given in eqn(5.5.7(a)), then,

$$\frac{\partial u}{\partial X} = \frac{1}{\det[J]}\,(\vec{\eta} \cdot \hat{Y})\,\frac{\partial u}{\partial \xi}, \qquad \text{eqn(5-B.12)}$$

and,

$$\frac{\partial v}{\partial X} = \frac{1}{\det[J]}\,(\vec{\eta} \cdot \hat{Y})\,\frac{\partial v}{\partial \xi},$$

$$= \frac{1}{\det[J]}\,(\vec{\eta} \cdot \hat{Y})\sum_{i=1}^{i=8}\frac{\partial N_i}{\partial \xi} \cdot v_i. \qquad \text{eqn(5-B.13)}$$

where the final form of eqn(5-B.13) may be obtained by using eqn(5.3.3.7) and eqn(5.3.2.2).

Since in the vicinity of the point A, v is zero throughout the element, eqn(5-B.13) may be rewritten as,

$$\left.\frac{\partial v}{\partial X}\right|_A = 0. \qquad \text{eqn(5-B.14)}$$

Substituting eqn(5-B.14) into eqn(5-B.11) yields,

$$\frac{\partial \delta}{\partial X} = \left\{\frac{\partial u}{\partial X}\,\underline{i} + 0\,\underline{j}\right\}. \qquad \text{eqn(5-B.15)}$$

Noting that, at the point A,

$$\hat{X}\Big|_A = \left\{0\,\underline{i} + 1\,\underline{j}\right\}, \qquad \text{eqn(5-B.16)}$$

with the substitution of the right hand side of eqn(5-B.15) and eqn(5-B.16) into eqn(5.6.15(b)), and making use of eqn(5.6.21), gives,

$$\left.\frac{\partial U}{\partial X}\right|_A = 0.. \qquad \text{eqn(5-B.17)}$$

Similarly, at the point A, given that,

$$\frac{\partial V}{\partial X} = \frac{\partial \delta}{\partial X} \cdot \hat{Y}, \quad \text{and,} \quad \hat{Y} = \left\{ -1\,\underline{i} + 0\,\underline{j} \right\}, \qquad \text{eqn(5-B.18)}$$

then,

$$\left.\frac{\partial V}{\partial X}\right|_A = \left.\frac{\partial \delta}{\partial X} \cdot \hat{Y}\right|_A = -\left.\frac{\partial u}{\partial X}\right|_A . \qquad \text{eqn(5-B.19)}$$

Therefore, substitution of eqn(5-B.17) and eqn(5-B.19) into eqn(5-B.9) yields,

$$\left.\frac{\partial U^t}{\partial X}\right|_A = \frac{1}{2}\left[-\frac{\partial u}{\partial X} \right]^2_A . \qquad \text{eqn(5-B.20)}$$

Eqn(5-B.20) indicates that, regardless of the magnitude of the global displacement vector $\{ \underline{\delta} \}$, the higher order terms of strain as given by eqn(5-B.7) must be included if the overall strains of the membrane are to be represented adequately, and therefore the true equilibrium state described, by the proposed numerical model. This is demonstrated further by the fact that the omission of such higher order terms would result in eqn(5-B.20) being equal to zero (irrespective of the magnitude of the vector $\{ \underline{\delta} \}$) as the first order term does not appear on the right side.

5.12. Appendix 5-C - Displacement Vectors for Examples 5.2, 5.3, and 5.4 (Figure 5.17 (a)-(c)).

The displacement vector, $\underline{\delta}$, corresponding to the element illustrated in Figure 5.17(a) (Example 5.2), is given as,

$$\underline{\delta} = \begin{Bmatrix} u_1, v_1 \\ u_2, v_2 \\ u_3, v_3 \\ u_4, v_4 \\ u_5, v_5 \\ u_6, v_6 \\ u_7, v_7 \\ u_8, v_8 \end{Bmatrix} = \begin{Bmatrix} +5.75, +3.25 \\ +7.50, +4.50 \\ +8.00, +6.50 \\ +7.00, +6.30 \\ +6.50, +6.00 \\ +6.00, +6.40 \\ +4.50, +4.75 \\ +6.00, +4.30 \end{Bmatrix}.$$

where $\{u_i, v_i\}$ $(i = 1 \rightarrow 8)$, are the displacements in the global x and y co-ordinate directions respectively, at the element nodes. (The nodal displacements, w_i, corresponding to the global z direction, are assumed to be zero.)

In the case of the element illustrated in Figure 5.17(b) (Example 5.3), $\underline{\delta}$ is,

$$\underline{\delta} = \begin{Bmatrix} 0.00, 0.00 \\ +4.00, 0.00 \\ +6.00, 0.00 \\ +5.00, +0.50 \\ +4.00, +1.00 \\ +1.00, +2.00 \\ +2.00, -1.00 \\ +1.00, -0.50 \end{Bmatrix},$$

and of the element illustrated in Figure 5.17(c) (Example 5.4), $\underline{\delta}$ is,

$$\underline{\delta} = \begin{Bmatrix} 0.00, 0.00 \\ +2.00, 0.00 \\ +4.00, 0.00 \\ +2.00, 0.00 \\ 0.00, 0.00 \\ 0.00, 0.00 \\ 0.00, 0.00 \\ 0.00, 0.00 \end{Bmatrix}.$$

5.13. References.

[5.1] Cook, R.D. *Concepts and Applications of Finite Element Analysis, a Treatment of the Finite Element Method as Used for the Analysis of Displacement, Strain and Stress.*

Wiley, London, 1974.

[5.2] Barnes, M.R., Wakefield, D.,

"Dynamic Relaxation Applied to Interactive Form-finding and Analysis of Air- supported Structures."

IStructE Conference on Design of Air-supported Structures, Bristol, 1984.

[5.3] Oden, J.T.,

Finite Elements of Non-linear Continua.

McGraw-Hill Advanced Engineering Series, 1972.

[5.4] Ergatoudis, I., Irons, B., Zienkiewicz, O.C.,

"Curved Isoparametric, 'Quadrilateral' Elements for Finite Element Analysis."

International Journal of Solids and Structures, Volume 4, Number 1, 1968, pages 31-42.

[5.5] Lewis, P.E., Ward, J.P.,

Vector Analysis for Engineers and Scientists.

Modern Applications of Mathematics Series, Addison Wisley Publishing Company, 1989, pages 269-278.

[5.6] Borisenko, A.I., Tarapov, I.E.,

Vector and Tensor Analysis with Applications.

Dover Publications Inc., New York, 1968, pages 82-86.

[5.7] Irons, B., Ahmad, S.,

Techniques of Finite Elements.

Ellis Horwood Series in Engineering Science, 1980, pages 77-79, & 443-445.

[5.8] Zienkiewicz, O.C., Taylor, R.C.,

The Finite Element Method.

Fourth Edition, Volume 1, Basic Formulation and Linear Problems, 1989, pages 35-37.

[5.9] Green, A.E., Zerna, W.,

Theoretical Elasticity.

Second Edition, Oxford (Clarendon) Press, 1968, pages 18-19, & 53-57.

[5.10] Ford, H., Alexander, J.M.,

Advanced Mechanics of Materials.

Longmans Publishing Group, 1963, pages 113-121.

[5.11] Zienkiewicz, O.C.,

The Finite Element Method in Engineering Science.

McGraw-Hill, London, 1971, pages 413-434.

[5.12] Scarborough, J.B.,

Numerical Mathematical Analysis.

John Hopkins Press, 1966, pages 152-159.

[5.13] Arden, B.W., Astill, K.N.,

Numerical Algorithms : Origins and Applications.

Addison Wesley Publishing Company, 1970, pages 86-96.

[5.14] Cook, R.D., Malkus, D.S., Plesha, M.E.,

Concepts and Applications of Finite Element Analysis.

John Wiley and Sons, 1989, pages 170-173, & 190-194.

[5.15] Lewis, W.J.

"A Comparative Study of Numerical Methods for the Solution of Pretensioned Cable Networks."

Proc. Int. Conf. Non-conventional Structures, Civil-Comp Press 2, pages 27-33, 1987.

[5.16] Barnes, M.R.

"Non-linear Numerical Solution Methods for Static and Dynamic Analysis of Tension Structures."

Symposium on Air Supported Structures, IStructE, London, 1980.

[5.17] Celia, M.A., Gray, W.G.

"An Improved Isoparametric Transformation for Finite Element Analysis."

International Journal for Numerical Methods in Engineering, Volume 20, pages 1443-1459, 1987.

[5.18] Jeffrey, A.

Mathematics for Engineers and Scientists.

Thomas Nelson & Sons Limited, 1969.

[5.19] Parry Lewis, J.

An Introduction to Mathematics.

M^{c} Millan & Co. Limited., London, 1964.

[5.20] Korn, G.A., Korn, T.M.

Mathematical Handbook for Scientists and Engineers.

M^{c} Graw Hill Book Co., Inc., 1961.

[5.21] Ahmad, S.

Finite Elements in the Analysis of Solid, Shell, and Plate Structures.

Ph.D. Thesis, School of Engineering, Division of Civil Engineering, University College Swansea, April 1969.

[5.22] Liu, W., Yang, Y-B.

"General Eigenvalue Test for Non-linear Finite Elements."

Proceedings of 4th International Conference on Civil and Structural Engineering Computing, CIVIL COMP 89, London, Sept. 19-21, 1989, Civil-Comp Limited, Edinburgh, pages 345-350, 1989.

Chapter 6

24 Degrees-of-Freedom Quadratic Quadrilateral Finite Element for the Investigation of Stable Minimal Energy Forms - An Appraisal of the Quality of the Element Formulation.

6.1. Introduction.

The general finite element theory is based on the assumptions that the element shape functions satisfy certain continuity requirements, and that the integrals contained in the equations describing the discretisation, are calculated exactly [6.1]. In addition, the ability of the element to represent accurately a desired response, relies extensively on the assumptions made during the formulation. The selection of the degrees of freedom, describing either translation or rotation, and the location and number of element nodes, are some of the variables which directly influence the suitability of an element to a particular application.

For example, the omission of rotational degrees of freedom and a lack of continuity of slope in the shape functions of a shell element, may lead to significant errors when analysing a thick shell structure or plate. The error decreases however with a reduction in the thickness of the shell, as there is an increased reliance on pure membrane action and a reduction in bending stiffness.

The consequences of the failure to fulfill the requirements which validate the basic finite element theory, and the effect of subsequent assumptions made during the element formulation, can be assessed by the "Patch Test" and the "Eigenvalue Test". The results of these fundamentally "single element" tests are presented in the following two sections of this chapter. The implementation of the element formulation with the Dynamic Relaxation algorithm is discussed, and an assessment is made of the inherent assumptions in the derivation of the element equations in this respect. The quality of the element formulation is also appraised in a global sense through the investigation of several minimal surfaces presented in the latter part of the chapter.

6.2. Patch Test.

6.2.1. General Formulation.

The concept of the Patch Test is simple, and may be expressed as in the subsequent statement - if it can be verified that an arbitrary "patch" of elements reproduces exactly the behaviour of a linear elastic solid material when it has been subjected to boundary conditions which are consistent with a state of constant straining, then both the necessary and the sufficient conditions for the convergence of the finite element discretisation to the exact solution with mesh refinement, are obtained [6.2].

A patch of elements is analysed and a solution obtained for the nodal displacements. It is required that, for the Patch Test to be passed, the computed displacements agree exactly with those obtained from a mathematical or closed form solution [1] . The application of the Patch Test is described below.

A small number of elements are assembled into a "patch" such that at least one node of the discretisation lies within (but not on) the boundary of the patch. Furthermore, this node must be shared by two or more elements so that one or more common element boundary exists. The patch is subsequently provided with sufficient constraints (placed on the nodal displacements) in order to prevent the rigid body motion of the complete discretisation. The internal nodes are neither constrained nor loaded. The unconstrained boundary nodes are loaded with a consistently derived nodal force vector $\{F_{eq}\}$, representing the uniform stress vector, $\{\sigma\}$, (Appendix 6-A).

The numerical solution to the element nodal displacements is obtained through the compilation of the global stiffness matrix $[K_t^g]$ initially. The matrix $[K_t^g]$ represents the elastic and the geometric stiffness of the complete "patch" of elements. The displacement constraints are applied by the removal of the appropriate rows and columns (corresponding to the constrained degrees-of-freedom) from the matrix $[K_t^g]$. This operation generates the reduced stiffness matrix $[K_t^{red}]$.

An LU decomposition algorithm [6.1] is used to invert the matrix $[K_t^{red}]$. The resulting flexibility matrix is post-multipled by the vector of equivalent nodal forces $\{F_{eq}\}$, yielding the required numerical solution to the element nodal displacements.

A suitable patch of elements is illustrated in Figure 6.1. The numerical model is intended to represent a thin plate or membrane, subjected to an axial tensile stress, $\sigma_x = 1500.\ \text{kN.m}^{-2}$, in the global x direction. The elastic modulus of the plate, E, is assumed to be $1.\times10^{+4}\ \text{kN.m}^{-2}$, with Poissons's ratio, υ, equal to 0.1. The thickness of the plate is taken as $1.\times10^{-3}$ m. In addition to

1

The phrase "agree exactly" permits only deviations in the solutions which can be attributed to computational noise or rounding errors.

the externally applied stress, σ_x, a prestress has been applied to all elements of the discretisation in the global x and y directions. The magnitude of the prestress is equivalent to $1.\times10^{-4}$ % of the elastic modulus of the plate [2].

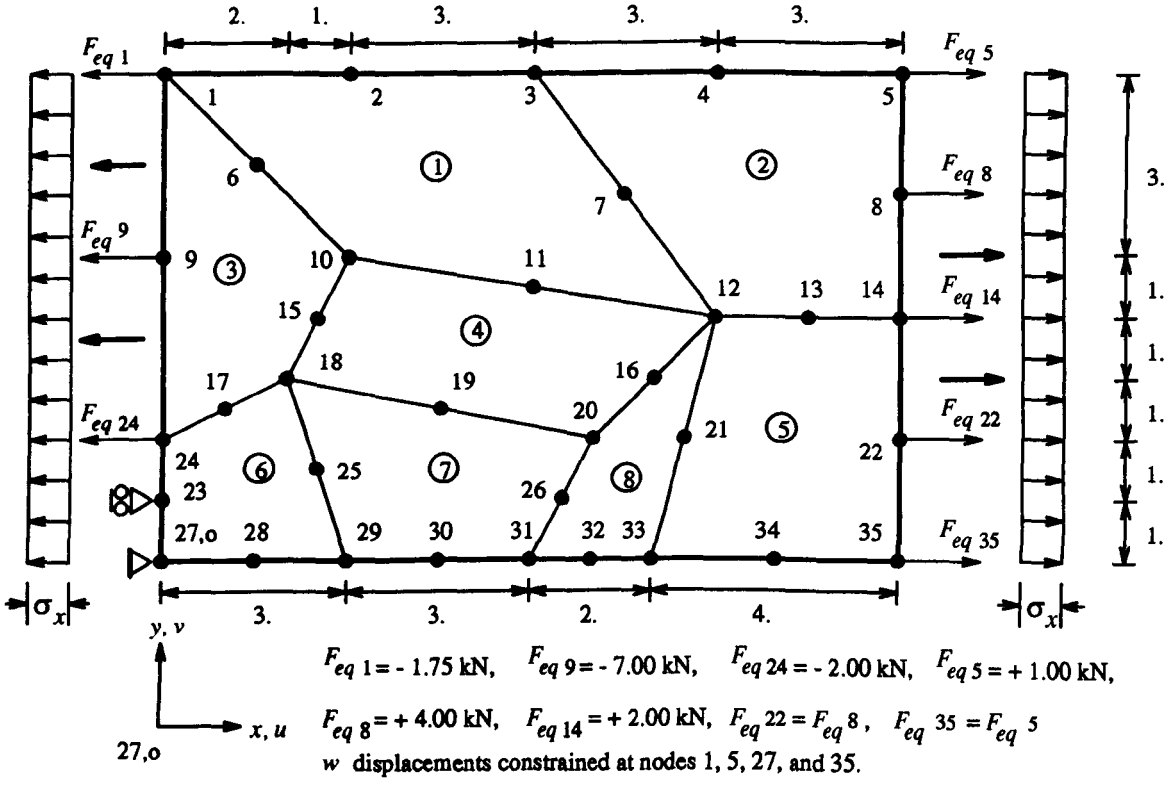

Figure 6.1 - General Patch of Quadratic Quadrilateral Finite Elements.

The numerical solution to the element nodal displacements (Figure 6.1) is presented in the last two columns of Table 6.1. As described below, the exact solution to the displacements is obtained from the fundamental theory of elasticity.

In the case of in-plane, uni-directional loading, the plate can be treated as a wide bar. Consequently, the stiffness of the plate in the x direction is $\frac{EA_x}{L_x}$, where A_x is the cross-sectional area and L_x the length of the plate [3] [6.7]. Using a simple stiffness approach therefore, the total extension of the plate in the x direction, e_x, is given as $e_x = \frac{\sigma_x A_x L_x}{E A_x} = \frac{\sigma_x L_x}{E}$. In addition, Poisson's ratio, υ, gives the extension of the bar in the y direction, e_y, as $e_y = -\upsilon e_x$ [6.7].

---

2 An explanation of the inclusion of this additional prestress is presented in Appendix 6-B.

3 The cross-sectional area of the plate, A_x, is calculated as the product of the dimension of the plate in the y direction with the thickness of the plate. The length of the plate, L_x, is the dimension of the plate in the x direction (Figure 6.1).

The extension of the plate is represented by a state of constant strain. The values of the displacements within the plate are thus proportional to the extensions e_x and e_y. Consequently, if a point p is at the position, $x = x_p$, where $x_p = \frac{L_x}{3}$, then the displacement of the point p in the x direction, δ_p, is $\delta_p = \frac{e_x}{L_x}\frac{L_x}{3} = \frac{e_x}{3}$.

Based on this approach, the exact solution to the displacements of the plate at the positions of the element nodes is obtained. The exact solution is presented in the second and third columns of Table 6.1.

By comparing column 2 with column 4, and column 3 with column 5, small disparities between the exact and the numerical solutions to the displacements of the axially loaded plate (Figure 6.1) can be identified (Table 6.1). These disparities can be attributed to rounding errors and to the conditioning of the global stiffness matrix, $[K_t^{plate}]$ [4]. Consequently, it is demonstrated that the element formulation presented in the preceding chapter passes the Patch Test.

Node	Exact Displacements (m)		Calculated Displacements (m)	
i	u_i^{ex}	v_i^{ex}	u_i^{cal}	v_i^{cal}
1	0.00000000	-0.12000000	0.00000000	-0.11999976
2	0.45000000	-0.12000000	0.44999955	-0.11999976
3	0.90000000	-0.12000000	0.89999909	-0.11999976
4	1.35000000	-0.12000000	1.34999864	-0.11999976
5	1.80000000	-0.12000000	1.79999818	-0.11999976
6	0.22500000	-0.09750000	0.22499977	-0.09749980
7	1.12500000	-0.09000000	1.12499886	-0.08999982
8	1.80000000	-0.09000000	1.79999820	-0.08999982
9	0.00000000	-0.06750000	0.00000001	-0.06749987
10	0.45000000	-0.07500000	0.44999955	-0.07499985
11	0.90000000	-0.67500000	0.89999909	-0.06749986
12	1.35000000	-0.06000000	1.34999864	-0.05999988
13	1.57500000	-0.06000000	1.57499841	-0.05999988
14	1.80000000	-0.06000000	1.79999818	-0.05999988
15	0.37500000	-0.06000000	0.37499962	-0.05999988

Table 6.1 - Patch Test Results (Figure 6.1) - *continued.*

[4] The magnitude of the condition number of the global stiffness matrix, $[K_t^{plate}]$, is discussed in Appendix 6-B.

Node	Exact Displacements (m)		Calculated Displacements (m)	
i	u_i^{ex}	v_i^{ex}	u_i^{cal}	v_i^{cal}
16	1.20000000	-0.04500000	1.19999879	-0.04499991
17	0.15000000	-0.03000000	0.14999985	-0.02999994
18	0.30000000	-0.04500000	0.29999970	-0.04499991
19	0.67500000	-0.03750000	0.67499932	-0.03749992
20	1.05000000	-0.03000000	1.04999893	-0.02999994
21	1.27500000	-0.03000000	1.27499871	-0.02999994
22	1.80000000	-0.03000000	1.79999818	-0.02999994
23	-	-0.00750000	-	-0.07499985
24	0.00000000	-0.01500000	0.00000001	-0.01499997
25	0.37500000	-0.02250000	0.37499962	-0.02249995
26	0.97500000	-0.01500000	0.97499902	-0.01499997
28	0.22500000	0.00000000	0.22499977	-0.00000001
29	0.45000000	0.00000000	0.44999955	-0.00000001
30	0.67500000	0.00000000	0.67499932	-0.00000001
31	0.90000000	0.00000000	0.89999909	-0.00000001
32	1.05000000	0.00000000	1.04999893	-0.00000001
33	1.20000000	0.00000000	1.19999879	-0.00000001
34	1.50000000	0.00000000	1.49999955	-0.00000001
35	1.80000000	0.00000000	1.79999818	-0.00000001

Table 6.1 - Patch Test Results (Figure 6.1) - *continued.*

6.2.2. An "Implicit" Patch Test for Geometrically Non-linear Finite Elements.

The Patch Test can demonstrate the ability of the element formulation to model accurately the condition of constant strain. It is usually applied to the situation of geometrically linear elasticity, where it is assumed that the external load vector acts in the plane of the discretisation, and that the geometries of the elements are flat (Section 6.2.2). The standard Patch Test does not assess the correctness or the convergence of the out-of-plane (or geometrically non-linear) response of the element formulation however.

A Patch Test could be devised based on the closed form, or the semi-analytical solutions to the displacements of a laterally loaded rectangular plate. However, significant approximations are made during the derivation of the appropriate governing equations [6.6]. The solutions from the closed form, or semi-analytical approaches are not sufficiently rigorous therefore to adopt as the basis of comparison with the solution from the finite element formulation. Consequently, an

"implicit" Patch Test for geometrically non-linear finite elements is proposed below.

If the Patch Test is passed in a geometrically linear elastic sense, then the convergence of the finite element model to the exact solution with mesh refinement is ensured [6.2]. Therefore, if it can be shown that a geometrically non-linear finite element model converges to the exact (predicted) solution with mesh refinement, then the "implicit" Patch Test is passed. Consequently, the correctness of the geometrically non-linear finite element formulation is demonstrated. The application of the proposed "implicit" Patch Test is described below.

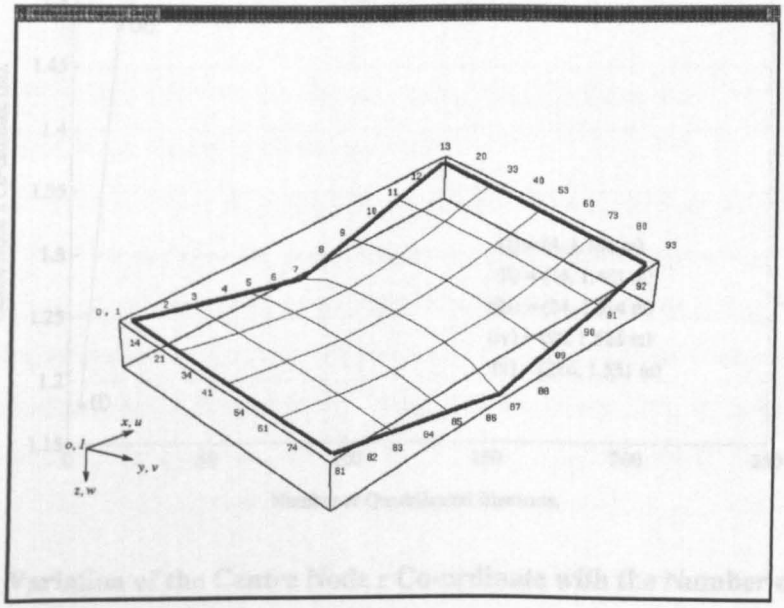

Table 6.2 - Boundary Conditions (Symmetrical).

Nodes	2, 82	3, 83	4, 84	5, 85	6, 86	7, 87
z co-ord. (m)	0.500	1.000	1.500	2.000	2.500	3.000

Figure 6.2 - Surface Discretised using Quadrilateral Elements - Example 6.1.

The surface illustrated in Figure 6.2 is defined by the overall dimensions of 24.m and 16.m in the global x and y directions respectively. The initial element sizes are assumed to be equal (on plan). The surface is subjected to a uniform stress vector, $\{\sigma_o\}$, defined by $\sigma_x = \sigma_y = 5.\times10^{+6}$ kN.m^{-2} and $\tau_{xy} = 0.$ kN.m^{-2}. The stiffness of the surface is derived from prestress only, while the thickness of the membrane is assumed to be $1.\times10^{-3}$m. The geometrical boundary conditions of the surface are presented in Table 6.2. The condition of equilibrium is satisfied to an error residual, Er, equal to 0.025 % of the maximum element equivalent nodal force.

Figure 6.3 shows the variation of the global z co-ordinate of the central node of the membrane at equilibrium (Figure 6.2), with the number of elements used to discretise the surface. As the number of elements is increased from four to 216, the solution to the central node z co-ordinate

of the surface is shown to converge rapidly and asymptotically from an under-estimate of the exact (predicted) solution to a solution of 1.535 m (approximately).

The convergence of the numerical solution to the exact (predicted) solution with mesh refinement is demonstrated (Figure 6.3). Consequently, it is recommended that, in the case of the proposed geometrically non-linear element formulation (Chapter 5), the "implicit" Patch Test is passed [5] .

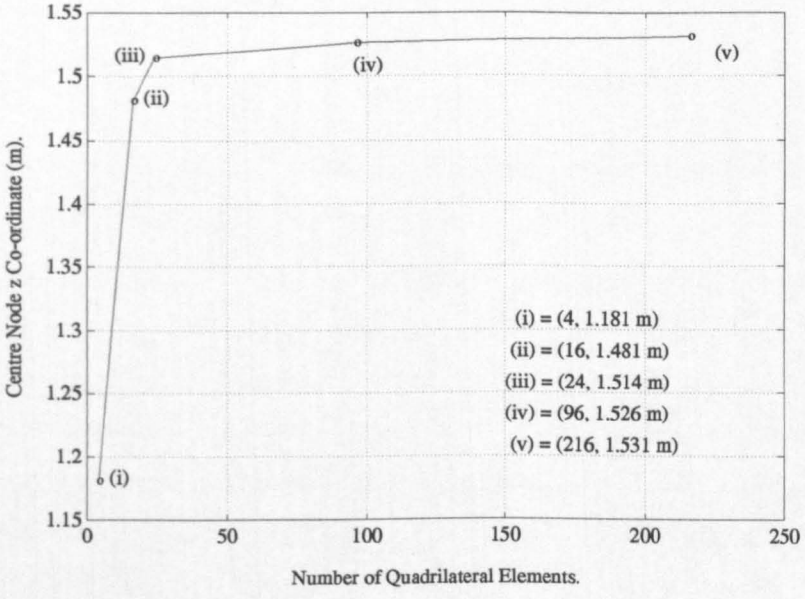

Figure 6.3 - Variation of the Centre Node z Co-ordinate with the Number of Elements.

6.2.3. Effects of the Assumptions of Small Displacements in the Derivation of the Element Shape Functions.

Section 5.3.3 of the preceding chapter outlines the mathematical bases behind the generation of the element shape functions. In the case of the shape functions derived using the small displacement theory (Section 5.3.3.1 Chapter 5), it is assumed that the position of the element side nodes remain at or very close to the centre of the element side on which the node appears. The standard Patch Test (Section 6.2.1) can be used to assess the magnitude of the error induced in the numerical model as this assumption is increasingly violated. The error is measured through a non-dimensional norm, $|e|$. As demonstrated below, the results of this study can be used to

5

The solutions to the element nodal displacements presented in this and the preceding section (Table 6.1, Figure 6.3), have been based on the calculation of the integrands (representing the element stiffness matrices and equivalent nodal force vectors), by the technique of reduced integration (Section 10.2 of Chapter 5). A numerical 2×2 Gauss integration scheme has been adopted, rendering the element elastic and geometric stiffness matrices rank deficient, and prone to exhibit spurious zero energy modes. The proposed element formulation (Chapter 5) is shown therefore to pass the standard Patch Test and the "implicit" Patch Test when the element integrands are evaluated using the technique of reduced integration.

determine an upper bound limit to the admissible deviation of the side nodes from the central position.

An appropriate basis for the error norm, $|e|$, is the disparity between the numerical and the exact strains. By assuming a plane stress element of constant thickness, t, the error norm, $|e|$, may be written as [6.3],

$$|e|^2 = t \iint \left\{ \{\varepsilon\}^{nume.} - \{\varepsilon\}^{exact} \right\}^T [E] \left\{ \{\varepsilon\}^{nume.} - \{\varepsilon\}^{exact} \right\} dX\, dY \qquad \text{eqn(6.2.3.1)}$$

where $\{\varepsilon\}^{nume.}$ and $\{\varepsilon\}^{exact}$ are the numerical and the exact strain vectors respectively, and where $[E]$ is the matrix of elastic constants.

A suitable patch of elements is presented in Figure 6.4. The numerical model is intended to represent a thin plate or membrane, subjected to an axial tensile stress, σ_x, in the global x direction. The stress, σ_x, is simulated by a vector of equivalent nodal forces, given by equations of a similar form to that of eqn(6-A.4) (Appendix 6-A). The patch of elements is assumed to deform in a symmetrical and a geometrically linear manner. In addition, the initial stress and the initial displacements of the plate are assumed to be zero [6]. Consequently, the strains within a typical element, k, may be calculated from a simplified form of eqn(5.7.1.6) written as,

$$\{\varepsilon\} = \begin{Bmatrix} \varepsilon_X \\ \varepsilon_Y \\ \gamma_{XY} \end{Bmatrix}_k = \begin{Bmatrix} \varepsilon_x \\ \varepsilon_y \\ \gamma_{xy} \end{Bmatrix}_k = [B_o\ (\xi, \eta)]_k\ \{\delta\}_k \qquad \text{eqn(6.2.3.2)}$$

where the matrix $[B_o\ (\xi, \eta)]_k$ contains the linear terms of the strain displacement relationships, and $\{\delta\}_k$ represents the vector of nodal displacements corresponding to the element k.

6

In the situation that the initial stress is zero, the stiffness of the plate is derived from elasticity only. Furthermore, the matrix $[B_L]$ has been shown to be linearly dependent on the element nodal displacements (Section 5.7.3, Chapter 5). Therefore, by assuming that the initial displacements within the plate are zero, the element matrix $[B_L]$ is a null matrix (initially). Consequently, the element strains are a function of the small strain displacement matrix, $[B_o]$, only (Section 5.7.1, Chapter 5).

Substituting eqn(6.2.3.2) into eqn(6.2.3.1), and rewriting the resulting expression in terms of the natural co-ordinates, $\{\xi, \eta\}$, gives [7],

$$|e|^2 = \int_{-1}^{+1}\int_{-1}^{+1} \left([B_o(\xi,\eta)]_k \{\delta\}_k^{nume.} - [B_o(\xi,\eta)]_k \{\delta\}_k^{exact} \right)^T [E] \cdot \left([B_o(\xi,\eta)]_k \{\delta\}_k^{nume.} - [B_o(\xi,\eta)]_k \{\delta\}_k^{exact} \right) \det[J]\, d\xi\, d\eta$$

eqn(6.2.3.3)

where $\{\delta\}_k^{nume.}$ and $\{\delta\}_k^{exact}$ are the numerical and the exact vectors of element nodal displacements, respectively.

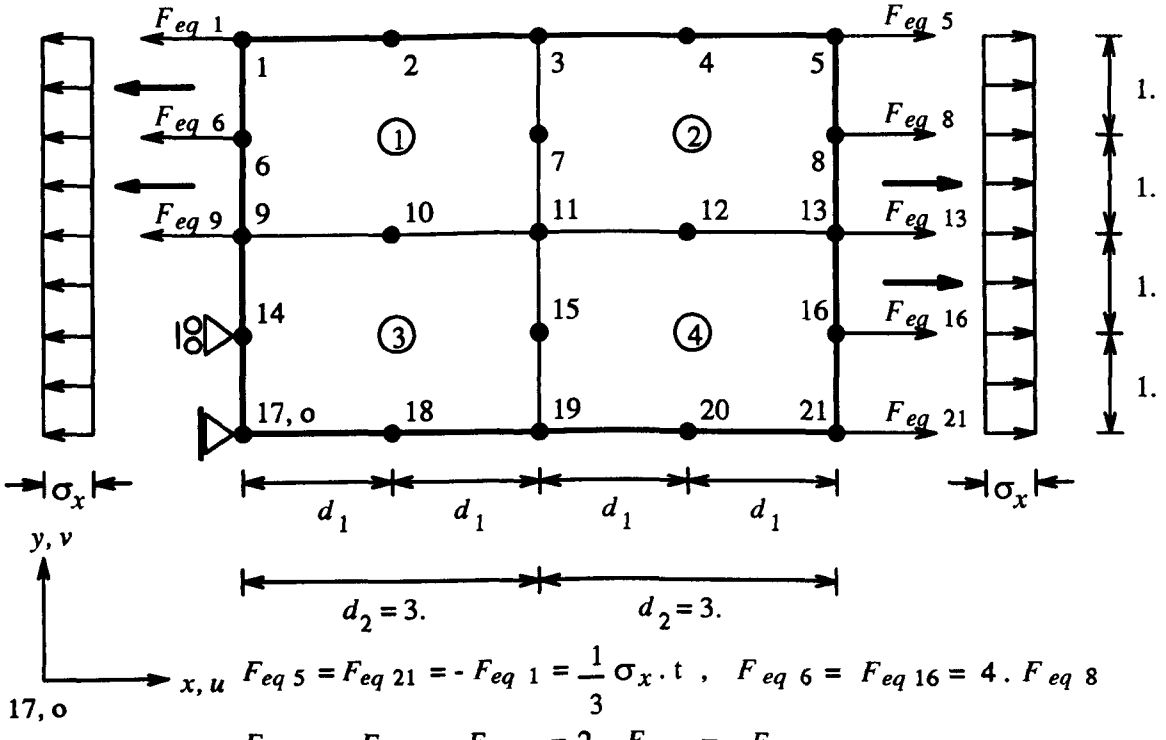

Figure 6.4 - Regular Patch of Quadratic Quadrilateral Finite Elements.

7

Since the matrix $[B_o]_k$ is a function of the natural co-ordinates, $\{\xi, \eta\}$, a change of variable is required in order to evaluate the integral given in eqn(6.2.3.1). It can be shown that $dX\, dY = \det[J]\, d\xi\, d\eta$ [6.5]. The coefficient, $\det[J]$, is the determinant of the Jacobian matrix, $[J]$, (eqn(5.5.7(b), Chapter 5) and is a scaling factor that yields the area of the distorted parent element (Figure 5.2(a), Chapter 5), $dX\, dY$, from the area of the mapped element (Figure 5.2(c), Chapter 5), $d\xi\, d\eta$.

As demonstrated below, the effects of the violation of the assumption of small displacements in the derivation of the element shape functions given in Table 5.1 (Chapter 5), can be investigated by monitoring the error norm, $|e|$, as the ratio $\frac{d_1}{d_2}$ is varied for the element nodes 2, 4, 10, 12, 18, and 20 (Figure 6.4). Figure 6.5 shows the error norm in the strain calculation, $|e|$, for the variation of the ratio $\frac{d_1}{d_2}$ in the range $0.1 \leq \frac{d_1}{d_2} \leq 0.9$. The element node is considered to be at the centre of the side when $\frac{d_1}{d_2} = 0.5$. The error norm, $|e|$, is presented using a logarithmic scale, and is obtained as the sum of the error norms at nine Gauss points for the element **3** (Figure 6.4) [8] . The strains which are calculated using the shape functions based on the small displacement theory (Section 5.3.3.1), produce the variation of the error norm, $|e|$, with the ratio $\frac{d_1}{d_2}$, represented by the dashed line in Figure 6.5.

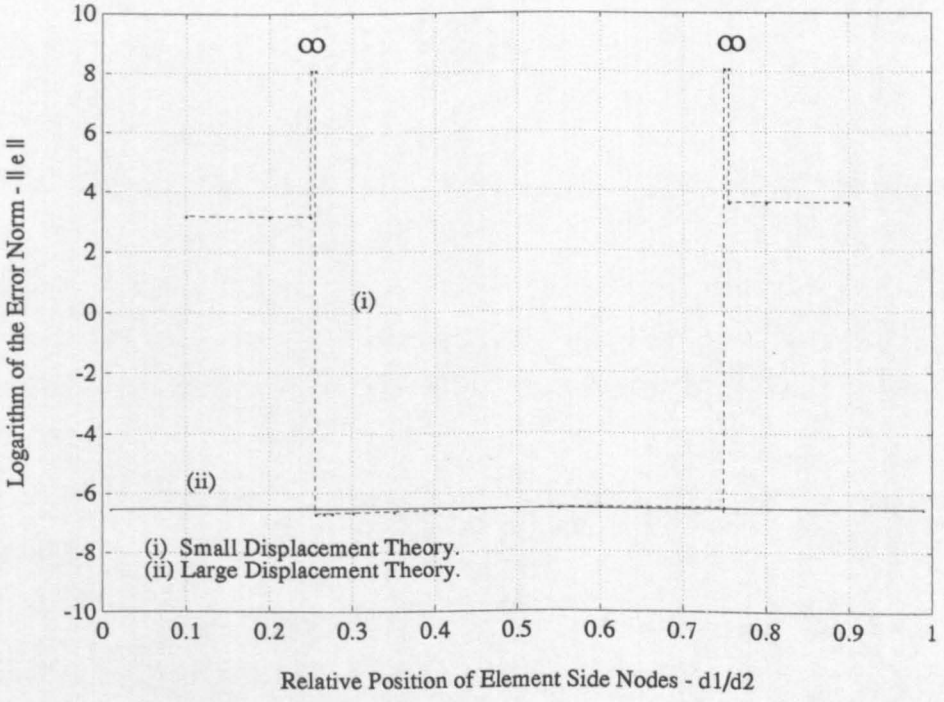

Figure 6.5 - Variation of the Ratio $\frac{d_1}{d_2}$ with the Error Norm $|e|$.

The error norm is shown to be constant at approximately 0.25×10^{-6} ($\log_{10}(0.25\times10^{-6}) = -6.6$) for the range $0.25 < \frac{d_1}{d_2} < 0.75$. At exactly $\frac{d_1}{d_2} = 0.25$ and $\frac{d_1}{d_2} = 0.75$ the error norm tends to infinity

8

Nine Gauss points (3×3 quadrature) have been adopted in this case, in order to minimise the error from the numerical integration technique, and therefore to prevent corruption of the strain based error norm, $|e|$, by the under integration of the element integrands.

and arithmetic errors are indicated [9]. For values of $\frac{d_1}{d_2} < 0.25$ and $\frac{d_1}{d_2} > 0.75$, $|e|$ returns to a stable (though unacceptably high) value of approximately $0.35\times10^{+4}$ ($\log_{10}(0.35\times10^{+4}) = 3.5$).

It is recommended therefore, that the application of the shape functions derived with the assumption of small displacements, is only valid within the range $0.25 < \frac{d_1}{d_2} < 0.75$. Beyond these limits large errors are introduced into the finite element formulation.

The solid line shown in Figure 6.5 reflects the results obtained through the application of the large displacement theory to the derivation of the element shape functions (Section 5.3.3.3, Chapter 5). A consistently low value for the error norm, $|e|$ (approximately 0.28×10^{-6} ($\log_{10}(0.28\times10^{-6}) = -6.55$)), is obtained across the range $0.05 \leq \frac{d_1}{d_2} \leq 0.95$. The stable magnitude of $|e|$, indicates the suppression of the errors induced through the application of the small displacement theory (dashed line, Figure 6.5). Consequently, the validity of the shape functions derived using large displacement theory (Section 5.3.3.3, Chapter 5) is demonstrated as the element side nodes are displaced from the central position ($\frac{d_1}{d_2} = 0.5$).

In the preceding example (Figure 6.4 and Figure 6.5), large nodal displacements have been assumed to cause the element side nodes to move in the plane of the edge of the element. Such displacements may be described as those generating a topological distortion. This does not result in a change of the shape of the element. The effects of geometric distortion (causing a change in the element geometry), on the accuracy of the proposed element formulation (Chapter 5), are illustrated below.

In the case of the simple patch of elements illustrated in Figure 6.6, the element side nodes are moved through the equal ratios $\frac{d_{1l}}{d_{2l}}$ and $\frac{d_{1s}}{d_{2s}}$. The nodal displacements are normal to the edge of the element on which the node is positioned, and generate the geometric distortions of the elements illustrated in Figure 6.6. In addition, prior and subsequent to the displacement, the side nodes are assumed to remain in the centre of the respective element side.

9

Celia and Gray have shown that if it is assumed that the side node remains at the centre of the element side in the derivation of the element shape functions, then the derivative of the shape functions with respect to the natural co-ordinates, $\{\xi, \eta\}$, becomes zero at some location within the element. [6.8]. This has the effect of yielding a zero determinant for the Jacobian matrix, $[J]$ (eqn(5.5.7(a))). Consequently, when calculating the local strain, $\frac{\partial U}{\partial X}$, (eqn(5.7.2.4), Chapter 5) for example, with eqn(5.5.7(a)), the reciprocal of the determinant of the Jacobian, det $[J]$, induces a solution of infinity.

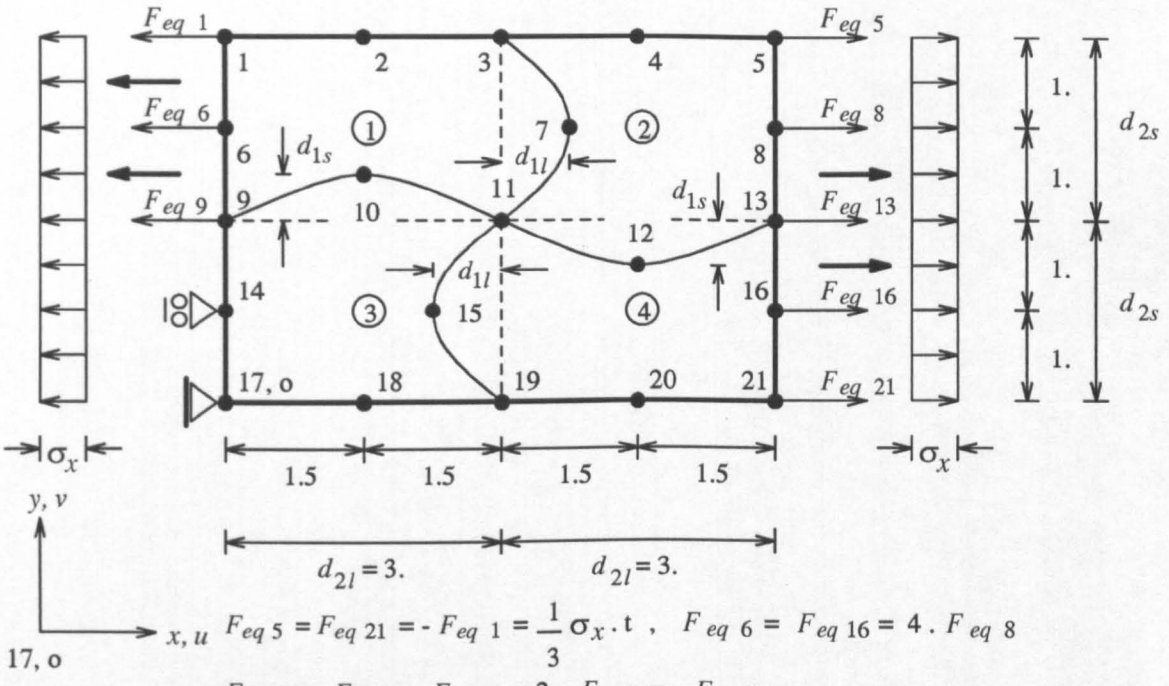

$F_{eq\,5} = F_{eq\,21} = -F_{eq\,1} = \frac{1}{3}\sigma_x \cdot t$, $F_{eq\,6} = F_{eq\,16} = 4 \cdot F_{eq\,8}$

$F_{eq\,6} = -F_{eq\,8}$, $F_{eq\,13} = 2 \cdot F_{eq\,5} = -F_{eq\,9}$

w displacements constrained at nodes 1, 5, 17, and 21.

Figure 6.6 - Distorted Patch of Quadratic Quadrilateral Finite Elements.

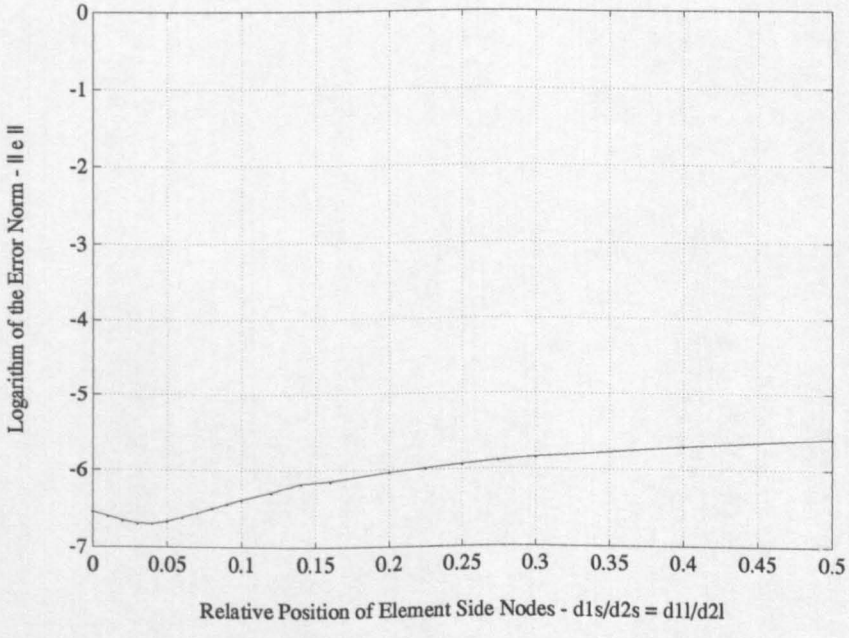

Figure 6.7 - Variation of the Ratios $\frac{d_{1s}}{d_{2s}}$ and $\frac{d_{1l}}{d_{2l}}$ with the Error Norm $|e|$.

Figure 6.7 illustrates the results of the Patch Test for the values of $\frac{d_{1l}}{d_{2l}} = \frac{d_{1s}}{d_{2s}}$ ranging from 0 to 0.5 [10] . It is shown that the element formulation based on shape functions derived using large displacement theory (Section 5.3.3.3), is insensitive to the geometric distortion of the element. For example, the log of the error norm, $\|e\|$, is shown to increase by a small amount, from -6.5 to around -5.5 in the range $0 \leq \frac{d_{1l}}{d_{2l}} = \frac{d_{1s}}{d_{2s}} \leq 0.5$ (Figure 6.7). Consequently, the accuracy of the overall numerical solution is not compromised significantly by the effects of the errors generated through a geometric distortion of the elements.

6.2.4. Summary.

From the studies presented in this section, the following points can be highlighted:

i) The Patch Test is passed for the case of geometrically linear elasticity (Figure 6.1, Table 6.1).

ii) Convergence to the exact (predicted) solution is achieved with mesh refinement. Consequently, the "Implicit" Patch Test is passed for the geometrically non-linear case (Figure 6.2).

iii) The proposed element formulation is valid for the analysis of systems undergoing large displacements, in which the large displacements cause a topological distortion (Figure 6.5).

iv) The error in the proposed element formulation is insensitive to large geometric distortions (in the range $0 \leq \frac{d_{1l}}{d_{2l}} = \frac{d_{1s}}{d_{2s}} \leq 0.5$, Figure 6.7).

6.3. Eigenvalue Test.

6.3.1. General Formulation.

The Eigenvalue Test may be used in addition to the Patch Test to assess the correctness of a finite element formulation. Whereas the Patch Test is able to check that a state of constant strain can be modelled and so assure convergence to the exact solution with mesh refinement, the Eigenvalue Test can detect zero energy or spurious deformation modes, and can assess the ability of the element to model rigid body motion adequately [6.4]. The eigen-problem is formulated as described below [6.5].

10

The values of $\frac{d_{1l}}{d_{2l}}$ and of $\frac{d_{1s}}{d_{2s}}$ have been limited to a maximum of 0.5 in the current investigation, in order to reflect an acceptable upper bound on the geometric distortion of the elements.

The vector of element nodal forces $\{fe\}$ may be related to the vector of resulting nodal displacements $\{\delta\}_i$, through a factor λ, such that,

$$[K_t^e]\,\{\delta\}_i = \{fe\} = \lambda\,\{\delta\}_i \qquad \text{eqn(6.3.1)}$$

or,

$$([K_t^e] - \{\lambda_i\}\,[I])\,\{\delta_v\}_i = 0 \qquad \text{eqn(6.3.2)}$$

where $\{\lambda_i\}$ is a vector of scaling factors, or "eigenvalues" of the stiffness matrix $[K_t^e]$.

There are as many eigenvalues of the matrix $[K_t^e]$ as there are degrees-of-freedom. Associated with each eigenvalue is an eigenvector $\{\delta_v\}_i$, which describes the deformation mode of the system (the finite element in this case). The eigenvalue gives the stiffness of the respective deformation mode. It is not necessary that all of the eigenvalues are different. Instead, the eigenvectors with the same eigenvalues may illustrate a symmetric mode. If each of the eigenvectors, $\{\delta_v\}_i$, is normalised such that $\{\delta_v\}_i^T\,\{\delta_v\}_i = 1$, then premultiplication of eqn(6.3.2) by $\{\delta_v\}_i^T$ yields,

$$\{\delta_v\}_i^T\,[K_t^e]\,\{\delta_v\}_i = \lambda_i \qquad \text{eqn(6.3.3)}$$

or,

$$2\,U_{oi} = \lambda_i \qquad \text{eqn(6.3.4)}$$

where U_{oi} is the strain energy associated with the deformation mode described by the eigenvector $\{\delta_v\}_i$ and the eigenvalue λ_i.

An eigenvalue analysis is usually performed on a single element stiffness matrix with all of the element degrees-of-freedom unrestrained. Therefore, $[K_t^e]$ in eqn(6.3.3) is the complete element stiffness matrix. It should be found that the value zero is returned for the eigenvalue λ_i when the corresponding eigenvector $\{\delta_v\}_i$ represents any rigid body deformation mode (eqn(6.3.4)).

A count of the number of zero eigenvalues (or strain free deformation modes) may be used as a direct measure of the correctness of the element formulation. In the case of an element formulated with three translational degrees-of-freedom at each node, six zero eigenvalues are required to show that all of the rigid body modes are represented adequately. These comprise three translational and three rotational modes. The Eigenvalue Test is passed if the correct number of zero eigenvalues are obtained from an eigenvalue analysis performed on the element stiffness matrix, $[K_t^e]$.

The element formulation presented in the preceding chapter has been assessed further, through the solutions to a series of Eigenvalue Tests [11] . In order to display the eigenvectors clearly, a square, flat element has been assumed (unless stated otherwise). The "reference" element is taken to have a side length of 1.m, with the side nodes positioned at the mid-points of the intervals. A value of unity is assumed for the thickness of the element, while (where applicable) the elastic modulus and the Poisson's ratio are taken to be $1.\times10^{+0}$ kN.m^{-2} and 0.1, respectively. The prestress in the element is specified individually for each test, along with the orientation of the element in the global $\{x, y, z\}$ space. The descriptions of various Eigenvalue Tests are presented below, with the respective eigenvalues given in Table 6.3.

Eigenvalue Test 1 (Eig-1): The results of the Eigenvalue Test on the elastic stiffness matrix $[\overline{K_E{}^e}]^1$ of the reference element are presented in the second column of Table 6.3. The reference element is orientated in the global x,y plane, such that the element natural co-ordinate directions, $\{\xi, \eta\}$, are aligned with the global co-ordinate directions, $\{x, y\}$, respectively.

The initial displacements of the element are assumed to be zero, such that the matrix $[B_L]$ is a null matrix (eqn(5.7.3.9), Chapter 5). Consequently, the elastic stiffness matrix, $[\overline{K_E{}^e}]^1$, is derived from small displacement theory only (eqn(5.7.1.7), Chapter 5). The numerical integration of eqn(5.7.1.7) has been carried out using 3×3 Quadrature [12] .

An eigenvalue analysis of the matrix $[\overline{K_E{}^e}]^1$ yields eleven zero and thirteen non-zero eigenvalues (Table 6.3). The eleven zero eigenvalues represent six strain free rigid body deformation modes and five superfluous spurious modes. As described below, the superfluous zero eigenvalues reflect the lack of coupling between the in-plane and the out-of-plane terms in the element elastic stiffness matrix $[\overline{K_E{}^e}]^1$, and represent spurious strain free out-of-plane deformation modes.

It is demonstrated in Appendix 6-B (Section 6.7.1) that in the case of a flat element, orientated in the global xy plane, the out-of-plane components of the element elastic stiffness matrix, $[K_E{}^e]$ (derived from small displacement theory), are zero. Consequently, any deformations out of the plane of the element appear as strain free ($\lambda_i = 0$), since the stretching of the middle surface (arising from the lateral deformation) is not represented. Subsequent to the suppression of the strain free rigid body modes of the element (by the removal of the appropriate rows and columns of the matrix $[\overline{K_E{}^e}]^1$), the reduced elastic stiffness matrix $[\overline{K_E{}^{red}}]^1$ remains singular therefore,

---

11

The eigenvalues and the eigenvectors have been obtained using the *Matlab* computational package [6.9]. Details of the calculation of the eigenvalues and the eigenvectors of a matrix as performed by the *Matlab* package are presented in Appendix 6-C.

12

A 3×3 Quadrature rule has been assumed in this case in order to suppress any spurious deformation mode arising from the under integration of the element integrands (Section 5.10.2, Chapter 5).

irrespective of the magnitude of the in-plane stiffness components.

Two procedures presented in the Eigenvalue Tests, **Eig-2** and **Eig-3**, illustrate the use of pre-conditioning as an effective means of negating the initially singular nature of the element elastic stiffness matrix $[\overline{K_E{}^e}]^1$.

Eigenvalue	Eig-1	Eig-2	Eig-3	Eig-4	Eig-5(a)	Eig-5(b)	Eig-6
1	0.	0.	0.	0.	0.	0.	0.
2	0.	0.	0.	0.	0.	0.	0.
3	0.	0.	0.	0.	0.	0.	0.
4	0.	0.	0.	0.	0.4795	0.	0.
5	0.	0.	0.	0.	0.4795	0.	0.
6	0.	0.	0.	0.	0.4795	0.	0.
7	0.	0.0087	0.0007	0.	0.4795	0.4795	0.6561
8	0.	0.1283	0.0244	0.	0.4795	0.4795	0.6667
9	0.	0.1283	0.0244	0.	0.4795	0.4795	0.9490
10	0.	0.1371	0.0271	0.	0.6667	0.6667	0.9724
11	0.	0.2858	0.0502	0.	0.6667	0.6667	1.0000
12	0.1603	0.3880	0.1631	0.	0.6667	0.6667	1.0000
13	0.3005	0.5198	0.3156	0.3005	1.8539	1.0000	1.0941
14	0.3005	0.5658	0.3156	0.3005	1.8539	1.0000	1.0941
15	0.4774	0.5658	0.4957	0.4667	1.8539	1.0000	2.2121
16	0.5327	0.7488	0.6834	0.4897	1.8539	1.8541	2.5863
17	1.0181	1.1471	1.0493	0.9091	1.8539	1.8541	2.6667
18	1.3333	1.3240	1.3333	1.2121	1.8539	1.8541	3.6842
19	1.6461	1.3240	1.6600	1.6461	2.6667	2.6667	3.7749
20	1.6461	1.6332	1.6600	1.6461	2.6667	2.6667	4.4282
21	2.0343	1.7921	2.0365	1.8335	2.6667	2.6667	4.4282
22	2.0598	1.9303	2.0601	1.9239	5.3333	5.3333	5.3333
23	4.4001	3.9896	4.4128	4.4001	5.3333	5.3333	9.4912
24	4.4001	3.9896	4.4128	4.4001	5.3333	5.3333	9.4912

Table 6.3 - Conditional Eigenvalues for a Quadratic Quadrilateral Element.

Eigenvalue Test 2 (Eig-2): As demonstrated below, a non-singular form of the reduced elastic stiffness matrix, $[\overline{K_E{}^{red}}]^1$, can be established by specifying a fictitious (temporary) geometry for the reference element.

The geometry of the element described in the preceding test is revised initially, by the prescription of fictitious values of $\pm 0.2m.$ for the z co-ordinates of the mid-side nodes. The signs

of the z co-ordinates are selected so that the element geometry resembles a saddle form. Consequently, the vector normal to the middle surface of the element is characterised by a direction which varies with the natural co-ordinates $\{\xi, \eta\}$. The corner nodes are located in the global xy plane. The eigenvalues of the pre-conditioned elastic stiffness matrix, $[\overline{K_E{}^e}]^2$, are presented in Table 6.3.

It is shown that six zero eigenvalues are returned for the matrix $[\overline{K_E{}^e}]^2$, corresponding to three translational and to three rotational strain free rigid body modes. The five superfluous zero eigenvalues displayed by the matrix $[\overline{K_E{}^e}]^1$, are suppressed by the components of the local in-plane element elastic stiffness terms acting in the local Z co-ordinate direction. These components are induced as outlined below.

The introduction of out-of-plane curvature to the surface of the element has the effect of invoking the terms of the unit vectors $\hat{X}$ and $\hat{Y}$ representing the global z direction. These terms (corresponding to the element nodes) are denoted as $\hat{X}^k{}_i$ and as $\hat{Y}^k{}_i$ respectively, where i is the element node number ($i = 1 \rightarrow 8$). In the situation that the element is curved the (first order) strains, $\frac{\partial U}{\partial X}$, and $\frac{\partial V}{\partial Y}$, comprise components which act in the global z direction. The magnitudes of these components are proportional to the terms $\hat{X}^k{}_i$ and $\hat{Y}^k{}_i$ (eqn(6-B.4), Appendix 6-B). Consequently, the strains induced by a lateral deformation are accounted for (in part) by components of the strains derived from the small displacement theory (first order, Section 5.7.2, Chapter 5) [13].

Eigenvalue Test 3 (Eig-3): It is shown below, that the assumption of non-zero values for the initial element nodal displacements can be used to suppress the five superfluous zero eigenvalues present in the elastic stiffness matrix $[\overline{K_E{}^e}]^1$.

The general element elastic stiffness matrix, $[\overline{K_E{}^e}]$ has been shown to be linearly dependent on the element nodal displacements (Section 5.7.3, Chapter 5). As demonstrated in Appendix 6-D, the out-of-plane stiffness terms can be invoked therefore, through the assumption of a fictitious initial displacements, acting in the global z direction. If a fictitious (initial) displacement of 0.05 m is applied to the mid side nodes of the reference element, (**Eig-1**), in the positive z direction, the eigenvalues presented in Table 6.3 are obtained for the elastic stiffness matrix $[\overline{K_E{}^e}]^3$.

Six zero eigenvalues are returned for the matrix $[\overline{K_E{}^e}]^3$. It is shown that the magnitudes of the first five non-zero eigenvalues are relatively small, however. The associated eigenvectors may be

13

The same effects are not achieved if the element remains flat and is rotated about the global x or y co-ordinate axes. In this case the out-of-plane components of the (first order) strains $\frac{\partial U}{\partial X}$, and $\frac{\partial V}{\partial Y}$, cancel as the direction cosines are constant over the surface of the element.

seen to tend to zero energy modes therefore. By increasing the magnitude of the fictitious displacements, it can be demonstrated that the tendency of the deformations modes identified with the first five non-zero eigenvalues, to act as mechanisms, can be eliminated. A comparison of the eigenvalues in the second and in the fourth columns of Table 6.3 shows that, in general, the stiffnesses of the element deformation modes are increased by the application of an assumed vector of initial displacements.

Eigenvalue Test 4 (Eig-4): The technique of reduced integration is used to improve the accuracy and the rate of convergence of the isoparametric finite element formulated in Chapter 5. An assessment of the effects of using reduced integration when calculating the element elastic stiffness matrix, $[\overline{K_E{}^e}]$, are made through the eigenvalue analysis presented below.

The elastic stiffness matrix $[\overline{K_E{}^e}]^4$, representing the element described in **Eig-1**, but with the element integrands calculated using reduced 2×2 Gauss Quadrature, is characterised by the eigenvalues given in Table 6.3. Of the twelve zero eigenvalues, six represent the rigid body deformation modes of the element. The remaining zero eigenvalues indicate that six spurious mechanisms are represented in addition.

The introduction of changes in the element shape, **(Eig-2)**, or of a vector of initial displacements, **(Eig-3)**, fail to reduce the number of superfluous zero eigenvalues. Consequently, the spurious mechanisms described by the matrix, $[\overline{K_E{}^e}]^4$, cannot be attributed to the presence of zero stiffness terms out of the plane of the element. Instead, they are generated through the under integration of the element integrands, arising from the application of the technique of reduced integration. This proposal is confirmed by an appraisal of the rank of a general elastic element stiffness matrix evaluated using 2×2 Gauss Quadrature, (Section 5.8.2, Chapter 5). It is shown that the matrix is rank deficient by an order of six, inferring the existence of six spurious mechanisms ($\lambda_i = 0.$).

Eigenvalue Test 5 (Eig-5): The concept of the Eigenvalue Test has been used further to assess the adequate representation of rigid body deformation modes, and to investigate the possible existence of mechanisms, in the formulation of the geometric (or initial stress) stiffness matrix $[K_\sigma{}^e]$.

Adopting the geometry described in the Eigenvalue Test **Eig-1**, it is assumed that the element is prestressed as in, $\sigma_x = \sigma_y = +1.$ kN.m^{-2}, and $\tau_{xy} = 0.$ kN.m^{-2}. The element integrands are evaluated using the technique of reduced integration. Using the basic formulation for $[K_\sigma{}^e]$ (Section 5.7.4, Chapter 5), an eigenvalue analysis yields only three zero eigenvalues in the case of the geometric stiffness matrix, $[K_\sigma{}^e]^1$ **(Eig-5(a)**, Table 6.3). The associated eigenvectors can be shown to represent the strain free rigid body translation deformation modes.

Repeating the analysis subsequent to the adequate representation of the element rigid body rotation modes (Section 5.9, Chapter 5), returns six zero eigenvalues. The eigenvectors associated

with the zero eigenvalues represent three translational and three rotational rigid body deformation modes. The results of the latter eigenvalue analysis performed on the geometric stiffness matrix $[K_\sigma{}^e]^2$ are presented in the penultimate column of Table 6.3 (**Eig-5(b)**.

The theory defining explicitly the adequate representation of the rigid body rotation modes of the element, (Section 5.9, Chapter 5), is validated therefore. Furthermore, despite the use of the technique of reduced integration (2×2 Gauss Quadrature) to evaluate the element integrands (describing the geometric stiffness matrices, $[K_\sigma{}^e]^1$ and $[K_\sigma{}^e]^2$), the eigenvectors associated with the zero eigenvalues comprise no spurious deformation modes.

Eigenvalue Test 6 (Eig-6): The eigenvalues of an element stiffness matrix, $[\overline{K_T{}^e}]$, obtained by combining $[\overline{K_E{}^e}]^4$ with $[K_\sigma{}^e]^2$, are presented in the last column of Table 6.3. It is shown that six of the twenty-four eigenvalues are zero. When comparing the solutions to the eigenvalue analyses **Eig-4** and **Eig-6**, it is demonstrated, that the addition of the stress stiffness matrix $[K_\sigma{}^e]^2$ to the elastic stiffness matrix $[\overline{K_E{}^e}]^4$ effectively suppresses the spurious modes in $[\overline{K_E{}^e}]^4$, generated through the adoption of the technique of reduced integration.

The eigenvectors associated with the eigenvalues given in the last column of Table 6.3 are presented in Figures 6.10 (a)-(d). The undeformed element is shown in outline only, by a solid dark line. The deformed element is shaded, with equally spaced "contours" to aid visualisation of the particular mode shape. (The "contour" lines are not intended to represent the borders of additional quadrilateral elements.)

The mode shapes associated with the six zero eigenvalues are illustrated in Figure 6.8(a), and represent the rigid body deformation modes of the element. They are manifested by a series of linear combinations of the three rigid body translation modes with the three rigid body rotation. Of the remaining eighteen deformation modes, numbers 8, 11, 12, 17, and 22 are identified as representing a series of deformation modes of both the syn-clastic and the anti-clastic types. A combination of these mode shapes may be seen to occur locally across the surface of a minimal energy form.

6.3.2. Summary.

The following points can be summarised from the results presented in this section:

i) In the case of a flat, rectangular quadrilateral element without initial stress, spurious deformation modes may occur, irrespective of the order of Quadrature used to evaluate the element integrand. The spurious modes arise from a lack of coupling between the in-plane strains and the out-of-plane deformations of the membrane in the small displacement theory (Section 5.7.2, Chapter 5). A suppression of the spurious deformation modes can be achieved by distorting the element, or by introducing fictitious (initial) displacements to the

element (Eigenvalue Tests **Eig-2** and **Eig-3** respectively).

ii) The adoption of the technique of reduced integration can cause the elastic element stiffness matrix $[\overline{K_E{}^e}]$ to display zero energy modes (Eigenvalue Test **Eig-4**). An elimination of the zero energy modes can be achieved by the introduction of an initial stress to the element (Eigenvalue Test **Eig-6**).

iii) Subsequent to the application of the theory to include explicitly the strain free rigid body rotation modes of the element (Section 5.9, Chapter 5), six zero eigenvalues values are obtained for the geometric stiffness matrix $[K_\sigma{}^e]^2$ (Eigenvalue Test **Eig-5(b)**). The zero eigenvalues represent the rigid body translation and rigid body rotation element deformation modes.

iv) Subject to pre-conditioning, (Eigenvalue Tests **Eig-2** and **Eig-3**), the element formulated in Chapter 5 passes the Eigenvalue Test.

v) Several of the deformation modes exhibited by the proposed element formulation (Figures 6.10 (a)-(d)) are suited to the analysis of minimal energy forms [14].

14

The eigenvectors of a matrix are not unique, unlike its eigenvalues. Instead, the magnitudes of the eigenvectors can be altered, for example, by performing a co-ordinate transformation on the matrix, or by assigning a different value to the arbitrary eigenvector arising subsequent to the decomposition of the matrix [6.11]. Consequently, the deformation modes displayed in Figures 6.10 (a)-(d) are only indicative of a perhaps wider family, comprising combinations of the basic eigenvectors.

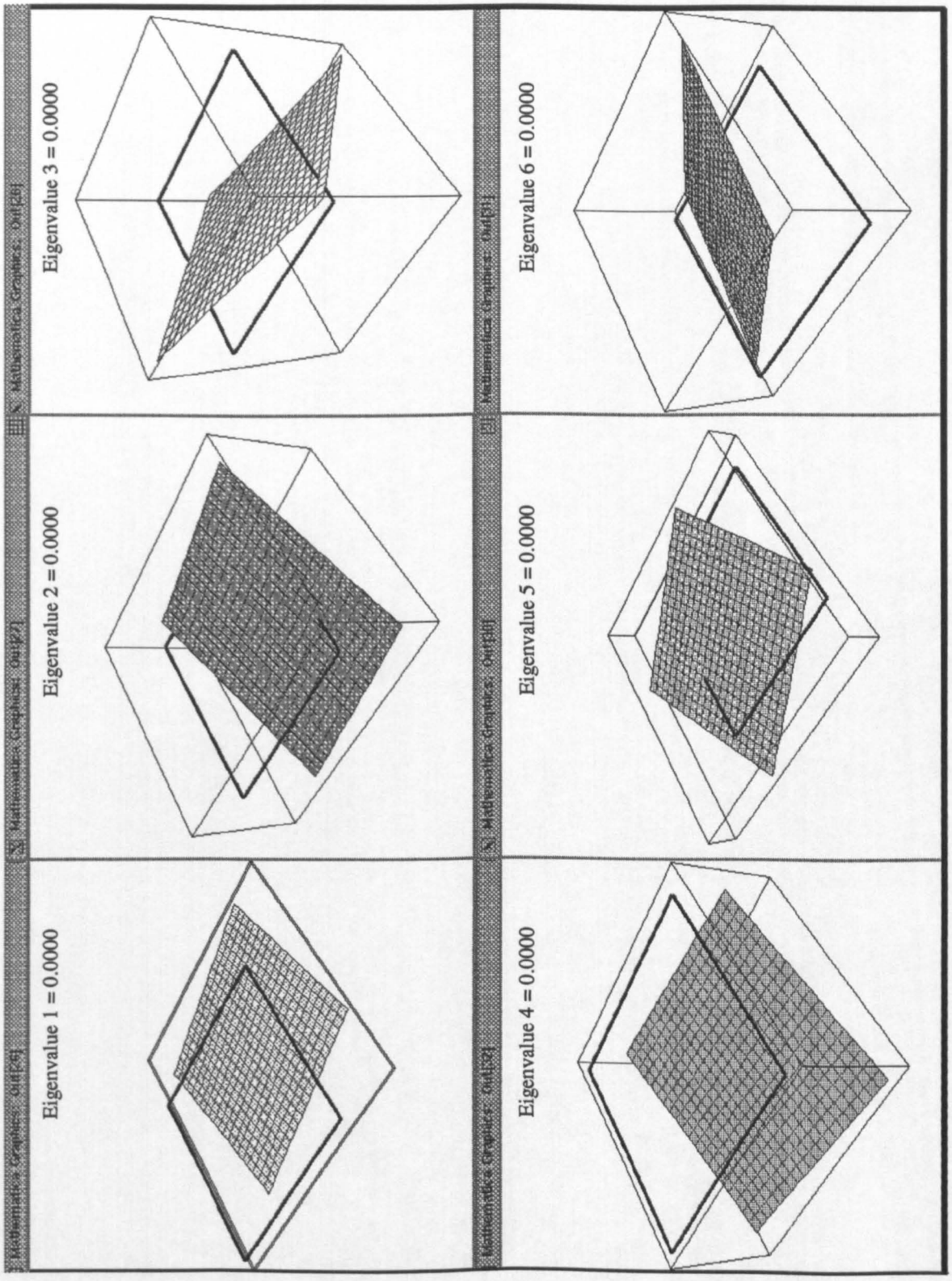

Figure 6.8(a) - Associated Eigenvectors for Eigenvalues 1-6.

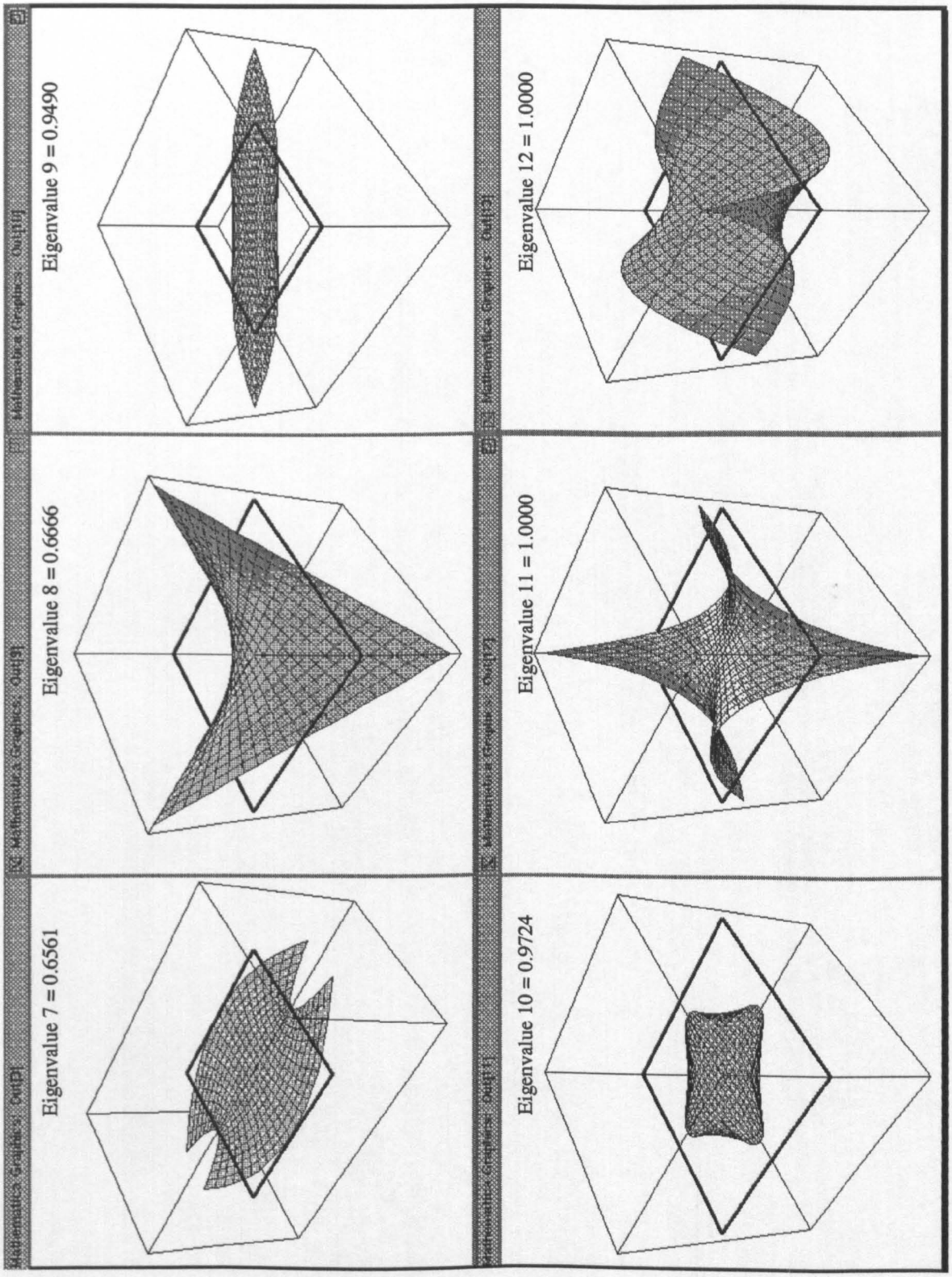

Figure 6.8(b) - Associated Eigenvectors for Eigenvalues 7-12.

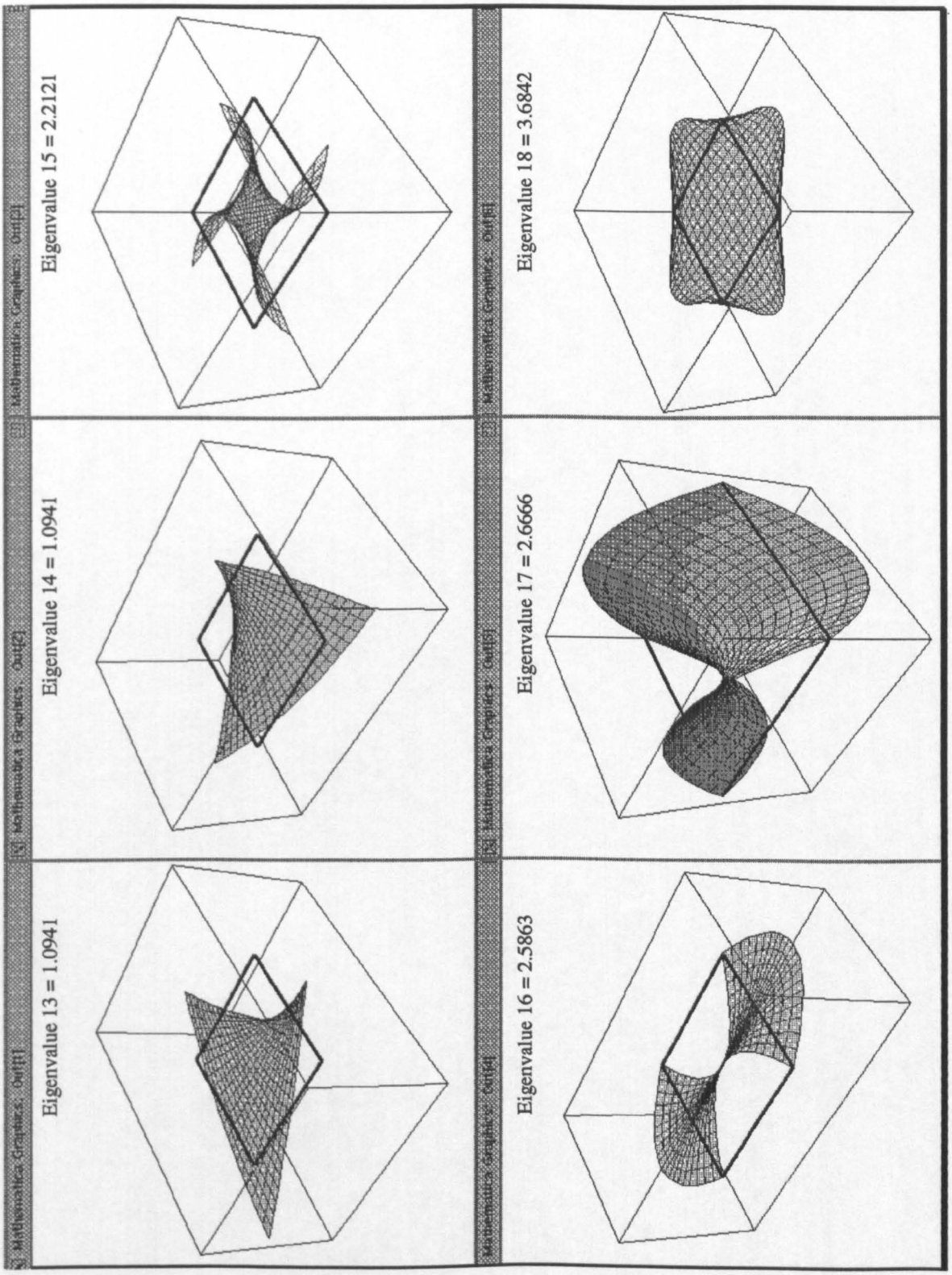

Figure 6.8(c) - Associated Eigenvectors for Eigenvalues 13-18.

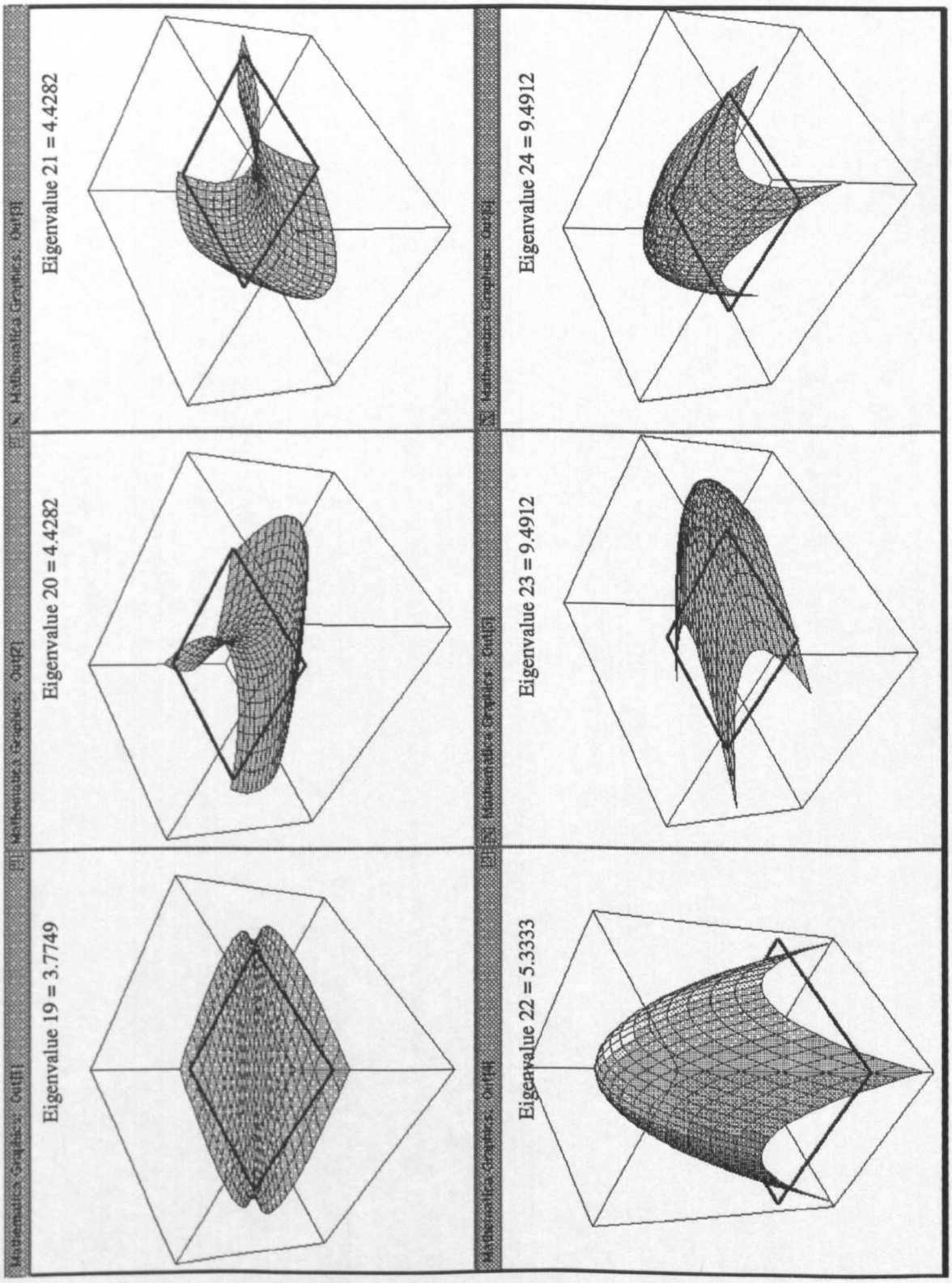

Figure 6.8(d) - Associated Eigenvectors for Eigenvalues 19-24.

6.4. Adoption of the 24 Degrees-of-Freedom Quadrilateral Element with the Dynamic Relaxation Algorithm.

6.4.1. Solution Procedure.

The quadrilateral finite element formulated in the preceding chapter, is used in conjunction with the Dynamic Relaxation algorithm as described below.

The element nodal stiffnesses are calculated according to eqn(5.7.4.8). For each element the total stiffness matrix $[K_t^e]$ is transformed into the global $\{x, y, z\}$ co-ordinate directions, and the appropriate diagonal terms summed at the respective element nodes to give the terms $\underline{K_{pq}}$ (eqn(4.2.4)). The vectors of element equivalent nodal forces $\{fe\}$ (eqn(5.7.5.1)) are similarly calculated in the local co-ordinate system and transformed into the global co-ordinate directions. All of the terms of the element vector $\{fe\}$ are assigned to the relevant element nodes. These are added to the contributions from adjacent elements, to give the out-of-balance force vector, or residual force $\underline{R_{pq}}$, for each node of the discretised system (eqn(4.2.4)).

Through the application of eqn(4.2.9) and of eqn(4.2.10) the nodal displacements are obtained as a function of $\underline{K_{pq}}$ and of $\underline{R_{pq}}$. The nodal co-ordinates are updated as in,

$$\{x, y, z\}^j = \{x, y, z\}^{j-1} + \{\delta\}^j \qquad \text{eqn(6.4.1.1)}$$

where j is the current iteration number.

At each iteration the element matrix $[K_t^e]$ and the element vector $\{fe\}$ are recalculated, based on the revised surface geometry. As before, Kinetic Damping is used to attenuate the oscillations of the discretised surface. The solution method is stopped when all the nodal force residuals, $\underline{R_{pq}}$, are acceptably close to zero.

6.4.2. Effects of the Element Formulation on the Solution Procedure.

6.4.2.1. Sensitivity to Large Geometric Changes.

The 24 degrees-of-freedom element (Chapter 5) is highly sensitive to large geometrical changes. This feature, when combined with the generation of relatively large geometric and topological distortions allowed for in the Dynamic Relaxation algorithm, leads to rapid variations in the magnitudes and directions of the element stiffness terms and equivalent nodal force vectors. Consequently, large changes are induced in the magnitudes and directions of the element nodal displacements. Numerical instability of the solution algorithm can arise therefore, particularly during the initial stages of the form-finding procedure.

By the selection of only the diagonal terms of the element stiffness matrix, $[K_t{}^e]$, to control the iterative step of the solution algorithm, the sensitivity of the element can be reduced [15] . The element sensitivity is decreased further by the adoption of the technique of reduced integration (Section 5.8, Chapter 5).

Paradoxically, the decoupling of and the softening of the element stiffness matrix $[K_t{}^e]$ (through the selection of the diagonal terms only), has the secondary effect of increasing the tendency to instability of the solution algorithm. This phenomenon arises as the diagonal terms underestimate the exact stiffnesses of the element. Consequently, the element nodal displacements are overestimated (eqn(4.2.9), Chapter 4). If the element nodal displacements are overestimated significantly, the solution algorithm may become unstable. The technique of scaling the nodal stiffnesses (Section 4.3.6, Chapter 4), can be adopted to restore the stability of the algorithm.

6.4.2.2. Assumption of Large Strains.

The expression for the element equivalent nodal force vector, $\{fe\}$ (eqn(5.7.5.1)), has been shown to be a function of the matrix $[\bar{B}] = [B_o] + [B_L]$. The matrix $[B_L]$ is linearly dependent on the element nodal displacements, and represents part of the geometric non-linearity of the system (eqn(5.7.3.9)). Therefore, at equilibrium, the magnitudes of the terms held in the vector $\{fe\}$ are based on the element stress vector $\{\sigma_o\}$, and the elment geometry through the matrix $[B_o]$. In addition, the history of element nodal displacements contribute (in a non-linear sense) to the terms of the vector, $\{fe\}$, through the matrix $[B_L]$.

Assuming that the surface has displaced in order to satisfy the condition of equilibrium, the equilibriated surface geometry is similarly a function of both the stress vector, $\{\sigma_o\}$, and the element nodal displacements. Consequently, if the stress vector, $\{\sigma_o\}$, is applied to the same equilibriated surface, but with the nodal displacements reset to zero (such that the matrix $[B_L] = [0]$), the condition of equilibrium is no longer satisfied.

Furthermore, if the form-finding procedure is commenced from two different initial surfaces, for a particular set of boundary conditions, dissimilar solutions to the same surface are obtained. This phenomenon arises as a result of the differing displacement histories of the two solutions, leading to differing element equivalent nodal force vectors $\{fe\}$, based on the accumulated nodal displacement terms in the matrix $[B_L]$ of each solution.

However, at equilibrium, if it is assumed that there is no displacement history, a non-uniform stress vector, $\{\sigma_o{}'\}$, exists therefore (at each of the element Gauss Points (Section 5.8)), which is

---

15

This effect is achieved in a similar manner to that in the case of the linear and triangular elements (Section 4.3, Chapter 4).

in equilibrium with the current (equilibriated) element geometry [16] . As demonstrated below, by comparing the required surface stress vector, $\{\sigma_o\}$, with the non-uniform stress vector, $\{\sigma_o'\}$, the vector of element stress deviations, $\{\Delta\sigma\}$, can be obtained.

Assuming the use of 2×2 Gaussian Quadrature (Section 5.8, Chapter 5), the vector of element nodal forces, $\{fe\}$ (eqn(5.7.5.1)), may be written as,

$$\{fe\} = \int_{vol} [\bar{B}]^T \{\sigma_o\} \, dV$$

$$= \sum_{i=1}^{i=4} [\bar{B}]_i^T \{\sigma_o\}_i \det [J]_i \, . t \, . Wt_i \qquad \text{eqn(6.4.2.2.1)}$$

where t is the thickness of the element, and Wt_i is the weight associated with the Gauss point i.

Considering each Gauss point individually and pre-multiplying both sides of eqn(6.4.2.2.1) by the matrix $[\bar{B}]_i$, it follows that,

$$\{fe'\}_i = [\bar{B}]_i \, [\bar{B}]_i^T \{\sigma_o\}_i \det [J]_i \, . t \, . Wt_i \qquad \text{eqn(6.4.2.2.2)}$$

where the vector $\{fe'\}_i$ is the vector of pseudo loads representing the relationship between the element geometry, the nodal displacement history, and the stress vector $\{\sigma_o\}_i$, at the Gauss point i, and is written as $\{fe'\}_i = [\bar{B}]_i \{fe\}_i$.

If it is assumed that the matrix $[\bar{B}]_i$ describes the geometry and the displacement history of an element at equilibrium, then neglecting the displacement history (such that $[\bar{B}]_i = [B_o]_i$), yields the expression,

$$\{fe'\}_i = [B_o]_i \, [B_o]_i^T \{\sigma_o'\}_i \det [J]_i \, . t \, . Wt_i$$

or,

$$\{\sigma_o'\}_i = \frac{1}{\det [J]_i \, . t \, . Wt_i} \left[[B_o]_i \, [B_o]_i^T \right]^{-1} \{fe'\}_i \qquad \text{eqn(6.4.2.2.3)}$$

where $\{\sigma_o'\}_i$ is the vector of non-uniform stress that must be applied to the element Gauss Point, i, at the commencement of the form-finding procedure, in order to obtain an equilibriated surface upon the first iteration of the solution algorithm.

16

The term, "displacement history", refers to the displacements which the elements (surface) undergo during the form-finding procedure. If there is no displacement history, the surface is at equilibrium at the first iteration of the numerical algorithm, and the matrix $[B_L]$ is a null matrix.

The vector of element stress deviations at each Gauss point i, $\{\Delta\sigma\}_i$, may be written simply as,

$$\{\Delta\sigma\}_i = \{\sigma_o\}_i - \{\sigma_o'\}_i \qquad \text{eqn(6.4.2.2.4)}$$

As demonstrated below, if the magnitude of the terms in the vector of element stress deviations, $\{\Delta\sigma\}_i$, are found to be unacceptably high, then the re-imposition of the required stress vector, $\{\sigma_o\}_i$, and the subsequent satisfaction of the condition of equilibrium, can be used to improve the stress distribution within the surface. (Moreover, by using this approach, the same solution to the surface is obtained if two different initial geometries are assumed at the commencement of the form-finding procedure.)

Figure 6.2 shows the equilibriated surface generated in conjunction with the boundary conditions given in Table 6.2. The initial surface of the form has been described using Hermitian polynomials with the factor $\lambda_s = 2$ [17], while the numerical stability of the solution algorithm is ensured with $\lambda_A = 2$ [6.10]. The condition of uniform stress, $\{\sigma_o\}_i$, is given as $\sigma_x = \sigma_y = 5.\times10^{-6}$ kN.m^{-2}, and $\tau_{xy} = 0.$ kN.m^{-2}. The thickness of the membrane is assumed to be $1.\times10^{-3}$ m, with the elasticity matrix $[E]$ taken as a null matrix. The error residual, Er, is assumed to be 0.025 % of the maximum equivalent nodal force [18]. The maximum and the average element stress deviations (at the Gauss points) are presented in Table 6.4 (overleaf) for the first five and for the tenth global re-impositions ($N_{GI} = 1 \rightarrow 5, 10$) of the uniform stress vector $\{\sigma_o\}_i$.

Subsequent to the re-imposition of the uniform stress vector $\{\sigma_o\}_i$, the magnitudes of the element stress deviations are shown to reduce in general (at equilibrium). The reductions in the magnitudes of the element stress deviations reflect the increasing proximity of the form to the truly minimal surface. Furthermore, as N_{GI} is increased the changes in the maximum and the average element stress deviations (when compared with the preceding values at equilibrium), tend to zero. As described below, the values to which the element stress deviations converge, can be used as a measure of the adequacy of the discretisation, in a similar way to that described in the case of the triangular elements (Chapter 4).

If the equilibriated surface is not a minimal energy form, the re-imposition of the uniform stress vector $\{\sigma_o\}_i$ induces relative nodal displacements. These displacements are related to the element stresses through the non-linear strain displacement matrix, $[B_L]$, at each Gauss Point, i (eqn(6.4.2.2.2) and eqn(6.4.2.2.3)). Therefore, by monitoring the element stress deviations, areas of an inappropriate discretisation, or areas where the boundary conditions will not permit the

17

The coefficient, λ_s, is defined in footnote 4, Chapter 4.

18

The error residual, Er, equal to 0.025 % of the maximum element equivalent nodal force, has been assumed for all subsequent examples, unless otherwise stated.

generation of a minimal energy form, can be highlighted.

N_{GI}	N_{IT}	$\Delta\sigma_X^{max}$	$\Delta\sigma_Y^{max}$	$\Delta\tau_{XY}^{max}$	$\overline{\Delta\sigma_X}$	$\overline{\Delta\sigma_Y}$	$\overline{\Delta\tau_{XY}}$
1	60	-1.00%	+8.76%	+2.03%	+0.26%	+0.91%	+0.35%
2	57	+0.52%	+4.04%	+0.85%	+0.18%	+0.63%	+0.24%
3	53	+0.31%	+2.70%	+0.46%	+0.15%	+0.51%	+0.18%
4	74	-0.30%	+2.33%	-0.39%	+0.11%	+0.46%	+0.14%
5	57	+0.31%	+2.22%	-0.36%	+0.09%	+0.44%	+0.13%
10	63	-0.33%	+2.01%	-0.32%	+0.07%	+0.40%	+0.10%

Table 6.4 - Variation of the Maximum and Average Element Stress Deviations with the Factor N_{GI} - Example 6.1.

6.4.3. Performance of the Proposed Element Formulation.

6.4.3.1. Effects of the Assumption of Quadratic Element Shape Functions.

Table 6.5 presents the variation in the maximum and the average element stress deviations at the element Gauss points for the equilibriated surface illustrated in Figure 6.2 ($N_{GI} = 10$), and the number of elements comprising the discretisation.

Number of Elements	Initial Element Size on Plan	$\Delta\sigma_X^{max}$	$\Delta\sigma_Y^{max}$	$\Delta\tau_{XY}^{max}$	$\overline{\Delta\sigma_X}$	$\overline{\Delta\sigma_Y}$	$\overline{\Delta\tau_{XY}}$
4	12.m x 12.m	-0.33%	+1.06%	-0.04%	+0.21%	+0.67%	+0.04%
24	4.m x 4.m	-0.33%	+2.01%	-0.32%	+0.07%	+0.40%	+0.10%
96	2.m x 2.m	-0.32%	+2.83%	+0.04%	+0.02%	+0.15%	+0.04%
216	$1\frac{1}{3}$m x $1\frac{1}{3}$m	-0.32%	+3.27%	-0.42%	+0.01%	+0.09%	+0.03%

Table 6.5 - Variation of the Maximum and Average Element Stress Deviations with Mesh Refinement - Example 6.1.

As the number of elements is increased, it is shown that the average stress deviations in the surface are reduced, so that, with 216 elements the average element stress deviations are < 0.1%

(Table 6.5). With the adoption of a finer discretisation, it should be found that the numerical model represents the truly minimal form more closely, with the individual element stress deviations tending to zero. Conversely, in certain regions of the surface, the numerical solution drifts from the minimal energy form. This is inferred by an increase in the maximum element stress deviation, $\Delta\sigma_Y{}^{max}$, as the element size is reduced (Table 6.5).

The maxima in the stress deviation, $\Delta\sigma_Y$, occur at the Gauss points immediately adjacent to the discontinuities of slope in the boundary of the surface (Figure 6.2). It is proposed below that the increases in the direct stress deviation $\Delta\sigma_Y{}^{max}$ with a reduction in the size of the element, can be attributed to two possible causes.

Firstly, as the element size is decreased, the contribution of the element nodal displacements to the vector of equivalent nodal forces $\{fe\}$ increases due to the dominance of the matrix $[B_L]$ in the expression for $[\bar{B}]$ (eqn(5.7.1.6), Chapter 5).

Secondly, it is assumed that the element shape functions vary quadratically with the natural co-ordinates $\{\xi, \eta\}$ (eqn(5.3.3.1)). As the element size is reduced, the elements in the areas around the boundary discontinuities (Figure 6.2) become increasingly distorted and constrained. Meanwhile, the majority of the elements contribute to the formation of local minimal surfaces [19]. With an increase in the element geometric and topological distortion, the element geometry and the element displacements no longer vary quadratically. This leads to a violation of the inherent assumption in the derivation of the element shape functions. Consequently, an error is introduced into the element stiffness matrix $[K_t{}^e]$, and in the vector of equivalent nodal forces $\{fe\}$.

As demonstrated subsequently, in the cases of surfaces bounded by a combination of curves and straight lines (which are devoid of discontinuities of slope out of the plane of the surface), the violation of the assumption of quadratic element shape functions can be avoided, and the associated errors in the numerical solution, eliminated.

The surface illustrated in Figure 6.9, is characterised by the same elastic and the geometric constants assumed for the surface shown in Figure 6.2. This is with the exception that the boundary of the surface illustrated in Figure 6.9 is defined by the parabola,

$$z = -0.020833\,y^2 + 0.5\,y\,, \qquad \text{eqn(6.4.3.1.1)}$$

such that $z_{max} = 3.000$ (as before, Table 6.2). The initial surfaces of both examples are generated by Hermitian polynomials with the factor $\lambda_s = 2$.

Table 6.6 presents the maximum and the average element stress deviations for the first five and for the tenth global re-impositions ($N_{GI} = 1 \rightarrow 5, 10$) of the uniform stress vector $\{\sigma_o\}_i$, for the

19

The formation of such local minimal surfaces is indicated by the low average element stress deviations (Table 6.5).

surface illustrated in Figure 6.9. By comparing Table 6.6 with Table 6.4, the magnitudes of the maximum element stress deviations, $\Delta\sigma_Y{}^{max}$, (and therefore the errors in the numerical solution to the truly minimal surface) are shown to decrease when the boundary of the surface is parabolic [20].

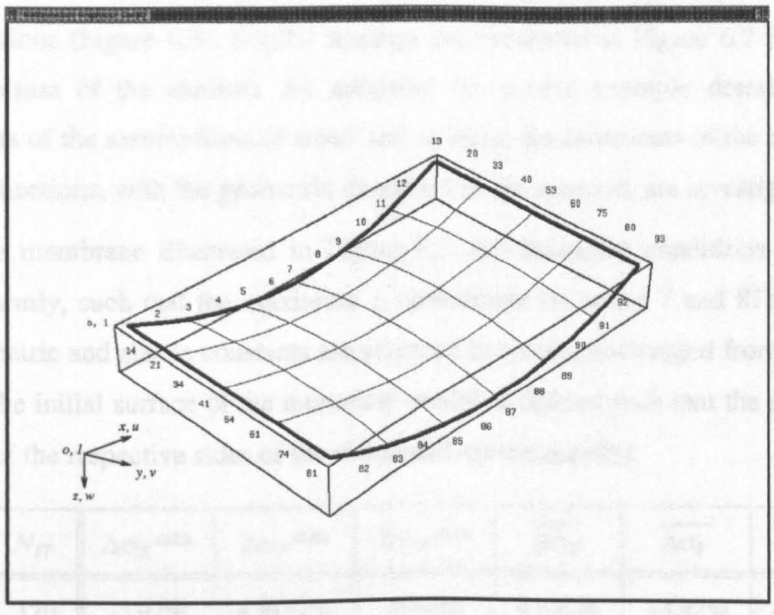

Figure 6.9 - Surface Discretised using Quadrilateral Elements - Example 6.2.

N_{GI}	N_{IT}	$\Delta\sigma_X{}^{max}$	$\Delta\sigma_Y{}^{max}$	$\Delta\tau_{XY}{}^{max}$	$\overline{\Delta\sigma_X}$	$\overline{\Delta\sigma_Y}$	$\overline{\Delta\tau_{XY}}$
1	94	+0.83%	-1.35%	-0.40%	+0.41%	+0.46%	+0.13%
2	88	+0.49%	-0.58%	-0.22%	+0.20%	+0.22%	+0.08%
3	83	+0.34%	-0.26%	-0.13%	+0.12%	+0.11%	+0.05%
4	76	+0.28%	-0.15%	+0.09%	+0.08%	+0.06%	+0.04%
5	60	+0.26%	-0.11%	+0.08%	+0.07%	+0.04%	+0.04%
10	52	+0.23%	+0.17%	+0.08%	+0.06%	+0.04%	+0.03%

Table 6.6 - Variation of the Maximum and Average Element Stress Deviations with the Factor N_{GI} - Example 6.2.

[20] The constraints of the assumption that the element shape functions vary quadratically with the natural co-ordinates $\{\xi, \eta\}$, are shown subsequently, to introduce a geometric error into the numerical solution (Section 6.5.1).

6.4.3.2. Combined Effects of Geometric Distortion [21] and of the Assumption of Small Displacements in the Element Shape Functions.

The results of the Patch Test presented in Section 6.2 have shown that the assumption of large displacements in the derivation of the element shape functions, produces an element formulation exhibiting a low and a stable error norm, $|e|$ (eqn(6.2.3.3)), as the side nodes move away from the central positions (Figure 6.5). Similar findings are presented in Figure 6.7 for the case of a geometric distortion of the element. By adopting the simple example described below, the combined effects of the assumptions of small and of large displacements in the derivation of the element shape functions, with the geometric distortion of the element, are investigated.

Considering the membrane illustrated in Figure 6.3, the boundary conditions (Table 6.2) are magnified uniformly, such that the maximum z co-ordinate (at nodes 7 and 87) is 6.000m. The remaining geometric and elastic constants are assumed to remain unchanged from those given for Example 6.1. The initial surface of the numerical model is defined such that the side nodes are at the mid points of the respective sides of the elements (approximately).

N_{GI}	N_{IT}	$\Delta\sigma_X{}^{max}$	$\Delta\sigma_Y{}^{max}$	$\Delta\tau_{XY}{}^{max}$	$\overline{\Delta\sigma_X}$	$\overline{\Delta\sigma_Y}$	$\overline{\Delta\tau_{XY}}$
1	120	-3.97%	+30.47%	-8.05%	+1.22%	+3.47%	+1.16%
2	126	-2.09%	+15.66%	+3.81%	+0.57%	+2.74%	+0.82%
3	93	-1.54%	+10.85%	+2.25%	+0.45%	+2.46%	+0.64%
4	98	-1.51%	+9.09%	+1.06%	+0.37%	+2.38%	+0.55%
5	95	-1.51%	+8.31%	-1.29%	+0.34%	+2.38%	+0.50%
10	99	-1.31%	+8.15%	-1.75%	+0.39%	+2.79%	+0.56%
12	105	-1.27%	+9.00%	+2.36%	+0.46%	+3.21%	+0.68%
15	110	-1.98%	+15.84%	+6.04%	+0.91%	+5.44%	+1.32%
16	Numerical Instability - No Solution.						

Table 6.7 - Variation of the Maximum and Average Element Stress Deviations with the Factor N_{GI} - Small Displacement Theory.

Table 6.7 and Table 6.8 present the maximum and the average element stress deviations for the surface at equilibrium, when the element shape functions are derived according to the small

21 Geometric distortion is defined as a distortion causing a change in the shape of the element.

displacement theory (Section 5.3.3.1, Chapter 5), and according to the large displacement theory (Section 5.3.3.2, Chapter 5), respectively.

N_{GI}	N_{IT}	$\Delta\sigma_X{}^{max}$	$\Delta\sigma_Y{}^{max}$	$\Delta\tau_{XY}{}^{max}$	$\overline{\Delta\sigma_X}$	$\overline{\Delta\sigma_Y}$	$\overline{\Delta\tau_{XY}}$
1	118	-4.04%	+29.79%	+7.72%	+1.02%	+3.03%	+1.13%
2	141	-1.88%	+13.47%	-3.41%	+0.56%	+2.03%	+0.77%
3	116	-1.08%	+8.11%	+1.78%	+0.44%	+1.61%	+0.56%
4	107	-0.85%	+6.20%	+1.14%	+0.32%	+1.42%	+0.44%
5	98	-0.85%	+5.38%	+1.07%	+0.24%	+1.32%	+0.37%
10	94	-0.90%	+4.33%	-0.96%	+0.21%	+1.14%	+0.28%
12	90	-0.92%	+4.26%	-0.98%	+0.22%	+1.12%	+0.27%
15	99	-1.02%	+3.99%	-1.03%	+0.24%	+1.05%	+0.26%
16	106	-1.05%	+3.92%	-1.05%	+0.25%	+1.04%	+0.26%
18	107	-1.13%	+3.78%	-1.07%	+0.27%	+1.01%	+0.27%
20	105	-1.22%	+3.64%	-1.09%	+0.29%	+0.99%	+0.27%

Table 6.8 - Variation of the Maximum and Average Element Stress Deviations with the Factor N_{GI} - Large Displacement Theory.

By comparing Table 6.7 with Table 6.8, it is shown that immediately after the first imposition of the uniform stress vector, $\{\sigma_o\}$, ($N_{GI} = 1$), the disparities between the maximum and average element stress deviations are small. This infers that significant movements of the side nodes away from the mid point of the interval have not occurred as the surface is equilibriated initially. With an increase in the number of re-impositions of the uniform stress vector $\{\sigma_o\}$, the magnitudes of the corresponding element stress deviations are shown to diverge however. This is demonstrated by the maximum disparities of 88% in the maximum and 144% in the average element stress deviations at $N_{GI} = 10$ (Table 6.7 and Table 6.8).

The divergence of the element stress deviations suggests an increasing violation of the assumption of small displacements in the derivation of the element shape functions. After 16 re-impositions of the stress vector $\{\sigma_o\}$, numerical instability of the solution algorithm occurs for the case in which the element shape functions are derived using the small displacement theory. Conversely, when adopting the assumption of large displacements, the solution algorithm

remains stable and continues to show an improvement in the accuracy of the surface at equilibrium. (This is indicated by a comparison of the corresponding values presented in the last three rows of Table 6.8.)

From the solution at N_{GI} = 16 it is found that the minimum value of the ratio $\frac{d_1}{d_2}$ (Figure 6.4), is 0.34, with the corresponding maximum value given as 0.66 [22] . With reference to the dashed line in Figure 6.5 (representing the small displacement theory , in which the system is geometrically linear, and the elements are not subjected to geometric distortion), a value of $\frac{d_1}{d_2} = 0.34$ (or 0.66) corresponds to an error norm, $|e|$, of approximately 0.25×10^{-6}. This value of $|e|$ indicates a small loss in the accuracy of the geometrically linear solution, when the assumption of small displacements, adopted in the derivation of the element shape functions, is violated.

This feature is not demonstrated in the geometrically non-linear case, where the combined effects of the violation of the assumption of small displacements with those of the geometric distortion of the element, leads to large errors in the analysis. The last row of Table 6.7 indicates that these errors, present in the evaluation of both the element total stiffness matrix $[K_t{}^e]$ and in the evaluation of the vector of equivalent nodal forces $\{fe\}$, can lead to the numerical instability and to the divergence of the solution algorithm ultimately.

6.4.3.3. Effects of the Fictitious Stiffness Terms in the Element Geometric Stiffness Matrix, $[K_\sigma{}^e]$.

The theory presented in Section 5.9 (Chapter 5) yields expressions for the fictitious stiffness terms which arise when the element undergoes rigid body rotation. To assess the effects of these terms on the solution algorithm, the surface illustrated in Figure 6.10 has been investigated [23] .

22

The ratio, $\frac{d_1}{d_2}$ (Figure 6.4), is used as a measure of the relative position of the element side node. When the side node is at the mid-point of the element side $\frac{d_1}{d_2} = 0.5$.

23

The correctness of the theory presented in Section 5.9 (Chapter 5) has been demonstrated by an eigenvalue analysis of the geometric stiffness matrix representing a flat rectangular element, orientated in the global xy plane (Section 6.3). The arguments formulated in this section assume that the theory presented in Section 5.9 (Chapter 5), eliminates adequately the fictitious stiffness terms which are generated by the rigid body rotation of a general curved element, however. In order to determine the effectiveness of the theory presented in Section 5.9 (Chapter 5) in this case, an eigenvalue analysis has been performed on the geometric stiffness matrix of the element 9 comprising the surface illustrated in Figure 6.10 and described in the subsequent paragraph. The solution to this eigenvalue analysis is presented in Appendix 6-E.

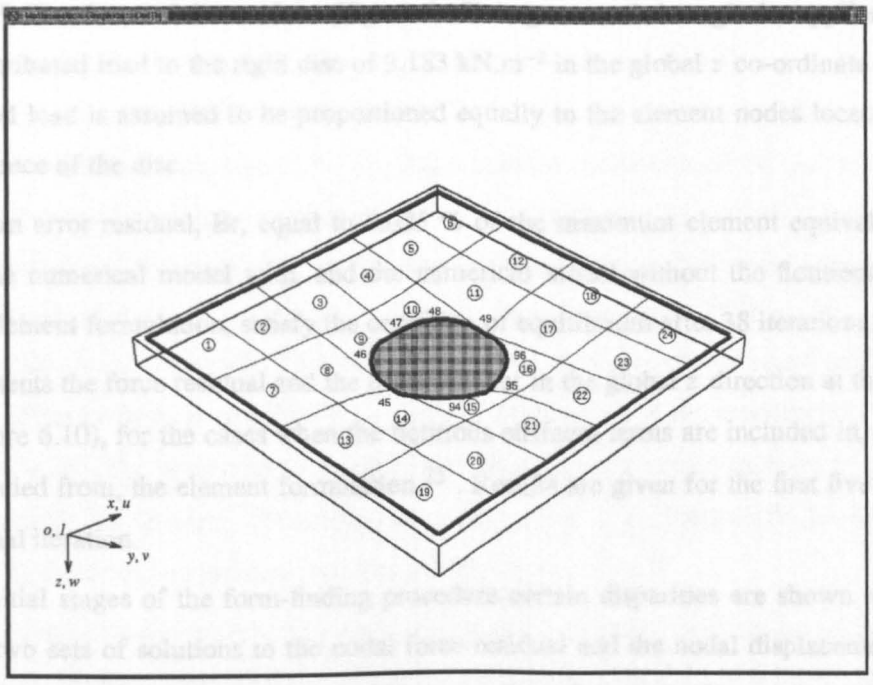

Figure 6.10 - Surface Discretised using Quadrilateral Elements - Example 6.3.

N_{IT}	Residual (kN) R.B.R. Included	Residual (kN) R.B.R. Excluded	Disparity	Accumulated Displacement (m) R.B.R. Included	Accumulated Displacement (m) R.B.R. Excluded	Disparity
1	20.0000	20.0000	0.%	0.193369	0.193369	0.%
2	6.3384	5.2173	17.71%	0.515308	0.490498	4.81%
3	6.5098	4.0471	37.83%	0.967798	0.866913	10.42%
4	-3.3480	-0.9719	70.97%	1.345508	1.222800	9.12%
5	-5.4987	-5.4839	0.27%	1.594611	1.454600	8.78%
38	-3.30×10^{-2}	1.15×10^{-2}	65.15%	1.904650	1.904960	0.016%

Table 6.9 - Comparison of Solutions to Example 6.3. [24]

The surface is square on plan with overall dimensions of 24. m in the global x and y directions. A rigid disc (shaded), with a diameter of 8. m is located at the centre of the membrane. The stiffness of the membrane is derived from the initial stress (or geometric) stiffness matrix $[K_\sigma{}^e]$ only, based on the assumed stress field, $\sigma_x = \sigma_y = 5.95\times10^{+3}$ kN.m^{-2} and $\tau_{xy} = 0.$ kN.m^{-2}. A thickness of $1.\times10^{-3}$m has been taken for the membrane, while a value of 1.85 is assumed for the stabilising

[24] The abbreviation "R.B.R." denotes "Rigid Body Rotation". "R.B.R. Included" refers to the suppression of the fictitious stiffness terms in the element geometric stiffness matrix, $[K_\sigma{}^e]$, associated with the rigid body rotation of the element.

factor λ_A [6.10]. The form of the surface (Figure 6.10) is generated through the application of a uniformly distributed load to the rigid disc of 3.183 kN.m^{-2} in the global z co-ordinate direction. The distributed load is assumed to be proportioned equally to the element nodes located around the circumference of the disc.

By adopting an error residual, Er, equal to 0.025 % of the maximum element equivalent nodal force, both the numerical model with, and the numerical model without the fictitious stiffness terms in the element formulation, satisfy the condition of equilibrium after 38 iterations.

Table 6.9 presents the force residual and the displacement in the global z direction at the element node 47 (Figure 6.10), for the cases when the fictitious stiffness terms are included in, and when they are excluded from, the element formulation [25]. Results are given for the first five iterations and for the final iteration.

During the initial stages of the form-finding procedure certain disparities are shown to develop between the two sets of solutions to the nodal force residual and the nodal displacement (Table 6.9). As the number of iterations is increased however, the solutions tend to converge, such that, at equilibrium, the accumulated vertical displacement of the node 47 deviates by < 0.02%. The solutions are also shown to be notably similar when comparing the maximum and the average element stress deviations (Table 6.10) for the element **9** (Figure 6.10). The average element stress deviations can be seen to be identical to the second place after the decimal point, with the maximum disparity in the remaining figures equivalent to 0.37%.

Rigid Body Rotations	$\Delta\sigma_X{}^{max}$	$\Delta\sigma_Y{}^{max}$	$\Delta\tau_{XY}{}^{max}$	$\overline{\Delta\sigma_X}$	$\overline{\Delta\sigma_Y}$	$\overline{\Delta\tau_{XY}}$
Explicitly Included	26.55%	32.46%	21.78%	4.46%	4.93%	3.32%
Excluded	26.49%	32.40%	21.70%	4.46%	4.93%	3.32%
Disparity	0.23%	0.18%	0.37%	0.%	0.%	0.%

Table 6.10 - Comparison of Element Stress Deviations for Example 6.3.

As described below, the convergence of the differing element formulations (with and without the adequate representation of the element rigid body rotation modes) to the same solution (approximately) is achieved by solving the equations of equilibrium of the surface by the Dynamic Relaxation algorithm.

25

The element **9** has been highlighted as this element (in conjunction with the symmetric elements **10**, **15**, and **16**), undergoes the largest components of rigid body rotation (Figure 6.10). In addition, node 47 (comprising the element 9) is subjected to the maximum relative magnitude of displacement in the global z direction, and therefore to the largest out-of-balance force in that direction.

The pseudo oscillations of the discretised system are controlled by the out-of-balance force vector and by the stiffnesses at the element nodes (eqn(4.2.9), Chapter 4). Consequently, the fictitious stiffness terms in the matrix $[K_\sigma{}^e]$ (arising from an inadequate representation of the element rigid body rotation modes) have the effect of inducing a pseudo oscillation of the surface which is different to the oscillation obtained subsequent to the removal of these terms. (The disparities between the solutions to the nodal force residual and to the nodal displacement (node 47) for the first five iterations of the solution algorithm, demonstrate this feature (Table 6.9)). However, because the surface form is generated by the application of a stress vector of constant magnitude, the geometry of the surface (at equilibrium) is unique, irrespective of the straining of the surface (Table 6.9, $N_{IT} = 38$). The subsequent paragraph describes how the unique solution to the surface is obtained through the Dynamic Relaxation algorithm, even when the pseudo oscillations are contaminated by the fictitious stiffness terms of the matrix, $[K_\sigma{}^e]$.

If the surface overshoots the equilibrium configuration (as a result of the fictitious stiffness terms in the matrix, $[K_\sigma{}^e]$), then re-application of the uniform stress vector, $\{\sigma_o\}$ (in conjunction with the updated element geometry), has the effect of increasing the proximity of the surface to the equilibrium state. For example, as the surface passes the equilibrium position, a peak in the kinetic energy of the system is detected. At this point, the nodal velocities are reset to zero, and the uniform stress vector, $\{\sigma_o\}$, is reapplied. The analysis is recommenced from the updated configuration. In this procedure the stiffness terms of the matrix, $[K_\sigma{}^e]$, define simply how far past the true equilibrium position the surface has moved when the kinetic energy peak is observed. Therefore, the fictitious stiffness terms in the matrix, $[K_\sigma{}^e]$, may cause the surface to become remote from the true equilibrium position. Meanwhile, the condition of equilibrium is given by the magnitude of the nodal out-of-balance force vectors, $\underline{R_{pq}}$, only. If the elasticity of the membrane is assumed to be zero, the vector, $\underline{R_{pq}}$, is simply a function of the element geometry (and therefore of the surface geometry) and of the uniform stress vector, $\{\sigma_o\}$. Consequently, the fictitious stiffness terms in the matrix, $[K_\sigma{}^e]$, affect only the rate of convergence of the solution to the condition of equilibrium, and do not contribute to a misrepresentation of the equilibriated geometry of the surface.

By a similar argument the iterative procedure of a geometrically non-linear matrix analysis can be shown to suppress the effects of the fictitious stiffness terms in the matrix, $[K_\sigma{}^e]$. In this case the surface overshoots the equilibrium configuration by an amount which is defined by the global flexibility matrix of the system. In both the Dynamic Relaxation and the matrix iteration analyses of an elastic geometrically non-linear system, the effects of the fictitious stiffness terms in the matrix, $[K_\sigma{}^e]$, are negated, provided that the elastic stiffness matrix of the element is represented accurately. In this case the associated fictitious displacements are compensated by a change in the element stresses arising from the elastic straining of the surface. A geometrically linear matrix

analysis is forced into error however by the fictitious stiffness terms in the matrix, $[K_\sigma{}^e]$. The error arises as the displacements are calculated from a single application of the global flexibility matrix of the system. The updated geometry of the system is assumed to be at equilibrium. In the Dynamic Relaxation algorithm, an iterative procedure is adopted despite the assumption that the system is linear. Therefore, no error is induced by the fictitious stiffness terms in the matrix, $[K_\sigma{}^e]$, during the analysis of a linear system by the Dynamic Relaxation algorithm.

6.4.3.4. Summary.

The following points can be summarised from the results presented in this section:

i) The high sensitivity of the element formulation to large geometrical changes can lead to rapid variations in the magnitudes and directions of the element stiffnesses and equivalent nodal forces, and so induce instability into the solution algorithm.

ii) The non-linear terms in the strain-displacement matrix, $[\bar{B}]$, give rise to a vector of element stress deviations, $\{\Delta\sigma\}_i$, at each Gauss point i. The adequacy of the finite element discretisation, and the proximity of the equilibriated surface to the local minimal energy form can be assessed through the magnitude of the components of the vector $\{\Delta\sigma\}_i$.

iii) A violation of the assumption of a quadratic variation of displacements and of geometry in the element formulation can lead to errors in the element stiffness matrix $[K_t{}^e]$ and in the vector of equivalent nodal forces $\{fe\}$.

iv) The combined effects of topological and geometric distortions of the element, can amplify the errors generated through the violation of the assumption of small displacements in the derivation of the element shape functions, when analysing a geometrically non-linear surface.

v) The fictitious terms in the element stiffness matrix, $[K_\sigma{}^e]$, associated with the element rigid body rotation modes, fail to produce significant errors in a geometrically linear or geometrically non-linear solutions, provided that;

- the Dynamic Relaxation algorithm is adopted as the solution algorithm, and
- the terms of the matrix $[K_\sigma{}^e]$ are calculated using the technique of reduced integration.

6.5. Verification of the Numerical Solution Method.

6.5.1. Introduction.

In this section the results of the investigations into the stability and the accuracy of the solution algorithm to various soap-film models are presented. Particular attention is paid to the effects of the assumptions which are inherent in the element formulation, on the accuracy of the numerical solutions.

6.5.2. Single Minimal Surfaces with Fixed Boundaries.

Figure 6.11 shows the equilibriated surface of the soap-film model illustrated in Plates 3.1 & 3.2 (Example 6.4). The surface is discretised by 216 quadrilateral elements of the type formulated in Chapter 5. The element dimensions correspond approximately to 5.55% of the overall x dimension of the surface in the global x direction, and to 8.33% of the overall y dimension in the global y dimension. The condition of uniform stress is modelled as $\sigma_x = \sigma_y = 1.\times10^{+6}$ kN.m^{-2} and $\tau_{xy} = 0.$ kN.m^{-2}. The stiffness of the surface is derived from prestress only.

The form-finding procedure is commenced from a mathematically defined initial surface, based on the Hermitian cubic polynomial, with the value of λ_s equal to 2.0 [26] . In order to ensure the numerical stability of the solution algorithm the factor $\lambda_A = 2.0$ [6.10] has been adopted. The magnitude of the error residual, Er, has been taken as 0.025 % of the maximum element equivalent nodal force.

An increase in the rate of convergence to both the condition of equilibrium and to the condition of (approximately) uniform stress, has been achieved through the introduction of an additional factor, λ_D, into the solution algorithm. Scaling the vector of accumulated nodal displacements, $\{\delta\}_i^{accum.}$, by the factor, λ_D, such that $\lambda_D < 1.0$, reduces the contribution of the vector, $\{\delta\}_i^{accum.}$, to the vector of element equivalent nodal forces, $\{fe\}$, through the matrix $[B_L]$ (eqn(5.7.5.1) with eqn(5.7.1.6), Chapter 5). Consequently, the element stress deviations are diminished at equilibrium (eqn(6.4.2.2.4)). In the current example, a value of $\lambda_D = 0.6$ is assumed. (A decrease in this figure gives rise to an inadequate representation of the contribution of the large displacement terms to the element strains, and to a loss of convergence of the solution algorithm).

26

The coefficient, λ_s, is defined in footnote 4, Chapter 4.

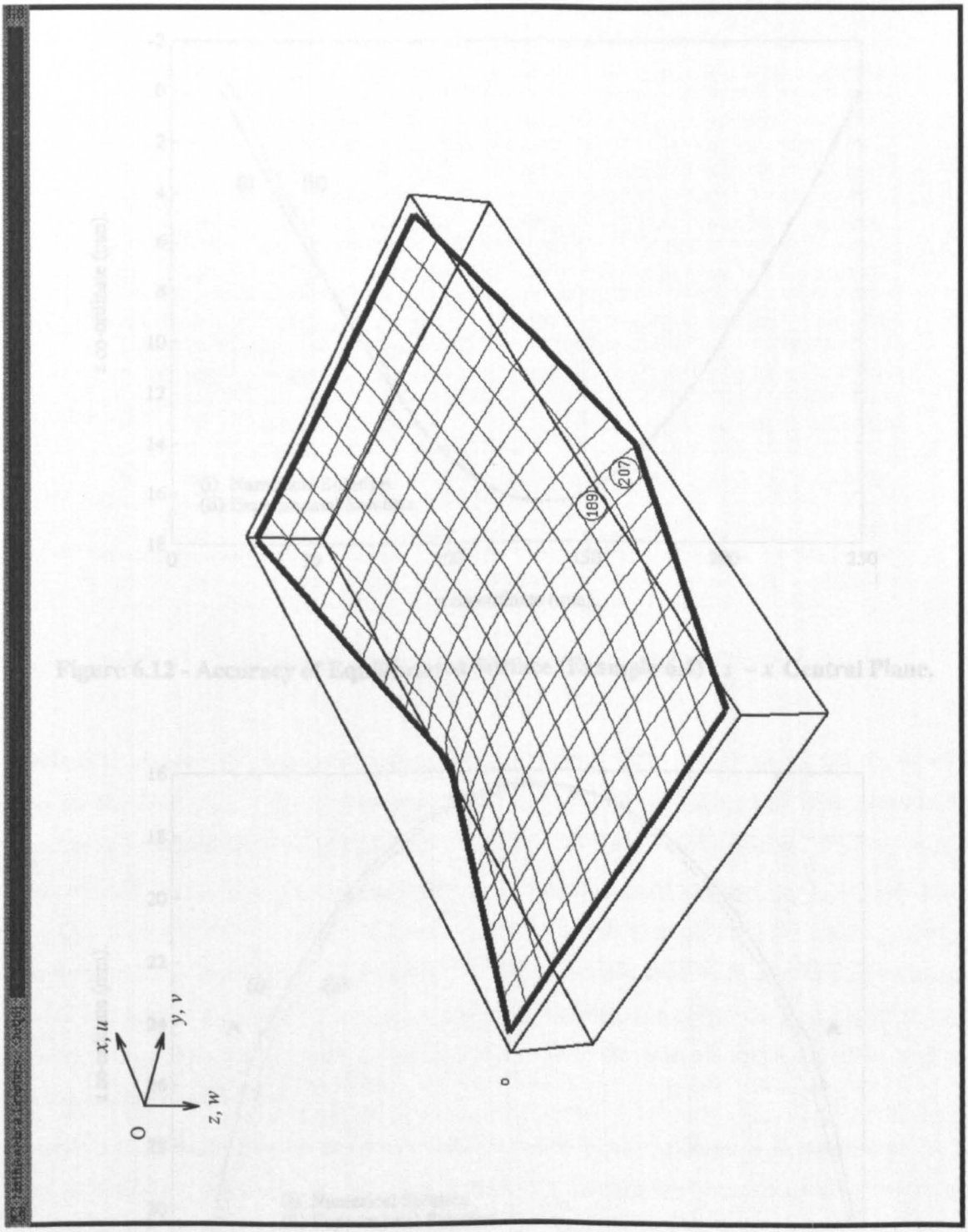

Figure 6.11 - Surface Discretised using Quadrilateral Elements - Example 6.4.

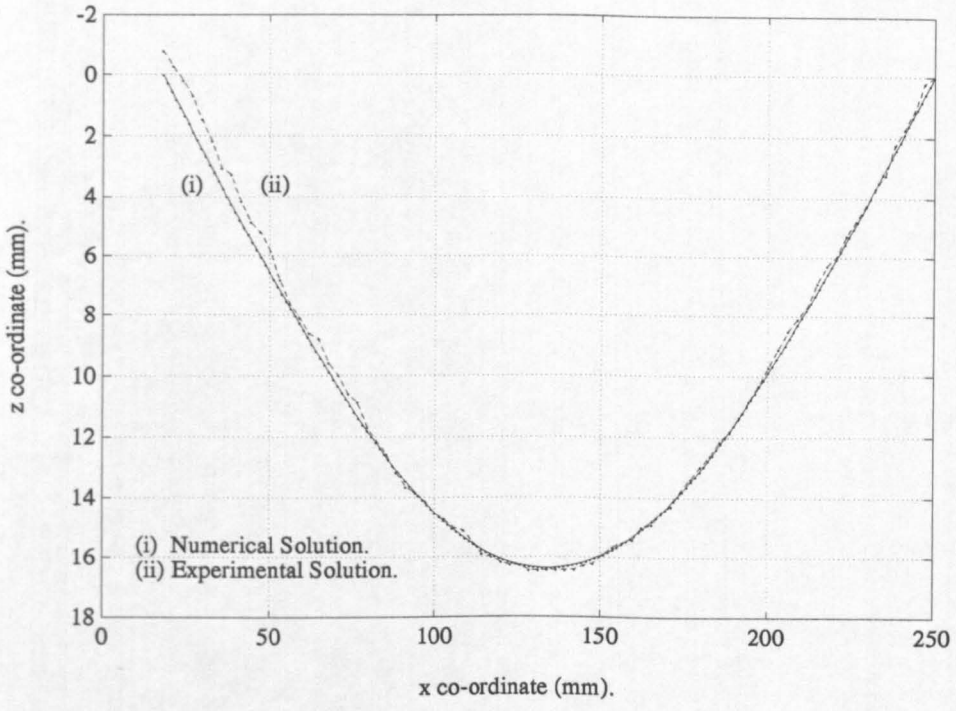

Figure 6.12 - Accuracy of Equilibriated Surface (Example 6.4) - $z - x$ Central Plane.

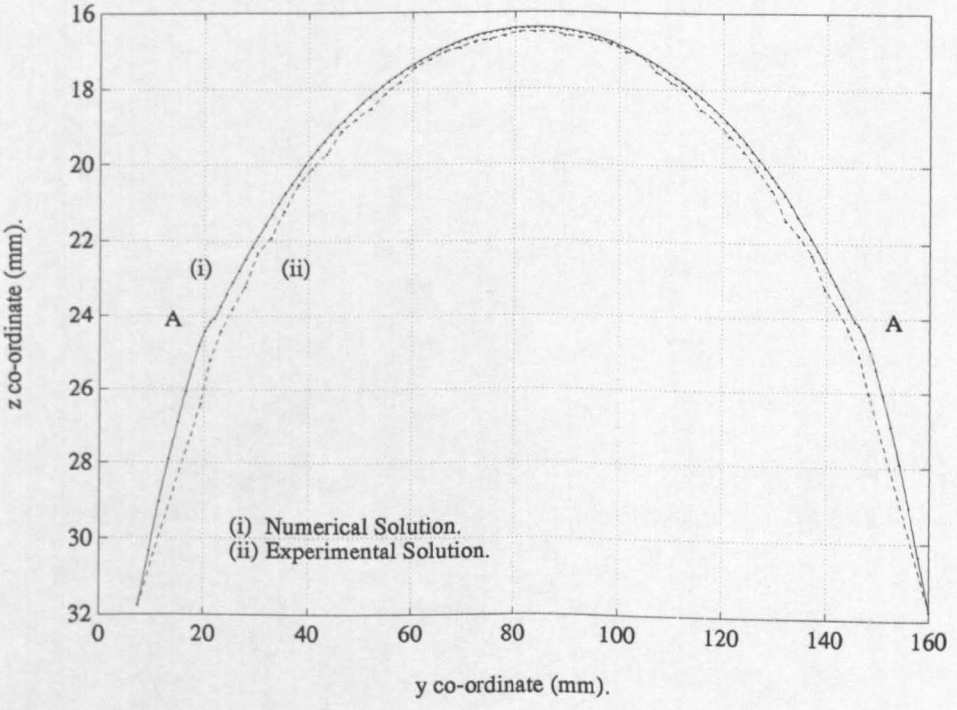

Figure 6.13 - Accuracy of Equilibriated Surface (Example 6.4) - $z - y$ Central Plane.

N_{GI}	N_{IT}	$\Delta\sigma_X{}^{max}$	$\Delta\sigma_Y{}^{max}$	$\Delta\tau_{XY}{}^{max}$	$\overline{\Delta\sigma_X}$	$\overline{\Delta\sigma_Y}$	$\overline{\Delta\tau_{XY}}$
1	144	-1.29%	+19.24%	+4.23%	+0.18%	+0.56%	+0.32%
2	142	-0.52%	+7.32%	-1.60%	+0.13%	+0.25%	+0.14%
3	127	-0.39%	+4.75%	-0.86%	+0.08%	+0.17%	+0.08%
4	136	-0.36%	+3.93%	+0.59%	+0.04%	+0.12%	+0.05%
5	109	-0.35%	+3.41%	-0.50%	+0.02%	+0.10%	+0.04%
6	93	-0.36%	+3.38%	-0.48%	+0.01%	+0.10%	+0.03%
7	108	-0.36%	+3.18%	-0.47%	+0.01%	+0.09%	+0.03%
8	93	-0.36%	+2.96%	-0.47%	+0.01%	+0.09%	+0.03%
9	93	-0.36%	+2.75%	-0.47%	+0.01%	+0.09%	+0.03%
10	93	-0.36%	+2.54%	-0.47%	+0.01%	+0.09%	+0.03%
20	89	-0.38%	+2.23%	-0.50%	+0.01%	+0.07%	+0.02%

Table 6.11 - Variation of the Maximum and Average Element Stress Deviations with the Factor N_{GI}.

Table 6.11 presents the maximum and the average element stress deviations for the the first ten and for the final ($N_{GI} = 20$) re-imposition of the uniform stress vector $\{\sigma_o\}$. Also given is the number of iterations required to equilibriate the surface for each re-imposition. With $N_{GI} = 10$ a total of 1138 iterations is required to obtain the surface illustrated in Figure 6.11, corresponding to a Cpu time of 21008.9u. Figure 6.12 and Figure 6.13 display graphically the central planes of the membrane, $z-x$ and $z-y$, respectively [27] . The numerical solution is plotted at the element nodes and also at the intermediate points , so as to represent the curvature of the element. The intermediate points are obtained by interpolation, using the element shape functions and the element nodal co-ordinates.

Excellent agreement between the numerical and experimental solutions is demonstrated in the $z-x$ central plane (Figure 6.12). In the orthogonal direction however, some disparity between the numerical solution and the experimental can be identified. It can be seen, in particular, in the vicinity of the discontinuity of slope in the boundary of the model (Figure 6.13). This geometric disparity is coincident with the maximum element stress deviations presented in Table 6.11.

27

In Figure 6.12 and Figure 6.13, and in subsequent figures of this type, the scale along the ordinate has been exaggerated in order to illustrate the accuracy of the numerical solution to the minimal surface more clearly.

The condition of uniform stress is approximated to within –0.38% in the global x direction, and to within +2.23% in the global y direction (Table 6.11). The maximum of the average element stress deviations is given as +0.07%, indicating the existence of at least one local minimal surface comprising the overall form. The maximum element stress deviation in the global y direction has the effect of over constraining the surface. Consequently, the numerical solution should overestimate the z co-ordinates of the surface. The fact that the numerical solution is shown to underestimate the z co-ordinates (Figure 6.13), implies that the deviations of the element stresses from the condition of uniform surface stress, do not contribute significantly to the disparity between the numerical and experimental solutions. In the subsequent paragraphs it is proposed conversely, that the constraints of certain assumptions in the element formulation, can be attributed to the dissimilarities between the numerical and experimental solutions.

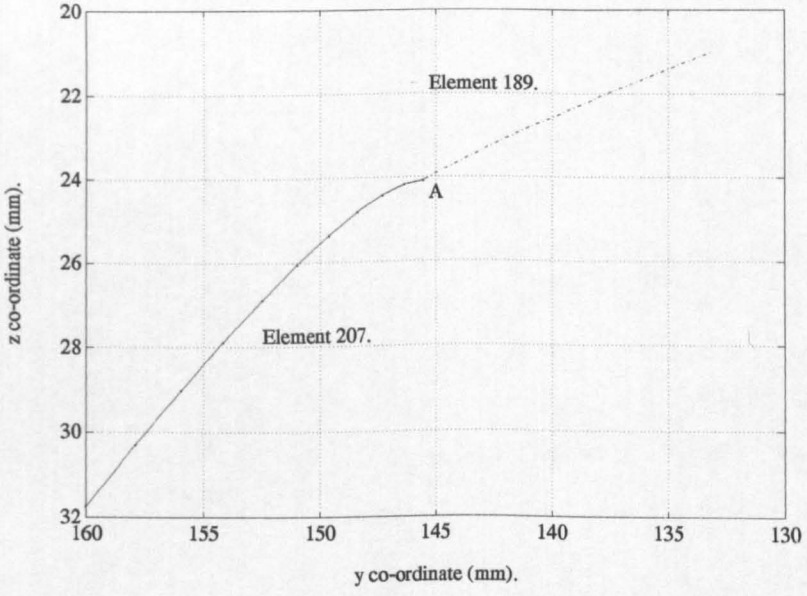

Figure 6.14 - Accuracy of Equilibriated Surface (Example 6.4) - $z-y$ Central Plane (Part-plot).

Figure 6.14 illustrates a sub-plot of the numerical solution to the surface given in Figure 6.13 for the range $y = 130.$mm to $y = 160.$mm. The geometries of the elements **207** and **189** (Figure 6.11), defined along the natural co-ordinate $\xi = +1.$ (corresponding to the z–y central plane), are presented. At the common boundary of the elements **207** and **189** (point "A" in Figure 6.14), the slope of the surface, as given by the numerical solution, is discontinuous. The curvatures of adjacent elements (determined by the numerical solution) are shown to be different at the common element boundaries, giving rise to a loss of "smoothness" when compared with the truly minimal form. This "geometric error" in the numerical model, arises from the assumption that the element shape functions are derived from the current element nodes only, and do not take into account the effects of the geometries of adjacent elements.

The element geometry and the element displacements are assumed to vary quadratically with the natural co-ordinates $\{\xi, \eta\}$ (eqn(5.3.3.7), Chapter 5). The violation of this assumption, arising during the numerical representation of the truly minimal form, has been identified with the generation of numerical errors in the formulation of the element characteristic matrices (Section 6.4.3.1). As described below, the constraints of the same assumption can be associated with a further error in the geometric representation of the element.

The geometry of element **207** at $\xi = +1.$, is characterised by a section from $y = 160.$ mm to $y = 150.$ mm which is approximately linear (Figure 6.14). The profile then curves sharply, until, at the interface with the element **189**, the surface of the element **207** is almost horizontal. As the side node (at the natural co-ordinate $\xi = +1.$) is displaced towards the point "A" (Figure 6.14), both the topological and (consequently) the geometric distortions of the element can be shown to increase. The subsequent paragraph describes how this combined topological and geometric distortion of the element may lead to an erroneous condition of equilibrium.

A vector can be established in the global y direction which is tangential to the middle surface of the element **207** at the common boundary with element **189**. This vector can be shown to be approximately horizontal. Consequently, transforming the vector of equivalent nodal forces, $\{fe\}$, into the global $\{x, y, z\}$ co-ordinate directions, and summing the resulting terms to the contributions from element **189**, gives rise to an erroneous and dominant out-of-balance force vector in the global y direction, at the common element boundary. In order to equilibriate the form, the surface is displaced in the global y direction (predominantly), until the error residual is equal to or less than the specified limit. Therefore, the surface is effectively "pulled away" from the truly minimal form (Figure 6.13).

By comparing Figure 4.34(a) (Chapter 4) with Figure 6.12, and Figure 4.34(b) (Chapter 4) with Figure 6.13, the quadrilateral element discretisation can be seen to exhibit a greater disparity between the numerical and experimental solutions, than that demonstrated by the triangular element discretisation (Figure 4.33, Chapter 4). The triangular discretisation comprises 784 elements, compared to the 216 quadrilateral elements of the discretisation illustrated in Figure 6.11. A significant increase in computational effort is required in order to generate the element matrices and to calculate the individual terms of the quadrilateral element formulation, however. This is reflected by the Cpu times of 111.8u and 21008.9u demanded by the triangular and quadrilateral element discretisations in order to establish the surfaces illustrated in Figure 4.33 (Chapter 4) and in Figure 6.11, respectively. The corresponding numbers of iterations are given as 589 and 1138. (The error residual, Er, expressed as a percentage of the maximum equivalent nodal forces, is the same for both the triangular and quadrilateral element discretisations.)

Figure 6.15 shows the equilibriated surface of the soap-film model illustrated in Plates 3.5 & 3.6 (Example 6.5). 216 quadrilateral elements are used to discretise the surface. The elements are arranged such that the initial element size is the same as that adopted in the preceding example when measured relative to the overall dimensions of the physical model. The condition of uniform stress is modelled as $\sigma_x = \sigma_y = 1.\times10^{+6}$ kN.m^{-2}, and $\tau_{xy} = 0.$ kN.m^{-2}. The elastic modulus of the surface is assumed to be zero, while the thickness of the membrane is taken to be $1.\times10^{-3}$m.

Due to the rapidly changing curvatures of the surface (Plate 3.5), the numerical stability of the solution algorithm cannot be assured by scaling the components of the nodal stiffnesses with the factor, λ_A [6.10]. Therefore, the procedure described below has been devised in order to enhance the numerical stability of the solution algorithm in this case.

The initial surface is defined mathematically, in the first instance, by Hermitian polynomials, with the factor $\lambda_s = 4.0$. Equilibriating the form in the global z direction only (while suppressing displacements in the global x and the global y directions) gives rise to a revised "initial" surface. The revised "initial" surface resembles the truly minimal energy form more closely than obtained using the Hermitian polynomials.

In order to reduce the out-of-balance force vector in the global x and the global y directions, while maintaining the numerical stability of the solution algorithm, a temporary fictitious condition of equilibrium is imposed. This is done by assuming that the out-of-balance force vector in the global x and in the global y directions is zero at each element node, until a peak in the kinetic energy of the system is detected. All of the terms of the current out-of-balance force vector are then calculated, and used to establish the element nodal displacements in the global x, y, and z directions. The surface geometry is subsequently updated according to eqn(6.4.1.1). The out-of-balance force vector in the global x and in the global y directions are then reset to, and maintained at, zero until the next peak in the kinetic energy of the system is observed, when the same procedure is repeated. In order to prevent exaggerated deformations of the surface at the kinetic energy peaks, the nodal displacements in the global x and in the global y directions are scaled by a factor of $\frac{1}{5}$.

Subsequent to a total of 5500 iterations ($N_{GI} = 1.$), with a corresponding Cpu time of 102774.6u (28.5 hours), the surface illustrated in Figure 6.15 is obtained. The maximum and the average element stress deviations are presented in Table 6.12, while the central planes of the surface, $z-x$ and $z-y$, are shown in Figure 6.16 and Figure 6.17 respectively.

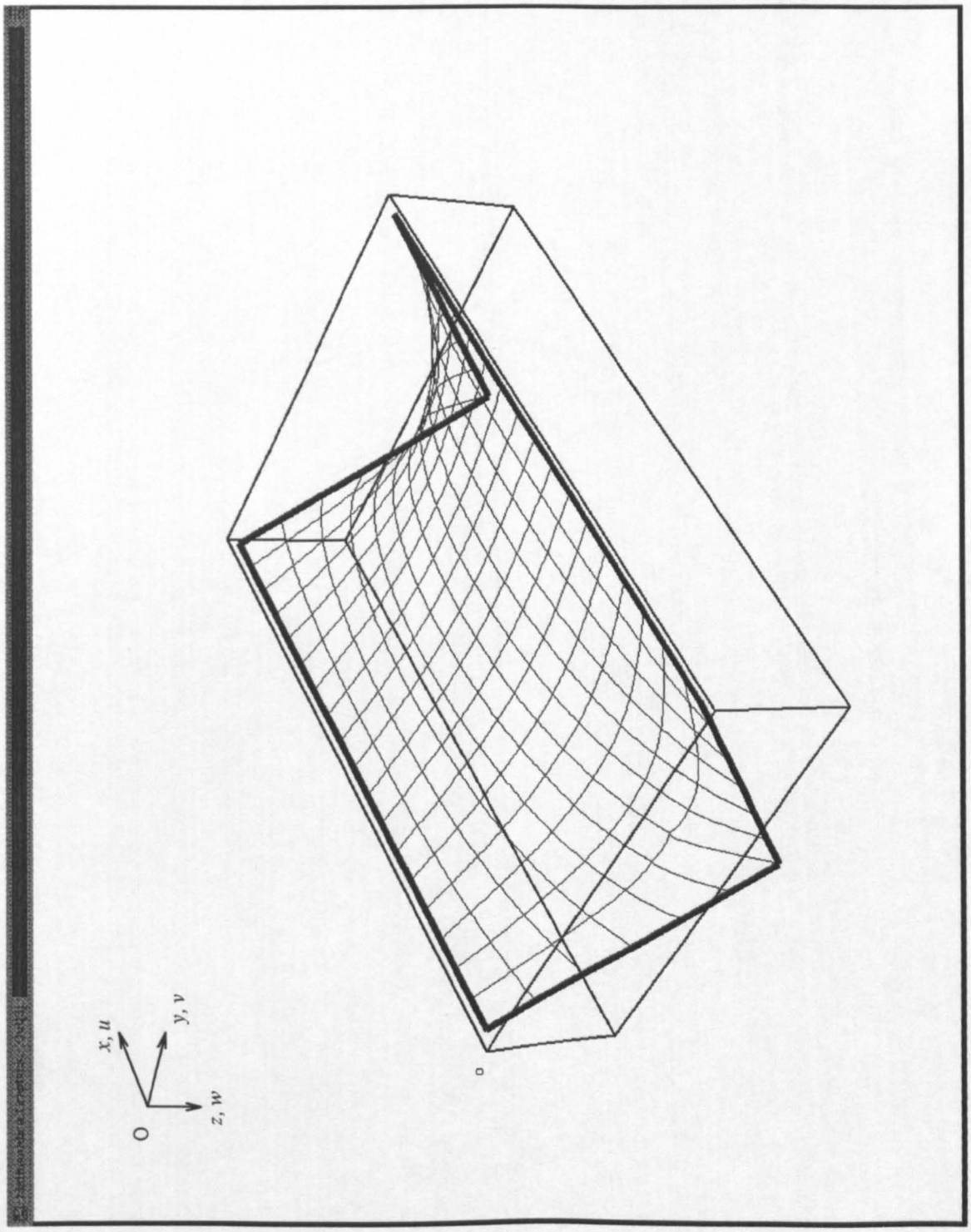

Figure 6.15 - Surface Discretised using Quadrilateral Elements - Example 6.5.

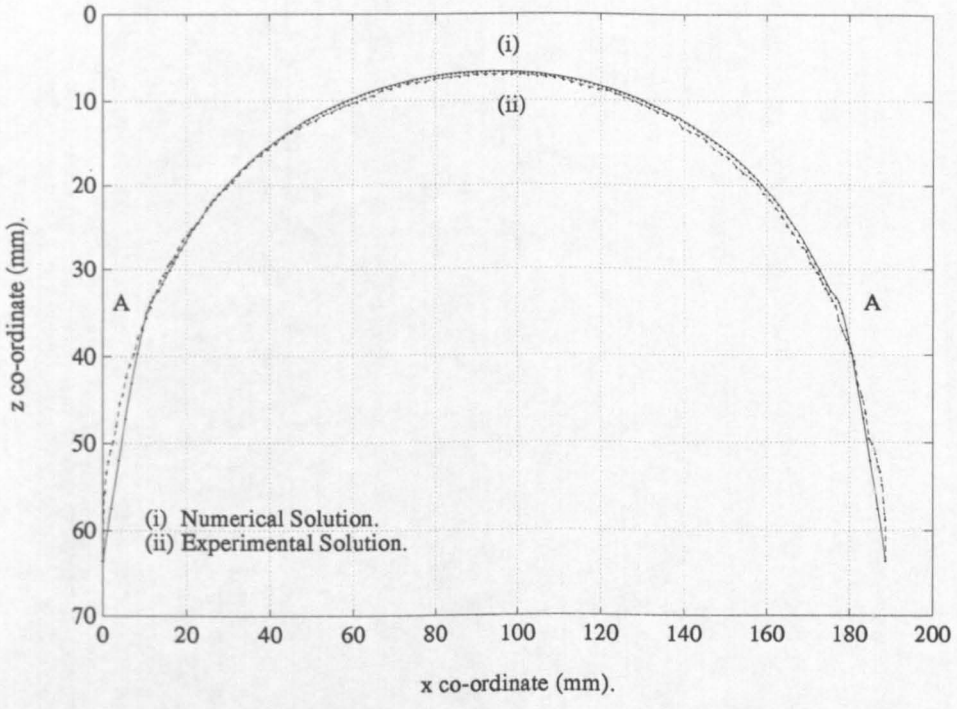

Figure 6.16 - Accuracy of Equilibriated Surface (Example 6.5) - $z-x$ Central Plane.

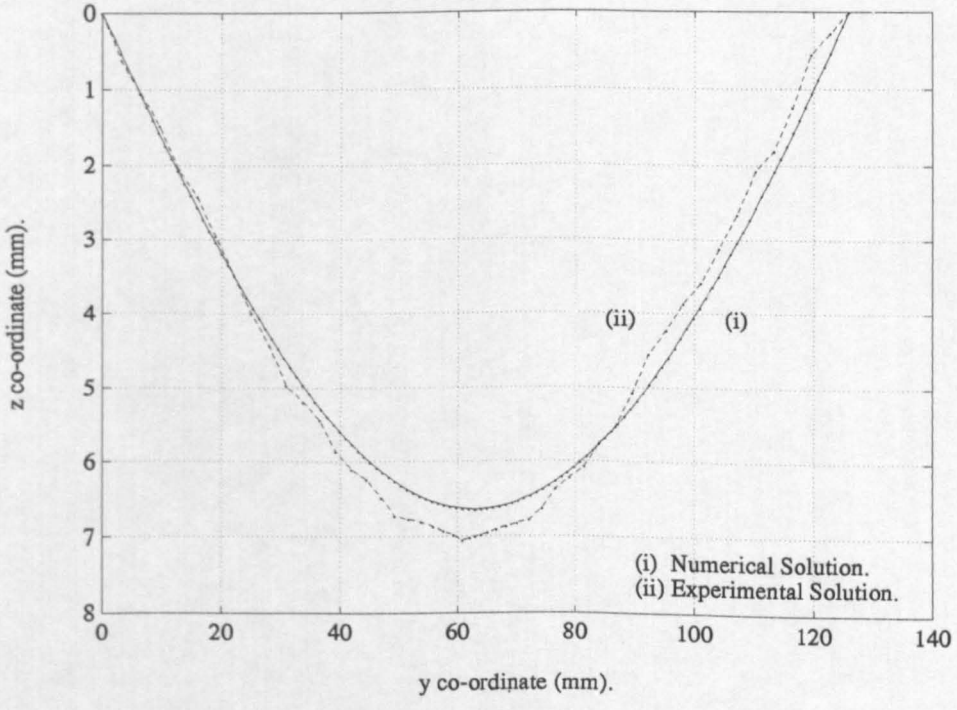

Figure 6.17 - Accuracy of Equilibriated Surface (Example 6.5) - $z-y$ Central Plane.

At the termination of the analysis however, the surface is deemed not to be fully equilibriated, as it fails to satisfy the criterion established for the maximum error residual, Er, at certain nodes of the discretisation. For example, the out-of-balance force in the global x direction is equal to $+0.1868\times10^{+1}$kN, in the global y direction to $+0.3054\times10^{+2}$kN, and in the global z direction to $+0.2471\times10^{+0}$kN, with the value of Er equal to $1.\times10^{-1}$ kN (approximately equal to 0.025 % of the maximum element equivalent nodal force). These figures correspond to 61.1%, to 28.8%, and to 0.02%, of the values at the commencement of the form-finding procedure, respectively.

$\Delta\sigma_X{}^{max}$	$\Delta\sigma_Y{}^{max}$	$\Delta\tau_{XY}{}^{max}$	$\overline{\Delta\sigma_X}$	$\overline{\Delta\sigma_Y}$	$\overline{\Delta\tau_{XY}}$
+48.82%	-8.75%	+23.10%	+2.37%	+0.63%	+1.15%

Table 6.12 - Maximum and Average Element Stress Deviations - Example 6.5.

Furthermore, the maximum and the average element stress deviations are shown to be large at the same stage of the analysis ($N_{IT} = 5500$, Table 6.12). An attempt to reduce the element stress deviations (by re-imposing the uniform stress vector $\{\sigma_o\}$) leads to the numerical instability of the solution algorithm. As in the case of the surface illustrated in Figure 6.11, the maximum element stress deviations are found to occur in the elements immediately adjacent to the discontinuities of slope in the element boundary. The high positive magnitude of the maximum element stress deviation in the global x direction is shown to over-constrain the numerical representation of the surface in the vicinity of the model boundary (Figure 6.16). Therefore, the numerical solution overestimates the z co-ordinates of the surface in this region.

The discontinuities of slope identified in the numerical solution of the preceding example, can also be seen in Figure 6.16 (marked as "A"). However, the effects of the constraints imposed on the numerical solution through the assumption of a quadratic variation of element shape functions with the natural co-ordinates $\{\xi, \eta\}$ (eqn(5.3.3.7)), and of the positive element stress deviations in the global x direction, tend to cancel. Consequently, good agreement between the numerical and experimental solutions can be observed (Figure 6.16 and Figure 6.17). However, the numerical solution to the surface is not fully equilibriated, and the approximate cancelling of the effects mentioned above, must be considered as coincidental.

An adequate numerical solution to the soap-film surface illustrated in Plates 3.3 & 3.4 has been found difficult to establish when adopting a discretisation of quadrilateral elements, formulated in the Chapter 5.

Figure 6.18 (Example 6.6) and Figure 6.19 (Example 6.7) illustrate two alternative discretisations of the same physical model. (The initial surfaces of the numerical models are displayed).

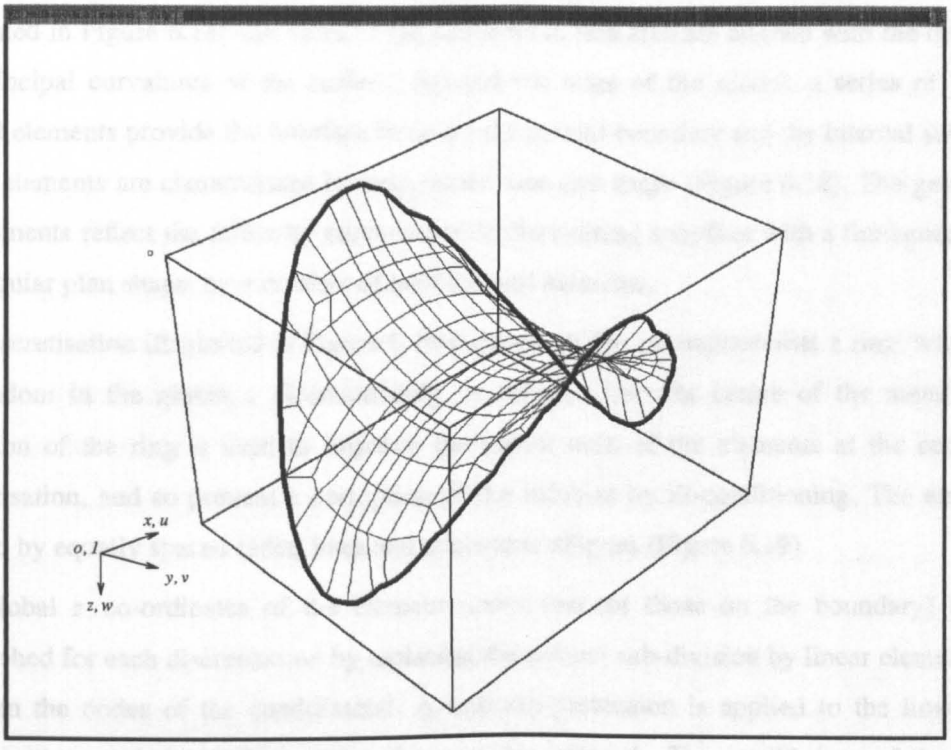

Figure 6.18 - Surface Discretised using Quadrilateral Elements - Example 6.6.

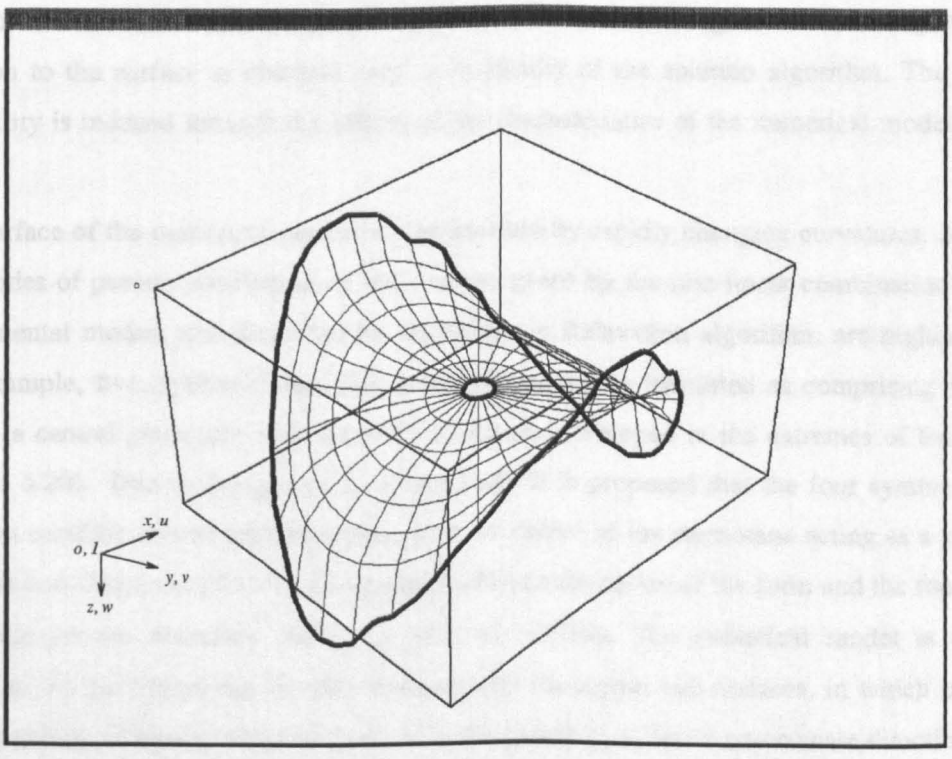

Figure 6.19 - Surface Discretised using Quadrilateral Elements - Example 6.7.

A mesh of regularly shaped quadrilateral elements constitutes the main body of the sub-division illustrated in Figure 6.18. The sides of the elements in this area are aligned with the directions of the principal curvatures of the surface. Around the edge of the model, a series of irregularly shaped elements provide the interface between the curved boundary and the internal sub-division. These elements are characterised by both varied size and shape (Figure 6.18). The geometries of the elements reflect the difficulty encountered in discretising a surface with a fundamentally non-rectangular plan shape, by a number of quadrilateral elements.

The discretisation illustrated in Figure 6.19 is based on the assumption that a ring, with degrees-of-freedom in the global z direction only, is inserted into the centre of the membrane. The inclusion of the ring is used to improve the aspect ratio of the elements at the centre of the discretisation, and so prevent a corruption of the solution by ill-conditioning. The elements are defined by equally spaced radial lines and concentric ellipses (Figure 6.19).

The global z co-ordinates of the element nodes (except those on the boundary) have been established for each discretisation by replacing the current sub-division by linear elements, placed between the nodes of the quadrilateral. A uniform pretension is applied to the linear element discretisation, and the surface analysed as a cable network. The equilibrium of the surface is established in the global z direction only, while displacements in the global x and in the global y directions are suppressed. An approximation to the truly minimal form is established in this way.

It is found that, in the case of the discretisations illustrated in Figure 6.18 and Figure 6.19, no solution to the surface is obtained, due to instability of the solution algorithm. The numerical instability is induced through the effects of the characteristics of the numerical model described below.

The surface of the numerical model is characterised by rapidly changing curvatures. In addition, the modes of pseudo oscillations of the surface, given by the non-linear combination of several fundamental modes, and described by the Dynamic Relaxation algorithm, are highly complex. For example, five, approximately flat, sub-surfaces can be identified as comprising the overall form - a central plane and four symmetrical planes developed in the extremes of the boundary (Figure 6.20). Due to the geometry of the form, it is proposed that the four symmetrical sub-surfaces oscillate almost independently, with the centre of the membrane acting as a point about which the surfaces can pivot, and with lines between the centre of the form and the four points of inflection on the boundary, acting as axes of rotation. The numerical model is dominated therefore, by four relatively flexible and partially decoupled sub-surfaces, in which large nodal displacements of similar magnitude occur in the global x, y, and z co-ordinate directions. These large nodal displacements can induce rapid changes in the geometries of the elements, and give rise to an exaggeration of the out-of-balance force vectors at the element nodes (through the contribution of the non-linear strain-displacement matrix $[B_L]$ (eqn(5.7.5.1) with eqn(5.7.1.6))). It

is demonstrated below, that the sensitivity of the numerical model can be shown to be reduced, and the stability of the solution algorithm enhanced by the adoption of a coarse mesh of elements.

Figure 6.20 (Example 6.8) shows the surface illustrated in Plates 3.3 & 3.4 discretised by four quadrilateral elements. Assuming a similar initial surface to that illustrated in Figure 6.19, and a uniform stress vector $\{\sigma_o\}$ given as $\sigma_x = \sigma_y = 5.\times10^{+6}$ kN.M^{-2}, and $\tau_{xy} = 0.$ kN.M^{-2}, the condition of equilibrium can be shown to be satisfied to an error residual, Er, equal to 0.25 % of the maximum element equivalent nodal force, in the global x, y and z co-ordinate directions. The technique of imposing a temporary fictitious condition of equilibrium in the x and y directions between the kinetic energy peaks, has been adopted, in order to maintain the stability of the solution algorithm.

Table 6.13 presents the maximum and the average element stress deviations for the first five re-impositions of the uniform stress vector $\{\sigma_o\}$, with the number of iterations necessary to achieve equilibrium after each re-imposition.

Subsequent to to the first re-imposition of the uniform stress vector, $\{\sigma_o\}$, ($N_{GI} = 1$), the magnitude of the maximum element stress deviation can be seen to stablise at around +20.0%, with the maximum of the average element stress deviations converging to approximately +10.0%. These relatively high figures reflect the inability of the numerical model (Figure 6.20) to model accurately the curvatures of the truly minimal surface. This is due primarily to an insufficient number of elements comprising the discretisation.

By comparing the numerical solution (based on the discretisation illustrated in Figure 6.20) with the experimental solution, the numerical model can be seen to provide an adequate representation of the minimal surface illustrated in Plates 3.3 & 3.4 (Figure 6.21 and Figure 6.22) [28] . The relatively small disparity between the solutions for such a low number of elements, is indicative of the ability of the quadratic element shape functions to define the central orthogonal planes of the surface accurately ($N_{GI} = 1$). At the same time the effects of the inaccuracies of the boundaries of the numerical representation of the physical model, counteract those of the element stress deviations.

28

With the re-imposition of the stress vector $\{\sigma_o\}$, the element nodes 9, 10, 11, and 12, (Figure 6.20), can be shown to move significantly in the plane of the surface. This phenomenon gives rise to topological and (consequently) geometric distortions of the elements. Therefore, an error is induced in the numerical solution to the surface. For this reason the solution to the surface at $N_{GI} = 1$ has been chosen for comparison with the experimental solution.

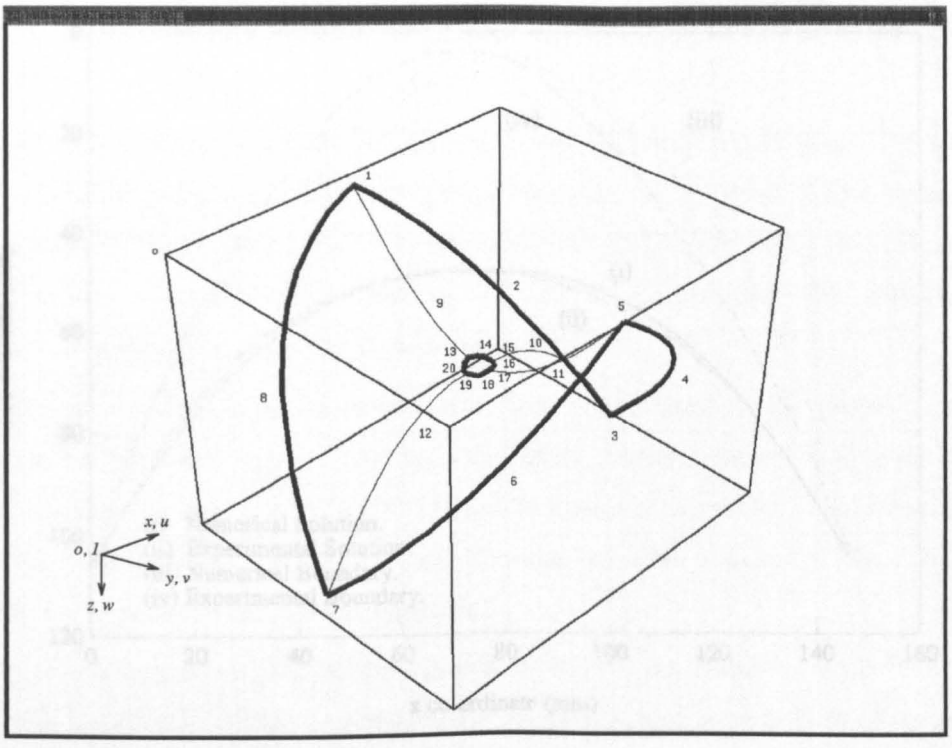

Figure 6.20 - Surface Discretised using Quadrilateral Elements - Example 6.8.

N_{GI}	N_{IT}	$\Delta\sigma_X{}^{max}$	$\Delta\sigma_Y{}^{max}$	$\Delta\tau_{XY}{}^{max}$	$\overline{\Delta\sigma_X}$	$\overline{\Delta\sigma_Y}$	$\overline{\Delta\tau_{XY}}$
1	187	+15.76%	+27.71%	+15.58%	+8.17%	+15.52%	+8.10%
2	181	+7.45%	-21.48%	+10.07%	+4.67%	+12.72%	+5.09%
3	172	+4.58%	-20.62%	+7.09%	+3.03%	+10.92%	+3.66%
4	174	-4.05%	-20.16%	+5.42%	+2.75%	+10.01%	+3.14%
5	183	-3.94%	-19.87%	+5.13%	+2.57%	+9.45%	+2.90%

Table 6.13 - Variation of the Maximum and Average Element Stress Deviations with the Factor N_{GI}.

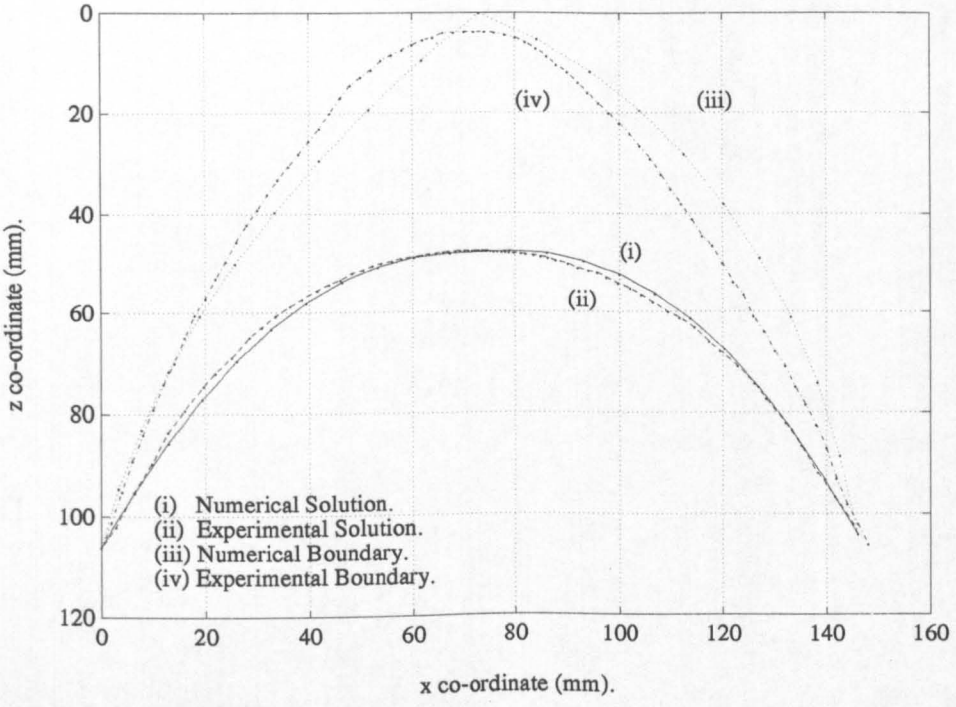

Figure 6.21 - Accuracy of Equilibriated Surface (Example 6.8) - $z - x$ Central Plane.

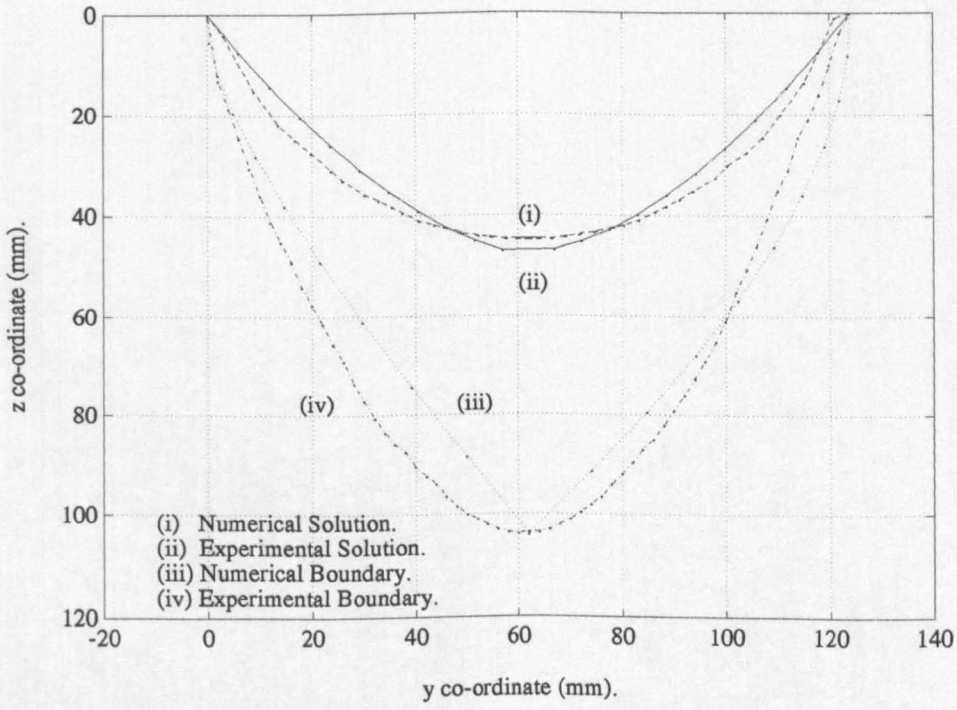

Figure 6.22 - Accuracy of Equilibriated Surface (Example 6.8) - $z - y$ Central Plane.

6.5.3. Minimal Surfaces With Internal and External Flexible Boundary Elements.

Further numerical solutions to the minimal surfaces shown in Plates 3.14 - 3.19, are presented in this section [29] .

Figure 6.23 illustrates the equilibriated surface to the soap-film model shown in Plate 3.15 (Example 6.9). The surface is initially sub-divided by sixteen square quadrilateral elements, with a sides of length of 4. m and a constant thicknesses of 1×10^{-3}m. A uniform stress vector, $\{\sigma_o\}$, given as $\sigma x = \sigma y = 1.\times10^{+6}$ kN.m^{-2} and $\tau_{xy} = 0.$ kN.m^{-2} is assumed. The stiffness of the membrane is considered to be derived from prestress only.

The membrane is bounded by linear elements, and is restrained in the global x, y, and z directions at the four corner points. The boundary cable elements are assumed to be uniformly tensioned initially by a prestress of $7\times10^{+3}$ kN, and to have a constant elastic modulus of $1.\times10^{+4}$ kN.m^{-2}. The cross sectional areas of the linear elements are taken to be unity. The initial surface of the form is illustrated in the insert in Figure 6.23.

To ensure the numerical stability of the solution algorithm, the factor $\lambda_A = 5.0$ [6.10] has been adopted with $\lambda_D = 1.0$ [30] , while the error residual, Er, is assumed to be 0.25 % of the maximum element equivalent nodal force. Table 6.14 presents the maximum and the average element stress deviations for ten re-impositions of the uniform stress vector $\{\sigma_o\}$, and the numbers of iterations required to satisfy the condition of equilibrium.

A total of 824 iterations, corresponding to a Cpu time of 1101.7u are required to establish the form illustrated in Figure 6.23 ($N_{GI} = 10$). From the magnitude of the element stress deviations ($N_{GI} = 1$, Table 6.14), and from the distortion of the elements demonstrated by comparing the initial and equilibriated surfaces presented in Figure 6.23, a significant straining of the surface can be seen to have occurred during the form-finding procedure.

With the re-imposition of the uniform stress vector $\{\sigma_o\}$ the maximum element stress deviation is shown to converge to approximately -45.0%, with the maximum of the average stress deviations to around +5.1% (Table 6.14). The maximum element stress deviation exists in the elements at the four corners of the discretisation, where the boundary elements can be seen to have merged, in order to establish an approximation to the minimal energy form (Figure 6.23). The relatively high figure to which the maximum element stress deviation converges, is as a result of the

---

29

The relevant figures can be found at the end of this section.

30

The factor, λ_D, is used to scale the vector of accumulated nodal displacements, $\{\delta\}_{i\,accum.}$, in order to reduce the contribution of the vector, $\{\delta\}_{i\,accum.}$, to the vector of element equivalent nodal forces, $\{fe\}$, through the matrix $[B_L]$ (eqn(5.7.5.1) with eqn(5.7.1.6), Chapter 5). Consequently, the element stress deviations are diminished at equilibrium (eqn(6.4.2.2.4)).

geometric distortions of the corner elements. As demonstrated below, the excessive geometric distortions of the elements, which are characterised by the very large and the very small internal angles at the element extremes, give rise to errors in the element formulation.

If the initial boundary natural forces are increased to $2\times10^{+4}$ kN, while the other geometric and material constants are assumed to remain unchanged, the surface illustrated in Figure 6.24 (Example 6.10) is obtained. Table 6.15 presents the maximum and the average element stress deviations at equilibrium, for the first eight re-impositions of the uniform stress vector $\{\sigma_o\}$. With reference to Table 6.15 the condition of uniform stress is shown to be represented very closely when the element distortion is low (Figure 6.24). Furthermore, in the case of the surface illustrated in Figure 6.23, it is found that at equilibrium ($N_{GI} = 10$), the natural forces in the boundary elements vary by up to 1.8%. This figure may be compared with a zero variation in the case of the experimental solution. With the revised boundary element pretensions, the natural forces are found to be invariant to the first five digits, or constant to within 0.02%. A comparison of the solutions to the surfaces illustrated in Figure 6.23 and Figure 6.24 indicates that the contribution of the errors in the numerical solution, arising from large geometric distortions of the elements, can be significant.

Figure 6.25 illustrates the equilibriated surface of the soap-film model shown in Plates 3.17 (Example 6.11). A total of 60 quadrilateral elements are used to discretise the membrane, with 72 linear elements representing the flexible boundaries. The initial surface of the form is illustrated in the insert in Figure 6.25. To ensure the numerical stability of the solution algorithm, the factor $\lambda_A = 5$. [6.10] is adopted. In addition, a value of 0.75 is assumed for the factor λ_D, in order to increase the rate of convergence of the solution to the condition of uniform stress.

The elastic modulus of the external boundary elements has been taken as $1.\times10^{+2}$ kN.m^{-2} and for the internal elements as $1.\times10^{+4}$ kN.m^{-2}. In both sets of boundary cables the prestress is assumed to be $8.\times10^{+3}$ kN, with the cross-sectional area as unity. The membrane is prestressed by the vector of uniform stress, $\{\sigma_o\}$, with the magnitudes of the stresses the same as those assumed for the preceding example. Table 6.16 presents the maximum and the average element stress deviations for ten re-impositions of the uniform stress vector $\{\sigma_o\}$, and the numbers of iterations required to satisfy the condition of equilibrium after each re-imposition.

For $N_{GI} = 10$, a total of 855 iterations is required to establish the form illustrated in Figure 6.25, with a corresponding Cpu time of 4123.5u. The maximum element stress deviation can be seen to converge to around -12.0% (occurring in the corner elements), with the maximum of the average element stress deviations to approximately +1.0%. The less severe geometric distortion of the corner elements (Figure 6.25) (compared with the surface illustrated in Figure 6.23) permits an improved satisfaction of the condition of uniform surface stress. This is reflected by the reduced magnitude of the maximum element stress deviations given in Table 6.16 (cf. Table 6.14). The

natural forces in the external boundary elements are found to be constant to within 0.28%, with those in the internal boundary elements to within 0.13%, at $N_{GI} = 10$. These figures suggest good agreement between the numerical and experimental solutions.

Figure 6.26 illustrates the equilibriated surface of the soap-film model shown in Plates 3.19 (Example 6.12). The discretisation is similar to that in the previous example, except that, the central hole in the membrane is translated by -4.m in the global x direction and +4.m in the global y direction (Figure 6.26). The elastic modulus of all of the boundary cable elements is assumed to be $1.\times10^{+4}$ kN.m^{-2}, with the cross-sectional area of the elements taken as unity. The prestress in the external boundary elements is given as $1.\times10^{+4}$ kN, with $1.\times10^{+3}$ kN in the internal. The remaining details are as those adopted for the preceding example.

Table 6.17 gives the maximum and the average element stress deviations for ten re-impositions of the uniform stress vector $\{\sigma_o\}$, and the numbers of iterations to achieve equilibrium after each re-imposition. A total of 1075 iterations, corresponding to a Cpu time of 5176.1u are required to establish the form illustrated in Figure 6.26 ($N_{GI} = 10$).

A significant straining of the surface can be seen to have occurred in the elements in the regions marked "A" (Figure 6.26), when the geometries of the elements are compared with those of the initial surface (insert, Figure 6.26). For the first seven re-impositions of the uniform stress vector $\{\sigma_o\}$, the maximum element stress deviations in the global x and the global y directions, correspond to the elements in these regions. The magnitudes of the stress deviations (Table 6.17, $1 \leq N_{GI} \leq 7$) reflect the stability of the solution algorithm during the large straining of these elements (Figure 6.26).

In the case of $N_{GI} \geq 8$, the effects of the errors in the numerical solution, arising from the geometric distortion of the elements at the corners of the discretisation, tend to dominate the magnitudes of the element stress deviations. Consequently, the maximum element stress deviation is -13.36% with a maximum of the average element stress deviations of +1.20%, at $N_{GI} = 10$. The natural forces in the external boundary elements are found to be constant to within 1.1%, and those in the internal to within 2.3%. These relatively high figures indicate a loss of accuracy from the numerical solution, due to the heavy geometric distortion and the poor aspect ratios of some elements comprising the discretisation.

Figure 6.23 can be compared with Plates 3.15, Figure 6.25 with Plates 3.17, Figure 6.26 with Plates 3.19. The accuracies of the numerical solutions are demonstrated when comparing the element stress deviations and the boundary element natural forces with the values anticipated from the physical models.

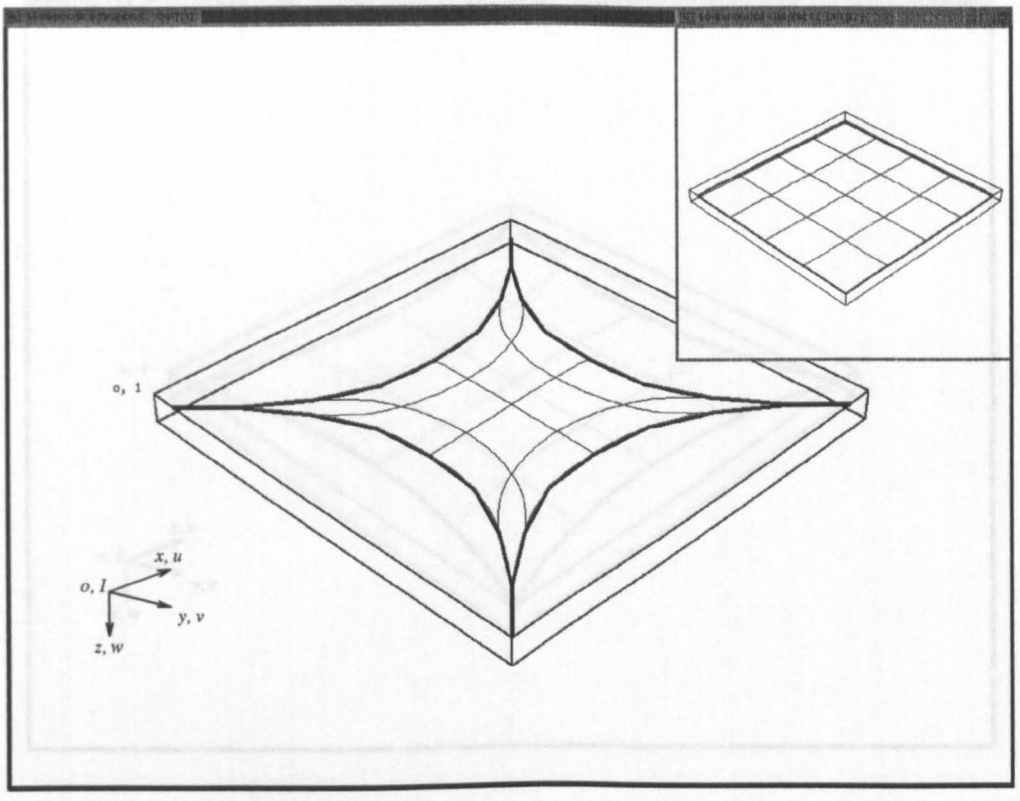

Figure 6.23 - Surface Discretised using Quadrilateral Elements - Example 6.9.

N_{GI}	N_{IT}	$\Delta\sigma_X{}^{max}$	$\Delta\sigma_Y{}^{max}$	$\Delta\tau_{XY}{}^{max}$	$\overline{\Delta\sigma_X}$	$\overline{\Delta\sigma_Y}$	$\overline{\Delta\tau_{XY}}$
1	73	-72.47%	-72.47%	+81.20%	+39.90%	+39.90%	+25.01%
2	76	-43.77%	-43.77%	+53.12%	+25.84%	+25.84%	+21.08%
3	77	-41.26%	-41.26%	+47.36%	+18.73%	+18.73%	+16.11%
4	81	-41.94%	-41.94%	+45.28%	+14.25%	+14.25%	+12.57%
5	72	-42.49%	-42.49%	-44.50%	+11.23%	+11.23%	+10.09%
6	75	-43.09%	-43.09%	+44.39%	+9.14%	+9.14%	+9.14%
7	80	-43.72%	-43.72%	+44.59%	+7.64%	+7.64%	+7.07%
8	83	-44.32%	-44.32%	+44.91%	+6.53%	+6.53%	+6.53%
9	92	-44.84%	-44.84%	+45.26%	+5.72%	+5.72%	+5.43%
10	115	-45.25%	-45.25%	+45.46%	+5.10%	+5.11%	+4.89%

Table 6.14 - Variation of the Maximum and Average Element Stress Deviations with the Factor N_{GI}.

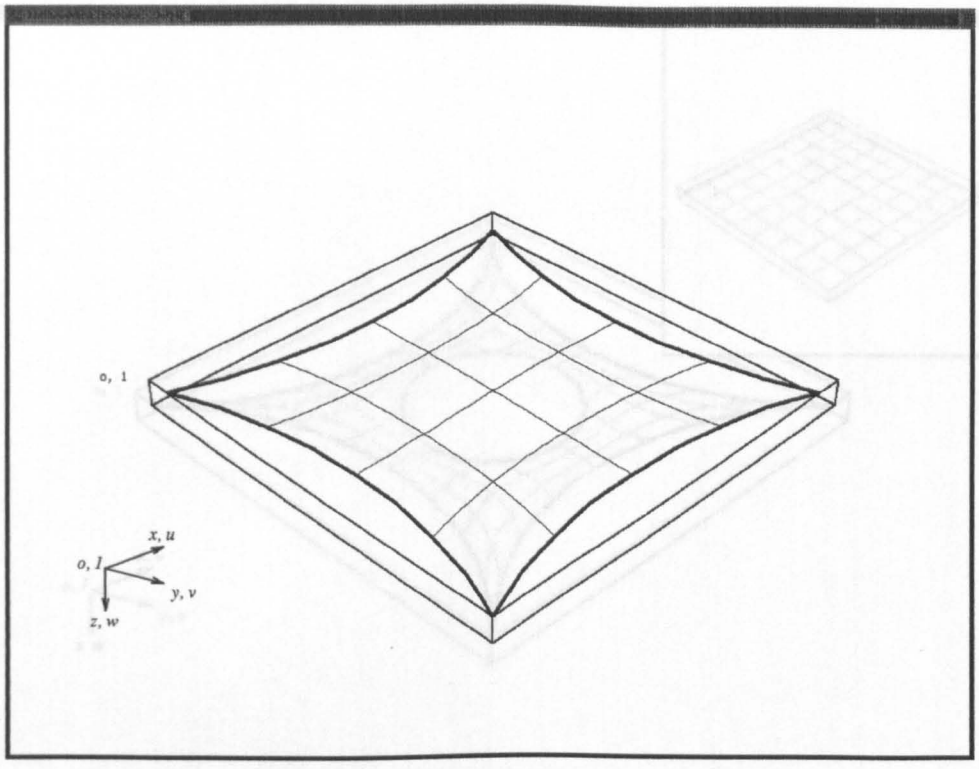

Figure 6.24 - Surface Discretised using Quadrilateral Elements - Example 6.10.

N_{GI}	N_{IT}	$\Delta\sigma_X{}^{max}$	$\Delta\sigma_Y{}^{max}$	$\Delta\tau_{XY}{}^{max}$	$\overline{\Delta\sigma_X}$	$\overline{\Delta\sigma_Y}$	$\overline{\Delta\tau_{XY}}$
1	76	-42.70%	-42.70%	+49.93%	+22.56%	+22.56%	+13.71%
2	62	-13.23%	-13.23%	+17.33%	+7.28%	+7.28%	+6.01%
3	44	-6.24%	-6.24%	+6.92%	+2.58%	+2.58%	+2.32%
4	41	-2.56%	-2.56%	+2.74%	+0.96%	+0.96%	+0.88%
5	35	-1.01%	-1.01%	+1.05%	+0.36%	+0.36%	+0.33%
6	31	-0.39%	-0.39%	+0.41%	+0.14%	+0.14%	+0.13%
7	21	-0.15%	-0.15%	+0.16%	+0.05%	+0.05%	+0.05%
8	28	-0.05%	-0.05%	+0.05%	+0.02%	+0.02%	+0.01%

Table 6.15 - Variation of the Maximum and Average Element Stress Deviations with the Factor N_{GI}.

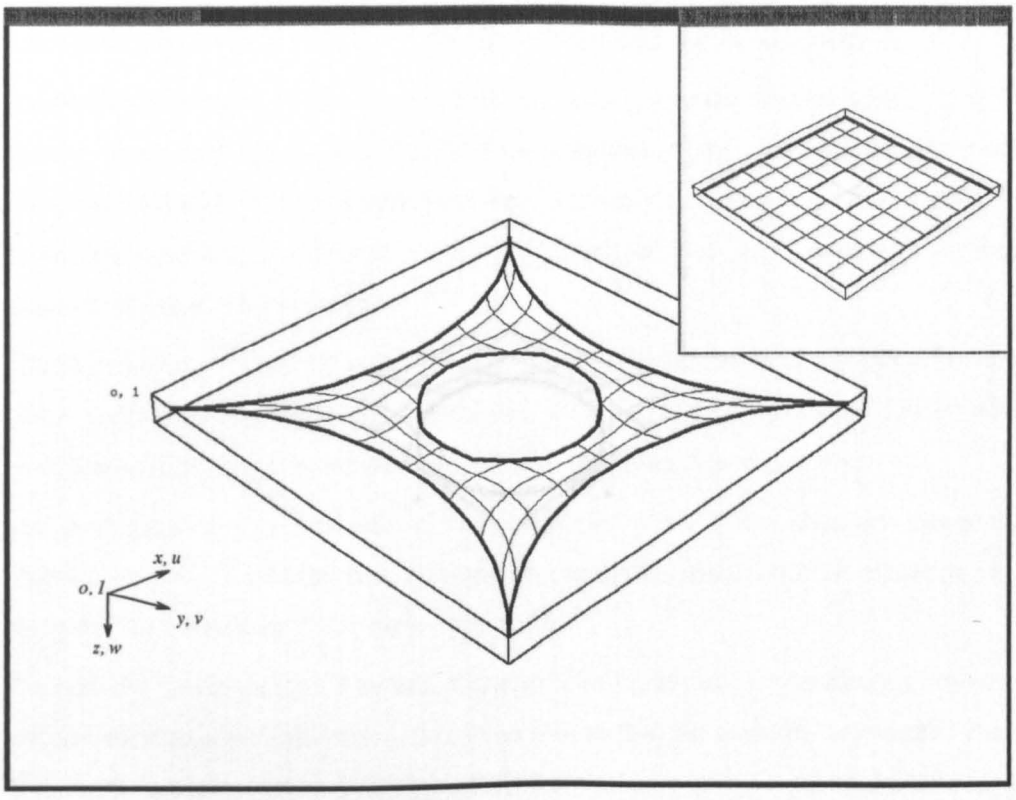

Figure 6.25 - Surface Discretised using Quadrilateral Elements - Example 6.11.

N_{GI}	N_{IT}	$\Delta\sigma_X{}^{max}$	$\Delta\sigma_Y{}^{max}$	$\Delta\tau_{XY}{}^{max}$	$\overline{\Delta\sigma_X}$	$\overline{\Delta\sigma_Y}$	$\overline{\Delta\tau_{XY}}$
1	127	-84.84%	-84.48%	+67.73%	+32.73%	+32.73%	+17.51%
2	112	-51.82%	-51.82%	+38.76%	+19.90%	+19.90%	+11.31%
3	106	-31.21%	-31.21%	+30.84%	+12.54%	+12.54%	+7.14%
4	84	-24.24%	-24.24%	+25.74%	+8.14%	+8.14%	+4.70%
5	73	-21.21%	-21.21%	+22.13%	+5.46%	+5.46%	+3.24%
6	73	-18.72%	-18.72%	+19.26%	+3.76%	+3.76%	+2.28%
7	80	-16.51%	-16.51%	+16.90%	+2.65%	+2.65%	+1.66%
8	67	-14.80%	-14.80%	+15.04%	+1.91%	+1.91%	+1.23%
9	62	-13.33%	-13.33%	+13.50%	+1.41%	+1.41%	+0.93%
10	71	-11.92%	-11.92%	+12.03%	+1.04%	+1.04%	+0.70%

Table 6.16 - Variation of the Maximum and Average Element Stress Deviations with the Factor N_{GI}.

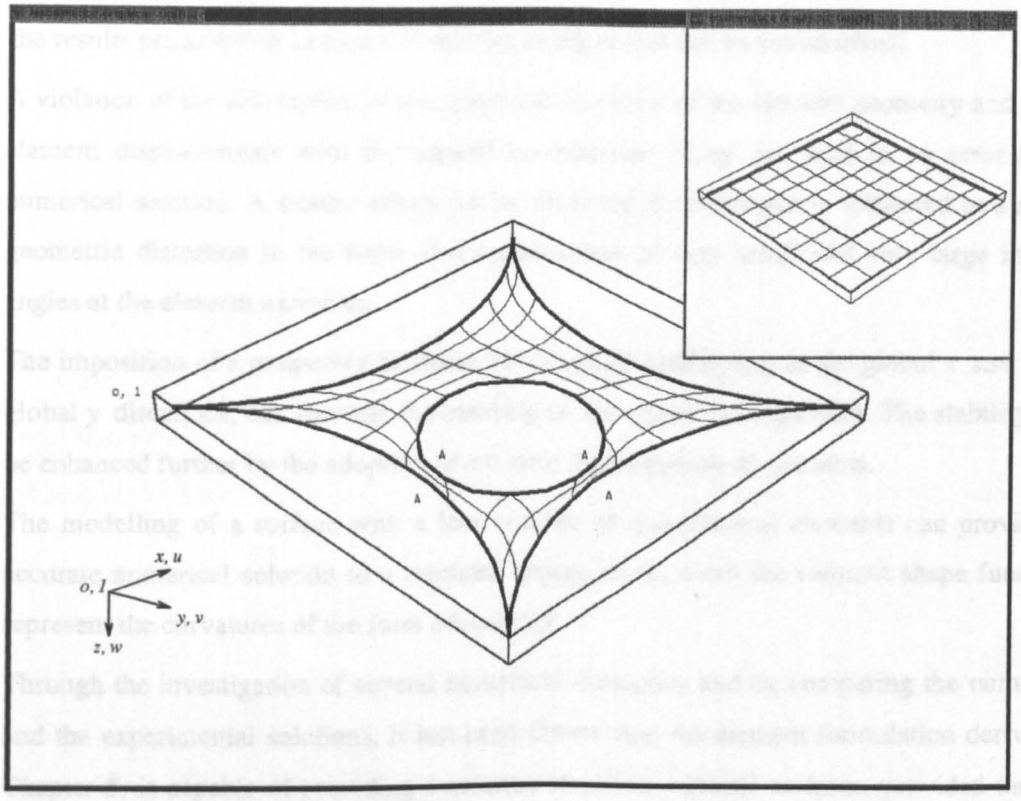

Figure 6.26 - Surface Discretised using Quadrilateral Elements - Example 6.12.

N_{GI}	N_{IT}	$\Delta\sigma_X{}^{max}$	$\Delta\sigma_Y{}^{max}$	$\Delta\tau_{XY}{}^{max}$	$\overline{\Delta\sigma_X}$	$\overline{\Delta\sigma_Y}$	$\overline{\Delta\tau_{XY}}$
1	159	-88.32%	-88.32%	+66.62%	+32.70%	+32.70%	+19.55%
2	141	-64.04%	-64.04%	+39.52%	+19.16%	+19.16%	+13.08%
3	122	-45.87%	-45.87%	+31.58%	+12.12%	+12.12%	+8.51%
4	102	-33.86%	-33.86%	+26.39%	+8.01%	+8.01%	+5.79%
5	102	-25.47%	-25.47%	+22.59%	+5.49%	+5.49%	+4.08%
6	100	-19.56%	-19.56%	+19.65%	+3.88%	+3.88%	+2.96%
7	104	-17.53%	-17.53%	+17.21%	+2.81%	+2.81%	+2.21%
8	95	-15.89%	-15.89%	+15.18%	+2.08%	+2.08%	+1.66%
9	85	-14.56%	-14.56%	+13.53%	+1.58%	+1.58%	+1.29%
10	65	-13.36%	-13.36%	+12.02%	+1.20%	+1.20%	+0.99%

Table 6.17 - Variation of the Maximum and Average Element Stress Deviations with the Factor N_{GI}.

6.5.4. Summary.

From the results presented in section 6.5, the following points can be summarised:

i) A violation of the assumption of the quadratic variation of the element geometry and of the element displacements with the natural co-ordinates $\{\xi, \eta\}$ can lead to an error in the numerical solution. A similar effect can be observed if an element is subjected to a severe geometric distortion in the form of a combination of very small and very large internal angles at the element extremes.

ii) The imposition of a temporary fictitious condition of equilibrium in the global x and in the global y directions, can increase the stability of the numerical algorithm. The stability may be enhanced further by the adoption of a coarse discretisation of elements.

iii) The modelling of a surface with a low number of quadrilateral elements can provide an accurate numerical solution to a minimal energy form, when the element shape functions represent the curvatures of the form adequately.

iv) Through the investigation of several numerical examples, and by comparing the numerical and the experimental solutions, it has been shown that the element formulation derived in Chapter 5, is capable of providing a solution to stable minimal surfaces, provided that the problems outlined in (i) can be overcome.

6.6. Appendix 6-A - Derivation of the Vector of Equivalent Nodal Forces, $\{F_{eq}\}$, Describing the Uniform Stress Vector, $\{\sigma\}$.

The vector, $\{F_{eq}\}$ is obtained from the equation [6.1],

$$\{F_{eq}\} = \int_{surface} [N^{**}]^T \{\sigma\} \, ds \,, \qquad \text{eqn(6-A.1)}$$

where $\{\sigma\}$ represents the external uniform stress vector, and is written as $\{\sigma\} = \{\sigma_x, \sigma_y, \tau_{xy}\}^T$. The matrix $[N^{**}]$ contains shape functions drawn from the Lagrangian set.

For example, with reference to Figure 6-A.1, the Lagrangian polynomial may be written as,

$$L_j(x) = \frac{(x-x_0)(x-x_i)\cdots\cdots(x-x_{j-1})(x-x_{j+1})\cdots(x-x_n)}{(x_j-x_0)(x_j-x_1)\cdots\cdots(x_j-x_{j-1})(x_j-x_{j+1})\cdots(x_j-x_n)} \qquad \text{eqn(6-A.2)}$$

where eqn(6-A.2) defines $L_j(x)$ to be unity at $x = x_j$ and zero at $x_{i \neq j}$

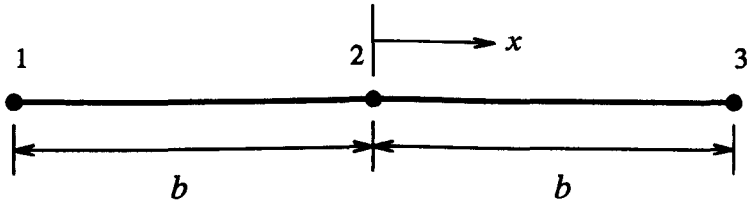

Figure 6-A.1 - Lagrangian Element.

Thus, considering the element side with the nodes (14), (8), and (5) (Element 2, Figure 6.1), the shape functions $N_{14}^{**}, N_8^{**}, N_5^{**}$ may be written as,

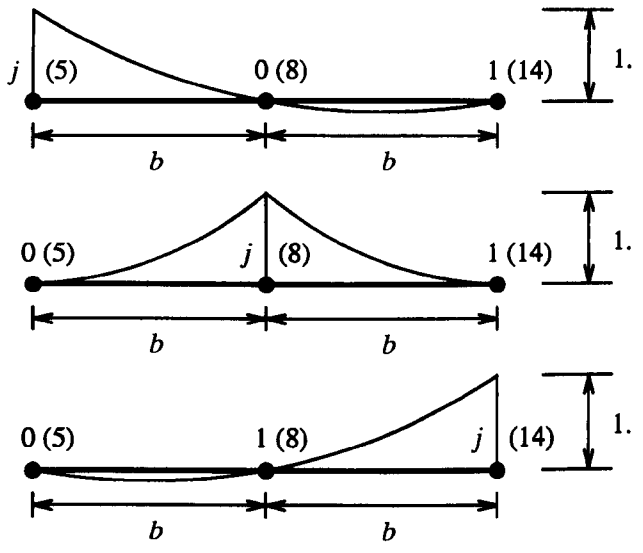

$$N_5^{**} = \frac{x\,(x-b)}{2\,b^2} \qquad \text{eqn(6-A.3(a))}$$

$$N_8^{**} = \frac{(x+b)\,(x-b)}{-b^2} \qquad \text{eqn(6-A.3(b))}$$

$$N_{14}^{**} = \frac{(x+b)\,x}{2\,b^2} \qquad \text{eqn(6-A.3(c))}$$

Figure 6-A.2 - Lagrangian Shape Functions.

Substituting eqn(6-A.3(a)) into eqn(6-A.1) and assuming an element thickness of t, gives for example, the equivalent nodal force in the global x direction for the node 5 (Figure 6.1), as,

$$F_{eq\,5} = \int_{-b}^{+b} \frac{x\,(x-b)}{2b^2}\, t\, dx = \frac{1}{3}\, b\, \sigma_x\, t \qquad \text{eqn(6-A.4)}$$

Similar expressions can be obtained for the remaining element nodes (8), (14), (22) and (35).

6.7. Appendix 6-B - Contribution of the Out-of-plane Stiffness Components of the Geometric Stiffness Matrix $[K_\sigma]$ to the Total Stiffness Matrix, $[K_t]$.

6.7.1. Out-of-plane Elastic Stiffness Components of a Flat Element.

In the case of a flat rectangular element orientated in the global xy plane, the out-of-plane components of the elastic stiffness matrix, $[K_E{}^{plate}]$, are zero. This feature is demonstrated below by calculating the direct out-of-plane stiffness component, $[K_E{}^e(3, 3)]$, corresponding to the W displacement at the element node 1.

The general element elastic stiffness matrix, $\left[\overline{K_E{}^e}\right]$, is given is given by the expression, (Section 5.7.1, Chapter 5),

$$\left[\overline{K_E{}^e}\right] = \int_{vol} [\bar{B}]^T [E] [\bar{B}] \, dV, \qquad \text{eqn(5.7.1.7)}$$

where $[\bar{B}] = [B_o] + [B_L]$, with $[B_o]$ and $[B_L]$ the small and large strain-displacement matrices, respectively, and $[E]$ is the matrix of elastic constants.

If it is assumed that the initial displacements of the element are zero, then the elastic stiffness matrix, $[K_E{}^e]$, can be written as,

$$[K_E{}^e] = \int_{vol} [B_o]^T [E] [B_o] \, dV. \qquad \text{eqn(6-B.1)}$$

where the matrix, $[B_o]$, is given as,

$$[B_o] =$$

$$\begin{bmatrix} \hat{X}^i{}_1 \frac{\partial N_1}{\partial X} & \hat{X}^j{}_1 \frac{\partial N_1}{\partial X} & \hat{X}^k{}_1 \frac{\partial N_1}{\partial X} & \rightarrow & \hat{X}^k{}_8 \frac{\partial N_8}{\partial X} \\ \hat{Y}^i{}_1 \frac{\partial N_1}{\partial Y} & \hat{Y}^j{}_1 \frac{\partial N_1}{\partial Y} & \hat{Y}^k{}_1 \frac{\partial N_1}{\partial Y} & \rightarrow & \hat{Y}^k{}_8 \frac{\partial N_8}{\partial Y} \\ \hat{X}^i{}_1 \frac{\partial N_1}{\partial Y} + \hat{Y}^i{}_1 \frac{\partial N_1}{\partial X} & \hat{X}^j{}_1 \frac{\partial N_1}{\partial Y} + \hat{Y}^j{}_1 \frac{\partial N_1}{\partial X} & \hat{X}^k{}_1 \frac{\partial N_1}{\partial Y} + \hat{Y}^k{}_1 \frac{\partial N_1}{\partial X} & \rightarrow & \hat{X}^k{}_8 \frac{\partial N_8}{\partial Y} + \hat{Y}^k{}_8 \frac{\partial N_8}{\partial X} \end{bmatrix},$$

eqn(5.7.2.8)

and (assuming plane stress), the matrix, $[E]$, is given as,

$$[E] = \frac{E}{1-\upsilon^2} \begin{bmatrix} 1 & \upsilon & 0 \\ \upsilon & 1 & 0 \\ 0 & 0 & \frac{1-\upsilon}{2} \end{bmatrix} \qquad \text{eqn(6-B.2)}$$

where, E is the modulus of elasticity, and υ is Poisson's ratio.

The direct out-of-plane stiffness component, $[K_E{}^e(3,3)]$, is obtained by calculating the third column of the matrix product, $[E][B_o]$, initially (denoted as $[E.B_o(r_1,3)]$, where $r_1 = 1 \rightarrow 3$, given as,

$$[E.B_o(r_1,3)] = \frac{E}{1-\upsilon^2}\begin{bmatrix} \hat{X}^k{}_1 \dfrac{\partial N_1}{\partial X} + \upsilon\, \hat{Y}^k{}_1 \dfrac{\partial N_1}{\partial Y} \\ \upsilon\, \hat{X}^k{}_1 \dfrac{\partial N_1}{\partial X} + \hat{Y}^k{}_1 \dfrac{\partial N_1}{\partial Y} \\ \left(\dfrac{1-\upsilon}{2}\right)\left(\hat{X}^k{}_1 \dfrac{\partial N_1}{\partial Y} + \hat{Y}^k{}_1 \dfrac{\partial N_1}{\partial X}\right) \end{bmatrix} \qquad \text{eqn(6-B.3)}$$

By multiplying the third column of the matrix, $[B_o]$, with the column matrix, $[E.B_o(r_1,3)]$, the stiffness component, $[K_E{}^e(3,3)]$, is obtained as,

$$[K_E{}^e(3,3)] = \frac{E}{1-\upsilon^2}\int_{vol}\left[\left(\hat{X}^k{}_1 \frac{\partial N_1}{\partial X}\right)^2 + 2\upsilon\, \hat{X}^k{}_1\, \hat{Y}^k{}_1 \frac{\partial N_1}{\partial X}\frac{\partial N_1}{\partial Y} + \left(\hat{Y}^k{}_1 \frac{\partial N_1}{\partial Y}\right)^2 + \left(\frac{1-\upsilon}{2}\right)\left(\left(\hat{X}^k{}_1 \frac{\partial N_1}{\partial Y}\right)^2 + 2\,\hat{X}^k{}_1\, \hat{Y}^k{}_1 \frac{\partial N_1}{\partial X}\frac{\partial N_1}{\partial Y} + \left(\hat{Y}^k{}_1 \frac{\partial N_1}{\partial X}\right)^2\right)\right] dV .$$

eqn(6-B.4)

In the situation that the element is flat and orientated in the global xy plane it follows that the direction cosines in the global z direction, $\hat{X}^k{}_1$, and $\hat{Y}^k{}_1$, are zero. Substitution of these values of $\hat{X}^k{}_1$ and $\hat{Y}^k{}_1$ into eqn(6-B.4), can be seen to lead to a zero coefficient for the stiffness component $[K_E{}^e(3,3)]$.

6.7.2. Derivation of the Out-of-plane Terms of the Element Geometric Stiffness Matrix $[K_\sigma{}^e]$.

The derivation of the out-of-plane stiffness term $[K_\sigma{}^e(3,3)]$ of the element geometric stiffness matrix $[K_\sigma{}^e]$ is presented in this section [31]. It is assumed that the element is of a rectangular, flat geometry and is located in the global xy plane [32]. The orientation of the element is such that the local co-ordinate directions coincide with the global co-ordinate directions.

31

The term $[K_\sigma{}^e(3,3)]$ is the direct out-of-plane stiffness component associated with the W displacement at the element node 1. The subsequent derivation can be followed to obtain similar expressions for the remaining out-of-plane stiffnesses. It can be demonstrated that the remaining out-of-plane stiffness terms along the leading diagonal of the geometric stiffness matrix $[K_\sigma{}^e]$ are non zero.

32

If the constraint that the element geometry is rectangular is removed, similar but more complicated expressions than those presented subsequently are obtained.

The unit vectors $\hat{X}_i$, $\hat{Y}_i$, and $\hat{Z}_i$, at each node i ($i = 1 \rightarrow 8$) of the element are thus obtained as,

$$\hat{X}_i = \{ 1\,\underline{i} + 0\,\underline{j} + 0\,\underline{k} \}, \qquad \text{eqn(6-B.5(a)}$$

$$\hat{Y}_i = \{ 0\,\underline{i} + 1\,\underline{j} + 0\,\underline{k} \}, \qquad \text{eqn(6-B.5(b)}$$

$$\hat{Z}_i = \{ 0\,\underline{i} + 0\,\underline{j} + 1\,\underline{k} \}. \qquad \text{eqn(6-B.5(c)}$$

The geometric stiffness matrix of an individual element, $[K_\sigma{}^e]$, is given by the expression (Section 5.7.4, Chapter 5),

$$[\,K_\sigma{}^e\,] = \int_{vol} [\,G\,]^T\,[\,M\,]\,[\,G\,]\;\mathrm{dV} \qquad \text{eqn(5.7.4.6)}$$

where the matrix $[\,G\,]$ is a function of the natural co-ordinates ξ, η and is written as,

$$[\,G\,] = \begin{bmatrix}
\hat{X}^i{}_1 \frac{\partial N_1}{\partial X}(\xi,\eta) & \hat{X}^j{}_1 \frac{\partial N_1}{\partial X}(\xi,\eta) & \hat{X}^k{}_1 \frac{\partial N_1}{\partial X}(\xi,\eta) & \rightarrow \hat{X}^k{}_8 \frac{\partial N_8}{\partial X}(\xi,\eta) \\
\hat{Y}^i{}_1 \frac{\partial N_1}{\partial X}(\xi,\eta) & \hat{Y}^j{}_1 \frac{\partial N_1}{\partial X}(\xi,\eta) & \hat{Y}^k{}_1 \frac{\partial N_1}{\partial X}(\xi,\eta) & \rightarrow \hat{Y}^k{}_8 \frac{\partial N_8}{\partial X}(\xi,\eta) \\
\hat{Z}^i{}_1 \frac{\partial N_1}{\partial X}(\xi,\eta) & \hat{Z}^j{}_1 \frac{\partial N_1}{\partial X}(\xi,\eta) & \hat{Z}^k{}_1 \frac{\partial N_1}{\partial X}(\xi,\eta) & \rightarrow \hat{Z}^k{}_8 \frac{\partial N_8}{\partial X}(\xi,\eta) \\
\hat{X}^i{}_1 \frac{\partial N_1}{\partial Y}(\xi,\eta) & \hat{X}^j{}_1 \frac{\partial N_1}{\partial Y}(\xi,\eta) & \hat{X}^k{}_1 \frac{\partial N_1}{\partial Y}(\xi,\eta) & \rightarrow \hat{X}^k{}_8 \frac{\partial N_8}{\partial Y}(\xi,\eta) \\
\hat{Y}^i{}_1 \frac{\partial N_1}{\partial Y}(\xi,\eta) & \hat{Y}^j{}_1 \frac{\partial N_1}{\partial Y}(\xi,\eta) & \hat{Y}^k{}_1 \frac{\partial N_1}{\partial Y}(\xi,\eta) & \rightarrow \hat{Y}^k{}_8 \frac{\partial N_8}{\partial Y}(\xi,\eta) \\
\hat{Z}^i{}_1 \frac{\partial N_1}{\partial Y}(\xi,\eta) & \hat{Z}^j{}_1 \frac{\partial N_1}{\partial Y}(\xi,\eta) & \hat{Z}^k{}_1 \frac{\partial N_1}{\partial Y}(\xi,\eta) & \rightarrow \hat{Z}^k{}_8 \frac{\partial N_8}{\partial Y}(\xi,\eta)
\end{bmatrix},$$

eqn(5.7.3.7)

and the matrix $[\,M\,]$ is given as,

$$[\,M\,] = \begin{bmatrix} \sigma_x\,[\,I_3\,] & \tau_{xy}\,[\,I_3\,] \\ \tau_{xy}\,[\,I_3\,] & \sigma_y\,[\,I_3\,] \end{bmatrix},$$

$$= \begin{bmatrix}
\sigma_x & 0 & 0 & \tau_{xy} & 0 & 0 \\
0 & \sigma_x & 0 & 0 & \tau_{xy} & 0 \\
0 & 0 & \sigma_x & 0 & 0 & \tau_{xy} \\
\tau_{xy} & 0 & 0 & \sigma_y & 0 & 0 \\
0 & \tau_{xy} & 0 & 0 & \sigma_y & 0 \\
0 & 0 & \tau_{xy} & 0 & 0 & \sigma_y
\end{bmatrix}. \qquad \text{eqn(5.7.4.7)}$$

The stiffness component $[K_\sigma{}^e(3,3)]$ is obtained by calculating the third column of the matrix product $[\,M\,]\,[\,G\,]$ (denoted as $[M.G(r_2,3)]$, where $r_2 = 1 \rightarrow 6$), initially. Substituting eqn(6-B.5 (a)-(c)) into eqn(5.7.3.7), and performing the matrix product $[\,M\,]\,[\,G\,]$, yields the expression for

the column matrix, $[M.G(r_2,3)]$, as,

$$[M.G(r_2,3)] = \begin{bmatrix} 0 \\ 0 \\ \sigma_x \frac{\partial N_1}{\partial X}(\xi,\eta) + \tau_{xy} \frac{\partial N_1}{\partial Y}(\xi,\eta) \\ 0 \\ 0 \\ \tau_{xy} \frac{\partial N_1}{\partial X}(\xi,\eta) + \sigma_y \frac{\partial N_1}{\partial Y}(\xi,\eta) \end{bmatrix} \qquad \text{eqn(6-B.6)}$$

By multiplying the third column of the matrix [G] with the column matrix $[M.G(r_2,3)]$, the stiffness term $[K_\sigma{}^e(3,3)]$ is obtained as,

$$[K_\sigma{}^e(3,3)] = \int_{vol} \left[\sigma_x \left[\frac{\partial N_1}{\partial X}(\xi,\eta) \right]^2 + 2\,\tau_{xy} \frac{\partial N_1}{\partial X}(\xi,\eta) \frac{\partial N_1}{\partial Y}(\xi,\eta) + \sigma_y \left[\frac{\partial N_1}{\partial Y}(\xi,\eta) \right]^2 \right] dV\,. \qquad \text{eqn(6-B.7)}$$

The evaluations of the partial derivatives comprising eqn(6-B.3) are presented below.

Assuming that the side nodes are at the mid-points of the element sides, the shape function $N_1(\xi,\eta)$, can be written as (Table 5.1, Chapter 5),

$$N_1 = \frac{1}{4}(1-\xi)(1-\eta)(-\xi-\eta-1)$$

$$= \frac{1}{4}(\xi^2+\eta^2-\xi^2\eta-\xi\eta^2+\xi\eta-1) \qquad \text{eqn(6-B.8)}$$

The change of variable given in eqn(5.5.7(a)) (Chapter 5) is used to express the partial derivatives $\frac{\partial N_1}{\partial X}$ and $\frac{\partial N_1}{\partial Y}$ in terms of the natural co-ordinates $\{\xi,\eta\}$, as,

$$\frac{\partial N_1}{\partial X} = \vec{\eta}\,.\,\hat{Y_1} \frac{\partial N_1}{\partial \eta} - \vec{\xi}\,.\,\hat{Y_1} \frac{\partial N_1}{\partial \xi}\,, \qquad \text{eqn(6-B.9(a))}$$

and,

$$\frac{\partial N_1}{\partial Y} = -\vec{\eta}\,.\,\hat{X_1} \frac{\partial N_1}{\partial \eta} + \vec{\xi}\,.\,\hat{X_1} \frac{\partial N_1}{\partial \xi}\,, \qquad \text{eqn(6-B.9(b))}$$

where (from eqn(6-B.8)),

$$\frac{\partial N_1}{\partial \xi} = \frac{1}{4}(2\xi - 2\xi\eta - \eta^2 + \eta)\,, \qquad \text{eqn(6-B.10(a))}$$

$$\frac{\partial N_1}{\partial \xi} = \frac{1}{4}(2\eta - \xi^2 - 2\xi\eta + \xi). \qquad \text{eqn(6-B.10(b))}$$

In the situation that the global and local co-ordinate directions are aligned and the element is rectangular, it can be shown that the vector products $\vec{\xi} \,.\, \hat{Y_i}$ and $\vec{\eta} \,.\, \hat{X_i}$ are zero, and that the vector products $\vec{\eta} \,.\, \hat{Y_i}$ and $\vec{\xi} \,.\, \hat{X_i}$ are non-zero (where i is the node number, with $i = 1 \rightarrow 8$). [33]

Using these results, and substituting eqn(6-B.9 (a)&(b)) into eqn(6-B.7), the (non-zero) geometric stiffness term, $[K_\sigma{}^e(3,3)]$, is obtained as [34],

$$[K_\sigma{}^e(3,3)] = \int_{vol} \left[\sigma_x \left(\vec{\eta} \,.\, \hat{Y_1} \frac{\partial N_1}{\partial \eta} \right)^2 + 2\,\tau_{xy}\, \vec{\eta} \,.\, \hat{Y_1} \frac{\partial N_1}{\partial \eta} \vec{\xi} \,.\, \hat{X_1} \frac{\partial N_1}{\partial \xi} + \sigma_y \left(\vec{\xi} \,.\, \hat{X_1} \frac{\partial N_1}{\partial \eta} \right)^2 \right] dV .$$

eqn(6-B.11)

6.7.3. Suppression of the Singular Form of the Matrix $[K_E{}^{plate}]$.

As demonstrated in Section 6.7.1, in the case of a flat plate (or membrane), in which the stiffness is derived from elasticity only, the out-of-plane components of the elastic stiffness matrix of the plate $[K_E{}^{plate}]$ are zero. Consequently, the determinant of the matrix, $[K_E{}^{plate}]$, is also zero. This indicates a singular form of the matrix, $[K_E{}^{plate}]$, and infers a condition number of infinity.

In the preceding section (Section 6.7.2), the introduction of prestress is shown to invoke the contribution of the out-of-plane stiffness components of the geometric stiffness matrix $[K_\sigma{}^{plate}]$ to the total stiffness matrix $[K_t{}^{plate}]$ (where $[K_t{}^{plate}] = [K_E{}^{plate}] + [K_\sigma{}^{plate}]$). The inclusion of these (non-zero) terms has the effect of reducing the condition number of the total stiffness matrix, $[K_t{}^{plate}]$, from infinity. This effect arises as the tendency of the out-of-plane deformation modes to act as mechanisms is negated by the appropriate (out-of-plane) terms of the matrix $[K_\sigma{}^{plate}]$. The inverse of the matrix $[K_t{}^{plate}]$ can be computed therefore.

In the case of the discretisation illustrated in Figure 6.1, the condition number of the matrix $[K_t{}^{plate}]$ is reduced to $2.374 \times 10^{+8}$ when a prestress equivalent to $1. \times 10^{-4}$ % of the elastic modulus of the plate is assumed in all elements of the discretisation. Consequently, the solution to the

---

33

In the case that the global and the local co-ordinate directions are the same, and the element geometry is rectangular, the directions of the element natural co-ordinates, $\{\xi, \eta\}$, coincide with the directions of the local co-ordinates, $\{X, Y\}$. Consequently, the vector $\vec{\xi}$ is orthogonal to the vector $\hat{Y_i}$, and the vector $\vec{\eta}$ is orthogonal to the vector $\hat{X_i}$. These properties give rise to the zero vector products $\vec{\xi} \,.\, \hat{Y_i}$ and $\vec{\eta} \,.\, \hat{X_i}$.

34

Eqn(6-B.11) is evaluated using Gaussian Integration (Section 5.8, Chapter 5).

element nodal displacements are assumed accurate to the first six digits only [6.12] (based on the LU decomposition algorithm [6.1]).

The condition number of the matrix $[K_t{}^{plate}]$ may be reduced further by the adoption of a higher element prestress. However, additional errors are then introduced into the elastic solution by the terms of the geometric stiffness matrix $[K_t{}^{plate}]$.

6.8. Appendix 6-C - Calculation of the Eigenvalues and Eigenvectors of a Matrix [6.9] [35] .

The eigenvalue problem is to determine the non-trivial solutions to the equation,

$$A\,x = \lambda x\,, \qquad \text{eqn(6-C.1)}$$

where A is an n-by-n matrix, x is a column vector of length n, and λ is a scalar.

The n values of λ that satisfy eqn(6-C.1) are the eigenvalues, and the corresponding values of x are the "*right eigenvectors*". In *Matlab* the eigenvectors are normalised so that the largest element of each eigenvector is unity.

The generalised eigenvalue problem is to determine the non-trivial solutions to the equation,

$$B^{-1}A\,x = \lambda x\,, \qquad \text{eqn(6-C.2)}$$

with A replaced by $B^{-1}A$.

But since the matrix, B, could be singular, an alternative algorithm, called the "QZ" method, is used. The algorithm used in *Matlab* is described below.

In the case of real matrices, the real general matrix is converted to a Hessenberg form using orthogonal similarity transformations [36] . The eigenvalues and eigenvectors of a real Hessenberg matrix are subsequently found using the "QR" [6.11] algorithm.

The "QR" algorithm performs an orthogonal-triangular decomposition of square or rectangular matrices. It expresses the matrix as the product of a real orthonormal matrix and an upper triangular matrix. An iterative procedure is adopted to find the eigenvalues. If an eigenvalue is not found after $30n$ iterations then the algorithm gives a warning of no convergence.

35

Acknowledgement - some sections of Appendix 6-C have been copied directly from reference [6.9].

36

A Hessenberg matrix is a matrix in which all terms are zero below the first sub-diagonal.

6.9. Appendix 6-D - Out-of-plane Stiffness Components of the General Elastic Stiffness Matrix, $[\overline{K_E{}^e}]$.

The derivation of the out-of-plane stiffness term $[K_{(B_L)}{}^e(3,3)]$ of the element stiffness matrix $[K_{(B_L)}{}^e]$ is presented in this section [37] . The element is assumed to be of a rectangular, flat geometry and to be located in the global xy plane. The orientation of the element is such that the local co-ordinate directions coincide with the global co-ordinate directions.

The terms of the large displacement elastic stiffness matrix, $[K_{(B_L)}{}^e]$, can be obtained by assuming that the strain displacement matrix, $[B_o]$, is a null matrix (eqn(5.7.1.6)). Therefore, from eqn(5.7.1.7), the expression for the matrix, $[K_{(B_L)}{}^e]$, is obtained as,

$$\left[K_{(B_L)}{}^e \right] = \int_{vol} [B_L]^T [E] [B_L] \, dV, \qquad \text{eqn(6-D.1)}$$

where the matrix $[B_L]$ represents the large strain displacement equations (eqn(5.7.3.1)), and, $[E]$, is the matrix of elastic constants, written as,

$$[E] = \frac{E}{1-\upsilon^2} \begin{bmatrix} 1 & \upsilon & 0 \\ \upsilon & 1 & 0 \\ 0 & 0 & \frac{1-\upsilon}{2} \end{bmatrix}, \qquad \text{eqn(6-B.2)}$$

with, E is the modulus of elasticity, and υ is Poisson's ratio.

The matrix $[B_L]$ is expressed as the product of two matrices, as in,

$$[B_L] = [A][G], \qquad \text{eqn(6-D.2)}$$

where,

$$[A] = \begin{bmatrix} \frac{\partial U}{\partial X} & \frac{\partial V}{\partial X} & \frac{\partial W}{\partial X} & 0 & 0 & 0 \\ 0 & 0 & 0 & \frac{\partial U}{\partial Y} & \frac{\partial V}{\partial Y} & \frac{\partial W}{\partial Y} \\ \frac{\partial U}{\partial Y} & \frac{\partial V}{\partial Y} & \frac{\partial W}{\partial Y} & \frac{\partial U}{\partial X} & \frac{\partial V}{\partial X} & \frac{\partial W}{\partial X} \end{bmatrix}, \qquad \text{eqn(6-D.3)}$$

and,

37

The large displacement terms comprise the out-of-plane elastic stiffness of the matrix, $[\overline{K_E{}^e}]$. These terms are represented in the matrix $[B_L]$ (eqn(5.7.3.9), Chapter 5). Consequently, the subscript (B_L) is intended to indicate that the large displacement components of the general elastic stiffness matrix, $[K_E{}^e]$, are being considered in this section.

$$[G] = \begin{bmatrix} \hat{X}^i{}_1 \frac{\partial N_1}{\partial X}(\xi,\eta) & \hat{X}^j{}_1 \frac{\partial N_1}{\partial X}(\xi,\eta) & \hat{X}^k{}_1 \frac{\partial N_1}{\partial X}(\xi,\eta) & \rightarrow \hat{X}^k{}_8 \frac{\partial N_8}{\partial X}(\xi,\eta) \\ \hat{Y}^i{}_1 \frac{\partial N_1}{\partial X}(\xi,\eta) & \hat{Y}^j{}_1 \frac{\partial N_1}{\partial X}(\xi,\eta) & \hat{Y}^k{}_1 \frac{\partial N_1}{\partial X}(\xi,\eta) & \rightarrow \hat{Y}^k{}_8 \frac{\partial N_8}{\partial X}(\xi,\eta) \\ \hat{Z}^i{}_1 \frac{\partial N_1}{\partial X}(\xi,\eta) & \hat{Z}^j{}_1 \frac{\partial N_1}{\partial X}(\xi,\eta) & \hat{Z}^k{}_1 \frac{\partial N_1}{\partial X}(\xi,\eta) & \rightarrow \hat{Z}^k{}_8 \frac{\partial N_8}{\partial X}(\xi,\eta) \\ \hat{X}^i{}_1 \frac{\partial N_1}{\partial Y}(\xi,\eta) & \hat{X}^j{}_1 \frac{\partial N_1}{\partial Y}(\xi,\eta) & \hat{X}^k{}_1 \frac{\partial N_1}{\partial Y}(\xi,\eta) & \rightarrow \hat{X}^k{}_8 \frac{\partial N_8}{\partial Y}(\xi,\eta) \\ \hat{Y}^i{}_1 \frac{\partial N_1}{\partial Y}(\xi,\eta) & \hat{Y}^j{}_1 \frac{\partial N_1}{\partial Y}(\xi,\eta) & \hat{Y}^k{}_1 \frac{\partial N_1}{\partial Y}(\xi,\eta) & \rightarrow \hat{Y}^k{}_8 \frac{\partial N_8}{\partial Y}(\xi,\eta) \\ \hat{Z}^i{}_1 \frac{\partial N_1}{\partial Y}(\xi,\eta) & \hat{Z}^j{}_1 \frac{\partial N_1}{\partial Y}(\xi,\eta) & \hat{Z}^k{}_1 \frac{\partial N_1}{\partial Y}(\xi,\eta) & \rightarrow \hat{Z}^k{}_8 \frac{\partial N_8}{\partial Y}(\xi,\eta) \end{bmatrix},$$

eqn(5.7.3.7)

The out-of-plane stiffness term $[K_{(B_L)^e}(3,3)]$, is obtained by calculating the third column of the matrix $[B_L] = [A][G]$, initially (denoted as $[B_L(r_1,3)]$, where $r_1 = 1 \rightarrow 3$), given as,

$$[B_L(r_1,3)] = \begin{bmatrix} \left\{ \frac{\partial U}{\partial X} \hat{X}^k{}_1 \frac{\partial N_1}{\partial X} + \frac{\partial V}{\partial X} \hat{Y}^k{}_1 \frac{\partial N_1}{\partial X} + \frac{\partial W}{\partial X} \hat{Z}^k{}_1 \frac{\partial N_1}{\partial X} \right\} \\ \left\{ \frac{\partial U}{\partial Y} \hat{X}^k{}_1 \frac{\partial N_1}{\partial Y} + \frac{\partial V}{\partial Y} \hat{Y}^k{}_1 \frac{\partial N_1}{\partial Y} + \frac{\partial W}{\partial Y} \hat{Z}^k{}_1 \frac{\partial N_1}{\partial Y} \right\} \\ \left\{ \frac{\partial U}{\partial Y} \hat{X}^k{}_1 \frac{\partial N_1}{\partial X} + \frac{\partial V}{\partial Y} \hat{Y}^k{}_1 \frac{\partial N_1}{\partial X} + \frac{\partial W}{\partial Y} \hat{Z}^k{}_1 \frac{\partial N_1}{\partial X} + \right. \\ \left. \frac{\partial U}{\partial X} \hat{X}^k{}_1 \frac{\partial N_1}{\partial Y} + \frac{\partial V}{\partial X} \hat{Y}^k{}_1 \frac{\partial N_1}{\partial Y} + \frac{\partial W}{\partial X} \hat{Z}^k{}_1 \frac{\partial N_1}{\partial Y} \right\} \end{bmatrix}.$$

eqn(6-D.4)

In the situation that the element is flat and orientated in the global xy plane it follows that the direction cosines in the global z direction, $\hat{X}^k{}_1$, and $\hat{Y}^k{}_1$, are zero, while $\hat{Z}^k{}_1$ has a value of unity. Substitution of these values of $\hat{X}^k{}_1$, $\hat{Y}^k{}_1$, and $\hat{Z}^k{}_1$ into eqn(6-D.4) yields the simplified expression,

$$[B_L(r_1,3)] = \begin{bmatrix} \frac{\partial W}{\partial X} \frac{\partial N_1}{\partial X} \\ \frac{\partial W}{\partial Y} \frac{\partial N_1}{\partial Y} \\ \frac{\partial W}{\partial Y} \frac{\partial N_1}{\partial X} + \frac{\partial W}{\partial X} \frac{\partial N_1}{\partial Y} \end{bmatrix}.$$

eqn(6-D.5)

The calculation of the out-of-plane stiffness term $[K_{(B_L)^e}(3,3)]$ is continued by establishing the third column of the matrix product, $[E][B_L]$, (denoted as $[EB_L(r_1,3)]$), given as,

$$[EB_L(r_1,3)] = \frac{E}{1-\upsilon^2}\begin{bmatrix} \left[\frac{\partial W}{\partial X}\frac{\partial N_1}{\partial X}\right] + \upsilon\left[\frac{\partial W}{\partial Y}\frac{\partial N_1}{\partial Y}\right] \\ \upsilon\left[\frac{\partial W}{\partial X}\frac{\partial N_1}{\partial X}\right] + \left[\frac{\partial W}{\partial Y}\frac{\partial N_1}{\partial Y}\right] \\ \frac{(1-\upsilon)}{2}\left[\frac{\partial W}{\partial Y}\frac{\partial N_1}{\partial X} + \frac{\partial W}{\partial X}\frac{\partial N_1}{\partial Y}\right] \end{bmatrix} \qquad \text{eqn(6-D.6)}$$

By multiplying the third column of the matrix, $[B_L]$, with the column matrix, $[EB_L(r_1,3)]$, the stiffness term, $[K_{(B_L)^e}(3,3)]$, is obtained as,

$$[K_{(B_L)^e}(3,3)] = \frac{E}{1-\upsilon^2}\int_{vol}\left[\left[\frac{\partial W}{\partial X}\frac{\partial N_1}{\partial X}\right]^2 + 2\upsilon\left[\frac{\partial W}{\partial X}\frac{\partial N_1}{\partial X}\right]\left[\frac{\partial W}{\partial Y}\frac{\partial N_1}{\partial Y}\right] + \left[\frac{\partial W}{\partial Y}\frac{\partial N_1}{\partial Y}\right]^2 + \frac{(1-\upsilon)}{2}\left[\frac{\partial W}{\partial Y}\frac{\partial N_1}{\partial X} + \frac{\partial W}{\partial X}\frac{\partial N_1}{\partial Y}\right]^2\right] dV \qquad \text{eqn(6-D.7)}$$

From equations of the form of eqn(5.7.2.7) (Section 5.7.2, Chapter 5), the local strain, $\frac{\partial W}{\partial X}$, can be written as,

$$\frac{\partial W}{\partial X} = \sum_{i=1}^{i=8} \hat{Z}^i{}_i \frac{\partial N_i(\xi,\eta)}{\partial X} u_i + \sum_{i=1}^{i=8} \hat{Z}^j{}_i \frac{\partial N_i(\xi,\eta)}{\partial X} v_i + \sum_{i=1}^{i=8} \hat{Z}^k{}_i \frac{\partial N_i(\xi,\eta)}{\partial X} w_i \,. \qquad \text{eqn(6-D.8)}$$

with the vectors, $\hat{Z}_i$ (for $i = 1 \rightarrow 8$), given as,

$$\hat{Z}_i = \left\{ \hat{Z}^i{}_i \underline{i} + \hat{Z}^j{}_i \underline{j} + \hat{Z}^k{}_i \underline{k} \right\} = \left\{ 0\underline{i} + 0\underline{j} + 1\underline{k} \right\} \qquad \text{eqn(6-D.9)}$$

Substituting the coefficients of eqn(6-D.9) into eqn(6-D.8) leads to expression for the local strain, $\frac{\partial W}{\partial X}$, as

$$\frac{\partial W}{\partial X} = \sum_{i=1}^{i=8} \frac{\partial N_i(\xi,\eta)}{\partial X} w_i \,, \qquad \text{eqn(6-D.10)}$$

with a similar expression for the local strain, $\frac{\partial W}{\partial Y}$, as,

$$\frac{\partial W}{\partial Y} = \sum_{i=1}^{i=8} \frac{\partial N_i(\xi, \eta)}{\partial Y} w_i \,, \qquad \text{eqn(6-D.11)}$$

Substitution of eqn(6-D.10) and eqn(6-D.11) into eqn(6-D.7) yields the out-of-plane stiffness term, $[K_{(B_L)}{}^e(3, 3)]$, as a function of the global displacement, w.

6.10. Appendix 6-E - Effectiveness of the Suppression of the Fictitious Terms in the General Geometric Stiffness Matrix, $[K_\sigma{}^e]$.

Assuming the surface configuration defined at equilibrium, two Eigenvalue Tests have been performed on the stress stiffness matrix $[K_\sigma{}^e]$ of the element **9** (Figure 6.10). The element matrix $[K_\sigma{}^e]$ has been formulated with ($[K_\sigma{}^e]_{incl.}$) and without ($[K_\sigma{}^e]_{excl.}$) the inclusion of the fictitious stiffness terms associated with the rigid body rotation of the element. The first eight eigenvalues of the stiffness matrices, $[K_\sigma{}^e]_{incl.}$ and $[K_\sigma{}^e]_{excl.}$, (listed in ascending order) are presented in Table 6-E.1.

In the case of the element formulation in which the fictitious stiffness terms are not removed, it is shown that the eigenvalue analysis returns three zero eigenvalues only (corresponding to the translational rigid body modes). The explicit removal of the fictitious stiffness terms from the matrix, $[K_\sigma{}^e]$, yields the eigenvalues 0.01, 0.03, and 0.60, as approximations to zero (Table 6-E.1). The proximities of the eigenvalues 4, and 5, to zero, suggest that two of the three rigid body rotation modes are represented adequately. By displaying the corresponding eigenvectors it and can be shown that these modes represent the out-of-plane type.

Conversely, the magnitude of the sixth eigenvalue infers that the in-plane rigid body rotation mode is not represented adequately. In the derivation of the expression for the rigid body rotation angle, $\theta_r{}^{ip}$, it is assumed that the element strains are uniform and equal in the local X and Y directions (Section 5.9, Chapter 5). A violation of this assumption in the case of the element **9** (Figure 6.10), arising from the irregular geometry of the element, can be attributed to the high value for the eigenvalue 6.

The out-of-plane rigid body rotation modes dominate the terms in the displacement vectors, $\{\delta\}_i$, of the elements comprising the surface illustrated in Figure 6.10. Consequently, it is recommended that the rigid body rotation modes which are most likely to occur during the form-finding procedure, are represented adequately when the associated fictitious stiffness terms of the element matrices, $[K_\sigma{}^e]_i$, are removed explicitly in accordance with the theory presented in Section 5.9, Chapter 5.

Eigenvalue	1	2	3	4	5	6	7	8
$[K_\sigma{}^e]_{incl.}$	0.000	0.000	0.000	1.220	1.220	1.220	5.250	5.250
$[K_\sigma{}^e]_{excl.}$	0.000	0.000	0.000	0.010	0.030	0.600	1.220	3.230

Table 6-E.1 - First Eight Eigenvalues for the Element 9 at Equilibrium - Example 6.3

6.11. References.

[6.1] Zienkiewicz, O.C.

The Finite Element Method.

Third Edition, McGraw-Hill Book Company, 1977.

[6.2] Irons, B.M., Razzaque, A.

"Experience with the Patch Test for Convergence of the Finite Element Method."

The Mathematical Foundations of the Finite Element Method with Applications to Partial Differential Equations. Ed. A.K. Aziz, Academic Press, 1972, pages 557-587.

[6.3] Zienkiewicz, O.C.

The Finite Element Method.

Fourth Edition, McGraw-Hill Book Company, 1989.

[6.4] Irons, B.M.

"Testing and Assessing Finite Elements by an Eigenvalue Technique."

Proceedings of Conference on Recent Advances in Stress Analysis. J.B.C.S.A., Royal Aeronautical Society, London, 1968, pages 6-22.

[6.5] Cook, R.D., Malkus, D.S., Plesha, M.E.,

Concepts and Applications of Finite Element Analysis.

John Wiley and Sons, 1989, pages 166-170 & 563-565.

[6.6] Coates, R.C., Coutie, M.G., Kong, F.K.

Structural Analysis.

Van Nostrand Reinhold (UK) Co. Ltd., Third Edition, 1988, pages 428-457.

[6.7] Megson, T.H.G.

Strength of Materials for Civil Engineers.

Thomas Nelson and Sons Ltd., 1980, pages 42-43 & 68-70.

[6.8] Celia, M.A., Gray, W.G.

"An Improved Isoparametric Transformation for Finite Element Analysis."

Int. Journal Numerical Methods in Engineering. Volume 20, 1984, pages 1443-1459.

[6.9] Moler, C., Little, j., Bangert, S.

Pro-matlab for Sun Workstations, User's Guide.

The MathWorks, Inc., 1989, pages 3.35-3.37.

[6.10] Lewis, W.J., Gosling, P.D.

"Computer Modelling of Stable Minimal Surfaces."

Research Report CE32, University of Warwick, November 1990.

[6.11] Froeberg, C.-E.

Numerical Mathematics.

The Benjamin/Cummings Publishing Company, Inc., 1985, pages 22-24 & 203-206.

[6.12] Gerald, C.F.

Applied Numerical Analysis.

Addison-Wesley Publishing Company., Second Edition, 1978, pages 110-113.

Chapter 7

Conclusions and Suggestions for Further Work

7.1. Conclusions.

The work presented in this thesis relates to the form-finding of stable minimal surfaces. In particular, it is focused on the aspect of the formulation of elements of finite size used to discretise a continuum, modelling a state of plane stress. From the studies presented so far, the conclusions presented below can be drawn.

Linear Elements.

i) In order to represent the uniform stress field of the discretised continuous membrane, the linear elements are arranged in the form of an orthogonal mesh, with the element natural co-ordinates aligned with the directions of either of the principal direct stresses, and subjected to uniform and constant pretensions. Under these conditions, the linear elements tend to follow geodesic lines over the surface. This can give rise to distortion of the final form.

ii) A discretisation of linear elements can provide an accurate solution to a minimal surface when the principal curvatures are low. A large number of linear elements is required to model the surface accurately. With careful modelling, an accurate solution to a surface exhibiting high curvatures can be obtained, provided the final form is known.

Triangular Elements.

iii) The continuum based triangular element may be represented by a triplet of pseudo cables possessing appropriate elastic and geometric stiffness coefficients. The invariant stress field of the element is represented by natural forces in the pseudo cables. These forces can be tensile or compressive, dependent on the geometry and the orientation of the triangular element in the global co-ordinate system.

iv) The element is characterised by constant strain. This can lead to a buckling type of phenomenon, and may result in the divergence of the solution algorithm. If the constraint of uniform surface stress in the numerical model is released (after a specified number of kinetic energy peaks in the Dynamic Relaxation algorithm), the onset of the buckling type phenomenon can be prevented. A critical number of admissible kinetic energy peaks exists, beyond which the accuracy of the solution is reduced. An expression has been proposed to

relate the geometrical accuracy of the equilibriated surface to the condition of uniform stress and the maximum overall dimension of the triangular elements comprising the discretised surface.

v) By violating the assumption of small strains inherent in the triangular element formulation, errors can be induced in the numerical solution. These errors occur predominantly in the element nodal displacements, and can lead to the inversion of certain elements, and to the divergence of the solution algorithm. The effects of the violation of this assumption have been shown to be negated by introducing elasticity into the numerical model.

vi) An accurate solution to a minimal surface can be obtained from a relatively coarse discretisation of triangular elements. The degree to which the condition of uniform surface stress is satisfied, can be used to assess the proximity of the equilibriated surface to the local minimal surface. By modifying the existing boundaries and monitoring the element stress deviations, the numerical model can be amended to obtain the minimal surface which is local to the original topology.

24 Degrees-of-freedom Quadrilateral Elements.

vii) The formulation of a 24 degrees-of-freedom membrane finite element has been presented. The element strains are calculated by performing the differentiation of the global displacements with respect to the local variable, prior to transformation into the local co-ordinate directions.

viii) If the system is geometrically non-linear, such that an iterative technique is used to establish the condition of equilibrium, then the fictitious terms in the element geometric stiffness matrix fail to corrupt the numerical solution. This applies to both the Dynamic Relaxation and matrix inversion based solution algorithms. Conversely, if the system is geometrically linear, the matrix based solution algorithms is forced into error by these terms.

ix) The proposed element formulation is valid for the analysis of systems subjected to large displacements, in which the large displacements cause a topological distortion. The strain based error norm is insensitive to large geometric distortions.

x) In the case of a flat, rectangular element without initial stress, spurious deformation modes may occur, irrespective of the order of Gauss quadrature used to evaluate the element integrands. A suppression of the spurious deformation modes can be achieved by distorting the element, or by introducing fictitious (initial) displacements into the element. The adoption of the technique of reduced integration can also cause the element elastic stiffness matrix to display zero energy modes.

xi) The 24 degrees-of-freedom element is highly sensitive to large changes in geometry. Therefore, numerical instability can arise, particularly during the initial stages of the form-finding procedure. Adopting only the diagonal terms of the element stiffness matrices reduces the sensitivity of the formulation. The technique of reduced integration has a similar affect.

xii) When the element shape functions simulate the curvatures of the surface adequately, a small number of elements can produce an accurate solution to that minimal surface. If the assumption that the element shape functions vary quadratically with the element natural co-ordinates is violated, then errors are introduced into the terms of the element stiffness matrices and into the vectors of equivalent nodal forces.

xiii) The combined effects of topological and geometric distortions of the element can amplify the errors generated through the violation of the assumption of small displacements. In the case of surfaces exhibiting rapidly changing curvatures, the assumption that the element shape functions are derived from the current element only (ignoring the elements adjacent to it), can lead to a loss of smoothness from the numerical solution.

xiv) The representation of the non-linear components of the strain displacement relations in the element formulation, gives rise to a deviation from the condition of uniform stress at equilibrium.

xv) The 24 degrees-of-freedom finite element formulation is too sensitive to be applied effectively to the form-finding of minimal surfaces. The derivation of the element equations to model accurately the effects of large displacements and large strains has been completed successfully. Provided the problems stated in (xi), (xii), and (xiii), can be overcome, an accurate solution to a minimal surface can be obtained.

7.2. Suggestions for Further Work.

It is recommended that the adaptation of the 24 degrees-of-freedom finite element formulation should be investigated further. In particular, the sensitivity of the proposed formulation to large changes in in geometry (in terms of geometric and topological distortions) should be examined in the context of the Dynamic Relaxation algorithm.

For example, the number of element degrees of freedom could be decreased (and therefore the sensitivity reduced) by limiting the movements of the element nodes to those normal to the surface. This proposed simplification is valid in the case of the analysis of an inelastic membrane, subjected to a state of uniform stress, as the condition of equilibrium is satisfied in the plane of the surface automatically. The vector normal to the surface at the point of interest could be constructed at the beginning of each time increment, and used to define the direction along which the element node could move. The magnitude of the nodal displacement would be controlled by the out-of-balance force vector and the stiffness as before.

An additional control over the in-plane movements of the element nodes could be achieved by making the boundaries of the quadrilateral elements follow geodesic lines. Geodesic lines may be defined by a uniformly tensioned cable placed between boundary points. The cable, discretised by a sufficient number of linear elements, would be equilibriated by displacements in the plane of the surface, such that the surface form remained undistorted. Furthermore, the fabric cutting patterns of the membrane could be generated automatically when following this procedure. The position of the element nodes along the length of the geodesic line, may be controlled by maintaining an equal spacing of the nodes. This type of restraint may prove particularly effective

in increasing the stability and convergence of the solution algorithm when applied to the element side nodes (which are prone to unnecessarily large displacements in the plane of the surface.

Furthermore, it is recommended that the triangular element should be resumed, and reformulated using the finite element techniques, taking into account the second order strain displacement equations. This proposed element formulation, it is anticipated, would negate the effects of the violation of the assumption of small strains, present in the triangular element appraised in this thesis, and would be less sensitive to changes in geometry than the 24 degrees-of-freedom quadrilateral element formulated here.